Can human beings sense magnetic fields? *p. 1508*

Challenges of encoding morality into autonomous vehicles *pp. 1514 & 1573*

The true measures of carrier mobility *p. 1521*

Science

$15
24 JUNE 2016
sciencemag.org

AAAS



STAYING IN SHAPE

Disorder puts a damper on atoms spreading out *p. 1547*

Science
AAAS
1200 New York Avenue, NW, Washington, DC 20005
Bateman House, 82-88 Hills Road, Cambridge, UK CB2 1LQ

Editor-in-Chief Marcia McNutt
Executive Editor Monica M. Bradford **News Editor** Tim Appenzeller
Managing Editor, Research Journals Katrina L. Kelner
Deputy Editors Lisa D. Chong, Andrew M. Sugden(UK), Valda J. Vinson, Jake S. Yeston

Research and Insights

DEPUTY EDITOR, EMERITUS Barbara R. Jasny **SR. EDITORS** Caroline Ash(UK), Gilbert J. Chin, Julia Fahrenkamp-Uppenbrink(UK), Pamela J. Hines, Stella M. Hurtley(UK), Paula A. Kiberstis, Marc S. Lavine(Canada), Kristen L. Mueller, Ian S. Osborne(UK), Beverly A. Purnell, L. Bryan Ray, Guy Riddihough, H. Jesse Smith, Jelena Stajic, Peter Stern(UK), Phillip D. Szuromi, Sacha Vignieri, Brad Wible, Nicholas S. Wigginton, Laura M. Zahn **ASSOCIATE EDITORS** Brent Grocholski, Keith T. Smith **ASSOCIATE BOOK REVIEW EDITOR** Valerie B. Thompson **LETTERS EDITOR** Jennifer Sills **CHIEF CONTENT PRODUCTION EDITOR** Cara Tate **SR. CONTENT PRODUCTION EDITORS** Harry Jach, Lauren Kmec **CONTENT PRODUCTION EDITORS** Jeffrey E. Cook, Chris Filiatreau, Cynthia Howe, Barbara P. Ordway, Catherine Wolner **SR. EDITORIAL COORDINATORS** Carolyn Kyle, Beverly Shields **EDITORIAL COORDINATORS** Aneera Dobbins, Joi S. Granger, Lisa Johnson, Anita Wynn **PUBLICATIONS ASSISTANTS** Jeffrey Hearn, Dona Mathieu, Le-Toya Mayne Flood, Shannon McMahon, Scott Miller, Caitlyn Phillips, Jerry Richardson, Alice Whaley(UK), Brian White **EXECUTIVE ASSISTANT** Anna Bashkirova **ADMINISTRATIVE SUPPORT** Janet Clements(UK), Lizanne Newton(UK), Maryrose Madrid

News

NEWS MANAGING EDITOR John Travis **INTERNATIONAL EDITOR** Richard Stone **DEPUTY NEWS EDITORS** Robert Coontz, Elizabeth Culotta, David Grimm, David Malakoff, Leslie Roberts **CONTRIBUING EDITOR** Martin Enserink(Europe) **SR. CORRESPONDENTS** Daniel Clery(UK), Jeffrey Mervis, Elizabeth Pennisi **NEWS WRITERS** Adrian Cho, Jon Cohen, Jennifer Couzin-Frankel, Carolyn Gramling, Eric Hand, Jocelyn Kaiser, Catherine Matacic, Kelly Servick, Robert F. Service, Erik Stokstad(Cambridge, UK), Emily Underwood **INTERNS** Patrick Monahan **CONTRIBUTING CORRESPONDENTS** John Bohannon, Warren Cornwall, Ann Gibbons, Mara Hvistendahl, Sam Kean, Eli Kintisch, Kai Kupferschmidt(Berlin), Andrew Lawler, Christina Larson(Beijing), Mitch Leslie, Charles C. Mann, Eliot Marshall, Virginia Morell, Dennis Normile(Shanghai), Heather Pringle, Tania Rabesandratana(London), Gretchen Vogel(Berlin), Lizzie Wade(Mexico City) **CAREERS** Donisha Adams, Rachel Bernstein(Editor) **COPY EDITORS** Julia Cole, Dorie Chevlen, Jennifer Levin (Chief) **ADMINISTRATIVE SUPPORT** Jessica Adams

Executive Publisher Rush D. Holt
Publisher Bill Moran **Chief Digital Media Officer** Rob Covey

BUSINESS OPERATIONS AND PORTFOLIO MANAGEMENT DIRECTOR Sarah Whalen **PRODUCT DEVELOPMENT DIRECTOR** Will Schweitzer **PRODUCT DEVELOPMENT ASSOCIATE** Hannah Heckner **BUSINESS SYSTEMS AND FINANCIAL ANALYSIS DIRECTOR** Randy Yi **MANAGER OF FULFILLMENT SYSTEMS** Neal Hawkins **SYSTEMS ANALYST** Nicole Mehmedovich **DIRECTOR, BUSINESS OPERATIONS & ANALYSIS** Eric Knott **MANAGER, BUSINESS OPERATIONS** Jessica Tierney **SENIOR BUSINESS ANALYST** Cory Lipman **BUSINESS ANALYSTS** David Garrison, Meron Kebede, Sandy Kim **FINANCIAL ANALYST** Drew Sher **DIRECTOR, COPYRIGHTS LICENSING SPECIAL PROJECTS** Emilie David **PERMISSIONS ASSOCIATE** Elizabeth Sandler **RIGHTS, CONTRACTS, AND LICENSING ASSOCIATE** Lili Kiser **RIGHTS & PERMISSIONS ASSISTANT** Alexander Lee

MARKETING DIRECTOR Elise Swinehart **ASSOCIATE MARKETING DIRECTOR** Stacey Burke Bowers **MARKETING ASSOCIATE** Steven Goodman **CREATIVE DIRECTOR** Scott Rodgerson **SENIOR ART ASSOCIATES** Paula Fry **ART ASSOCIATE** Kim Huynh

PROGRAM DIRECTOR, AAAS MEMBER CENTRAL Peggy Mihelich **FULFILLMENT SYSTEMS AND OPERATIONS** membership@aaas.org **MANAGER, MEMBER SERVICES** Pat Butler **SPECIALISTS** Terrance Morrison, Latasha Russell **MANAGER, DATA ENTRY** Mickie Napoleoni **DATA ENTRY SPECIALISTS** Brenden Aquilino, Fiona Giblin **MARKETING ASSOCIATE** Isa Sesay-Bah

PUBLISHER RELATIONS, EASTERN REGION Keith Layson **PUBLISHER RELATIONS, WESTERN REGION** Ryan Rexroth **SALES RESEARCH COORDINATOR** Aiesha Marshall **MANAGER, SITE LICENSE OPERATIONS** Iquo Edim **SENIOR OPERATIONS ANALYST** Lana Guz **FULFILLMENT ANALYST** Judy Lillibridge

WEB TECHNOLOGIES PORTFOLIO MANAGER Trista Smith **TECHNICAL MANAGER** Chris Coleman **PROJECT MANAGER** Nick Fletcher **DEVELOPERS** Ryan Jensen, Jimmy Marks, Brandon Morrison

DIGITAL MEDIA DIRECTOR OF ANALYTICS Enrique Gonzales **DIGITAL REPORTING ANALYST** Eric Hossinger **SR. WEB PRODUCER** Sarah Crespi **WEB PRODUCER** Alison Crawford **VIDEO PRODUCER** Nguyen Nguyen **SOCIAL MEDIA PRODUCER** Brice Russ

DIRECTOR OF OPERATIONS PRINT AND ONLINE Lizabeth Harman **DIGITAL/PRINT STRATEGY MANAGER** Jason Hillman **QUALITY TECHNICAL MANAGER** Marcus Spiegler **PROJECT ACCOUNT MANAGER** Tara Kelly **DIGITAL PRODUCTION MANAGER** Lisa Stanford **ASSISTANT MANAGER DIGITAL/PRINT** Rebecca Doshi **SENIOR CONTENT SPECIALISTS** Steve Forrester, Antoinette Hodal, Lori Murphy, Anthony Rosen **CONTENT SPECIALISTS** Jacob Hedrick, Kimberley Oster

DESIGN DIRECTOR Beth Rakouskas **DESIGN EDITOR** Marcy Atarod **SENIOR DESIGNERS** Garvin Grullón, Chrystal Smith **GRAPHICS MANAGING EDITOR** Alberto Cuadra **SENIOR SCIENTIFIC ILLUSTRATORS** Chris Bickel, Katharine Sutliff **SCIENTIFIC ILLUSTRATOR** Valerie Altounian **INTERACTIVE GRAPHICS EDITOR** Jia You **SENIOR ART ASSOCIATES** Holly Bishop, Nathalie Cary **PHOTOGRAPHY MANAGING EDITOR** William Douthitt **SENIOR PHOTO EDITOR** Christy Steele

DIRECTOR, GLOBAL COLLABORATION, CUSTOM PUBLICATIONS, ADVERTISING Bill Moran **EDITOR, CUSTOM PUBLISHING** Sean Sanders: 202-326-6430 **ADVERTISING MARKETING MANAGER** Justin Sawyers: 202-326-7061 science_advertising@aaas.org **ADVERTISING SUPPORT MANAGER** Karen Foote: 202-326-6740 **ADVERTISING PRODUCTION OPERATIONS MANAGER** Deborah Tompkins **SR. PRODUCTION SPECIALIST/GRAPHIC DESIGNER** Amy Hardcastle **SR. TRAFFIC ASSOCIATE** Christine Hall **SALES COORDINATOR** Shirley Young **ASSOCIATE DIRECTOR, COLLABORATION, CUSTOM PUBLICATIONS/CHINA/TAIWAN/KOREA/SINGAPORE** Ruolei Wu: +86-186 0082 9345, rwu@aaas.org **COLLABORATION/CUSTOM PUBLICATIONS/JAPAN** Adarsh Sandhu + 81532-81-5142 asandhu@aaas.org **EAST COAST/E. CANADA** Laurie Faraday: 508-747-9395, FAX 617-507-8189 **WEST COAST/W. CANADA** Lynne Stickrod: 415-931-9782, FAX 415-520-6940 **MIDWEST** Jeffrey Dembksi: 847-498-4520 x3005, Steven Loerch: 847-498-4520 x3006 **UK EUROPE/ASIA** Roger Goncalves: TEL/FAX +41 43 243 1358 **JAPAN** Katsuyoshi Fukamizu(Tokyo): +81-3-3219-5777 kfukamizu@aaas.org **CHINA/TAIWAN** Ruolei Wu: +86-186 0082 9345, rwu@aaas.org

WORLDWIDE ASSOCIATE DIRECTOR OF SCIENCE CAREERS Tracy Holmes: +44 (0) 1223 326525, FAX +44 (0) 1223 326532 tholmes@science-int. co.uk **CLASSIFIED** advertise@sciencecareers.org **U.S. SALES** Tina Burks: 202-326-6577, Nancy Toema: 202-326-6578 **EUROPE/ROW SALES** Sarah Lelarge **SALES ASSISTANT** Kelly Grace **JAPAN** Hiroyuki Mashiki(Kyoto): +81-75-823-1109 hmashiki@aaas.org **CHINA/TAIWAN** Ruolei Wu: +86-186 0082 9345 rwu@aaas.org **MARKETING MANAGER** Allison Pritchard **MARKETING ASSOCIATE** Aimee Aponte

AAAS BOARD OF DIRECTORS, CHAIR Geraldine L. Richmond **PRESIDENT** Barbara A. Schaal **PRESIDENT-ELECT** Susan Hockfield **TREASURER** David Evans Shaw **CHIEF EXECUTIVE OFFICER** Rush D. Holt **BOARD** Cynthia M. Beall, May R. Berenbaum, Carlos J. Bustamante, Stephen P.A. Fodor, Claire M. Fraser, Michael S. Gazzaniga, Laura H. Greene, Elizabeth Loftus, Mercedes Pascual

SUBSCRIPTION SERVICES For change of address, missing issues, new orders and renewals, and payment questions: 866-434-AAAS (2227) or 202-326-6417, FAX 202-842-1065. Mailing addresses: AAAS, P.O. Box 96178, Washington, DC 20090-6178 or AAAS Member Services, 1200 New York Avenue, NW, Washington, DC 20005

INSTITUTIONAL SITE LICENSES 202-326-6730 **REPRINTS:** Author Inquiries 800-635-7181 **COMMERCIAL INQUIRIES** 803-359-4578 **PERMISSIONS** 202-326-6765, permissions@aaas.org **AAAS Member Services** 202-326-6417 or http://membercentral.aaas.org/discounts

Science serves as a forum for discussion of important issues related to the advancement of science by publishing material on which a consensus has been reached as well as including the presentation of minority of conflicting points of view. Accordingly, all articles published in *Science*—including editorials, news and comment, and book reviews—are signed and reflect the individual views of the authors and not official points of view adopted by AAAS or the institutions with which the authors are affiliated.

INFORMATION FOR AUTHORS See pages 624 and 625 of the 5 February 2016 issue or access www.sciencemag.org/authors/science-information-authors

SENIOR EDITORIAL BOARD
Gary King, *Harvard University,* **Susan M. Rosenberg,** *Baylor College of Medicine,*
Ali Shilatifard, *Northwestern University Feinberg School of Medicine*

BOARD OF REVIEWING EDITORS (Statistics board members indicated with **(S)**

Adriano Aguzzi, *U. Hospital Zürich*
Takuzo Aida, *U. of Tokyo*
Leslie Aiello, *Wenner-Gren Foundation*
Judith Allen, *U. of Edinburgh*
Sonia Altizer, *U. of Georgia*
Sebastian Amigorena, *Institut Curie*
Kathryn Anderson, *Memorial Sloan-Kettering Cancer Center*
Meinrat O. Andreae, *Max-Planck Inst. Mainz*
Paola Arlotta, *Harvard U.*
Johan Auwerx, *EPFL*
David Awschalom, *U. of Chicago*
Clare Baker, *University of Cambridge*
Nenad Ban, *ETH Zurich*
Jordi Bascompte, *University of Zurich*
Franz Bauer, *Instituto de Astrofisica*
Ray H. Baughman, *U. of Texas, Dallas*
David Baum, *U. of Wisconsin*
Carlo Beenakker, *Leiden U.*
Kamran Behnia, *ESPCI-ParisTech*
Yasmine Belkaid, *NIAID, NIH*
Philip Benfey, *Duke U.*
May Berenbaum, *U. of Illinois*
Gabriele Bergers, *U. of California, San Francisco*
Bradley Bernstein, *Massachusettes General Hospital*
Peer Bork, *EMBL*
Bernard Bourdon, *Ecole Normale Supérieure de Lyon*
Chris Bowler, *École Normale Supérieure*
Ian Boyd, *U. of St. Andrews*
Emily Brodsky, *U. of California, Santa Cruz*
Ron Brookmeyer, *U. of California Los Angeles* **(S)**
Christian Büchel, *U. Hamburg-Eppendorf*
Joseph A. Burns, *Cornell U.*
Carter Tribley Butts, *U. of California, Irvine*
Gyorgy Buzsaki, *New York U. School of Medicine*
Blanche Capel, *Duke U.*
Mats Carlsson, *U. of Oslo*
Ib Chorkendorff, *U. of Denmark*
David Clapham, *Children's Hospital Boston*
Joel Cohen, *Rockefeller U., Columbia U.*
James J. Collins, *MIT*
Robert Cook-Deegan, *Duke U.*
Lisa Coussens, *Oregon Health & Science U.*
Alan Cowman, *Walter & Eliza Hall Inst.*
Robert H. Crabtree, *Yale U.*
Roberta Croce, *Vrije Universiteit*
Janet Currie, *Princeton U.*
Jeff L. Dangl, *U. of North Carolina*
Tom Daniel, *U. of Washington*
Frans de Waal, *Emory U.*
Stanislas Dehaene, *Collège de France*
Robert Desimone, *MIT*
Claude Desplan, *New York U.*
Dennis Discher, *U. of Pennsylvania*
Gerald W. Dorn II, *Washington U. School of Medicine*
Jennifer A. Doudna, *U. of California, Berkeley*
Bruce Dunn, *U. of California, Los Angeles*
William Dunphy, *Caltech*
Christopher Dye, *WHO*
Todd Ehlers, *U. of Tuebingen*
David Ehrhardt, *Carnegie Inst. of Washington*
Tim Elston, *U. of North Carolina at Chapel Hill*
Gerhard Ertl, *Fritz-Haber-Institut, Berlin*
Barry Everitt, *U. of Cambridge*
Ernst Fehr, *U. of Zurich*
Anne C. Ferguson-Smith, *U. of Cambridge*
Michael Feuer, *The George Washington U.*
Toren Finkel, *NHLBI, NIH*
Kate Fitzgerald, *U. of Massachusetts*
Peter Fratzl, *Max-Planck Inst.*
Elaine Fuchs, *Rockefeller U.*
Daniel Geschwind, *UCLA*
Karl-Heinz Glassmeier, *TU Braunschweig*
Ramon Gonzalez, *Rice U.*
Julia R. Greer, *Caltech*
Elizabeth Grove, *U. of Chicago*
Nicolas Gruber, *ETH Zurich*
Kip Guy, *St. Jude's Children's Research Hospital*
Taekjip Ha, *U. of Illinois at Urbana-Champaign*
Wolf-Dietrich Hardt, *ETH Zurich*
Christian Haass, *Ludwig Maximilians U.*
Sharon Hammes-Schiffer, *U. of Illinois at Urbana–Champaign*
Michael Hasselmo, *Boston U.*
Martin Heimann, *Max-Planck Inst. Jena*
Yka Helariutta, *U. of Cambridge*
James A. Hendler, *Rensselaer Polytechnic Inst.*
Janet G. Hering, *Swiss Fed. Inst. of Aquatic Science & Technology*
Kai-Uwe Hinrichs, *U. of Bremen*
David Hodell, *U. of Cambridge*
Lora Hooper, *UT Southwestern Medical Ctr. at Dallas*
Tamas Horvath, *Yale University*
Raymond Huey, *U. of Washington*
Fred Hughson, *Princeton U.*
Auke Ijspeert, *EPFL Lausanne*
Stephen Jackson, *USGS and U. of Arizona*
Steven Jacobsen, *U. of California, Los Angeles*
Kai Johnsson, *EPFL Lausanne*
Peter Jonas, *Inst. of Science & Technology (IST) Austria*
Matt Kaeberlein, *U. of Washington*
William Kaelin Jr., *Dana-Farber Cancer Inst.*
Daniel Kahne, *Harvard U.*
Daniel Kammen, *U. of California, Berkeley*
Abby Kavner, *U. of California, Los Angeles*
Masashi Kawasaki, *U. of Tokyo*
V. Narry Kim, *Seoul National U.*
Joel Kingsolver, *U. of North Carolina at Chapel Hill*
Robert Kingston, *Harvard Medical School*
Etienne Koechlin, *Ecole Normale Suprieure*
Alexander Kolodkin, *Johns Hopkins U.*
Thomas Langer, *U. of Cologne*
Mitchell A. Lazar, *U. of Pennsylvania*
David Lazer, *Harvard U.*
Thomas Lecuit, *IBDM*
Virginia Lee, *U. of Pennsylvania*
Stanley Lemon, *U. of North Carolina at Chapel Hill*
Ottoline Leyser, *Cambridge U.*
Wendell Lim, *U.C. San Francisco*
Marcia C. Linn, *U. of California, Berkeley*
Jianguo Liu, *Michigan State U.*
Luis Liz-Marzan, *CIC biomaGUNE*
Jonathan Losos, *Harvard U.*
Ke Lu, *Chinese Acad. of Sciences*
Christian Lüscher, *U. of Geneva*
Laura Machesky, *CRUK Beatson Inst. for Cancer Research*
Anne Magurran, *U. of St. Andrews*
Oscar Marin, *CSIC & U. Miguel Hernández*
Charles Marshall, *U. of California, Berkeley*
C. Robertson McClung, *Dartmouth College*
Graham Medley, *U. of Warwick*
Tom Misteli, *NCI*
Yasushi Miyashita, *U. of Tokyo*
Mary Ann Moran, *U. of Georgia*
Richard Morris, *U. of Edinburgh*
Alison Motsinger-Reif, *NC State U.* **(S)**
Thomas Murray, *The Hastings Center*
Daniel Neumark, *U. of California, Berkeley*
Kitty Nijmeijer, *U. of Twente*
Helga Nowotny, *European Research Advisory Board*
Ben Olken, *MIT*
Joe Orenstein, *U. of California Berkeley & Lawrence Berkeley National Lab*
Harry Orr, *U. of Minnesota*
Pilar Ossorio, *U. of Wisconsin*
Andrew Oswald, *U. of Warwick*
Margaret Palmer, *U. of Maryland*
Steve Palumbi, *Stanford U.*
Jane Parker, *Max-Planck Inst. of Plant Breeding Research*
Giovanni Parmigiani, *Dana-Farber Cancer Inst.* **(S)**
John H. J. Petrini, *Memorial Sloan-Kettering Cancer Center*
Samuel Pfaff, *Salk Institute for Biological Studies*
Joshua Plotkin, *U. of Pennsylvania*
Albert Polman, *FOM Institute AMOLF*
Philippe Poulin, *CNRS*
Jonathan Pritchard, *Stanford U.*
David Randall, *Colorado State U.*
Felix Rey, *Institut Pasteur*
Trevor Robbins, *U. of Cambridge*
Jim Roberts, *Fred Hutchinson Cancer Research Ctr.*
Barbara A. Romanowicz, *U. of California,Berkeley*
Amy Rosenzweig, *Northwestern University*
Mike Ryan, *U. of Texas, Austin*
Mitinori Saitou, *Kyoto U.*
Shimon Sakaguchi, *Kyoto U.*
Miquel Salmeron, *Lawrence Berkeley National Lab*
Jürgen Sandkühler, *Medical U. of Vienna*
Alexander Schier, *Harvard U.*
Vladimir Shalaev, *Purdue U.*
Robert Siliciano, *Johns Hopkins School of Medicine*
Denis Simon, *Arizona State U.*
Uri Simonsohn, *U. of Pennsylvania*
Alison Smith, *John Innes Centre*
Richard Smith, *U. of North Carolina* **(S)**
John Speakman, *U. of Aberdeen*
Allan C. Spradling, *Carnegie Institution of Washington*
Jonathan Sprent, *Garvan Inst. of Medical Research*
Eric Steig, *U. of Washington*
Paula Stephan, *Georgia State U. and National Bureau of Economic Research*
Molly Stevens, *Imperial College London*
V. S. Subrahmanian, *U. of Maryland*
Ira Tabas, *Columbia U.*
Sarah Teichmann, *Cambridge U.*
John Thomas, *North Carolina State U.*
Shubha Tole, *Tata Institute of Fundamental Research*
Christopher Tyler-Smith, *The Wellcome Trust Sanger Inst.*
Herbert Virgin, *Washington U.*
Bert Vogelstein, *Johns Hopkins U.*
Cynthia Volkert, *U. of Göttingen*
David Wallach, *Weizmann Inst. of Science*
Ian Walmsley, *U. of Oxford*
Jane-Ling Wang, *U. of California, Davis* **(S)**
David A. Wardle, *Swedish U. of Agric. Sciences*
David Waxman, *Fudan U.*
Jonathan Weissman, *U. of California, San Francisco*
Chris Wikle, *U. of Missouri* **(S)**
Ian A. Wilson, *The Scripps Res. Inst.* **(S)**
Timothy D. Wilson, *U. of Virginia*
Rosemary Wyse, *Johns Hopkins U.*
Jan Zaanen, *Leiden U.*
Kenneth Zaret, *U. of Pennsylvania School of Medicine*
Jonathan Zehr, *U. of California, Santa Cruz*
Len Zon, *Children's Hospital Boston*
Maria Zuber, *MIT*

BOOK REVIEW BOARD
David Bloom, *Harvard U.,* **Samuel Bowring,** *MIT,* **Angela Creager,** *Princeton U.,*
Richard Shweder, *U. of Chicago,* **Ed Wasserman,** *DuPont*

Published by AAAS

EDITORIAL

Fast horses



Marcia McNutt
Editor-in-Chief
Science *Journals*

Those who know me well appreciate my passion for fast horses—those with spirit and stamina, as well as speed. And thus I devote my final words as editor-in-chief of the *Science* journals to the incredible team of thoroughbreds who accomplished more in a short time than I ever thought was possible. The changes that have come to the publishing enterprise at the American Association for the Advancement of Science (AAAS, the publisher of *Science* journals) have touched all facets of what we do and how we deliver it to our readers.

In the past 3 years, *Science* has doubled the size of its portfolio from three to six journals. *Science Advances*, our first foray into open-access publishing, is already into its second year and reaching a broad audience with premier content. *Science Immunology* will publish its first issue next month, and *Science Robotics* is open for submissions. I am grateful to two Chief Executive Officers (Alan Leshner and now Rush Holt), two past Publishers and one current one (Beth Rosner, Kent Anderson, and now Bill Moran), and the AAAS Board of Directors for supporting these new projects. The success of these ventures would not have been possible, however, without the dedication of the *Science* editors, who worked overtime to set up the processes and procedures for the new journals, helped select the new staff, and recruited quality content for these publications.

Next, kudos to Rob Covey, Chief Digital Media Officer, and the digital media team for the redesign of the print journal (a blazing sprint!) and launching a more responsive web version of *Science* journals (more an endurance trial than a derby). Rob's team populated the new design with beautiful covers, photos, and videos. They have demonstrated that multimedia can drive traffic to articles and communicate the research story in new, compelling ways.

Finally, all of us at *Science* have been on a crusade for the past 3 years to raise the standards for transparency and reproducibility in research, publishing a series of editorials, policy pieces, and research articles on this topic. Our special partners have been the Laura and John Arnold Foundation, the Center for Open Science, and many top publishers and funding agencies. The American Statistical Association helped us create a special Statistical Board of Reviewing Editors (S-BoRE) that is now being expanded to serve all *Science* journals. We recently announced our implementation of the Transparency and Openness Promotion (TOP) guidelines, effective 1 January 2017. Our terrific News team at *Science*, led by Tim Appenzeller, has worked to ferret out and bring to light questionable practices in scientific publishing, such as paper brokers selling authorships, institutions offering bounties for publishing in high-impact journals, and publishers forgoing promised peer-review services. Our new product, PRE (Peer Review Evaluation), gives readers greater insight into the peer-review process for each article published.



"...be sure to let those fast horses run."

After such a wild ride, it was with some trepidation that I awaited the outcome of the search for my successor as editor-in-chief of the *Science* journals. The new journals still need a champion. The quest to improve the transparency and reproducibility of research and to remove any bias in access to scientific resources continues. Would the new editor care about these matters as much as I have?

I am most pleased to say that the search committee, led by former AAAS Board chair Gerry Fink, has chosen very wisely. Professor Jeremy Berg is a superb pick to take the reins of the *Science* journals. He is highly respected and thoughtful, cares about what is important, commands an exceptionally broad view of science, and is a very quick study.

So hold on and enjoy the ride, Jeremy. And be sure to let those fast horses run.

– Marcia McNutt

PODCAST

Hear the interview with Marcia at http://bit.ly/6293_pod

10.1126/science.aag3351

PHOTOS: (INSET) © INGA SPENCE/ALAMY STOCK PHOTO; (TOP RIGHT) STACEY PENTLAND PHOTOGRAPHY

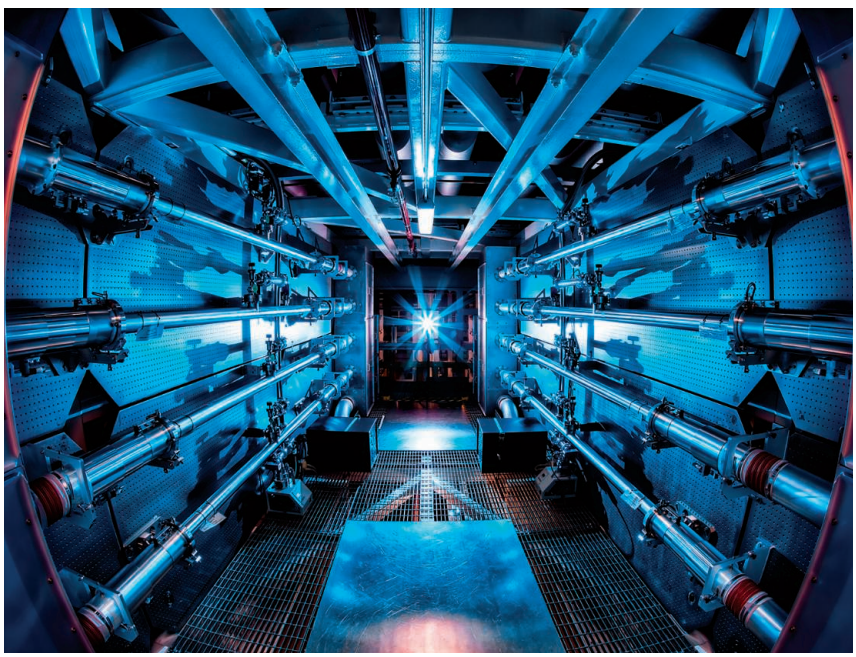
Downloaded from http://science.sciencemag.org/ on June 28, 2016

Published by AAAS

> “We could map the entire deep oceans for $3 billion—no more than a single Mars mission.”
>
> **Oceanographer Larry Mayer** of the University of New Hampshire, Durham, to BBC News about calls from a group called General Bathymetric Chart of the Oceans for a “NASA-style” effort to map the entire sea floor; only 5% has been mapped to date.

IN BRIEF

Fusion laser may never ignite



NIF’s preamplifiers increase the energy of laser beams aimed at the target chamber.

An independent report on the progress of fusion research at the $3.5 billion National Ignition Facility (NIF) at Lawrence Livermore National Laboratory in California suggests that the titular goal—attaining ignition, a self-sustaining fusion burn that produces excess energy—may not be achievable. NIF, which uses lasers to heat and compress capsules of hydrogen isotopes until they fuse and release energy, has struggled to live up to its name since its opening in 2009. After a concerted effort to reach the goal between 2010 and 2012 failed to deliver, researchers turned to understanding the physics of the compressed fusion fuel, as well as to studying the physics of nuclear weapons as part of the Stockpile Stewardship Program. The May report, which was sponsored by the Department of Energy and first described in *Physics Today*, marks the end of that 3-year campaign. It suggests research should now shift from identifying the obstacles in the path to ignition to investigating whether ignition is even possible. “The question is *if* the NIF will be able to reach ignition in its current configuration and not *when* it will occur,” the report says. http://scim.ag/NIFignite

AROUND THE WORLD

Climate change claims mammal

QUEENSLAND STATE, IN AUSTRALIA | A tiny rodent known as the Bramble Cay melomys (*Melomys rubicola*) has the dubious distinction of being the first mammal to go extinct because of human-caused climate change, Australian scientists say. The melomys’s entire habitat was a 4-hectare spit of land in east Torres Strait in Queensland, near the northern end of the Great Barrier Reef, which has been subject to encroaching sea level. The last reported sighting of the animal was in 2009; an “exhaustive” survey effort in 2014 failed to discover a single one, “confirming that the only known population of this rodent is now extinct,” the researchers stated in their report last week to the Queensland Department of Environment and Heritage Protection. However, they noted, there is a chance that a previously unknown population of the species, or a close relative, persists in the largely unsurveyed Fly River delta of Papua New Guinea.

Human CRISPR trial proposed

BETHESDA, MARYLAND | Researchers have for the first time asked to use the gene-editing tool CRISPR to modify genes in people. A University of Pennsylvania team this week discussed their proposal to use CRISPR to engineer immune cells to fight cancer before the U.S. Recombinant DNA Advisory Committee (RAC) at the National Institutes of Health, which reviews the safety of gene therapy research. Gene editing has already been used to modify the same type of immune cells, called T cells, in patients with HIV and leukemia. But the trial could be the first clinical application of CRISPR, the easiest gene-editing method to date. The study would be funded by the $250 million Parker Institute for Cancer Immunotherapy, launched in April by tech entrepreneur Sean Parker. RAC approved the study, which must now undergo formal regulatory review. http://scim.ag/CRISPRtrial

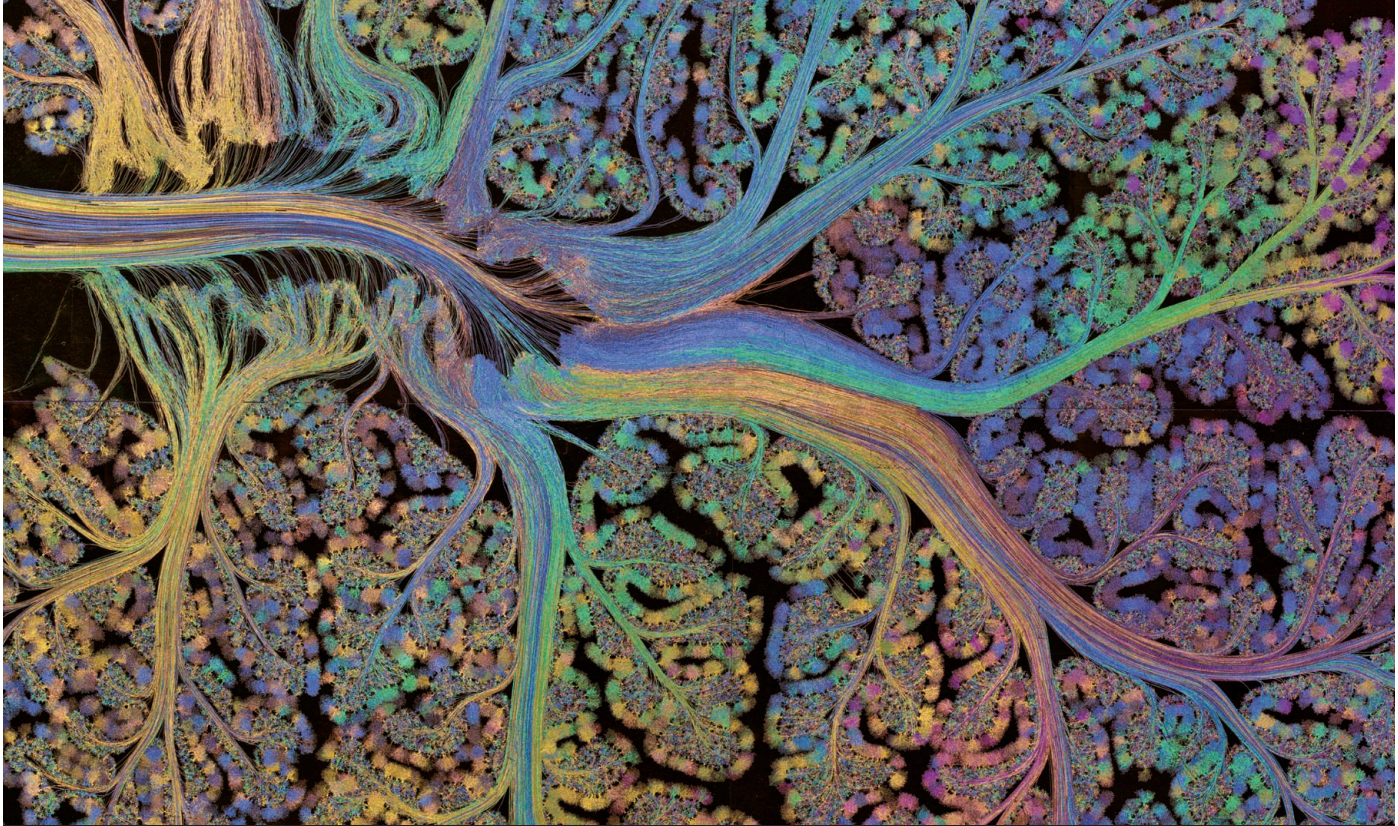
Stretching yellow fever vaccine

GENEVA, SWITZERLAND | An expert panel at the World Health Organization (WHO) says lower doses of yellow fever vaccine

Downloaded from http://science.sciencemag.org/ on June 28, 2016

PHOTO: DAMIEN JEMISON/NIF

Published by AAAS



A new art installation shows the human brain in intricate detail, including this closeup of the cerebellum.

'A brief moment of wonder'

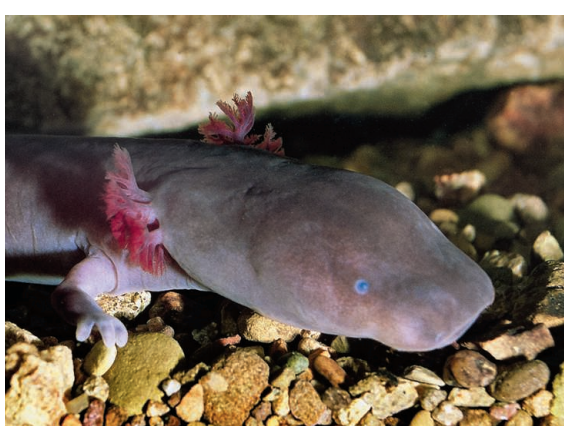
The Franklin Institute in Philadelphia, Pennsylvania, is now home to what may be the most detailed piece of brain art ever made. The image, a 2.4-by-3.7-meter illustration of a slice through the human brain, shows more than 500,000 individual neurons. Its appearance changes as visitors walk around the installation because microscopic waves etched into the polymer surface, which was then coated with gold leaf, only reflect light from certain angles. An LED light source will illuminate different parts of the image at different times to mimic the flow of electrical activity through the brain. The permanent installation, which opens 25 June, is the result of a 2-year collaboration between Greg Dunn, a local neuroscientist-turned-artist, and Brian Edwards, an applied physicist at the University of Pennsylvania. The work, funded by a $261,000 grant from the National Science Foundation, is grounded in science, Dunn says. "But what it's really about is giving people a brief moment of wonder."

can be used in an emergency. The Strategic Advisory Group of Experts on Immunization found sufficient evidence that a dose of 0.1 milliliters (ml) instead of the usual 0.5 ml would still protect people from the disease for at least 12 months. Massive vaccination campaigns targeting millions of people depleted global stocks earlier this year, although the stock has since been replenished (*Science*, 27 May, p. 1036). However, "WHO and partners are seriously considering the use of this dose-sparing strategy" because the continuing transmission of the mosquito-borne virus in Angola and in the Democratic Republic of the Congo, as well as the risk of spread to other countries, could quickly outpace the world's ability to produce the vaccine, says Jon Abramson, chair of the expert group. The lower dose is not being recommended for routine vaccination because it is not clear whether it will confer lifelong immunity.

Tracking the Slovenian dragon

FAYETTEVILLE, ARKANSAS | The blind cave salamander *Proteus anguinus* lives in underground aquifers in Slovenia, surfacing only when floodwaters sweep it from its lair. At 30 centimeters long, it is the world's largest cave animal—but it's rarely seen. Now, molecular biologists have a new way to track this elusive "dragon": a probe that detects the animal's DNA in springs. In a forensic technique borrowed from law enforcement, the probe sorts through "environmental DNA" from skin cells, hair, or other cells released into the environment—to monitor animals that live where humans can't go. By providing information on how big or widespread the salamander populations are, the probe, described last week at the 2016 International Conference on Subterranean Biology here, opens up new possibilities for protecting the salamander. Early data are also providing tantalizing evidence that a rare black subspecies of the typically white creature might actually be a separate species.

http://scim.ag/dragonDNA



Scientists use environmental DNA to map this salamander's lairs.

PHOTOS: (TOP TO BOTTOM) GREG DUNN; GREGOR ALJANCIC/TULAR CAVE LABORATORY

Downloaded from http://science.sciencemag.org/ on June 28, 2016

Published by AAAS



HIGH-PERFORMANCE COMPUTING

China overtakes U.S. supercomputing lead

A new machine propels China to first place in combined supercomputing power

By **Robert F. Service**

China has claimed two computing crowns. A new supercomputer at China's National Supercomputing Center in Wuxi in Jiangsu province has snagged the top spot on the latest TOP500 list of supercomputers, which was unveiled earlier this week at the 2016 International Supercomputing Conference in Frankfurt, Germany. The new machine, known as the Sunway TaihuLight, has a peak performance of 93 petaflop per second (Pflop/s), or 93 quadrillion calculations per second. That's nearly three times the performance of its closest competitor, Tianhe-2, another Chinese supercomputer, and nearly 2 million times faster than a standard laptop. More important, for the first time China has overtaken the United States as the country with the largest installed supercomputing capacity.

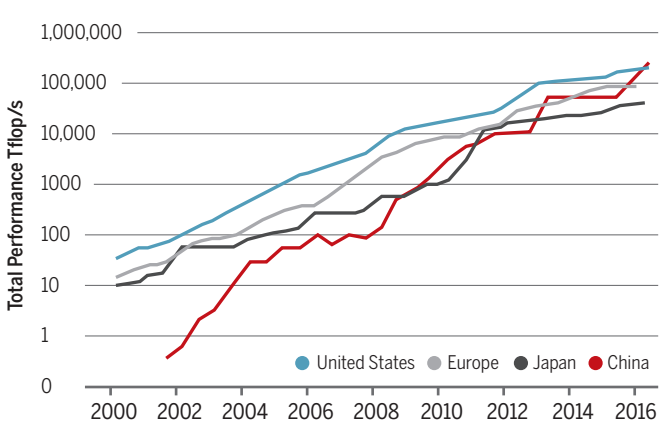
"We're seeing an inflection point," says Horst Simon, a supercomputing expert and deputy director of the Lawrence Berkeley National Laboratory in Berkeley, California. Simon and a few other supercomputer experts update the TOP500 list twice a year to track trends in their field. Countries other than the United States have previously claimed the top spot for an individual machine's performance, but this is the first time another country has eclipsed the United States in total supercomputing power. "We've seen this trend building for the last few years," says Wu Feng, a supercomputing expert at the Virginia Polytechnic Institute and State University in Blacksburg. "It shows that China is committed to a sustained investment in high-performance computing."

According to the TOP500 list, China now has 167 of the world's top 500 supercomputers, with a total capacity of 211 Pflop/s. The United States has 165 of the top machines, with a cumulative capacity of 173 Pflop/s. That's a reversal of the rankings 15 years ago, when the United States had more than half of the world's top 500 supercomputers, Simon says. Europe's share, meanwhile, has dropped to 105 systems with a combined capacity of 115 Pflop/s. China's supercomputing crown could pay off not just for research and engineering, but for commerce: Chinese companies already have a 34% market share in the global market for supercomputers, a percentage that is growing fast. And Haohuan Fu, a supercomputer expert at Tsinghua University in Beijing, says the Chinese government is making a concerted effort to support supercomputing to propel advances in everything from life sciences research to manufacturing design for its companies.

According to Jack Dongarra, a supercomputing expert at the University of Tennessee, Knoxville, who keeps close tabs on international trends, China is expected to add another machine comparable to the

Steep climb

China has rocketed from having no supercomputers in the year 2000 to leading the world in supercomputing power, a position it says it plans to maintain.



CREDITS: (PHOTO) JACK DONGARRA; (CHART) TOP500 LIST

Downloaded from http://science.sciencemag.org/ on June 28, 2016

Published by AAAS

China's new Sunway TaihuLight supercomputer is the country's first to use only Chinese-built processors instead of U.S. technology.

Sunway supercomputer either late this year or early in 2017. The United States, meanwhile, isn't expected to have one in the 100 Pflop/s range until the end of 2017. The most powerful U.S. machine, ranked third overall, is Titan, a 17.59-Pflop/s supercomputer at the U.S. Department of Energy's (DOE's) Oak Ridge National Laboratory in Tennessee.

China is now looking to extend its lead. Chinese officials announced recently that they expect to produce their first machine capable of running at 1000 Pflop/s, or 1 exaflop/s, in 2020. Such exascale machines should dramatically speed up a host of scientific and industrial computing tasks, such as modeling climate change and the activity of the human brain, searching for new high-performance materials, and designing energy-efficient car engines. DOE, which heads U.S. supercomputing efforts, has said it doesn't expect to build its first exascale supercomputer until 2023 at the earliest, a target that has already slipped several years.

The Sunway machine marks a noteworthy step toward those goals, Dongarra says. The new supercomputer is powered by more than 10.6 million processor chips, which were designed and built in China, and consumes 15.4 megawatts (MW) of power. That means the Sunway machine carries out 6 billion calculations per watt, making it the third most efficient supercomputer ever designed. "That's quite remarkable," Simon says. "Usually the top systems are not at the top in efficiency."

Even so, simply scaling up the current Sunway system to exascale is impractical, as the resulting machine would require on the order of 150 MW, enough to power thousands of homes. It's more likely, Simon says, that achieving the computational efficiency needed to get to exascale will require technologies still under development, such as low-power 3D memory chips and links between processors that pass data as light instead of electrons.

An exascale machine could have payoffs beyond high-end computing. Although the worldwide market for supercomputers themselves is modest—far smaller than sales of conventional consumer electronics—Simon and others note that supercomputing technology often trickles down to consumer markets. So if China's researchers are the first to come up with the technology breakthroughs needed to reach exascale, the feat could supercharge their consumer electronics industry and spell danger for other electronics giants around the globe. ■

PHOTO: KRISTYNA WENTZ-GRAFF/*THE OREGONIAN* VIA AP

CLIMATE

How a 'Godzilla' El Niño shook up weather forecasts

Departing climate event left fires, drought, and questions

By **Eli Kintisch**

From cyclones and coral bleaching in the tropical Pacific to drought in Peru and South Africa, the El Niño that ended this month drove record-setting weather extremes across the planet. What some forecasters called the "Godzilla" El Niño mostly conformed to regional forecasts, based on past events. But some key aspects of the 14-month climate disruption flouted predictions, especially along the U.S. West Coast, where parched Southern California—usually a beneficiary of El Niños—remained largely dry while storms battered the Pacific Northwest.

That's spurring introspection among atmospheric scientists—and a flurry of manuscripts as the community tries to improve forecasts for the next time El Niño rears its head. "Every El Niño is different, and we're hoping we can learn from this one to improve our models," says Jon Gottschalck, a forecaster with the National Oceanic and Atmospheric Administration (NOAA) in College Park, Maryland.

Heat sloshing from the western tropical Pacific to the chillier eastern side, off South America, is El Niño's main driver. This time, temperatures in the central tropical Pacific rose as much as 3°C above average, putting this event among the three strongest El Niños ever. That heat made some impacts, like widespread coral bleaching in the central Pacific, depressingly easy to forecast. Oceanographer Kim Cobb of the Georgia Institute of Technology in Atlanta says that the devastation to the reef off the island nation of Kiribati, for example, "was beyond my worst fears."

High Pacific temperatures also were key to an Indian government forecast of a "deficient" monsoon last summer. During El Niños, atmospheric convection over the Western Pacific often weakens, robbing the monsoon of its energy. For scientists under intense pressure not to scare the public, that forecast "took a lot of courage and conviction," says Rupa Kumar Kolli, a meteorologist at the World Meteorological Organization in Geneva, Switzerland. It was correct: Last summer drought and wildfires spread across India, Southeast Asia, and Indonesia.

But on the U.S. West Coast, other factors intervened to stymie forecasters. There, models had suggested that this event would play out like previous large El Niños. As abnormal heat drives convection and rainfall in the eastern Pacific, the jet stream usually pushes that moisture toward southern California. There, it fuels storms that quench the state's perennial thirst, while the northern West



El Niño veered off script in the Pacific Northwest, dumping heavy rain on Portland, Oregon, in December 2015.

Downloaded from http://science.sciencemag.org/ on June 28, 2016

Published by AAAS

Coast grows drier. Last fall, using models trained with that historical tendency, NOAA forecasters put the chance of increased winter precipitation over southern California at 60%. Instead the region experienced a fourth straight year of dry conditions.

In the Pacific Northwest, meanwhile, the El Niño started as expected last summer and fall, with heat that brought drought to farmers and ranchers. But then it confounded meteorologists, contributing to heavy winter precipitation that delivered both misery, like flooding and snow-clogged roads, and joy. "All this moisture has been kind of a happy surprise," acknowledged Washington state climatologist Nick Bond at the time. "Certainly our snowpack is in good shape." Heavy rains in northern California also refilled reservoirs that send water south, bringing some relief to the southern part of the state.

Why did the El Niño dump precipitation so far from its usual target? Daniel Swain, a climate scientist at Stanford University in Palo Alto, California, points to the Pacific subtropics north of the equator. At least partly because of global warming, waters there were "drastically, drastically" warmer than during past whopper El Niños in 1982 and 1997. The jet stream's position is determined by north-south temperature differences, his thinking goes, so as the ocean warming extended northward, the jet settled into a more northerly track. That could have driven storms far north of their usual El Niño position.

Another unusual aspect of Godzilla could have played a role as well, says Michael Ventrice, a meteorologist with the Weather Company in Metuchen, New Jersey. During this El Niño, the warmest water and strongest convection occurred hundreds of kilometers farther west along the equator than in other El Niños. A similar pattern characterized an El Niño episode in 1992, when the jet stream also veered northward. Gottschalck, of NOAA, wonders whether the anomalous West Coast rainfall might also reflect the Madden-Julian Oscillation (MJO), a weather phenomenon that alters rain in an eastern progression around the global tropics (*Science,* 2 October 2015, p. 22). The MJO is often absent during El Niño events, he notes, but in this case the oscillation was active.

To test that hypothesis and others, climate scientists are devising "hindcasting" model experiments that replay the El Niño event with the same Pacific heating while factors are varied. It could be years before they understand why this El Niño played out as it did, Gottschalck says. But forecasters have little time for second-guessing: They say a La Niña event, typified by cooling in the Pacific and its own set of global weather disruptions, is due in the fall. ■

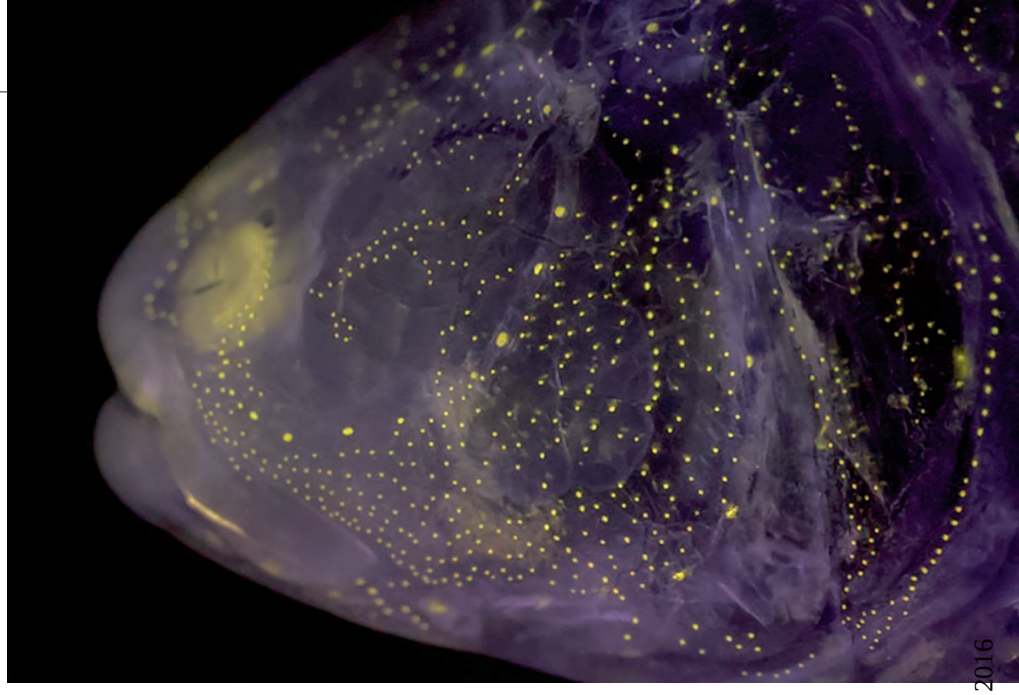


PHOTO: AMANDA POWERS/JOSHUA GROSS

ECOLOGY

Blind cave fish may provide insights into human health

Cave adaptations are connected to diabetes, eye problems, and other conditions that afflict people

By **Elizabeth Pennisi**, *in Fayetteville, Arkansas*

Degenerated retinas, globs of liver fat, wildly fluctuating blood sugar and insulin levels—all can spell trouble for people. But they are a way of life for *Astyanax mexicanus*, better known as the blind cave fish or Mexican tetra.

For decades, biologists have studied these pale 6-centimeter-long fish to understand the ecological and evolutionary effects of subterranean life. Now, some researchers argue that the fishes' adaptations can shed light on human diseases including retinal degeneration and diabetes. "Studies of cave fishes have tremendous potential for advancing our understanding of a host of human problems," says biologist Danté Fenolio of the San Antonio Zoo in Texas, who spoke here last week at the 2016 International Conference on Subterranean Biology. "Once we understand how the problems occur in fish, we can look at the human system through an educated lens."

Reflecting its evolution from sighted surface-dwellers, the blind Mexican tetra begins to build eyes while an early embryo, but they degenerate as it matures. Pinning down how the fish dismantles its eyes has been William Jeffery's goal for years, and at the meeting the developmental biologist from the University of Maryland, College Park, reported the first gene responsible. The cave fish, but not its surface relatives, possesses a mutation in a gene called *cbsa*, which codes for the enzyme cystathionine β synthase. The cave fish variant causes excessive buildup of homocysteine, a building block for the amino acid cysteine. In the developing fish eye, this excess leads to cell death that drives the tissue's degeneration. It also may lead to fat deposits in the liver and elsewhere, including the eye socket, Jeffery reported.

In humans, a deficiency of the same enzyme causes a disorder called homocystinuria, which affects not only the eye but also skeletal growth and metabolism. "Some of the genes underlying adaptation to the cave environment also define disease in humans," says Jeffery, who hopes further exploring the effects produced by the *cbsa* mutation in cave fish will lead to a better understanding of homocystinuria. Houmam Araj, a molecular biologist at the National Eye Institute in Bethesda, Maryland, agrees. "One has to look for targets of opportunity. *Astyanax* is an excellent such example."

Joshua Gross, an evolutionary developmental biologist at the University of Cincinnati in Ohio, sees a similar opportunity in developing cave fish skulls. They are often asymmetric, he and his graduate student Amanda Powers noticed a while back: The

Downloaded from http://science.sciencemag.org/ on June 28, 2016

Published by AAAS

In blind cave fish, sensory cells called neuromasts (yellow) may influence the growth of bone (purple).

left and right sides of the head do not match exactly. Such unevenness is rare in the surface fish, but not in humans, whose faces can be a little uneven, leading to conditions such as crossbite, or asymmetric to the point of disfigurement.

Cave fish skulls could help explain how human face development goes awry, Gross and Powers propose. They have focused on the cave fish's sensory neuromasts, nerve receptors that enable the fish to detect vibrations set off by insects falling in the water. At the meeting, Gross showed that neuromast patterns are closely associated with facial bone shape and that cave fish have about twice the number of neuromasts on their faces as surface fish, despite having much smaller bones. The neuromasts could be fragmenting the cave fish's facial bones during development, creating asymmetry as a "morphological 'byproduct' of selection for enhanced sensation in the darkness of the cave," he says. Humans don't have these same receptors on their faces, but Gross suspects other nonbone, noncartilaginous cells may similarly skew our skull symmetry.

Evolutionary biologist Nicolas Rohner of the Stowers Institute for Medical Research in Kansas City, Missouri, is probing cave fish adaptations that help the animals cope with the scanty food supply in caves—and mimic other human diseases in the process. He reported, for example, that the livers of cave fish are larded with energy-storing glycogen and fat. In people, such deposits signal a potentially lethal condition called nonalcoholic fatty liver disease, but in cave fish they may serve to tide the animal through periods of starvation. When cave fish do eat, Rohner adds, their blood glucose skyrockets to levels three times those seen in surface fish, then plummet a few hours later to levels so low "that it's a miracle they don't faint." Such fluctuations characterize diabetes in humans, he notes—as does a scarcity of insulin-producing cells, also found in cave fish.

"We argue that [cave fish] have evolved these metabolic alterations as a strategy to be more starvation resistant," Rohner says. But unlike people, "cave fish stay healthy." Figuring out how they do so could suggest ways to protect the health of people with diabetes or liver disease, he proposes.

The U.S. National Institutes of Health sees promise in cave fish as well, having agreed to fund Gross's work and that of a few other cave fish biologists. This subterranean creature, Gross says, "gives us the power to understand something that we don't entirely understand in humans." ■

BIOLOGY

Step aside, E. coli

Can a faster-growing microbe replace lab favorite?

By **Ben Panko**

Fresh from co-organizing a controversial project to synthesize the human genome, Harvard University geneticist George Church is looking to rock microbiology. In a preprint article published online last week on bioRxiv, he and colleagues argue that scientific experiments are unnecessarily prolonged as researchers wait for their workhorse microbe, *Escherichia coli*, to grow and reproduce. The team wants to replace *E. coli* with *Vibrio natriegens*, a salt marsh denizen that is the fastest-growing bacterium known.

Since its discovery 131 years ago, *E. coli* has become the go-to bacterium for microbiology, analyses of gene function, and much more. It is easy to grow and safe—the strains commonly studied no longer can infect the human intestines. *E. coli* also reproduces reasonably quickly, doubling in number as fast as every 20 minutes. (The bacterium that causes tuberculosis takes 12 to 16 hours.) But the biggest factor driving its popularity may be inertia. "We use *E. coli* just because we know the most about it," says Harvard geneticist Henry Lee.

Originally an electrical engineer, Lee was dismayed at the time biologists spend waiting for the microbe to grow. He went looking for a better alternative, and he landed on *V. natriegens*, which doubles every 10 minutes in ideal conditions. (It shares a genus with *V. cholerae*, the bacterium behind cholera, but seems harmless to people.) Lee, Church, and colleagues have sequenced its full genome, making the data—along with a list of tested growing conditions—public. They've also shown the CRISPR genome-editing system works on the bacterium. "We want to develop tools that would make it a drop-in, turnkey alternative for *E. coli*," Lee says.

Biologist Richard Lenski of Michigan State University in East Lansing, who has charted the evolution of a batch of *E. coli* for more than 28 years, is intrigued by the idea, but suggests *E. coli* may be tough to beat. "I don't know whether most research and applications are really limited by rapid growth, once you're already down into the range where cultures easily replace themselves in a day," he says. "But time will tell." ■

Published by AAAS

Downloaded from http://science.sciencemag.org/ on June 28, 2016



Drinks hotter than 65°C can cause cancer of the esophagus, a new report says.

EPIDEMIOLOGY

High-profile cancer reviews trigger controversy

IARC reports create mostly confusion, scientists say

By **Kai Kupferschmidt**

Officially released at 3 p.m. EST on 15 June, the news immediately raced around the world, spread by hundreds of websites. Judging by reader comments, many found it reassuring, whereas others were spooked. The message: Coffee doesn't give you cancer after all, but very hot drinks might, according to the International Agency for Research on Cancer (IARC), the cancer research arm of the World Health Organization.

But scientists grumbled that the hot drink verdict left the public none the wiser, because IARC couldn't say how big the risk is. And the next day, Germany's Federal Institute for Risk Assessment (BfR) in Berlin warned that blanket assessments, such as the one on coffee, are "of limited usefulness" to consumers. "Like almost any food, coffee is a complicated mixture of many different chemicals, some of which we know can cause cancer and others that are beneficial," says BfR President Andreas Hensel.

It has become a recurring pattern: an IARC announcement, followed by confusion, controversy, and criticism. In October 2015, IARC made headlines when it declared processed meat a carcinogen, putting it alongside plutonium and smoking in its classification scheme. Statisticians and risk communication experts, however, were quick to point out that the risk was very low. A few months earlier, IARC announced that glyphosate, the world's most widely used herbicide, was "probably carcinogenic," a verdict that helped fuel efforts to ban the chemical in the European Union, but was at odds with that of many other agencies, including BfR and the U.S. Environmental Protection Agency.

"What is the public supposed to do with these judgments?" asks Geoffrey Kabat, a cancer epidemiologist at the Albert Einstein College of Medicine in New York City. "No matter how much I observe IARC, I find it baffling."

IARC, formed in 1965 and based in Lyon, France, helps set up cancer registries around the world, and tries to harmonize data collection. "Some of these databases are incredibly useful," says Paul Pharoah, a cancer epidemiologist at the University of Cambridge in the United Kingdom. The agency also trains epidemiologists and conducts excellent research, he says. But IARC's most visible products are "monographs on the evaluation of carcinogenic risks to humans" that it started producing in 1971. They group substances and environmental exposures (almost a thousand so far) into one of five categories, ranging from "carcinogenic" to "probably not carcinogenic" (see table, below).

In the case of coffee, IARC announced that a review of recent research had prompted it to move the beverage from the "possibly carcinogenic" category, where it had been since 1991, to "not classifiable as to its carcinogenicity." The agency also said that drinking beverages at temperatures higher than 65°C probably causes cancer of the esophagus—but without quantifying the risk. "That's interesting for science but does not provide the information for making decisions," says David Spiegelhalter, a statistician at Cambridge.

Observers say several developments have helped IARC become a controversy catalyst. One is that the agency often evaluates widely used products such as mobile phones and coffee that are of great interest to a global public. Another is that IARC "aggressively seeks media coverage for its assessments," sending out press releases and organizing news conferences, says Peter Sandman, an independent expert on risk communication based in New York City. He accuses the agency of publicizing relatively vague statements "knowing they will be widely misperceived. I have to think this is intentional … [IARC] believes, probably correctly, that this misperception motivates people to change their behavior."

Veronique Terrasse, IARC's press officer, says that the agency's solid technical reputation means it "doesn't need to seek media coverage as such," and that its outreach is primarily intended to promote transparency. "I think the general public has the right to know what expert scientists with no conflicts of interest came up with," adds Kurt Straif, who heads IARC's monographs program. Much of the criticism, he says, is coming from

Weighing the evidence

Since 1971, IARC has issued almost 1000 verdicts on human carcinogenicity for a wide variety of products and environmental factors. Here's a sample, with reviews published in the past 12 months in red.

Carcinogenic (118 substances/exposures)
Processed meat, outdoor air pollution, asbestos, estrogen therapy, hepatitis B and C viruses, plutonium, solar radiation, tamoxifen (a breast cancer drug), alcohol, smoking

Probably carcinogenic (80)
Red meat, very hot beverages, glyphosate, shift work, working as a hairdresser or barber, acrylamide

Possibly carcinogenic (289)
Lead, nickel, cellphone use, AZT (an HIV drug), styrene

Not classifiable as to carcinogenicity (502)
Coffee, anesthetics, static electric fields, mineral wool, saccharin, tea, printing inks

Probably not carcinogenic (1)
Caprolactam (a precursor to nylon)

PHOTO: REDROCKSCHOOL/ISTOCKPHOTO.COM

Downloaded from http://science.sciencemag.org/ on June 28, 2016

Published by AAAS

"people who are directly or indirectly affiliated with stakeholders that are not happy with us," such as the pesticide and meat industries. Straif concedes, however, that it's less than ideal that IARC often announces its findings first in a relatively brief scientific summary, followed months later by the full monograph.

Further complicating IARC's communications effort is the distinction, often not appreciated by the public, between hazard and risk. An exposure is a cancer hazard if it can cause the disease under some circumstances; the risk is how likely one is to get cancer if exposed. Although IARC uses the word "risk" in monograph titles, a preamble cautions that the agency's aim is to "identify cancer hazards even when risks are very low at current exposure levels," because new uses could increase exposures.

But looking only at hazard has downsides. For one, it is very hard to prove that something will never cause cancer. Indeed, IARC has classified just one compound—caprolactam, a nylon precursor—as "probably not carcinogenic." And critics note IARC has no "not carcinogenic" category. Straif says that's also because IARC reviews prioritize substances suspected of carcinogenicity.

The classification is confusing for consumers because the different categories say nothing about how dangerous a substance is—only about how sure the agency is that there is a danger. IARC places smoking and processed meat in the same category, for instance, despite smoking's vastly higher risks. "People end up worrying about the wrong things and concluding that everything causes cancer, so why bother to stop smoking?" Kabat says.

Scientifically, the focus on hazard is outdated, Hensel adds, in part because the world is full of carcinogenic substances that are harmless at low levels. IARC's Straif says there often isn't enough scientific evidence to quantify the risk. But when there is, the agency "does try to move in that direction," he says.

In the meantime, scientists are bracing for more high-impact IARC pronouncements. The agency plans to produce monographs on controversial substances such as the cooking byproduct acrylamide and the plastic component bisphenol A. Hensel, for one, fears that IARC's seemingly black and white verdicts will lead to further politicization of regulatory debates.

At least the report about very hot drinks—although perhaps not particularly helpful—didn't play into a political issue, Pharoah says. "It's hard to see a big downside," he says, "to telling people to leave their tea to cool for 5 minutes." ■

PUBLIC HEALTH

California approves publicly funded gun research center

University of California to run $5 million center that could tap state's extensive database on firearm transfers

By **Emily Underwood**

For 2 decades, firearm advocates in Congress have blocked taxpayer-funded research into the causes and consequences of gun violence, which kills more people in the United States than in any other developed nation. Last week, California's state legislature bucked that trend, voting to establish the nation's first publicly funded center for studying gun violence.

The new California Firearm Violence Research Center will be run by the University of California (UC) system. Its lean budget—$1 million per year over the next 5 years—will likely preclude large-scale studies, but backers hope it will demonstrate the value of publicly funded gun research and perhaps help build support in Congress for a similar federal effort. The 16 June vote to create the center poses "a very stark" contrast to the continuing gridlock in Congress, says epidemiologist Garen Wintemute, who studies firearm violence at UC Davis. Last fall, he worked with state Senator Lois Wolk (D) to develop plans for the center.

> ***"We know that using real data and scientific methods, our best researchers can help policy makers get past the politics and find real answers to this public health crisis."***
>
> **Lois Wolk**, California legislator

Coincidentally, the California vote came just 4 days after a gunman killed 49 people and injured 53 at a gay nightclub in Orlando, Florida, sparking renewed debate in Congress over proposals to impose new federal rules on gun purchases. Events like the Orlando massacre—one of the country's worst mass shootings—"leave us searching for answers," Wolk said in a statement. "We know that using real data and scientific methods, our best researchers can help policy makers get past the politics and find real answers to this public health crisis."

"This shows the kind of thing states can do" in the absence of federal action, says David Hemenway, a health policy researcher at Harvard University. In 1996, the National Rifle Association and other groups successfully lobbied Congress to stifle federally funded gun research. Led by then-Representative Jay Dickey (R–AR), lawmakers barred the U.S. Centers for Disease Control and Prevention from funding any activity that would "advocate or promote gun control" and eliminated a $2.5 million pot of money for gun-related studies.

Dickey, now retired, has since reversed his position and advocates for more gun research. But the lack of public funding means that few young scientists are drawn to the field, says Wintemute, who has spent more than $1 million of his own funds to sustain his research.

The new center will focus on interdisciplinary research "to provide the scientific evidence upon which to base sound firearm violence prevention policies and programs," according to Wolk. "You name it, we need to know about it," says Hemenway, citing the need for more information on everything from firearm training and gun thefts to their role in suicide and homicide.

Wintemute adds that the center could enable a small team of researchers to examine California's unique data set on statewide gun transfers and other firearm-related activities. One pressing question, he says, is why California's annual fatalities from gun violence have dropped by roughly 20% since 2000, even as the nationwide rate has not changed. "We don't know why that is," Wintemute says. "Are we doing something right? Or are we not doing something wrong that other [states] are?"

The location of the new center is not yet "locked in," but Wintemute believes UC Davis is the most likely candidate. And he hopes the state funding will help researchers attract additional money from private donors. ■

Downloaded from http://science.sciencemag.org/ on June 28, 2016

Published by AAAS

DRUG DEVELOPMENT

Beleaguered phage therapy trial presses on

Setbacks suggest difficult road for much-needed antibiotic alternatives

By **Kelly Servick**

As drug-resistant infections thwart even our last-resort antibiotics, a growing number of researchers see promise in a therapy long on the back burner: bacteria-killing viruses known as bacteriophages. Now, phage therapy is facing its first major trial under modern regulatory standards—and it's proving challenging to test. The ambitious phase I/II clinical trial in Europe was expected to have its first results this summer. But the trial has faced a series of delays and shrunk in size and scope, hinting at some of the many barriers phages will confront in getting to market.

First discovered more than a century ago, phages largely fell by the wayside in the West as big pharmaceutical companies pursued broad-spectrum antibiotic compounds. Anecdotal evidence abounds that phages can sometimes defeat obstinate, life-threatening infections, and they are already used to treat patients in Eastern Europe. But to date, most clinical studies have included only small groups of patients and have lacked rigorous oversight.

PhagoBurn was supposed to change that. In response to a 2012 European Commission call for grant proposals on new antibacterial products, the French Ministry of Defense partnered with pharmaceutical companies and military and civilian hospitals in France, Switzerland, and Belgium to design a 3-year test of phage therapy in burn patients with infected wounds. In 2013, the project launched with €3.8 million in European Commission support.

"The expectations are high," says Sandra Morales, vice president of research at AmpliPhi Biosciences in Sydney, Australia, which earlier this year began two small phage therapy clinical trials in Australia and the United States. "Almost scarily high!"

Pherecydes Pharma, based in Romainville, France, was to develop two topical phage treatments for the trial, aimed at *Escherichia coli* and *Pseudomonas aeruginosa* infections, which are often antibiotic-resistant. Pherecydes collected most of its phages from the bacteria-rich sewage flowing underground from Parisian hospitals, then grew and purified them into two cocktails of 12 and 13 phages each to ensure multiple modes of action against ever-evolving bacterial strains.

Technically, that process is "not too tricky," says Laurent Bretaudeau, director of research and development for Clean Cells in Boufféré, France, which handled PhagoBurn's manufacturing. But the burden of validating and documenting the production steps grows exponentially with each new phage. The project budgeted 12 months to establish good manufacturing practice for the treatments, but ended up taking 20.

The company then planned to enroll 220 patients from 11 participating hospitals. Half would receive phages, and the other half silver sulfadiazine, an antibacterial cream routinely used on burn infections. That number seemed realistic based on the hospitals' previous patient data, says Jérôme Gabard, CEO of Pherecydes. But in the 6 months after recruitment began last July, PhagoBurn found just 15 eligible patients with *P. aeruginosa* infections and one with *E. coli*. "All of the clinicians in the trial are surprised" by the poor numbers, Gabard says.

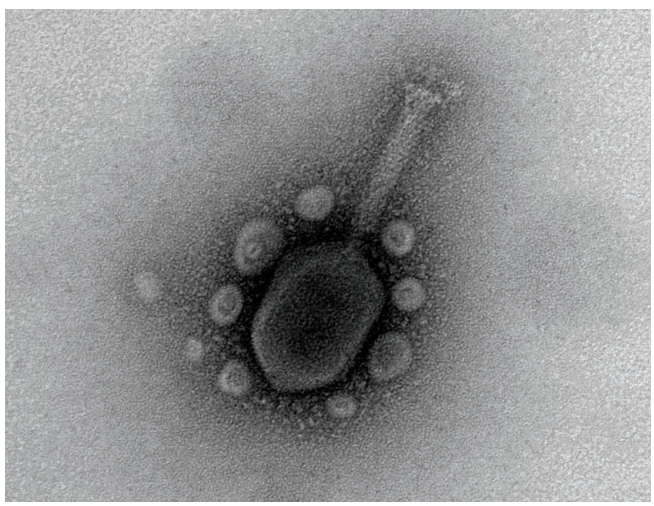
PhagoBurn's recruitment effort struggled in part because phages' attack mechanisms are highly targeted to one bacterial species. As a result, only patients with a single infection were eligible, and yet most infected burn patients are colonized with more than one type of bacterium. Last month, the team decided to drop the *E. coli* study altogether, leaving just the intended 110-person *P. aeruginosa* study.

The project hit another snag when regulators with France's National Agency for the Safety of Medicines and Health Products asked Pherecydes to show that the concentrations of the various phage components were stable over time. Demonstrating stability is usually straightforward for drugs with just one or a few active ingredients. But it's a major hurdle for an elaborate cocktail made up of highly similar phages, Gabard explains. When the deadline for these data came up in January, Pherecydes put recruitment for the trial on hold.

This month, regulators accepted provisional measures showing that the product remained sterile and retained its antibacterial activity, and the trial started back up. The company is now exploring ways to limit the formula to just a handful of distinct and potent strains, though Gabard notes that reducing the diversity of a cocktail too much could render it less effective as bacteria evolve resistance.

PhagoBurn's struggles come as little surprise to those who work with phages. "It's not like there's been some transformative development or technology that means that it's open season on phage therapy," says Paul Bollyky, a microbiologist and physician at the Stanford University Medical Center in Palo Alto, California. "It's just the problems have gotten so extensive with drug resistance that people are willing to try to get around some of the regulatory and composition issues and give this a try."

And despite the disappointments, many in the field have a certain reverence for PhagoBurn, which still plans to get as close as possible to its 110-patient goal by the end of the year and reveal efficacy data next February or March. At the very least, they say, the project will establish new manufacturing approaches and push regulators to clarify their policies for evaluating phages. "In some ways, it doesn't matter at all if it works or not," says Ry Young, a phage biologist with the Center for Phage Technology at Texas A&M University, College Station. "The very fact that it's being tried is a very positive step for the field." ■



A big European trial is testing whether bacteria-killing viruses, like the bacteriophage above, could be an effective alternative to antibiotics.

IMAGE: PHERECYDES PHARMA

Downloaded from http://science.sciencemag.org/ on June 28, 2016

Published by AAAS



Joe Kirschvink, sporting an EEG sensor cap, was the first subject in his magnetic-sensing tests.

Downloaded from http://science.sciencemag.org/

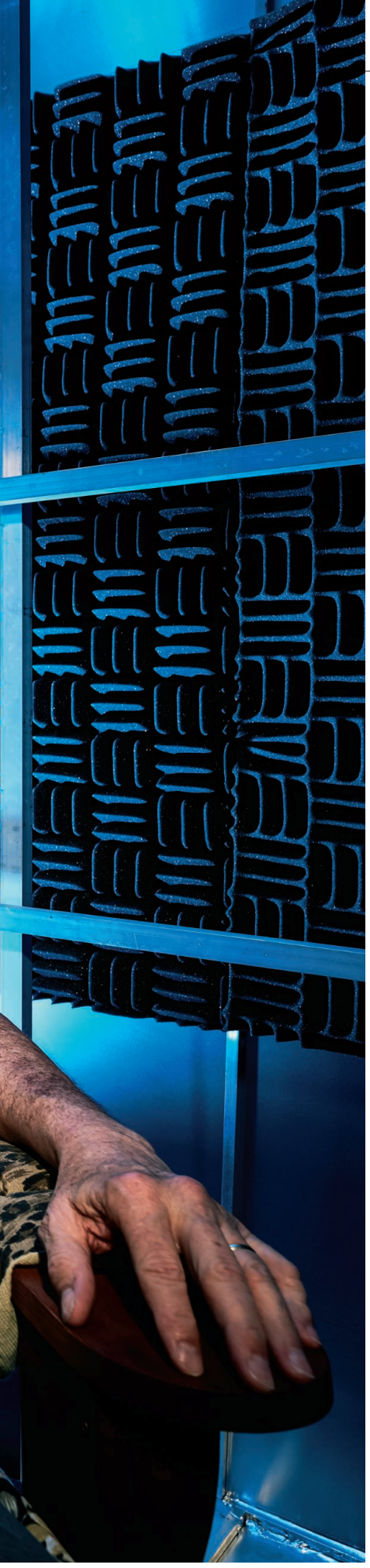


PHOTO: SPENCER LOWELL

POLAR EXPLORER

Joe Kirschvink thinks he has found a magnetic sixth sense in humans

By **Eric Hand**

Birds do it. Bees do it. But the human subject, standing here in a hoodie—can he do it? Joe Kirschvink is determined to find out. For decades, he has shown how critters across the animal kingdom navigate using magnetoreception, or a sense of Earth's magnetic field. Now, the geophysicist at the California Institute of Technology (Caltech) in Pasadena is testing humans to see if they too have this subconscious sixth sense. Kirschvink is pretty sure they do. But he has to prove it.

He takes out his iPhone and waves it over Keisuke Matsuda, a neuroengineering graduate student from the University of Tokyo. On this day in October, he is Kirschvink's guinea pig. A magnetometer app on the phone would detect magnetic dust on Matsuda—or any hidden magnets that might foil the experiment. "I want to make sure we don't have a cheater," Kirschvink jokes.

They are two floors underground at Caltech, in a clean room with magnetically shielded walls. In a corner, a liquid helium pump throbs and hisses, cooling a superconducting instrument that Kirschvink has used to measure tiny magnetic fields in everything from bird beaks to martian meteorites. On a lab bench lie knives—made of ceramic and soaked in acid to eliminate magnetic contamination—with which he has sliced up human brains in search of magnetic particles. Matsuda looks a little nervous, but he will not be going under the knife. With a syringe, a technician injects electrolyte gel onto Matsuda's scalp through a skullcap studded with electrodes. He is about to be exposed to custom magnetic fields generated by an array of electrical coils, while an electroencephalogram (EEG) machine records his brain waves.

For much of the 20th century, magnetoreception research seemed as unsavory as the study of dowsing or telepathy. Yet it is now an accepted fact that many animals sense the always-on, barely-there magnetic field of Earth. Birds, fish, and other migratory animals dominate the list; it makes sense for them to have a built-in compass for their globetrotting journeys. In recent years, researchers have found that less speedy creatures—lobsters, worms, snails, frogs, newts—possess the sense. Mammals, too, seem to respond to Earth's field: In experiments, wood mice and mole rats use magnetic field lines in siting their nests; cattle and deer orient their bodies along them when grazing; and dogs point themselves north or south when they urinate or defecate.

The mounting scientific evidence for magnetoreception has largely been behavioral, based on patterns of movement, for example, or on tests showing that disrupting or changing magnetic fields can alter animals' habits. Scientists know that animals can sense the fields, but they do not know how at the cellular and neural level. "The frontier is in the biology—how the brain actually uses this information," says David Dickman, a neurobiologist at the Baylor College of Medicine in Houston, Texas, who in a 2012 *Science* paper showed that specific neurons in the inner ears of pigeons are somehow involved, firing in response to the direction, polarity, and intensity of magnetic fields.

Finding the magnetoreceptors responsible for triggering these neurons has been like

Published by AAAS

Downloaded from http://science.sciencemag.org/ on June 28, 2016

looking for a magnetic needle in a haystack. There's no obvious sense organ to dissect; magnetic fields sweep invisibly through the entire body, all the time. "The receptors could be in your left toe," Kirschvink says.

Scientists have come up with two rival ideas about what they might be (see sidebar, right). One is that magnetic fields trigger quantum chemical reactions in proteins called cryptochromes. Cryptochromes have been found in the retina, but no one has determined how they might control neural pathways. The other theory, which Kirschvink favors, proposes that miniature compass needles sit within receptor cells, either near the trigeminal nerve behind animals' noses or in the inner ear. The needles, presumed to be made up of a strongly magnetic iron mineral called magnetite, would somehow open or close neural pathways.

The same candidate magnetoreceptors are found in humans. So do we have a magnetic sense as well? "Perhaps we lost it with our civilization," says Michael Winklhofer, a biophysicist at the University of Oldenburg in Germany. Or, as Kirschvink thinks, perhaps we retain a vestige of it, like the wings of an ostrich.

KIRSCHVINK SPECIALIZES in measuring remanent magnetic fields in rock, which can indicate the latitude at which the rock formed, millions or billions of years ago, and can trace its tectonic wanderings. The technique has led him to powerful, influential ideas. In 1992, he marshaled evidence that glaciers nearly covered the globe more than 650 million years ago, and suggested that their subsequent retreat from "Snowball Earth" (a term he coined) triggered an evolutionary sweepstakes that would become the Cambrian explosion 540 million years ago. In 1997, he worked out a provocative explanation for the abnormally speedy drift of continental plates about the same time as the Cambrian explosion: Earth's rotational axis had tipped over by as much as 90°, Kirschvink proposed. The climatic havoc from this geologically sudden event also would have spurred the biological innovations seen in the Cambrian. And he was prominent among a group of scientists who in the 1990s and 2000s argued that magnetic crystals in a famous martian meteorite, Allan Hills 84001, were fossilized signs of life on the Red Planet. Although the significance of Allan Hills 84001 remains controversial, the idea that life leaves behind magnetofossils is an active area of research on Earth.

"He's not afraid to go out on a limb," says Kenneth Lohmann, a neurobiologist who studies magnetoreception in lobsters and sea turtles at the University of North Carolina, Chapel Hill. "He's been right about some things and not right about other things."

In support of his hypotheses, Kirschvink has gathered rocks from all over the world: South Africa, China, Morocco, and Australia. But looking for magnets in animals—and humans—in his windowless subbasement lab has remained an abiding obsession. Just ask his first-born son, who arrived in 1984, as Kirschvink and his wife—Atsuko Kobayashi, a Japanese structural biologist—published the discovery of magnetite in the sinus tissue of yellowfin tuna. At Kirschvink's suggestion, they named him Jiseki: magnet stone, or magnetite.

Kirschvink, 62, could never decide between geology and biology. He remembers the day in 1972 when, as an undergraduate at Caltech, he realized that the two were intertwined. A professor held the tongue plate of a chiton, a type of mollusk, and dragged it around with a bar magnet. Its teeth were capped with magnetite. "That blew me away," recalls Kirschvink, who still keeps the tongue plate on his desk. "Magnetite is typically something that geologists expect in igneous rocks. To find it in an animal is a biochemical anomaly."

For many years, scientists thought chitons had evolved a way to synthesize magnetite simply because the hard mineral makes for a good, strong tooth. But in 1975, Richard Blakemore at the Woods Hole Oceanographic Institution in Massachusetts suggested that in certain bacteria, magnetite is a magnetic sensor. Studying bacteria from Cape Cod marsh muds, Blakemore found that when he moved a small magnet around his glass slides, the bacteria would rush toward the magnet. Looking closer, he found that the microbes harbored chains of magnetite crystals that forced the cells to align with the lines of Earth's own magnetic field, which in Massachusetts dip down into the ground at 70°, toward the North Pole. Many bacteria search randomly for the right balance of oxygen and nutrients, utilizing a motion called "tumble and run." But as swimming compass needles, Blakemore's bacteria knew up-mud from down-mud. They could surf this gradient more efficiently and would swim downward along it whenever the mud was disturbed.

These bacterial magnetoreceptors are still the only ones scientists have definitively located and studied. To Kirschvink, their presence indicates that magnetoreception is ancient, perhaps predating Earth's first eukaryotic cells, which are thought to have evolved nearly 2 billion years ago after a host cell captured free-living bacteria that became the cell's energy-producing mitochondria. "I'm suggesting that the original mitochondria were magnetic bacteria," Kirschvink says, which could mean that all eukaryotes have a potential magnetic sense.

What and where are the body's magnetometers?

By **Eric Hand**

That many animals sense and respond to Earth's magnetic field is no longer in doubt, and people, too, may have a magnetic sense (see main story, p. 1508). But how this sixth sense might work remains a mystery. Some researchers say it relies on an iron mineral, magnetite; others invoke a protein in the retina called cryptochrome.

Magnetite has turned up in bird beaks and fish noses and even in the human brain, as Joe Kirschvink of the California Institute for Technology in Pasadena reported in 1992, and it is extremely sensitive to magnetic fields. As a result, Kirschvink and other fans say, it can tell an animal not only which way it is heading (compass sense) but also where it is. "A compass cannot explain how a sea turtle can migrate all the way around the ocean and return to the same specific stretch of beach where it started out," says neurobiologist Kenneth Lohmann of the University of North Carolina, Chapel Hill. A compass sense is enough for an animal to figure out latitude, based on changes in the inclination of magnetic field lines (flat at the equator, plunging into the earth at the poles). But longitude requires detecting subtle variations in field strength from place to place—an extra map or signpost sense that magnetite could supply, Lohmann says.

Except in bacteria, however, no one has seen magnetite crystals serving as a magnetic sensor. The crystals could be something else—say, waste products of iron metabolism, or a way for the body to sequester carcinogenic heavy metals. In the early 2000s, scientists found magnetite-bearing cells in the beaks of pigeons. But a follow-up study found that the supposed magnetoreceptors were in fact scavenger immune cells that had nothing to do with the neural system. And because there is no unique stain or marker for magnetite, false sightings are easy to make.

Cryptochrome, too, offers much

Downloaded from http://science.sciencemag.org/ on June 28, 2016

Published by AAAS

Reading about Blakemore's work, Kirschvink wondered which way magnetic bacteria swim in the Southern Hemisphere: northward like the Massachusetts microbes, or southward toward their own pole, or in some other direction? He flew to Australia to search stream beds for Blakemore's antipodal counterparts. They were most abundant in a sewage treatment pond near Canberra. "I just went with a magnet and hand lens," he says. "They're all over the place." Sure enough, they swam down toward the South Pole. They had evolved south-seeking magnetite chains.

By then, Kirschvink was a postdoc at Princeton University, working with biologist James Gould. He had also graduated up the food chain of animals. In 1978, he and Gould found magnetite in the abdomen of honey bees. Then, in 1979, in the heads of pigeons. Unbeknownst to Kirschvink, across the Atlantic Ocean a young, charismatic University of Manchester, U.K., biologist named Robin Baker was setting his sights on the magnetic capabilities of larger, more sophisticated animals: British students. In a series of experiments, he gathered blindfolded students from a "home" point onto a Sherpa mini-bus, took them on a tortuous route into the countryside, and asked them the compass direction of home. In *Science* in 1980, Baker reported something uncanny: The students could almost always point in the quadrant of home. When they wore a bar magnet in the elastic of their blindfolds, that pointing skill was thwarted, whereas controls who wore a brass bar still had what appeared to be a magnetic sense.

In later variations, Baker claimed to find a human compass sense in "walkabout" experiments, in which subjects pointed home after being led on a twisty route; and "chair" experiments, in which they were asked for cardinal directions after being spun around. Baker performed some of his experiments for live television, and he announced some of his results prior to peer review in books and popular science magazines—a flair for the dramatic that rubbed other academics the wrong way.

In an email, Baker says there was a "base hostility" among his U.S. counterparts. Kirschvink and Gould were among the skeptics. In 1981, they invited Baker to Princeton for a chance to perform the experiments, one whistle stop on a reproducibility tour of several U.S. campuses in the Northeast. At Princeton and elsewhere, the replication efforts failed. After Baker claimed in a 1983 *Nature* paper that human sinus bones were magnetic, Kirschvink showed that the results were due to contamination. In 1985, Kirschvink failed to replicate a version of the chair experiment.

Although the Manchester experiments cast a pall over human magnetoreception, Kirschvink quietly took up Baker's mantle, pursuing human experiments on the side for 30 years. He never gave up running students through a gauntlet of magnetic coils and experimental protocols. "The irritating thing was, [our] experiments were not negative," he says. "But from day to day, we couldn't reproduce them."

Now, with a $900,000 grant from the Human Frontier Science Program, Kirschvink; Shinsuke Shimojo, a Caltech psychophysicist and EEG expert; and Ayumu Matani, a neuroengineer at the University of Tokyo, are making their best effort ever to test Baker's claims.

Baker finds it ironic that his onetime antagonist is now leading the charge for human magnetoreception. "Joe is probably in a better position to do this than most," he writes. As for whether he thinks his results still indicate something real, Baker says there is "not a shadow of doubt in my mind: Humans can detect and use the Earth's magnetic field."

NEXT DOOR to Kirschvink's magnetics lab is the room where he tests his human subjects. In it is a box of thin aluminum siding, known as a Faraday cage, just big enough to hold the test subject. Its role is to screen out electromagnetic noise—from computers, elevators, even radio broadcasts—that might confound the experiment. "The Faraday cage is key," Kirschvink says. "It wasn't until the last few years, after we put the damned Faraday shield in, that we went, 'Wait a minute.'"

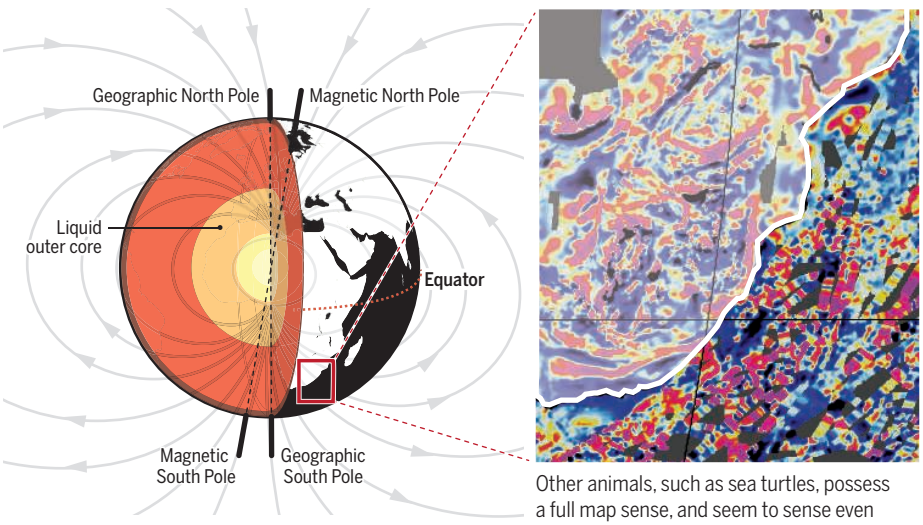
Kirschvink added it after an experiment led by one of Winklhofer's Oldenburg colleagues, Henrik Mouritsen, showed that electromagnetic noise prevents European robins from orienting magnetically. The stray fields would probably affect any human compass, Kirschvink says, and the noise is most disruptive in a band that overlaps with AM radio broadcasts. That could explain why Baker's experiments succeeded in Manchester, which at the time did not have strong AM radio stations. The U.S. Northeast, however, did, which could explain why scientists there couldn't replicate the findings.

In the current setup, the Faraday cage is lined with squares of wire coils, called Merritt coils. Electricity pulsed through the coils induces a uniform magnetic field running through the center of the box. Because the coils are arranged in three perpendicular directions, the experimenters can control the orientation of the field. A fluxgate magnetometer to check field strength dangles above a wooden chair that has had all of its iron-containing parts replaced with nonmagnetic brass screws and aluminum brackets.

Kirschvink, Shimojo, and Matani's idea is to apply a rotating magnetic field, similar in strength to Earth's, and to check EEG recordings for a response in the brain. Finding one would not reveal the magnetoreceptors themselves, but it would prove that such a sense exists, with no need to interpret often-ambiguous human behavior. "It's a really fantastic idea," Winklhofer says. "I'm wondering why nobody has tried it before."

The experiments began at the end of 2014.

Playing the field Earth's magnetic field, generated by its liquid outer core, is similar to that of a giant off-axis bar magnet. Its strength ranges from 25 microtesla (μT) near the equator to 60 μT at the poles. That is weak: An MRI's field is more than 100,000 times stronger.



Some animals, such as birds, gain a compass by sensing the field lines and their inclination.

Other animals, such as sea turtles, possess a full map sense, and seem to sense even finer variations in strength due to magnetic rocks in the crust.

CREDITS: (DIAGRAM) ADAPTED BY G. GRULLÓN/*SCIENCE*; (IMAGE) WDMAM/CIRES

Downloaded from http://science.sciencemag.org/ on June 28, 2016

Published by AAAS

Kirschvink was human subject No. 1. No. 19 is Matsuda, on loan from Matani's lab, which is replicating the experiment in Tokyo with a similar setup. Matsuda signs a consent form and is led into the box by the technician, who carries the EEG wires like the train of a wedding veil. "Are we ready to start?" the technician asks, after plugging in the electrodes. Matsuda nods grimly. "All right, I'll shut the box." He lowers the flap of aluminum, turns off the lights, and shuts the door. Piped into the box is Kirschvink's nasal, raspy voice. "Don't fall asleep," he says.

Matsuda will sit in the box for an hour in total blackness while an automated program runs through eight different tests. In half of them, a magnetic field roughly as strong as Earth's rotates slowly around the subject's head. In the others, the Merritt coils are set to cancel out the induced field so that only Earth's natural magnetism is at work. These tests are randomized so that neither experimenter nor subject knows which is which.

EVERY FEW YEARS, the Royal Institute of Navigation (RIN) in the United Kingdom holds a conference that draws just about every researcher in the field of animal navigation. Conferences from years past have dwelt on navigation by the sun, moon, or stars—or by sound and smell. But at this year's meeting, in April at Royal Holloway, University of London, magnetoreception dominated the agenda. Evidence was presented for magnetoreception in cockroaches and poison frogs. Peter Hore, a physical chemist at the University of Oxford in the United Kingdom, presented work showing how the quantum behavior of the cryptochrome system could make it more precise than laboratory experiments had suggested. Can Xie, a biophysicist from Peking University, pressed his controversial claim that, in the retina of fruit flies, he had found a complex of magnetic iron structures, surrounded by cryptochrome proteins, that was the long-sought magnetoreceptor.

Then, in the last talk of the first day, Kirschvink took the podium to deliver his potentially groundbreaking news. It was a small sample—just two dozen human subjects—but his basement apparatus had yielded a consistent, repeatable effect. When the magnetic field was rotated counterclockwise—the equivalent of the subject looking to the right—there was sharp drop in α waves. The suppression of α waves, in the EEG world, is associated with brain processing: A set of neurons were firing in response to the magnetic field, the only changing variable. The neural response was delayed by a few hundred milliseconds, and Kirschvink says the lag suggests an active brain response. A magnetic field can induce electric currents in the brain that could mimic an EEG signal—but they would show up immediately.

Kirschvink also found a signal when the applied field yawed into the floor, as if the subject had looked up. He does not understand why the α wave signal occurred with up-down and counterclockwise changes, but not the opposite, although he takes it as a sign of the polarity of the human magnetic compass. "My talk went *really* well," he wrote jubilantly in an email afterwards. "Nailed it. Humans have functioning magnetoreceptors."

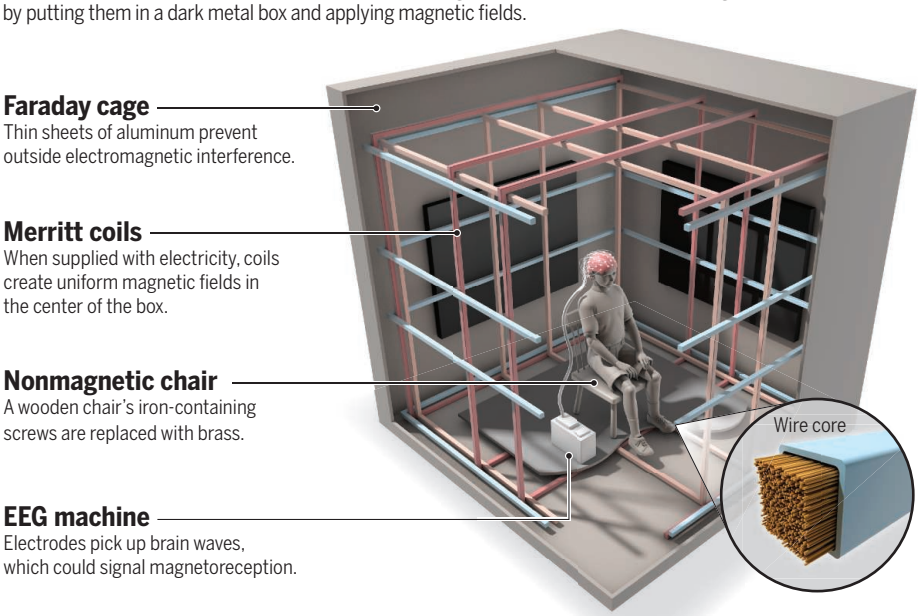
Others at the talk had a guarded response: amazing, if true. "It's the kind of thing that's hard to evaluate from a 12-minute talk," Lohmann says. "The devil's always in the details." Hore says: "Joe's a very smart man and a very careful experimenter. He wouldn't have talked about this at the RIN if he wasn't pretty convinced he was right. And you can't say that about every scientist in this area."

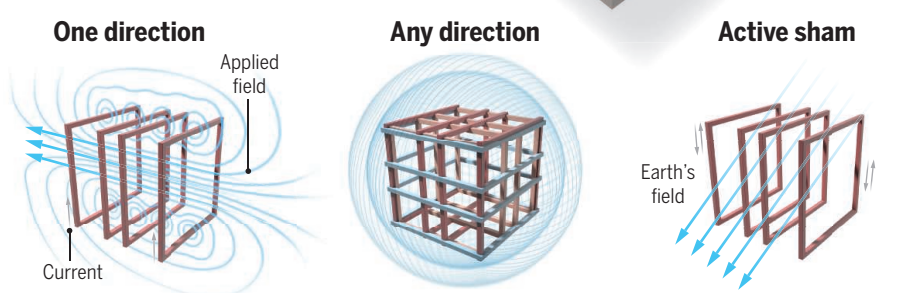
Two months later, in June, Kirschvink is in Japan, crunching data and hammering out experimental differences with Matani's group. "Alice in Wonderland, down the rabbit hole, that's what it feels like," he says. Matani is using a similarly shielded setup, except his cage and coils are smaller—just big enough to encompass the heads of subjects, who must lie on their backs. Yet this team, too, is starting to see repeatable EEG effects. "It's absolutely reproducible, even in Tokyo," Kirschvink says. "The doors are opening."

Kirschvink's lifelong quest seems to be on the cusp of resolution, but it also feels like a beginning. A colleague in New Zealand says he is ready to replicate the experiment in the Southern Hemisphere, and Kirschvink wants money for a traveling Faraday cage that he could take to the magnetic equator. There are papers to write, and new subjects to recruit. Just as Baker's results ricocheted through the research community for years, Kirschvink knows that the path toward getting his idea accepted is long, and uphill.

But he relishes the thought of showing, once and for all, that there is something that connects the iPhone in his pocket—the electromagnetic laws that drive devices and define modernity—to something deep inside him, and the tree of life. "It's part of our evolutionary history. Magnetoreception may be the primal sense." ■

Center of attraction Researchers are testing humans for a subconscious magnetic sense by putting them in a dark metal box and applying magnetic fields.





One set of Merritt coils produces a field along the axis of the coils.

Using all three sets of coils, a field can be created in any direction.

Alternating currents cancel out applied field, leaving only Earth's.

DIAGRAM: C. BICKEL/SCIENCE

Downloaded from http://science.sciencemag.org/ on June 28, 2016

Published by AAAS



Downloaded from http://science.sciencemag.org/ on June 28, 2016

ETHICS

Our driverless dilemma

When should your car be willing to kill you?

By **Joshua D. Greene**

Suppose that a driverless car is headed toward five pedestrians. It can stay on course and kill them or swerve into a concrete wall, killing its passenger. On page 1573 of this issue, Bonnefon *et al.* (*1*) explore this social dilemma in a series of clever survey experiments. They show that people generally approve of cars programmed to minimize the total amount of harm, even at the expense of their passengers, but are not enthusiastic about riding in such "utilitarian" cars—that is, autonomous vehicles that are, in certain emergency situations, programmed to sacrifice their passengers for the greater good. Such dilemmas may arise infrequently, but once millions of autonomous vehicles are on the road, the improbable becomes probable, perhaps even inevitable. And even if such cases never arise, autonomous vehicles must be programmed to handle them. How should they be programmed? And who should decide?

Bonnefon *et al.* explore many interesting variations, such as how attitudes change when a family member is on board or when the number of lives to be saved by swerving gets larger. As one might expect, people are even less comfortable with utilitarian sacrifices when family members are on board and somewhat more comfortable when sacrificial swerves save larger numbers of lives. But across all of these variations, the social dilemma remains robust. A major determinant of people's attitudes toward utilitarian cars is whether the question is about utilitarian cars in general or about riding in them oneself.

In light of this consistent finding, the authors consider policy strategies and pitfalls. They note that the best strategy for utilitarian policy-makers may, ironically, be to give up on utilitarian cars. Autonomous vehicles are expected to greatly reduce road fatalities (*2*). If that proves true, and if utilitarian cars are unpopular, then pushing for utilitarian cars may backfire by delaying the adoption of generally safer autonomous vehicles.

Department of Psychology, Center for Brain Science, Harvard University, Cambridge, MA 02138, USA.
Email: jgreene@wjh.harvard.edu

ILLUSTRATION: DARIA KIRPACH/@SALZMANART

Published by AAAS



Moral dilemma. Should autonomous vehicles protect their passengers or minimize the total amount of harm?

As the authors acknowledge, attitudes toward utilitarian cars may change as nations and communities experiment with different policies. People may get used to utilitarian autonomous vehicles, just as some Europeans have grown accustomed to opt-out organ donation programs (*3*) and Australians have grown accustomed to stricter gun laws (*4*). Likewise, attitudes may change as we rethink our transportation systems. Today, cars are beloved personal possessions, and the prospect of being killed by one's own car may feel like a personal betrayal to be avoided at all costs. But as autonomous vehicles take off, car ownership may decline as people tire of paying to own vehicles that stay parked most of the time (*5*). The cars of the future may be interchangeable units within vast transportation systems, like the cars of today's subway trains. As our thinking shifts from personal vehicles to transportation systems, people might prefer systems that maximize overall safety.

In their experiments, Bonnefon *et al.* assume that the autonomous vehicles' emergency algorithms are known and that their expected consequences are transparent. This need not be the case. In fact, the most pressing issue we face with respect to autonomous vehicle ethics may be transparency. Life-and-death trade-offs are unpleasant, and no matter which ethical principles autonomous vehicles adopt, they will be open to compelling criticisms, giving manufacturers little incentive to publicize their operating principles. Manufacturers of utilitarian cars will be criticized for their willingness to kill their own passengers. Manufacturers of cars that privilege their own passengers will be criticized for devaluing the lives of others and their willingness to cause additional deaths. Tasked with satisfying the demands of a morally ambivalent public, the makers and regulators of autonomous vehicles will find themselves in a tight spot.

Software engineers—unlike politicians, philosophers, and opinionated uncles—don't have the luxury of vague abstraction. They can't implore their machines to respect people's rights, to be virtuous, or to seek justice—at least not until we have moral theories or training criteria sufficiently precise to determine exactly which rights people have, what virtue requires, and which trade-offs are just. We can program autonomous vehicles to minimize harm, but that, apparently, is not something with which we are entirely comfortable.

Bonnefon *et al.* show us, in yet another way, how hard it will be to design autonomous machines that comport with our moral sensibilities (*6*–*8*). The problem, it seems, is more philosophical than technical. Before we can put our values into machines, we have to figure out how to make our values clear and consistent. For 21st-century moral philosophers, this may be where the rubber meets the road. ■

REFERENCES

1. J.-F. Bonnefon *et al.*, *Science* **352**, 1573 (2016).
2. P. Gao, R. Hensley, A. Zielke, *A Road Map to the Future for the Auto Industry* (McKinsey & Co., Washington, DC, 2014).
3. E. J. Johnson, D. G. Goldstein, *Science* **302**, 1338 (2003).
4. S. Chapman *et al.*, *Injury Prev.* **12**, 365 (2006).
5. D. Neil, "Could self-driving cars spell the end of car ownership?", *Wall Street Journal*, 1 December 2015; www.wsj.com/articles/could-self-driving-cars-spell-the-end-of-ownership-1448986572.
6. I. Asimov, *I, Robot* [stories] (Gnome, New York, 1950).
7. W. Wallach, C. Allen, *Moral Machines: Teaching Robots Right from Wrong* (Oxford Univ. Press, 2010).
8. P. Lin, K. Abney, G. A. Bekey, *Robot Ethics: The Ethical and Social Implications of Robotics* (MIT Press, 2011).

10.1126/science.aaf9534

IMMUNOLOGY

Converting to adapt

Gut microbiota affect T cell plasticity in the intestinal lining

By **Marco Colonna** *and* **Luisa Cervantes-Barragan**

Effective immune responses rely on balancing lymphocyte stability and plasticity. Lymphocytes have regulatory circuits that control phenotypic and functional identity. Stable circuits maintain homeostasis and prevent autoimmunity. But plasticity is needed to integrate new environmental inputs and generate immune responses that subdue the eliciting agent without damaging tissue. Regulatory T cells (T_{regs}) are a subset of $CD4^+$ T cells that control effector T cell responses and prevent excessive inflammation and autoimmunity (*1*, *2*). On page 1581 in this issue, Sujino *et al.* (*3*) report that intestinal T_{regs} convert into $CD4^+$ intraepithelial T cells ($CD4_{IELs}$) to adapt to the local intestinal environment, thus identifying the intestinal epithelium as a compartment that enforces lymphocyte plasticity.

"...Foxp3⁺ cells might rapidly convert into another T cell subtype."

$CD4_{IELs}$ are implicated in various immune responses, including tolerance to dietary antigens (*4*). They originate from $CD4^+$ T helper cells in the intestinal lamina propria, and can produce interferon-γ (IFN-γ), a cytokine that triggers immune responses to infection, as well as promote cytolysis. Differentiation of T cells into $CD4_{IELs}$ is governed by the reduced expression of ThPOK (T helper–inducing POZ/Kruppel factor), a transcription factor that drives the $CD4^+$ T helper cell program. Moreover, increased expression of Runx3 (runt-related transcription factor 3) drives the $CD8^+$ T cell program, i.e. IFN-γ production and cytolysis (*5*, *6*). $CD4_{IELs}$ in the intestinal

Department of Pathology and Immunology, Washington University School of Medicine, St. Louis, MO, USA. Email: mcolonna@pathology.wustl.edu

Downloaded from http://science.sciencemag.org/ on June 28, 2016

Published by AAAS

T cell conversion

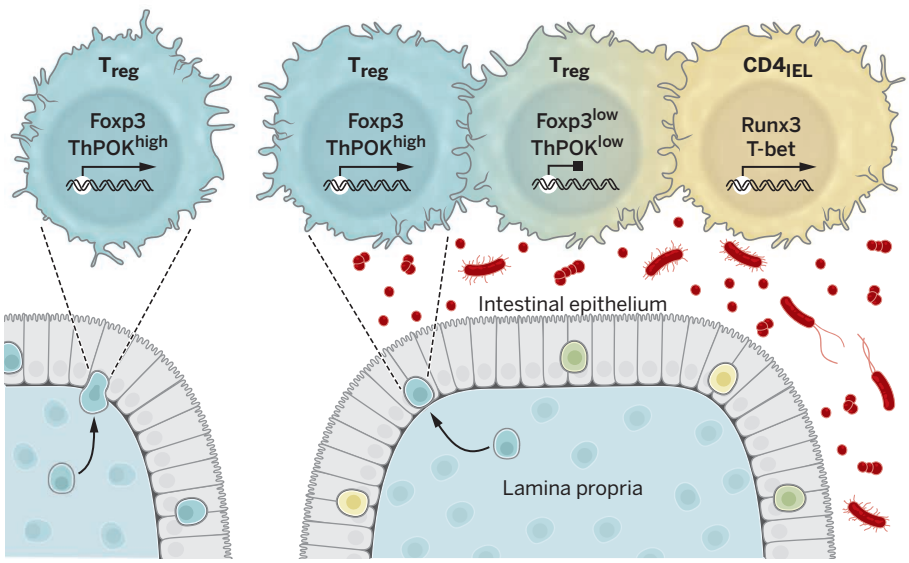
In the presence of microbiota, T_{regs} convert into $CD4_{IELs}$ via altered expression of the transcription factors ThPOK, Foxp3, Runx3, and T-bet. This results in the expression of cell surface proteins (CD8α, 2B4, and CRTAM), which may support localization of $CD4_{IELs}$ to the epithelium.

Migration
$Foxp3^+$ T_{regs} migrate to intestinal epithelium. In germ-free mice, ThPOK prevents conversion.

Stimulation
Environmental cues from microbiota trigger T_{regs} to rapidly convert into $CD4_{IELs}$.

Down-regulation
Runx3 and T-bet cooperate in turning off ThPOK and Foxp3.

Regulation
$CD4_{IELs}$ control local inflammation and tolerance to dietary antigens.



epithelium are sustained by retinoic acid and transforming growth factor β (TGFβ), which promote Runx3 expression (*6*).

Sujino *et al.* defined the localization and migration of T_{regs} [those expressing the transcription factor forkhead box P3 (Foxp3)] in the small intestinal mucosa by intravital multiphoton microscopy. Experiments were performed in a mouse model that allows inducible tracing of $Foxp3^+$ cells by marking cells that currently express Foxp3 as well as cells that once expressed Foxp3 (ex-Foxp3). Although $Foxp3^+$ cells were largely present in the lamina propria, some migrated into the intestinal epithelium, but not vice versa. Given that $Foxp3^+$ T_{regs} are barely detectable in the intestinal epithelium ex vivo, this suggested that the epithelial $Foxp3^+$ cells might rapidly convert into another T cell subtype (see the figure).

To determine whether these T cell dynamics were associated with changes in ThPOK expression, Sujino *et al.* used a transgenic mouse model in which all $CD4^+$ T cells express an ovalbumin-specific T cell receptor (OTII T cells) and also express a fluorescence reporter for ThPOK. Mice fed ovalbumin had OTII T cells with reduced ThPOK activity, found mostly in the intestinal epithelium. The authors further found that a large percentage of ex-$Foxp3^+$ T cells in the intestinal epithelium expressed low amounts of ThPOK. Thus, T_{regs} are plastic within the intestinal epithelium and can convert into $CD4_{IELs}$.

Does the gut microbiota affect T_{reg} plasticity in the intestinal epithelium? Germ-free mice had more intestinal $Foxp3^+$ T_{regs} than specific-pathogen-free mice, but very few $CD4_{IELs}$. The frequency of ThPOK-expressing T cells in the epithelium was also greater in germ-free mice. Treatment of mice with antibiotics impaired conversion of T_{regs} into $CD4_{IELs}$. Thus, the gut microbiota destabilizes T_{regs} in the intestinal epithelium. Interestingly, when OTII transgenic mice were treated with antibiotics, repeated antigenic stimulation of intestinal OTII T cells with dietary ovalbumin (a model of dietary antigens) overcame the requirement for microbiota. Thus, conversion of T_{regs} in the intestinal epithelium depends on antigenic stimulation.

Sujino *et al.* interrogated the impact of T_{reg} plasticity on the intestinal immune response to dietary antigens. Ovalbumin was fed to OTII transgenic mice in which $CD4^+$ T cells were prevented from generating $CD4_{IELs}$. Antigenic challenge resulted in diarrhea. Ovalbumin was also fed to OTII transgenic mice engineered to have fewer T_{regs} and more $CD4_{IELs}$. Despite decreased T_{regs}, no intestinal intolerance to ovalbumin was detected. Thus, $CD4_{IELs}$ can control local intestinal inflammation. Moreover, ovalbumin challenge of transgenic mice that could not generate T_{regs} (because of a mutation in Foxp3 in OTII T cells) did not cause inflammation and diarrhea unless $CD4_{IELs}$ were also depleted (by injecting mice with an anti-CD8 antibody). Thus, T_{regs} and $CD4_{IELs}$ have complementary roles in tolerance to dietary antigens.

Although some plasticity of T_{regs} had been previously reported in other settings (*7*, *8*), the study by Sujino *et al.* conclusively demonstrates that the intestinal epithelium is a compartment that supports the plasticity of T_{regs} and converts them into $CD4_{IELs}$. This finding opens exciting new research avenues. Whereas TGFβ and retinoic acid produced by intestinal epithelial cells and dendritic cells may be among the crucial signals that trigger this conversion (*6*, *9*), the impact of defined microbial antigens and metabolites remains to be determined (*10*, *11*). The cytokine interleukin-15 (IL-15) in the intestinal epithelial microenvironment also seems to contribute to certain $CD4_{IEL}$ functions, such as cytolysis (*5*). Besides Runx3 and the T-box transcription factor T-bet, other transcription factors may contribute to $CD4_{IEL}$ differentiation and function. The induced expression of certain cell surface molecules, such as CRTAM (class I major histocompatibility complex–restricted T cell–associated molecule) and 2B4 (*12*), may be particularly important in sustaining $CD4_{IEL}$ location. More studies will be required to examine $CD4_{IEL}$ functions.

Although the study of Sujino *et al.* demonstrates a function of $CD4_{IELs}$ in tolerance to dietary antigens, it is not clear how this function is carried out. Moreover, given that $CD4_{IELs}$ produce IFN-γ and that IFN-γ can induce dysbiosis (*13*), $CD4_{IELs}$ may contribute to pathology if inappropriately stimulated by IL-15 (*14*) or other stimuli. The study of $CD4_{IELs}$ in humans has just begun (*15*) and is likely to rapidly progress in both physiological and pathological settings. ■

REFERENCES

1. S. Z. Josefowicz, L. F. Lu, A. Y. Rudensky, *Annu. Rev. Immunol.* **30**, 531 (2012).
2. S. Sakaguchi *et al.*, *Nat. Rev. Immunol.* **13**, 461 (2013).
3. T. Sujino *et al.*, *Science* **352**, 1581 (2016).
4. H. Cheroutre, M. M. Husain, *Semin. Immunol.* **25**, 273 (2013).
5. D. Mucida *et al.*, *Nat. Immunol.* **14**, 281 (2013).
6. B. S. Reis *et al.*, *Nat. Immunol.* **14**, 271 (2013).
7. S. L. Bailey-Bucktrout *et al.*, *Immunity* **39**, 949 (2013).
8. M. Tsuji *et al.*, *Science* **323**, 1488 (2009).
9. D. Mucida *et al.*, *Science* **317**, 256 (2007).
10. M. G. Rooks, W. S. Garrett, *Nat. Rev. Immunol.* **16**, 341 (2016).
11. L. V. Hooper *et al.*, *Science* **336**, 1268 (2012).
12. V. S. Cortez *et al.*, *J. Exp. Med.* **211**, 623 (2014).
13. M. Raetz *et al.*, *Nat. Immunol.* **14**, 136 (2013).
14. B. Jabri, V. Abadie, *Nat. Rev. Immunol.* **15**, 771 (2015).
15. A. Takeuchi *et al.*, *J. Exp. Med.* **213**, 123 (2016).

10.1126/science.aag1719

ILLUSTRATION: K. SUTLIFF/*SCIENCE*

Downloaded from http://science.sciencemag.org/ on June 28, 2016

Published by AAAS

CLIMATE CHANGE

How climate change affects extreme weather events

Research can increasingly determine the contribution of climate change to extreme events such as droughts

By **Peter Stott**[1,2]

Human-induced climate change has led to an increase in the frequency and intensity of daily temperature extremes and has contributed to a widespread intensification of daily precipitation extremes (*1*, *2*). But has it also made specific extreme weather and climate events—such as floods, droughts, and heat waves—more likely? Although it has been said that individual climate events cannot be attributed to anthropogenic climate change (*3*), a recent assessment by the National Academies of Science concludes that "this is no longer true as an unqualified blanket statement" (*4*). Robust event attribution can support decisions such as how to rebuild after a disaster and how to price insurance by quantifying the current risk of such events.

The first annual report explaining extreme events of the previous year from a climate perspective was published in 2011 with six contributions (*5*). The latest report explaining events of 2014 (*6*) included 32 papers looking at 28 different events from all seven continents, covering a greatly increased range of event type, location, and impact. According to the National Academies of Science, this rapidly advancing scientific capability now makes it possible to "make and defend quantitative statements about the extent to which human-induced climate change has influenced either the magnitude or the probability of specific types of event or event classes" (*4*).

Most researchers use one of two methods for event attribution. In the first, they perform coupled climate model runs to simulate the likely evolution of climate with and without anthropogenic climate change (see the figure, top panel). They then choose a suitable index (such as seasonal mean temperature over a particular region) and calculate the likelihood of exceeding this index with and without climate change. For example, Sun *et al.* used this method to analyze the summer of 2013, the hottest on record in eastern China. They found that the likelihood of such extreme temperatures had increased by a factor of >60 as a result of human-induced climate change (*7*).

In the second method, researchers generate large ensembles of atmosphere-only models that sample the occurrence of the rare event of interest (such as rainfall in a river basin exceeding an extreme value), given observed sea surface temperature conditions (see the figure, bottom panel). They then compare the return periods of such events in ensembles with and without anthropogenic climate and calculate their changed likelihood. Using this method, Schaller *et al.* found no evidence that human-induced climate change had made the extreme precipitation in the Upper Danube and Elbe basins in May to June 2013 more likely (*8*).

A further proposed method assumes that the circulation regime or weather event is unchanged and determines whether climate change has altered its impact—for example, through altering the thermodynamic state of the atmosphere (*9*). A conditional approach to attribution can be helpful. Indeed, the second method described above estimates how the risk of events has changed, assuming that large-scale patterns of sea surface temperatures due to natural variability (for example, associated with El Niño or La Niña conditions) remain unchanged. But to relate recent events to their future likelihood of occurrence, attribution assessments cannot ignore the effects of circulation changes.

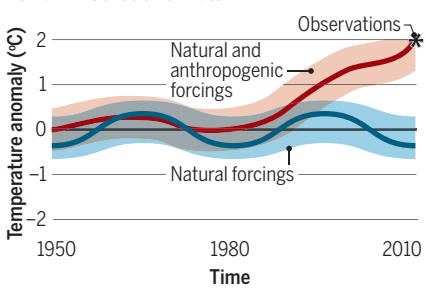
Attribution findings related to extreme temperature events tend to show much stronger evidence of human influence than for other types of events. This is because there tends to be a wealth of data on extreme hot and cold events, they can be captured accurately by models, and their relationship with anthropogenic climate change is usually well simulated. In contrast, extreme rainfall

Robust event attribution

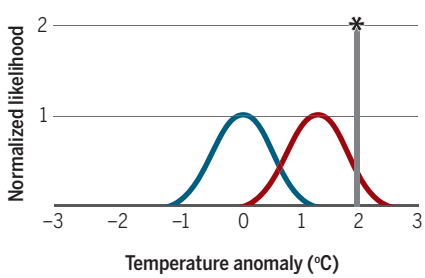
Scientists use two main approaches to determine the contribution of climate change to extreme weather events.

Approach 1

Observed and modeled temperature changes
Scientists compare changes in observed temperatures to modeled temperatures with or without human influence on climate.

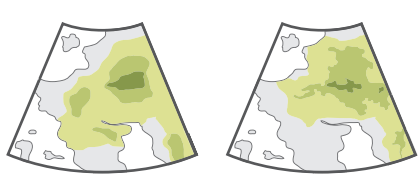


Distribution of possible temperatures
They use this comparison to assess how likely the observed temperatures are with and without human-induced climate change.

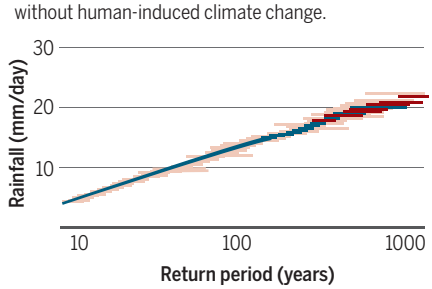


Approach 2

Observed and modeled rainfall distributions
Researchers look for rainfall events in the large ensembles of model runs that are similar to the observed rainfall event.



Return times for extreme rainfall events
They determine return times for such events in large model ensembles of model runs with and without human-induced climate change.



GRAPHIC: V. ALTOUNIAN/*SCIENCE*

[1]*Met Office Hadley Centre, Fitzroy Road, Exeter, EX1 3PB, UK.*
[2]*Department of Mathematics, University of Exeter, Exeter, EX4 4QF, UK. Email: peter.stott@metoffice.gov.uk*

Downloaded from http://science.sciencemag.org/ on June 28, 2016

Published by AAAS

events are often poorly observed, models can fail to represent them adequately, and their relationship with climate variability and change is often not well understood (*4*). Improved climate models, observational data sets, and theoretical understanding will be needed to improve the reliability of attribution findings for such events.

Recent initiatives, including the European project EUCLEIA (European Climate and Weather Events: Interpretation and Attribution) and the World Weather Attribution effort, seek to develop the science of event attribution. For such science to help societies become more resilient to climate variability and change, event attribution results need to be credible and relevant (*10*). Further improvements are needed in techniques for analyzing extreme events, tools to evaluate and communicate the robustness of event attribution results (*11*, *12*), and methodologies to link the effects of extreme events to their meteorological drivers (*13*). A model-based result by itself does not guarantee its utility (*3*). A convincing physically based storyline describing the event and its effects is also needed to support the legitimate use of such information for robust decision-making (*14*).

The increasingly routine nature of some temperature-based studies points the way toward an operational attribution capability in which trusted providers issue routine updates on recent events (*15*). The National Academies of Science recommended that such a capability be linked to the provision of probabilistic forecasts of extreme events at lead times of days to seasons or longer (*4*). Placing recent extreme events in the context of past and future climate variability and change would enhance the ability of societies to manage weather and climate-related risks. ■

REFERENCES

1. N. Bindoff *et al.*, in *Climate Change 2013: The Physical Science Basis. Contribution of Working Group I to the Fifth Assessment Report of the Intergovernmental Panel on Climate Change*, T. Stocker *et al.*, Eds. (Cambridge Univ. Press, Cambridge/New York, 2013), pp. 867–952.
2. X. Zhang *et al.*, *Geophys. Res. Lett.* **40**, 5252 (2013).
3. A. Solow, *Science* **349**, 1444 (2015).
4. *Attribution of Extreme Weather Events in the Context of Climate Change* (National Academies Press, Washington, DC, 2016).
5. T. Peterson *et al.*, *Bull. Am. Meteorol. Soc.* **93**, 1041 (2012).
6. S. Herring *et al.*, Eds., Explaining extreme events of 2014 from a Climate Perspective, *Bull. Am. Meteorol. Soc.* **96**, special supplement (2015).
7. Y. Sun *et al.*, *Nat. Clim. Change* **4**, 1082 (2014).
8. N. Schaller *et al.*, *Bull. Am. Meteorol. Soc.* **95**, S69 (2014).
9. K. E. Trenberth *et al.*, *Nat. Clim. Change* **5**, 725 (2015).
10. S. Sippel, *Weather Clim. Soc.* **7**, 224 (2015).
11. O. Bellprat, F. Doblas Reyes, *Geophys. Res. Lett.* **43**, 10.1002/2015GL067189 (2016).
12. F. Lott, P. Stott, *J. Clim.* 10.1175/JCLI-D-15-0566.1 (2016).
13. F. Otto, *Nat. Clim. Change* **6**, 342 (2016).
14. T. Shepherd, *Curr. Clim. Change. Rep.* **2**, 28 (2016).
15. P. Stott *et al.*, *WIRES Clim. Change* **7**, 23 (2016).

10.1126/science.aaf7271

OCEAN BIOLOGY

Corals' microbial sentinels

The coral microbiome will be key to future reef health

By **Tracy D. Ainsworth**[1] *and* **Ruth D. Gates**[2]

In 2005, Pandolfi *et al.* (*1*) asked whether U.S. coral reefs would in the future be overgrown and dominated by algae as a result of rapid change in the marine environment. Over a decade later, an increasing number of reefs worldwide have declined, and severe and lasting environmental changes are altering the composition of coral reefs that were once pristine and resilient. In the past 2 years, many reefs around the world have suffered from repeated bleaching (see the photo) as a result of high water temperatures caused by a strong El Niño event combined with climate change. Corals that survive the multiple impacts of climate change and local disturbance will form the basis of future reefs that will differ in fundamental ways from those considered healthy today (*2*). Changes to the coral microbiome on these reefs will play a vital part in future coral reef health (see the figure).

Microbial communities play central roles in animal health and ecosystem stability. Factors such as nutritional status, stress response, and disease are linked to shifts in the taxonomic composition of—and the interactions between—microbiomes and their hosts (*3*). There are also correlations between an organism's life span and its microbial complexity, structure, and function (*4*). Corals form integral and functionally important symbioses with prokaryotic microbes (forming a core symbiotic microbiome) (*5*). The implications of altered prokaryotic microbial partnerships for coral reefs are difficult to predict because little is known about the functional complexity of the undisturbed coral microbiome. However, knowledge from other systems suggests that altered microbiomes, representing a new stable state after disturbance, impair the host's metabolic state, disease resistance, and functional capacity (*6*).

One of the most extreme examples of the impacts of environmental stress on coral function is bleaching. Temperature stress of only 1°C above the physiological upper limit, as seen on coral reefs worldwide in the past 3 years, causes tropical reef corals to bleach. Bleaching reflects a reduced density of endosymbiotic algae (belonging to the dinoflagellate genus *Symbiodinium*) in the coral tissues. When these nutritionally beneficial endosymbionts are lost, coral health suffers and nutritional resources are depleted. These effects continue as long as adverse temperature conditions persist and can ultimately lead to the death of the coral.

In corals that bleach but survive, external conditions

Microbiome shifts

The shifting microbial complexity indicates the impact of climate change on the coral microbiome, host health, and population stability on coral reefs. The challenge to coral research is to understand the microbial contribution to alternate stable states on coral reefs.

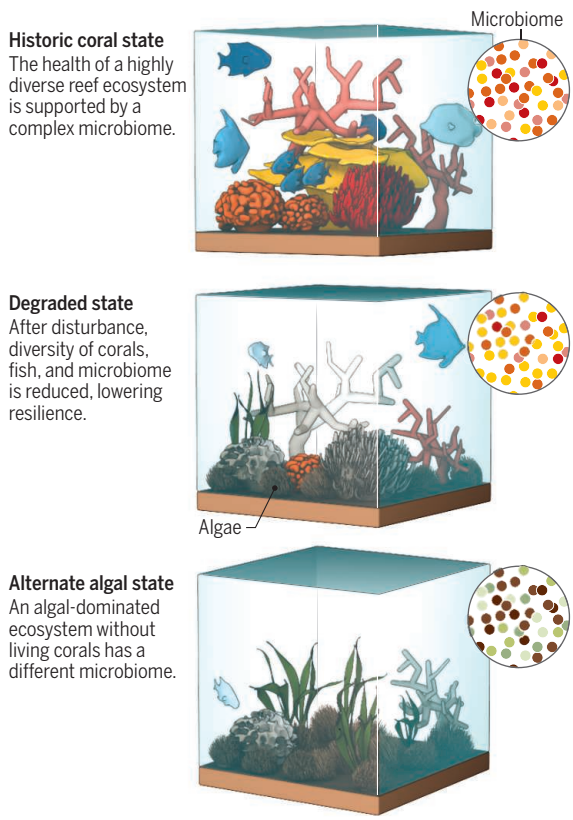


ILLUSTRATION: V. ALTOUNIAN/*SCIENCE*

Downloaded from http://science.sciencemag.org/ on June 28, 2016

Published by AAAS



Stress response. The past 2 years have seen widespread bleaching in coral reefs around the world, as shown here in the Maldives.

PHOTO: XL CATLIN SEAVIEW SURVEY

must return to normal for the repopulation of endosymbiotic algae and regeneration of the host tissue to occur. The drastic impact of bleaching on the coral animal and, ultimately, its microbiome can influence the immune system, alter the metabolic capacity, and impair the stress resistance of the surviving corals. Maintaining and/or reestablishing crucial functional contributions from the prokaryotic microbiome after events such as bleaching are key to coral survival, recovery, and prevention of disease. A microbial signature dominated by pathogens has been associated with bleaching mortality (*7, 8*), whereas in corals that survive bleaching, there is no rise in primary pathogens (*8, 9*). For example, of over 25,000 bacterial phylotypes identified on surviving Acroporid corals, only 14 bacteria of the pathogenic Vibrio genera were found; these pathogens were associated with just 2 of the 63 corals analyzed (*10*).

A shift toward a phylogenetically and functionally less diverse core symbiotic microbiome after bleaching, and in catastrophic stress survivors, would indicate the formation of a new metaorganism. As seen in other systems, new stable-state metaorganisms have altered functional capacity that can influence life history. In corals, the loss of beneficial bacteria has been linked to the development of lesions and tissue necrosis (*11*, *12*). Such changes to the surviving adult coral microbiome are likely to have far-reaching implications, including intergenerational impacts, as has been found in other organisms (*13*). As outlined by Pandolfi *et al.* (*1*), many factors shift the balance between survival and mortality on reefs. The influence of these environmental factors on the coral microbiome is not yet accounted for in estimates of coral response to climate change (*14*, *15*).

"The emergence of new ecosystem norms on coral reefs will be underpinned by changes to the microbiome...."

The coral microbiome is a critical element to the health of the corals that can influence the reef-wide response to growing environmental pressures. The emergence of new ecosystem norms on coral reefs will be underpinned by changes to the microbiome and the microbial contribution to organism health and stress resistance, under new environmental norms. Accounting for the influence of microbes in coral ecosystem stability will require an advance in our fundamental understanding of the establishment, diversity, and complexity of prokaryotic symbioses. Differentiating the elements of the microbiome that signify a loss of functional redundancy, altered stress resistance, mortal states (such as the rise of opportunistic microbes and primary pathogenesis), and disease will be crucial. ■

[1]ARC Centre of Excellence for Coral Reef Studies, James Cook University, Townsville, Australia, 4811. [2]Hawai'i Institute of Marine Biology, University of Hawai'i at Manoa, Honolulu, HI 96744, USA. Email: tracy.ainsworth@jcu.edu.au

REFERENCES AND NOTES

1. J. M. Pandolfi *et al.*, *Science* **307**, 1725 (2005).
2. I. A. van de Leemput, T. P. Hughes, E. H. van Nes, M. Scheffer, *Coral Reefs* 10.1007/s00338-016-1439-7 (2016).
3. S. Krause *et al.*, *Front. Microbiol.* **5**, 251 (2014).
4. L. Fontana, L. Partridge, *Cell* **161**, 106 (2015).
5. T. D. Ainsworth *et al.*, *ISME J.* **9**, 2261 (2015).
6. C. Zhang *et al.*, *Nat. Commun.* **4**, (2013).
7. R. Vega Thurber *et al.*, *Environ. Microbiol.* **11**, 2148 (2009).
8. J. R. Zaneveld *et al.*, *Nat. Comm.* **7**, 11833 (2016).
9. R. Littman, B. L. Willis, D. G. Bourne, *Environ. Microbiol.* **3**, 651 (2011).
10. D. Ogawa, thesis, James Cook University, Townsville, Australia (2014).
11. J. L. Meyer, V. J. Paul, M. Teplitski, *PLOS ONE* **9**, e100316 (2014).
12. B. Glas, G. J. Herndl, P. R. Frade, *ISME J.* 10.1038/ismej.2016.9 (2016).
13. J. K. Goodrich, E. R. Davenport, J. L. Waters, A. G. Clark, R. E. Ley, *Science* **352**, 532 (2016).
14. N. Knowlton, M. Leray, in *Coral Reefs in the Anthropocene*, C. Birkeland, Ed. (Springer, Dordrecht, Netherlands, 2015), pp. 117–132.
15. T. D. Ainsworth, R. V. Thurber, R. D. Gates, *Trends Ecol. Evol.* **25**, 233 (2010).

ACKNOWLEDGMENTS

We acknowledge funding from the Australian Research Council (Discovery Program Grant DP130101421; Super Science Program FS110200046; and Centre of Excellence for Coral Reef Studies CE0561435) and the University of Hawai'i. We thank B. Leggat for editorial assistance and D. Tracy for graphic design.

10.1126/science.aad9957

Published by AAAS

Downloaded from http://science.sciencemag.org/ on June 28, 2016

ASTRONOMY

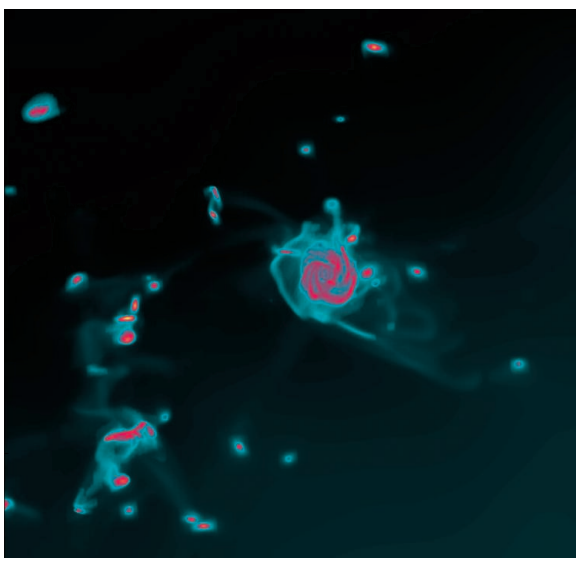
When the universe became dusty

Observations from high-redshift galaxies reveal details of early universe evolution

By **Carlos De Breuck**

Observations of the most distant galaxies known are now reaching into the epoch when the first generations of stars were being formed. As stars are the main factories of elements heavier than hydrogen and helium, one also expects to see a reduced abundance of these heavy elements and of the dust that condenses out of them. Recent observations of galaxies within 1 billion years of the Big Bang have shown that the far-infrared (far-IR) emission from dust in these galaxies indeed becomes fainter. Also, the usually strong far-IR emission line from ionized carbon remains undetected in an increasing number of galaxies of redshift $z > 7$ (*1*–*3*). Hence, it has been assumed that detailed studies of the interstellar medium (ISM) in these galaxies will be very challenging, even with the powerful Atacama Large Millimeter/submillimeter Array (ALMA). On page 1559 of this issue, Inoue *et al*. (*4*) detect doubly ionized oxygen at a rest wavelength of 88 μm from a galaxy at $z = 7.2$, where neither dust nor ionized carbon was detected. The oxygen to far-ultraviolet luminosity ratio in this galaxy is similar to nearby dwarf galaxies with an oxygen abundance of 10 to 60% that of the Sun (*5*), which suggests that some substantial chemical enrichment has already occurred. However, the similarities stop there; in dwarf galaxies, the dust and ionized carbon lines are not as faint. It appears that the dust in this young galaxy may not have formed yet, or that it was destroyed, for example, by supernova shock waves.

As in several other galaxies at similar redshifts (*3*), there is an indication that faint ionized carbon is detected a few kiloparsecs from the galaxy. These offsets have been explained in galaxy evolution models (*6*) and are consistent with the idea that the first generations of stars disrupt the central parts of primordial galaxies from the inside, while the outer regions are still seen as they trace the accreting gas fueling the stars. This effect is further strengthened by the low amounts of heavy elements and dust that normally shield the molecules inside gas clouds from the highly energetic photons emitted by the young stars. In slightly less distant galaxies of similar mass at $z = 5$ to 6, the carbon emission is already detected, but the far-IR dust emission still appears an order of magnitude fainter than in $z < 3$ galaxies that have nearly solar fractions of heavy elements (*7*). It thus appears that the epoch around $z = 6$ is a key moment in the history of the dust production in typical galaxies, where sufficient heavy elements have been produced to allow the dust to survive the strong ultraviolet radiation field from the very energetic young stars.



Dust building up. Gas density distribution of the simulated $z \approx 7$ galaxy "Dahlia," similar to the one observed by Inoue *et al*. (*4*). The image is 5 arc sec on a side, corresponding to about 30 kpc. Note that the gas in Dahlia is distributed in a disklike structure; note also the large number of infalling satellites (*14*).

The appearance of dust is a lot faster in more massive galaxies. Recent observations with ALMA and the Plateau de Bure Interferometer of the Institut de Radio Astronomie Millimetrique of quasars at $6.6 < z < 7.1$ show strong detections in both the dust and carbon line (*8*), and dusty star-forming galaxies selected by means of their copious dust emission have now also been found at similar redshifts. They also emit strong carbon (*9*, *10*) and oxygen (*11*) lines. The dust production in these galaxies thus appears to be more efficient (*12*), and/or the more massive host galaxies are more efficient in preventing the destruction of the dust by the massive young stars.

To understand the different evolution of these normal and more massive galaxies, further information on their ISM is essential. Because of the high redshift of these objects, they can no longer be detected with optical telescopes, and these galaxies are often too faint to detect any other line than Lyman-α with ground-based near-IR instruments. Deep integrations with the soon-to-be-launched James Webb Space Telescope would be required to detect these faint tracers of heavy elements.

Good alternatives are the far-IR fine-structure lines from carbon, nitrogen, and oxygen, which can normally only be observed from space. At $z > 5$, these lines conveniently shift into the atmospheric windows that can be observed from the ground with ALMA. Combined studies of these lines can constrain the ionization state, gas density, temperature, and even the amount of heavy elements. Modeling of the ionized gas regions with varying amounts of heavy elements shows that the 88-μm oxygen line remains the strongest among the bright far-IR fine structure lines (*13*). The far-IR oxygen line detection of Inoue *et al*. thus shows that the future of ISM studies of galaxies in the epoch of reionization is very promising. ■

European Southern Observatory, 85748 Garching, Germany, and Kavli Institute for Theoretical Physics, Santa Barbara, CA 93106, USA. Email: cdebreuc@eso.org

REFERENCES AND NOTES

1. M. Ouchi *et al*., *Astrophys. J.* **778**, 102 (2013).
2. D. Schaerer *et al*., *Astron. Astrophys.* **574**, A19 (2015).
3. R. Maiolino *et al*., *Mon. Not. R. Astron. Soc.* **452**, 54 (2015).
4. A. K. Inoue *et al*., *Science* **352**, 1559 (2016).
5. D. Cormier *et al*., *Astron. Astrophys.* **578**, A53 (2015).
6. L. Vallini *et al*., *Astrophys. J.* **813**, 36 (2015).
7. P. Capak *et al*., *Nature* **522**, 455 (2015).
8. B. Venemans *et al*., *Astrophys. J.* **816**, 37 (2016).
9. D. Riechers *et al*., *Nature* **496**, 329 (2013).
10. B. Gullberg *et al*., *Mon. Not. R. Astron. Soc.* **449**, 2883 (2015).
11. C. Ferkinhoff *et al*., *Astrophys. J.* **714**, L147 (2010).
12. M. Mancini *et al*., *Mon. Not. R. Astron. Soc.* **451**, L70 (2015).
13. A. Inoue *et al*., *Astrophys. J.* **780**, L18 (2014).
14. S. Gallerani *et al*., http://arxiv.org/abs/1604.05714 (2016).

ACKNOWLEDGMENTS

Supported by NSF grant NSF PHY11-25915.

10.1126/science.aaf9761

PHOTO: ANDREA PALLOTINI

Downloaded from http://science.sciencemag.org/ on June 28, 2016

Published by AAAS

ORGANIC DEVICES

Avoid the kinks when measuring mobility

Transistor measurements can overstate organic semiconductor charge carrier mobility

By **Iain McCulloch,[1,2] Alberto Salleo,[3] Michael Chabinyc[4]**

The ability to make flexible electronics enables us to envision new types of devices such as durable displays, implantable bioelectronics, and sensors seamlessly integrated in everyday items (*1*). Furthermore, the power and flexibility of organic chemistry to design new semiconductors has been a strong driver for an unprecedented effort in materials development worldwide (*2*). A key materials parameter is the mobility of charge carriers, which is often determined by building a field-effect transistor (FET) with the material. We outline why such measurements, which are indirect and depend on the appropriate use of device models, only provide apparent mobilities that can, in some cases, overstate the real values by more than an order of magnitude.

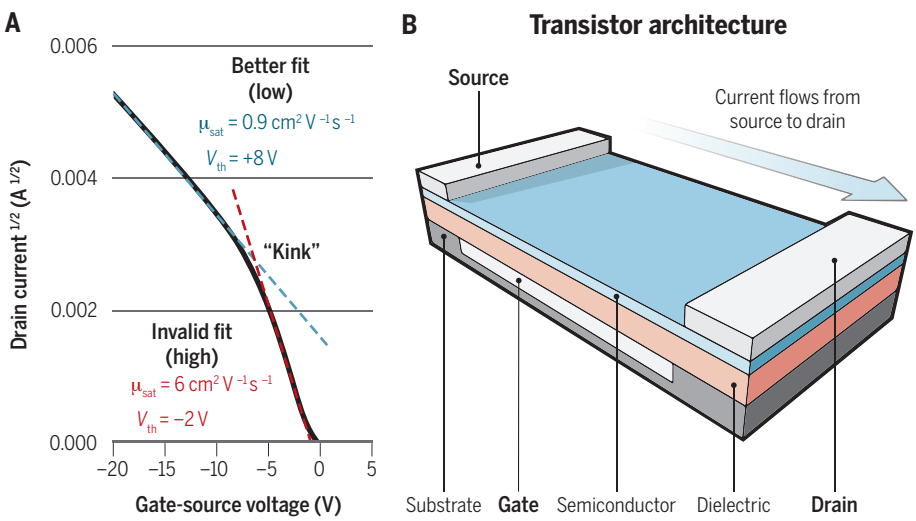
Electronic devices operate by controlling how charge carriers—electrons and holes—move through semiconductors, and higher carrier mobilities lead to faster circuitry. Carrier mobility is the first materials property measured to benchmark improved performance of new organic semiconductors. Targeted mobility values in FETs, often considered the building blocks of electronic circuits, are on the order of 10 $cm^2\ V^{-1}\ s^{-1}$ or larger. Accurate mobility values are needed by synthetic chemists to validate molecular design concepts aimed at improving charge transport and by circuit designers to ensure that devices can perform their functions.

Nonetheless, a correct measurement of carrier mobility in organic semiconductors has proven challenging (*3*, *4*). Organic semiconductors are van der Waals solids with weak intermolecular interactions and strong structural anisotropy, so their properties are at the edge of the applicability of well-known transport models developed for inorganic semiconductors (*5*). Furthermore, the presence of disorder and nonconventional transport mechanisms has severely limited the use of common techniques such as the measurement of the Hall voltage. Finally, the strong dependence of mobility on thin-film microstructure, originating from specific fabrication conditions, compels experimentalists to measure these electronic properties in the actual devices of interest rather than in idealized model structures.

As a result, carrier mobility is often measured in FETs. However, transistor characteristics only provide a current-voltage relation that aggregates contributions from many factors present in a device, including charge injection and carrier concentration effects, and do not directly measure carrier mobility. In principle, detailed modeling is needed to extract the mobility rigorously, but the most popular transistor model used in organic electronics relies on the gradual-channel approximation, which posits a simple carrier distribution comprising only one type of carrier in the channel and neglects contact effects. The characterization of an FET based on a fit to a particular model provides an "apparent mobility of carriers in a device," and the numbers are meaningful only if device operation conforms to the model's assumptions.

The carrier mobility is frequently derived from transfer characteristics, which describe the dependence of the device current on charge density, which is in turn controlled by the voltage on the gate electrode. Mobility is calculated by making use of the ideal gradual-channel approximation, which was sufficient in the early development of organic electronics when the current was limited by the organic semiconductor. For newer, high-performance materials, the organic semiconductor, in many cases, is not the limiting factor. The emergence of this new condition is apparent in many recent reports (*6*–*8*), where substantial nonidealities in the characteristics of FETs are observed. The typical manifestation of this nonideality is the existence of a downward kink in the transfer characteristics of the FET, as shown in the figure, as well as a pronounced dependence on the history of electrical biasing of the device.

Recently, several groups have taken a closer look at some irregularities in the characteristics of previously reported high-performance organic FETs, drawing the common conclusion that the conventional methods to extract carrier mobility cannot be used when devices exhibit nonideal characteristics (*9*–*11*). For example, deviations from ideal behavior have been observed



A misleading kink. (**A**) An example of the "kink-down" feature exhibited in the nonideal transfer characteristics of a rubrene small-molecule semiconductor device [reproduced from (*8*)]. The difference in the extracted apparent mobility of the two regions of the plot is shown as red and blue extrapolations. The true mobility of the semiconductor is closer to the value in blue. (**B**) Illustration of a FET architecture, with bottom gate, top contacts (light gray), dielectric (red), semiconductor (blue), and substrate (dark gray).

[1]*King Abdullah University of Science and Technology, KSC, Thuwal 23955-6900, Saudi Arabia.* [2]*Department of Chemistry and Centre for Plastic Electronics, Imperial College London, London SW7 2AZ, UK.* [3]*Department of Materials Science and Engineering, Stanford University, Stanford, CA 94305, USA.* [4]*Materials Department, University of California Santa Barbara, Santa Barbara, CA 93106-5050, USA. Email: i.mcculloch@imperial.ac.uk*

GRAPHIC: C. BICKEL/*SCIENCE*

Downloaded from http://science.sciencemag.org/ on June 28, 2016

Published by AAAS

with polymers where both electrons and holes can be injected into the channel of the device. Localized electron trapping near one contact invalidated a key assumption of the gradual-channel approximation. The use of the simple transistor equations resulted in an overestimation of the hole mobility by a factor exceeding 20, 14 $cm^2 V^{-1} s^{-1}$, rather than a more likely value of 0.6 $cm^2 V^{-1} s^{-1}$ (*10*). Another type of nonideality occurs when non-ohmic injection from the electrodes generates a gate-bias dependence of the contact resistance. Single-crystal rubrene FETs with severely non-ohmic contacts also led to an overestimation of the mobility by more than an order of magnitude (*9*).

Without a robust and reliable method to determine carrier mobility as an intrinsic materials property, chemists dedicated to the synthesis of improved organic semiconductors can easily pursue erroneous design principles based on inaccurate literature values of mobility. For example, notable instances of these nonidealities are observed in the characteristics of recent polymers synthesized from a highly polar, electron-deficient diketopyrrolopyrrole (DPP) conjugated monomer (*12*). This repeat unit generates a high electron affinity that can facilitate electron injection in hole-based devices, thereby invalidating the use of formulas derived from the gradual-channel approximation to extract mobility. Molecular design principles for this class of polymers developed from these mobility values may thus be unsubstantiated and, in fact, impede an understanding of the fundamental structure-property relations. Furthermore, high mobilities obtained from nonideal characteristics may set erroneous benchmarks for device design. Until better models and solutions to eliminate nonidealities are found, the best prescription is conservatism on absolute metrics and trends, particularly with small differences in electrical properties, as suggested in a number of recent commentaries (*13*). ■

REFERENCES

1. A. C. Arias, J. D. MacKenzie, I. McCulloch, J. Rivnay, A. Salleo, *Chem. Rev.* **110**, 3 (2010).
2. A. Facchetti, *Chem. Mater.* **23**, 733 (2011).
3. C. Reese, Z. Bao, *J. Appl. Phys.* **105**, 024506 (2009).
4. H. T. Yi, Y. Chen, K. Czelen, V. Podzorov, *Adv. Mater.* **23**, 5807 (2011).
5. N. F. Mott, E. A. Davis, *Electronic Processes in Non-Crystalline Materials* (Oxford Univ. Press, 1979).
6. J. Li *et al.*, *Sci. Rep.* **2**, 754 (2012).
7. Z. Chen *et al.*, *Adv. Mater.* **24**, 647 (2012).
8. H.-R. Tseng *et al.*, *Adv. Mater.* **26**, 2993 (2014).
9. E. G. Bittle, J. I. Basham, T. N. Jackson, O. D. Jurchescu, D. J. Gundlach, *Nat. Commun.* **7**, 10908 (2016).
10. T. Okachi, T. Kashiki, K. Ohya, *Proc. SPIE* **9568**, 10.1117/12.2187572 (2015).
11. T. Uemura *et al.*, *Adv. Mater.* **28**, 151 (2016).
12. C. B. Nielsen, M. Turbiez, I. McCulloch, *Adv. Mater.* **25**, 1859 (2013).
13. H. Sirringhaus, *Adv. Mater.* **26**, 1319 (2014).

10.1126/science.aaf9062

BIOMEDICAL ENGINEERING

Capitalizing on convergence for health care

Integrate physical sciences, engineering, and biomedicine

By **Phillip Sharp, Tyler Jacks, Susan Hockfield***

POLICY

For decades, scientists have called for more collaboration between the life and physical sciences, and in the past 5 years, we have been among those calling for a new national research strategy—one we call "convergence"—that would integrate engineering, physical, computational, and mathematical sciences with biomedical science (*1*). Thanks to the accelerating pace of biological discovery, the expanding power of computation, and a new focus in engineering on biocompatible materials and nanotechnology, the potential of such a strategy for advances in health care is greater than ever (see the photo). Technologies emerging from such efforts have potential implications far beyond health care: creating jobs; speeding products to market; and improving everything from agriculture and the environment to defense, the economy, and energy production. It all adds up to a moment of unprecedented opportunity, if we choose to invest in it meaningfully. But so far we have not. We detail below, and in greater depth in a new report with colleagues from across the country (*2*), the stakes in the convergence revolution and what we should do to capitalize on it.

> ***"The report recommends...an interagency working group on convergence with NIH, NSF, Department of Defense, FDA, and DOE...."***

Convergence and interdisciplinary research are closely allied, but convergence goes beyond collaboration. It involves integration of historically distinct disciplines and technologies into a unified whole that creates new pathways and opportunities. It is this integration that offers potentially revolutionary change for biomedical sciences. Consider the changes resulting from the 20th century's great convergence, which brought together physical sciences and engineering and which gave us tools that have reshaped our world—radios, telephones, cars, planes, computers, nuclear power, satellites, and the Internet. We can promote another era of transformational tools and technologies in health care if we invest in and commit our agencies, institutions, and ingenuity.

Yet only 3% of the principal scientists receiving research grants today from the U.S. National Institutes of Health, the major source of research funding for biomedical science, come from physics, biophysics, mathematics, engineering, or bioengineering (*3*). The National Institute of Biomedical Imaging and Bioengineering (NIBIB, NIH), which is primarily focused on convergence-related research, has a 2016 budget just short of $345 million (*4*). That amounts to only ~1% of the total NIH budget. Among federal agencies, the National Science Foundation (NSF) is the primary source of support for basic engineering and physical sciences, but the level of funding in the convergence of these disciplines with biomedical science is miniscule, because NSF has historically deferred to NIH on medical research (*5*, *6*). Although other federal agencies—such as the Department of Energy (DOE), Defense Advanced Research Projects Agency (DARPA), and Food and Drug Administration (FDA)—are beginning to recognize the promise of convergence, to date, no federal agency or office has the primary responsibility to promote the convergence of engineering, physical, and mathematical sciences with biomedical sciences. Difficulty in securing federal funding for projects that cross disciplines has impeded progress.

HOW FAR HAVE WE COME? Although investment has been far too modest in our view, we applaud efforts already under way that can serve as models and test beds for efforts to come. Several federal agencies have embraced convergence initiatives. The NIBIB has been awarding convergence-related grants since 2002. DARPA launched a Biological Technologies Office in 2014 to harness "the power of natural systems" as it develops smart prosthetics and strategies to combat brain disorders and infectious disease. The recently launched BRAIN Initiative (*7*), designed to revolutionize our

*Massachusetts Institute of Technology, Cambridge, MA 02139, USA. *Correspondence to: hockfield@mit.edu*

Downloaded from http://science.sciencemag.org/ on June 28, 2016

Published by AAAS



Convergence at work. Microfabricated device by Stephen Quake, Stanford University, for sequencing DNA from one sperm.

CREDIT: PHOTO COURTESY OF THE LEMELSON-MIT PROGRAM

understanding of the human brain, and the Precision Medicine Initiative (*8*), which aims to use big data analytics to evaluate information about disease at the level of individuals, both have built the interdisciplinary potential of convergence into their research models. The same is true for the recent National Microbiome Initiative (*9*). These initiatives have been encouraged by early support from foundations such as Kavli, Howard Hughes, Raymond and Beverly Sackler, and Simons and from the Burroughs Wellcome Fund.

Several academic institutions have made promising commitments to convergence in the recent past. Northwestern University's International Institute for Nanotechnology has brought together chemistry, bioscience, and engineering to develop tools for nanomedicine and nano-oncology. At the University of California, the California Institute for Quantitative Biosciences applies the techniques of physics, chemistry, and computer science to challenges of molecular biology. The Wyss Institute for Biologically Inspired Engineering at Harvard crosses disciplinary and institutional lines to develop innovative engineering solutions, commercial products, and therapies in multiple fields. At Massachusetts Institute of Technology (MIT), the David H. Koch Institute for Integrative Cancer Research has brought together engineers, biologists, and clinical oncologists to develop new insights and create tools to better diagnose, treat, and prevent cancer.

These programs, along with many others like them, are uncoordinated and modest in the big picture but have already generated impressive results (*2*). Dozens of companies have been spun out, many with products now in clinical trials: nanoparticles that home in on cancer cells to deliver chemotherapy directly, imaging technologies that allow surgeons to more accurately spot and remove cancer cells, and much more. These efforts have the important benefit of training a generation of scientists and engineers across disciplines to become facile and conversant in a range of fields in order to take full advantage of opportunities.

Many businesses have also moved into this space. Verily (formerly Google Life Sciences) is combining genomics with high-content and high-resolution imaging to develop individualized treatments based on biological, genetic, behavioral, and environmental data. Companies such as Apple, IBM, and Microsoft have invested and brought to market innovations that allow people and institutions to track and monitor individual health, fitness, and disease.

HOW CAN WE GO FURTHER? Despite these indicators of progress, there is reason for concern, and there are lessons to be learned. The new report makes several recommendations to improve and accelerate convergence: a substantial and sustained increase in federal funding for biomedical research that explicitly targets funds for convergence programs; a revision of grant-review mechanisms to include expertise from engineering, computation, and physical sciences; and, at colleges and universities, a realignment of academic structures to facilitate research and educational collaborations among biologists, clinicians, mathematicians, physicists, engineers, and computational scientists. The NIH will have a major role to play: It should aggressively develop convergence-technology strategies and recruit mathematicians, engineers, physicists, and computational scientists to apply their expertise to our biomedical challenges, in both fundamental and applied research. Although several federal agencies have already embarked on programs that embrace convergence, these efforts should expand. We are encouraged by NSF's new convergence-research emphasis and its planned changes to its grant reviews and new education models to support convergence models.

Big things will happen if we can align objectives across disciplines and provide funding and programs to foster working together. The report recommends creating an interagency working group on convergence with NIH, NSF, Department of Defense, FDA, and DOE, coordinated through the Office of Science and Technology Policy. In addition, a specific strategic plan for advancing biomedical science through convergence patterned on the Nanotechnology and Plant Genome initiatives should be developed. NIH's Common Fund mechanism should support convergence across multiple institutes and centers. Federal agencies should consider more traineeships with convergence research tracks and on a larger scale. Transformation of biomedical and health care by convergence depends on openness to change and the will to work together. This is clearly emerging but needs to be further strengthened. ■

REFERENCES AND NOTES

1. P.A. Sharp, R. Langer, *Science* **333**, 527 (2011).
2. MIT, "Convergence: The future of health" (MIT, Cambridge, MA, 24 June 2016).
3. NIH, RePorter Data; https://projectreporter.nih.gov/reporter.cfm.
4. NBIB, Budget (NIH, Bethesda, MD, 2016); https://www.nibib.nih.gov/about-nibib/budget.
5. For example, the highly convergent Chemical, Bioengineering, Environmental, and Transport Systems Division at NSF received just $184 million in fiscal year (FY) 2016 to fund not only research in biomedical engineering and engineering health care but in environmental and transportation research, as well (*6*).
6. AAAS, Guide to the President's Budget: Research & Development FY 2017 (AAAS, Washington, DC, 2016), p. 51; www.aaas.org/sites/default/files/AAAS%20R%26D%20Report%20FY17%20web.pdf.
7. The White House, Brain Initiative (WhiteHouse.gov, 2013); https://www.whitehouse.gov/BRAIN.
8. The White House, President Obama's Precision Medicine Initiative (WhiteHouse.gov, 2015); https://www.whitehouse.gov/precision-medicine.
9. The White House, National Microbiome Initiative (WhiteHouse.gov, 2016); http://bit.ly/MicrobiomeInitiative.

10.1126/science.aag2350

Downloaded from http://science.sciencemag.org/ on June 28, 2016

Published by AAAS



Cutting-edge research and technological advances are ushering in a new era of human reproduction.

HUMAN REPRODUCTION

Making babies

Advances in genetics introduce new promise and perils into the business of being born

By **Dov Greenbaum**

In the 200 years since the genesis of Mary Shelley's *Frankenstein*, many have found the story to be a useful source of metaphors for rebuffing efforts to extend science beyond society's comfort zones. Perhaps the clearest example is the widespread application of the "Franken" prefix as a tool to reflect a prevalent uneasiness with areas of science research that seem instinctively "wrong." However, perhaps a more apt metaphor can be found in the 1931 film adaptation's enraged mob. Here, seemingly, without second-guessing their sources, the townspeople set out to destroy the monster. Despite extraordinary advances in recent years, and substantial research supporting its safety and efficacy, there remain large and loud factions who not only are fearful of the use of genetic technologies in modern medicine but also actively campaign to prevent further advancements and applications.

Two authors have recently tried to enlighten readers on this topic: Paul S. Knoepfler, a prolific blogger and well-known stem cell researcher at the University of California, Davis, and Henry T. Greely, professor of law at Stanford University and director of the Center for Law and the Biosciences.

Knoepfler's *GMO Sapiens* is a down-to-earth introduction to the human use of new genetic technologies. An easy and enjoyable read, the book is targeted to an audience that has a general interest in, but perhaps a minimal understanding of, science. Knoepfler cautiously guides his reader through the emerging technologies that will allow humans to more easily alter our genetic codes. Throughout, he generously sprinkles personal anecdotes and interviews with many of the relevant personalities. In appreciation of his audience, Knoepfler provides only short and relatively simplified explanations of a number of complicated technological issues, including in vitro fertilization (IVF), stem cells, cloning, genetically modified organisms (GMOs), CRISPR, sex selection, and other technologies and their applications. He also addresses a number of relevant legal concerns, including, for example, the Genetic Information Nondiscrimination Act (GINA). Perhaps best summarizing his position, in the penultimate chapter, Knoepfler invites readers to imagine the promise of human genetic modification: "Totally new types of people could be made in such a fearless new world. It could be both wondrous and disastrous. I am inclined to believe it would be more disastrous, but it is thought-provoking and even fun to think about the possibilities from a strictly hypothetical perspective."

Readers looking for a more in-depth analysis of human genome modifications and reproductive technologies and their legal and ethical implications should strongly consider picking up Greely's *The End of Sex and the Future of Human Reproduction*. Whereas Knoepfler's book will make you look smart at your next cocktail party, Greely's will prepare you to attend a professional symposium on human reproduction or, alternatively, a legal conference on the relevant bioethics.

Greely's breezy first-person narrative belies the extraordinary depth and impressive quality of information provided, both scientific and legal. He does not dumb down the material; rather, he expects his audience to look up medical and legal terminology and jargon themselves, when necessary.

The End of Sex is organized into three distinct sections, punctuated by brief interludes that summarize the material covered and outline the goals of the next section. In "The Science," Greely describes the underlying advances in stem cell and genetics technology that will result in cheap, easy, and reliable alternatives to current technologies. "The Pathway" outlines Greely's speculation about the eventual outcomes of these technologies. One particular projection involves a reproduction technique that will allow for the relatively easy selection of a child's genetic attributes, an option Greely refers to as easy preimplantation genetic diagnosis or "easy PGD." In the book's third section, "The Implications," Greely provides a thorough analysis of the ethical, legal, and social implications of easy PGD. Here, he substantially tackles issues including safety, family relationships, fairness, justice, equality, coercion, enforcement, and implementation. He also engages with the visceral reactions that may play a significant role in guiding potential policies. Many of the tools Greely provides are also relevant in other bioethical questions.

Although both books have the potential to empower readers to make informed decisions about the implementation of advancements in genetics technologies, it is unlikely that either will convince the enraged mobs to put aside their pitchforks. At least the rest of us will be better informed.

10.1126/science.aaf8469

GMO Sapiens
The Life-Changing Science of Designer Babies
Paul Knoepfler
World Scientific, 2016. 282 pp.

The End of Sex and the Future of Human Reproduction
Henry T. Greely
Harvard University Press, 2016. 391 pp.



The reviewer is at the Zvi Meitar Institute for Legal Implications of Emerging Technologies, Radzyner Law School, Interdisciplinary Center, Herzliya, Israel; and Department of Molecular Biophysics and Biochemistry, Yale University, New Haven, CT, USA. Email: dov.greenbaum@yale.edu

PHOTO: SAMI SERT/ISTOCKPHOTO.COM

Downloaded from http://science.sciencemag.org/ on June 28, 2016

Published by AAAS

PUBLIC HEALTH

The best-studied people on the planet

A history of the longest-running birth cohort study reveals how much has been learned from the lives of 70,000 Britons

By **Alireza Salehi Nejad**

Cohort studies, the empirical longitudinal research of people with a common characteristic, have played a crucial role in enhancing medical care and have dramatically reduced the risk of early death by revealing potential risk factors and unanticipated dangers. In *The Life Project: The Extraordinary Story of 70,000 Ordinary Lives*, Helen Pearson explores the world's oldest and longest-running birth cohort study, which has tracked the lives of five generations of Britons for seven decades.

A few months after the end of World War II, researchers with the National Survey of Health and Development set out to record details about the births of almost every child born in England, Scotland, and Wales in the first full week of March 1946. The researchers conducted elaborate interviews with a total of 13,687 mothers, asking them everything from how many rooms were in the family's home to how many diapers had been purchased for the new arrival. The study has been carefully following the lives of 5362 of those children ever since, with new cohorts added in 1958, 1970, 1991, and 2000. The more than 70,000 Britons who are being tracked are some of the best-studied people on the planet.

The Life Project draws from more than 150 interviews that Pearson conducted with people involved in the project over the course of 5 years and is enriched with historical details attained from academic publications and historical archives. In addition to scrutinizing the subjects' health, well-being, and life circumstances, comprehensive survey data have been collected from their parents, teachers, school doctors and nurses, youth employment officers, and other administrative sources. Blood, placental tissue, fingernails, hair, and teeth have been collected from later cohorts, prompted by advances in our understanding of genetics and enthusiasm for the Human Genome Project. Nearly 1.5 million biological samples have been archived from the 1991 cohort alone.

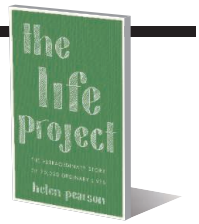
Early data collected via the cohort studies revealed that low income was a major source of risk to a child's health and survival. For example, women in the lowest socioeconomic classes were found to be 70% more likely to have stillborn babies than women of higher socioeconomic status, and children from poor families tended to grow more slowly, ending up shorter, on average, than their wealthier counterparts. Disadvantaged children were also more likely to struggle in school and were more likely to be under- or unemployed in adulthood. "It seems obvious today that social conditions such as poverty or poor housing should affect people's health," writes Pearson. "… [But] in an era in which huge swathes of the population were struggling to get enough to eat, the sorry truth is that many doctors just weren't that concerned about the effects of poverty on health." These and other analyses of social equality prompted major improvements in health services and were an important driver behind the decision to provide free, government-sponsored perinatal care when the National Health Service was launched in 1948.



Members of the first cohort celebrated their 70th birthday in March 2016.

The reviewer is at the Faculty of World Studies, University of Tehran, Tehran, Iran. Email: arash@a-salehi.co.uk

The Life Project
The Extraordinary Story of 70,000 Ordinary Lives
Helen Pearson
Soft Skull Press, 2016.
409 pp.



Whereas the cards are clearly stacked against some before birth, the studies also revealed that it is possible to escape from disadvantage and triumph over adversity. The scientists identified several factors—including parents who are interested in their children's lives, rigorous school environments, inherent motivation, and geographical location—as among the predictors of future prosperity and success.

Since their inception, the birth cohort studies have tackled an impressive array of topics, including corporal punishment in schools, the risks associated with home versus hospital births, the health effects of smoking and pollution, and the rise of chronic diseases. More than 2500 papers and books have been published on the 1958 cohort alone; more than 770 have been published on the 1970 cohort.

In March 2011, the same week that members of the original cohort celebrated their 65th birthdays, funding for a new cohort was announced. The scale of the proposed study would have been ambitious: "80,000 babies, warehouses of stool samples and placentas, gigabytes of video clips, several hundred thousand questionnaires and much more."

Unfortunately, funding for the study was cut when researchers were unable to recruit a sufficient number of expectant mothers. Scientists had expected to sign on some 16,000 women in the first 18 months of the study. Only 249 had signed up between January and June.

New cohorts were proposed in 2012 and again in 2015; however, neither succeeded in attaining the required funding. Given how much more there is left to learn about human health, there is little doubt that another cohort study will be proposed in the future. "Maybe your children or grandchildren will be enrolled in it—or perhaps they will even run it," writes Pearson. "Perhaps those children will help resolve some of the mysteries about science and society that 70,000 lives, so far, have not."

10.1126/science.aaf8256

PHOTO: © ROGER ALLEN PHOTOGRAPHY/STOCKIMONEWS/ALAMY STOCK PHOTO

Downloaded from http://science.sciencemag.org/ on June 28, 2016

Published by AAAS

LETTERS

Edited by **Jennifer Sills**

Reduce, relegalize, and recycle food waste

J. ASCHEMANN-WITZEL ("WASTE not, want not, emit less," Perspectives, 22 April, p. 408) describes the challenges and benefits of reducing food waste, but does not discuss what to do with the food waste that remains. Because not all food waste is avoidable, it is critically important to pair efforts to reduce food waste with legislation that allows resource-efficient recycling of food waste when it does arise. Europe has yet to seize this opportunity for sustainability.

Countries such as South Korea already understand the importance of twinning food waste reductions with improved disposal. Since 2005, South Korea has reduced household and restaurant food waste by 30 to 40% while simultaneously improving food waste recycling. The disposal of food waste in landfills is banned, and 85% of food waste is recycled as animal feed or compost (*1*).

Europe lags behind. The European Union's Waste Directive stipulates that by 2025 no biodegradable waste (including food waste) should be sent to landfills, but progress toward this target is highly variable. Although some nations, including Germany and the Netherlands, do divert food waste, across the whole of the EU-27 approximately 40% of municipal waste (including food waste) is still sent to landfills (*2*). Worse, some EU legislation prevents resource-efficient use of food waste. Despite evidence of the potential economic and environmental benefits (*1*, *3*) and tentative steps to reclassify some surplus food as fit for animal feed (*4*), it remains illegal to use the vast majority of food waste as animal feed in the European Union because of historical disease control concerns (*1*). Meanwhile, countries such as Japan, South Korea, and Taiwan are all operating systems that safely recycle more than one-third of their food waste as animal feed (*1*). When it comes to reducing the impact of food waste, the European Union has much to learn from the Far East.

Erasmus K. H. J. zu Ermgassen,[1]* Andrew Balmford,[1] Ramy Salemdeeb[2]

[1]Conservation Science Group, Department of Zoology, University of Cambridge, Cambridge, CB2 3QZ, UK. [2]Department of Engineering, University of Cambridge, Cambridge, CB2 1PZ, UK.

*Corresponding author. Email: ekhjz2@cam.ac.uk



Unlike some countries in Asia, the European Union still disposes of food waste in landfills.

REFERENCES

1. E. K. H. J. zu Ermgassen, B. Phalan, R. E. Green, A. Balmford, *Food Policy* **58**, 35 (2016).
2. Eurostat, 2016 (http://ec.europa.eu/eurostat/web/environment/waste/main-tables).
3. S. Salemdeeb, E. K. H. J. zu Ermgassen, M. H. Kim, A. Balmford, A. Al-Tabbaa, *J. Clean. Prod.* 10.1016/j.jclepro.2016.05.049 (2016).
4. European Commission, "Closing the loop—An EU action plan for the circular economy" (2015); http://eur-lex.europa.eu/legal-content/EN/TXT/?uri=CELEX:52015DC061.

10.1126/science.aaf9630

Burial law impedes scientific discovery

THE NEWS AT A GLANCE item "'Ancient One' to get Native American burial" (6 May, p. 634) reports the reburial of the 9300-year-old skeletal remains of Kennewick Man after 2 decades of legal wrangling between Native American communities and scholars. The story does not address the scientific ramifications of this decision.

The legal battles are the result of the dissolution of American skeletal and archaeological museum collections mandated by the 1990 Native American Graves Protection and Repatriation Act (NAGPRA). This law requires museums receiving federal money to turn over skeletal remains and archaeological objects to local Native American communities who can trace genetic or cultural affiliation to the human or cultural remains. NAGPRA was enacted by the U.S. Congress in response to political agitation and concerns about social justice.

The skeletal remains of about 50,000 people and 1.4 million archaeological objects have subsequently left major museums in the United States, and are therefore lost to science (*1*). Museum skeletal and archaeological collections constitute the raw data for biological anthropological and archaeological research. The reburial of the Kennewick material is deeply unfortunate for science. Scholars had only 2 weeks to examine the skeleton, and their results can never be replicated. Furthermore, no future refinements to ancient DNA analysis or the chemical analysis of prehistoric bone and enamel can be applied to the Kennewick specimen. In the context of war in the Middle East, the destruction of museum collections is routinely deplored as a crime against the cultural heritage of humankind. As a scientist, I feel a similar sense of loss when I hear the results of the NAGPRA legislation.

S. Cachel

Rutgers University, New Brunswick, NJ 08901-1414, USA. Email: Cachel@rci.rutgers.edu

REFERENCE

1. S. J. Redman, *Bone Rooms: From Scientific Racism to Human Prehistory in Museums* (Harvard Univ. Press, 2016).

10.1126/science.aag1641

Modeling the effects of climate engineering

IN THEIR POLICY FORUM "Opportunities for advances in climate change economics" (15 April, p. 292), M. Burke *et al.* highlight three areas of climate change economics research: social cost of carbon, climate policy impacts, and developing economies. They overlook an important avenue of research that affects all three: climate engineering technologies, in particular solar radiation management (SRM).

SRM is an engineered change in Earth's radiative forcing in an effort to reduce climate changes (*1*). Direct costs are low (*2*). SRM acts quickly (years) so it reduces part of the effective inertia of the climate system, profoundly altering the dynamics of any climate policy. SRM would substantially change the profile of climate impacts, disconnecting temperature from other changes caused by CO_2, such as ocean acidification. It would also alter the distribution of climate impacts and policy choices across countries (*3*). Importantly, SRM would introduce new risks to the equation (*4*).

Integrated assessment models have a damage function that is largely calibrated in terms of temperatures. Recent versions

Downloaded from http://science.sciencemag.org/ on June 28, 2016

PHOTO: ZELJKOSANTRAC/ISTOCKPHOTO.COM

Published by AAAS

also add sea-level rise (*5*). This is a good approximation when damages from carbon concentrations and temperature are linked. SRM would change this relationship by reducing temperature without lowering carbon concentrations. Integrated assessment models must recognize the newly differentiated impacts. Naïvely introducing SRM into these models without further consideration would bias the results toward implementation of SRM.

SRM is an important part of the future climate policy research agenda, as illustrated by the latest National Academy of Sciences report (*6, 7*). Economists need to embrace research on SRM technologies, recognize their capacity to disrupt the climate policy agenda, focus on understanding the new impacts and risks introduced, and integrate this new understanding into models and policy design.

David Keith,[1] Gernot Wagner,[1] Juan Moreno-Cruz[2]*

[1]Harvard School of Engineering and Applied Sciences, Cambridge, MA 02138, USA. [2]Georgia Institute of Technology, Atlanta, GA 30332, USA.

*Corresponding author. Email: jmc3@gatech.edu

REFERENCES

1. D. W. Keith, *Annu. Rev. Energy Environ.* **25**, 245 (2000).
2. J. McClellan, D. Keith, J. Apt, *Environ. Res. Lett.* **7**, 034019 (2010).
3. J. B. Moreno-Cruz, K. L. Ricke, D. W. Keith, *Clim. Change* **110**, 649 (2012).
4. G. Wagner, M. L. Weitzman, *Climate Shock* (Princeton Univ. Press, 2015).
5. U.S. Interagency Working Group on Social Cost of Carbon, "Technical support document: Technical update of the social cost of carbon for regulatory impact analysis under Executive Order 12866" (Washington, DC, 2015).
6. National Research Council, *Climate Intervention: Reflecting Sunlight to Cool Earth* (National Acad. Press, 2015).
7. M. McNutt, *Engineering* **2**, 50 (2016).

10.1126/science.aag1630

TECHNICAL COMMENT ABSTRACTS

Comment on "The Atlantic Multidecadal Oscillation without a role for ocean circulation"

Rong Zhang, Rowan Sutton, Gokhan Danabasoglu, Thomas L. Delworth, Who M. Kim, Jon Robson, Stephen G. Yeager

Clement *et al.* (Reports, 16 October 2015, p. 320) claim that the Atlantic Multidecadal Oscillation (AMO) is a thermodynamic response of the ocean mixed layer to stochastic atmospheric forcing and that ocean circulation changes have no role in causing the AMO. These claims are not justified. We show that ocean dynamics play a central role in the AMO.

Full text at http://dx.doi.org/10.1126/science.aaf1660

Response to Comment on "The Atlantic Multidecadal Oscillation without a role for ocean circulation"

Amy Clement, Mark A. Cane, Lisa N. Murphy, Katinka Bellomo, Thorsten Mauritsen, Bjorn Stevens

Zhang *et al.* interpret the mixed-layer energy budget in models as showing that "ocean dynamics play a central role in the AMO." Here, we show that their diagnostics cannot reveal the causes of the Atlantic Multidecadal Oscillation (AMO) and that their results can be explained with minimal ocean influence. Hence, we reaffirm our findings that the AMO in models can be understood primarily as the upper-ocean thermal response to stochastic atmospheric forcing.

Full text at http://dx.doi.org/10.1126/science.aaf2575

Downloaded from http://science.sciencemag.org/ on June 28, 2016

TECHNICAL COMMENT

OCEAN VARIABILITY

Comment on "The Atlantic Multidecadal Oscillation without a role for ocean circulation"

Rong Zhang,[1]* Rowan Sutton,[2] Gokhan Danabasoglu,[3] Thomas L. Delworth,[1] Who M. Kim,[3] Jon Robson,[2] Stephen G. Yeager[3]

Clement *et al*. (Reports, 16 October 2015, p. 320) claim that the Atlantic Multidecadal Oscillation (AMO) is a thermodynamic response of the ocean mixed layer to stochastic atmospheric forcing and that ocean circulation changes have no role in causing the AMO. These claims are not justified. We show that ocean dynamics play a central role in the AMO.

Without analyzing the Atlantic Multidecadal Oscillation (AMO) mechanisms in fully coupled general circulation models (CGCMs) that include ocean dynamics, Clement *et al.* (*1*) conclude that the AMO in CGCMs is generated by the same mechanism as in slab-ocean models (SOMs), which lack ocean dynamics. They suggest that the AMO is a direct response of the ocean mixed layer to stochastic surface heat fluxes without a role for ocean heat transport/circulation changes.

Here, we show that the above conclusions are not justified. Any claims about the mechanisms governing the AMO, such as those in (*1*), must be based on direct analyses of these mechanisms. It is not possible to make robust inferences about mechanisms causing the AMO from a simple analysis of sea surface temperature (SST) patterns and power spectra. We refute the claims in (*1*) through analyses of the same models employed in (*1*) and show that the mechanism causing the AMO in CGCMs is different from that in SOMs—i.e., time-varying ocean heat transport convergence is a leading cause of the AMO in CGCMs (Figs. 1 and 2).

Figure 1, A and B, shows the SST tendency ($\frac{dSST'}{dt}$) at low frequencies regressed on the AMO index with a 4-year lead time. The AMO index used for regression analyses should be the "low-pass filtered" detrended North Atlantic basin–averaged SST anomalies (SST′) to reflect the "multidecadal" variability that gives the AMO its name (*2*). The 4-year lead time is not chosen arbitrarily. With 10-year low-pass filtering, the AMO tendency ($\frac{dAMO}{dt}$) leads the AMO index by 4 years at their maximum correlation in all CGCMs, and the multi-model mean lead time for SOMs is 3 to 4 years. The SST tendency ($\frac{dSST'}{dt}$) at low frequencies has a similar pattern to the simulated AMO pattern [figure S1 in (*1*)], with the largest amplitude in the subpolar region. At low frequencies, the positive SST tendency in SOMs (Fig. 1B) is induced mainly by reduced upward sensible heat flux (not shown) leading to a positive net surface heat flux anomaly ($F'_{Net} = \rho C_p h \frac{dSST'}{dt} > 0$, where the positive sign denotes downward heat flux into the ocean) (Fig. 1D). In contrast, in CGCMs the positive SST tendency in the subpolar region (Fig. 1A) is induced by enhanced ocean heat transport convergence (Fig. 1E) (OHTC′, diagnosed approximately as $OHTC' \approx \rho C_p h \frac{dSST'}{dt} - F'_{Net}$, where h is 50 m for SOMs and is the thickness of the top ocean model layer for each CGCM (not a constant across models). The residual term $\rho C_p h \frac{dSST'}{dt}$ is negligible, compared with F'_{Net} that is almost in balance with OHTC′ (Fig. 1, C and E). Consistent with observations (*3*), the enhanced turbulent heat fluxes (not shown) and negative net surface heat flux ($F'_{Net} < 0$) (Fig. 1C) damp the surface warming induced by positive OHTC′ in the subpolar region at low frequencies.

Similar regression patterns also appear at other lead times (Fig. 2, A to D) and at zero-lag. With 20- or 30-year low-pass filtering, the multimodel mean correlation between $\frac{dAMO}{dt}$ and the AMO peaks at longer lead times (8 or 10 to 11 years, respectively) due to the broad AMO spectra in CGCMs. The SOM simulations are too short to apply longer low-pass filtering cutoff periods, but in SOMs the same mechanism holds at all frequencies. Our results are robust for a wide range of lead times and different low-pass filtering cutoff periods, and our conclusions about causality are not a consequence of the filtering. The leading role of ocean dynamics that we identify in CGCMs is consistent with a wealth of evidence that the AMO is associated with coherent multidecadal variability in multiple variables (ocean heat/salt content, overturning circulation and heat transport, and ocean-driven surface turbulent heat fluxes) (*3*–*11*). Our results (Figs. 1 and 2) refute the claims in (*1*) that "the current generation models analyzed here do not support the idea that ocean circulation drives the AMO" and "simulations of the AMO using fully coupled atmosphere-ocean models…are essentially indistinguishable from those produced by the equivalent slab-ocean model versions." They are clearly distinguishable if one examines the mechanisms, even if the models have similar SST patterns and power spectra.

Curiously, Clement *et al.* comment at the end of their Report that "Our analysis does not rule out that the ocean circulation may contribute to low-frequency variability in parts of the ocean, such as the subpolar gyre." This curious statement contradicts their central claim that "the AMO is the response to stochastic forcing from the mid-latitude atmospheric circulation" in which "ocean circulation changes would be largely a response to, not a cause of, the AMO". Our analyses demonstrate that in the subpolar region, ocean dynamics is the leading cause of the AMO, whereas the varying surface heat fluxes are a passive response to, not a cause of, the AMO, contrary to the claims in (*1*) (Fig. 2, E and F). The largest low-frequency SST anomalies in the observed AMO pattern are in the subpolar region (*12*). The simulated AMO in CGCMs [figure S1 in (*1*)] is dominated by the subpolar gyre variability induced by ocean dynamics. The weaker low-latitude AMO signal responds to the stronger subpolar AMO signal through combined oceanic and atmospheric teleconnections (including changes in the Hadley circulation, wind-evaporation-SST feedback, and cloud feedback) (*12*–*15*) (Fig. 2E). Changes in the subpolar ocean state also induce tropical North Atlantic subsurface temperature variations through the oceanic teleconnection, which are anticorrelated with the tropical AMO signal (*5*, *7*, *13*) (Fig. 2E). If the tropical AMO signal were forced by stochastic F'_{Net}, as in SOMs, its anticorrelation with oceanic-driven tropical subsurface temperature variations found in both observations and CGCMs (*5*, *7*, *13*) would not exist (Fig. 2, E and F). The climate impacts associated with the tropical AMO have high decadal predictability only when the subpolar ocean state is initialized (*14*). The successful decadal predictions (*9*–*11*), with initialized observed ocean states, suggest that ocean dynamics is the leading cause of the AMO (Fig. 2E). The mechanism in SOMs implies no decadal predictability other than simple persistence (Fig. 2F). Our results show that the subpolar gyre is the key region for generating the AMO and that our most realistic models indicate that ocean circulation indeed plays a leading role in driving this variability.

[1]National Oceanic and Atmospheric Administration, Geophysical Fluid Dynamics Laboratory, Princeton, NJ, USA. [2]National Centre for Atmospheric Science, Department of Meteorology, University of Reading, Reading, UK. [3]Climate and Global Dynamics Laboratory, National Center for Atmospheric Research, Boulder, CO, USA.
*Corresponding author. Email: rong.zhang@noaa.gov

REFERENCES AND NOTES

1. A. Clement *et al*., *Science* **350**, 320–324 (2015).
2. D. B. Enfield, A. M. Mestas-Nunez, P. J. Trimble, *Geophys. Res. Lett.* **28**, 2077–2080 (2001).
3. S. K. Gulev, M. Latif, N. Keenlyside, W. Park, K. P. Koltermann, *Nature* **499**, 464–467 (2013).
4. R. Zhang, *Geophys. Res. Lett.* **35**, L20705 (2008).
5. C. Wang, S. Dong, E. Munoz, *Clim. Dyn.* **34**, 953–968 (2010).
6. R. Zhang *et al*., *J. Atmos. Sci.* **70**, 1135–1144 (2013).
7. C. Wang, L. Zhang, *J. Clim.* **26**, 6137–6162 (2013).

Downloaded from http://science.sciencemag.org/ on June 28, 2016

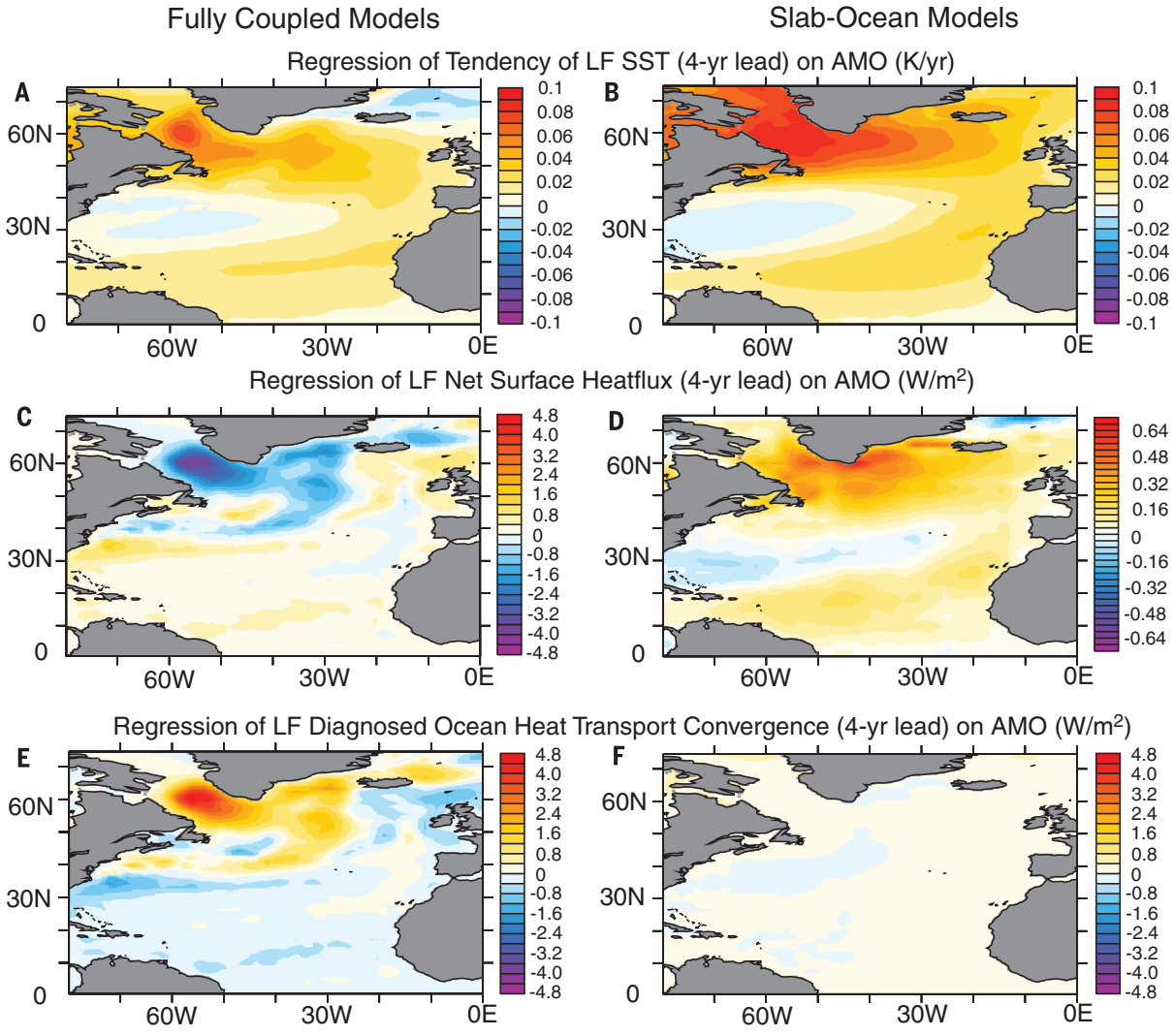


Fig. 1. Regression of 10-year low-pass filtered (LF) variables on the standardized AMO index when the variables lead the AMO index by 4 years, using the same 10 Coupled Model Intercomparison Project phase 3 (CMIP3) preindustrial control fully coupled and SOMs, as listed in table 1 in Clement *et al*. (*1*). (**A**, **C**, and **E**) Multimodel ensemble mean of 10 fully coupled models (CGCMs). (**B**, **D**, and **F**) Multimodel ensemble mean of 10 SOMs. (The GISS SOM has an unrealistic discontinuity of longwave surface fluxes at year 101, so only the first 100 years of GISS SOM are used.) [(A) and (B)] Regression of tendency of LF SST ($\frac{dSST'}{dt}$). [(C) and (D)] Regression of LF net surface heat flux (F'_{Net}, positive sign denotes downward heat flux into the ocean). [(E) and (F)] Regression of LF diagnosed ocean heat transport convergence ($OHTC' \approx \rho C_p h \frac{dSST'}{dt} - F'_{Net}$). h is 50 m for SOMs and is the thickness of the top ocean model layer to calculate SST (top ocean model layer temperature) heat budget for each fully coupled model (h is not a constant across models), and ρ and C_p are the density and heat capacity of ocean water. Regression values correspond to one standard deviation of the AMO index. The AMO index is defined as 10-year LF basin–averaged SST anomalies in the North Atlantic (80°W to 0°, 0° to 60°N). All variables are detrended.

8. J. Robson, R. Sutton, K. Lohmann, D. Smith, M. Palmer, *J. Clim.* **25**, 4116–4134 (2012).
9. J. I. Robson, R. Sutton, D. Smith, *Geophys. Res. Lett.* **39**, L19713 (2012).
10. S. Yeager, A. Karspeck, G. Danabasoglu, J. Tribbia, H. Teng, *J. Clim.* **25**, 5173–5189 (2012).
11. R. Msadek *et al*., *J. Clim.* **27**, 6472–6496 (2014).
12. A. Ruiz-Barradas, S. Nigam, A. Kavvada, *Clim. Dyn.* **41**, 3301–3315 (2013).
13. R. Zhang, *Geophys. Res. Lett.* **34**, L12713 (2007).
14. N. J. Dunstone, D. M. Smith, R. Eade, *Geophys. Res. Lett.* **38**, L14701 (2011).
15. D. L. R. Hodson, J. I. Robson, R. T. Sutton, *J. Clim.* **27**, 8229–8243 (2014).

ACKNOWLEDGMENTS

We appreciate the cordial exchanges with Clement *et al*. on our disagreement discussed in this Comment. We thank I. Held for internal review of the Comment. We also thank two anonymous reviewers for their constructive suggestions. We acknowledge the modeling groups, the Program for Climate Model Diagnosis and Intercomparison (PCMDI), and the World Climate Research Programme's (WCRP's) Working Group on Coupled Modelling (WGCM) for their roles in making available the WCRP CMIP3 multimodel data set. Support of this data set is provided by the Office of Science, U.S. Department of Energy. National Center for Atmospheric Research (NCAR) is supported by the National Science Foundation. Support from the NOAA Climate Program Office, Climate Variability and Predictability Program to NCAR is also acknowledged.

12 January 2016; accepted 16 May 2016
10.1126/science.aaf1660

Downloaded from http://science.sciencemag.org/ on June 28, 2016

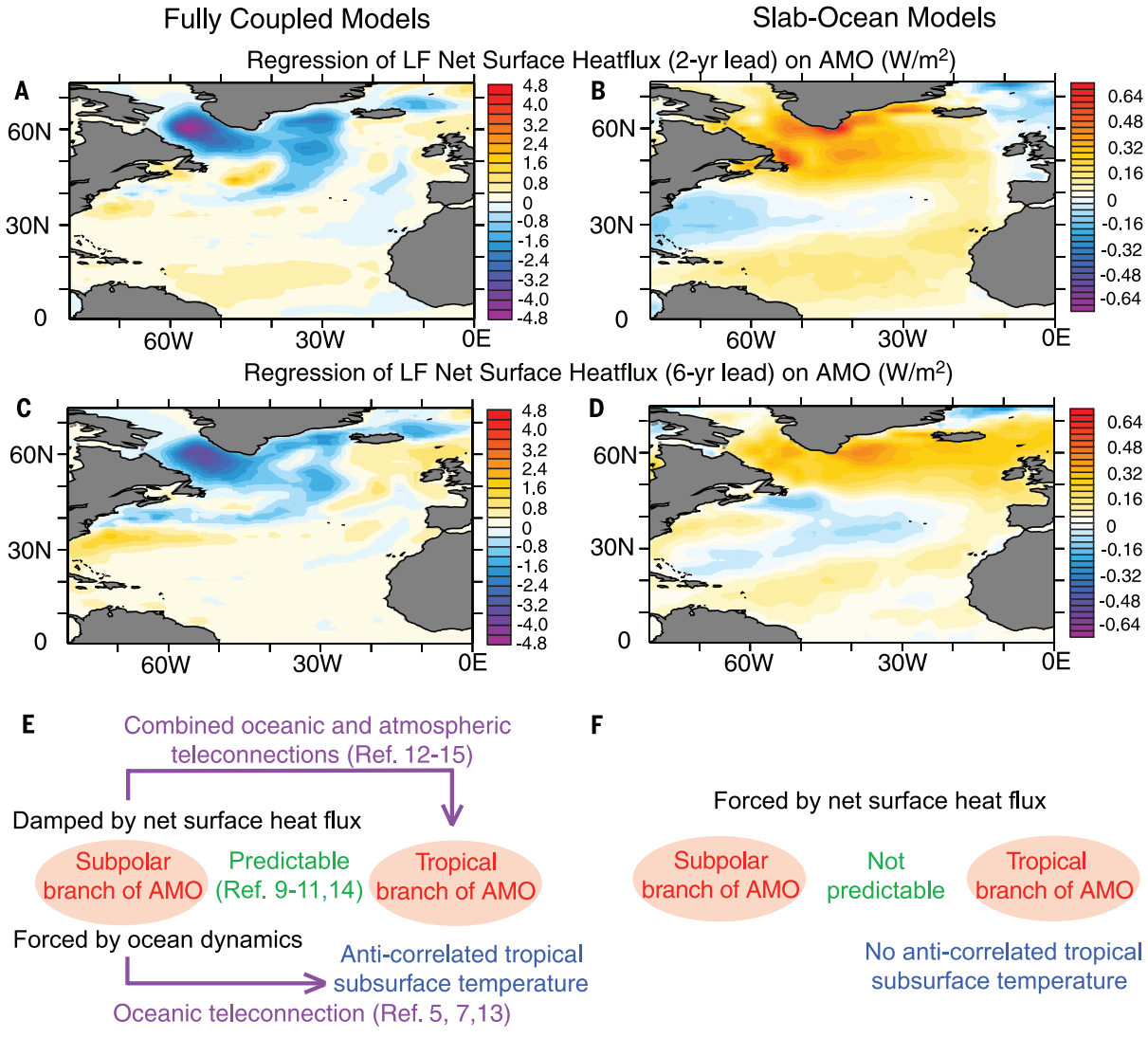


Fig. 2. Regression of 10-year LF net surface heat flux on the standardized AMO index when the heat flux leads by 2 and 6 years and schematic mechanisms of the AMO. (**A** and **C**) Multi-model ensemble mean of 10 fully coupled models (CGCMs). (**B** and **D**) Multimodel ensemble mean of 10 SOMs. (**E** and **F**) Schematic diagrams of different mechanisms of the AMO. In fully coupled models (E), the subpolar AMO is forced by time-varying ocean heat transport convergence and damped by net surface heat flux anomalies. The weaker tropical AMO responds to the stronger subpolar AMO through combined oceanic and atmospheric teleconnections (*12*–*15*). Changes in the subpolar North Atlantic ocean state also induce tropical North Atlantic subsurface temperature variations through oceanic teleconnection, which is anticorrelated with the tropical AMO, suggesting that the tropical AMO is linked to subpolar oceanic variability (*5*, *7*, *13*). The subpolar AMO and the climate impacts associated with the tropical AMO have decadal predictability when initializing the subpolar North Atlantic ocean state (*9*–*11*, *14*). In SOMs (F), both subpolar and tropical AMO branches are forced by stochastic net surface heat flux anomalies and thus have no decadal predictive skill other than simple persistence. The mechanism in SOMs cannot explain the anticorrelation between the tropical AMO and tropical North Atlantic subsurface temperature variations found in both observations and fully coupled models.

Downloaded from http://science.sciencemag.org/ on June 28, 2016

TECHNICAL RESPONSE

OCEAN VARIABILITY

Response to Comment on "The Atlantic Multidecadal Oscillation without a role for ocean circulation"

Amy Clement,[1]* Mark A. Cane,[2] Lisa N. Murphy,[1] Katinka Bellomo,[2] Thorsten Mauritsen,[3] Bjorn Stevens[3]

Zhang *et al*. interpret the mixed-layer energy budget in models as showing that "ocean dynamics play a central role in the AMO." Here, we show that their diagnostics cannot reveal the causes of the Atlantic Multidecadal Oscillation (AMO) and that their results can be explained with minimal ocean influence. Hence, we reaffirm our findings that the AMO in models can be understood primarily as the upper-ocean thermal response to stochastic atmospheric forcing.

In their Comment on Clement *et al.* (*1*), Zhang *et al.* (*2*) show that several years before the peak of the AMO (Atlantic Multidecadal Oscillation) in coupled models, the net surface heat flux in parts of the subpolar North Atlantic is out of the ocean and into the atmosphere. They interpret this signal as indicative that ocean dynamics is the leading cause of the AMO.

We do not share this interpretation, foremost because cause and effect cannot be inferred from this budget. At low frequencies (long time scales), the heat storage in the upper ocean, $\rho C_p h dT/dt$, is negligible; hence, the heat fluxes, which must balance on such time scales, do not inform a causal analysis. This is apparent in the maps shown in Zhang *et al.*, where there is almost complete cancellation between the net surface heat flux [figure 1C in (*2*)] and what they call the ocean residual [figure 1E in (*2*)]. The ocean residual may or may not have caused the warming, but the equilibrium heat budget is not informative about how this state came about. In addition, the ocean residual in their calculation should not be called the ocean heat transport convergence because it also includes the effect of local mixed-layer physics.

The problem with the budget approach is illustrated by the analysis shown in Fig. 1. Following Zhang *et al.*, we calculate average quantities for the region 40° to 55°N, 20° to 60°W, a region of the subpolar ocean that they argue contains the seed of the AMO warming. The main finding of Zhang *et al.* is recovered in this analysis (here based on correlation values rather than regression coefficients so as to give equal weight when averaging across models). The multimodel mean correlation of net surface heat flux is slightly negative leading the temperature (Fig. 1C, heavy blue line), and the ocean residual is slightly positive (Fig. 1D, heavy blue line). However, the same relationships are also found at positive lags, when the temperature is cooling (dT/dt is negative) (Fig. 1B). Following the logic of Zhang *et al.*, we would be forced to the opposite conclusion, that the atmosphere is driving the temperature. This serves to illustrate the difficulty of inferring causality from such an analysis.

Zhang *et al.*'s diagnostic does show that the net effect of the ocean at low frequencies is not zero in some regions of the subpolar gyre and Labrador sea, in contrast to what is found in the slab-ocean models. The net ocean influence is zero in the slab-ocean models by design. Hence, the net surface heat flux is approximately zero (to within 0.5 W/m^2), as shown in figure 1D in (*2*) (note the change of color scale in that panel), as required by the lack of heat storage on these time scales. Just because the AMO is correlated with a coherent pattern of surface fluxes in models where it is not forced to be zero does not mean that the ocean is the leading cause of the AMO.

To further illustrate this point, a comparison of the GCM results with a simple stochastically forced model is instructive. Assume that

$$dT/dt = -\alpha T + aN_a + bN_o \quad (1)$$

where N_a and N_o are the atmosphere and ocean forcing, respectively, and $-\alpha T + aN_a$ can be interpreted as the net surface heat flux, Q_s in this model. Here, both N_a and N_o are unit amplitude white noise and uncorrelated with each other. The parameter α is set to 4 year^{-1}, which is the best fit to the multimodel mean, and is consistent with observed values (*3*). We take $a^2 + b^2 = 1$, which means that a^2 and b^2 are the fractions of forcing variance contributed by the atmosphere and ocean. A case with strong atmospheric driving is shown in Fig. 1, where $a^2 = 0.9$ (which is 90% atmosphere forcing and only 10% ocean). The sign of the relationship between Q_s and dT/dt predicted by this model (Fig. 1, B and C) is the same as in the multimodel mean with negative values of heat flux both leading and lagging temperature. The sign of the ocean residual (Fig. 1D) also matches the multimodel mean.

This example illustrates that the multimodel mean results and the findings of Zhang *et al.* can be explained with a small amount of ocean noise. Zhang *et al.*'s analysis does not show that the ocean is necessary for the AMO but rather that a particular diagnostic has some influence from the ocean. This is consistent with the main findings of Clement *et al.*. The virtue of that study was to show that eliminating variations in the ocean heat transport convergence, in the manner of the usual process attribution studies (turn off some process and see how the result changes), did not change the AMO space and time characteristics. Thus, while ocean processes may be doing something to the mixed-layer energy budget in parts of the subpolar gyre and Labrador Sea in coupled models, its effect on the AMO is small compared with the stochastic atmospheric forcing.

Although the AMO is defined as the average SST in the entire North Atlantic, it is worth remembering that over most of the North Atlantic, the net surface heat flux is as negligible in the coupled models as it is in the slab-ocean models [figure 1, C and D, in (*2*)]. Zhang *et al.* confine their discussion to the subpolar gyre, which they assert is "the key region for generating the AMO." Because of its implications for prediction studies, this idea is an attractive one, but this is far from settled science. Studies of the AMO are commonly motivated by the effects on rainfall and temperature patterns on land around the Atlantic, and many studies—e.g., (*4*)—have shown that these effects originate in the tropical North Atlantic. Both Clement *et al.* and previous studies cited therein showed that in this region the atmosphere is strongly influenced by the ocean through thermal coupling. If the subpolar gyre is important for warming the rest of the Atlantic basin and associated effects, then its influence must be communicated through the atmosphere. Not withstanding the studies cited by Zhang *et al.*, other studies come to different conclusions, and as recently reviewed by Buckley and Marshall (*5*), the debate remains contentious. The finding in Clement *et al.* is another challenge to the idea that the subpolar gyre is the hinge on which the whole Atlantic swings.

Finally, all of the "coherent multidecadal variability in multiple variables" mentioned by Zhang *et al.* as "associated" with the AMO can be accounted for as additional responses to the same atmospheric forcing that we find to be responsible for the AMO in models. As ever, neither association nor correlation implies causality.

[1]Rosenstiel School of Marine and Atmospheric Science, University of Miami, Miami, USA. [2]Lamont-Doherty Earth Observatory of Columbia University, Palisades, NY, USA. [3]Max Planck Institute for Meteorology, Hamburg, Germany.
*Corresponding author. Email: aclement@rsmas.miami.edu

REFERENCES AND NOTES

1. A. Clement *et al.*, *Science* **350**, 320–324 (2015).
2. R. Zhang *et al.*, *Science* **352**, 1527 (2016).
3. S. Park, C. Deser, M. A. Alexander, *J. Clim.* **18**, 4582–4599 (2005).
4. R. T. Sutton, D. L. Hodson, *Science* **309**, 115–118 (2005).
5. M. W. Buckley, J. Marshall, *Rev. Geophys.* **54**, 5–63 (2016).

ACKNOWLEDGMENTS

This work was supported by the National Science Foundation Climate and Large-Scale Dynamics and Paleo Perspectives on

Downloaded from http://science.sciencemag.org/ on June 28, 2016

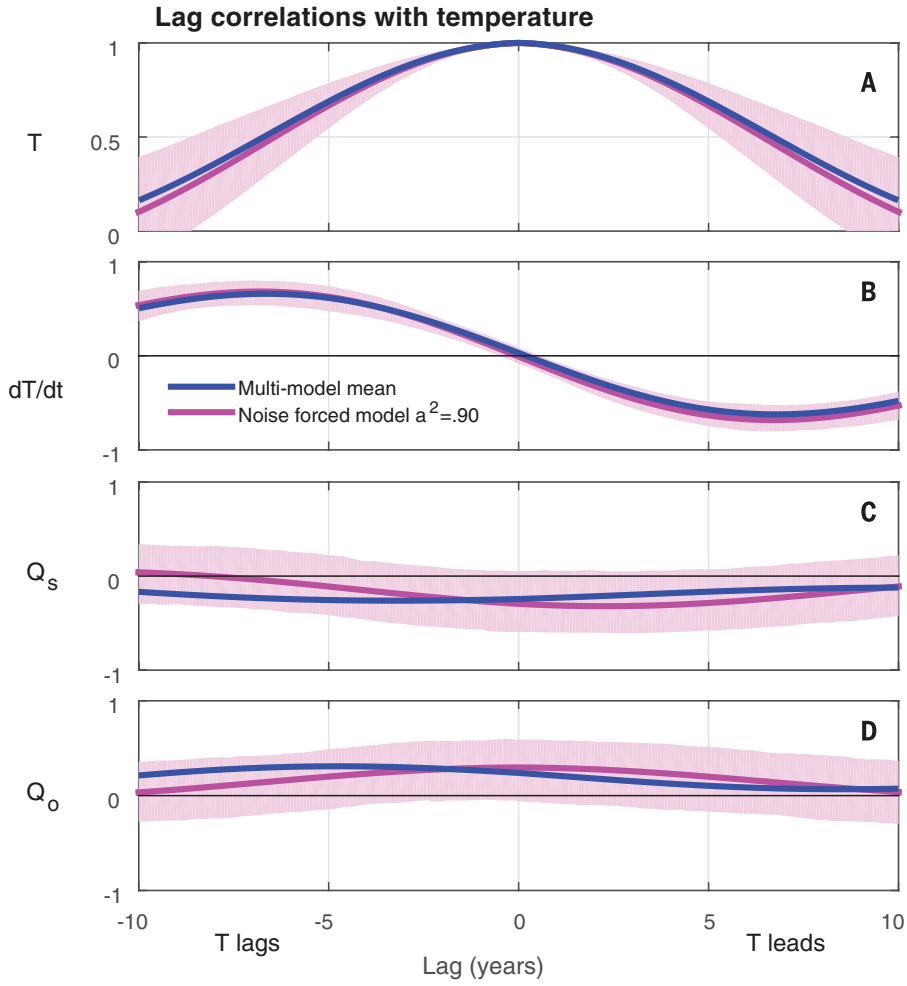


Fig. 1. Lead-lag relationships with the AMO index. Here, we reproduce similar diagnostics as in Zhang *et al*. for the region 40° to 55°N, 20° to 60°W, with eight of the CMIP3 fully coupled models that were used in their comment and in Clement *et al*., along with the same quantities calculated from the simple noise-forced model from Eq. 1. (We limit our analysis to 55°N to avoid the effects of sea ice on the mixed-layer heat budget.) We exclude two models (mri_cgcm2_3_2a and miroc3_2_hires_coupled_40_55N_20_60W) because their published data contain less than 200 years. We analyze only the last 300 years of the model time series to remove any effect of adjustment (and the last 200 years in the hadgem1). Data are detrended and then low-pass filtered, with a 20-year cutoff Butterworth fourth-order filter. The multi-model mean is shown in heavy blue for (**A**) the autocorrelation of temperature, (**B**) the lag correlation of d*T*/d*t* and temperature, (**C**) the lag correlation of net surface heat flux (defined as positive downward) and temperature, and (**D**) the lag correlation of the "ocean residual" (defined as positive for convergence of heat) and temperature. Superimposed on these curves are the results from the simple noise-forced model, with $a^2 = 0.9$ (pink lines). The pink shading shows the 5% and 95% confidence intervals based on a nonparametric estimation using 500 300-year long realizations of the noise-forced model.

Climate Change programs. M.A.C. was supported by Office of Naval Research grant N00014-12-1-0911. We thank Y. Kushnir for comments. We acknowledge the contributors to the Coupled Model Intercomparison Project phase 3 (CMIP3) archive. The CMIP3 data are available at http://cmip-pcmdi.llnl.gov/.

3 February 2016; accepted 16 May 2016
10.1126/science.aaf2575

Downloaded from http://science.sciencemag.org/ on June 28, 2016



PHOTO: ABRAHAM MIRMALEK

Panel of experts encourages scientific collaboration with Iran

AAAS conference examines partnership potential since signing of nuclear agreement

By **Michaela Jarvis**

Increased collaboration with Iranian scientists could speed the development of important solutions to global challenges in many fields, experts said at the AAAS Science Diplomacy 2016 conference, and a broadening range of organizations, including AAAS and the National Academies, can help make it happen.

Throughout the "Opening Doors to Iran" session of the 5 May conference, one of eight sessions on diverse topics in science diplomacy, panelists cited far-ranging evidence of the capability of Iran's scientific community as a collaborative partner. They described the problems Iran is experiencing—such as energy shortages, HIV/AIDS, and air and water pollution—as opportunities for science and technology engagement to positively impact people's lives. Referring to the nuclear agreement signed last July and subsequent statements signed or released by the United States, Iran, and five other nations, panelist Ali Douraghy, of the National Academies of Sciences, Engineering and Medicine, said, "There are certainly very positive opportunities for potential scientific cooperation outlined."

Over the years, Iranian scientists, physicians, and other health experts have collaborated with their U.S. counterparts through partnerships fostered by the National Academies, the National Institutes of Health, AAAS, and CRDF Global, on topics such as water, foodborne diseases, neuroscience and drug abuse, noncommunicable and infectious diseases, health disparities, and bioethics. The 5 May panel was convened by CRDF Global, a nonprofit that connects emerging scientific communities with the international scientific community.

"Scientific collaboration is among the best ways to show that the two countries can productively work together, as opposed to work against each other, by helping tackle the world's greatest challenges and to build trust," said Tom Wang, AAAS's chief international officer and director of the AAAS Center for Science Diplomacy.

In October 2013, newly elected Iranian President Hassan Rouhani made a speech about restoring academic freedom at the country's universities following nearly a decade of interference in academic affairs by a conservative government. *Science* International News Editor Richard Stone, who had visited Iran back in 2005, saw this as a crucial moment. "I thought, 'This is a message that is interesting for the international science community. I'd like to see what it means on the ground,'" said Stone, who also participated in the conference panel.

His subsequent visit in 2015 resulted in a series of articles documenting the state of science and technology in Iran. As his reporting bore out, some of the projects he had seen beginning to blossom back in 2005, such as plans for a top-caliber Iranian National Observatory, were regaining momentum after years of halting progress due to internal political pressures and international sanctions imposed on Iran over its nuclear program.

Stone described how Iranian scientists were able to push ahead on international-quality research despite the sanctions. The Iranian Light Source Facility, a synchroton project, has made remarkable progress in overcoming sanctions, thanks in large part to improvisation. Similarly, when scientists were unable to import sensors to measure seismic stress on infrastructure such as dams and bridges in a country laced with faults, they invented their own that are now used throughout the country and are even starting to be exported.

"I was struck by the ingenuity of many of the Iranian scientists in the face of sanctions," said Stone.

Downloaded from http://science.sciencemag.org/ on June 28, 2016

Published by AAAS

The receding of Lake Urmia is creating a salt desert, threatening ecosystems and agriculture.

Somewhat surprisingly, stem cell research was one of the fields that progressed, after Iranian scientists, unsure of what was permissible, petitioned Iran's Supreme Leader Seyyed Ayatollah Ali Khamenei to issue a fatwa on stem cells. The ruling in 2002 legalized any kind of stem cell research except for human cloning, a policy more liberal than that of the United States. Iranians, given the go-ahead from Khamenei, actively advanced the research, Stone said.

Alex Dehgan, who has worked for the U.S. Department of State and has also served as chief scientist at USAID—invoking one of his main requirements for successful science diplomacy—said that the benefits of scientific engagement with Iran would accrue to both partners because of the strength of science and technology in Iran. The Iranian Revolution of 1979 brought university education to a much broader segment of the population than is seen in other countries in the region, and Iranians have long cultivated a cultural pride in scholarship and creativity. Iran is now ranked fourth in the world in terms of its growth rate in publishing scientific articles, said Dehgan, co-founder of Conservation X Labs.

At Stanford University's Ph.D. program in electrical engineering, said panelist Douraghy, Iran's Sharif University of Technology is known as the world's top institution for preparing undergraduates in the field. Dehgan pointed out that Iranian students who studied at Stanford and other U.S. universities and then stayed in this country went on to found companies ranging from eBay, to Dropbox, to Hot Pockets.

"We're missing out," said Dehgan, "[if we're not] engaging that community."

Whatever their talents and preparation, though, Iranian scientists have been isolated from the rest of the world, said Stone, and organizations like AAAS can perform a crucial function in connecting them to the international science community.

"Western scientists are not aware of who the talented scientists are in Iran and North Korea and other isolated countries," said Stone. "A role for nongovernmental organizations like AAAS and the National Academies is to bring those people together."

Still, there are significant challenges to collaboration, panelists said. Rouhani was able to oversee the nuclear agreement with the West and is seen as having a mandate from the Iranian public for opening up the country. However, an ongoing tension exists between elected officials like Rouhani and other extremely influential leaders.

Furthermore, although the nuclear agreement is gradually lifting nuclear-related sanctions, other sanctions remain in place, and panelists reported extensive confusion over what kinds of scientific collaboration are permitted and can get licenses required to proceed. William Colglazier, a senior scholar in the AAAS Center for Science Diplomacy and editor-in-chief of the *Science & Diplomacy* quarterly, asked the panelists how the U.S. government could best encourage science diplomacy and engagement with Iran. Colglazier is a former science and technology advisor to the U.S. Secretary of State.



About 175 people attended the Science Diplomacy 2016 conference.

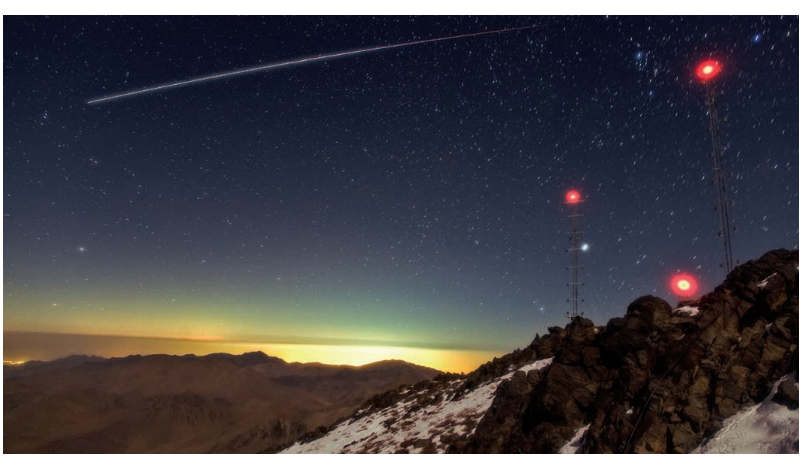
"Where the government can help," said Dehgan, "is by giving signals, guidelines" regarding what is permissible, and perhaps granting "larger blanket licenses" for research projects.

U.S. universities, said panel moderator Siri Oswald, sometimes misunderstand the restrictions on scientific exchanges and needlessly abandon efforts to engage. "They back off of opportunities that, frankly, they could engage in," said Oswald, interim vice president for programs at CRDF Global. A publication by the Institute of International Education entitled "Reinventing Academic Ties," which contains a helpful guide on the impact of sanctions on academic exchanges, offers information for U.S. scientists and institutions looking to collaborate with Iranian researchers, said Douraghy, who is a senior international programs officer for the National Academies.

"In this time, we should take advantage of the good will and test the system, and see what kind of collaborations we can start under current conditions," said Stone, who urged environmental scientists to turn their attention to a catastrophe occurring in northwestern Iran, where poor water management and drought have caused Lake Urmia to lose 80% of its water, creating a salt desert that threatens crops and people.

"These sorts of environmental problems are really amenable to international cooperation," he said. "They're an easy sell" to the U.S. government, the Iranian government, and to funders, Stone added, "and if they're successful, they're going to sow a lot of good will with the Iranian people."

Meanwhile, Dehgan sees the current generation of technology entrepreneurs in Iran as having the most potential to build bridges with partners in the West. "There's an unbelievable tech community in Iran right now that I think gives us the most hope," said Dehgan, citing an opportunity for change in Iran that will come, not necessarily through government, "but change driven by the people themselves, driven by entrepreneurs, driven by scientists."



Iran plans to build its national astronomy observatory on Mount Gargash.

PHOTOS: (TOP TO BOTTOM) AAAS/EPNAC.COM; BABAK TAFRESHI/THE WORLD AT NIGHT

Downloaded from http://science.sciencemag.org/ on June 28, 2016

Published by AAAS

REVIEW SUMMARY

MICROBIOTA

Childhood undernutrition, the gut microbiota, and microbiota-directed therapeutics

Laura V. Blanton, Michael J. Barratt, Mark R. Charbonneau, Tahmeed Ahmed, Jeffrey I. Gordon*

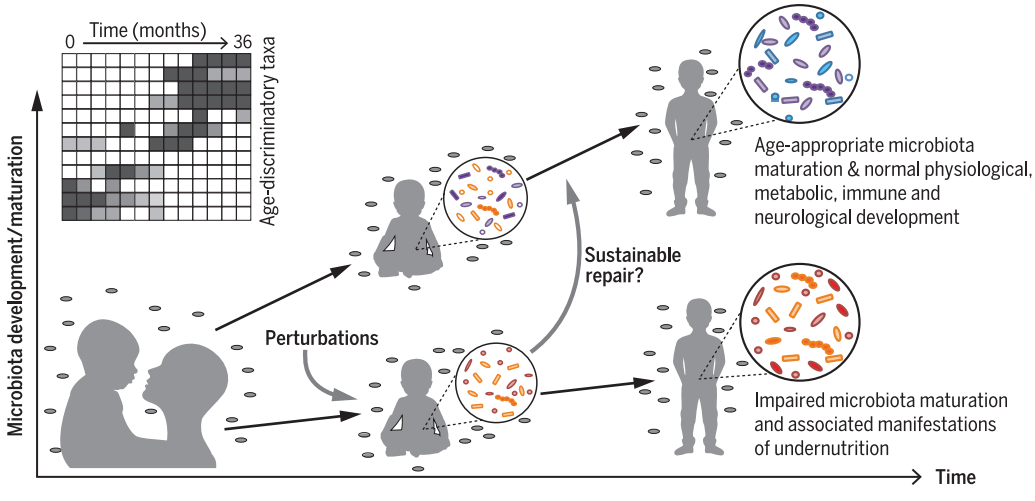
BACKGROUND: Childhood undernutrition is a global health challenge. Undernutrition in early life is associated with a number of adverse outcomes, including persistent stunting, immune dysfunction, and neurocognitive deficits. Current approaches to treatment have only modest effects in correcting these long-term sequelae, suggesting that certain features of host biology are not being adequately repaired. This has led to the hypothesis that healthy growth is dependent, in part, on normal postnatal development of the gut microbiota and that perturbations in its development are causally related to undernutrition. Testing this hypothesis illustrates a number of the challenges that human microbial ecology research faces: (i) defining "normal," both in terms of community structure and expressed functions; (ii) determining whether normal in one population generalizes to other populations; (iii) ascertaining whether deviations from normal correlate with disease and are a cause rather than an effect of pathology; (iv) determining whether abnormal microbial community configurations can be repaired in a sustained fashion, and what route and time course are optimal for such repair; (v) deciphering the short- and long-term effects and safety of repair; and (vi) proactively addressing the ethical, regulatory, and other societal implications of microbiota-directed food and/or microbial interventions designed to deliberately manipulate this facet of postnatal human development.

ON OUR WEBSITE

Read the full article at http://dx.doi.org/10.1126/science.aad9359

ADVANCES: Culture-independent studies of the gut microbiota of members of birth cohorts with healthy growth phenotypes have identified a program of community assembly ("maturation") defined by the changing representation of a group of age-discriminatory bacterial taxa. Features of this program are shared across individuals living in several low-income countries. Applying metrics for defining deviations from this program (microbiota-for-age Z score) has disclosed that children with severe acute malnutrition have gut microbial communities that appear younger than would be expected on the basis of their chronological age. The resulting microbiota "immaturity" is not repaired by current therapeutic food interventions. Compared with healthy children, microbiota from undernourished children transmit impaired growth phenotypes to recipient gnotobiotic mice fed diets representative of those of the human donors; moreover, some of the transplanted age-discriminatory strains are growth-discriminatory. These findings provide early preclinical proof-of-concept that gut microbiota immaturity is causally related to a number of the manifestations of childhood undernutrition.

OUTLOOK: Gnotobiotic animal models can be used to test a number of concepts. Gut microbiota immaturity, increased enteropathogen burden, and gut barrier dysfunction are interrelated factors that affect disease risk and pathogenesis. Microbiota development is linked to maturation of the gut mucosal immune system, metabolic function in multiple host tissues, plus musculoskeletal and brain development. Age- and growth-discriminatory bacterial strains identified in the normally developing microbiota represent therapeutic targets in children with undernutrition. The representation of these strains provides a way not only for defining the efficacy of these therapeutic interventions but also for assessing the effects of various parameters postulated to contribute to disease risk and pathogenesis (such as maternal health status, breast milk composition, history and quality of complementary feeding, poor sanitation and enteropathogen burden, and antibiotic exposures). Microbiota-directed strategies for treating and ultimately preventing childhood undernutrition raise intriguing questions about the mechanisms that define human development. They also highlight the need to add a microbial dimension to our conceptualization of human biological immaturity and its associated adaptations and compensations, and to consider whether interventions that promote healthy microbiota development can spawn a form of preventative medicine that has lifelong benefits. ■



The concept that impaired postnatal gut microbiota development (maturation) is causally related to childhood undernutrition. The representation of age-discriminatory bacterial taxa defines a program of normal gut microbiota development. Disrupting the coordinated functional codevelopment of microbiota and host affects multiple biological regulatory systems through largely unknown mechanisms. Developing effective strategies for sustained repair of microbiota immaturity through food or microbial interventions requires preclinical studies of these mechanisms and modeling of the effects of different rates and routes of repair.

The list of author affiliations is available in the full article online.
*Corresponding author. Email: jgordon@wustl.edu
Cite this article as L. V. Blanton *et al.*, *Science* 352, aad9359 (2016). DOI: 10.1126/science.aad9359

Downloaded from http://science.sciencemag.org/ on June 28, 2016

REVIEW

MICROBIOTA

Childhood undernutrition, the gut microbiota, and microbiota-directed therapeutics

Laura V. Blanton,[1,2] Michael J. Barratt,[1,2] Mark R. Charbonneau,[1,2] Tahmeed Ahmed,[3] Jeffrey I. Gordon[1,2]*

Childhood undernutrition is a major global health challenge. Although current therapeutic approaches have reduced mortality in individuals with severe disease, they have had limited efficacy in ameliorating long-term sequelae, notably stunting, immune dysfunction, and neurocognitive deficits. Recent work is providing insights about the role of impaired development of the human gut microbiota in disease pathogenesis, leading to new concepts for treatment and prevention. These findings raise intriguing basic questions about the mechanisms that direct normal gut microbial community assembly and functional maturation. Designing and implementing new microbiota-directed therapeutics for undernutrition highlights the need to simultaneously consider a variety of features of human biology as well as broader societal issues.

Childhood undernutrition is a vexing, pressing, and in many respects overwhelming global health issue. Undernutrition contributes to more than 40% of deaths worldwide among children under 5 years old (*1*). Acute undernutrition affects more than 50 million children and is defined by a low weight-for-height Z (WHZ) score [the number of standard deviations from the median value for a reference, multinational World Health Organization (WHO) cohort of children with healthy growth phenotypes (*2*)]. Preschool children with severe wasting (WHZ < −3) have a 10-fold higher mortality rate than that of their well-nourished counterparts. In 2014, chronic undernutrition, which manifests as stunting [low height-for-age Z score (HAZ)], affected 159 million children, with almost all living in low-income countries (*3*). Despite these categorical distinctions, deficits in ponderal and linear growth frequently coexist and increase the risk that children will experience persistent stunting, defective immune responses, and impaired neurocognitive function into adulthood (*4*).

Epidemiologic studies have emphasized that undernutrition cannot be ascribed to food insecurity alone and reflects the intersection of multiple factors that operate within and across generations (*4*, *5*). Genetic analyses of risk factors have produced few leads. Longitudinal studies of a cohort of 317 Malawian twin pairs, aged 0 to 3 years and living in rural villages, revealed a high incidence of discordance (>40%) for either severe acute malnutrition (SAM) or moderate acute malnutrition (MAM). The rate of discordance (in which one twin was healthy by anthropometry and the other was diagnosed with SAM or MAM) was not significantly different between mono- versus dizygotic pairs, suggesting that early life environmental exposures play a key role in disease pathogenesis (*6*).

Breast milk

For many infants, breast milk represents one of the earliest postnatal environmental exposures. WHO/United Nations Children's Emergency Fund (UNICEF) recommends exclusive breastfeeding for the first 6 months of postnatal life and non-exclusive breastfeeding up to 24 months (*7*). Breast milk reduces infant mortality from common infections, including those that cause diarrhea and pneumonia (*8*). Despite the biological importance of breast milk, large gaps in knowledge remain, including how breast milk composition varies as a function of maternal nutritional status and whether and how variation in its composition affects risk for undernutrition in offspring. Fortunately, recent advances in mass spectrometric (MS) methods have set the stage for addressing how breast milk components vary as a function of age, genotype, parity, length of pregnancy, time after parturition, and health status in geographically and culturally diverse populations of women (*9*). Human milk oligosaccharides (HMOs) represent attractive targets for MS-based analyses, particularly if they are incorporated into birth cohort studies that couple serial breast milk sampling with comprehensive assessments of maternal and infant health status (*9*). HMOs contain a lactose core and linked glucose, galactose, N-acetyl galactosamine, fucose, and/or sialic acid residues [3–20 monosaccharides per HMO structure; ≥100 structures present in a given mother's breast milk (*9*)]. HMOs do not directly provide nutrition to the host. HMOs act as prebiotics that promote colonization of the infant gut with bifidobacterial taxa associated with multiple benefits to the host, including improved vaccine responses (*10*), enhanced gut barrier function (*10*, *11*), and protection from enteropathogen infection (*12*).

A recent study documented reduced levels of total, fucosylated, and sialylated HMOs in the breast milk of Malawian mothers with severely stunted compared with healthy 6-month-old infants (*13*). In follow-up preclinical experiments, young gnotobiotic mice were colonized with a consortium of bacterial strains cultured from the fecal microbiota of a severely stunted 6-month-old Malawian infant and fed a prototypic micro- and macronutrient-deficient Malawian diet, with or without added purified sialylated bovine milk oligosaccharides (S-BMOs) that are structurally similar to sialylated HMOs (*13*). A separate group of animals was fed the same Malawian diet supplemented with fructo-oligosaccharides, which are present in a number of current infant formulas. Even though all diets were isocaloric and animals in each of the groups consumed the same amount of diet, S-BMO but not fructo-oligosaccharide supplementation significantly augmented the rate of lean body mass gain. Growth augmentation was microbiota-dependent. S-BMO supplementation also produced changes in liver, muscle, and brain metabolic profiles indicative of increased capacity to use nutrients for anabolism in the fed condition and break down lipids during fasting [a state of increased metabolic flexibility (*14*)]. S-BMO–treated animals also manifested alterations in bone morphometry (*13*). The effects of S-BMOs were also observed in gnotobiotic piglets fed the same prototypic Malawian diet and colonized with cultured bacterial components of the same donor's microbiota (*13*). These findings underscore the need to understand genetic, physiologic, metabolic, and environmental factors that influence the representation of different HMO structures in lactating mothers' milk, how these structures are processed by the gut microbiota of healthy versus undernourished infants, and whether HMOs and the products of their biotransformation by the microbiota correlate with infant growth outcomes. In addition, these preclinical results illustrate how S-BMOs can be used as a tool to explore the mechanisms by which at least one class of HMOs operate, via the microbiota, to influence postnatal growth and metabolism.

Enteropathogen burden

Enteropathogens represent another common early life environmental exposure. The breadth of exposure is enormous: ~2.5 billion people currently live under unsanitary conditions, although efforts to sponsor innovations that yield affordable and sustainable solutions are under way (for example, www.gatesfoundation.org/What-We-Do/Global-Development/Reinvent-the-Toilet-Challenge).

[1]Center for Genome Sciences and Systems Biology, Washington University School of Medicine, St. Louis, MO 63110, USA. [2]Center for Gut Microbiome and Nutrition Research, Washington University School of Medicine, St. Louis, MO 63110, USA. [3]Nutrition and Clinical Services Division, International Centre for Diarrhoeal Disease Research, Dhaka 1212, Bangladesh.
*Corresponding author. Email: jgordon@wustl.edu

Downloaded from http://science.sciencemag.org/ on June 28, 2016

The development and implementation of robust, high-throughput methods for simultaneous quantitative polymerase chain reaction assays of multiple enteropathogens in a single fecal sample (*15*) is critical, enabling large-scale surveys of the relationship between enteropathogen burden and undernutrition. Birth cohort studies designed to address this question are now under way that also include serial anthropometric assessments as well as tests of immune and neurocognitive function (*16*).

Environmental enteric dysfunction (EED)

EED is an enigmatic disorder prevalent in low-income countries where sanitation is poor and enteropathogen burden is high. EED is often invoked as a key factor underlying the pathogenesis of undernutrition. However, accurate diagnosis remains a challenge. The "gold standard" for diagnosis is small intestinal biopsy, in which histopathologic manifestations of disease include infiltration of the lamina propria with $CD8^+$ T cells and villus atrophy (*17*). These changes are accompanied by marked reductions in the surface area available for active nutrient uptake and disruption of gut barrier function (*17*, *18*).

The fact that small intestinal biopsies carry substantial risk for children with undernutrition has limited the ability to assess the specificity or sensitivity of current fecal-, serum-, and urine-based biomarkers (*19*). Nonetheless, reports indicate that biomarkers of gut inflammation, intestinal permeability, and systemic immune activation are inversely correlated with linear growth and the efficacy of oral vaccines (*20*, *21*). Preclinical models with features of EED (*22*) provide an opportunity to help identify disease mechanism–based biomarkers and to dissect interactions between dietary components, enteropathogens, community members, gut barrier function, and inflammatory responses. For example, some gut microbes appear to elicit and benefit from inflammation (*23*), whereas others appear to blunt the immune response (*24*, *25*).

The limitations of current therapies and our knowledge of their long-term effectiveness

There is ongoing debate about the role of antibiotics in treating children at risk for or with already manifest acute or chronic undernutrition (*26*, *27*). A recent large, double-blind, placebo-controlled trial involving children with SAM living in Niger found no benefit of routine antibiotic use on nutritional recovery (*26*). Using random effects models, a meta-analysis of 10 randomized control trials (RCTs) involving children living in low- and middle-income countries given a variety of oral antibiotics for different indications and durations concluded that treatment was associated with modest improvement in ponderal growth and smaller improvements in linear growth (*28*). Extrapolating, these effects would correspond to a 0.2 to 0.3 increase in WAZ and a 0.1 increase in HAZ over 6 months in the most vulnerable populations (*28*).

Current nutritional interventions also have limited efficacy. A meta-analysis of RCTs, conducted in low- and higher-income countries, involving various forms of antenatal diet supplementation indicated that these interventions contributed to improved birth outcomes, including gestational age and birth weight (*1*). However, because primary end points were assessed at birth, the long-term effects on child growth and development remain unclear (*1*, *29*). The levels of certain micronutrients in breast milk that are essential for growth (such as vitamins A, B1, B2, B6, B12, and D and choline, selenium, and iodine) are influenced by maternal nutritional status (*30*). A meta-analysis of 16 controlled clinical studies of "multiple micronutrient powders" (MNPs) found no evidence of substantial effects on linear growth, despite improvements in micronutrient status (*31*). A separate analysis of seven clinical trials conducted in 6- to 24-month-old children living in food-insecure populations indicated that provision of complementary foods with or without nutritional education did not significantly reduce the risk of stunting (*1*). As with antenatal supplementation, studies have generally not examined the long-term effects of postnatal interventions on immune function or neurodevelopmental outcomes (*1*).

Energy-dense, micronutrient-fortified, ready-to-use therapeutic foods (RUTFs) are effective in accelerating short-term weight gain in individuals with SAM (*1*). Nutritional recovery (defined as attaining WHZ > −2) is believed to be facilitated by the provision of high-quality dietary protein in RUTFs, resulting in a switch from fatty acid to amino acid oxidation, with accompanying promotion of fat deposition and weight gain. Concomitant increases in insulin and IGF-1 and decreases in cortisol levels limit protein catabolism and permit accretion of muscle mass (*32*). However, in SAM as well as MAM there is a general lack of information on the appropriate timing and duration of current nutritional interventions or their overall effectiveness in overcoming the long-term morbidities that ensue from childhood undernutrition (*33*, *34*).

What are we missing in our understanding of the pathogenesis of undernutrition, and how can new therapeutic strategies be identified that more durably repair its short and long-term effects? Recent work points to a persistent developmental abnormality in children with undernutrition that affects their gut microbiota.



Box 1. A hypothesis about gut microbiota development and the pathogenesis of undernutrition.

- Initial gut community assembly is disrupted by one or more factors (for example, failure to acquire organisms with key metabolic capabilities, whether due to insufficient exposure, deficiency of required nutrients, antibiotic administration, undefined host biological features, and/or enteropathogen competition).
- Disrupted microbiota development provides opportunities for enteropathogens to establish themselves and/or the virulence potential of pathobionts to be expressed, further disrupting already impaired microbiota maturation.
- Impaired microbiota development impairs codevelopment of the mucosal immune system, compromising barrier function, defense against enteropathogens, and vaccine responses and impeding further maturation.
- Disrupting the coordinated, mutually beneficial, functional codevelopment of the microbiota and host affects multiple biological regulatory systems through mechanisms that are largely unknown but manifested in part by impaired muscle and bone growth, impaired metabolism that jeopardizes the supply of nutrients and energy required by the developing brain, and impaired immune/gut barrier function.

(Left) Young girl in Dhaka, Bangladesh, consuming a meal with a diversity of dietary ingredients. Identifying those ingredients that promote healthy development of the gut microbiota may yield more effective treatments for undernutrition. [Photo courtesy of Mustafa Mahfuz] (Right) Measurement of mid-upper-arm circumference (MUAC) to assess for acute wasting in a child in Mitondo, Malawi. [Photo courtesy of Indi Trehan]

Postnatal development of the gut microbiota and the pathogenesis of undernutrition

Defining "normal" gut microbiota development

The tens of trillions of microbes that inhabit the human gut are tasked in part with the biotransformation of dietary ingredients into products that affect various aspects of our physiology, metabolism, and immune function. Asking whether and how postnatal assembly of the microbial community is related to the risk for and pathogenesis of undernutrition requires a definition of normal microbiota development. One approach used machine learning (Random Forests) to mine bacterial 16*S* ribosomal RNA (rRNA) data sets generated from fecal samples, collected monthly from birth through the first 2 to 3 years of postnatal life from infants and children living in an urban slum in Bangladesh who had healthy growth phenotypes (as judged with serial anthropometry). The results yielded a group of the most age-discriminatory

Downloaded from http://science.sciencemag.org/ on June 28, 2016

bacterial taxa; changes in their relative abundance provided a microbial signature that described a program of normal gut microbiota development shared by biologically unrelated healthy Bangladeshi infants/children (*35*).

This approach is being applied to additional birth cohorts living in different regions of the world, including low-income countries where the burden of undernutrition is great as well as high-income countries where the level of sanitation and consumption of processed foods is considerably higher. The results are beginning to provide information about the degree to which this program of gut community development is shared (*36*, *37*). Applying advances in genome assembly by using shotgun sequencing data sets generated from fecal DNA, as well as advances in culturing phylogenetically diverse members of the gut microbiota, should reveal the extent of strain-level variation and insights into the functional potential of these age-discriminatory bacterial taxa, both within and between different human populations. The representation of archaeal, eukaryotic, and viral components [including phage (*38*)] in the developing microbiota of healthy infants and children also needs to be delineated. One of the many motivations for obtaining this expanded view comes from recent work emphasizing how enteric viruses affect, and are affected by, members of these other domains of life ["transkingdom interactions" (*39*)].

Gut microbiota "immaturity" in undernourished children

Bacterial 16*S* rRNA–based Random Forests–generated models composed of age-discriminatory bacterial taxa allow a microbiota-for-age Z (MAZ) score to be computed that defines the degree of deviation of an unhealthy individual's microbiota age (state of development) from a reference cohort of chronologically age-matched children with normal growth. Applying this metric disclosed that community assembly is perturbed in Bangladeshi and Malawian children with undernutrition, resulting in persistent gut microbiota "immaturity"; their microbial community configuration looks "younger" than in chronologically age-matched healthy individuals (*35*, *36*). Children with MAM also have microbiota immaturity, albeit less severe than those with SAM (*35*, *36*). MAZ scores documented at 12 months of age in members of a Malawian birth cohort with minimal antibiotic exposure were predictive of anthropometric scores at 18 months [WHZ, WAZ, and to a lesser degree HAZ (*36*)]. Although additional studies of birth cohorts are needed to define the degree of correlation between MAZ and growth phenotypes, applying this metric in a randomized clinical study that assessed the effects of two different RUTFs given to Bangladeshi children with SAM revealed that neither RUTF rescued microbiota immaturity; improvement was partial and transitory (*35*).

Cause versus effect

What is the biological consequence of persistent gut microbiota immaturity? Preclinical proof-of-concept (POC) that it is a contributing cause rather than simply an effect of undernutrition has come from transplanting immature gut microbiota from undernourished Malawian infants and children, or normally maturing microbiota from those with healthy growth phenotypes, into young recently weaned germ-free mice fed a macro- and micronutrient-deficient diet representative of those consumed by the human donors (*36*). Immature microbiota from undernourished infants and children transmitted significantly reduced lean body mass gain phenotypes, alterations in bone morphometric phenotypes, and metabolic abnormalities evident in muscle, liver, and brain. Remarkably, the gain in lean body mass was significantly greater when the microbiota were from 6-month-old as compared with 18-month-old donors, although in each chronological age bin, growth promotion in recipient mice was greater when the microbial community originated from a healthy individual (*36*). These latter findings provide evidence supporting the hypothesis that microbiota maturation is functionally linked to the growth rate of the host.

Random Forests–based analysis of bacterial 16*S* rRNA data sets generated from the fecal microbiota of these recipient mice identified groups of bacterial taxa whose representation was discriminatory for several host phenotypes, including rate of lean body mass gain and bone morphologic features (*36*). These "growth-discriminatory" taxa included a subset of the age-discriminatory taxa, suggesting that the latter include taxa that are not only biomarkers but also mediators of host development. The overlapping membership of taxa in the different Random Forests models generated from different features of host biology leads to a testable hypothesis: Different configurations of microbiota from undernourished children can transmit different manifestations of disease.

Taking advantage of the coprophagy of mice, cohousing gnotobiotic animals shortly after they received microbiota transplants from 6-month-old infants with either normal linear and ponderal growth or severe stunting and underweight phenotypes resulted in invasion of age- and growth-discriminatory strains from cagemates with the transplanted healthy donor microbiota into the microbiota of cagemates harboring the undernourished donor's microbiota. Invasion was associated with prevention of growth faltering. Addition of a number of cultured invasive taxa to an undernourished donor's microbiota ameliorated growth-faltering and metabolic abnormalities present in control mice that received the undernourished donor's microbiota alone (*36*).

This approach of tracking microbial exchange during cohousing, followed by culturing invasive taxa, can be applied to numerous combinations of healthy and undernourished microbiota to determine the extent to which acquisition of members of a healthy donor's microbiota (or extirpation of members of an undernourished donor's microbiota) can prevent or treat transmissible disease–associated phenotypes. The results could yield probiotic candidates and provide an opportunity to define mechanisms underlying microbial promotion of healthy growth. Relevant to this issue is a report showing that the gut microbiota enhances sensitivity to growth hormone (*40*). In this study, young germ-free mice exhibited significantly reduced rates of weight gain and bone growth as compared with their conventionally raised counterparts. Moreover, the difference between groups was greater when animals consumed a nutrient-deficient compared to -sufficient diet. Whereas levels of growth hormone were comparable, insulin-like growth factor 1 (IGF-1) and IGF-1–binding protein 3 (IGFBP-3) concentrations were significantly lower in animals lacking a microbiota. Remarkably, this growth hormone–resistance was overcome if germ-free animals were monocolonized at birth with one but not another strain of *Lactobacillus plantarum*.

Characterizing codevelopment of the microbiota and gut mucosal immune system

Another important aspect of postnatal development involves functional maturation of the gut mucosal immune system. Quantifying immunoglobulin A (IgA) responses to members of the developing gut microbiota provides one way to characterize this process. IgA is the major class of antibody secreted by the gut mucosa. The intestinal IgA repertoire of breastfeeding infants initially consists of a mixture of antibodies produced locally within the mucosa and antibodies present in breast milk but becomes entirely host-derived as IgA-secreting plasma cells populate the intestinal lamina propria through both T cell–dependent and –independent pathways. Fecal samples can be serially collected from members of birth cohorts and subjected to fluorescence-activated cell sorting (FACS) so as to distinguish IgA-targeted from nontargeted taxa [defined by means of 16*S* rRNA analysis of the IgA^+ and IgA^- populations and expressed as an IgA index for each taxon (*37*, *41*)]. Applying this method to samples collected from 40 pairs of healthy U.S.-born mono- and dizygotic twins revealed IgA responses to 30 bacterial taxa that converge on a pattern shared across pairs by the second postnatal year. This convergence is not simply due to changes in the abundance of the targeted bacterial taxa. Several of the targeted bacteria are age-discriminatory taxa defined by Random Forests–based analysis of microbiota development in this healthy U.S. birth cohort. Zygosity, mode of delivery, and breast versus formula feeding all had small but statistically significant effects on targeting (*37*).

These approaches for quantifying development of gut mucosal IgA responses and development of the gut microbiota can be applied to healthy and undernourished members of birth cohorts representing different geographic areas, distinctive cultural and dietary traditions, and varying degrees of sanitation. The results should reveal the extent to which features of the maturation of gut mucosal IgA responses generalize across populations and whether they correlate with MAZ scores, anthropometry, enteropathogen burden, and vaccine responses. (If the latter is true, this may help inform vaccination strategies

Downloaded from http://science.sciencemag.org/ on June 28, 2016

in populations with poor responses.) Intriguingly, analysis of feces obtained from gnotobiotic mice colonized with fecal microbiota obtained from twin pairs discordant for SAM revealed a group of IgA-targeted bacterial taxa in the SAM donor microbiota. The FACS protocol allowed these strains to be recovered in a viable form. Germ-free mice receiving the purified consortium of SAM-associated IgA-targeted taxa and fed a Malawian diet developed an enteropathy characterized by disruption of small intestinal and colonic barrier function. The effects were diet-dependent (they did not occur if animals were fed a macro- and micronutrient-sufficient diet) and were prevented when a consortium of purified IgA-targeted bacterial strains from the healthy co-twin's microbiota was added just before transfer of the SAM-derived strains (*41*). These findings indicate that the IgA response can be used to identify and characterize bacterial effectors of enteropathy, strains that are potential therapeutic candidates, as well as the impact of specified dietary ingredients on pathogenesis (*42*).

A recent mouse study demonstrated a role for maternal microbial exposure in programming the immune responses of their pups (*43*). Pregnant germ-free mice were colonized with a genetically engineered *E. coli* strain that transiently colonizes the host, allowing dams to return to a germ-free state and deliver germ-free offspring. Transient maternal colonization was associated with changes in expression of pup intestinal genes involved in various facets of barrier function. This transmissible phenotype appears to be mediated in part by components of maternal microbes transferred, via antibodies, during pregnancy and in breast milk.

Mechanisms and future directions

Identifying age- and growth-discriminatory bacterial taxa in preclinical models provides an opportunity to use serially collected biospecimens and clinical metadata from completed, ongoing, or future birth cohort studies to examine, in a focused and hypothesis-driven manner, the effects of a variety of factors implicated in the pathogenesis of childhood undernutrition on the gut microbiota. One conceptualization of pathogenesis is presented in Box 1. Birth cohort studies also offer an opportunity to examine the extent to which microbiota immaturity arises through a failure to progress through a normal developmental program and/or through a regression owing to harmful perturbations (with an attendant failure to recover). Given the high rates of discordance for undernutrition documented in twins (*6*), incorporating them into these birth cohorts studies should be very informative.

Deciphering mechanisms that direct microbial community assembly

Although progression from milk feeding to complementary feeding to a fully weaned state has a large effect on gut microbial community configuration, the mechanisms that shape postnatal assembly of the human gut microbiota remain poorly understood. Preclinical gnotobiotic models should help address this challenge. The ability to generate clonally arrayed and genome-sequenced collections of cultured bacterial strains that represent the diversity present in a given individual's gut community makes it possible to introduce subsets of these organisms that represent different stages of community assembly into young germ-free animals. This will permit assessments of how each subset affects host biology, how varying the order of presentation of these community subsets affects community "fate," and what the effects of manipulating host genes have on community assembly. High-resolution time series studies need to be applied to these models that look beyond defining community structure, to expressed functions. If cultured strains are amenable to whole-genome transposon mutagenesis, then gene-level definitions of the origin of their fitness in the evolving community can be ascertained (*44*). These approaches can also be used to model the effects of enteropathogen invasion and/or antibiotic administration at various stages of community assembly, including analyses of how the extent and route of recovery from these perturbations (resiliency) relate to stages of community development and composition. Intriguingly, recovery from cholera infection in adults living in Bangladesh recapitulates many of the features of normal gut microbial community assembly seen in healthy infants and children, albeit over a much shorter time scale [weeks as opposed to years (*45*)]. Yet another opportunity provided by these types of defined gnotobiotic models is to characterize the effects of these manipulations along the length of the gut (at least at the time of euthanasia); this includes the proximal small intestine, where substantial host nutrient absorption occurs, and the ileum, where there is considerable cross-talk between microbes and the immune system.

At a minimum, these gnotobiotic experiments require that representative human diets be developed, including those that support early colonizers of the human gut (including milk-based components if the recipient germ-free animals have already been weaned). More detailed biochemical knowledge of the composition of commonly consumed dietary components is needed if their effects on the structural and functional maturation of the microbiota are to be deciphered. Developing





Box 2. Societal considerations for microbiota-directed interventions for childhood undernutrition.

- Educating women about the microbiota and health
- Envisioning the impact of this knowledge and empowerment on child-rearing practices
- Assessing the cultural acceptability of microbiota-directed food products (includes labeling and associated public educational/advertising efforts)
- Defining price points for "affordability" and development of strategies that promote consumer compliance
- Identification of sources of ingredients, and designing manufacturing systems and distribution infrastructures that provide local economic benefit in order to ensure sustainable production of these products
- Ensuring partnerships between governmental, nongovernmental organization, and other potential stakeholders to enable broad implementation and mitigate risk for investment by industrial partners
- Understanding and shaping national views and policies related to ownership of foods (cultivars and recipes), their manufacture, branding, and associated intellectual property
- Assessing the downstream consequences of success in demonstrating the interrelationship between food, the gut microbiota, and healthy growth on national policies regarding (i) nutritional recommendations for children (including school age), (ii) the identification of more affordable nutritious sources of foods, and (iii) how best to define and ensure food safety (and support associated costs of implementing surveillance/testing)
- Delineating policies about the preservation, stewardship, and ownership of human-associated microbial resources within and across generations, within national borders, as well as policies related to the distribution of these resources across national borders
- Supporting anthropologic studies of how views about the association between microbes and humans ("self") are shaped by cultural traditions and religious beliefs
- Conducting analyses of the ethical and regulatory implications and long-term consequences of deliberately shaping human development through manipulating the assembly of microbial communities

(Left) Woman cooking food in a slum in Dhaka City, Bangladesh. [Photo courtesy of Mustafa Mahfuz] (Right) Rural village of Makhwira in Chikwawa District, Malawi, an area with some of the highest rates of stunting and wasting in sub-Saharan Africa. [Photo courtesy of Indi Trehan]

Downloaded from http://science.sciencemag.org/ on June 28, 2016

improved methods for quantifying spatial relationships between community members on partially digested food particles and at the mucosal-luminal interface would also add value to these analyses.

The massive data sets emanating from these preclinical studies should provide unprecedented opportunities (and requirements for new tools) to model microbe-microbe interactions, including the underpinnings of syntrophic relationships and competition. The results of the modeling can be tested in vivo by using the types of gnotobiotic models described above, or in vitro including in microfluidic systems (*46*). Throughput is a bottleneck for gnotobiotic experiments involving mice, but new caging systems offer the promise of increasing the ability to simultaneously test multiple combinations of defined collections of cultured gut microbes, or intact uncultured microbiota from multiple donors, outside of traditional flexible-film isolators. A variety of nonmammalian, genetically manipulatable vertebrate and invertebrate model organisms (such as *Danio rerio*, *Drosophila melanogaster*, and *Caenorhabditis elegans*) have been, are being, and need to be adopted for gnotobiotic studies. Moreover, in contrast to the hunt for genetic polymorphisms that affect susceptibility to infections in childhood with various pathogens (*47*), the search for polymorphisms that influence host-microbe interactions in undernutrition has produced few leads (*48*). Genetically manipulatable preclinical models will hopefully help fill this gap in knowledge.

Communication between the microbiota and host

Identifying the mechanisms by which normally developing versus immature gut microbiota regulate host physiology and metabolism is a formidable and intimidating yet inspiring challenge because it offers an opportunity to greatly advance our fundamental understanding of biological regulation in holobionts (hosts together with all of their microbial symbionts, both stable and transient). Basic principles can be gleaned by using preclinical models of the type described above, in which microbial community membership, host genotype, and environmental exposures can be systematically manipulated. The therapeutic implications could be great. For example, there is a dearth of metabolomic studies of undernourished children before, during, and/or after treatment and of suitable healthy controls (*32*). Understanding how immature microbiota from undernourished donors transmit a reduced metabolic flexibility phenotype to recipient gnotobiotic animals is important for a number of reasons, including the fact that low-income countries are experiencing the dual burden of under- and overnutrition [obese individuals with metabolic syndrome also manifest reduced metabolic flexibility (*14*)].

Therapeutic considerations

We need clinical POC that "catch-up" maturation of immature microbiota is feasible and sustainable. If the means are identified for sustained repair, then appropriately powered follow-on studies can be conducted to ascertain the effect on clinically meaningful growth outcomes, enteropathogen burden, gut barrier function and EED biomarkers, vaccine responses, and neurologic function.

One approach for shaping microbial community maturation is through development of microbiota-directed therapeutic foods that target age- and growth-discriminatory taxa. Commonly consumed complementary foods represent a source of culturally accessible, locally available, and affordable food ingredients that have "co-evolved" with a human population and its microbiota. One testable hypothesis is that some of the ingredients in these foods promote the representation of growth-discriminatory taxa in proportions that are age-appropriate. Testing this hypothesis requires databases of food consumption patterns and in vivo models in order to efficiently test different combinations and concentrations of these dietary ingredients for their effects on targeted age- or growth-discriminatory organisms. Fortunately, methods have already been described for performing diet oscillation studies in gnotobiotic mice colonized with defined consortia of bacterial strains and using linear modeling to identify which ingredients correlate with the abundances of given strains (*49*). A related question is whether the effects generalize to strain-level phylotypes obtained from different donors representing a population or populations of interest.

Complementary food-derived "leads" emerging from preclinical models can be advanced to human studies, assuming proper attention is paid to ethical, safety, and regulatory issues involved when enrolling children in vulnerable populations. Children who exhibit persistent MAM after the treatment of SAM represent a more stratified population with a history of severe microbiota immaturity than that of individuals who first present with MAM. Moreover, there is a clear unmet medical need, given the observed failures to progress beyond MAM with current short-term therapeutic protocols (*35*). This issue of what subset of children to enroll in future POC studies emphasizes the need to develop affordable point-of-care diagnostics for defining microbiota maturity.

Until the POC clinical studies are performed, we will not know whether and to what extent these types of food-based interventions can durably repair microbiota immaturity. We will also not know whether there are host factors that operate to regulate the rate of restoration of normal microbiota maturity and what the effects are when an age-appropriate state is achieved over a time frame that is shorter than the extent of immaturity (for example, if rescue occurs over 2 months when the child has a microbiota that at the time of diagnosis is 8 months younger than what is appropriate for his/her chronological age). The finding that microbiota from 6-month-old infants conferred greater growth than those from 18-month-old children in recipient mice has to be repeated by using samples serially collected from multiple individuals representing different populations in order to gain better understanding of the impact of rate (and route) of restoration of a perturbed microbiota on host biology.

In this conceptualization, the primary end-point biomarker for testing lead microbiota-directed food prototypes would be MAZ scores, with enteropathogen burden and assays of gut mucosal immune function (such as IgA responses) serving as secondary end-point markers. A selected affordable lead can then be advanced to studies so as to determine its effects on growth and development outcomes and, if therapeutic efficacy is established, whether it has utility in preventing disease.

It is possible that sustained repair of severely perturbed gut communities will require combinations of food-based and microbial interventions—the latter with defined consortia of cultured strains, including those representing targets of the dietary interventions. The regulatory path for microbial interventions in children, especially for organisms that are not classified as "generally regarded as safe" (GRAS), is uncertain at present, as is the safety (both short and long term) of fecal microbiota transplants in this population in which enteropathogen load is great and barrier function often compromised. To date, clinical trials of probiotics classified as GRAS in children with undernutrition have failed to show efficacy (*50*).

Societal implications of deliberate microbiota-directed interventions in children

The impact of increasing knowledge of the role of the microbiota in defining nutritional status will likely manifest itself in many ways. For these reasons, it is important that a holistic proactive view of the implications of this work be embraced and efforts made to prepare many elements of society through thoughtful engagement (Box 2). As clinical trials of the type described above are being planned, we issue a call for a comprehensive public dialogue about their benefits and perceived risks. Achieving a deep understanding of the biological as well as socioeconomic origins of this pervasive health problem will require "antedisciplinary" people (*51*). The same is true if we are to develop and implement effective treatment and prevention strategies. As such, this area provides an opportunity and need for universities to creatively evolve their educational strategies, policies (including access to their course content), and partnerships (within and across countries) in order to inspire and empower their students to acknowledge, confront, and overcome this daunting 21st-century challenge during their lifetimes.

REFERENCES AND NOTES

1. Z. A. Bhutta *et al*., Evidence-based interventions for improvement of maternal and child nutrition: What can be done and at what cost? *Lancet* **382**, 452–477 (2013). doi: 10.1016/S0140-6736(13)60996-4; pmid: 23746776
2. M. de Onis, A. W. Onyango, J. Van den Broeck, W. C. Chumlea, R. Martorell, Measurement and standardization protocols for anthropometry used in the construction of a new international growth reference. *Food Nutr. Bull.* **25** (suppl.), S27–S36 (2004). doi: 10.1177/15648265040251S104; pmid: 15069917
3. UNICEF, World Health Organization, W. B. Group, Levels and trends in child malnutrition, 1–6 (WHO, 2015).
4. A. J. Prendergast, J. H. Humphrey, The stunting syndrome in developing countries. *Paediatr. Int. Child Health* **34**, 250–265

Downloaded from http://science.sciencemag.org/ on June 28, 2016

(2014). doi: 10.1179/2046905514Y.0000000158; pmid: 25310000
5. R. Martorell, A. Zongrone, Intergenerational influences on child growth and undernutrition. *Paediatr. Perinat. Epidemiol.* **26** (suppl. 1), 302–314 (2012). doi: 10.1111/j.1365-3016.2012.01298.x; pmid: 22742617
6. M. I. Smith *et al*., Gut microbiomes of Malawian twin pairs discordant for kwashiorkor. *Science* **339**, 548–554 (2013). doi: 10.1126/science.1229000; pmid: 23363771
7. World Health Organization, Infant and young child feeding; Fact sheet no. 342, 1–5 (WHO, 2016).
8. B. L. Horta, C. G. Victora, Short-term effects of breastfeeding. *World Health Organization*, 1–54 (2013).
9. J. T. Smilowitz, C. B. Lebrilla, D. A. Mills, J. B. German, S. L. Freeman, Breast milk oligosaccharides: Structure-function relationships in the neonate. *Annu. Rev. Nutr.* **34**, 143–169 (2014). doi: 10.1146/annurev-nutr-071813-105721; pmid: 24850388
10. M. N. Huda *et al*., Stool microbiota and vaccine responses of infants. *Pediatrics* **134**, e362–e372 (2014). doi: 10.1542/peds.2013-3937; pmid: 25002669
11. M. Weng, K. Ganguli, W. Zhu, H. N. Shi, W. A. Walker, Conditioned medium from Bifidobacteria infantis protects against Cronobacter sakazakii-induced intestinal inflammation in newborn mice. *Am. J. Physiol. Gastrointest. Liver Physiol.* **306**, G779–G787 (2014). doi: 10.1152/ajpgi.00183.2013; pmid: 24627567
12. S. Fukuda *et al*., Bifidobacteria can protect from enteropathogenic infection through production of acetate. *Nature* **469**, 543–547 (2011). doi: 10.1038/nature09646; pmid: 21270894
13. M. R. Charbonneau *et al*., Sialylated milk oligosaccharides promote microbiota-dependent growth in models of infant undernutrition. *Cell* **164**, 859–871 (2016). doi: 10.1016/j.cell.2016.01.024; pmid: 26898329
14. D. M. Muoio, Metabolic inflexibility: When mitochondrial indecision leads to metabolic gridlock. *Cell* **159**, 1253–1262 (2014). doi: 10.1016/j.cell.2014.11.034; pmid: 25480291
15. J. Liu *et al*., A laboratory-developed TaqMan Array Card for simultaneous detection of 19 enteropathogens. *J. Clin. Microbiol.* **51**, 472–480 (2013). doi: 10.1128/JCM.02658-12; pmid: 23175269
16. A. M. Acosta *et al*., The MAL-ED study: A multinational and multidisciplinary approach to understand the relationship between enteric pathogens, malnutrition, gut physiology, physical growth, cognitive development, and immune responses in infants and children up to 2 years of age in resource-poor environments. *Clin. Infect. Dis.* **59** (suppl. 4), S193–S206 (2014). doi: 10.1093/cid/ciu653; pmid: 25305287
17. P. S. Korpe, W. A. Petri Jr., Environmental enteropathy: Critical implications of a poorly understood condition. *Trends Mol. Med.* **18**, 328–336 (2012). doi: 10.1016/j.molmed.2012.04.007; pmid: 22633998
18. S. McKay, E. Gaudier, D. I. Campbell, A. M. Prentice, R. Albers, Environmental enteropathy: New targets for nutritional interventions. *In Health* **2**, 172–180 (2010). doi: 10.1016/j.inhe.2010.07.006; pmid: 24037697
19. M. Kosek *et al*., Assessment of environmental enteropathy in the MAL-ED cohort study: Theoretical and analytic framework. *Clin. Infect. Dis.* **59** (suppl. 4), S239–S247 (2014). pmid: 25305293
20. M. Kosek *et al*., Fecal markers of intestinal inflammation and permeability associated with the subsequent acquisition of linear growth deficits in infants. *Am. J. Trop. Med. Hyg.* **88**, 390–396 (2013). doi: 10.4269/ajtmh.2012.12-0549; pmid: 23185075
21. C. Naylor *et al*., Environmental enteropathy, oral vaccine failure and growth faltering in infants in Bangladesh. *EBioMedicine* **2**, 1759–1766 (2015). doi: 10.1016/j.ebiom.2015.09.036; pmid: 26870801
22. E. M. Brown *et al*., Diet and specific microbial exposure trigger features of environmental enteropathy in a novel murine model. *Nat. Commun.* **6**, 7806 (2015). doi: 10.1038/ncomms8806; pmid: 26241678
23. S. E. Winter *et al*., Host-derived nitrate boosts growth of E. coli in the inflamed gut. *Science* **339**, 708–711 (2013). doi: 10.1126/science.1232467; pmid: 23393266
24. E. Quévrain *et al*., Identification of an anti-inflammatory protein from *Faecalibacterium prausnitzii*, a commensal bacterium deficient in Crohn's disease. *Gut* **65**, 415–425 (2016). doi: 10.1136/gutjnl-2014-307649; pmid: 26045134
25. S. Guo *et al*., Secreted metabolites of *Bifidobacterium infantis* and *Lactobacillus acidophilus* protect immature human enterocytes from IL-1β-induced inflammation: A transcription profiling analysis. *PLOS ONE* **10**, e0124549 (2015). doi: 10.1371/journal.pone.0124549; pmid: 25906317
26. S. Isanaka *et al*., Routine amoxicillin for uncomplicated severe acute malnutrition in children. *N. Engl. J. Med.* **374**, 444–453 (2016). doi: 10.1056/NEJMoa1507024; pmid: 26840134
27. I. Trehan *et al*., Antibiotics as part of the management of severe acute malnutrition. *N. Engl. J. Med.* **368**, 425–435 (2013). doi: 10.1056/NEJMoa1202851; pmid: 23363496
28. E. K. Gough *et al*., The impact of antibiotics on growth in children in low and middle income countries: Systematic review and meta-analysis of randomised controlled trials. *BMJ* **348** (apr15 6), g2267 (2014). doi: 10.1136/bmj.g2267; pmid: 24735883
29. P. C. Papathakis, L. N. Singh, M. J. Manary, How maternal malnutrition affects linear growth and development in the offspring. *Mol. Cell. Endocrinol.* (2016). doi: 10.1016/j.mce.2016.01.024; pmid: 26820126
30. L. H. Allen, B vitamins in breast milk: Relative importance of maternal status and intake, and effects on infant status and function. *Adv. Nutr.* **3**, 362–369 (2012). doi: 10.3945/an.111.001172; pmid: 22585913
31. R. A. Salam, C. MacPhail, J. K. Das, Z. A. Bhutta, Effectiveness of Micronutrient Powders (MNP) in women and children. *BMC Public Health* **13** (suppl. 3), S22 (2013). pmid: 24564207
32. S. Bartz *et al*., Severe acute malnutrition in childhood: Hormonal and metabolic status at presentation, response to treatment, and predictors of mortality. *J. Clin. Endocrinol. Metab.* **99**, 2128–2137 (2014). doi: 10.1210/jc.2013-4018; pmid: 24606092
33. C. Y. Chang *et al*., Children successfully treated for moderate acute malnutrition remain at risk for malnutrition and death in the subsequent year after recovery. *J. Nutr.* **143**, 215–220 (2013). doi: 10.3945/jn.112.168047; pmid: 23256140
34. L. M. Lenters, K. Wazny, P. Webb, T. Ahmed, Z. A. Bhutta, Treatment of severe and moderate acute malnutrition in low- and middle-income settings: A systematic review, meta-analysis and Delphi process. *BMC Public Health* **13** (suppl. 3), S23 (2013). doi: 10.1186/1471-2458-13-S3-S23; pmid: 24564235
35. S. Subramanian *et al*., Persistent gut microbiota immaturity in malnourished Bangladeshi children. *Nature* **510**, 417–421 (2014). pmid: 24896187
36. L. V. Blanton *et al*., Gut bacteria that prevent growth impairments transmitted by microbiota from malnourished children. *Science* **351**, aad3311 (2016). doi: 10.1126/science.aad3311; pmid: 26912898
37. J. Planer *et al*., Development of the gut microbiota and mucosal IgA responses in twins and gnotobiotic mice. *Nature* 10.1038/nature17940 (2016). doi: 10.1038/nature17940
38. A. Reyes *et al*., Gut DNA viromes of Malawian twins discordant for severe acute malnutrition. *Proc. Natl. Acad. Sci. U.S.A.* **112**, 11941–11946 (2015). doi: 10.1073/pnas.1514285112; pmid: 26351661
39. J. K. Pfeiffer, H. W. Virgin, Transkingdom control of viral infection and immunity in the mammalian intestine. *Science* **351**, aad5872 (2016). doi: 10.1126/science.aad5872; pmid: 26816384
40. M. Schwarzer *et al*., Lactobacillus plantarum strain maintains growth of infant mice during chronic undernutrition. *Science* **351**, 854–857 (2016). doi: 10.1126/science.aad8588; pmid: 26912894
41. A. L. Kau *et al*., Functional characterization of IgA-targeted bacterial taxa from undernourished Malawian children that produce diet-dependent enteropathy. *Sci. Transl. Med.* **7**, 276ra24 (2015). doi: 10.1126/scitranslmed.aaa4877; pmid: 25717097
42. T. Hashimoto *et al*., ACE2 links amino acid malnutrition to microbial ecology and intestinal inflammation. *Nature* **487**, 477–481 (2012).
43. M. Gomez de Agüero *et al*., The maternal microbiota drives early postnatal innate immune development. *Science* **351**, 1296–1302 (2016). doi: 10.1126/science.aad2571; pmid: 26989247
44. M. Wu *et al*., Genetic determinants of in vivo fitness and diet responsiveness in multiple human gut Bacteroides. *Science* **350**, aac5992 (2015). doi: 10.1126/science.aac5992; pmid: 26430127
45. A. Hsiao *et al*., Members of the human gut microbiota involved in recovery from *Vibrio cholerae* infection. *Nature* **515**, 423–426 (2014). doi: 10.1038/nature13738; pmid: 25231861
46. H. J. Kim, H. Li, J. J. Collins, D. E. Ingber, Contributions of microbiome and mechanical deformation to intestinal bacterial overgrowth and inflammation in a human gut-on-a-chip. *Proc. Natl. Acad. Sci. U.S.A.* **113**, E7–E15 (2016). doi: 10.1073/pnas.1522193112; pmid: 26668389
47. J.-L. Casanova, Severe infectious diseases of childhood as monogenic inborn errors of immunity. *Proc. Natl. Acad. Sci. U.S.A.* **112**, E7128–E7137 (2015). pmid: 26621750
48. C. O. Marginean, C. Banescu, S. Voidazan, C. Duicu, IL-6 572 C/G, 190 C/T, and 174 G/C gene polymorphisms in children's malnutrition. *J. Pediatr. Gastroenterol. Nutr.* **59**, 666–673 (2014). doi: 10.1097/MPG.0000000000000492; pmid: 25023587
49. J. J. Faith, N. P. McNulty, F. E. Rey, J. I. Gordon, Predicting a human gut microbiota's response to diet in gnotobiotic mice. *Science* **333**, 101–104 (2011). doi: 10.1126/science.1206025; pmid: 21596954
50. M. Kerac *et al*., Probiotics and prebiotics for severe acute malnutrition (PRONUT study): A double-blind efficacy randomised controlled trial in Malawi. *Lancet* **374**, 136–144 (2009). doi: 10.1016/S0140-6736(09)60884-9; pmid: 19595348
51. S. R. Eddy, "Antedisciplinary" science. *PLOS Comput. Biol.* **1**, e6 (2005). doi: 10.1371/journal.pcbi.0010006; pmid: 16103907

ACKNOWLEDGMENTS

Work cited from the authors' laboratory was supported in part by a grant from the Bill & Melinda Gates Foundation. J.I.G. is cofounder of Matatu, a company characterizing the role of diet-by-microbiota interactions in animal health. Upon completion of his Ph.D., M.R.C. has joined Matatu as a research scientist.

10.1126/science.aad9359

Downloaded from http://science.sciencemag.org/ on June 28, 2016

RESEARCH ARTICLE SUMMARY

DNA NANOTECHNOLOGY

Designer nanoscale DNA assemblies programmed from the top down

Rémi Veneziano,* Sakul Ratanalert,* Kaiming Zhang,* Fei Zhang, Hao Yan, Wah Chiu, Mark Bathe†

INTRODUCTION: Synthetic DNA can be programmed by using canonical Watson-Crick base pairing to form highly structured nanometer-scale assemblies that rival many natural protein and RNA assemblies in structural complexity. The use of a single-stranded scaffold DNA molecule that traverses the entire DNA architecture offers near-quantitative yield of target DNA-based objects, in addition to full control over their asymmetric three-dimensional (3D) structure and site-specific functionalization for applications that include cellular delivery, nanoscale photonic materials, single-molecule imaging, and structured metamaterials, among others. Design of these versatile DNA assemblies is currently limited, however, to experts who are knowledgeable in the sequence design rules needed to fold a target DNA shape.

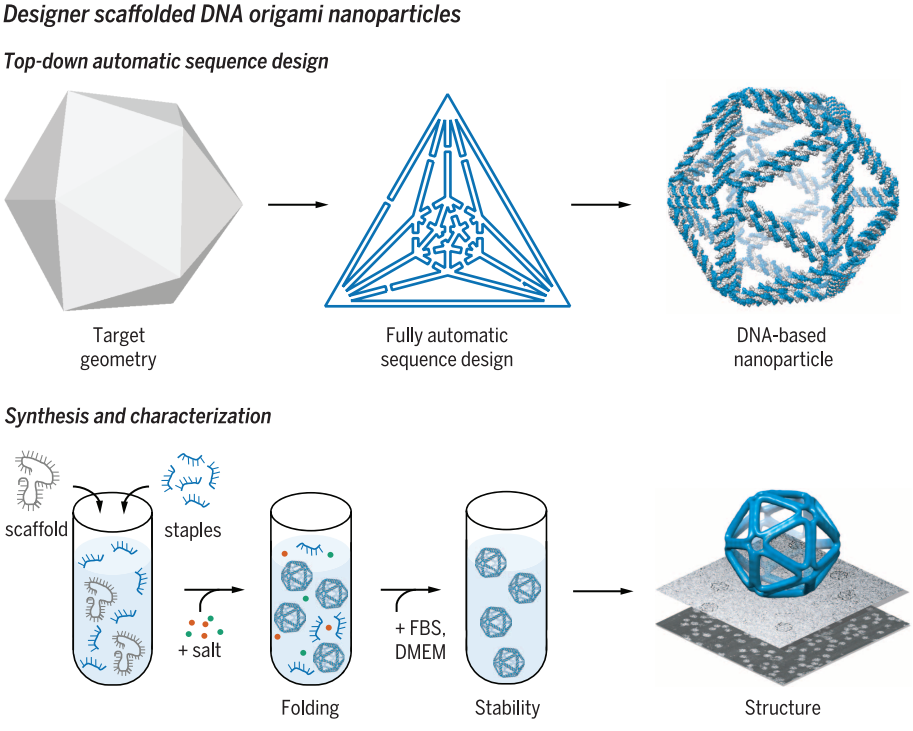
RATIONALE: A fully autonomous design procedure that computes the single-stranded DNA (ssDNA) sequences needed to fold an arbitrary 3D shape offers the potential for broadening participation in this powerful molecular design paradigm. Toward this end, we present the algorithmic framework DAEDALUS (http://daedalus-dna-origami.org) that uses a simple surface-based representation of target 3D geometry to automatically generate the ssDNA needed to synthesize the object. Target shapes are rendered with parallel DNA duplexes that are folded to form nanoparticles of high structural fidelity that are also biologically compatible. Our approach realizes the fully automatic, top-down sequence design of nearly arbitrary structured 3D DNA assemblies based only on simple geometric representation, offering non-experts the ability to design synthetic DNA-based molecular architectures.

RESULTS: We apply our computational algorithm to design a broad palette of 45 complex nanoparticle geometries including Platonic, Archimedean, Catalan, and Johnson solids, as well as more than 10 arbitrarily shaped solids that include both symmetric and asymmetric shapes. We apply asymmetric polymerase chain reaction (aPCR) to generate custom ssDNA scaffolds that result in high-fidelity folding of DNA nanoparticles of diverse shapes and sizes, which are also verified to fold in low salt concentrations due to their open wireframe design. We use single-particle cryo–electron microscopy (cryo-EM) to obtain 3D reconstructions of six target objects that are consistent with 3D atomic model predictions within the nanometer-scale resolution obtained, and demonstrate versatility of our algorithm in realizing both rigid and toroidal-like objects. Nanoparticles are demonstrated to be stable in cellular buffers including Dulbecco's modified Eagle's medium (DMEM) and fetal bovine serum (FBS). Our aPCR procedure offers facile amplification of target natural or synthetic DNA scaffolds for assays requiring high amounts of material, such as the cryo-EM reconstructions realized here.

ON OUR WEBSITE

Read the full article at http://dx.doi.org/10.1126/science.aaf4388

CONCLUSION: Inverse sequence design of structured DNA assemblies with full control over asymmetric 3D structure and sequence properties is a long-standing aim of molecular engineering. We present a general solution to this problem that offers the ability for nonspecialists to design and synthesize nearly arbitrary DNA-based nanoparticles using only a simple surface representation of the target object. We provide open-source software together with a versatile synthesis strategy to self-assemble complex nanoparticles that are stable in diverse buffers, including in physiological conditions, which offers the opportunity for their potential use in numerous in vitro as well as biomedical applications. ■



DNA nanoparticle design, synthesis, and characterization. (**Top**) Top-down geometric specification of the target geometry is followed by fully automatic sequence design and 3D atomic-level structure prediction. (**Bottom**) aPCR is used to synthesize object-specific ssDNA scaffold for folding. Nanoparticle stability is characterized in cellular media with serum and nanoparticle 3D structure is characterized by single-particle cryo-EM.

The list of author affiliations is available in the full article online.
*These authors contributed equally to this work.
†Corresponding author. Email: mark.bathe@mit.edu
Cite this article as R. Veneziano *et al.*, *Science* 352, aaf4388 (2016). DOI: 10.1126/science.aaf4388

Downloaded from http://science.sciencemag.org/ on June 28, 2016

RESEARCH ARTICLE

DNA NANOTECHNOLOGY

Designer nanoscale DNA assemblies programmed from the top down

Rémi Veneziano,[1]* Sakul Ratanalert,[1,2]* Kaiming Zhang,[3]* Fei Zhang,[4,5] Hao Yan,[4,5] Wah Chiu,[3] Mark Bathe[1]†

Scaffolded DNA origami is a versatile means of synthesizing complex molecular architectures. However, the approach is limited by the need to forward-design specific Watson-Crick base pairing manually for any given target structure. Here, we report a general, top-down strategy to design nearly arbitrary DNA architectures autonomously based only on target shape. Objects are represented as closed surfaces rendered as polyhedral networks of parallel DNA duplexes, which enables complete DNA scaffold routing with a spanning tree algorithm. The asymmetric polymerase chain reaction is applied to produce stable, monodisperse assemblies with custom scaffold length and sequence that are verified structurally in three dimensions to be high fidelity by single-particle cryo-electron microscopy. Their long-term stability in serum and low-salt buffer confirms their utility for biological as well as nonbiological applications.

DNA nanotechnology offers the ability to synthesize highly structured nanometer-scale assemblies that in principle could rival the geometric complexity found in natural protein and nucleic acid assemblies. The past decade has witnessed dramatic growth in the diversity of structured DNA assemblies that can be programmed from the bottom up to self-assemble into target shapes by complementary Watson-Crick base pairing (*1*–*7*). Scaffolded DNA origami is a particularly powerful means of synthesizing structured DNA assemblies, offering full control over both molecular weight and intricate nanometer-scale structure, with near-quantitative yield of the programmed product that relies on a single-stranded DNA (ssDNA) template (*2*, *5*, *8*, *9*). Wireframe topologies based on the scaffolding principle have further demonstrated highly versatile control over two-dimensional (2D) and three-dimensional (3D) spatial architecture (*10*–*13*).

Similar to the challenge of structure-based protein sequence design, which seeks to infer the amino acid sequence needed to fold a target protein structure of interest (*14*, *15*), achieving a general strategy for structure-based design of synthetic DNA assemblies represents a major challenge as well as opportunity for nanotechnology. Although numerous computational design tools exist to aid in the bottom-up, manual programming of scaffolded DNA origami (*16*), which requires complex scaffold routing and staple design to realize a target geometry based on Watson-Crick base complementarity, only one approach offers a solution to the inverse problem of sequence design based on specification of target geometry (*13*). However, this approach is only semi-automated and relies on single duplex DNA arms and multiway junctions to represent polyhedral geometries, which may result in compliant and unstable assemblies that are unsuitable for many applications. Moreover, programmed geometries must be topologically equivalent to a sphere, substantially limiting its scope.

As an alternative, here we introduce the fully automatic inverse design procedure DAEDALUS (DNA Origami Sequence Design Algorithm for User-defined Structures) that programs arbitrary wireframe DNA assemblies based on an input wireframe mesh without reliance on user feedback or limitation to spherical topologies. We apply our procedure to design 35 Platonic, Archimedean, Johnson, and Catalan solids; six asymmetric structures; and four polyhedra with nonspherical topologies; each of which is specified using surface geometry alone. Designed sequences are used to synthesize icosahedral, tetrahedral, cuboctahedral, octahedral, and reinforced hexahedral structures by the asymmetric polymerase chain reaction (aPCR) for facile production of single-stranded scaffolds of custom length and sequence. Programmed objects are confirmed by cryo–electron microscopy (cryo-EM), folding, and stability assays to be both high-fidelity structurally and stable under low-salt buffer conditions important to biological as well as in vitro applications. These results demonstrate the broad applicability of our design and synthesis strategy for numerous potential applications in biomolecular science and nanotechnology, including nanoparticle (NP) delivery (*17*, *18*), photonics (*19*, *20*), inorganic NP synthesis (*21*, *22*), memory storage (*23*–*25*), and single-particle cryo-EM analysis (*3*, *26*–*28*), among others (*7*, *29*, *30*). The ability to synthesize nearly arbitrary geometric shapes that are automatically rendered from the top down should enable the broad participation of nonexperts in this powerful molecular design paradigm.

Top-down automatic sequence design

To enable the fully automatic and robust inverse design of programmed DNA assemblies, we chose to render arbitrary geometries as node-edge networks based on the DX-based wireframe motif in which interconnected edges consist of two duplexes joined by means of antiparallel double crossovers (DX) (Fig. 1) (*3*, *10*–*12*, *31*). This strategy offered application of our procedure to any closed geometric surface, including nonspherical topologies such as a torus, provided that it can be rendered with polyhedral surface meshes. By means of this approach, the spatial coordinates of all vertices, the edge connectivities between vertices, and the faces to which vertices belong fully specify the target object (*32*). Standard polyhedron file formats containing this information are converted into this set of arrays, providing input to our scaffold routing and staple design procedure (Fig. 1, step i, and Fig. 2A). Programmed edges are required to consist of multiples of 10.5 base pairs (bp) rounded to the nearest nucleotide (nt), as commonly assumed in DNA origami design to satisfy the natural helicity of B-form DNA. Obeying the natural geometry of DNA ensures that no over- or underwinding in duplexes occurs (*33*, *34*), which may otherwise result in shape distortions that force deviation from the target geometry and would require iterative, ad hoc adjustment of edge lengths and sequence design (*13*). Notably, our algorithm has no theoretical limitation on the length of scaffold that can be used to program the target DNA origami object.

Representing the target geometry as a polyhedral mesh that satisfies the preceding design criteria guarantees that a single-stranded scaffold can be routed uniquely throughout the entire object with an Eulerian circuit, without modifications to the target geometry. From the mesh, the graph of the target structure is computed, containing the vertex, edge, and face information (Fig. 1, step i). Scaffold routing is then assigned by using a spanning tree (Fig. 1, step ii) generated with Prim's algorithm (fig. S1) (*35*). Each of the edges that is a member of the spanning tree is assigned no scaffold crossover, whereas each remaining edge is assigned one scaffold crossover. For a given graph, every spanning tree therefore corresponds to a unique scaffold routing, where, by default, Prim's algorithm generates a maximally branching spanning tree (figs. S1 and S2) that has been suggested for folding 2D nets to self-assemble more reliably than linear trees (*36*). The use of DX arms to represent edges ensures that a solution to the scaffold routing problem is obtained efficiently in solution

[1]Department of Biological Engineering, Massachusetts Institute of Technology, Cambridge, MA 02139, USA. [2]Department of Chemical Engineering, Massachusetts Institute of Technology, Cambridge, MA 02139, USA. [3]National Center for Macromolecular Imaging, Verna and Marrs McLean Department of Biochemistry and Molecular Biology, Baylor College of Medicine, Houston, TX 77030, USA. [4]School of Molecular Sciences, Arizona State University, Tempe, AZ 85287, USA. [5]Biodesign Center for Molecular Design and Biomimetics (at the Biodesign Institute) at Arizona State University, Tempe, AZ 85287, USA.
*These authors contributed equally to this work. †Corresponding author. Email: mark.bathe@mit.edu

Downloaded from http://science.sciencemag.org/ on June 28, 2016

time that scales as $E \log V$, where E and V are the numbers of edges and vertices, respectively (*35*). To complete the scaffold routing, a scaffold crossover is placed at the center of each edge that is not part of the preceding spanning tree. From the scaffold crossover positions and spanning tree, the circuit for the scaffold routing is determined, specifying the order in which the scaffold visits each vertex and crossover while ensuring that the scaffold does not intersect itself at vertices (Fig. 1, step iii) (*37*). A linear scaffold nick position is set to ensure that it is noncoincident with crossovers and other nicks, with the polarity of its routing chosen to be counterclockwise around each face because of the preference of the major groove to orient inwards at vertices (*38*). Thus, use of our spanning tree approach enables fully automatic conversion of the input polyhedral geometry to full scaffold routing based on the single circuit that traverses each duplex once.

With the scaffold routing determined, staple strands are assigned automatically by using distinct rules for vertex versus edge staples, enabling the assignment of staple strand sequences assuming Watson-Crick base complementarity (Fig. 1, step iv) (*32*). Vertex staples hybridize to the scaffold in the 10 to 11 bp closest to vertices, comprising 52- and 78-nt staples, the numbers of which are determined by the degree of the vertex (*32*). Edge staples occupy the intermediate regions, spanning across scaffold crossovers to help rigidify each edge by creating crossovers every 10, 11, or 21 bp (*32*). Finally, the positions and orientations of each nucleotide are modeled to predict the 3D structure of the NP (Fig. 1, step v, and fig. S3) (*32*). Critically, in contrast with previous tile-based approaches that used this DX-motif to synthesize NPs of diverse form (*3*), the use of a ssDNA scaffold that is routed throughout the entire object in our strategy offers near-quantitative yield of the final product in its self-assembly without dependence on relative multiarm junction tile concentrations, as well as full control over DNA sequence. This final feature is essential to biomolecular applications that use spatially specific asymmetric sequence programming for protein or RNA scaffolding, as well as other chemical functionalization.

To test the generality and robustness of our design procedure to be applied to diverse polyhedral geometries, we first applied it to design Platonic solids, which have equal edge lengths, angles, and vertex degrees; followed by geometries of increasing complexity, including Archimedean solids with unequal vertex angles; Johnson solids that include heterogeneity in vertex degrees; and Catalan solids that have unequal edge lengths (Fig. 2). Applicability to asymmetric and nonconvex objects specified on the basis of surface geometry alone (*13*) was also confirmed (Fig. 2 and fig. S4), in addition to nonspherical topologies, including a nested cube, a nested octahedron, and tori that have not been previously realized experimentally (*3*, *12*) and cannot be solved computationally with existing procedures (*13*). Fifteen of these structures required scaffolds longer than the 7249-nt M13mp18 (*39*), for which random sequences of appropriate length were generated (Fig. 2B). Taken together, these examples illustrate the broad ability of our procedure to automatically generate complex scaffold and staple routings for diverse geometries based on top-down geometric specification alone (Fig. 2).

Custom scaffold production with asymmetric PCR

To investigate the synthetic yield and homogeneity of self-assembled objects programmed with our computationally generated scaffold and staple designs, we used the aPCR (*40*) to generate object-specific scaffolds for folding (figs. S6 and S7) (*32*). These custom scaffolds minimize excess ssDNA in the final structure, which may result in nonspecific object aggregation or otherwise interfere with folding as well as downstream chemical functionalization (Fig. 3 and fig. S8) (*2*, *41*, *42*). Monodispersity of multiple custom linear short scaffold strands synthesized, ranging from 450 to 3400 nt, was first confirmed by gel electrophoresis of aPCR products based either on the M13pm18 ssDNA plasmid or double-stranded DNA (dsDNA) fragments as templates (Fig. 3). Custom scaffolds were used to fold tetrahedra of 31-, 42-, 52-, 63-, and 73-bp edge lengths in addition to an octahedron, two pentagonal bipyramids (42- and 52-bp edge lengths), a cube, a reinforced cube, an icosahedron, a cuboctahedron, and a nested cube (Fig. 4 and figs. S8 to S18) (*32*). Folded objects were analyzed by single-particle atomic force microscopy (AFM) after purification, which confirmed their folding yields of up to 90% (table S3) and particle homogeneity that is characteristic of scaffolded DNA origami objects (Fig. 2 and figs. S12 to 18). Notably, application of our aPCR approach offers folded sample purity that is similar to that of existing synthesis strategies that use restriction enzymes to generate subfragment scaffolds (Fig. 3 and figs. S6 and S7) (*43*), yet without dependence on restriction sites and with higher synthetic yield. Redesign of vertex staple nicks to be positioned at crossovers instead of interior segments of duplexes also resulted in increased folding stability (fig. S19) (*32*). Thus, diverse polyhedral origami objects from 270 kDa to 2 MDa programmed with our top-down, inverse sequence design procedure self-assembled robustly by using scaffolds of custom length and sequence, which may be natural or synthetic.

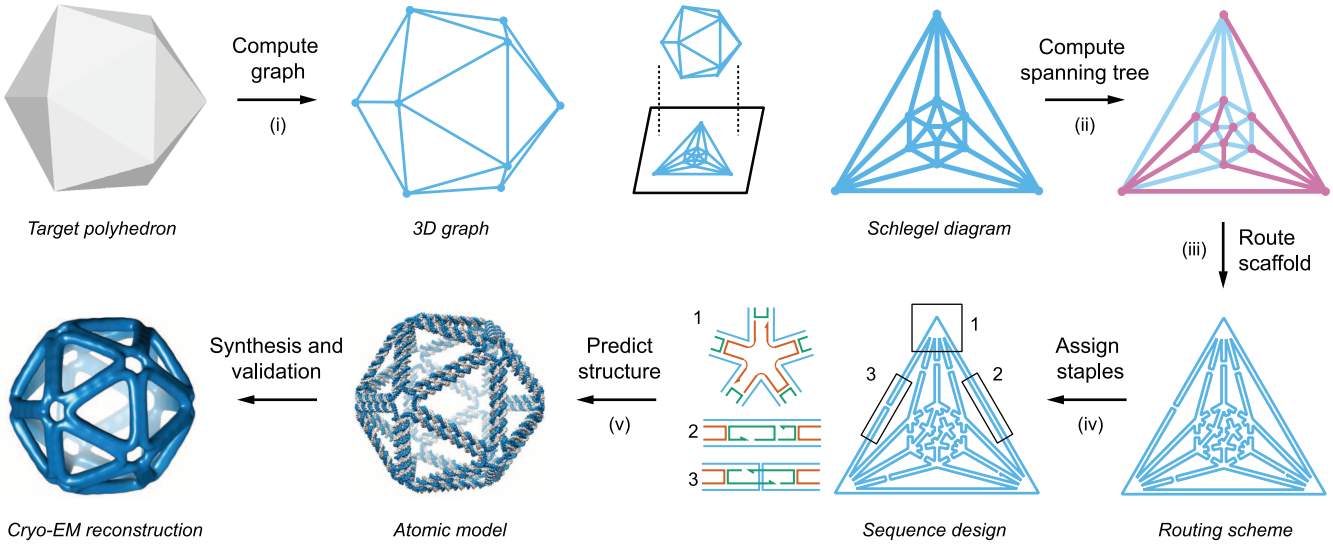


Fig. 1. Top-down sequence design procedure for scaffolded DNA origami nanoparticles of arbitrary shape. Specification of the arbitrary target geometry is based on a continuous, closed surface that is discretized with polyhedra. This discrete representation is used (step i) to compute the corresponding 3D graph and (step ii) spanning tree. The spanning tree is used (step iii) to route the ssDNA scaffold throughout the entire origami object automatically, which then enables (step iv) the assignment of complementary staple strands. Finally, (step v) a 3D atomic-level structural model is generated assuming canonical B-form DNA geometry, which is validated using 3D cryo-EM reconstruction.

Downloaded from http://science.sciencemag.org/ on June 28, 2016

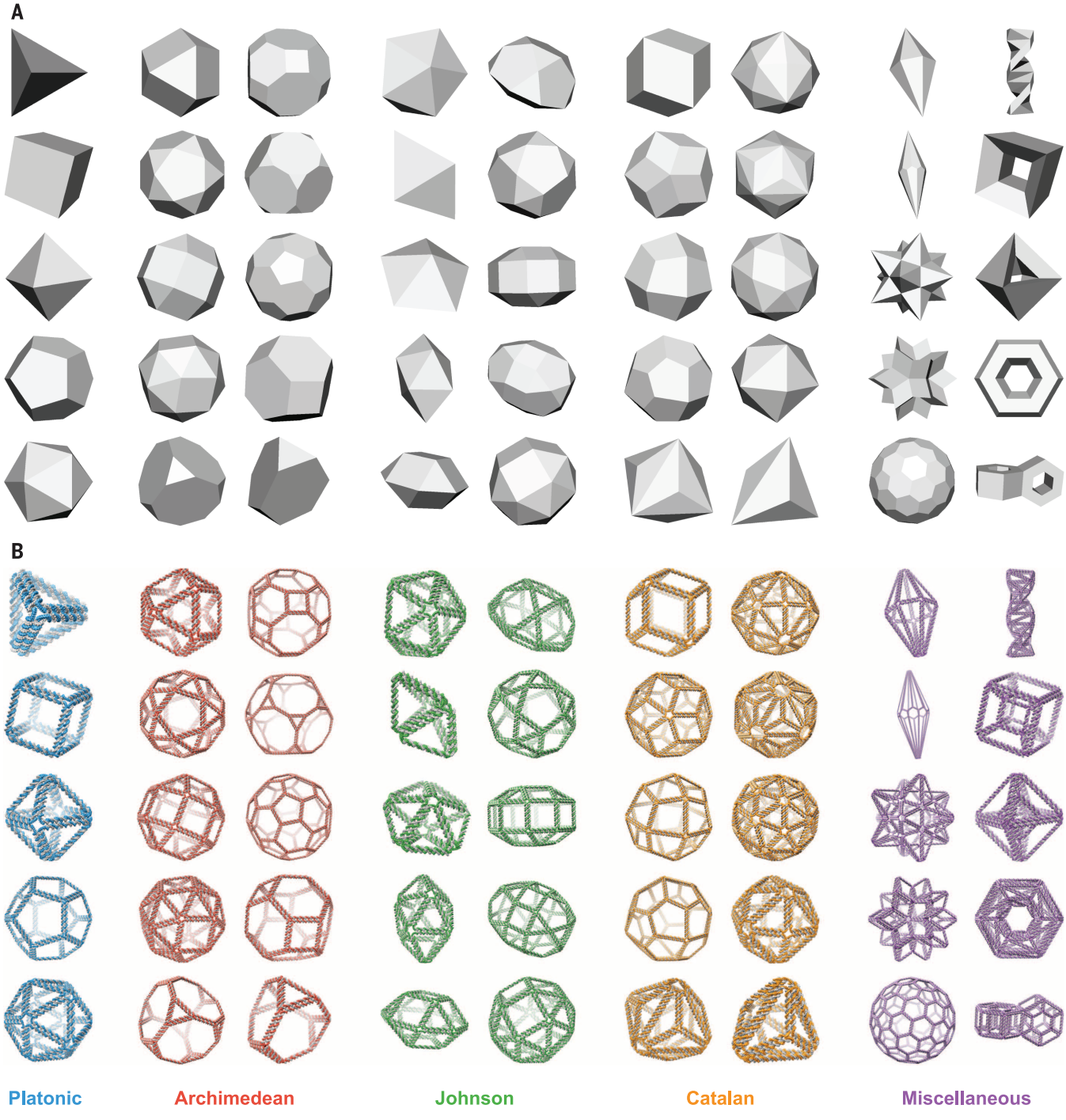


Fig. 2. Fully automatic sequence design of 45 diverse scaffolded DNA origami nanoparticles. (**A**) Face-shaded 3D representations of geometric models used as input to the algorithm. (**B**) Three-dimensional atomic models of DNA-rendered nanoparticles for (blue) Platonic, (red) Archimedean, (green) Johnson, (orange) Catalan, and (violet) miscellaneous polyhedra generated using the automatic scaffold routing and sequence design procedure (particles are not shown to scale). Miscellaneous polyhedra include (first column) heptagonal bipyramid; enneagonal trapezohedron; small stellated dodecahedron, a type of Kepler-Poinsot solid; rhombic hexecontahedron, a type of zonohedron; Goldberg polyhedron G(2,1) with symmetry of *Papillomaviridae*; (second column) double helix; nested cube; nested octahedron; torus; and double torus. Platonic, Archimedean, and Johnson solids each have 52-bp edge length, Catalan solids and the first column of miscellaneous polyhedra have minimum 42-bp edge length, and the second column of miscellaneous polyhedra have minimum 31-bp edge length. Thirty of the 45 structures shown have scaffolds smaller than the 7249-nt M13mp18, whereas 15 have scaffold lengths that exceed it (table S2).

Cryo-EM 3D reconstruction

Next, we evaluated the structural fidelity of programmed origami objects by using single-particle cryo-EM and 3D reconstruction (Fig. 5 and figs. S20 to S27) (*32*). Cryo-EM imaging confirmed the abundance of well-folded single DNA NPs of expected sizes and shapes, which were used to generate 3D density maps (Fig. 5). All maps were validated by matching class averages, map projections, and tilted-pair images (figs. S28 to S33) (*32*). Three-dimensional atomic structures of programmed DNA origami objects were predicted

Downloaded from http://science.sciencemag.org/ on June 28, 2016

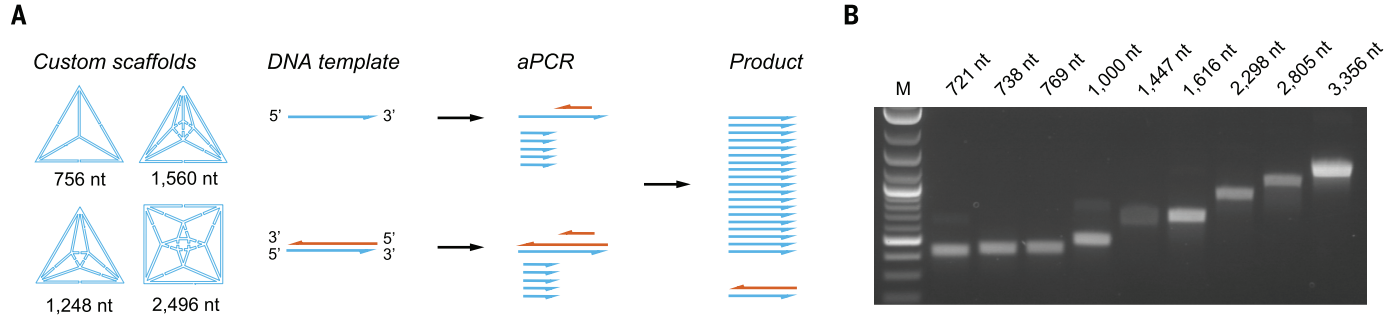


Fig. 3. aPCR strategy to synthesize custom ssDNA scaffolds. (**A**) ssDNA scaffolds of custom length and sequence for each target structure are amplified using either a single- or double-stranded DNA template mixed with appropriate primer pairs consisting of 50× sense primer and 1× antisense primer concentration relative to the scaffold concentration. (**B**) Amplified ssDNA products are purified and analyzed by agarose gel electrophoresis.

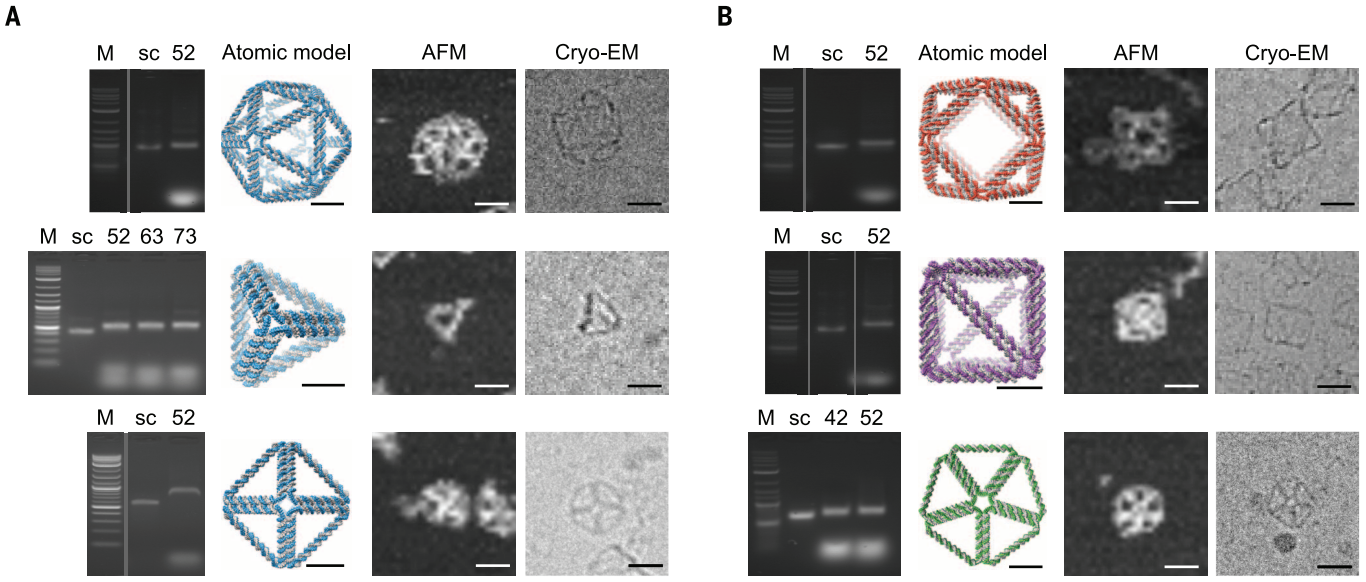


Fig. 4. Folding and 2D structural characterization of scaffolded DNA origami nanoparticles. (**A**) Characterization of folding for five platonic solids (52-, 63-, and 73-bp edge-length tetrahedra; 52-bp edge-length octahedron; 52-bp edge-length icosahedron) by agarose gel electrophoresis, AFM and cryo-EM. (**B**) Characterization of folding for one Archimedean solid (52-bp edge-length cuboctahedron), one miscellaneous solid (reinforced cube with 52- and 73-bp edge lengths), and one Johnson solid (42- and 52-bp edge-length pentagonal bipyramid), using agarose gel electrophoresis, AFM, and cryo-EM. M: DNA marker; sc: custom ssDNA scaffold. Scale bars: 20 nm for AFM and cryo-EM and 10 nm for atomic models.

by using a rigid duplex model in which each edge is composed of two parallel duplexes with the central axis of each edge meeting at a single point that is specified in the input graph (*32*). Quantitative comparison of model predictions with cryo-EM reconstructions revealed favorable agreement, with correlations ranging from 0.73 for the tetrahedron to 0.92 for the cuboctahedron, and resolutions comparable to those of previous wireframe DX designs based on tile assembly that produces polydisperse samples (Fig. 5A and fig. S28) (*3*). Interestingly, the tetrahedron exhibited outward bowing of its edges (Fig. 5B and fig. S29), which has been previously observed for single-duplex edges (*44*) and may be attributable to its smaller acute interior angles compared with those of other designed objects, which may result in steric overlap of adjoining DNA duplexes at vertices. Structure-based molecular modeling is of interest to test possible redesigns of the tetrahedral object that may improve agreement with the target, input geometry. Comparison of the cuboctahedron reconstruction with two competing models for vertex geometry suggested that duplex overlap is preferred over backbone stretching in determining overall equilibrium shape (Fig. 5D and figs. S3 and S30).

Notably, cryo-EM reconstructions suggested that origami objects assembled as designed instead of "inside-out" while satisfying programmed Watson-Crick base pairing from sequence design (*32*). This result reaffirms the suitability of our sequence design algorithm to choose to point the major groove inward at vertices, which was based on the previous observation that DNA origami folds in this manner (*38*). These two variants are distinguished experimentally by the designed asymmetry that places a 1-bp overhang on the 5′ end of the scaffold on each edge to keep the scaffold and staple crossovers perpendicular to the helical axis. Although 3′-end overhangs would have also achieved this, our choice of 5′-end overhangs anticipates a right-handed twist of the central hole of each vertex when the structures fold as prescribed, which is supported experimentally for the octahedron in which the chirality of the vertex twist is apparent (Fig. 5C and fig. S31). Notwithstanding, the extent to which the edges twist is not predicted by a simple geometric model that assumes that edges meet straight-on at vertices, deviating from the ~15° right-handed twist observed experimentally.

Although individual DX-based polyhedral edges are expected to be more structurally rigid than single-duplex edges used previously (*13*), some

Downloaded from http://science.sciencemag.org/ on June 28, 2016

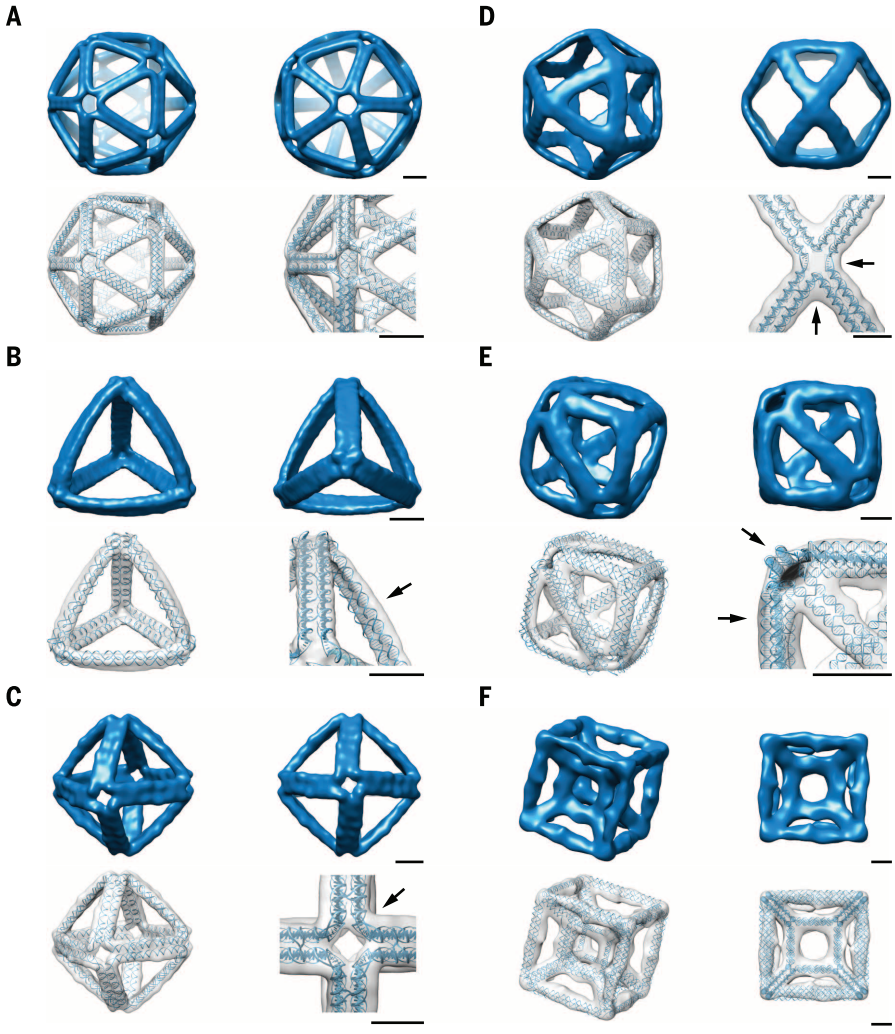


Fig. 5. Three-dimensional structural characterization of scaffolded DNA origami nanoparticles using cryo-EM reconstruction and comparison with model predictions. (**A**) Programmed edges of the 52-bp edge-length icosahedron are straight and vertices are rotationally symmetric, as designed. Cryo-EM resolution is 2.0 nm and correlation with the model is 0.85 (*55*). (**B**) Edges of the 63-bp edge-length tetrahedron reveal outward bowing (arrow) attributable to its acute interior angles that might result in steric hindrance. Cryo-EM resolution is 1.8 to 2.2 nm and correlation with the model is 0.72. (**C**) A 15° right-handed twist is visible at each vertex (arrow) of the 52-bp edge-length octahedron, which suggests that the structure folds as prescribed rather than "inside-out." Cryo-EM resolution is 2.5 nm and correlation with the model is 0.89. (**D**) A 52-bp edge-length cuboctahedron has unequal angles between edges that meet at vertices (arrows), which supports a rigid-duplex model in which phosphate backbone stretch is minimized (*32*). Cryo-EM resolution is 2.9 nm and correlation with the model is 0.92. (**E**) The addition of 73-bp reinforcing struts to a simple cube of 52-bp edge-length increases its structural homogeneity to produce a 3D reconstruction with 915 particles. With the reinforcement, the particles maintain right-angled vertices (upper arrow). The diagonal edges form a tetrahedral symmetry that exhibits outward bowing (lower arrow). Cryo-EM resolution is 2.7 nm and correlation with model is 0.72. (**F**) Three-dimensional reconstruction of a nested cube within a cube that has nonspherical topology. The 73-bp edge-length outer cube is connected to a 32-bp edge-length inner cube by eight 31-bp edge-length diagonals. Cryo-EM resolution is 4.0 to 4.5 nm and correlation with the model is 0.74. Scale bars: 5 nm.

surfaced-rendered polyhedral objects may still be expected to be structurally compliant because of their overall geometry, as in the case of the simple cube with 52-bp edge lengths that was initially observed by AFM and cryo-EM to fold into heterogeneous single particles (Fig. 2 and figs. S34 to S36). To test the ability of our algorithm to reprogram such flexible objects—to render them rigid for applications including single-particle cryo-EM at subnanometer resolution that requires highly homogeneous structural populations for reconstruction—we applied it to redesign a new, reinforced cube (Fig. 5E and fig. S32). We hypothesized that the observed heterogeneity in the simple cube resided in its vertex flexibilities, in which right-angle vertices can change in concert while maintaining constant edge lengths in shearing modes. To eliminate this compliant mode of deformation, we sought to introduce cross-bars on each face. Reinforced structures folded into highly homogeneous hexahedral objects that enabled single-particle cryo-EM imaging and reconstruction that agreed with 3D atomic model predictions (Fig. 5E and fig. S32). Surprisingly, constraining edge lengths to be multiples of 10.5 bp did not prove restrictive in achieving this target redesign, which required introduction of 73-bp cross-bars across each face (Fig. 5E and fig. S32). Although in principle this agreement may be attributable to the overall symmetry of the object, further bowing of edges may equally have been anticipated on the basis of steric overlap or duplex crowding at vertices. Given that uniform triangular polyhedra or other simple rules do not apply generally to the ultimate aim of rendering mechanically rigid surface geometries, generalizing this preceding redesign strategy from the hexahedron to other objects represents an important future challenge and demonstrates the versatility of our top-down sequence design procedure.

To test the ability of our algorithm to design scaffolded DNA origami objects of nonspherical topology and with internal structure that have not been previously realized experimentally (*3*, *12*) and cannot be designed with existing top-down computational design procedures (*13*), we synthesized the nested cube (Fig. 2B) and reconstructed its 3D structure using cryo-EM (Fig. 5F and fig. S33). Although the folding yield and cryo-EM resolution of this object were somewhat lower than for other objects (*32*), possibly due to the flexibility that is intrinsic to cubelike geometries, noted above, the ability to program internal structure substantially broadens the scope for synthesizing such complex scaffolded origami objects (*45*) in a one-step folding reaction.

Folding and stability characterization

An important limitation of DNA origami, for biological as well as in vitro applications, has been the requirement of high concentrations of either magnesium or monovalent cations for their folding and stability (*42*, *46*), which was recently shown to be alleviated by the use of single-duplex edge meshworks that fold and are stable in physiological buffer and salt conditions (*13*). Investigation of the folding properties of DX-based objects synthesized here revealed that objects fold effectively in cation concentrations as low as 4 mM Mg^{2+} and 500 mM Na^{+} (Fig. 6 and figs. S37 to S48), as well as in phosphate-buffered saline (PBS) alone (figs. S49 to S53). Although these results mirror those for wireframe structures employing single-duplex edges (*13*), our use of DX arms and multiway junctions (*11*, *12*) here results in structurally stable assemblies of enhanced rigidity that are crucial to many applications. To test the utility of our objects for cellular assays, after folding in TAE-Mg^{2+}, particles were transferred to PBS and Dulbecco's modified Eagle's medium (DMEM) containing 0 to

Downloaded from http://science.sciencemag.org/ on June 28, 2016

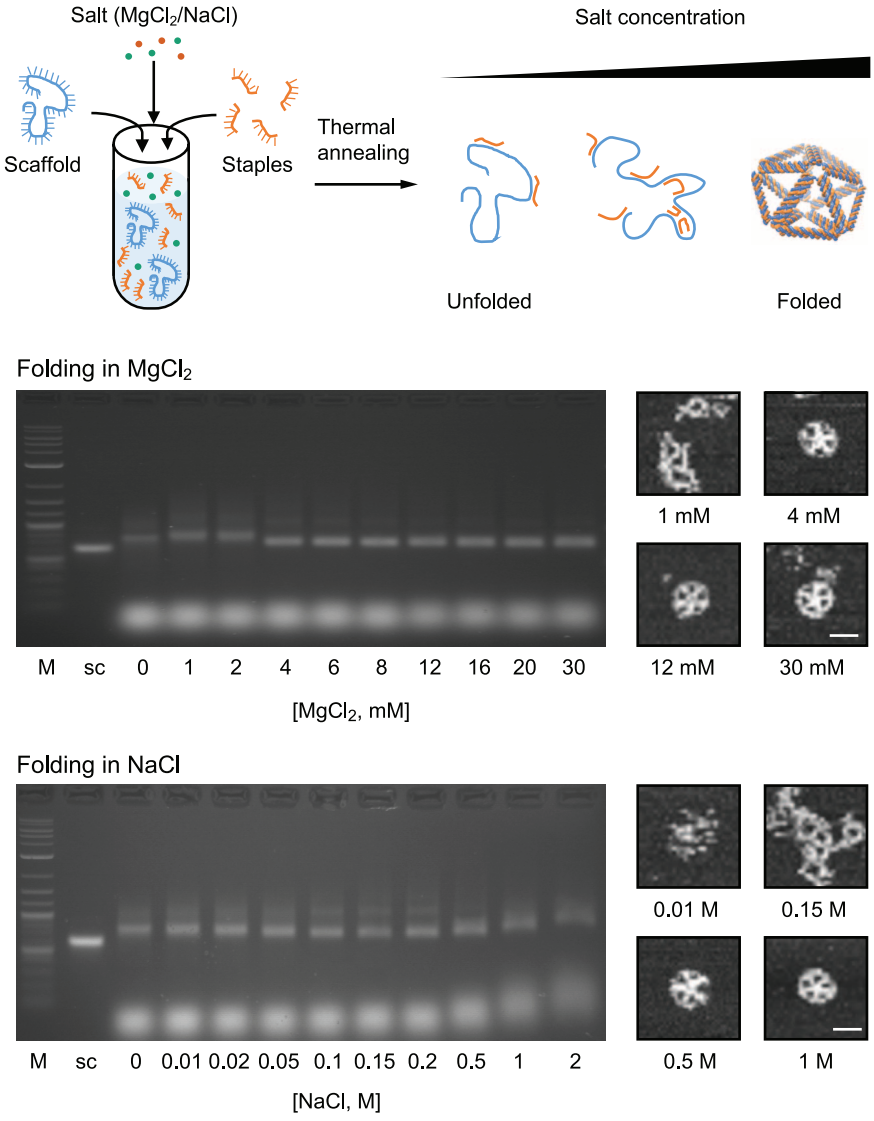


Fig. 6. Characterization of scaffolded DNA origami nanoparticle folding in variable concentrations of added salt. Characterization of folding of the 52-bp edge-length pentagonal bipyramid in increasing magnesium chloride ($MgCl_2$) and sodium chloride (NaCl) concentration using 2% agarose gel electrophoresis and AFM imaging. Critical concentrations for folding are 4 mM $MgCl_2$ and 500 mM NaCl in TRIS-acetate (pH 8.0). M: DNA marker; sc: custom ssDNA scaffold. Scale bars: 30 nm.

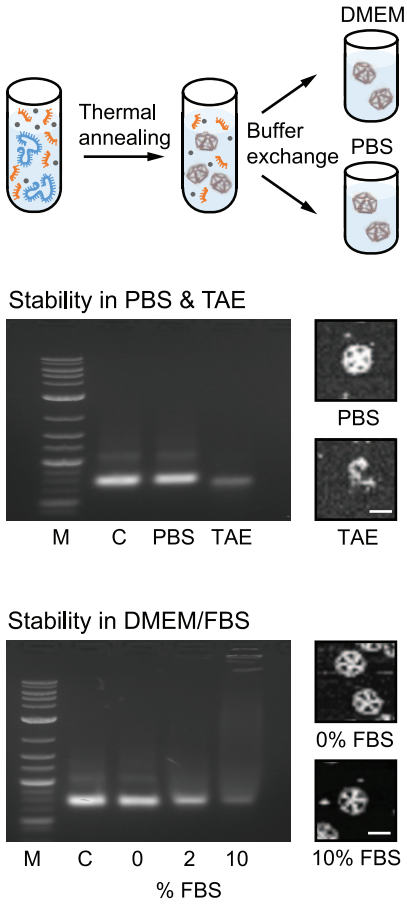


Fig. 7. Characterization of scaffolded DNA origami nanoparticle stability in physiological buffer and serum. Agarose gel electrophoresis and AFM structural characterization of the 52-bp edge-length pentagonal bipyramid after 6 hours in PBS, TAE (without added NaCl or $MgCl_2$), and DMEM buffer with increasing concentration of FBS (0, 2, and 10%) after folding in TAE-Mg^{2+} buffer (12 mM $MgCl_2$) followed by buffer exchange. Stability is observed for structures in PBS buffer but not in TAE owing to the absence of salt, which demonstrates the importance of a minimal salt concentration for stability. AFM imaging reveals the presence of intact objects after 6 hours in DMEM media in the presence of 2 to 10% FBS despite partial degradation observed in agarose gel electrophoresis. Scale bars: 30 nm.

10% fetal bovine serum (FBS), where they were found to be stable for at least 6 hours (Fig. 7 and figs. S54 to S59). When transferred to salt-free solution after folding, however, particles were observed to be unstable, confirming the well-known importance of a minimal amount of added salt for their longer-term stability (Fig. 7 and fig. S58). Interestingly, folding of the 52-bp tetrahedron with the full M13 scaffold instead of its custom scaffold also required higher magnesium concentrations to achieve folding, reaffirming the importance of the use of scaffolds that eliminate excess ssDNA (fig. S8).

Outlook

Structure-based, rational design of macromolecular assemblies, including both nucleic acids and proteins, is a long-standing aim of nanotechnology and biological engineering. Unlike proteins, which contain a myriad of specific and nonspecific interresidue interactions that determine their local and global folds, and RNA, which exhibits promiscuity in base pairing and secondary structure, synthetic DNA assemblies are well established to be highly programmable with Watson-Crick base pairing alone (*1*, *2*). In particular, wireframe polyhedral geometries offer the powerful ability to program nearly arbitrary 3D geometries on the nanometer scale, limited only by current size constraints imposed by single-stranded scaffold lengths. This important and versatile class of topologies therefore has broad potential for programming complex nanoscale geometries, including biomimetic systems inspired by viruses and photosynthetic systems, as well as other highly evolved natural macromolecular assemblies. Achieving full automation of inverse sequence design with this versatile wireframe approach has the potential to realize the original vision of Ned Seeman to program nanoscale materials with full 3D control over positioning of all atomic-level groups (*1*, *47*). As a major advance in this direction, we developed a top-down, geometry-driven sequence design procedure that uses a spanning tree algorithm to determine scaffold crossover positions. This enables efficient and unique routing of the single-stranded scaffold throughout any target origami object of arbitrary polyhedral shape and

Downloaded from http://science.sciencemag.org/ on June 28, 2016

molecular weight, as well as automated staple assignment to enable custom synthesis of programmed origami objects of near-quantitative yield and high-fidelity atomic-level structure. Asymmetric PCR is demonstrated to provide full control over scaffold sequence and length, verified between 449 to 3356 nt, and use of the DX-based design further confers folding capacity and stability under diverse conditions, including cell-compatible buffers. Our strategy to realize the top-down design of nanoscale DNA assemblies offers full control over both 3D structure and local sequence which, together with our broadly usable software and experimental protocols, provides a versatile approach to the design of functionalized DNA objects of nearly arbitrary shape for photonic applications (*19*, *48*, *49*), including self-assembled superlattices (*50*), cellular delivery (*18*, *51*), memory storage devices (*23*–*25*), and single-particle cryo-EM reconstruction assays (*3*, *26*–*28*) for proteins and RNAs that are not otherwise amenable to crystallography or nuclear magnetic resonance. Possible future generalizations of our approach may include rendering polyhedral networks with edges of arbitrary cross-section (*4*) for applications requiring further enhanced NP rigidity and closed surface topologies, such as inorganic nanoparticle synthesis (*21*, *22*) and hybrid nanoscale materials (*52*).

Materials and methods

Top-down sequence design

DAEDALUS is available for use as open-source software (*32*) and online at http://daedalus-dna-origami.org. Additional details can be found in Supplementary Materials (*32*) and in documentation provided with the software.

Single-stranded DNA scaffold amplification using aPCR

aPCR was performed with a sense primer concentration of 1 μM, an antisense primer concentration of 20 nM (table S2), 30 ng of M13mp18 ssDNA template or 10 ng of dsDNA gBlocks, 200 μM deoxynucleotide triphosphates mixed in a final volume of 50 μl and 1 unit of Accustart Taq DNA polymerase HiFi. The aPCR program used is as follows: 94°C, 1 min for the initial denaturation; followed by 30 to 40 cycles of 94°C, 20 s; 55° to 59°C, 30 s; 68°C, 1 min per kilobase to amplify. PCR products were run through 1% low–melting temperature agarose gel and were extracted and purified with Zymoclean Gel DNA recovery kit.

DNA origami assembly and purification

In a one-pot reaction, 5 to 40 nM scaffold strand was mixed with 50 to 800 nM of a staple strands mix in a Tris-acetate EDTA-$MgCl_2$ (TAE-Mg^{2+}) buffer [40 mM Tris, 20 mM acetic acid, 2 mM EDTA, 12 mM $MgCl_2$ (pH 8.0)]. Annealing was performed in a thermal cycler with the following program: 95°C for 5 min, 80° to 75°C at 1°C per 5 min, 75° to 30°C at 1°C per 15 min, and 30° to 25°C at 1°C per 10 min. Fresh DNA origami solutions were purified with an Amicon Ultra-0.5 ml centrifugal filter [molecular weight cut-off (MWCO) 100 kDa] to remove excess of staple strands and stored at 4°C.

Stability experiments

After buffer exchange with Amicon Ultra-0.5 (MWCO 100 kDa) DNA origami stability was evaluated for 6 hours in TAE, PBS, or DMEM buffer complemented with FBS.

Agarose gel electrophoresis

Samples were loaded in 2% agarose gel in Tris-acetate EDTA buffer supplemented with 12 mM $MgCl_2$ and prestained with EtBr. Gels were run on a BioRad electrophoresis unit at 4°C for 3 to 4 hours under a constant voltage of 70 V. Gels were imaged with a Gene flash gel imager (Syngene, Inc.), and yield was estimated by analyzing the band intensity with the Gel Analyzer program in the ImageJ software (*53*).

Atomic force microscopy (AFM)

Samples for AFM were annealed at a concentration of 5 nM in TAE-Mg^{2+} (12 mM) buffer and subsequently purified before AFM imaging. A 1.5-μl volume of the samples was deposited onto freshly peeled mica (Ted Pella, Inc.), and 10 μl of 1× TAE-Mg^{2+} buffer were added to enlarge the solution drop to cover the whole mica surface. A 1.5-μl volume of $NiCl_2$ (100 mM) was added to the drop immediately. After leaving about 30 s for adsorption to the mica surface, 70 μl of 1× TAE-Mg^{2+} buffer were added to the samples and an extra 40 μl of the same buffer were deposited on the AFM tip. The samples were scanned in "ScanAssyst mode in fluid" by using an AFM (Dimension FastScan, Bruker Corporation, Inc.) with SCANASSYST-FLUID+ tips.

Cryo-EM

Fifteen to 25 tubes of samples were freshly annealed at a scaffold concentration of 20 nM in 50 μl of TAE-Mg^{2+} buffer, pooled, purified, and concentrated with an Amicon column Ultra-0.5 ml centrifugal filter (MWCO 100 kDa) to a final volume of 20 to 30 μl. Two microliters of the freshly concentrated DNA nanostructure solution were applied onto the glow-discharged 200-mesh Quantifoil grid, blotted for 1.5 s, and rapidly frozen in liquid ethane with a Vitrobot Mark IV (FEI). All grids were screened on a JEM2200FS cryo–electron microscope (JEOL) operated at 200 kV with in-column energy filter with a slit of 20 eV. Micrographs of the icosahedron, tetrahedron, cuboctahedron, and octahedron were recorded with a direct detection device (DDD) (DE-20 4k×5k camera, Direct Electron, LP) operating in movie mode at a recording rate of 25 raw frames per second at 25,000× microscope magnification (corresponding to a calibrated sampling of 2.51 Å per pixel) and a dose rate of ~21 electrons s^{-1} $Å^{-2}$ with a total exposure time of 3 s. Micrographs of the reinforced cube and the nested cube were recorded on a 4k×4k charge-coupled device camera (Gatan, Inc.) at 40,000× microscope magnification (corresponding to a calibrated sampling of 2.95 Å per pixel) and a dose rate of ~20 electrons s^{-1} $Å^{-2}$ with a total exposure time of 3 s. A total of 180 images for the icosahedron, 91 images for the tetrahedron, 101 images for the cuboctahedron, 100 images for the octahedron, 36 images for the reinforced cube, and 152 images for the nested cube were collected with a defocus range of ~1.5 to 4 μm.

Single-particle image processing and 3D reconstruction

Particle images recorded on a DE-20 detector were motion corrected and radiation damage compensated (*24*). The motion correction was done with running averages of three consecutive frames by using the DE_process_frames.py script (Direct Electron, LP). Single-particle image processing and 3D reconstruction was performed with the image processing software package EMAN2 (*54*). EMAN2 was used for initial micrograph evaluation, particle picking, contrast transfer function correction, 2D reference-free class averaging, initial model building, and 3D refinement. All initial models for the DNA origami objects were built from 2D reference-free class averages. For final refinement, 3650 particles were used for the icosahedron, 2183 particles for the tetrahedron, 1758 particles for the cuboctahedron, 2678 particles for the octahedron, 915 particles for the reinforced cube, and 2008 particles for the nested cube, applying icosahedral, tetrahedral, octahedral, octahedral, tetrahedral, and octahedral symmetries, respectively. Resolutions for the final maps were estimated with the 0.143 criterion of the Fourier shell correlation curve without any mask. A Gaussian low-pass filter was applied to the final 3D maps displayed in the UCSF Chimera software package (*55*). Correlation of each map with its corresponding atomic model is calculated by the UCSF Chimera fitmap function.

Tilt-pair validation for the cryo-EM map (*56*) was performed by collecting data at two goniometer angles, 0° and −10°, for each region of the grid. The test was performed with the e2tiltvalidate.py program in EMAN2. Additional details on the tilt-pair validation are provided in table S3.

Quantitative PCR thermal analysis

Quantitative PCR (QPCR) analyses were performed in a Roche LightCycler® 480. A scaffold concentration of 80 nM was used for the tetrahedron folding analysis, and the concentrations of each strand were adjusted to 1 μM for the three-way junctions. Samples were complemented with 1× final concentration of SYBR Green in a final volume of 20 μl. Fluorescence curves obtained were analyzed with first-order derivatives to identify transition temperatures.

REFERENCES AND NOTES

1. N. C. Seeman, Nucleic acid junctions and lattices. *J. Theor. Biol.* **99**, 237–247 (1982). doi: 10.1016/0022-5193(82)90002-9; pmid: 6188926
2. P. W. K. Rothemund, Folding DNA to create nanoscale shapes and patterns. *Nature* **440**, 297–302 (2006). doi: 10.1038/nature04586; pmid: 16541064
3. Y. He *et al.*, Hierarchical self-assembly of DNA into symmetric supramolecular polyhedra. *Nature* **452**, 198–201 (2008). doi: 10.1038/nature06597; pmid: 18337818
4. S. M. Douglas *et al.*, Self-assembly of DNA into nanoscale three-dimensional shapes. *Nature* **459**, 414–418 (2009). doi: 10.1038/nature08016; pmid: 19458720

Downloaded from http://science.sciencemag.org/ on June 28, 2016

5. D. Han *et al*., DNA origami with complex curvatures in three-dimensional space. *Science* **332**, 342–346 (2011). doi: 10.1126/science.1202998; pmid: 21493857
6. Y. Ke, L. L. Ong, W. M. Shih, P. Yin, Three-dimensional structures self-assembled from DNA bricks. *Science* **338**, 1177–1183 (2012). doi: 10.1126/science.1227268; pmid: 23197527
7. M. R. Jones, N. C. Seeman, C. A. Mirkin, Nanomaterials. Programmable materials and the nature of the DNA bond. *Science* **347**, 1260901 (2015). doi: 10.1126/science.1260901; pmid: 25700524
8. W. M. Shih, J. D. Quispe, G. F. Joyce, A 1.7-kilobase single-stranded DNA that folds into a nanoscale octahedron. *Nature* **427**, 618–621 (2004). doi: 10.1038/nature02307; pmid: 14961116
9. C. E. Castro *et al*., A primer to scaffolded DNA origami. *Nat. Methods* **8**, 221–229 (2011). doi: 10.1038/nmeth.1570; pmid: 21358626
10. H. Yan, S. H. Park, G. Finkelstein, J. H. Reif, T. H. LaBean, DNA-templated self-assembly of protein arrays and highly conductive nanowires. *Science* **301**, 1882–1884 (2003). doi: 10.1126/science.1089389; pmid: 14512621
11. P. W. Rothemund, Scaffolded DNA origami: From generalized multicrossovers to polygonal networks, in *Nanotechnology: Science and Computation* (Springer, 2006), pp. 3–21.
12. F. Zhang *et al*., Complex wireframe DNA origami nanostructures with multi-arm junction vertices. *Nat. Nanotechnol.* **10**, 779–784 (2015). doi: 10.1038/nnano.2015.162; pmid: 26192207
13. E. Benson *et al*., DNA rendering of polyhedral meshes at the nanoscale. *Nature* **523**, 441–444 (2015). doi: 10.1038/nature14586; pmid: 26201596
14. J. C. Sinclair, K. M. Davies, C. Vénien-Bryan, M. E. M. Noble, Generation of protein lattices by fusing proteins with matching rotational symmetry. *Nat. Nanotechnol.* **6**, 558–562 (2011). doi: 10.1038/nnano.2011.122; pmid: 21804552
15. H. Gradišar *et al*., Design of a single-chain polypeptide tetrahedron assembled from coiled-coil segments. *Nat. Chem. Biol.* **9**, 362–366 (2013). doi: 10.1038/nchembio.1248; pmid: 23624438
16. S. M. Douglas *et al*., Rapid prototyping of 3D DNA-origami shapes with caDNAno. *Nucleic Acids Res.* **37**, 5001–5006 (2009). doi: 10.1093/nar/gkp436; pmid: 19531737
17. D. Bhatia, S. Surana, S. Chakraborty, S. P. Koushika, Y. Krishnan, A synthetic icosahedral DNA-based host-cargo complex for functional in vivo imaging. *Nat. Commun.* **2**, 339 (2011). doi: 10.1038/ncomms1337; pmid: 21654639
18. S. M. Douglas, I. Bachelet, G. M. Church, A logic-gated nanorobot for targeted transport of molecular payloads. *Science* **335**, 831–834 (2012). doi: 10.1126/science.1214081; pmid: 22344439
19. A. Kuzyk *et al*., DNA-based self-assembly of chiral plasmonic nanostructures with tailored optical response. *Nature* **483**, 311–314 (2012). doi: 10.1038/nature10889; pmid: 22422265
20. G. P. Acuna *et al*., Fluorescence enhancement at docking sites of DNA-directed self-assembled nanoantennas. *Science* **338**, 506–510 (2012). doi: 10.1126/science.1228638; pmid: 23112329
21. W. Sun *et al*., Casting inorganic structures with DNA molds. *Science* **346**, 1258361 (2014). doi: 10.1126/science.1258361; pmid: 25301973
22. S. Helmi, C. Ziegler, D. J. Kauert, R. Seidel, Shape-controlled synthesis of gold nanostructures using DNA origami molds. *Nano Lett.* **14**, 6693–6698 (2014). doi: 10.1021/nl503441v; pmid: 25275962
23. V. Zhirnov, R. M. Zadegan, G. S. Sandhu, G. M. Church, W. L. Hughes, Nucleic acid memory. *Nat. Mater.* **15**, 366–370 (2016). doi: 10.1038/nmat4594; pmid: 27005909
24. G. M. Church, Y. Gao, S. Kosuri, Next-generation digital information storage in DNA. *Science* **337**, 1628–1628 (2012). doi: 10.1126/science.1226355; pmid: 22903519
25. N. Goldman *et al*., Towards practical, high-capacity, low-maintenance information storage in synthesized DNA. *Nature* **494**, 77–80 (2013). doi: 10.1038/nature11875; pmid: 23354052
26. X. C. Bai, T. G. Martin, S. H. W. Scheres, H. Dietz, Cryo-EM structure of a 3D DNA-origami object. *Proc. Natl. Acad. Sci. U.S.A.* **109**, 20012–20017 (2012). doi: 10.1073/pnas.1215713109; pmid: 23169645
27. Z. Wang *et al*., An atomic model of brome mosaic virus using direct electron detection and real-space optimization. *Nat. Commun.* **5**, 4808 (2014). doi: 10.1038/ncomms5808; pmid: 25185801
28. R. N. Irobalieva *et al*., Structural diversity of supercoiled DNA. *Nat. Commun.* **6**, 8440 (2015). doi: 10.1038/ncomms9440; pmid: 26455586
29. Y. Krishnan, M. Bathe, Designer nucleic acids to probe and program the cell. *Trends Cell Biol.* **22**, 624–633 (2012). doi: 10.1016/j.tcb.2012.10.001; pmid: 23140833
30. A. V. Pinheiro, D. Han, W. M. Shih, H. Yan, Challenges and opportunities for structural DNA nanotechnology. *Nat. Nanotechnol.* **6**, 763–772 (2011). doi: 10.1038/nnano.2011.187; pmid: 22056726
31. T. J. Fu, N. C. Seeman, DNA double-crossover molecules. *Biochemistry* **32**, 3211–3220 (1993). doi: 10.1021/bi00064a003; pmid: 8461289
32. See supplementary materials on *Science* Online.
33. H. Dietz, S. M. Douglas, W. M. Shih, Folding DNA into twisted and curved nanoscale shapes. *Science* **325**, 725–730 (2009). doi: 10.1126/science.1174251; pmid: 19661424
34. D.-N. Kim, F. Kilchherr, H. Dietz, M. Bathe, Quantitative prediction of 3D solution shape and flexibility of nucleic acid nanostructures. *Nucleic Acids Res.* **40**, 2862–2868 (2012). doi: 10.1093/nar/gkr1173; pmid: 22156372
35. R. C. Prim, Shortest connection networks and some generalizations. *Bell Syst. Tech. J.* **36**, 1389–1401 (1957). doi: 10.1002/j.1538-7305.1957.tb01515.x
36. S. Pandey *et al*., Algorithmic design of self-folding polyhedra. *Proc. Natl. Acad. Sci. U.S.A.* **108**, 19885–19890 (2011). doi: 10.1073/pnas.1110857108; pmid: 22139373
37. S. W. Bent, U. Manber, On non-intersecting Eulerian circuits. *Discrete Appl. Math.* **18**, 87–94 (1987). doi: 10.1016/0166-218X(87)90045-X
38. Y. He *et al*., On the chirality of self-assembled DNA octahedra. *Angew. Chem. Int. Ed. Engl.* **49**, 748–751 (2010). doi: 10.1002/ange.200904513; pmid: 20017168
39. A. N. Marchi, I. Saaem, B. N. Vogen, S. Brown, T. H. LaBean, Toward larger DNA origami. *Nano Lett.* **14**, 5740–5747 (2014). doi: 10.1021/nl502626s; pmid: 25179827
40. C. I. Wooddell, R. R. Burgess, Use of asymmetric PCR to generate long primers and single-stranded DNA for incorporating cross-linking analogs into specific sites in a DNA probe. *Genome Res.* **6**, 886–892 (1996). doi: 10.1101/gr.6.9.886; pmid: 8889557
41. K. E. Dunn *et al*., Guiding the folding pathway of DNA origami. *Nature* **525**, 82–86 (2015). doi: 10.1038/nature14860; pmid: 26287459
42. J.-P. J. Sobczak, T. G. Martin, T. Gerling, H. Dietz, Rapid folding of DNA into nanoscale shapes at constant temperature. *Science* **338**, 1458–1461 (2012). doi: 10.1126/science.1229919; pmid: 23239734
43. H. Said *et al*., M1.3—a small scaffold for DNA origami. *Nanoscale* **5**, 284–290 (2013). doi: 10.1039/C2NR32393A; pmid: 23160434
44. T. Kato, R. P. Goodman, C. M. Erben, A. J. Turberfield, K. Namba, High-resolution structural analysis of a DNA nanostructure by cryoEM. *Nano Lett.* **9**, 2747–2750 (2009). doi: 10.1021/nl901265n; pmid: 19492821
45. Z. Liu *et al*., Self-assembly of responsive multilayered DNA nanocages. *J. Am. Chem. Soc.* **137**, 1730–1733 (2015). doi: 10.1021/ja5101307; pmid: 25628147
46. T. G. Martin, H. Dietz, Magnesium-free self-assembly of multi-layer DNA objects. *Nat. Commun.* **3**, 1103 (2012). doi: 10.1038/ncomms2095; pmid: 23033079
47. N. C. Seeman, N. R. Kallenbach, Design of immobile nucleic acid junctions. *Biophys. J.* **44**, 201–209 (1983). doi: 10.1016/S0006-3495(83)84292-1; pmid: 6197102
48. K. Pan, E. Boulais, L. Yang, M. Bathe, Structure-based model for light-harvesting properties of nucleic acid nanostructures. *Nucleic Acids Res.* **42**, 2159–2170 (2014). doi: 10.1093/nar/gkt1269; pmid: 24311563
49. P. K. Dutta *et al*., DNA-directed artificial light-harvesting antenna. *J. Am. Chem. Soc.* **133**, 11985–11993 (2011). doi: 10.1021/ja1115138; pmid: 21714548
50. W. Liu *et al*., Diamond family of nanoparticle superlattices. *Science* **351**, 582–586 (2016). doi: 10.1126/science.aad2080; pmid: 26912698
51. S. Surana, A. R. Shenoy, Y. Krishnan, Designing DNA nanodevices for compatibility with the immune system of higher organisms. *Nat. Nanotechnol.* **10**, 741–747 (2015). doi: 10.1038/nnano.2015.180; pmid: 26329110
52. Y. Tian *et al*., Lattice engineering through nanoparticle-DNA frameworks. *Nat. Mater.*; advance online publication (2016). doi: 10.1038/nmat4571; pmid: 26901516
53. G. Bellot, M. A. McClintock, C. Lin, W. M. Shih, Recovery of intact DNA nanostructures after agarose gel-based separation. *Nat. Methods* **8**, 192–194 (2011). doi: 10.1038/nmeth0311-192; pmid: 21358621
54. G. Tang *et al*., EMAN2: An extensible image processing suite for electron microscopy. *J. Struct. Biol.* **157**, 38–46 (2007). doi: 10.1016/j.jsb.2006.05.009; pmid: 16859925
55. E. F. Pettersen *et al*., UCSF Chimera—a visualization system for exploratory research and analysis. *J. Comput. Chem.* **25**, 1605–1612 (2004). doi: 10.1002/jcc.20084; pmid: 15264254
56. P. B. Rosenthal, R. Henderson, Optimal determination of particle orientation, absolute hand, and contrast loss in single-particle electron cryomicroscopy. *J. Mol. Biol.* **333**, 721–745 (2003). doi: 10.1016/j.jmb.2003.07.013; pmid: 14568533

ACKNOWLEDGMENTS

Funding from the Office of Naval Research (ONR) N000141410609, the Human Frontier Science Program (HFSP) RGP0029/2015, and National Science Foundation (NSF-EAGER) CCF-1547999 to M.B.; the National Science Foundation (NSF CMMI) 1334109 to M.B. and H.Y.; and the National Institutes of Health (NIH P41GM103832 and P50GM103297) to W.C. is gratefully acknowledged. Patent applications have been filed by the MIT Technology and Licensing Office on behalf of M.B., R.V., and S.R. related to this work. M.B. is scientific founder of Structured DNA Technologies LLC. K. Pan is acknowledged for technical assistance with atomic-level rendering of origami models and with website construction; C. Hill for technical assistance with website construction; V. Kaushik, A. Leed, and M. Adendorff for technical assistance with QPCR; and S. Ludtke for advice on cryo-EM image processing. Author contributions: R.V. designed and implemented the aPCR protocol; conducted the aPCR, the agarose gel electrophoresis characterization, and the QPCR experiments; prepared samples for AFM and cryo-EM; and analyzed the data. S.R. designed the algorithm; coded and implemented the algorithm computationally; analyzed the atomic models and cryo-EM maps; performed the QPCR experiments; and analyzed the data. K.Z. performed the cryo-EM imaging and the 3D reconstruction and analyzed the data. F.Z. performed the AFM imaging and analyzed the data. H.Y. supervised the AFM imaging and interpreted the data. W.C. supervised the cryo-EM imaging and interpreted the data. M.B. designed and supervised the study and interpreted the results. S.R., R.V., and M.B. wrote the manuscript. All authors commented on and edited the manuscript. Data repository: Cryo-EM maps have been deposited to EMDataBank (Tetrahedron EMD-3408; Icosahedron EMD-3409; Octahedron EMD-3410; Cuboctahedron EMD-3411; Reinforced cube EMD-3412; Nested cube EMD-3413).

SUPPLEMENTARY MATERIALS

www.sciencemag.org/content/352/aaf4388/suppl/DC1
Materials and Methods
Supplementary Text S1 to S7
Figs. S1 to S59
Tables S1 to S27
Movies S1 to S7
References (57–64)
DAEDALUS Software Package

17 February 2016; accepted 3 May 2016
Published online 26 May 2016
10.1126/science.aaf4388

Downloaded from http://science.sciencemag.org/ on June 28, 2016

RESEARCH ARTICLES

INNATE IMMUNITY

A sentinel goblet cell guards the colonic crypt by triggering Nlrp6-dependent Muc2 secretion

George M. H. Birchenough, Elisabeth E. L. Nyström, Malin E. V. Johansson, Gunnar C. Hansson*

Innate immune signaling pathways contribute to the protection of host tissue when bacterially challenged. Colonic goblet cells are responsible for generating the two mucus layers that physically separate the luminal microbiota from the host epithelium. Analysis of colonic tissues from multiple mouse strains allowed us to identify a "sentinel" goblet cell (senGC) localized to the colonic crypt entrance. This cell nonspecifically endocytoses and reacts to the TLR2/1, TLR4, and TLR5 ligands by activating the Nlrp6 inflammasome downstream of TLR- and MyD88-dependent Nox/Duox reactive oxygen species synthesis. This triggers calcium ion–dependent compound exocytosis of Muc2 mucin from the senGC and generates an intercellular gap junction signal; in turn, this signal induces Muc2 secretion from adjacent goblet cells in the upper crypt, which expels bacteria. Thus, senGCs guard and protect the colonic crypt from bacterial intruders that have penetrated the inner mucus layer.

The intestinal epithelium separates the luminal microbiota from the systemic tissues, but it is not the first line of defense. That function falls to the colonic mucus layers, which are composed of polymeric sheets of Muc2 mucin (*1*, *2*). The colonic mucus has an inner layer formed of closely packed Muc2 sheets and a less organized outer layer. The inner layer is impenetrable to bacteria, whereas the outer layer serves as a habitat for the microbiota (*1*). Deletion of Muc2 in mice eliminates the mucus, causing bacterial colonization of the crypts, inflammation, and carcinogenesis (*1*, *3*). The mucus layers are vital for preventing colitis, but they must function cooperatively with other elements of the epithelial innate immune system. These include TLR-MyD88 (Toll-like receptor–myeloid differentiation primary response gene 88) signaling and the Nlrp6 (NOD-like receptor family pyrin domain–containing 6) inflammasome; deletion of either TLR-MyD88 signaling or the Nlrp6 inflammasome renders the host susceptible to severe experimental colitis (*4*–*7*).

Mucus components, including Muc2, are produced by intestinal goblet cells (GCs). As GCs migrate up the colonic crypt, they manufacture, store, and release Muc2 by regulated secretion. The colonic surface GCs continuously secrete Muc2 and maintain the mucus layers (*8*). Colonic GCs express TLRs, MyD88, and the Nlrp6 inflammasome (*9*, *10*). Thus, the crucial platforms for tissue preservation under challenge are expressed by the GCs. Endogenous factors (e.g., acetylcholine) trigger Muc2 secretion from colonic GCs (*11*, *12*); however, it is unknown whether microbial TLR ligands—for example, lipopolysaccharide (LPS) or lipoteichoic acid (LTA)—might regulate mucin secretion.

Department of Medical Biochemistry, University of Gothenburg, 40530 Gothenburg, Sweden.
*Corresponding author. Email: gunnar.hansson@medkem.gu.se

Bacterial TLR ligands induce Muc2 secretion

We first investigated the capacity of bacterial TLR ligands to stimulate Muc2 secretion from murine colonic GCs (Fig. 1A). Using dynamic changes in explant mucus thickness as an indicator of secretion (*12*, *13*), we observed that LTA, bacterial DNA, and the peptidoglycan subcomponents muramyl dipeptide (MDP) and γ-D-glutamyl-meso-diaminopimelic acid (iE-DAP) failed to elicit any secretory response. Conversely, LPS, its subcomponent lipid A, the synthetic triacylated lipopeptide P3CSK4, and flagellin all stimulated an increase in mucus thickness similar to that observed with the acetylcholine analog carbachol (CCh). LPS and P3CSK4 treatment of intact colonic tissue verified that the effect was not related to ex vivo muscle removal (fig. S1A). Ileal GCs are also responsive to CCh treatment (*12*), but we found them to be insensitive to LPS, P3CSK4, and flagellin (Fig. 1B).

Mucus quantified in the tissue explant system is dependent on Muc2 (i.e., completely absent in *Muc2*$^{-/-}$ tissue); alterations in mucus thickness are primarily reflective of Muc2 secretion. However, mucus thickness alterations may also be affected by volume expansion. Transepithelial potential difference recordings indicated transient ionic flux after treatment with LPS (Fig. 1C). A similar effect has been linked to cholinergic Muc2 secretion (*12*). Imaging of colonic explants from an mCherry–human MUC2–expressing transgenic mouse (RedMUC2^{98trTg}) revealed secreted Muc2 only in treated tissues (Fig. 1D). As mucus expands in volume, it becomes more penetrable to bacteria-sized beads. The thickness of mucus increased after LPS treatment, but no evidence of increased penetrability was observed (Fig. 1, E and F). Thus, bacterial TLR ligands induced Muc2 secretion.

Colonic GCs are likely routinely exposed to high concentrations of the TLR ligands that stimulate Muc2 secretion ex vivo. To examine the in vivo activity of TLR ligand–induced secretion, we measured the sensitivity of the response (Fig. 1G). Similar response curves were produced for lipid A, P3CSK4, and flagellin, with half-maximal effective concentration (EC_{50}) values between 0.4 and 0.85 μM. To assess this sensitivity in the appropriate biological context, we estimated the concentration of soluble lipid A in two colonic luminal compartments, the stool and mucus, by *Limulus* amebocyte lysate (LAL) assay (Fig. 1H). LAL reactivity of stool was higher than that of mucus by a factor of 360, indicating a steep gradient in lipid A concentration between the mucus and the stool. This reflected the factor of 210 difference in bacterial 16*S* rRNA gene copy number between these compartments (Fig. 1I). LAL reactivity to 0.85 μM (EC_{50}) lipid A was less than LAL reactivity to stool by a factor of 20 and was higher than LAL reactivity to mucus by a factor of 18 (Fig. 1H). Estimated in vivo lipid A concentrations were plotted on the lipid A response curve and closely mirrored the response window (Fig. 1G). These results show that the TLR ligand–triggered Muc2 secretion in the distal colon was inactive under normal conditions, as the mucus layer close to the colonic GCs did not harbor sufficient lipid A concentrations to trigger secretion.

TLR ligands induce Muc2 secretion in specific GCs

Intestinal GCs are more functionally heterogeneous than previously expected (*8*, *9*). We therefore tested whether TLR ligands induced Muc2 secretion from a specific population of GCs. RedMUC2^{98trTg} colonic explants were treated with LPS, P3CSK4, flagellin, or CCh individually or in combination, and tissue sections were imaged (Fig. 2, A and B). Untreated tissue had large Muc2-filled GCs in the upper crypt and smaller GCs containing less Muc2 in the lower crypt. Upper-crypt GCs were emptied in tissues treated with TLR ligands. Conversely, CCh treatment resulted in secretion of Muc2 at the lower crypt without affecting the upper-crypt GCs. Combined treatment with LPS and CCh emptied both upper- and lower-crypt GCs. Mucus secretion was quantified from explants treated with LPS in combination with P3CSK4, flagellin, or CCh (Fig. 2C). Treatment with LPS combined with P3CSK4 or flagellin did not induce any additive secretory response, whereas combined LPS and CCh treatment did. Reversing the direction (apical versus serosal) of LPS and CCh treatment did not induce Muc2 secretion, indicating that responses were compartmentalized (Fig. 2D). Together, these observations indicated that LPS, P3CSK4, and flagellin all induced Muc2 secretion from the same upper-crypt GCs and

Downloaded from http://science.sciencemag.org/ on June 28, 2016

that these cells were distinct from the GCs targeted by CCh.

The intercrypt GCs are another apically exposed GC population (*8*). These cells do not store large amounts of mature glycosylated Muc2 and are frequently not observed by conventional mucin staining. However, they can be identified in RedMUC2^{98trTg} tissues and are distinguishable from upper-crypt GCs (Fig. 2E). Comparison of untreated and LPS-treated tissue identified upper-crypt GCs secreting Muc2 in LPS-treated tissue but did not show any alterations to the intercrypt GCs. These results confirmed that only the upper-crypt colonic GCs were responsive to LPS.

The Muc2 secretory signaling pathway

Colonic GCs express TLRs that recognize LPS, P3CSK4, and flagellin (*9*) and also express the Nlrp6 inflammasome, which has been suggested to regulate GC Muc2 secretion (*10*). To examine the role of these mediators in controlling TLR ligand–stimulated secretion, we quantified mucus secretion in colonic explants from a range of knockout (KO) mice (Fig. 3A).

P3CSK4, LPS, and flagellin are recognized by TLR2/1, TLR4, and TLR5, respectively, which activate signaling via proximal mediators such as MyD88 and TRIF. Loss of their cognate receptors and MyD88, but not TRIF, prevented both LPS- and P3CSK4-induced secretion (Fig. 3A). *Tlr5*$^{-/-}$ tissue was not examined; however, the response to flagellin was not lost in *MyD88*$^{-/-}$ or *Trif*$^{-/-}$ tissues, which indicates that neither TLR-MyD88 nor TLR-TRIF signaling was essential to flagellin-induced secretion. The response to all three TLR ligands was preserved in *Rag1*$^{-/-}$ tissue, ruling out a role for mucosal lymphocytes in mediating Muc2 secretion (fig. S1B). CCh responses were unaltered in the *Tlr2*$^{-/-}$, *Tlr4*$^{-/-}$, *MyD88*$^{-/-}$, *Trif*$^{-/-}$, and *Rag1*$^{-/-}$ tissues.

Examination of LPS-, P3CSK4-, and flagellin-induced mucus secretion in Nlrp-deficient tissues precluded the involvement of Nlrp3 and Nlrc4 but indicated that Nlrp6 signaling was essential for the response to all three TLR ligands (Fig. 3A). Similarly, no response was observed in *Caspase-1/11*$^{-/-}$ and *Caspase-11*$^{-/-}$ tissue. Caspase-1–mediated maturation of interleukin-1β (IL-1β) and IL-18 is the conventional purpose of activated inflammasomes; the response to all three TLR ligands was unaltered in *IL1α/β*$^{-/-}$ and *IL18*$^{-/-}$ tissue, indicating that Nlrp6 inflammasome signaling did not rely on IL-1β and IL-18.

It has been suggested that *Nlrp6*$^{-/-}$ and *Caspase-1/11*$^{-/-}$ colonic GCs lack normal Muc2 secretion and an intact inner mucus layer (*10*), which could account for an inability to secrete Muc2. However, all of the different inflammasome KO tissues responded normally to CCh stimulation, and all strains had an intact inner mucus layer when housed in our facility (fig. S2).

To dissect the cellular responses involved in TLR ligand–induced Muc2 secretion, we tested inhibitors targeting various cellular processes (Fig. 3B). Dynasore, which inhibits endocytosis, blocked the response to both LPS and P3CSK4 but not the response to flagellin. Identical results

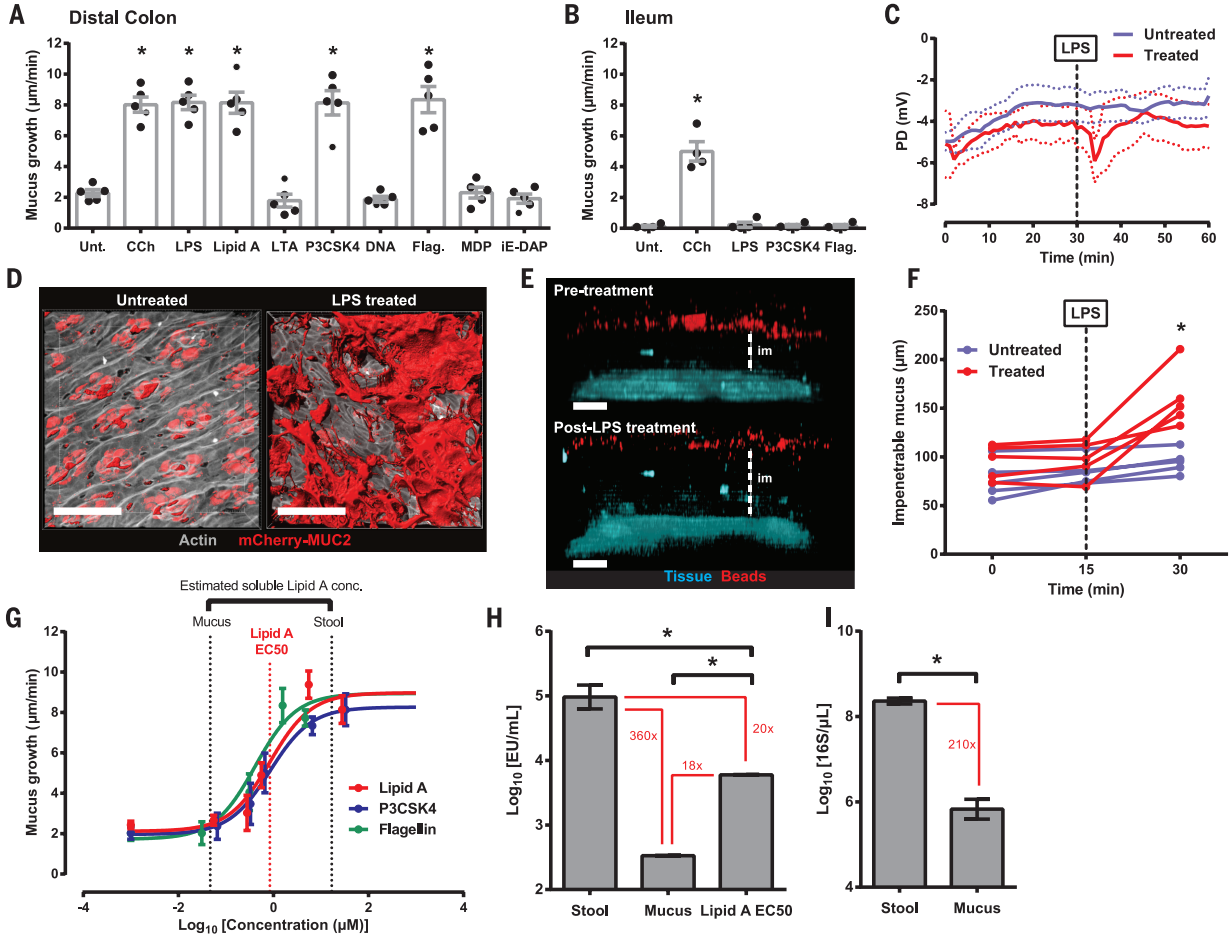


Fig. 1. Select TLR ligands induce Muc2 secretion in distal colon. In (A) to (G), intestinal explants were treated with TLR ligands or CCh. (**A** and **B**) Quantification of mucus growth from distal colonic (A) or ileal (B) explants. Unt., untreated; Flag., treated with flagellin. (**C**) Potential difference (PD) measurement: solid lines, mean; dashed lines, SEM. (**D**) Confocal micrographs of RedMUC2^{98trTg} tissue. Gray, actin; red, mCherry-MUC2. (**E**) Confocal z-stacks of tissue and 1-μm beads. Blue, tissue; red, beads; im, impenetrable mucus. (**F**) Impenetrable mucus thickness. (**G**) Concentration-response curves. Red dashed line, lipid A EC_{50}; black dashed lines, estimated mucus and stool lipid A concentrations. (**H**) LAL reactivity of stool, mucus, and lipid A EC_{50} (0.85 μM). (**I**) Quantification of 16S rRNA genes in stool and mucus by quantitative polymerase chain reaction. Data are means ± SEM (n = 4 or 5); *P < 0.05, Dunnett test [(A), (B), (H)], Sidak test (F), or Mann-Whitney test (I). Scale bars, 50 μm.

Downloaded from http://science.sciencemag.org/ on June 28, 2016

were obtained by using diphenyleneiodonium (DPI) to inhibit nicotinamide adenine dinucleotide phosphate/dual oxidase (Nox/Duox) reactive oxygen species (ROS) synthesis. Peptide-mediated inhibition of caspase-1 and caspase-11 activation mimicked results from caspase KO tissue, confirming the necessity for inflammasome activation. Atropine, a pan-muscarinic acetylcholine receptor inhibitor, blocked CCh-induced secretion but had no effect on tissue responses to TLR ligands.

ROS synthesis by Nox/Duox can be activated downstream of TLR signaling and can act as an upstream stimulator of inflammasome activation (*14*, *15*). DPI is a potent Nox/Duox inhibitor but can also inhibit mitochondrial ROS release. We clarified this element of the pathway using *N*-acetylcysteine (NAC), a nonspecific ROS scavenger, and Mito-TEMPO, a ROS scavenger that accumulates in mitochondria (Fig. 3C). NAC prevented LPS-stimulated Muc2 secretion, whereas Mito-TEMPO had no effect; thus, Nox/Duox was the likely source of LPS-induced ROS synthesis. We used the fluorogenic ROS probe DCFDA (2′,7′-dichlorofluorescin diacetate) to quantify LPS-induced ROS production in isolated colonic epithelial cells (Fig. 3D). ROS production was observed when cells were treated with LPS, and was inhibited by Dynasore, a MyD88 inhibitory peptide, DPI, and NAC, but not by a caspase inhibitory peptide. These results indicate that LPS-induced ROS synthesis is dependent on endocytosis and MyD88 signaling but takes place upstream of inflammasome activation. Intriguingly, flagellin treatment also induced ROS synthesis, which could be inhibited by both the endocytosis inhibitor Dynasore and the MyD88 inhibitory peptide (Fig. 3D); this finding shows that flagellin could activate a pathway similar to that activated by LPS.

Cotreatment of RedMUC2^{98trTg} tissue with caspase inhibitory peptide and fluorescent LPS allowed imaging of endocytotic GCs without triggering Muc2 secretion (Fig. 3E). Intracellular LPS was observed in only a small population of GCs. Thus, the endocytosis-dependent ROS synthesis observed in DCFDA-loaded cells was likely generated by these GCs, which supports the idea that a distinct population of GCs was responsive to the TLR ligands.

Together, these results suggested that LPS, P3CSK4, and flagellin stimulate Muc2 secretion from responsive GCs via activation of the Nlrp6 inflammasome. LPS- and P3CSK4-induced inflammasome activation occurred downstream of endocytosis and TLR-MyD88–induced ROS synthesis. Although it was apparent that endocytosis of flagellin could also induce TLR-MyD88–dependent ROS synthesis, it was also evident that flagellin-induced Muc2 secretion was not contingent on this element of the pathway, and we therefore focused our subsequent studies on the response to LPS and P3CSK4.

TLR ligands are endocytosed by senGCs

To identify LPS- and P3CSK4-sensitive GCs in intact colonic tissue, we treated RedMUC2^{98trTg} colonic explants with fluorescent LPS or P3CSK4 and imaged the tissue by confocal microscopy (Fig. 4, A to D). GCs that had taken up LPS or P3CSK4 were found exclusively in the apical regions of the crypt. Intriguingly, there appeared to be very few of these cells, with less than one cell per crypt (Fig. 4E). These cells were not observed in tissues pretreated with Dynasore, confirming the requirement for endocytosis. Inhibition of inflammasome activation significantly increased the number of endocytotic cells detected, as did loss of TLR or MyD88 signaling (Fig. 4, B and E). This result suggested that LPS- and P3CSK4-triggered TLR signaling and inflammasome activation resulted in loss of detectable endocytotic cells.

We investigated this possibility by treating explants with nonimmunogenic dextran. Dextran was also taken up by a small number of GCs, but without inducing the same loss of endocytotic cells seen with LPS and P3CSK4 treatment (Fig. 4, C and E). GCs that endocytosed dextran were identified as the same cells that endocytosed P3CSK4 (Fig. 4D), and examination of sections obtained from dextran-treated tissue demonstrated that endocytosis was entirely restricted to GCs in the upper-crypt region (fig. S3A). To ensure that GC endocytosis observed ex vivo reflected processes occurring in vivo, we administered dextran intrarectally to live RedMUC2^{98trTg} mice. Uptake of dextran was again observed in a limited number of upper-crypt GCs, confirming ex vivo observations (fig. S3B).

Thus, luminal material was nonspecifically endocytosed by a small subpopulation of upper-crypt GCs. These cells were lost after TLR-MyD88

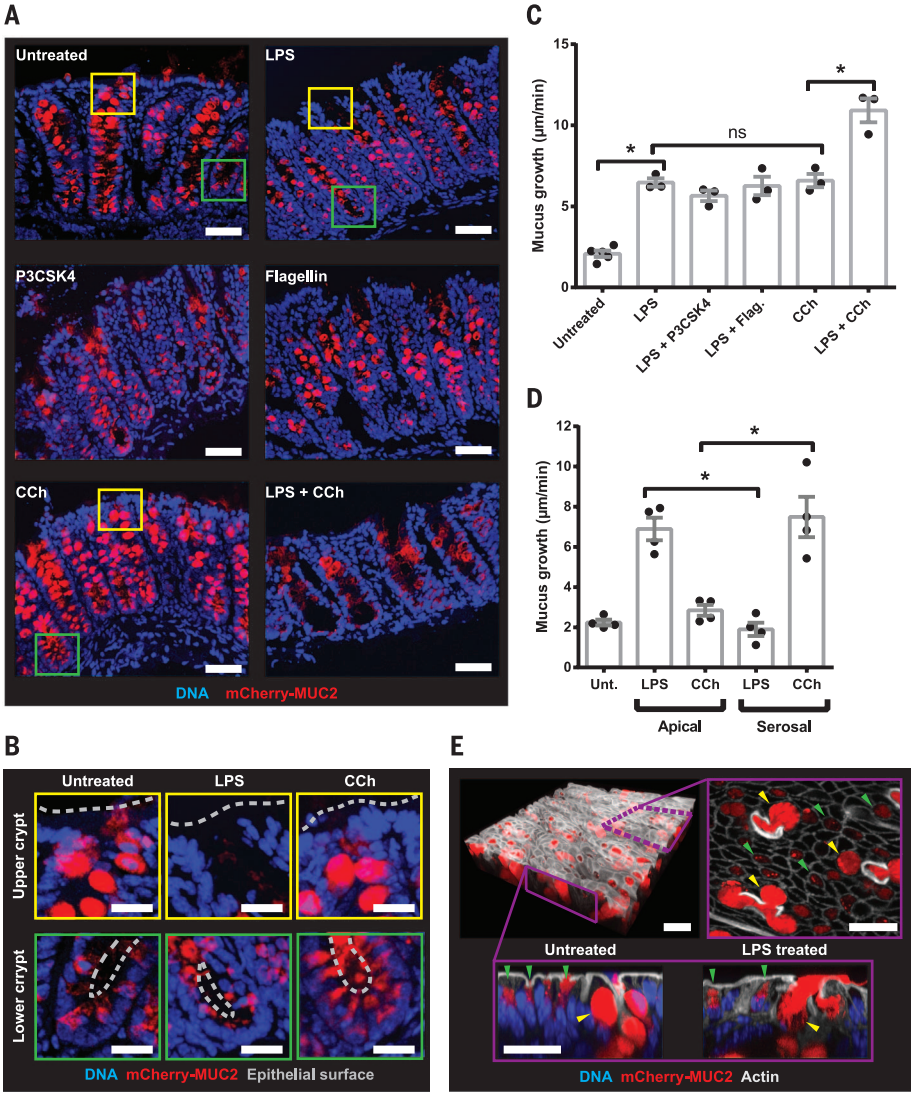


Fig. 2. TLR ligand–responsive GCs are localized to the upper crypt. Colonic explants were treated with TLR ligands or CCh. (**A**) Confocal micrographs of cryosections from RedMUC2^{98trTg} tissue. Red, MUC2; blue, DNA. (**B**) Upper crypt (yellow boxes) or lower crypt (green boxes) magnified from (A); a dashed gray line shows the epithelial surface. (**C** and **D**) Quantification of mucus growth rates. (**E**) Upper-crypt GCs (yellow arrowheads) and intercrypt GCs (green arrowheads) in RedMUC2^{98trTg} colon. Upper left: Confocal z-stack of tissue surface. Upper right: *x*/*y*-axis cross section. Lower left and right: *x*/*z*-axis cross sections. Blue, DNA; red, mCherry-MUC2; gray, actin. Data are means ± SEM (n = 3 or 4); *P < 0.05, Tukey multiple-comparisons test; ns, not significant. Scale bars, 50 μm (A), 20 μm [(B) and (E)].

Downloaded from http://science.sciencemag.org/ on June 28, 2016

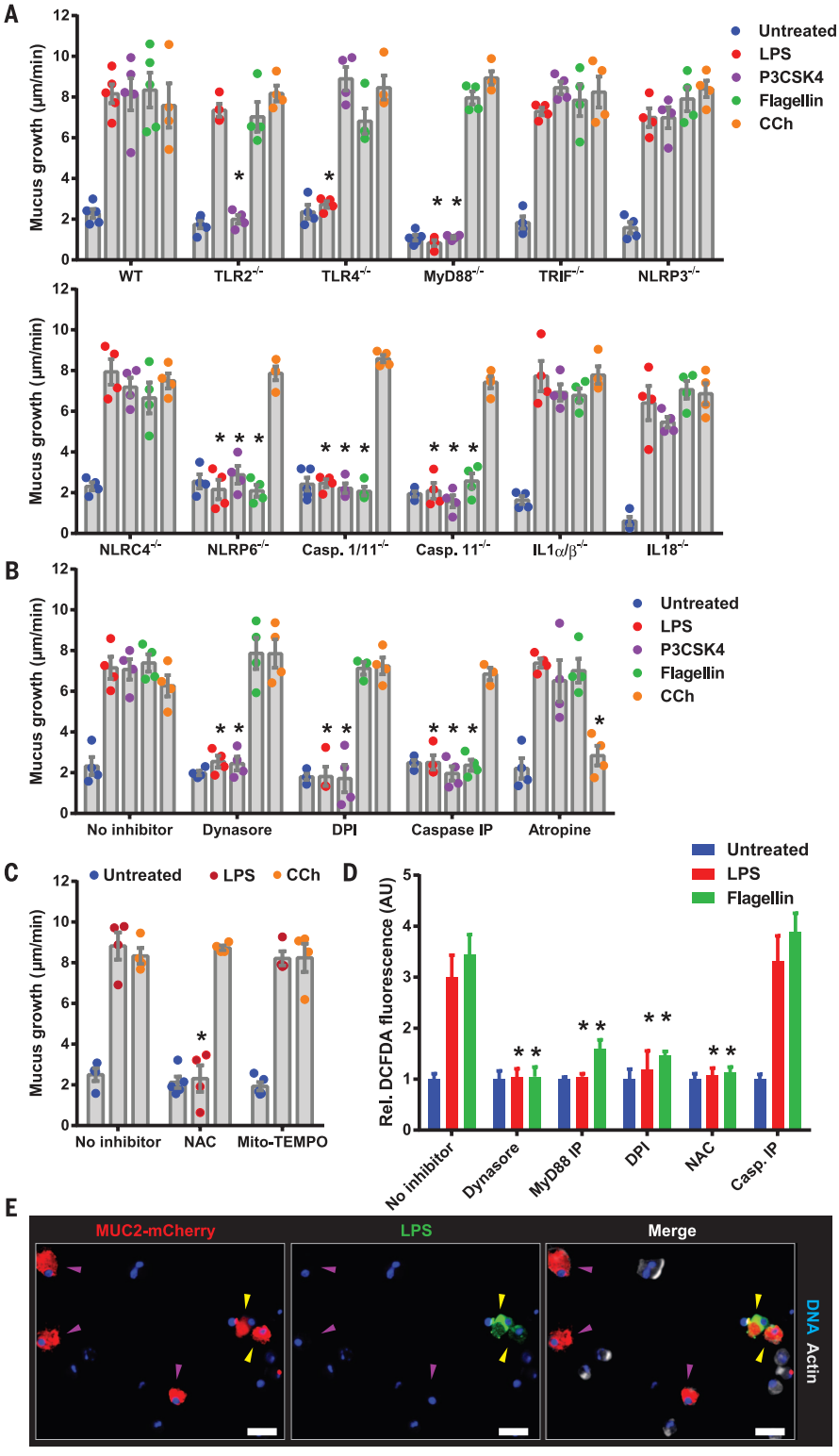


Fig. 3. TLR ligand–driven Muc2 secretion requires endocytosis, signaling, and ROS synthesis upstream of inflammasome activation. Colonic explants [(A) to (C)] or cell suspensions [(D) and (E)] were treated with TLR ligands or CCh. (**A**) Quantification of mucus growth in wild-type (WT) or KO explants. (**B**) Quantification of mucus growth in explants pretreated with inhibitors; IP, inhibitory peptide. (**C**) Quantification of mucus growth in explants pretreated with ROS scavengers. (**D**) DCFDA fluorescence in epithelial cells pretreated with inhibitors. (**E**) Confocal micrographs of RedMUC2^{98trTg} epithelial cells with caspase inhibitory peptide. Purple arrowheads, nonendocytotic GCs; yellow arrowheads, endocytotic GCs; red, mCherry-MUC2; blue, DNA; gray, actin. Data are means ± SEM (n = 4 or 5); *P < 0.05, Dunnett multiple-comparisons test of WT versus KO (A) or no inhibitor versus inhibitor [(B) to (D)]. Scale bars, 50 μm.

signaling and activation of the inflammasome. Crucially, only one or two such cells were typically detected per crypt. Because this represents only a fraction of the GCs secreted in response to TLR ligands, this finding suggested that activation of endocytotic GCs must control secretion from other responsive, but not endocytotic, upper-crypt GCs. The sampling and recognition of nonendogenous material is vital to the surveillance function of many types of host sentinel cell. Because this process was apparent in the endocytotic GCs, this cell was named sentinel GC (senGC) to distinguish it from other upper-crypt GCs.

Activated senGCs control Muc2 secretion

We examined the fate of senGCs lost after treatment and identified shed cells containing LPS or P3CSK4 and residual Muc2, which suggests that these were expelled senGCs (Fig. 5A). These were not present in tissue treated with dextran, indicating that expulsion was dependent on TLR engagement. Expelled cells were associated with diffuse extracellular Muc2 that was continuous with the remaining intracellular material (Fig. 5B). This implied that senGCs had undergone compound exocytosis (*16*) as well as expulsion. Intrarectal administration of P3CSK4 to live wild-type and RedMUC2^{98trTg} mice demonstrated that epithelial expulsion of GCs that had endocytosed P3CSK4 could also be observed in vivo (fig. S4, A and B). Intrarectal treatment of *Nlrp6*$^{-/-}$ mice identified cells that had endocytosed P3CSK4 but did not induce epithelial expulsion (fig. S4C). This confirmed that epithelial expulsion of senGCs was driven by Nlrp6 inflammasome activation.

Inflammasome activity was assessed using a fluorogenic peptide probe targeting active caspase-1 and caspase-11 (Casp1/11 FP). Tissue was loaded with Casp1/11 FP and then treated with LPS (Fig. 5C). Inflammasome activity was exclusively localized to cells that had been expelled from the upper crypt. Imaging of RedMUC2^{98trTg} tissue demonstrated that these cells were senGCs. Expelled senGCs were associated with long plumes of secreted Muc2, which confirmed that LPS treatment had triggered compound exocytosis of Muc2. No inflammasome activity or cellular expulsion was observed after LPS treatment of *Caspase-1/11*$^{-/-}$ or *Nlrp6*$^{-/-}$ tissue, but both were detected in treated *Nlrp3*$^{-/-}$ tissue. This demonstrated that activity observed in these cells was specifically dependent on a functional Nlrp6 inflammasome.

senGC-mediated secretion was studied by live imaging of RedMUC2^{98trTg} colonic explants. This revealed loss of Muc2 from upper-crypt GCs in LPS- or P3CSK4-treated tissues but not in vehicle-treated tissues (movies S1 and S2). Rapid Muc2 degranulation and epithelial expulsion were observed in a limited number of GCs per crypt (Fig. 5D and movies S3 and S4). Expulsion was used to designate the senGC, and the remaining upper-crypt GCs could be classified as "responsive" or "nonresponsive" according to whether they secreted Muc2 (Fig. 5D). Muc2 fluorescence was subsequently quantified from

Downloaded from http://science.sciencemag.org/ on June 28, 2016

different classes of GC and tracked over time (Fig. 5, E and F, and movies S5 and S6). Strikingly, this revealed that LPS- and P3CSK4-induced Muc2 secretion was sequential in nature. Degranulation occurred initially in senGCs and then in responsive GCs. Responsive GC secretion occurred in sequence, starting with cells closest to the senGC and progressing around the crypt (Fig. 5F). This indicates that activated senGCs triggered an intercellular signal that induced Muc2 secretion in adjacent responsive GCs.

Intercellular senGC signaling

Localized intercellular signals can use paracrine or juxtacrine mechanisms. The mammalian intestine is highly innervated, and paracrine signals can be generated by the enteric nervous system (ENS). Juxtacrine signals can be transmitted directly via intercellular cytoplasmic bridges formed by gap junction (GJ) connexons. We measured mucus secretion in colonic explants treated with inhibitors targeting each process. Tetrodotoxin (TTx) blocks ENS signaling, and carbenoxolone (CBX) can reduce GJ conductivity. Neither inhibitor affected CCh-induced secretion; however, although TLR ligand–induced secretion was unaffected by TTx, the response was blocked by CBX (Fig. 5G). To verify GJ decoupling, we used a FRAP (fluorescence recovery after photobleaching) assay to measure GJ conductivity. Vehicle- or CBX-treated explants were loaded with a GJ-permeable dye, and areas of epithelium were photobleached (fig. S5, A and B). Fluorescent recovery was significantly reduced in CBX relative to vehicle-treated explants, indicating that GJ conductivity had been inhibited and supporting a role for GJ signaling in controlling responsive GCs.

A recognized form of GJ signaling is mediated by calcium. Increased cytosolic Ca^{2+} is derived from extracellular influx or release from endoplasmic reticulum stores via inositol 1,4,5-trisphosphate receptor (IP_3R) or ryanodine receptor (RyR) channels. To investigate the role of Ca^{2+} signaling in TLR ligand–induced secretion, we pretreated explants with inhibitors before treatment with LPS or CCh (Fig. 5H). The cell-permeable Ca^{2+} chelator BAPTA-AM blocked secretion induced by either molecule, demonstrating the requirement for Ca^{2+} release in both types of secretion. The cell-impermeable Ca^{2+} chelator EGTA inhibited only the response to LPS. Intracellular Ca^{2+}-store release was targeted by the RyR inhibitor ryanodine and the IP_3R inhibitor xestospongin C (XeC). Inverse results were obtained for LPS and CCh, with LPS dependent on IP_3R-mediated Ca^{2+} release and CCh dependent on RyR-mediated Ca^{2+} release. The requirement for Ca^{2+} influx and intracellular store release indicated that Ca^{2+}-induced Ca^{2+} release was active in LPS-induced secretion. To probe the sequence of Ca^{2+} signaling events, we used the Ca^{2+} ionophore ionomycin (fig. S5C). Ionomycin transports Ca^{2+} across membranes mimicking the Ca^{2+} influx required for LPS-induced secretion. Ionomycin induced Muc2 secretion and was insensitive to inhibition of ROS synthesis and inflammasome activation, but was inhibited by EGTA and XeC. These findings suggest that Ca^{2+} influx has a role upstream of Ca^{2+} store release and that direct induction of Ca^{2+} signaling negates the requirement for inflammasome activation.

We used the fluorogenic Ca^{2+} indicator Fluo4 to detect Ca^{2+} signaling in LPS-treated RedMUC2^{98trTg} colonic explants (Fig. 5, I and J). Fluo4-positive GCs were observed after LPS treatment but not

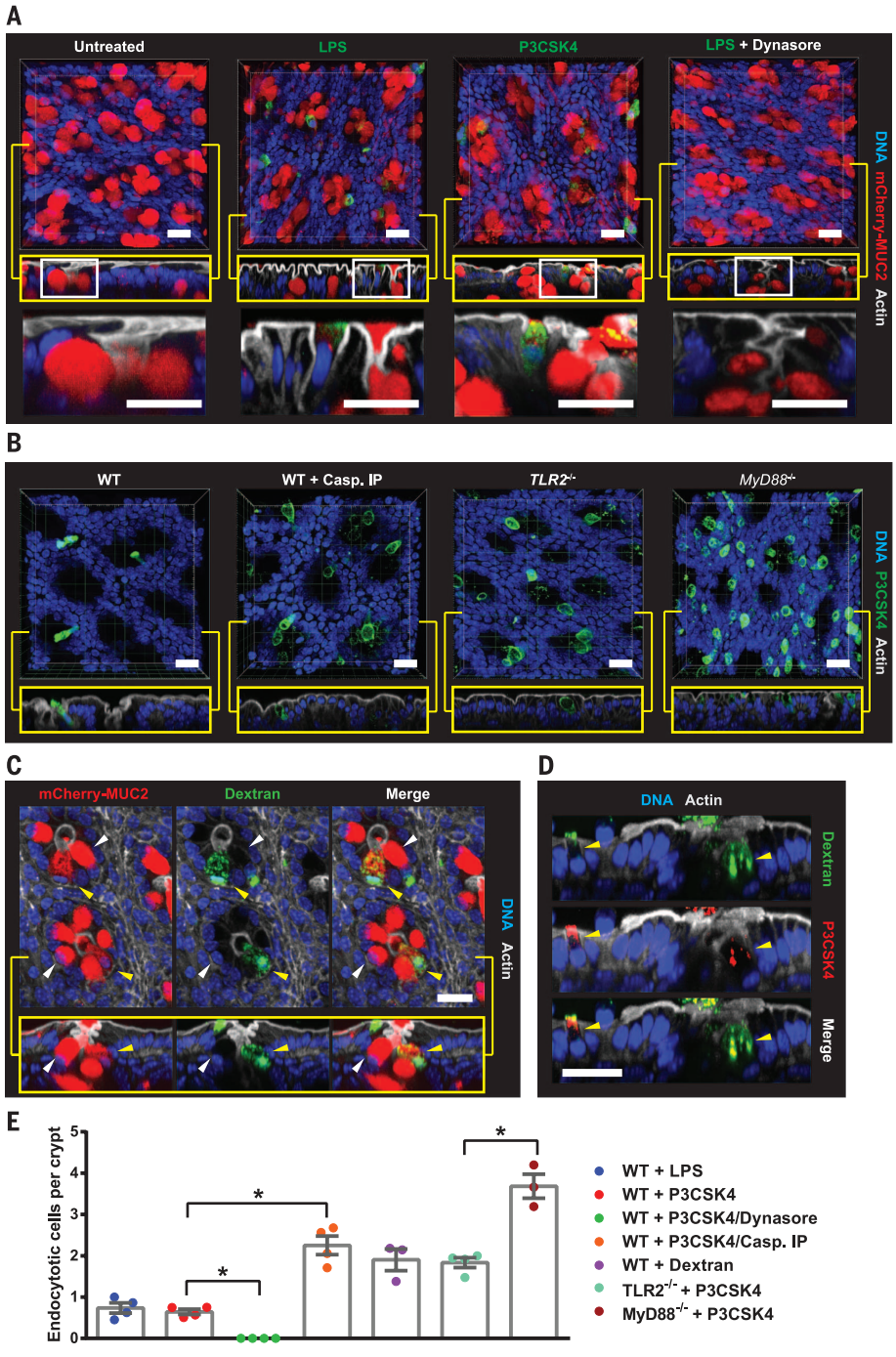


Fig. 4. TLR ligands are endocytosed by sentinel GCs (senGCs). In (A) to (D), colonic explants were treated as indicated, whole-mounted, and visualized by confocal microscopy; in (A) to (C), *x*/*y*-axis cross sections are at top; *x*/*z*-axis cross sections are in yellow boxes; blue, DNA; gray, actin. (**A**) RedMUC2^{98trTg} tissue; regions of *x*/*z*-axis cross sections magnified at bottom are indicated by white boxes. Green, LPS/P3CSK4; red, mCherry-MUC2. (**B**) WT with or without caspase inhibitory peptide, *Tlr2*$^{-/-}$, and *MyD88*$^{-/-}$ tissue. Green, P3CSK4. (**C**) RedMUC2^{98trTg} tissue. Yellow arrowheads, endocytotic GCs; white arrowheads, nonendocytotic GCs; red, mCherry-MUC2; green, dextran. (**D**) WT colon cotreated with P3CSK4 and dextran. Yellow arrowheads, endocytotic GCs. (**E**) Quantification of endocytotic cells. Data are means ± SEM (n = 3 or 4); *P < 0.05, Tukey multiple-comparisons test. Scale bars, 20 μm.

Downloaded from http://science.sciencemag.org/ on June 28, 2016

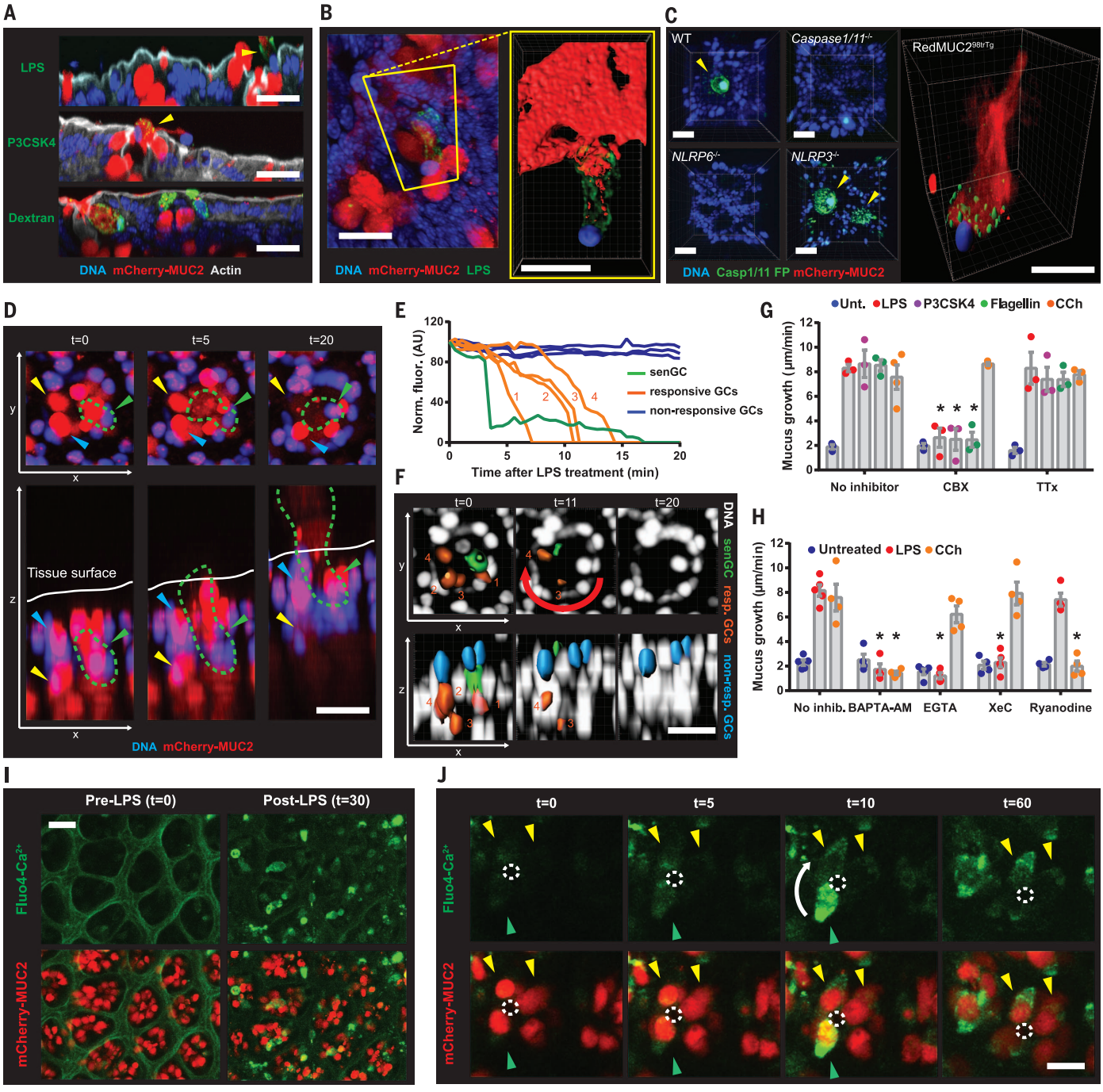


Fig. 5. Activated senGCs are expelled from the epithelium and trigger gap junction– and Ca^{2+}-dependent Muc2 secretion from responsive upper-crypt GCs. Colonic explants were treated with TLR ligands or CCh. (**A** and **B**) RedMUC2^{98trTg} tissue whole mounts visualized by confocal microscopy. Blue, DNA; gray, actin; red, mCherry-MUC2; green, LPS, P3CSK4, or dextran. (A) *x/z*-axis cross sections showing expelled senGCs (yellow arrowheads). (B) Expelled senGC overview (left) and isosurface enhanced view (right, yellow box). (**C**) Localization of inflammasome activity after LPS treatment of WT, KO, and RedMUC2^{98trTg} tissue. Green, caspase-1/caspase-11 fluorogenic probe (Casp1/11 FP); blue, DNA; yellow arrowheads, senGCs. (**D** to **F**) RedMUC2^{98trTg} tissue imaged by confocal microscopy. (D) *x/y*-axis view (top) and *x/z*-axis view (bottom) of a crypt at different time points after LPS treatment. Green arrowheads and green dashed lines, senGC; yellow arrowheads, responsive GC; blue arrowheads, nonresponsive GC. (E) Quantification of mCherry-MUC2 fluorescence of individual GCs from crypt in (D). (F) Fluorescent isosurfaces used to generate data in (E); responsive GC numbering corresponds to numbered plots in (E). Red arrow shows sequence of responsive cell secretion. White, DNA; green, senGC; orange, responsive GCs; blue, nonresponsive GCs. (**G** and **H**) Quantification of mucus growth with or without CBX, TTx, or Ca^{2+} signaling inhibitors. (**I** and **J**) RedMUC2^{98trTg} tissue loaded with fluorogenic Ca^{2+} indicator (Fluo4) and imaged by confocal microscopy. Green, Fluo4; red, mCherry-MUC2. (I) *x/y*-axis view of tissue before and after treatment. (J) *x/y*-axis view of a crypt at different time points after LPS treatment. White arrow shows sequence of GC secretion. White dashed line, crypt opening; green arrowheads, senGC; yellow arrowheads, responsive GCs. Data are means ± SEM (n = 4 or 5); *P < 0.05, Dunnett multiple-comparisons test. Scale bars, 20 µm.

Downloaded from http://science.sciencemag.org/ on June 28, 2016

vehicle treatment, indicating that LPS-induced Ca^{2+} signaling could be visualized ex vivo. senGCs appeared to have higher Fluo4 signal than the responsive GCs where the signal was relatively weak (Fig. 5J and movie S7). Sequential increases in cytoplasmic Ca^{2+} starting at the senGC appeared to follow the same pattern as observed for Muc2 secretion.

SenGCs flush bacteria away from crypt openings

Induced Muc2 secretion may remove bacteria from the crypt opening, and we tested this in our ex vivo tissue system. The inner mucus layer normally separates bacteria from the colonic tissue surface; therefore, this was first mechanically removed. Fluorescent bacteria were then applied to the tissue surface. Muc2 secretion was triggered by treatment with LPS, and images of tissue and bacteria were acquired and bacterial spatial distribution quantified (Fig. 6, A and B). Initially bacteria were identified at the tissue surface and close to the crypt openings. Treatment with LPS, but not vehicle, caused bacteria to be displaced from the crypt openings. Most bacteria remaining at the tissue surface after LPS treatment were in the intercrypt regions, thus supporting the notion that this mechanism functions to specifically protect the crypts in vivo.

Oral administration of dextran sodium sulfate (DSS) allows colonic bacteria to penetrate the inner mucus layer and contact the epithelium prior to the onset of inflammation (*17*). We hypothesized that if senGCs protect the crypt from bacteria, DSS treatment should trigger senGC activation in vivo. Short-term DSS treatment (84 hours) did not cause weight alterations (fig. S6A). However, the inner mucus layer became partially penetrable to bacteria-sized beads after 12 hours of DSS treatment and was largely disrupted after 84 hours (Fig. 6C). The Casp1/11 FP probe was used to quantify epithelial inflammasome activation (Fig. 6D and fig. S6B). This was detected in multiple cells after 12 hours of DSS treatment, but the number of these cells then declined. Inflammasome activity was visualized in both upper-crypt and shed cells with GC-like morphology (Fig. 6E), indicating that DSS had resulted in activation and epithelial expulsion of senGCs. That DSS treatment caused depletion of senGCs was confirmed by the loss of dextran endocytosis by upper-crypt cells after 36 hours (Fig. 6F). Endocytotic cells were clearly identified in untreated tissue but largely absent in tissue exposed to DSS, indicating that the senGCs had been activated and depleted.

Normally, colonocytes are separated from the microbiota by the inner mucus layer, and disruption of this process allows bacteria to approach the crypts (*1*, *18*–*20*) (fig. S7, A and B). Influx of bacteria increases the concentration of TLR ligands near the crypt and activates senGCs (fig. S7C). Our findings suggest that this sequence is initiated by TLR-MyD88 signaling downstream of endocytosis, preceding Nox/Duox ROS synthesis and Nlrp6 inflammasome activation. This causes Ca^{2+} signaling that drives compound secretion of Muc2, generation of GJ-dependent intercellular signaling, Muc2 secretion from responsive GCs, and the expulsion of the activated senGC. These events clear bacteria from the crypt opening (fig. S7D), thereby protecting the lower crypt and intestinal stem cells from bacterial intrusion. Mouse strains unable to trigger senGC activation had a functional inner mucus layer, which suggests that senGCs are less important for normal mucus layer generation.

The pathway activating senGCs is supported by other observations. Colonic GCs express the expected TLR repertoire and can take up luminal material (*9*, *21*, *22*). MyD88 signaling can induce Nox/Duox ROS synthesis (*23*) that has been coupled to inflammasome activation (*14*, *15*) and was recently linked to GC endocytosis and autophagy (*24*). The senGC Nlrp6 inflammasome activation resulted in expulsion of these cells; this mechanism could be important for clearing infected cells (*25*, *26*) and blocking the crypt.

Administration of DSS to mice is a commonly used colitis model. DSS disrupts the inner mucus layer, allowing bacteria to access the epithelial surface before the onset of inflammation (*17*). Increased sensitivity to DSS treatment in animals

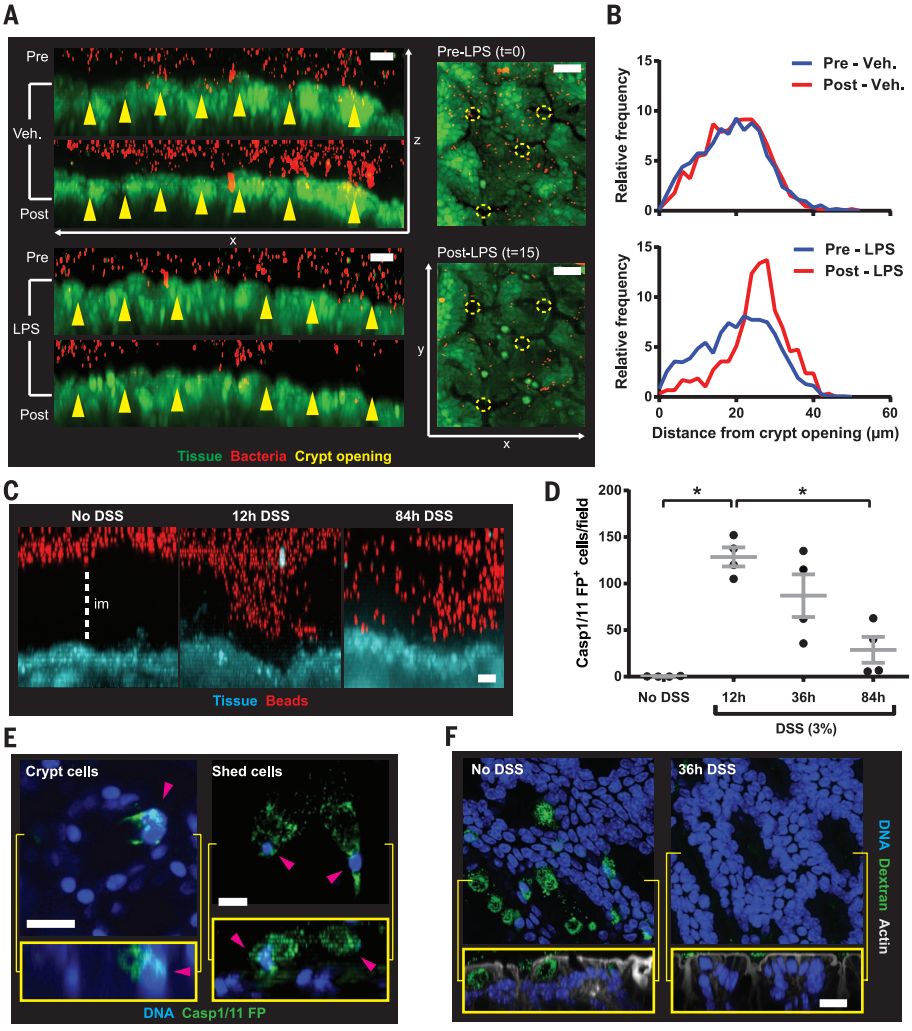


Fig. 6. senGC activation removes bacteria from crypt openings ex vivo and is triggered by disruption of the inner colonic mucus layer in vivo. (**A**) Fluorescent bacteria (red) applied to colonic explant tissue (green) and imaged before (top) and after (bottom) LPS or vehicle treatment. Left, *x*/*z*-axis view; right, *x*/*y*-axis view. Yellow arrowheads and dashed circles denote crypt openings. (**B**) Distribution of bacteria in relation to crypt openings as in (A). Data are representative of four independent experiments. In (C) to (F), mice were given 3% DSS in drinking water; samples were collected after 0 (no DSS), 12, 36, and 84 hours. (**C**) Confocal z-stacks of colonic explants and 1-μm beads. Blue, tissue; red, beads; im, impenetrable mucus. (**D**) Quantification of cells with inflammasome activity (Casp1/11 FP^+) detected in live tissue. (**E**) Casp1/11 FP^+ cells (pink arrows) with GC morphology in the upper crypt (left) and shed from tissue (right). Top, *x*/*y*-axis view; bottom, *x*/*z*-axis view. (**F**) Colonic explants were treated with fluorescent dextran, fixed, whole-mounted, and visualized by confocal microscopy. Top, *x*/*y*-axis view; bottom, *x*/*z*-axis view. Blue, DNA; green, dextran; gray, actin. Data are means ± SEM (n = 4); *P < 0.05, Dunn multiple-comparisons test. Scale bars, 20 μm.

Downloaded from http://science.sciencemag.org/ on June 28, 2016

lacking senGC activation mediators may be related to loss of senGC protection (*4*, *5*, *27*). DSS triggered inflammasome activity localized to upper-crypt cells and led to depletion of senGCs (Fig. 6, C to F). Ex vivo experiments confirmed that senGC-mediated mucus secretion displaced bacteria from crypt openings (Fig. 6, A and B), and senGC activation after inner mucus layer disruption likely generates a similar response. Depletion of senGCs by repeated challenge would leave the crypt without defense—an event that may be important in understanding the development of chronic colitis.

REFERENCES AND NOTES

1. M. E. V. Johansson *et al.*, *Proc. Natl. Acad. Sci. U.S.A.* **105**, 15064–15069 (2008).
2. D. Ambort *et al.*, *Proc. Natl. Acad. Sci. U.S.A.* **109**, 5645–5650 (2012).
3. A. Velcich *et al.*, *Science* **295**, 1726–1729 (2002).
4. S. Rakoff-Nahoum, J. Paglino, F. Eslami-Varzaneh, S. Edberg, R. Medzhitov, *Cell* **118**, 229–241 (2004).
5. A. L. Frantz *et al.*, *Mucosal Immunol.* **5**, 501–512 (2012).
6. M. Lamkanfi, V. M. Dixit, *Cell* **157**, 1013–1022 (2014).
7. E. Elinav *et al.*, *Cell* **145**, 745–757 (2011).
8. M. E. V. Johansson, *PLOS ONE* **7**, e41009 (2012).
9. K. A. Knoop, K. G. McDonald, S. McCrate, J. R. McDole, R. D. Newberry, *Mucosal Immunol.* **8**, 198–210 (2015).
10. M. Wlodarska *et al.*, *Cell* **156**, 1045–1059 (2014).
11. D. R. Halm, S. T. Halm, *Am. J. Physiol.* **277**, C501–C522 (1999).
12. J. K. Gustafsson *et al.*, *Am. J. Physiol.* **302**, G430–G438 (2012).
13. See supplementary materials on *Science* Online.
14. R. Zhou, A. Tardivel, B. Thorens, I. Choi, J. Tschopp, *Nat. Immunol.* **11**, 136–140 (2010).
15. F. Bauernfeind *et al.*, *J. Immunol.* **187**, 613–617 (2011).
16. R. D. Specian, M. R. Neutra, *J. Cell Biol.* **85**, 626–640 (1980).
17. M. E. V. Johansson *et al.*, *PLOS ONE* **5**, e12238 (2010).
18. H. E. Jakobsson *et al.*, *EMBO Rep.* **16**, 164–177 (2015).
19. M. E. V. Johansson *et al.*, *Gut* **63**, 281–291 (2014).
20. K. S. B. Bergstrom *et al.*, *PLOS Pathog.* **6**, e1000902 (2010).
21. J. R. McDole *et al.*, *Nature* **483**, 345–349 (2012).
22. P. C. Colony, R. D. Specian, *Anat. Rec.* **218**, 365–372 (1987).
23. A. Panday, M. K. Sahoo, D. Osorio, S. Batra, *Cell. Mol. Immunol.* **12**, 5–23 (2015).
24. K. K. Patel *et al.*, *EMBO J.* **32**, 3130–3144 (2013).
25. M. E. Sellin *et al.*, *Cell Host Microbe* **16**, 237–248 (2014).
26. L. A. Knodler *et al.*, *Cell Host Microbe* **16**, 249–256 (2014).
27. D. Demon *et al.*, *Mucosal Immunol.* **7**, 1480–1491 (2014).

ACKNOWLEDGMENTS

Supported by the Swedish Research Council, Swedish Cancer Foundation, Knut and Alice Wallenberg Foundation, Lundberg Foundation, Sahlgren's University Hospital (ALF), Torsten Söderbergs Stiftelse, National Institute of Allergy and Infectious Diseases grant U01AI095473, and Swedish Foundation for Strategic Research. We thank the Gothenburg Centre for Cellular Imaging for technical help, F. Svensson for generating the RedMUC2^{98trTg} mice, and W.-D. Hardt and the Mucosal Immunobiology and Vaccine Center at the University of Gothenburg for mouse strains.

SUPPLEMENTARY MATERIALS

www.sciencemag.org/content/352/6293/1535/suppl/DC1
Materials and Methods
Figs. S1 to S7
Movies S1 to S7
Reference (*28*)

23 March 2016; accepted 16 May 2016
10.1126/science.aaf7419

STRUCTURAL BIOLOGY

Atomic structure of Hsp90-Cdc37-Cdk4 reveals that Hsp90 traps and stabilizes an unfolded kinase

Kliment A. Verba,[1] Ray Yu-Ruei Wang,[1] Akihiko Arakawa,[2] Yanxin Liu,[1] Mikako Shirouzu,[2] Shigeyuki Yokoyama,[2] David A. Agard[1]*

The Hsp90 molecular chaperone and its Cdc37 cochaperone help stabilize and activate more than half of the human kinome. However, both the mechanism by which these chaperones assist their "client" kinases and the reason why some kinases are addicted to Hsp90 while closely related family members are independent are unknown. Our structural understanding of these interactions is lacking, as no full-length structures of human Hsp90, Cdc37, or either of these proteins with a kinase have been elucidated. Here we report a 3.9 angstrom cryo–electron microscopy structure of the Hsp90-Cdc37-Cdk4 kinase complex. Surprisingly, the two lobes of Cdk4 are completely separated with the β4-β5 sheet unfolded. Cdc37 mimics part of the kinase N lobe, stabilizing an open kinase conformation by wedging itself between the two lobes. Finally, Hsp90 clamps around the unfolded kinase β5 strand and interacts with exposed N- and C-lobe interfaces, protecting the kinase in a trapped unfolded state. On the basis of this structure and an extensive amount of previously collected data, we propose unifying conceptual and mechanistic models of chaperone-kinase interactions.

The human kinome is responsible for regulating about one-third of all proteins through phosphorylation (*1*). Proper regulation of this process is important, as misregulated kinase activity can lead to cell death and disease (*2*). To achieve fine regulation, kinase activity can be sensitively modulated by multiple allosteric inputs. Thus, kinase domains are organized so that dispersed small structural changes caused by binding of regulatory domains and proteins or phosphorylation can substantially alter kinase activity. Examples of such regulatory interactions abound, with SH2 and SH3 domains for Src family kinases, dimerization for epidermal growth factor receptor (EGFR) or Raf family kinases, and cyclin regulation for Cdks being well-characterized examples (*3*).

Beyond these specific regulators, the Hsp90 molecular chaperone, a member of the general cellular protein-folding machinery, also plays a fundamental role in the regulation of many kinases (*4*). Though chaperones usually facilitate the early steps of protein folding, Hsp90 also functions late in the process to help both fold and activate a set of protein "clients" (~10% of the proteome) (*5*). Notably, ~60% of the human kinome interacts with Hsp90, with the assistance of its kinase-specific cochaperone, Cdc37 (*6*). Pharmocologic inhibition of Hsp90 leads to rapid ubiquitinylation and degradation of client kinases. Because many Hsp90- and Cdc37-dependent kinases are key oncoproteins, (vSrc, bRafV600E, Her2, etc.), several Hsp90 inhibitors are undergoing clinical trials as cancer therapeutics (*7*).

Hsp90 is a well-conserved but highly dynamic molecular machine. Each monomer within the Hsp90 dimer has three structural domains: a C-terminal domain (CTD) responsible for dimerization, a middle domain (MD) implicated in client binding, and an N-terminal domain (NTD) that binds adenosine triphosphate (ATP). Without bound nucleotide, Hsp90 mostly populates a variety of open states, whereas nucleotide binding promotes the formation of a closed state in which the NTDs also dimerize, followed by hydrolysis (*8*, *9*). The rates of closure and hydrolysis are homolog-specific, with human cytosolic Hsp90s almost always open, whereas yeast Hsp90 preferentially adopts a fully closed state (*10*). Toward the end of the NTD is a highly charged region (i.e., a charged linker) that shows wide variation in length and composition between species. The function and structure of this charged linker are unclear, but deletion can affect Hsp90 function (*11*).

Cdc37 is less well studied. The monomeric protein can also be divided into three domains: an NTD of unknown structure that interacts with kinases, a globular MD that interacts with Hsp90, and an extended CTD of unknown function (*12*). Although there is a cocrystal structure of the Cdc37 MD and CTD (Cdc37 M/C) bound to the Hsp90 NTD (*13*), there is evidence that Cdc37 may also interact with the MD of Hsp90 (*14*). Phosphorylation of Cdc37 Ser^{13} plays an important role, providing stabilizing interactions in vitro (*15*) and being functionally necessary in vivo (*16*).

Although a wealth of in vivo data has been collected, a physical understanding of how Hsp90

[1]Howard Hughes Medical Institute (HHMI) and the Department of Biochemistry and Biophysics, University of California San Francisco, San Francisco, CA 94158, USA. [2]RIKEN Systems and Structural Biology Center, 1-7-22 Suehiro-cho, Tsurumi-ku, Yokohama 230-0045, Japan.
***Corresponding author. Email: agard@msg.ucsf.edu**

Downloaded from http://science.sciencemag.org/ on June 28, 2016

and Cdc37 facilitate kinase function is lacking. Equally unclear is why some kinases are strongly dependent on Hsp90, whereas closely related kinases function independently. Despite numerous attempts to identify a consistent motif responsible for Hsp90 interaction, the only general trend that has emerged is that client kinases appear to be less thermally stable than nonclients (*6*). Supporting this notion, the binding of kinase inhibitors or allosteric regulators reduces Hsp90 interactions (*17*, *18*). Though it is reasonable that less-stable kinases might depend on Hsp90, it remains unclear why this happens or what Hsp90 recognizes. Despite its obvious value, the crystal structure of an Hsp90-Cdc37-kinase complex has remained elusive, probably due to the dynamic nature of Hsp90-client interactions and challenges in reconstituting the complex. Encouraged by previous negative-stain electron microscopy (EM) studies (*19*) and the recent advances in cryo-EM detectors and processing methodologies that together make it feasible to analyze such a small, asymmetric complex (*20*), we undertook cryo-EM studies of the human 240-kDa Hsp90-Cdc37-Cdk4 kinase complex.

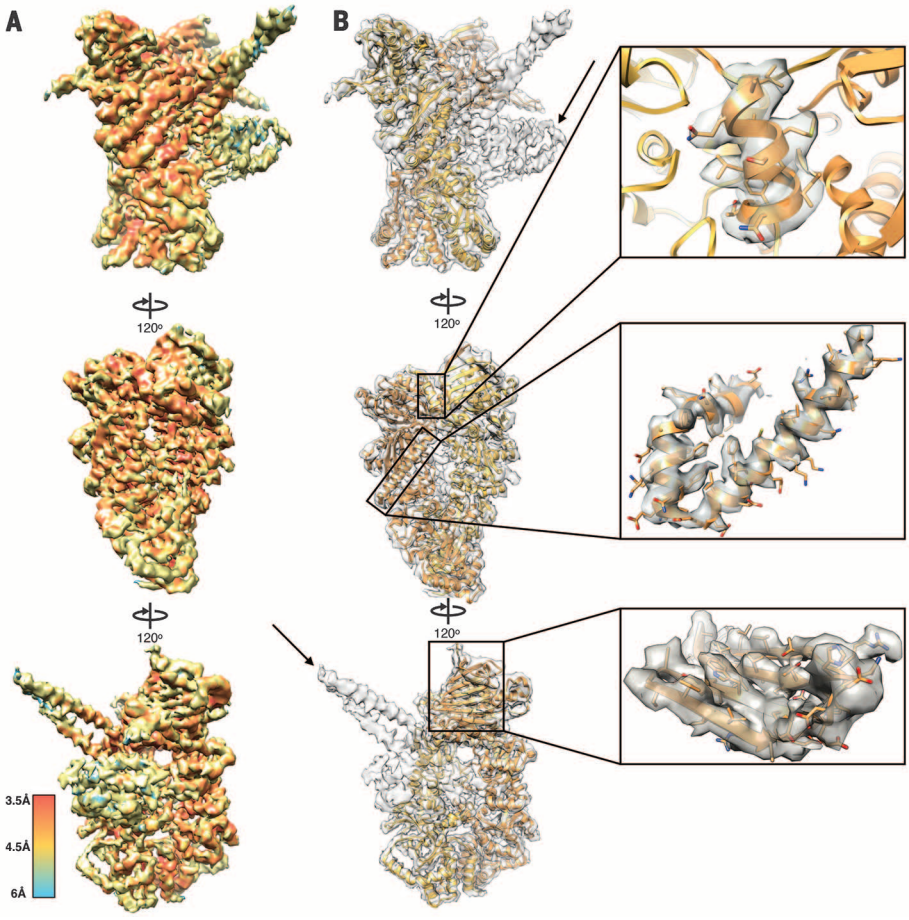


Fig. 1. The 4 Å map of Hsp90-Cdc37-Cdk4. (**A**) Density map colored by resolution. (**B**) hHsp90β model built into the density map, with different monomers depicted in shades of orange. Insets show high-resolution features. Arrows indicate density unaccounted for by Hsp90.

Complex formation and cryo-EM structural analysis

Human homologs of all three proteins were co-expressed in Sf9 insect cells. A stable ternary complex that survived rigorous dual-tag purification formed in the presence of molybdate (fig. S1). Although the mode of molybdate action is unknown, it affects Hsp90's hydrolysis rate and helps stabilize Hsp90-client interactions (*21*). Simply mixing components individually purified from insect cells did not yield any detectable complex; therefore, either posttranslational modifications specific to the complex or other components (like Hsp40 or Hsp70) are required. Despite considerable effort to optimize conditions and image processing, preferential particle orientation and conformational heterogeneity limited initial reconstructions from data collected in house to about 6 to 8 Å resolution. To move forward, a much larger data set was collected at the National Resource for Automated Molecular Microscopy (NRAMM) (*22*). Data quality was

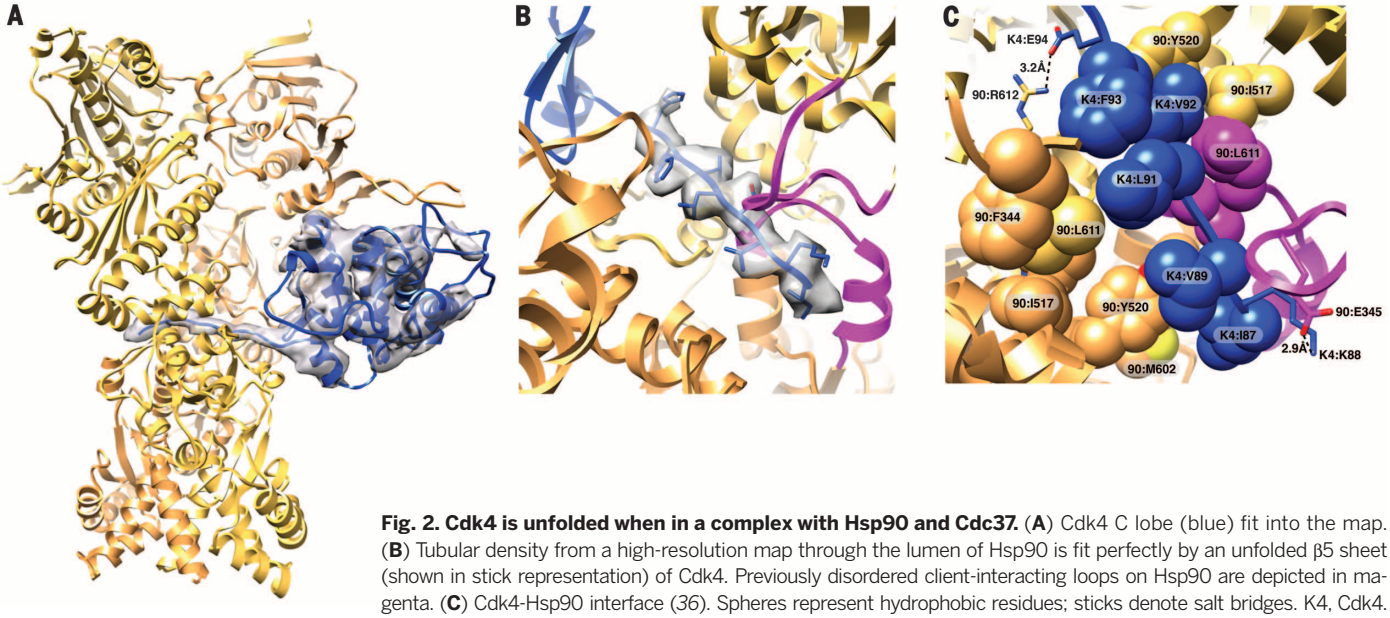


Fig. 2. Cdk4 is unfolded when in a complex with Hsp90 and Cdc37. (**A**) Cdk4 C lobe (blue) fit into the map. (**B**) Tubular density from a high-resolution map through the lumen of Hsp90 is fit perfectly by an unfolded β5 sheet (shown in stick representation) of Cdk4. Previously disordered client-interacting loops on Hsp90 are depicted in magenta. (**C**) Cdk4-Hsp90 interface (*36*). Spheres represent hydrophobic residues; sticks denote salt bridges. K4, Cdk4.

Downloaded from http://science.sciencemag.org/ on June 28, 2016

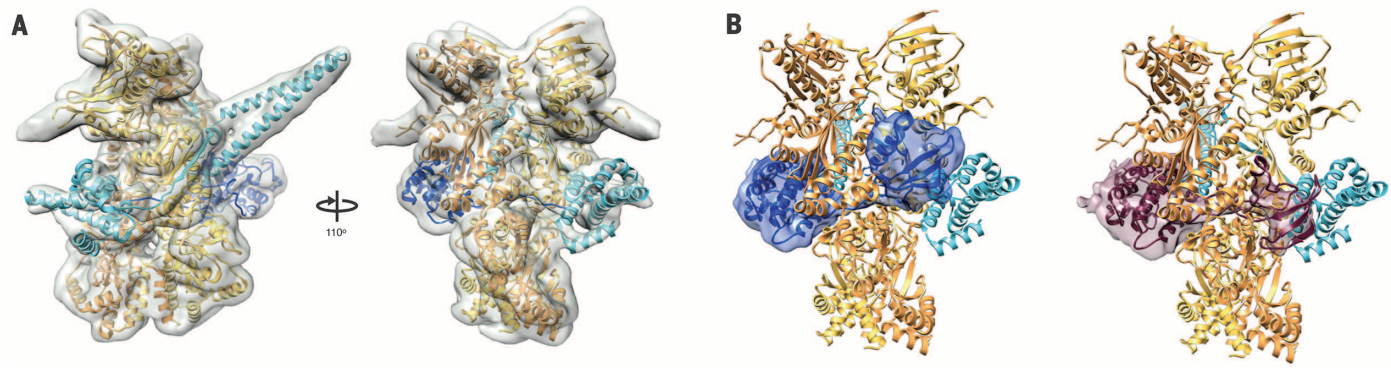


Fig. 3. Rounds of focused 3D classification yield distinct densities for Cdc37 and the Cdk4 N lobe. (**A**) One of the new classes has clear density for the Cdc37 M/C fragment crystal structure. Our complete Cdc37 model (residues 1 to 260) is shown in teal. Note the β strand wrapping around the outside of Hsp90, connecting the two major Cdc37 domains. (**B**) Two additional classes show previously unobserved density for the missing Cdk4 N lobe. These classes, minus the Hsp90-Cdc37 density highlight the two previously unseen Cdk4 N-lobe conformations (shown in blue and maroon, respectively). Fitted kinase models are illustrated as ribbons.

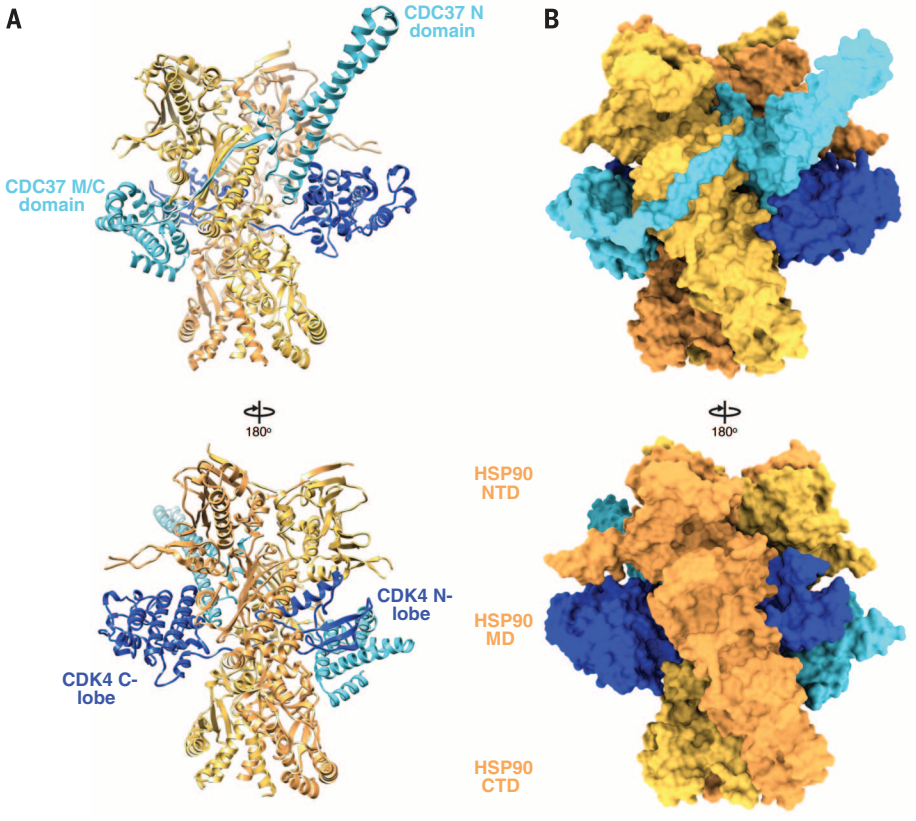


Fig. 4. Hsp90, Cdc37, and Cdk4 are intricately interwoven in the complex. Two views of the complete model, depicted in ribbon representation in (**A**) and surface representation in (**B**).

verified, as two-dimensional (2D) classification of ~800,000 initially chosen particles yielded classes with visible high-resolution features (fig. S2). Three-dimensional classification and refinement resulted in a 4 Å map (figs. S3 and S4 and table S1), with most of the Hsp90 structure being better resolved (3.5 Å), whereas the lowest-resolution regions were ~6 Å (Fig. 1A).

Hsp90 is in a closed conformation in the complex

Refining the 4 Å map with a tighter mask around Hsp90 resulted in a higher-resolution, 3.9 Å density for Hsp90 and neighboring regions (Fig. 1B, insets) (*22*). This map was of sufficient quality to accurately build and refine an atomic model of human Hsp90β based on a homology model derived from yeast Hsp90 (Fig. 1B and fig. S5). Surprisingly, reconstructions of the complex prepared with Hsp90 with a deleted charged linker never yielded good results, probably due to increased heterogeneity. Hsp90 adopts a symmetrical [root mean square deviation (RMSD) between monomers = 0.82 Å] closed conformation, which closely resembles the yHsp90 closed state (*23*). This result was unexpected, as without a cross-linker, closed hHsp90 had not been previously observed. Although the molybdate added during purification may contribute, the closed state is probably a consequence of the ternary complex. In our map, which was refined without symmetry, the strongest density is symmetric at the γ-phosphate location for nucleotide binding sites at both NTDs of Hsp90 (fig. S6). This suggests that either the complex traps Hsp90 in an ATP state or, more likely, ADP·molybdate acts as a posthydrolysis transition state inhibitor, thereby helping to stabilize the closed conformation. The hHsp90 model determined here is similar to the yeast Hsp90 structure (RMSD = 1.59 Å), with a small rotation in the CTD and correlated movements throughout (movie S1). Additionally, a number of loops disordered in the crystal structure were ordered in our model, as they were interacting with the kinase (Fig. 2B). The charged linker is visible in 2D classes but is absent from the 3D reconstruction, suggesting a highly flexible structure (fig. S2).

The N lobe of Cdk4 is substantially unfolded and threads through Hsp90

Two regions of the 4 Å map cannot be accounted for by Hsp90: a long coiled-coil like protrusion and a globular density on one side of Hsp90 (arrows in Fig. 1B). Although we initially suspected that these regions correspond to the Cdc37 M/C (globular domain with long helix), the globular domain fit became worse as our map improved. To obtain an unbiased fit, we performed an exhaustive search against all protein folds in the CATH database [~16,000 Protein Data Bank identifiers (PDB IDs)] (*22*). Disregarding algorithmic

Downloaded from http://science.sciencemag.org/ on June 28, 2016

errors, the top-scoring hits were all variations on the kinase C lobe, with Cdc37 M/C scoring considerably worse (fig. S7). Based on these findings, the Cdk4 C lobe was placed into the density (*24*), resulting in a high-quality fit (Fig. 2A). By contrast, not only does no suitable density exist for the folded kinase N lobe, but it would also sterically clash with Hsp90. Notably, however, tracing the kinase density from the C lobe toward the N terminus, there was a clear tubular region going through the lumen of Hsp90 (Fig. 2, A and B). Thus, a drastically altered conformation of the kinase N lobe is being stabilized by Hsp90 (movie S2). Threading the Cdk4 sequence into this density reveals that the β4 and β5 strands have been ripped apart, and instead β5 interacts with a previously mapped general Hsp90 client binding site via extensive hydrophobic interactions (*25*) and two salt bridges (Fig. 2C). Potentially due to these interactions, the Hsp90 CTD rotates toward the kinase (as compared to the yHsp90 structure) at the MD-CTD interface, which was identified as asymmetric in previous work (*26*) (movie S1). Altogether, this suggests that the MD-CTD interface may be used to communicate Hsp90's hydrolysis state to the client. Unfortunately, in the highest-resolution map, no density was visible for kinase residues at the N-terminal end of the β5 strand.

Cdc37 is split into two domains and wraps around Hsp90

Although there is no available 3D structural information for the Cdc37 NTD, sequence analysis (MARCOIL) predicts a significant coiled-coil structure. Supported by our observations of high helical content, as determined by circular dichroism and nuclear magnetic resonance (fig. S8), a coiled-coil provides a good candidate for the nonglobular map density (Fig. 1B). That density transitions from helical to strandlike, wrapping around the Hsp90 MD and adding an additional β strand to the 1AC β sheet (PDB ID 2CG9). Unfortunately, as with the kinase, this β strand does not connect to any density on the other side, thwarting a complete fit of Cdc37. Demonstrating the power of single-particle cryo-EM, local rounds of 3D classification yielded a 7 Å map (figs. S3 and S9) showing clear globular density that is connected through the β strand to the coiled-coil region (Fig. 3A). This previously unobserved density was unambiguously fit by the crystallized Cdc37 M/C fragment. Using a combination of the two maps, we were able to fit Cdc37 M/C residues 148 to 260 and de novo build residues 1 to 147 of human Cdc37 (Fig. 3A) (*22*). Although further classification revealed some density beyond residue 260, it was too weak to model with confidence.

Locating the remainder of the kinase N lobe and verification

The local 3D classification also revealed the remainder of the kinase N lobe (Fig. 3B and movie S3). In two of the classes, distinct globular densities were visible that connected to the tubular density derived from the unfolded Cdk4 N lobe. At the same time, the density for the MD of Cdc37 was either very weak or absent, suggesting an anticorrelation between Cdc37 M/C–Hsp90 interactions and kinase N-lobe–Hsp90 interactions. We were able to roughly fit the rest of the Cdk4 N lobe into these densities, allowing us to build a complete model of the Hsp90-Cdc37-Cdk4 complex (Fig. 4 and movie S4). Given the unusual split domain conformation for both the kinase and the cochaperone, it was important to verify our structural assignments. Toward that end, we used T4 lysozyme to covalently tag Cdc37 at its N terminus and Cdk4 at its C terminus. The two different complexes were expressed and purified from yeast, followed by cryo-EM reconstruction of each. These two structures clearly show lysozyme

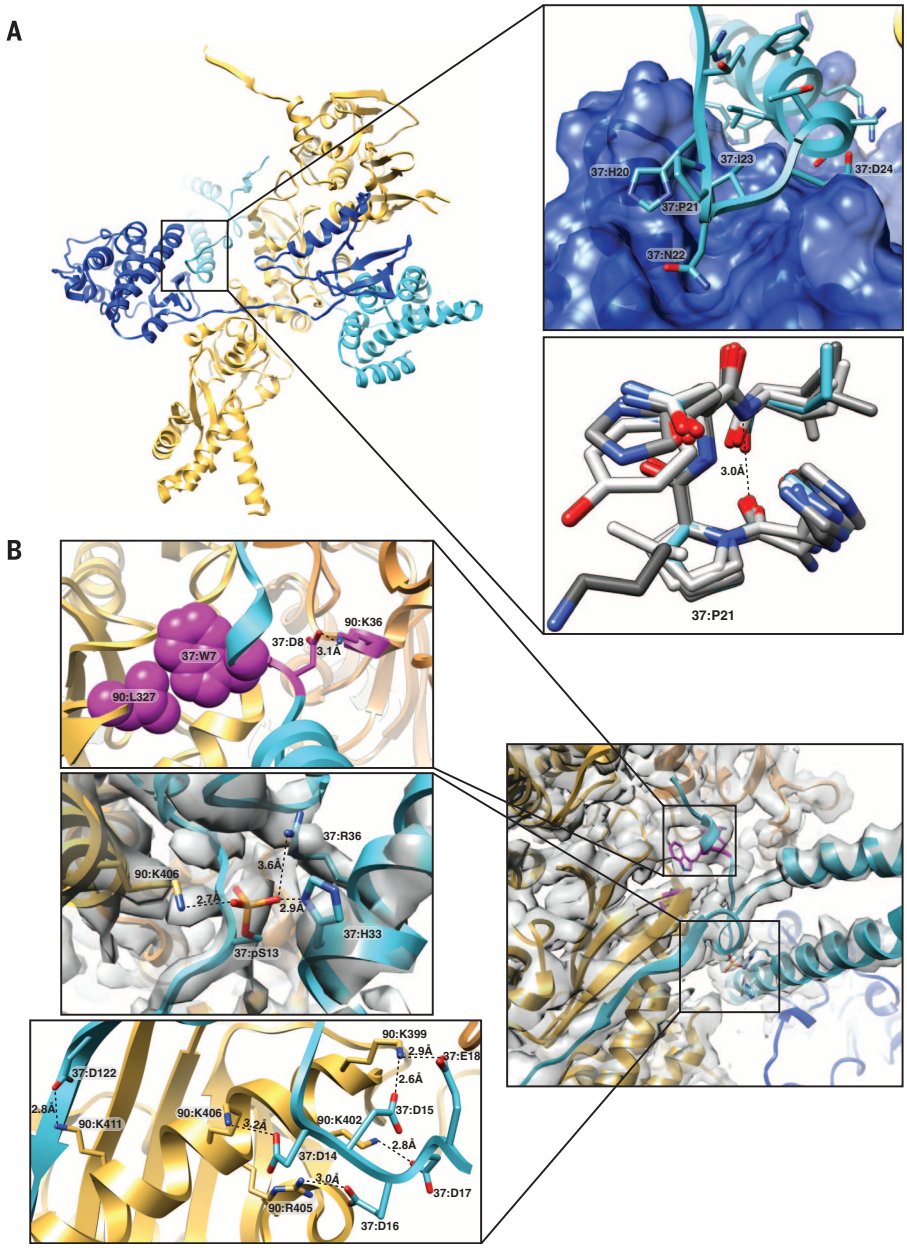


Fig. 5. High-resolution details of Cdc37 interactions with Hsp90 and Cdk4. (**A**) Overall arrangement of Hsp90-Cdc37-Cdk4 (one Hsp90 monomer removed for clarity). The insets highlight Cdc37-Cdk4 interaction features: (Top) Cdc37 and Cdk4 interact via hydrophobic interactions and backbone hydrogen bonds, with perfect shape complementarity. (Bottom) Overlay of Cdc37's conserved HPN motif (teal) perfectly mimicking a type I β turn of the αC-β4 loop of six different kinases (shades of gray) (PDB IDs: 3G33, 2ITP, 1QMZ, 3PP0, 1JNK, and 4FK3). (**B**) Zooming in on Hsp90-Cdc37 interactions. (Top inset) Cdc37-Hsp90 interactions mimic previously identified p23-Hsp90 interactions (magenta). (Middle inset) Phospho-Ser[13] stabilizes the local Cdc37 structure through interactions with conserved R36 and H33 and also interacts with Hsp90 at K406. (Bottom inset) Six salt bridges stabilize Hsp90-Cdc37 interactions.

Downloaded from http://science.sciencemag.org/ on June 28, 2016

density consistent with our map interpretation (fig. S10).

Cdc37 precisely mimics a conserved feature of kinase N-lobe–C-lobe interactions and makes previously unseen interactions with Hsp90

The resulting model (Fig. 4) contains a number of notable features that explain a wealth of accumulated, seemingly contradictory observations. The Cdc37 NTD forms a long coiled-coil with a leucine zipper-like motif. The N terminus of this coiled-coil interacts with Cdk4 through extensive hydrophobic and hydrogen bonding interactions, burying 725 Å^2 (table S2) in surface area, and mimicking interactions that the kinase αC-β4 loop normally makes with the C lobe (Fig. 5A). Additionally, the following loop in Cdc37 overlays perfectly with the αC-β4 loop of multiple kinases, packing tightly against the kinase C lobe (Fig. 5A, bottom inset), revealing why this Cdc37 region is so conserved (fig. S11). Thus, Cdc37 binds to the kinase C lobe by mimicking interactions the N lobe normally makes, stabilizing separation of the two kinase lobes.

The interactions between Cdc37 and Hsp90 are considerably different from those seen in the previous crystal structure of fragments of each protein. Instead of binding to an Hsp90 NTD surface that would be accessible only in the open state, Cdc37 M/C interacts with the Hsp90 MD in the Hsp90 closed state, although these interactions are fairly limited (only ~340 Å^2 out of 2650 Å^2 total buried surface area) (Fig. 4). Interactions with Cdc37 residues 120 to 129, which pack a β strand against Hsp90 MD (Fig. 5B), are more extensive. Additionally, part of the Cdc37 NTD binds to a new site on the closed Hsp90 NTD, somewhat mimicking interactions seen between p23 and Hsp90 (Fig. 5B, top inset). There is also an extensive network of ionic interactions between Cdc37 NTD and Hsp90 MD, which explains previously identified salt sensitivity of Cdc37-Hsp90 binding (Fig. 5B, bottom inset). Our structure thus helps to explain recent data indicating that *Caenorhabditis elegans* Cdc37 interacts with the MD of Hsp90 (*27*), rather than the NTD, as observed in previous human domain binding studies. Instead of assuming that *C. elegans* is different or that the interactions observed with isolated domains were incorrect, we propose that Cdc37-kinase first binds Hsp90 in its open conformation, as seen in the crystal structure, and then rearranges to the site on the MD upon Hsp90 closure, as seen in our structure.

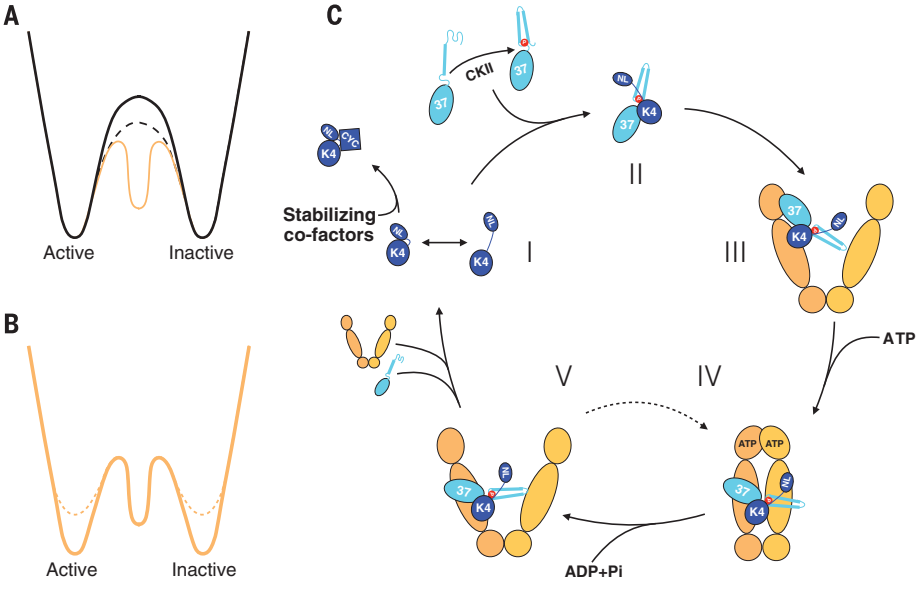


Fig. 6. Conceptual model for linkage between kinase folding and activation and proposed model for the Hsp90-Cdc37-kinase cycle. (**A**) Transitioning between states through an unfolded intermediate (black dashed line) has a lower energy barrier compared with that for transitioning through rigid-body motion (black solid line). The Hsp90-Cdc37 complex stabilizes such an unfolded intermediate (orange solid line). (**B**) By comparison with nonclients (orange solid line), the active and inactive states of client kinases (orange dashed lines) are destabilized. (**C**) Speculative model for an Hsp90-Cdc37-kinase cycle. (I) The kinase domain transiently samples an open state. Interactions with cofactors (such as cyclins, SH2 and SH3 domains, etc.) stabilize the kinase native state, disfavoring the open state (NL, N lobe; CYC, cyclin; K4, Cdk4). Casein kinase 2 (CKII)–phosphorylated Cdc37 (37) captures the open state by binding the kinase C lobe (II). Cdc37-kinase then binds to open Hsp90 (III). Hsp90 binds to ATP and closes upon the unfolded part of the kinase. Cdc37 migrates down, resulting in the structure described here (IV). Upon hydrolysis of ATP, Hsp90 opens with Cdc37-Cdk4 still bound, providing a chance for the kinase to fold (V). If it folds, it displaces Cdc37 and leaves the complex. If, however, it fails to displace Cdc37, then Hsp90 is able to rebind ATP and go back to state IV, repeating the process. At some point during this cycle, PP5 phosphatase is recruited to the complex to dephosphorylate Cdc37. Pi, phosphate.

Phosphorylation of Cdc37 stabilizes the kinase-bound conformation

Phosphorylation at the completely conserved Ser^{13} residue of Cdc37 is important for kinase function and was thought to be directly involved in kinase binding (*15*, *16*). In our structure, there is density for the phosphorylated Ser^{13}, which forms a salt bridge with Cdc37-Arg^{36} and Cdc37-His^{33}, stabilizing the N terminus of the coiled coil (Fig. 5B, middle inset). This provides a molecular rationale for previous observations of a Cdc37 conformational change upon phosphorylation (*28*). Of note, this phosphate also contributes to the overall electrostatic nature of Hsp90-Cdc37 interactions, by forming a salt bridge with Hsp90-Lys^{406}. The residues making up the Cdc37–Hsp90 NTD and Cdc37-kinase interaction surfaces are extremely well conserved (fig. S11), further validating the importance of the interactions observed here.

Hsp90 and Cdc37 capture and stabilize structural transitions within the kinase

In the ternary complex, Cdk4 assumes a conformation substantially different from those previously observed for any kinase structure. The kinase hinge region and the β4-β5 sheet are completely unfolded, with the N and C lobes being pried apart and stabilized by the interactions with Hsp90 and Cdc37. On the basis of this conformation, we propose a model where it is the propensity for the kinase to unfold to an N-lobe–C-lobe separated open state rather than a specific binding sequence that determines whether a particular kinase will be a client. Furthermore, the fact that many nonclient kinases depend on Hsp90 during initial folding would suggest that the open kinase state we observe is an on-pathway folding intermediate.

In agreement with the model, the β3-αC loop of Cdk4 (strong client) has seven glycine residues versus one or two glycines in the same loop of Cdk2 and Cdk6 (nonclient and weak client, respectively). Mutating this loop in Cdk4 to the Cdk6 sequence stabilizes the protein (*29*). In a similar manner, a single point mutation derived from EGFR (nonclient) in the αC-β4 loop was able to abrogate the interactions of HER2 (strong client) with, and its dependence on, Hsp90-Cdc37 (*30*). This point mutation would potentially introduce a salt bridge to stabilize the kinase loop (fig. S12) and, hence, the association between the kinase lobes.

Our model explains why a sequence motif responsible for Hsp90 interactions has yet to be found. The allosteric properties of kinases allow distant and seemingly unrelated mutations to destabilize the N-lobe–C-lobe interface, explaining often-confusing mutagenesis results. Thus, nonclient kinases would exit Hsp90 dependence after initial folding via stabilizing interactions with regulatory partners or extra domains (cyclin, dimerization partners, SH2 and SH3 domains, etc.).

Linking kinase unfolding to assembly and activity

Why might it be beneficial for a large percentage of human kinases to substantially populate a

Downloaded from http://science.sciencemag.org/ on June 28, 2016

folding intermediate, even when mature? Rather than being a vestige of kinase evolution with Hsp90 buffering gain-of-function destabilizing mutations (*31*), we argue that being able to safely populate such an open folding intermediate has a direct functional and regulatory benefit. Recent computational efforts have suggested a connection between folding and kinase activity (*32*, *33*). The concept is that the most favorable transition between the inactive and active states is through a more open, unfolded state rather than through a more classical rigid-body transition. Although the opening seen in simulations is far more subtle than what we observed, we suggest that the concept still applies (Fig. 6A). The generally lower stability of client kinases would lead to enhanced sampling of the open state, thereby encouraging chaperone binding (Fig. 6B). Chaperone stabilization of a kinase open state could increase the overall rates of interconversion and/or protect a potentially vulnerable state from aggregation or recognition by the ubiquitinylation machinery. Moreover, the open state could be the preferred substrate for adding and removing posttranslational modifications, as well as for critical stabilizing interactions.

Life cycle of kinase-Hsp90-Cdc37 interactions

Our structure also suggests how the observed state might arise and mature (Fig. 6C). Hsp90 would first interact with Cdc37-kinase via previously published crystal structure contacts (Fig. 6C, state III). Whether assistance from Hsp70 and/or Hsp40, as with the glucocorticoid receptor, would be required is still unclear (*34*), but the inability to directly form the complex from components and Chk1 reconstitution experiments (*35*) is suggestive. During the cycle, Cdc37 would act as a quality-control checkpoint, where it would dissociate from the kinase only upon proper folding of the N lobe. The long coiled-coil would allow Cdc37-kinase to stay attached to Hsp90 during multiple ATP hydrolysis events. If the kinase would fail to dissociate after many hydrolysis events, the degradation machinery might then be recruited to the complex. Although Fig. 6C captures the essence of the available data, other models are possible.

Beyond revealing the kinase open state, our cryo-EM reconstruction allowed us to build the first atomic models for human cytosolic Hsp90 and the kinase-interacting N terminus of Cdc37. The ability to collect a large number of particles, coupled with the capabilities of single-electron–counting detectors and 3D classification software, allowed us to visualize multiple conformations, providing a qualitative assessment for the dynamic nature of the complex. Overall, our structure has enabled us to explain a number of often-contradictory biochemical observations and to provide both mechanistic and conceptual models of Hsp90-kinase interactions that can be tested in future experiments. Our structure also indicates the potential for single-particle cryo-EM to facilitate exploration of other dynamic, asymmetric complexes at near-atomic resolution.

REFERENCES AND NOTES

1. S. S. Taylor, M. M. Keshwani, J. M. Steichen, A. P. Kornev, *Philos. Trans. R. Soc. Lond. B Biol. Sci.* **367**, 2517–2528 (2012).
2. J. Zhang, P. L. Yang, N. S. Gray, *Nat. Rev. Cancer* **9**, 28–39 (2009).
3. J. A. Endicott, M. E. Noble, L. N. Johnson, *Annu. Rev. Biochem.* **81**, 587–613 (2012).
4. J. Brugge, W. Yonemoto, D. Darrow, *Mol. Cell. Biol.* **3**, 9–19 (1983).
5. M. Taipale, D. F. Jarosz, S. Lindquist, *Nat. Rev. Mol. Cell Biol.* **11**, 515–528 (2010).
6. M. Taipale *et al.*, *Cell* **150**, 987–1001 (2012).
7. Y. Miyata, H. Nakamoto, L. Neckers, *Curr. Pharm. Des.* **19**, 347–365 (2013).
8. K. A. Krukenberg, T. O. Street, L. A. Lavery, D. A. Agard, *Q. Rev. Biophys.* **44**, 229–255 (2011).
9. M. P. Mayer, L. Le Breton, *Mol. Cell* **58**, 8–20 (2015).
10. D. R. Southworth, D. A. Agard, *Mol. Cell* **32**, 631–640 (2008).
11. S. Tsutsumi *et al.*, *Proc. Natl. Acad. Sci. U.S.A.* **109**, 2937–2942 (2012).
12. J. Shao, A. Irwin, S. D. Hartson, R. L. Matts, *Biochemistry* **42**, 12577–12588 (2003).
13. S. M. Roe *et al.*, *Cell* **116**, 87–98 (2004).
14. J. M. Eckl *et al.*, *J. Biol. Chem.* **288**, 16032–16042 (2013).
15. S. Polier *et al.*, *Nat. Chem. Biol.* **9**, 307–312 (2013).
16. C. K. Vaughan *et al.*, *Mol. Cell* **31**, 886–895 (2008).
17. M. Taipale *et al.*, *Nat. Biotechnol.* **31**, 630–637 (2013).
18. E. E. Boczek *et al.*, *Proc. Natl. Acad. Sci. U.S.A.* **112**, E3189–E3198 (2015).
19. C. K. Vaughan *et al.*, *Mol. Cell* **23**, 697–707 (2006).
20. Y. Cheng, *Cell* **161**, 450–457 (2015).
21. S. D. Hartson, V. Thulasiraman, W. Huang, L. Whitesell, R. L. Matts, *Biochemistry* **38**, 3837–3849 (1999).
22. Materials and methods are available as supplementary materials on *Science* Online.
23. M. M. Ali *et al.*, *Nature* **440**, 1013–1017 (2006).
24. T. Takaki *et al.*, *Proc. Natl. Acad. Sci. U.S.A.* **106**, 4171–4176 (2009).
25. O. Genest *et al.*, *Mol. Cell* **49**, 464–473 (2013).
26. L. A. Lavery *et al.*, *Mol. Cell* **53**, 330–343 (2014).
27. J. M. Eckl *et al.*, *J. Biol. Chem.* **290**, 30843–30854 (2015).
28. W. Liu, R. Landgraf, *Biochemistry* **54**, 1493–1504 (2015).
29. P. J. Day *et al.*, *Proc. Natl. Acad. Sci. U.S.A.* **106**, 4166–4170 (2009).
30. W. Xu *et al.*, *Nat. Struct. Mol. Biol.* **12**, 120–126 (2005).
31. J. Lachowiec, T. Lemus, E. Borenstein, C. Queitsch, *Mol. Biol. Evol.* **32**, 91–99 (2015).
32. O. Miyashita, J. N. Onuchic, P. G. Wolynes, *Proc. Natl. Acad. Sci. U.S.A.* **100**, 12570–12575 (2003).
33. Y. Shan, A. Arkhipov, E. T. Kim, A. C. Pan, D. E. Shaw, *Proc. Natl. Acad. Sci. U.S.A.* **110**, 7270–7275 (2013).
34. E. Kirschke, D. Goswami, D. Southworth, P. R. Griffin, D. A. Agard, *Cell* **157**, 1685–1697 (2014).
35. S. J. Arlander *et al.*, *J. Biol. Chem.* **281**, 2989–2998 (2006).
36. Single-letter abbreviations for the amino acid residues are as follows: A, Ala; C, Cys; D, Asp; E, Glu; F, Phe; G, Gly; H, His; I, Ile; K, Lys; L, Leu; M, Met; N, Asn; P, Pro; Q, Gln; R, Arg; S, Ser; T, Thr; V, Val; W, Trp; and Y, Tyr.

ACKNOWLEDGMENTS

We thank members of NRAMM-Scripps for help with collecting data; Y. Fan for the yeast expression vector; N. Ohbayashi and M. Niino (RIKEN Center for Life Science Technologies) for help with Sf9 protein expression; N. F. Rebbe (University of North Carolina at Chapel Hill) and E. Laue (University of Cambridge) for the plasmids encoding human HSP90b and Cdc37, respectively; D.A.A.'s lab members for helpful discussions; and N. Jura for reading the manuscript. Support for this work was provided by Protein Structure Initiative–Biology grant U01 GM098254 (to D.A.A.), American Association for Cancer Research–Breast Cancer Research Foundation grant 218084 for Translational Breast Cancer Research (to D.A.A.), a gift from the Cabala family (to D.A.A.), an HHMI Helen Hay Whitney Foundation Fellowship (to Y.L.), an HHMI International Student Research Fellowship (to K.A.V.), and the HHMI (to D.A.A.). Some of the work presented here was conducted at NRAMM, which is supported by a grant from the NIH National Institute of General Medical Sciences (9 P41 GM103310). Some of the work used the Extreme Science and Engineering Discovery Environment (XSEDE), which is supported by NSF grant ACI-1053575.

SUPPLEMENTARY MATERIALS

www.sciencemag.org/content/352/6293/1542/suppl/DC1
Materials and Methods
Figs. S1 to S13
Tables S1 and S2
References (*37*–*58*)
Movies S1 to S4

22 February 2016; accepted 13 May 2016
10.1126/science.aaf5023

QUANTUM SIMULATION

Exploring the many-body localization transition in two dimensions

Jae-yoon Choi,[1]*† Sebastian Hild,[1]* Johannes Zeiher,[1] Peter Schauß,[1]‡ Antonio Rubio-Abadal,[1] Tarik Yefsah,[1]§ Vedika Khemani,[2] David A. Huse,[2,3] Immanuel Bloch,[1,4] Christian Gross[1]

A fundamental assumption in statistical physics is that generic closed quantum many-body systems thermalize under their own dynamics. Recently, the emergence of many-body localized systems has questioned this concept and challenged our understanding of the connection between statistical physics and quantum mechanics. Here we report on the observation of a many-body localization transition between thermal and localized phases for bosons in a two-dimensional disordered optical lattice. With our single-site–resolved measurements, we track the relaxation dynamics of an initially prepared out-of-equilibrium density pattern and find strong evidence for a diverging length scale when approaching the localization transition. Our experiments represent a demonstration and in-depth characterization of many-body localization in a regime not accessible with state-of-the-art simulations on classical computers.

In his seminal work on localization in quantum mechanical systems, Philip Anderson emphasized the implications of localization on the thermodynamics of closed quantum systems (*1*). Recently, perturbative arguments suggested the existence of nonthermalizing, many-body localized systems at low energy (*2*, *3*). Soon thereafter, these arguments were extended to all interaction strengths and energy densities for systems with a bounded spectrum (*4*, *5*). The implication—nothing less than a breakdown of equilibrium statistical mechanics for certain generic

Downloaded from http://science.sciencemag.org/ on June 28, 2016

macroscopic systems—triggered tremendous theoretical efforts (*6*–*8*). Furthermore, the breakdown of the eigenstate thermalization hypothesis (*9*–*12*) caused by the failure of these systems to act as their own heat bath implies the persistence of initial state information, which might serve as a useful resource for quantum information technologies (*13*). Several other notable features of many-body localization (MBL) have been uncovered, such as the description of fully localized systems by coupled localized integrals of motion (*14*, *15*). This underlies the absence of particle transport but allows the transport of phase correlations, leading to a characteristic logarithmic growth of the entanglement entropy in the case of short-range interactions (*16*–*20*). Another distinctive feature of many-body localized systems, as compared with noninteracting low-dimensional systems, is the requirement of a nonzero disorder strength for the localized phase to appear (*21*, *22*).

Recently, the absence of thermalization due to MBL in a quasi-disordered one-dimensional (1D) Fermi lattice has been reported (*23*, *24*). These studies explored the system's behavior at long times and high energy density, as opposed to earlier experiments with noninteracting systems (*25*–*30*) or interacting ultracold atoms in lower-energy states (*31*–*36*). A recent experiment with 3D disordered lattice fermions provided evidence for the absence of particle transport, even at elevated temperatures (*37*). Indications for localization in Fock space, one characteristic property of MBL (*2*), have been reported in short ion chains (*38*), and MBL has been suggested as one possible explanation for the recently observed vanishing conductance in disordered superconductors at nonzero temperature (*39*). However, despite intensive theoretical and experimental efforts, some aspects of MBL, such as the details of the localization transition, including the identification of diverging length scales, are still not fully understood. Whereas in one dimension the localization transition is rather well studied (*21*, *22*, *40*, *41*), the nature of MBL in higher dimensions is an open question.

Here we address the open question of the nature of a MBL transition in two dimensions, which we observe experimentally and characterize. We report on the single-site–resolved study of thermalization and transport in a disordered 2D bosonic optical lattice, starting from a high–energy density initial state far from equilibrium. By tracking the time evolution of an initially prepared density domain wall for variable disorder strengths, we reveal the fairly sharp onset of nonthermalizing behavior above a critical value of disorder strength. The observed localization transition is found when the disorder, single-particle bandwidth, onsite interaction, and

[1]Max-Planck-Institut für Quantenoptik, 85748 Garching, Germany. [2]Department of Physics, Princeton University, Princeton, NJ 08544, USA. [3]Institute for Advanced Study, Princeton, NJ 08540, USA. [4]Fakultät für Physik, Ludwig-Maximilians-Universität, 80799 München, Germany.
*These authors contributed equally to this work. **†Corresponding author. Email: jae-yoon.choi@mpq.mpg.de** ‡Present address: Department of Physics, Princeton University, Princeton, NJ 08540, USA. §‡Present address: Laboratoire Kastler Brossel, CNRS, École Normale Supérieure, 75005 Paris, France.

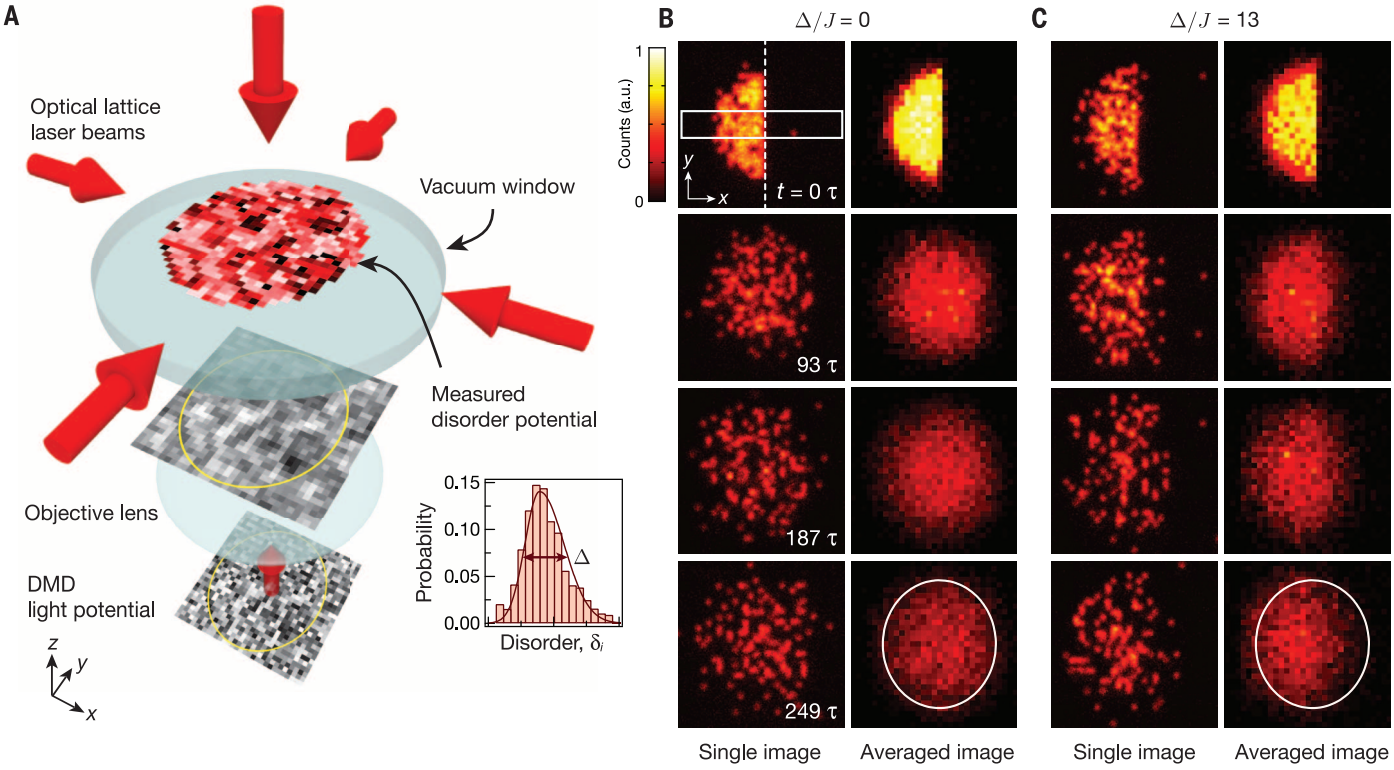


Fig. 1. Schematics of the experiment and raw images. (**A**) A 2D random disorder potential is imaged onto a single atomic plane in an optical lattice. The disorder is controlled by a digital mirror device (DMD), which converts a Gaussian laser intensity profile into a 2D random intensity distribution with spatially uniform mean light intensity (bottom image). The limited numerical aperture (NA = 0.68) of the microscope objective introduces a finite correlation length and leads to a smoothing of the disorder distribution. The histogram at bottom right (red bars) is the measured disorder distribution and its asymmetric Gaussian fit curve (red solid line), where Δ is the full width at half maximum of the disorder distribution. Distinct to the other two images showing the original (bottom) and smoothed (middle) light intensity distributions, the top image displays the local disorder potential determined by in situ spectroscopy (*42*). The yellow circles on the lower images indicate the spectroscopically calibrated region. (**B**) Raw fluorescence images (the red-to-yellow color scale corresponds to increasing detected light level) showing the evolution of the initial density step without disorder. The left column shows single images (isolated red dots are individual atoms) of the parity-projected atomic distribution for the indicated evolution times. The right column displays the mean density distribution averaged over 50 different disorder potentials. The top left image depicts the initial state for which the analysis region ($dx \times dy = 5 \times 31$) is indicated by the white box. For the high-disorder case shown in (**C**) the detected initial-state filling is slightly lower, which is an artifact of the parity projection (*42*). In contrast to (B), traces of the initial state remain at all times in the disordered case. The white circles in the averaged density profiles after $t = 249\tau$ highlight the difference. a.u., arbitrary units.

Downloaded from http://science.sciencemag.org/ on June 28, 2016

energy density are all of comparable strength. This regime of parameters, being far from the disorder-dominated (classical) and the interaction-dominated limits, is highly nontrivial from a theoretical perspective. Precise and direct characterization of the projected disorder potential by site-resolved spectroscopy allows for a direct comparison of our results with a numerical prediction for the noninteracting model, highlighting the dramatic differences and pointing out the key role of interactions. Furthermore, by locally comparing the observed density profiles to a thermalizing reference measured without disorder, we obtain strong evidence for a diverging length scale when approaching the transition from the localized side.

Experimental setup

We began by preparing a 2D approximately unity filled Mott insulator of bosonic ^{87}Rb atoms in a single plane of a cubic optical lattice with lattice spacing a_{lat} = 532 nm. To ensure that the initial state was separable, we froze out any motion at a lattice depth of $40E_r$ in the x and y directions, where $E_r = \hbar^2/8ma_{lat}^2$ is the recoil energy, $\hbar$ the Planck constant, and m is the atomic mass. Next, we used a digital mirror device–based spatial light modulator (*42*) to optically remove the right half of the atomic population such that about N = 125(11) atoms remained in the lattice sites located at $x < 0$, thus preparing a sharp density domain wall. For each experimental realization, a new computer-generated random disorder pattern drawn from a uniform distribution was displayed on the light modulator and subsequently projected onto the atoms (Fig. 1A). The optical projection results in a slightly asymmetric disorder distribution and a convolution of the disorder, with the point spread function of the imaging system leading to a finite disorder correlation length $0.6a_{lat}$ and a narrowing of the disorder distribution to a width Δ (Fig. 1A, inset) (*43*). We used single-site–resolved spectroscopy of the atomic sample to directly characterize the disorder. The topmost disorder picture in Fig. 1A displays the result of one such spectroscopic measurement for the configuration shown in the two images below. We then initiated the dynamics of the initial domain wall by lowering the x and y lattice depths to $12E_r$ in 5 ms, which is less than one tunneling time. Next, we allowed the system to evolve for a variable time t in the disorder potential, after which we used fluorescence imaging to measure the local parity-projected density (*44*).

During the dynamics, the system is described by a 2D Bose-Hubbard Hamiltonian with onsite disorder

$$\hat{H} = -J\sum_{\langle i,j\rangle}\hat{a}_i^\dagger\hat{a}_j + \frac{U}{2}\sum_i \hat{n}_i(\hat{n}_i - 1) + \sum_i(\delta_i + V_i)\hat{n}_i$$

Here, $\hat{a}_i^\dagger$ ($\hat{a}_j$) is the bosonic creation (annihilation) operator, $\hat{n}_i = \hat{a}_i^\dagger\hat{a}_i$ is the local density operator on site $\mathbf{i} = (i_x, i_y)$, and the first sum includes all neighboring sites. A harmonic trapping potential $V_i = ma_{lat}^2(\omega_x^2 i_x^2 + \omega_y^2 i_y^2)/2$ with frequencies $(\omega_x, \omega_y) = 2\pi \times (54, 60)$ Hz in the x and y direction confines the atoms around the trap minimum. The nearest-neighbor hopping strength at a lattice depth of $12E_r$ is J/h = 24.8 Hz, corresponding to a tunneling time of $\tau = \hbar/2\pi J$ = 6.4 ms. Longer-range hopping terms are neglected, as they are exponentially suppressed. The onsite interaction strength is U = 24.4J, and δ_i denotes the onsite disorder potential. For these parameters, in the absence of disorder, the system's ground state is in the Mott insulating phase, albeit with strong particle-hole fluctuations (*45*).

MBL in two dimensions

For reference, we first tracked the time evolution without any disorder potential applied. Even

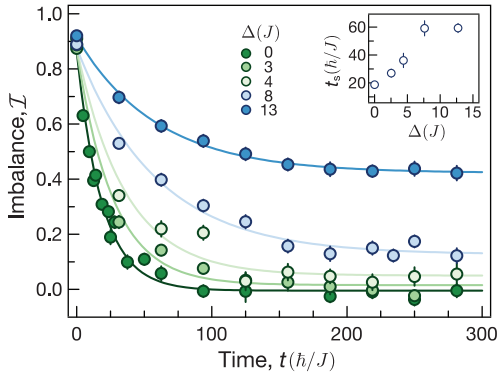


Fig. 2. Relaxation dynamics of a density domain wall. The evolution of the imbalance $\mathcal{I}$ shown for five different disorder strengths [Δ/J = 0 (dark green), 3 (medium green), 4 (light green), 8 (light blue), and 13 (dark blue)] displays a saturation behavior toward a quasi–steady state for all disorder strengths. For low disorders (green curves), the asymptotic value of the imbalance is vanishing, whereas a finite imbalance remains for higher disorder (blue). Solid curves are fits to the data with $\mathcal{I} = \mathcal{I}_0\exp(-t/t_s) + \mathcal{I}_\infty$, of which the decay time t_s is plotted versus disorder strength Δ in the inset. Error bars represent 1 SD of the mean in the main figure and 95% confidence bounds of the fit parameters in the inset. $\hbar$, Planck's constant h divided by 2π.

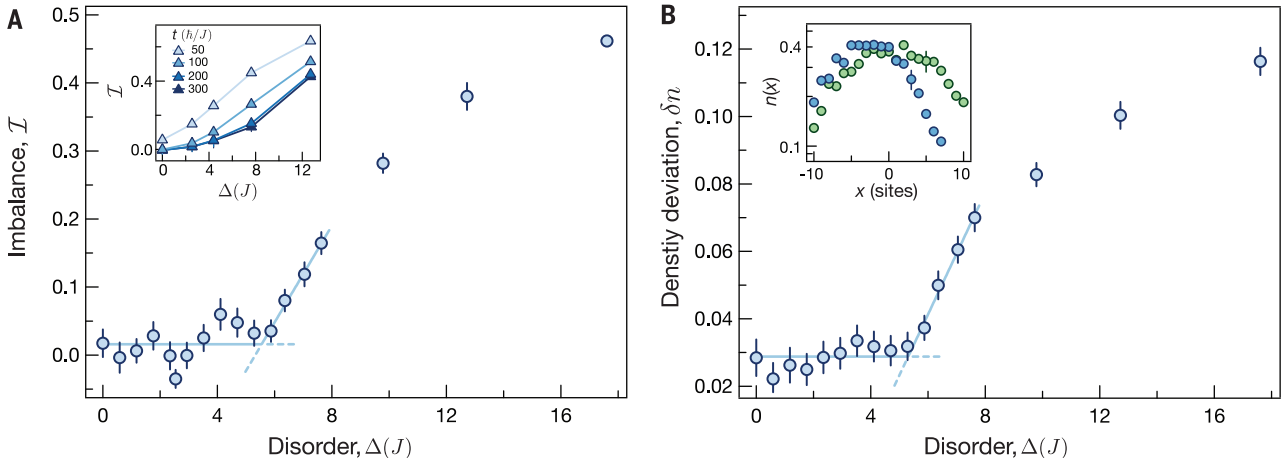


Fig. 3. Identifying the MBL transition. (**A**) Disorder dependence of the imbalance after equilibration of the dynamics [constant evolution time of 187τ, also in (B)]. The data show a sharp onset of nonzero quasi–steady-state imbalance $\mathcal{I}$ at a disorder strength of $\Delta_{c,\mathcal{I}} = 5.5(4)J$, and the solid line is a double linear fit (described in the text) to extract the critical disorder. The inset illustrates the sharpening of the transition versus time and demonstrates the saturation of its shape by showing the imbalance extracted from the fits in Fig. 2 at different evolution times. (**B**) Deviation from the zero-disorder thermal profile, as measured by the root mean square density difference δn at various disorder strengths. The relaxed density profiles differ by more than the random position-induced measurement noise from the thermal profile abruptly above the critical disorder strength $\Delta_{c,\delta n}$ = 5.3(2)J. The inset shows the averaged reference density profile for zero disorder (green) and the averaged profile at a high disorder of Δ = 13J (blue). Error bars represent 1 SD of the mean.

Downloaded from http://science.sciencemag.org/ on June 28, 2016

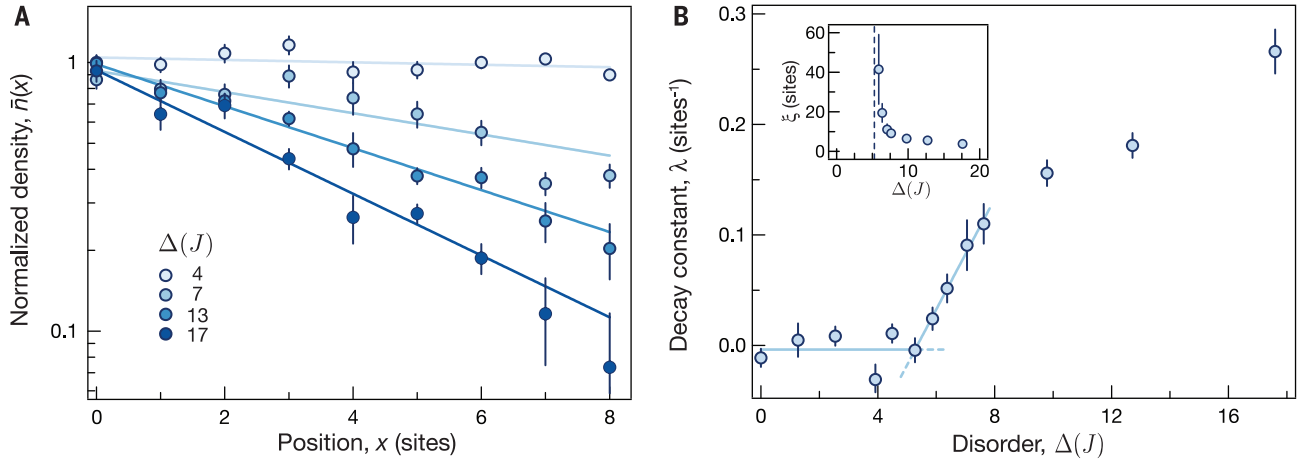


Fig. 4. Diverging density decay length at the localization transition. (**A**) The spatial dependence of the normalized average density $n(\Delta)/n(0)$ in the initially empty region is fitted by an exponentially decaying model (solid lines). The level of blue brightness encodes the disorder strength increasing from light to dark: Δ/J = 4, 7, 13, and 17. (**B**) Fitted decay constant λ as a function of disorder strength Δ. The solid light blue line is a double linear fit (described in the text) to locate the transition point $\Delta_{c,\delta n}$ = 5.3(2)J. The inset shows the diverging decay length $\xi = 1/\lambda$ near the critical disorder strength. Evolution time 187τ is for all data shown here. Error bars represent 1 SD of the mean in (A) and 95% confidence bounds of the fit parameters in (B).

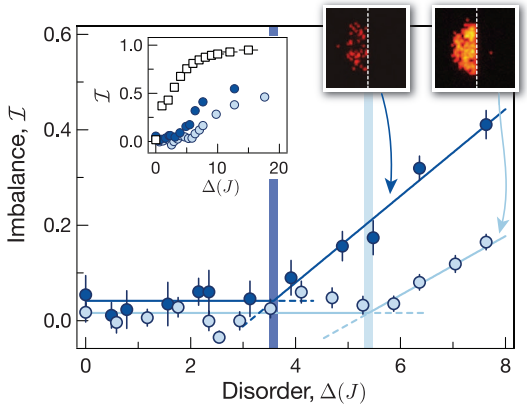


Fig. 5. Interaction dependence of the localization transition. Quasi–steady-state imbalance $\mathcal{I}$ versus disorder strength Δ for different initial densities (evolution time 187τ). The interaction effects are reduced by lowering the initial filling to 0.23, which is 25% of the value previously discussed in Fig. 3A (light blue). The clear difference in critical disorder strengths highlights the strong influence of interactions on the localization. The right two insets show representative fluorescence images of the initial density distribution for each case. The left inset is a zoomed-out view of the main figure where we added the results of exact diagonalization numerics for the noninteracting system with the same experimental conditions (black open squares). Here, the horizontal error bars denote the systematic uncertainty in the disorder strength. Vertical error bars represent 1 SD of the mean.

from the bare images (Fig. 1B), it is clear that the initially prepared density step is smeared out after a few tens of tunneling times τ, and after a longer time, no information about the initial density step remains. The observed density distribution appears thermal, and neglecting quantum fluctuations at 12E_r (that is, assuming decoupled sites), we extracted an upper limit of the temperature of $T < 0.54(1)U/k_B$, where k_B is the Boltzmann constant. This temperature estimate was obtained by a global fit to the radial density profile, assuming a grand canonical ensemble for each site with the chemical potential given by the local density approximation (*44*). The corresponding energy per particle of $E_r/N = 0.58(1)U$ might be overestimated by up to 0.15U, due to the finite band width, and agrees reasonably well with the expectation for a thermalized state, assuming that the lattice ramp to 12E_r was adiabatic with respect to the band gap. Here, the energy density of the initial out-of-equilibrium state contributes with $E_0/N = 0.28(3)U$ (where E_0 is the sum of the initial thermal and the potential energy due to the trap), determined by the initial thermal energy and the harmonic trap with frequency ω_x. An additional energy increase is present due to small heating during the 2-s evolution time [E_H/N = 0.18(6)U] used in this measurement (*43*). In contrast, upon repeating the measurement with strong disorder, traces of the initial state remain, and the system does not relax to a spatially symmetric density distribution expected for thermal state (Fig. 1C).

A direct and model-free quantity that can be used to identify a nonthermalized state is the density asymmetry quantified by a nonzero left (N_L) and right (N_R) atom number imbalance $\mathcal{I} = \frac{N_L - N_R}{N_L + N_R}$, which we analyze, as with all other extracted quantities, in a central region of interest extending over five lattice sites in the y direction. The zero line (x = 0) separating left and right is defined by the position of the initial density step and was precisely aligned to the closest lattice site to the trap center, resulting in an offset of up to ±1 lattice sites, corresponding to $\mathcal{I} \pm 0.05$. The evolution of the imbalance (Fig. 2) confirms that, for all disorder strengths, the system reaches a quasi–steady state within ~150τ. For small disorder strengths, we find a vanishing imbalance, whereas for large disorder, a nonzero imbalance remains, even for long evolution times. We interpret this latter regime as the many-body localized phase, where the observed quasi–steady state is clearly nonthermal and transport through the system is blocked. The relaxation time t_s, extracted from an exponential fit to the data, increases with disorder strength and hints at a saturation in the nonthermal regime (Fig. 2, inset). We now turn to a series of measurements in which we fix the evolution time to ~190τ, which is well in the quasi–steady-state regime but short enough to keep the effects of atom number loss and noise-induced coupling to higher-energy bands negligible. On this time scale, we also expect the effects of low-frequency noise on the disordered system to be small. Considering the measured heating rate in the nondisordered system as an upper bound for the energy increase, the energy per particle would change by only ~10% within one relaxation time t_s. Small couplings with the environment might lead to relaxation of the quasi–steady state on time scales much longer than our experimental time scale (*46*–*50*).

Identifying the MBL transition

The transition from zero to nonzero imbalance $\mathcal{I}_\infty$ for large disorder indicates the presence of a thermalizing phase for low disorder strengths and an apparent transition to a localized phase at higher disorder. To locate an MBL transition, we recorded a series of measurements with fixed evolution time in the quasi–steady-state regime and scanned the disorder around the critical value (Fig. 3). We find a fairly sharp onset of

Downloaded from http://science.sciencemag.org/ on June 28, 2016

nonzero–steady-state imbalance at a disorder strength $\Delta_{c,\mathcal{I}} = 5.5(4)J$, which indicates that the transition is taking place in the system, where we extracted the critical disorder from a simple double linear fit $\mathcal{I}(\Delta) = \mathcal{I}_0 + \mathcal{I}_1 \cdot \max[(\Delta - \Delta_{c,\mathcal{I}}), 0]$ with $\Delta/J \in [0, 8]$. In the vicinity of the transition, slow subdiffusive transport has been predicted (*21*, *22*, *51*–*53*), which suggests that our measurements might not have reached a true steady state in this regime. Because of this, it is possible that the resulting transition might move toward stronger disorder if we were able to study much longer times. Our high-resolution detection allows for a local comparison of the measured density profiles with the equilibrated thermal profile observed at vanishing disorder. As shown in Fig. 3B, we use this method as a more sensitive probe to detect deviations from the thermal profile by calculating the root mean square deviation $\delta n = \left\{ \sum_i [n_i(0) - n_i(\Delta)]^2 \right\}^{1/2}$ of the vertically (y direction) averaged reference profile $n_i(0) = \frac{1}{5} \sum_{j=-2}^{2} n_{i,j}(0)$ and the finite disorder profiles $n_i(\Delta)$. We observe that the profiles start to deviate at $\Delta_{c,\delta n} = 5.3(2)J$, with a fairly sharp kink signaling the transition, which is quantitatively consistent with the imbalance measurements. Whereas localization is predicted for vanishingly small disorder strength in the noninteracting case, the finite interaction U in our system promotes thermalization. This is consistent with our observation of a thermal behavior at nonzero Δ. However, as the disorder strength is increased above a critical value, the localization is restored, which is particularly notable because this transition takes place in the regime where the disorder Δ, the interaction U, and the single-particle bandwidth $8J$ are comparable.

The MBL phase transition is expected to be a continuous transition (*21*, *22*, *40*, *41*, *54*) for which one expects a characteristic diverging length scale when approaching the transition. With our experiments, we have direct access to the steady-state decay length $\xi(\Delta)$ of the initially prepared density step, which is directly related to a density-density correlation length. To minimize the influence of the external trap, we reference the density profile $n_i(\Delta)$ to the thermal profile $n_i(0)$ by calculating $\overline{n}_i(\Delta) = n_i(\Delta)/n_i(0)$ (Fig. 4A). The observed decay is found to be well captured by an exponential fit $\overline{n}_i(\Delta) \sim e^{-\lambda(\Delta) i}$ with a disorder-dependent decay constant $\lambda(\Delta) = 1/\xi(\Delta)$. A priori, we would have expected a crossover from an interaction-dominated decay to a single-particle–dominated decay at low densities present at the outer edge of our sample. However, within the experimental uncertainty we cannot identify such an effect. We directly observe the diverging behavior of the decay length $\xi(\Delta)$ when approaching the transition from the localized side (Fig. 4B, inset). The related decay constant $\lambda(\Delta)$ also shows a very sharp kink at $\Delta_{c,\lambda} = 5.3(3)J$, marking the onset of the localized region. We empirically obtain the critical disorder $\Delta_{c,\lambda}$ using the bilinear fit function, $\lambda(\Delta) = \lambda_0 + \lambda_1 \cdot \max[(\Delta - \Delta_{c,\lambda}), 0]$ with $\Delta/J \in [0, 8]$. We emphasize, that all three methods of extracting the critical disorder strength of the MBL transition in the experiments agree within the fit errors.

Interaction dependence

To experimentally verify that the observed behavior of the system is induced by interactions, we reduced the initial density and, therefore, the effects of the interaction on the dynamics while keeping the initial energy per particle (E_0/N) constant. Lower atomic densities are obtained by uniformly transferring a given fraction of the atoms by applying a microwave pulse to another hyperfine state and then optically removing the transferred population. When we reduced the density by factor of 4, we observed a clear shift of the localization transition toward lower disorder strength, as was expected (Fig. 5). Here, the left-right imbalance $\mathcal{I}(\Delta)$ displays a sharp transition behavior at a smaller critical disorder of $\Delta_{c,\mathcal{I}} \simeq 3.6(2)J$. Furthermore, the numerical prediction for a noninteracting system obtained by exact diagonalization (*43*) is fully incompatible and strongly differs from both measurements, showing that the interactions facilitate thermalization for low disorder strengths. Reducing the system size by the preparation of a smaller initial Mott insulator did not affect the observed critical disorder (*43*). From these observations, we conclude that the nonzero critical disorder strength is due to the interactions and that the measured critical disorder value is not strongly influenced by the small external driving caused by laser fluctuations discussed above.

Conclusions

Our experiments provide evidence for MBL in two dimensions by the observation of a transition from a thermalizing phase to a localized phase of interacting bosons in a disordered optical lattice. The system size analyzed in our experiment is far beyond numerically accessible scales, demonstrating a nontrivial quantum realization of the MBL system that challenges both analytical and numerical theory. Furthermore, we supplemented our observation of an MBL transition with the demonstration of a clear shift of the transition point for effectively smaller interaction energy. Even though it is difficult to distinguish a true phase transition from a sharp crossover within experiments, our results mark a first step in understanding MBL in more than one dimension and can be extended to obtain detailed information about the nature of the MBL transition, such as its dynamical critical exponent (*21*, *22*). Furthermore, supplementing transport experiments with density-density correlation measurements, or even measurements of the entanglement entropy (*55*, *56*), offers a promising possibility to demonstrate ongoing phase dynamics in the localized phase while the density or charge transport is frozen (*38*, *57*). Via detailed studies of the dynamics of transport, it should also be possible to study Griffiths effects and subdiffusive transport in the vicinity of the transition (*21*, *22*, *51*–*53*). In addition to dynamical properties, our technique might allow the investigation of many-body eigenstate–related properties, such as the local integrals of motion (*14*, *15*) defined via local operators (*54*).

REFERENCES AND NOTES

1. P. W. Anderson, *Phys. Rev.* **109**, 1492–1505 (1958).
2. D. Basko, I. Aleiner, B. Altshuler, *Ann. Phys.* **321**, 1126–1205 (2006) and references therein.
3. I. V. Gornyi, A. D. Mirlin, D. G. Polyakov, *Phys. Rev. Lett.* **95**, 206603 (2005) and references therein.
4. I. L. Aleiner, B. L. Altshuler, G. V. Shlyapnikov, *Nat. Phys.* **6**, 900–904 (2010).
5. V. Oganesyan, D. A. Huse, *Phys. Rev. B* **75**, 155111 (2007).
6. R. Nandkishore, D. A. Huse, *Annu. Rev. Condens. Matter Phys.* **6**, 15–38 (2015).
7. E. Altman, R. Vosk, *Annu. Rev. Condens. Matter Phys.* **6**, 383–409 (2015).
8. J. Eisert, M. Friesdorf, C. Gogolin, *Nat. Phys.* **11**, 124–130 (2015).
9. J. M. Deutsch, *Phys. Rev. A* **43**, 2046–2049 (1991).
10. M. Srednicki, *Phys. Rev. E* **50**, 888–901 (1994).
11. H. Tasaki, *Phys. Rev. Lett.* **80**, 1373–1376 (1998).
12. M. Rigol, V. Dunjko, M. Olshanii, *Nature* **452**, 854–858 (2008).
13. M. Serbyn *et al.*, *Phys. Rev. Lett.* **113**, 147204 (2014).
14. M. Serbyn, Z. Papić, D. A. Abanin, *Phys. Rev. Lett.* **111**, 127201 (2013).
15. D. A. Huse, R. Nandkishore, V. Oganesyan, *Phys. Rev. B* **90**, 174202 (2014).
16. M. Žnidarič, T. Prosen, P. Prelovšek, *Phys. Rev. B* **77**, 064426 (2008).
17. J. H. Bardarson, F. Pollmann, J. E. Moore, *Phys. Rev. Lett.* **109**, 017202 (2012).
18. R. Vosk, E. Altman, *Phys. Rev. Lett.* **110**, 067204 (2013).
19. M. Serbyn, Z. Papić, D. A. Abanin, *Phys. Rev. Lett.* **110**, 260601 (2013).
20. A. Nanduri, H. Kim, D. A. Huse, *Phys. Rev. B* **90**, 064201 (2014).
21. A. C. Potter, R. Vasseur, S. Parameswaran, *Phys. Rev. X* **5**, 031033 (2015).
22. R. Vosk, D. A. Huse, E. Altman, *Phys. Rev. X* **5**, 031032 (2015).
23. M. Schreiber *et al.*, *Science* **349**, 842–845 (2015).
24. P. Bordia *et al.*, *Phys. Rev. Lett.* **116**, 140401 (2016).
25. T. Schwartz, G. Bartal, S. Fishman, M. Segev, *Nature* **446**, 52–55 (2007).
26. J. Billy *et al.*, *Nature* **453**, 891–894 (2008).
27. G. Roati *et al.*, *Nature* **453**, 895–898 (2008).
28. S. S. Kondov, W. R. McGehee, J. J. Zirbel, B. DeMarco, *Science* **334**, 66–68 (2011).
29. F. Jendrzejewski *et al.*, *Nat. Phys.* **8**, 398–403 (2012).
30. G. Semeghini *et al.*, *Nat. Phys.* **11**, 554–559 (2015).
31. B. Deissler *et al.*, *Nat. Phys.* **6**, 354–358 (2010).
32. M. Pasienski, D. McKay, M. White, B. DeMarco, *Nat. Phys.* **6**, 677–680 (2010).
33. B. Gadway, D. Pertot, J. Reeves, M. Vogt, D. Schneble, *Phys. Rev. Lett.* **107**, 145306 (2011).
34. C. D'Errico *et al.*, *Phys. Rev. Lett.* **113**, 095301 (2014).
35. L. Tanzi *et al.*, *Phys. Rev. Lett.* **111**, 115301 (2013).
36. C. Meldgin *et al.*, *Nat. Phys.* 10.1038/nphys3695 (2016).
37. S. S. Kondov, W. R. McGehee, W. Xu, B. DeMarco, *Phys. Rev. Lett.* **114**, 083002 (2015).
38. J. Smith *et al.*, *Nat. Phys.* 10.1038/nphys3783 (2016).
39. M. Ovadia *et al.*, *Sci. Rep.* **5**, 13503 (2015).
40. A. Pal, D. A. Huse, *Phys. Rev. B* **82**, 174411 (2010).
41. J. A. Kjäll, J. H. Bardarson, F. Pollmann, *Phys. Rev. Lett.* **113**, 107204 (2014).
42. C. Weitenberg *et al.*, *Nature* **471**, 319–324 (2011).
43. See supplementary materials on *Science* Online.
44. J. F. Sherson *et al.*, *Nature* **467**, 68–72 (2010).
45. M. Endres *et al.*, *Science* **334**, 200–203 (2011).
46. R. Nandkishore, S. Gopalakrishnan, D. A. Huse, *Phys. Rev. B* **90**, 064203 (2014).
47. S. Johri, R. Nandkishore, R. N. Bhatt, *Phys. Rev. Lett.* **114**, 117401 (2015).
48. E. Levi, M. Heyl, I. Lesanovsky, J. P. Garrahan, *Phys. Rev. Lett.* **116**, 237203 (2016).

Downloaded from http://science.sciencemag.org/ on June 28, 2016

49. M. V. Medvedyeva, T. Prosen, M. Žnidarič, *Phys. Rev. B* **93**, 094205 (2016).
50. M. H. Fischer, M. Maksymenko, E. Altman, *Phys. Rev. Lett.* **116**, 160401 (2016).
51. Y. Bar Lev, G. Cohen, D. R. Reichman, *Phys. Rev. Lett.* **114**, 100601 (2015).
52. K. Agarwal, S. Gopalakrishnan, M. Knap, M. Müller, E. Demler, *Phys. Rev. Lett.* **114**, 160401 (2015).
53. Y. B. Lev, D. R. Reichman, *Europhys. Lett.* **113**, 46001 (2016).
54. A. Chandran, I. H. Kim, G. Vidal, D. A. Abanin, *Phys. Rev. B* **91**, 085425 (2015).
55. R. Islam *et al.*, *Nature* **528**, 77–83 (2015).
56. A. M. Kaufmann *et al.*, http://arxiv.org/abs/1603.04409 (2016).
57. M. Goihl, M. Friesdorf, A. H. Werner, W. Brown, J. Eisert, http://arxiv.org/abs/1601.02666 (2016).

ACKNOWLEDGMENTS

We thank M. Fischer, E. Altman, M. Knap, P. Bordia, H. Lüschen, A. Rosch, E. Demler, and S. Sondhi for discussions. D.A.H. is the A. and H. Broitman Member at the Institute for Advanced Study. We acknowledge funding by Max-Planck-Gesellschaft, Deutsche Forschungsgemeinschaft, the European Union (UQUAM, Marie Curie Fellowship to J.C.).

SUPPLEMENTARY MATERIALS

www.sciencemag.org/content/352/6293/1547/suppl/DC1
Supplementary Text
Figs. S1 to S4
Reference (*58*)

14 April 2016; accepted 31 May 2016
10.1126/science.aaf8834

REPORTS

QUANTUM PHYSICS

Quantum phase magnification

O. Hosten, R. Krishnakumar, N. J. Engelsen, M. A. Kasevich*

Quantum metrology exploits entangled states of particles to improve sensing precision beyond the limit achievable with uncorrelated particles. All previous methods required detection noise levels below this standard quantum limit to realize the benefits of the intrinsic sensitivity provided by these states. We experimentally demonstrate a widely applicable method for entanglement-enhanced measurements without low-noise detection. The method involves an intermediate quantum phase magnification step that eases implementation complexity. We used it to perform squeezed-state metrology 8 decibels below the standard quantum limit with a detection system that has a noise floor 10 decibels above the standard quantum limit.

The prospect of using quantum entanglement to improve the precision of atomic and optical sensors has been a topic of discussion for more than two decades. Examples of recent work using atomic ensembles include the preparation of spin-squeezed states (*1*–*12*), Dicke states (*13*–*15*), and other states with negative Wigner functions (*16*). An assumption common to all this work is that low-noise detection methods are required to properly measure and make use of the prepared quantum states. In fact, detection noise has thus far been the bottleneck in the performance of these systems. To this end, there has been dedicated work on improving state-selective detection of atoms with both optical cavity–aided measurements (*17*, *18*) and fluorescence imaging (*19*, *20*).

Here, we describe the concept and the implementation of a quantum phase magnification technique that relaxes stringent requirements in detection sensitivity for quantum metrology. This method is a generalization of a recent proposal for approaching the Heisenberg limit in measurement sensitivity without single-particle detection (*21*). We demonstrate the method in an ensemble of ^{87}Rb atoms. As in a typical atomic sensor or clock, the goal is to measure a differential phase shift accumulated between a pair of quantum states during a time interval. Making this measurement requires the phase shift to be converted into a population difference (*12*, *22*), after which the population difference is measured. Our scheme magnifies this population difference before the final detection, in effect magnifying the initial phase shift. The atomic ensemble is first spin-squeezed using atomic interactions aided by an optical cavity, and then small rotations—to be sensed—are induced on the atomic state. These rotations are magnified by stretching the rotated states (Fig. 1A), using cavity-aided interactions, and are finally detected via fluorescence imaging. Magnification allows for substantial reduction in the noise requirements for the final detection. Although the method is demonstrated in an atom/cavity system, it is broadly applicable to any quantum system that has a suitable nonlinear interaction [see below and (*23*)].

The collective state of an ensemble of N two-level atoms—here, the clock states of ^{87}Rb—can be described using the language of a pseudo–spin-$N/2$ system. The z-component of the spin, J_z, represents the population difference, and the orientation in the J_x - J_y plane represents the phase difference between the two states. As these angular momentum components do not commute, both the population and the phase possess uncertainties. For a state with $\langle J_x \rangle \approx N/2$, the uncertainties satisfy $\Delta J_z \cdot \Delta J_y \geq N/4$, where J_y is now identified with the phase of the ensemble. Coherent spin states (CSS) with noise $\Delta J_z = \Delta J_y = \sqrt{N}/2 \equiv \Delta_{CSS}$ establish the standard quantum limit (SQL) to minimum resolvable phase or population difference.

The magnification procedure (Fig. 1A) starts with a mapping of J_z onto J_y (Fig. 1B) via a shearing interaction. A rotation of J_y into J_z follows to complete the sequence. The interaction leading to the mapping (shearing) generates a rotation of the state about the J_z axis, with the rotation rate depending on J_z, and is represented by the one-axis twisting Hamiltonian (*24*) $H = \hbar\chi J_z^2$, where $\hbar$ is the Planck constant divided by 2π and χ is the shearing strength.

The Heisenberg equations of motion for the vector operator $\mathbf{J}$ yield $dJ/dt = {}^1/_2(\Omega \times \mathbf{J} - \mathbf{J} \times \Omega)$, where the rotation vector $\Omega = \hat{\mathbf{z}}2\chi J_z$ is also an operator, and $\hat{z}$ is a unit vector in the z-direction. We assume that the angular shifts we seek to measure are small (otherwise, they would readily be measurable without magnification) and that the uncertainties of the states after magnification occupy a small fraction of the Bloch sphere. With these assumptions and working with near-maximal initial x-polarization $J_x \approx J = N/2$, we can linearize the problem and focus our attention to a planar patch of the spherical phase space (Fig. 1, B to D). The equations of motion then yield $J_z(t) = J_z(0)$ and $J_y(t) = J_y(0) + MJ_z(0)$ with $M = N\int_0^t dt'\chi(t')$. Thus, the initial J_z is mapped onto J_y with a magnification factor M. This is analogous to free expansion of a gas if one identifies J_z with a particle's momentum and J_y with its position.

We implement the one-axis twisting Hamiltonian through a dispersive interaction between atoms and light in an optical cavity (*1*) (Fig. 2A). The underlying mechanism is a coupling between the intracavity power and atomic populations. The atom-cavity detuning is set such that the shift in the cavity resonance due to the atoms is proportional to J_z (Fig. 2C). Thus, J_z sets the cavity-light detuning, which in turn sets the intracavity power (Fig. 2D), which in turn provides a J_z-dependent ac-Stark shift—hence the J_z^2 interaction. Implemented this way, there is also a J_z-independent part of the ac-Stark shift, causing global rotations of the state about the J_z axis even for $J_z = 0$. The rotation angle ϕ_{AC} due to this effect is proportional to the pulse area of the interaction light incident on the cavity. By directly measuring ϕ_{AC} and offsetting the phase of the microwave oscillator by the same amount, we effectively work in a frame where the center of the states remains in the J_x - J_z plane (*23*). The magnification parameter

$$M = N\frac{\delta_c\delta_0}{\delta_0^2 + \left(\kappa/2\right)^2}\,\phi_{AC} \qquad (1)$$

obtained in this implementation directly relates to the measured quantity ϕ_{AC}. Here, $\delta_c = 5.5$ Hz is the

Department of Physics, Stanford University, Stanford, CA 94305, USA.
*Corresponding author. Email: kasevich@stanford.edu

Downloaded from http://science.sciencemag.org/ on June 28, 2016

cavity frequency shift per unit J_z, $\kappa = \{8.0, 10.4\}$ kHz is the cavity full linewidth at $N = \{0, 5 \times 10^5\}$, and δ_0 is the empty cavity-light detuning. The decay of the cavity field results in back-action noise that is not taken into account in the simple Hamiltonian analysis above. However, these effects are negligible in the parameter range we use for the magnification protocol and can be ignored (*23*).

The details of the experimental apparatus are described in (*12*, *25*). We load up to 5×10^5 atoms at 25 μK into an optical lattice inside the high-finesse (1.75×10^5) cavity (*23*). A 780-nm standing-wave cavity mode is used for generating the collective interactions and probing the atoms. The lattice holds the atoms at the intensity maxima of this 780-nm mode, ensuring uniform atom-cavity coupling (Fig. 2, A and B). The 1560-nm lattice light, whose frequency is stabilized to the cavity, generates the 780-nm light through frequency doubling, guaranteeing its frequency stability with respect to the cavity. By measuring the phase of a reflected probe pulse with homodyne detection, we can determine the empty cavity frequency down to a J_z equivalent of three spin-flips.

In our procedure, the low-noise cavity probe is used to obtain reference information about the states before magnification, which is then compared with the noisy fluorescence measurements after magnification.

We first prepare a CSS aligned with the J_x axis of the Bloch sphere using 2×10^5 atoms (*23*), then apply a small microwave-induced rotation about the J_y axis (±2 mrad) to displace the center of the CSS to a J_z value of ±200. As characterized by cavity measurements, the widths of the resulting J_z distributions read within 0.5 dB of the calibrated CSS noise level (*12*) (Fig. 3A). We illustrate the magnification protocol (Fig. 3) using these characterized states. We implement the following sequence (*23*): excite the cavity with a 200-μs light pulse, detuned by $\delta_0 = 36$ kHz, to shear the

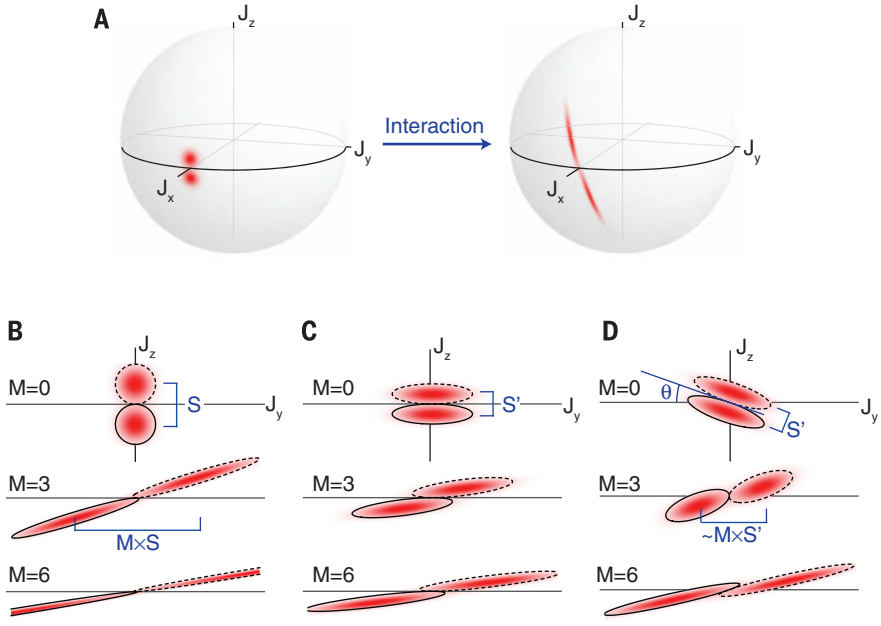


Fig. 1. Conceptual description of quantum phase magnification. (**A**) Illustration of the magnification protocol on the Bloch sphere. The Wigner quasi-probability distributions are shown for two separated initial CSSs (left) and after the states are magnified through collective interactions (right). Here this is shown with $N = 900$ atoms and a magnification of $M = 3$ for pictorial clarity. Experimentally we use up to $N = 5 \times 10^5$ and $M = 100$, permitting us to concentrate on a planar patch of the Bloch sphere. (**B** and **C**) Effect of the J_z^2 (shearing) interaction used for mapping J_z onto J_y for a pair of different initial states with separations S and $S' = S/2$; each panel shows three different magnification factors. Note that a $\pi/2$ rotation about the J_x axis needs to follow to complete the protocol. CSSs (B) and 6-dB squeezed states (C) together illustrate the requirement of larger magnifications to separate two initially squeezed states. (**D**) A small rotation θ about the J_x axis is added before the shearing step, eliminating the requirement of larger magnifications for squeezed states by giving rise to a refocusing of the J_y noise. At an optimal magnification (here $M = 3$), the noise-refocusing scheme maps the initial J_z onto J_y, preserving the SNR associated with the two initial states.

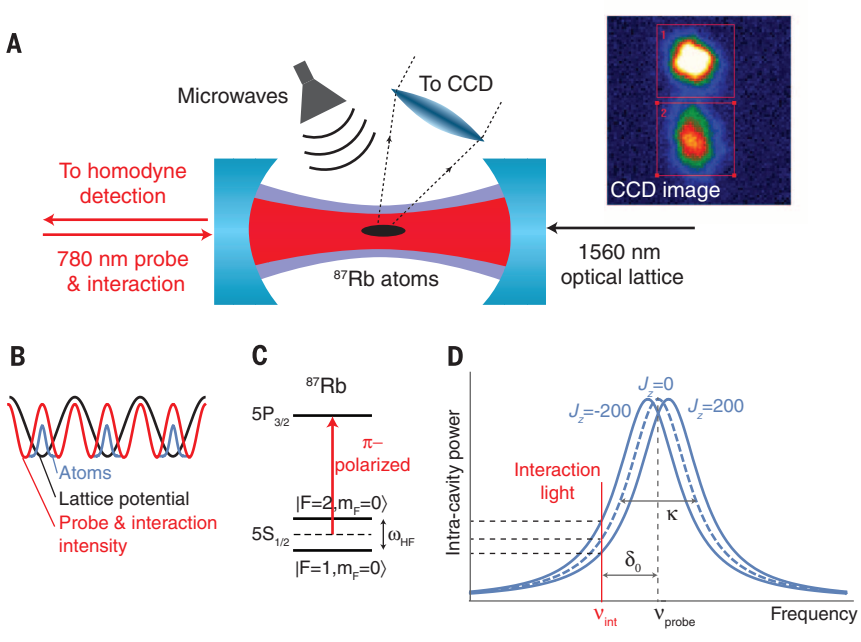


Fig. 2. Experimental setup implementing phase magnification. (**A**) ^{87}Rb atoms are trapped inside a high-finesse cavity (length 10.7 cm) using a 1560-nm cavity mode as a one-dimensional optical lattice. A 780-nm mode is used to generate collective atomic interactions and to probe the cavity resonance frequency (J_z measurements) by recording the phase of a reflected probe pulse (~10 pW, 200 μs). Microwaves are for atomic state rotations. A charge-coupled device (CCD) imaging system measures the population difference between the hyperfine states after releasing the atoms from the lattice and spatially separating the states. (**B**) Because of the commensurate frequency relationship between the trapping laser and the interaction/probe laser, all atoms are uniformly coupled to the 780-nm mode. (**C**) The 780-nm mode couples the two hyperfine clock states separated by ω_{HF} to the excited manifold with opposite detunings. Thus, the two states pull the intracavity index of refraction in opposite directions, leading to a cavity frequency shift proportional to J_z. (**D**) The mechanism leading to the collective atomic interactions (J_z^2 Hamiltonian) that enables the magnification process: linking of the intracavity power to J_z, producing a J_z-dependent ac-Stark shift. The frequencies of the interaction beam ν_{int} and probe beam ν_{probe} are indicated.

Downloaded from http://science.sciencemag.org/ on June 28, 2016

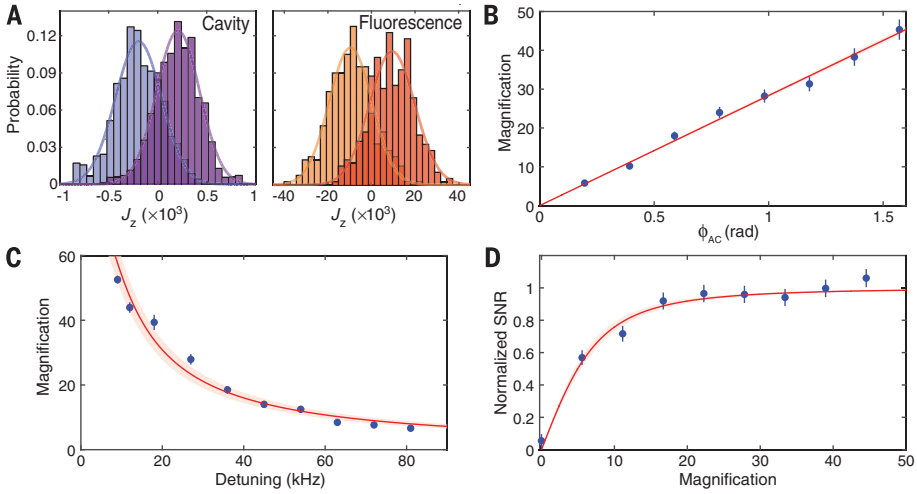


Fig. 3. Characterization of the basic magnification process with CSSs. (**A**) Sample distributions (400 samples each) comparing the cavity-based measurements of J_z with fluorescence imaging–based measurements after a magnification of $M = 45$. The two distributions in each plot correspond to different initial states with $\langle J_z \rangle = \pm 200$ prepared using 2×10^5 atoms. (**B** and **C**) Magnification of the separation between the two distributions as a function of accumulated ac-Stark shift phase ϕ_{AC} imparted on the atoms at fixed cavity-light detuning of 36 kHz (B) or as a function of cavity-light detuning δ_0 at fixed $\phi_{AC} = 0.6$ rad (C). Solid lines are fits to the data as a function of ϕ_{AC} and δ_0, respectively, in Eq. 1. Fitted curves agree with theoretical curves (not shown) to within 10%. (**D**) SNR associated with the two distributions as a function of the magnification parameter, normalized to that obtained by the cavity measurements (normalized SNR). Magnification is varied by changing ϕ_{AC}. The solid line is a fit of the form $M/(\alpha^2 + M^2)^{1/2}$; the fit parameter α contains information primarily about fluorescence detection noise. In (B) to (D), error bars and shaded regions denote the 68% statistical confidence interval for data and fits, respectively.

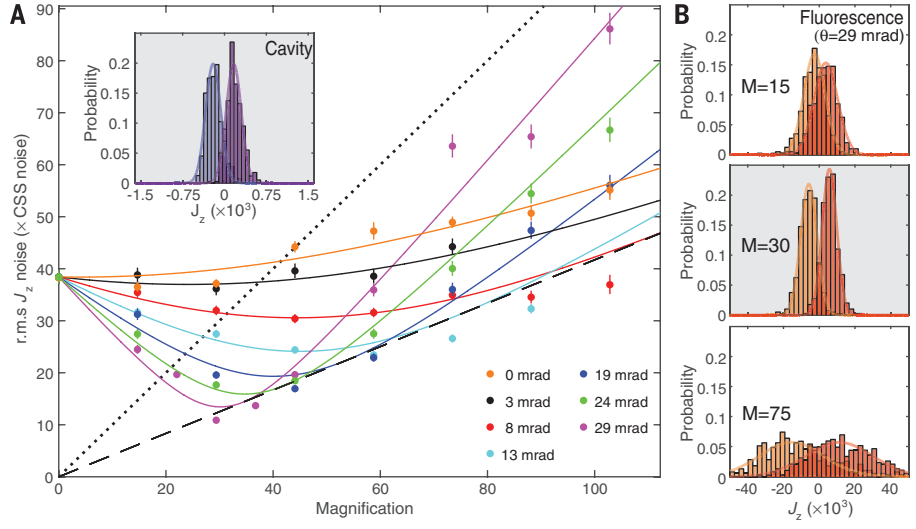


Fig. 4. Magnification process with noise refocusing using 8-dB squeezed spin states. (**A**) Post-magnification J_z noise in units of CSS noise for different amounts of prior rotation θ about the J_x axis (see Fig. 1D). Solid lines are a global fit to the entire data set with two free parameters: $d\theta/dt$ (the rate of change in θ with microwave pulse time) and the J_z noise of the initial squeezed states. Obtained values are within 15% of the calculated values. The inset shows the distribution of two separated 8-dB squeezed initial states (5×10^5 atoms) as identified by cavity measurements [to be compared with the $M = 30$ distribution in (B)]. The dashed line shows $M \times$ (J_z noise contribution from the initial squeezed states); the dotted line shows $M \times$ (CSS noise). Error bars denote the 68% statistical confidence interval. (**B**) The distributions after the magnification protocol at the indicated M values for $\theta = 29$ mrad. The normalized SNR becomes 0.96 ± 0.06 at $M \approx 1/|\theta|$ (middle histogram), where the dashed line is tangent to the $\theta = 29$ mrad noise curve in (A). For M values to either side of $1/|\theta|$, the two distributions blur into each other (top and bottom histograms).

state; apply a microwave $\pi/2$ rotation about the J_x axis; and count the atoms state-selectively using fluorescence imaging (*23*). The fluorescence detection setup has a technical noise floor of 1200 atoms RMS, which is ~{15, 11} dB above the SQL for {2×10^5, 5×10^5} atoms.

A comparison of the J_z distributions obtained separately by cavity and fluorescence measurements (Fig. 3A) allows for extraction of magnification parameters (*23*). The magnification increases linearly with incident shearing light power (Fig. 3B), quantified by ϕ_{AC}, and has the expected dependence on cavity-light detuning (Fig. 3C). In the large M limit, the signal-to-noise ratio (SNR) associated with the two states after magnification approaches the value measured by the cavity (Fig. 3D), set by the intrinsic sensitivity of the quantum state. Here, SNR is defined as the separation between the centroids of the two J_z distributions divided by the RMS width of their distributions.

For the mapping to be accurate in this protocol, the magnified J_z noise $M\,\Delta J_z(0)$ should exceed the initial J_y noise $\Delta J_y(0)$. If we magnify a J_z-squeezed state that has $\Delta J_z(0) = \Delta_{CSS}\xi$ and $\Delta J_y(0) = \Delta_{CSS}\xi'$ ($\xi' \cdot \xi \geq 1$, $\xi < 1$), the final noise becomes

$$\Delta J_y = \left[(\Delta_{CSS}\xi')^2 + (M\,\Delta_{CSS}\xi)^2\right]^{1/2} \quad (2)$$

Setting the fractional noise contribution of the second term to $1 - \varepsilon$ requires a magnification of $M_\varepsilon \approx (2\varepsilon)^{-1/2}\xi'/\xi$. This quantity grows unfavorably (at least quadratically) with the squeezing factor ξ.

The unfavorable scaling can be eliminated using a noise-refocusing version of the protocol (Fig. 1D), which enables, in principle, perfect mapping at a chosen magnification. By adding a small rotation θ before magnification, the J_y noise can be made to focus down through the course of magnification. The action of the small rotation is formally analogous to that of a lens on a beam of light. The final J_y noise in this version is

$$\Delta J_y \approx \left[(1 - M\theta)^2(\Delta_{CSS}\xi')^2 + (M\Delta_{CSS}\xi)^2\right]^{1/2} \quad (3)$$

(*23*). For $\theta = \theta_0$, the initial J_z noise becomes the sole noise contribution at $M = M_0 \equiv 1/\theta_0$.

We demonstrate the noise-refocusing protocol using squeezed spin states with 5×10^5 atoms (Fig. 4). The states are generated with the same shearing interaction later used for magnification (*1*, *23*). We start with states that are 8-dB squeezed in J_z and 32-dB antisqueezed in J_y ($\xi \sim 0.4$, $\xi' \sim 40$)—the best we can currently achieve without measurement-based methods. We apply a small microwave rotation θ about the J_x axis, and investigate the noise measured at the end of the magnification protocol (Fig. 4A). We observe a different optimal magnification value for each θ. The shown family of model curves (using Eq. 3) is a fit to the entire data set with only two free parameters, and the small deviations from these curves are attributable to slow drifts in the initial squeezing level (~1 dB). For the specific example of $\theta = 29$ mrad (Fig. 4B), we explicitly show that the optimal magnification $M \sim 30$ replicates the SNR of the initially prepared states. Had we not used noise refocusing, the required magnification

Downloaded from http://science.sciencemag.org/ on June 28, 2016

would have been $M_{0.05} \sim 320$ (for an infidelity $\varepsilon = 0.05$), which would have started wrapping the states around the Bloch sphere.

In assessing metrological gain obtained from spin squeezing, the degree of Bloch vector length (coherence) preservation is essential to prevent degradation of signal levels. Throughout all state preparation and magnification, the coherence of the states measured by Ramsey fringe contrasts remains above 96%. The small reduction arises from residual atom-cavity coupling inhomogeneities.

If the magnification technique developed here is used as the readout stage for the more effective measurement-based squeezing methods (*12*), we expect improvements in verifiable squeezing because the technique avoids degradation due to photon losses in the readout (*23*). The magnification protocol can be used on any kind of exotic initial state to ease characterization. Examples include the not yet demonstrated Schrödinger-cat spin states (*26*, *27*), where the spacing of inherent interference fringes can be magnified, or other states that possess negative Wigner functions (*16*). Because the only required key element is a nonlinear phase shift, the method could find broad use in systems that use, for example, collisional interactions in Bose-Einstein condensates (*11*, *28*, *29*), Rydberg blockade interactions in neutral atoms (*21*), Ising interactions in ion traps (*30*), nonlinearities in superconducting Josephson junctions, and nonlinearities in optics. In (*23*) we describe a photonic analog of the phase magnification concept using self-phase modulation.

REFERENCES AND NOTES

1. I. D. Leroux, M. H. Schleier-Smith, V. Vuletić, *Phys. Rev. Lett.* **104**, 073602 (2010).
2. M. H. Schleier-Smith, I. D. Leroux, V. Vuletić, *Phys. Rev. Lett.* **104**, 073604 (2010).
3. J. G. Bohnet *et al.*, *Nat. Photonics* **8**, 731–736 (2014).
4. K. C. Cox, G. P. Greve, J. M. Weiner, J. K. Thompson, *Phys. Rev. Lett.* **116**, 093602 (2016).
5. C. Gross, T. Zibold, E. Nicklas, J. Estève, M. K. Oberthaler, *Nature* **464**, 1165–1169 (2010).
6. C. D. Hamley, C. S. Gerving, T. M. Hoang, E. M. Bookjans, M. Chapman, *Nat. Phys.* **8**, 305–308 (2012).
7. J. Appel *et al.*, *Proc. Natl. Acad. Sci. U.S.A.* **106**, 10960–10965 (2009).
8. R. J. Sewell *et al.*, *Phys. Rev. Lett.* **109**, 253605 (2012).
9. W. Muessel, H. Strobel, D. Linnemann, D. B. Hume, M. K. Oberthaler, *Phys. Rev. Lett.* **113**, 103004 (2014).
10. T. Takano, M. Fuyama, R. Namiki, Y. Takahashi, *Phys. Rev. Lett.* **102**, 033601 (2009).
11. M. F. Riedel *et al.*, *Nature* **464**, 1170–1173 (2010).
12. O. Hosten, N. J. Engelsen, R. Krishnakumar, M. A. Kasevich, *Nature* **529**, 505–508 (2016).
13. B. Lücke *et al.*, *Phys. Rev. Lett.* **112**, 155304 (2014).
14. B. Lücke *et al.*, *Science* **334**, 773–776 (2011).
15. F. Haas, J. Volz, R. Gehr, J. Reichel, J. Estève, *Science* **344**, 180–183 (2014).
16. R. McConnell, H. Zhang, J. Hu, S. Ćuk, V. Vuletić, *Nature* **519**, 439–442 (2015).
17. H. Zhang *et al.*, *Phys. Rev. Lett.* **109**, 133603 (2012).
18. J. Volz, R. Gehr, G. Dubois, J. Estève, J. Reichel, *Nature* **475**, 210–213 (2011).
19. D. B. Hume *et al.*, *Phys. Rev. Lett.* **111**, 253001 (2013).
20. I. Stroescu, D. B. Hume, M. K. Oberthaler, *Phys. Rev. A* **91**, 013412 (2015).
21. E. Davis, G. Bentsen, M. Schleier-Smith, *Phys. Rev. Lett.* **116**, 053601 (2016).
22. I. D. Leroux, M. H. Schleier-Smith, V. Vuletić, *Phys. Rev. Lett.* **104**, 250801 (2010).
23. See supplementary materials on *Science* Online.
24. M. Kitagawa, M. Ueda, *Phys. Rev. A* **47**, 5138–5143 (1993).
25. J. Lee, G. Vrijsen, I. Teper, O. Hosten, M. A. Kasevich, *Opt. Lett.* **39**, 4005–4008 (2014).
26. R. McConnell *et al.*, *Phys. Rev. A* **88**, 063802 (2013).
27. S. Massar, E. S. Polzik, *Phys. Rev. Lett.* **91**, 060401 (2003).
28. H. Strobel *et al.*, *Science* **345**, 424–427 (2014).
29. W. Muessel *et al.*, *Phys. Rev. A* **92**, 023603 (2015).
30. J. G. Bohnet *et al.*, *Science* **352**, 1297–1301 (2016).

ACKNOWLEDGMENTS

Supported by grants from the Defense Threat Reduction Agency and the Office of Naval Research. We thank M. Schleier-Smith for crucial discussions over the course of this work.

SUPPLEMENTARY MATERIALS

www.sciencemag.org/content/352/6293/1552/suppl/DC1
Materials and Methods
Fig. S1
References (*31*–*33*)

28 January 2016; accepted 17 May 2016
10.1126/science.aaf3397

ORGANIC CHEMISTRY

Allosteric initiation and regulation of catalysis with a molecular knot

Vanesa Marcos, Alexander J. Stephens, Javier Jaramillo-Garcia, Alina L. Nussbaumer, Steffen L. Woltering, Alberto Valero, Jean-François Lemonnier, Iñigo J. Vitorica-Yrezabal, David A. Leigh*

Molecular knots occur in DNA, proteins, and other macromolecules. However, the benefits that can potentially arise from tying molecules in knots are, for the most part, unclear. Here, we report on a synthetic molecular pentafoil knot that allosterically initiates or regulates catalyzed chemical reactions by controlling the in situ generation of a carbocation formed through the knot-promoted cleavage of a carbon-halogen bond. The knot architecture is crucial to this function because it restricts the conformations that the molecular chain can adopt and prevents the formation of catalytically inactive species upon metal ion binding. Unknotted analogs are not catalytically active. Our results suggest that knotting molecules may be a useful strategy for reducing the degrees of freedom of flexible chains, enabling them to adopt what are otherwise thermodynamically inaccessible functional conformations.

Molecular knots are found in circular DNA (*1*) and approximately 1% of proteins in the Protein Data Bank (PDB) (*2*) and form spontaneously in polymer chains of sufficient length and flexibility (*3*). Molecules with the topology of some of the simplest prime knots have been synthesized (*4*–*13*), but, although knots are fundamental elements of structure, the potential benefits that could arise from tying molecules in knots are mostly unclear (*14*–*18*). Recently, Fe(II) complexes of some synthetic molecular knots and links were found to strongly and selectively bind halide anions (X^-) within their central cavities (*19*). This binding activity resembles a key feature of dehalogenase enzymes, which contain halide binding sites that facilitate the cleavage of carbon-halogen bonds (*20*, *21*). Here, we show that as little as 1 mole % (mol %) of a synthetic molecular pentafoil knot can induce Lewis acid–catalyzed reactions by the in situ generation of a carbocation by carbon-halogen bond scission promoted by CH···X^- hydrogen bonding and long range metal-cation···X^- electrostatic interactions.

School of Chemistry, University of Manchester, Oxford Road, Manchester, M13 9PL, UK.
***Corresponding author. Email: david.leigh@manchester.ac.uk**

We previously reported the synthesis of a molecular pentafoil knot [a 5_1 knot in Alexander-Briggs notation (*22*)], inspired by Lehn's cyclic double helicates (*23*) but modified so as to be assembled, and the end groups connected, through imine chemistry (*24*, *25*). The knot binds a chloride or bromide anion extremely strongly within its central cavity ($K_{Cl^-} = 3.6 \times 10^{10}\ M^{-1}$, $K_{Br^-} = 1.7 \times 10^{10}\ M^{-1}$ in MeCN) through a combination of CH···X^- hydrogen bonding and long-range Fe(II)···X^- electrostatic interactions (*19*). However, attempts to remove the metal ions while maintaining the pentafoil knot topology proved unsuccessful because of the lability of uncoordinated imine bonds (*25*). We therefore investigated an alternative route to a metal-free pentafoil knot based on ring-closing olefin metathesis (RCM) of a tris(bipyridine) [tris(bipy)] ligand strand (**1**) that had proved successful in the synthesis of a related Star of David catenane (*26*) (Fig. 1). [Detailed experimental procedures and full characterization data are given in sections S1 and S4 to S8 of the supplementary materials (SM).]

Heating ligand strand **1** with 1.25 equivalents (equiv.) of $FeCl_2$ in dimethylsulfoxide (DMSO) at 60°C resulted in an intensely colored red-purple solution indicative of the formation of low-spin Fe(II)–tris(bipy) complexes (Fig. 1, step i).

Downloaded from http://science.sciencemag.org/ on June 28, 2016

After 24 hours, the pentameric circular helicate $[Fe_5\mathbf{1}_5{\bullet}Cl](PF_6)_9$ was isolated in 89% yield by precipitation with aqueous KPF_6 (Fig. 1, step ii) and characterized by proton nuclear magnetic resonance (^{1}H NMR) spectroscopy (Fig. 2B) and electrospray ionization mass spectrometry (ESI-MS) (figs. S48 and S49). The end groups of each ligand strand were successfully connected to form the pentafoil knot $[Fe_5\mathbf{2}{\bullet}Cl](PF_6)_9$ by RCM using the Hoveyda-Grubbs second-generation catalyst (Fig. 1, step iii) (*27*). The ^{1}H NMR spectrum of $[Fe_5\mathbf{2}{\bullet}Cl](PF_6)_9$ (Fig. 2C) confirms the absence of terminal alkene protons (compare precursors **1** and $[Fe_5\mathbf{1}_5{\bullet}Cl](PF_6)_9$ in Fig. 2, A and B) and also two distinct environments for some sets of aromatic protons (e.g., H^6, H^7, and H^8) as a result of restricted rotamerization around the phenyl-bipyridine bond after RCM.

Single crystals of $[Fe_5\mathbf{2}{\bullet}Cl](PF_6)_9$ were obtained by slow evaporation of a solution of the knot in a mixture of acetonitrile and toluene containing excess $NaBPh_4$, and the solid-state structure was determined by x-ray crystallography (SM, section S8). The crystal structure (Fig. 3) confirmed the topology of the molecular pentafoil knot as a single 190-atom loop woven around five Fe(II) cations to create the five crossing points. As with the related imine-pentafoil knot, a chloride anion (present despite the large excesses of PF_6^- and BPh_4^- anions used in the purification and crystallization steps) is positioned within the central cavity of the pentafoil knot. The chloride ion is displaced by ~1.47 Å from the plane of the Fe(II) cations (Fig. 3B) and is in close contact with the 10 electron-poor aromatic CH^1 protons oriented toward the middle of the cavity (CH···Cl distance, 2.46 to 2.85 Å). The remaining anions are a ~2:1 mixture of PF_6^- and BPh_4^-.

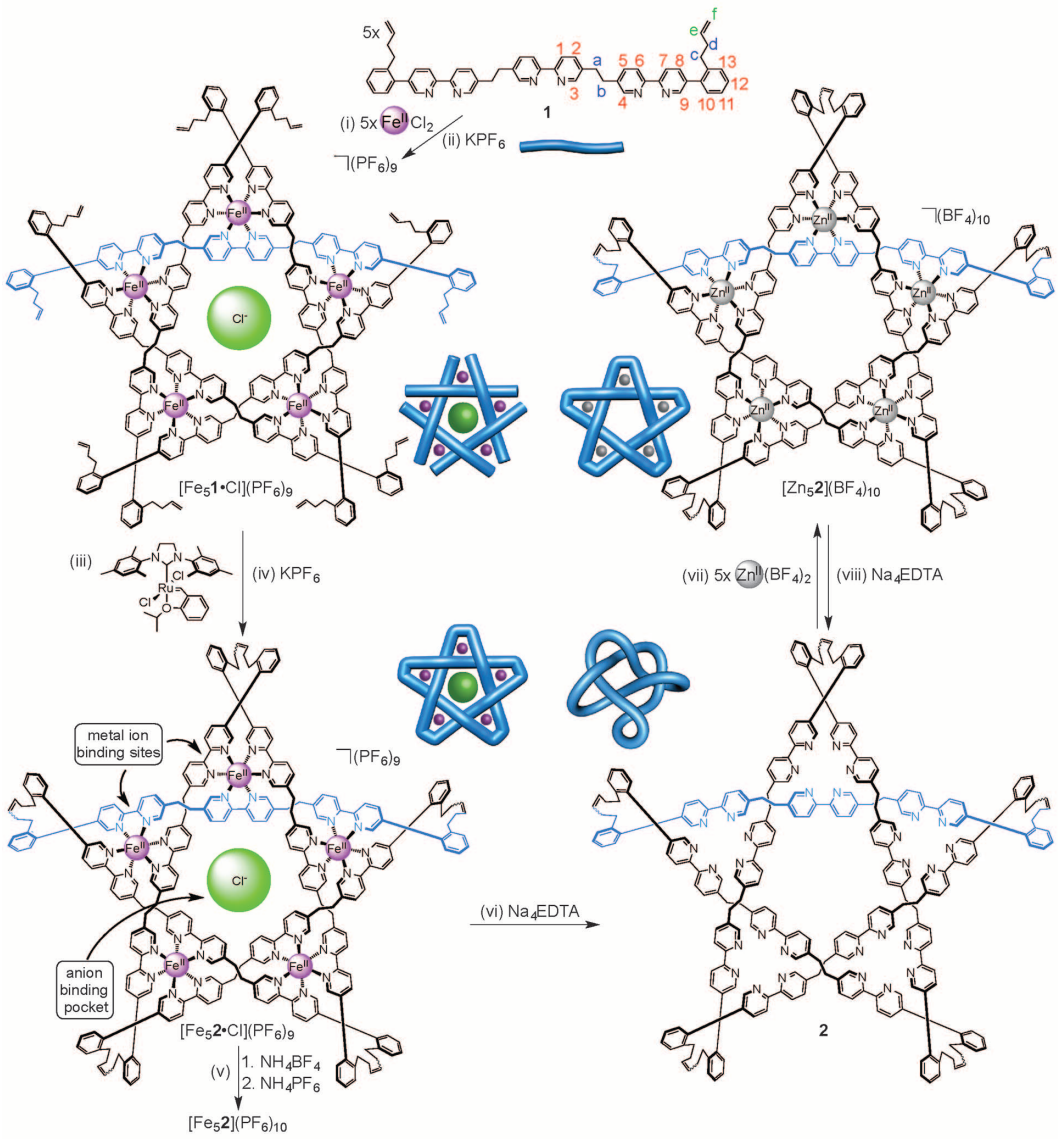


Fig. 1. Assembly of wholly organic pentafoil knot 2 and its reversible metallation with zinc(II) ions to form $[Zn_5\mathbf{2}](BF_4)_{10}$. Reagents and conditions: (i) $FeCl_2$, dimethylsulfoxide, 60°C, 24 hours; (ii) saturated aqueous KPF_6 solution (89% $[Fe_5\mathbf{1}_5{\bullet}Cl](PF_6)_9$ over two steps); (iii) Hoveyda-Grubbs second-generation catalyst, 1,2-dichloroethane/nitromethane (1/1), 60°C, 24 hours; (iv) saturated aqueous KPF_6 solution [98% $[Fe_5\mathbf{2}{\bullet}Cl](PF_6)_9$ over two steps]; (v) saturated aqueous NH_4BF_4, then saturated aqueous NH_4PF_6 [90% $[Fe_5\mathbf{2}](PF_6)_{10}$]; (vi) Na_4EDTA, acetonitrile/water (1/1), 80°C, 4 hours (69% **2**); (vii) $Zn(BF_4)_2$, dichloromethane/methanol (3/1), 40°C, 2 hours [98% $[Zn_5\mathbf{2}](BF_4)_{10}$]; (viii) Na_4EDTA, acetonitrile/water (1/1), room temperature (RT), 3 hours (98% **2**).

Unlike the imine pentafoil knot (*24*), the metal ions (and simultaneously the chloride ion) could be removed from $[Fe_5\mathbf{2}{\bullet}Cl](PF_6)_9$ by treatment with aqueous tetrasodium ethylenediaminetetraacetate (Na_4EDTA) solution at 80°C, forming the metal-free knotted ligand **2** in 69% yield (Fig. 1, step vi) (SM, p. 9). The ^{1}H NMR spectrum of **2** in CD_3CN/$CDCl_3$ (3/1 v/v) (Fig. 2D) is relatively broad in comparison with the metallated knot. Molecular modeling suggests that **2** does not exist in a single well-defined conformation, and the broadness of the ^{1}H NMR spectrum is apparently a consequence of reptation [the thermal motion of long, entangled polymer chains, which influences properties such as the viscous flow of amorphous polymers (*28*)] as the 190-atom-long knot backbone slowly slithers through transiently tightened loops and across over- and under-crossings. Despite possessing no elements of Euclidean chirality, the metal-free knot **2** is intrinsically chiral by virtue of its topology. The enantiomers could be separated by chiral high-performance liquid chromatography (HPLC) (SM, section S4), and the pentafoil knots of opposite handedness shown to have circular dichroism spectra of equal and opposite shape and sign (fig. S22).

The iron-coordinated pentafoil knot binds a chloride or bromide ion strongly within its central cavity [K_{Cl^-} ~2.6×10^{10} M^{-1} (MeCN), K_{Br^-} = $1.4 \pm 1.0 \times 10^{10}$ M^{-1} (MeCN)] (SM, section S9). Nevertheless, the halide anion could be removed while leaving the Fe(II) ions in place, forming $[Fe_5\mathbf{2}](PF_6)_{10}$, by treating $[Fe_5\mathbf{2}{\bullet}Cl](PF_6)_9$ or $[Fe_5\mathbf{2}{\bullet}Br](PF_6)_9$ first with saturated aqueous NH_4BF_4, which exchanges the majority of the anions—including the centrally bound halide—for BF_4^- and then saturated aqueous NH_4PF_6, which replaces the BF_4^- anions with PF_6^- (*19*) (Fig. 1, step v) (SM, pp. 7 and 8).

The reaction of tris(bipy) ligand strand **1** with divalent transition metal salts other than Fe(II) results in linear triple helicates, coordination

Downloaded from http://science.sciencemag.org/ on June 28, 2016

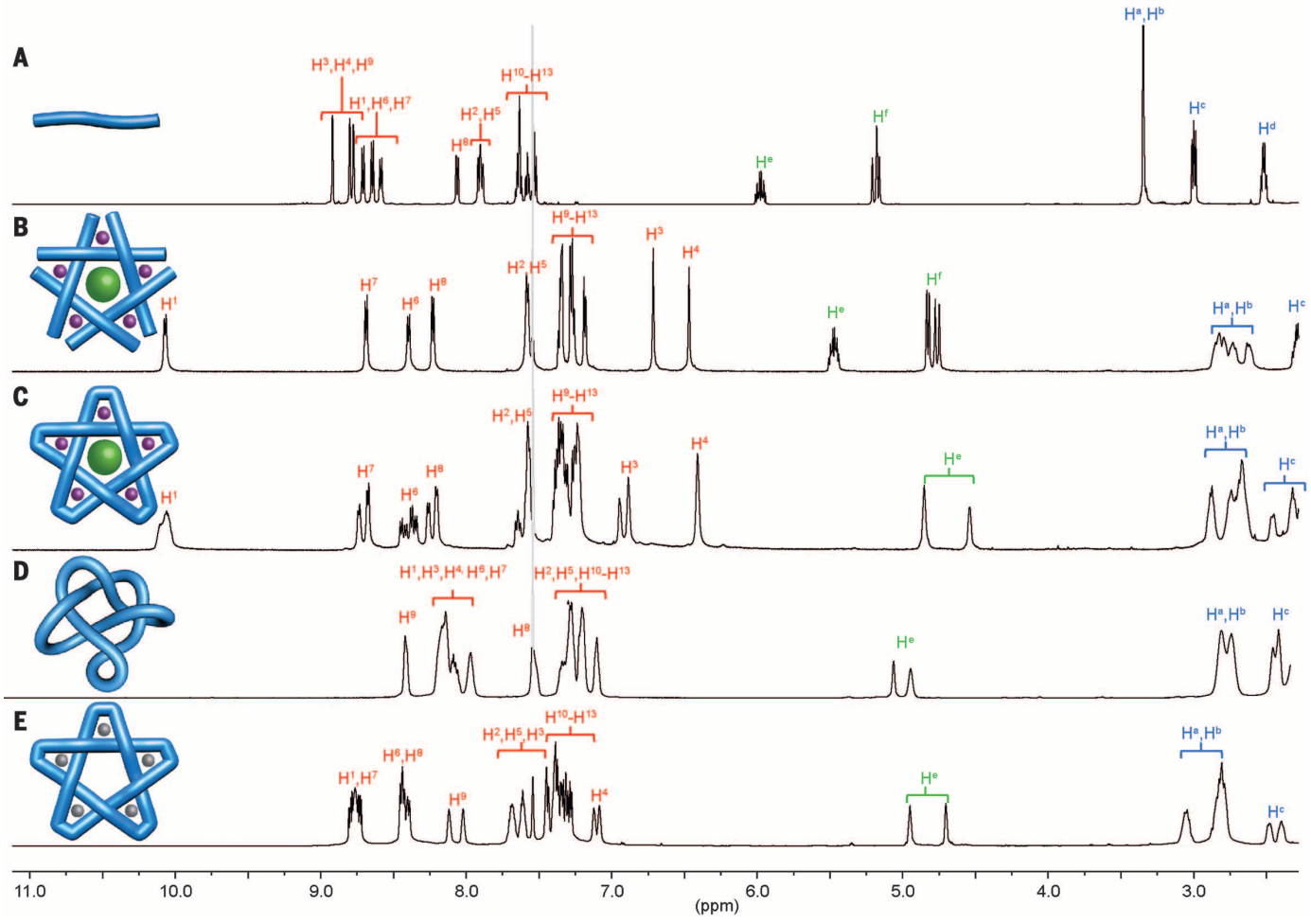


Fig. 2. Partial ^{1}H NMR spectra [600 MHz, 298 K, $CD_3CN/CDCl_3$ (3/1)]. (**A**) Ligand **1**. (**B**) Cyclic pentameric helicate $[Fe_5\mathbf{1}_5{\bullet}Cl](PF_6)_9$. (**C**) Fe(II)–pentafoil knot $[Fe_5\mathbf{2}{\bullet}Cl](PF_6)_9$. (**D**) metal-free pentafoil knot **2**. (**E**) Zn(II)–pentafoil knot $[Zn_5\mathbf{2}](BF_4)_{10}$. The signal assignments correspond to the labeling shown in Fig. 1. Signals from residual $CHCl_3$ are shown in gray.

polymers, or complex product mixtures (*29*). Therefore, it might seem that only iron(II)–complexed knots are accessible with this system. However, treatment of the metal-free pentafoil knot **2** with $Zn(BF_4)_2$ in a mixture of CD_2Cl_2/CD_3OD (3/1) (Fig. 1, step vii), gave an initially broad ^{1}H NMR spectrum (fig. S4) that sharpened after two hours at 40°C, indicating rearrangement to a single molecular species. After workup, the formation of the zinc(II) coordinated pentafoil knot $[Zn_5\mathbf{2}](BF_4)_{10}$ was confirmed by ^{1}H NMR spectroscopy (Fig. 2E) and ESI-MS (figs. S57 and S58). The restrictions on the chain conformation imposed by the topology of **2** prevent formation of linear triple helicates [as predominantly occurs with **1** and Zn(II) salts] and enable the ligand to adopt the higher-energy circular helicate structure with zinc(II) ions that is thermodynamically inaccessible with **1**. Zinc(II) ions typically exhibit much faster coordination kinetics than low-spin iron(II) ions, and the Zn(II)-pentafoil knot could be demetallated to reform **2** (Fig. 1, step viii) more readily and under milder conditions than the Fe(II)-pentafoil knot (Fig. 1, step

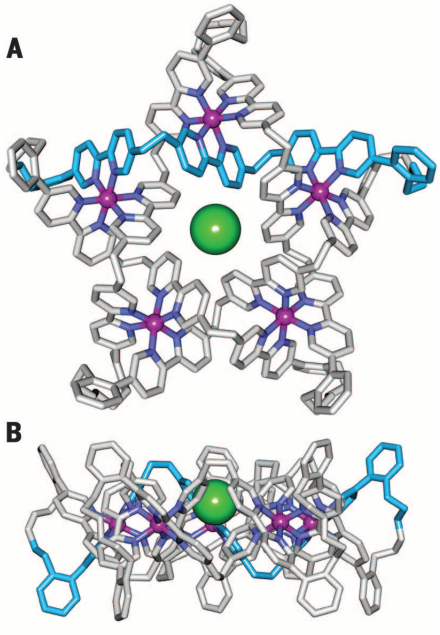


Fig. 3. X-ray crystal structure of pentafoil knot $[Fe_5\mathbf{2}{\bullet}Cl](PF_6)_6(BPh_4)_3$, shown as the Λ^5-enantiomer [Δ^5-$[Fe_5\mathbf{2}{\bullet}Cl](PF_6)_6(BPh_4)_3$ is present in equal amounts in the unit cell]. (**A**) Viewed from above the central cavity of the knot. (**B**) Viewed in the plane of the Fe(II) cations. Hydrogen atoms, solvent molecules, and anions (except for the central Cl^-) are omitted for clarity. The carbon atoms of one precursor ligand strand are colored light blue and the others light gray. N, dark blue; Fe, purple; Cl, green. Fe–Fe distances (Å): 8.305(7), 8.241(6), 8.313(7), 8.389(7), and 8.431(7). Fe–Fe–Fe angles (°): 107.80(7), 106.86(7), 108.37(7), 108.14(7), and 108.82(7). CH···Cl distances (Å): 2.461, 2.527, 2.539, 2.553, 2.629, 2.653, 2.669, 2.677, 2.714, and 2.858. Hydrogen bond distances were normalized using neutron diffraction data. Crystallographic data and experimental details of the structural refinement of $[Fe_5\mathbf{2}{\bullet}Cl](PF_6)_6(BPh_4)_3$ are provided in section S8 of the SM.

Downloaded from http://science.sciencemag.org/ on June 28, 2016

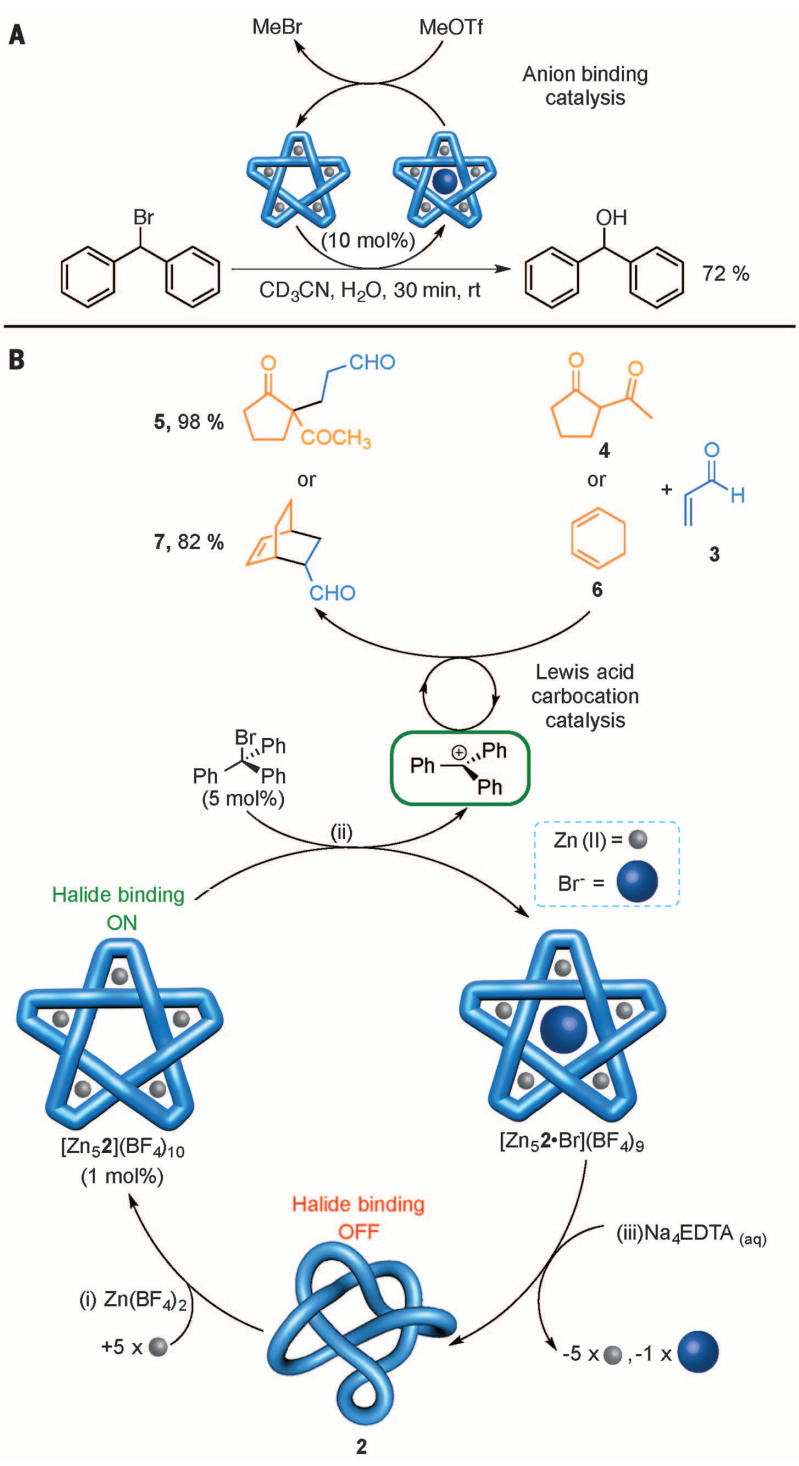


Fig. 4. Catalysis using a molecular knot. (**A**) Catalytic hydrolysis of Ph_2CHBr. Reaction conditions: Ph_2CHBr (2.0 μmol, 1 equiv.), wet CD_3CN (400 μL), $[Zn_5\mathbf{2}](BF_4)_{10}$ (0.2 μmol, 10 mol %), MeOTf (70 μmol, 35 equiv.), RT, 30 min, 72%. (**B**) Allosterically initiated catalysis of Michael addition and Diels-Alder reactions by in situ generation of a trityl cation via bromide abstraction using Zn(II)–pentafoil knot $[Zn_5\mathbf{2}](BF_4)_{10}$. Reaction conditions: (i) **2** (0.75 μmol, 1 mol % with respect to **3**), $Zn(BF_4)_2$ (3.71 μmol), CH_2Cl_2/CH_3OH (3/1) (400 μl), 40°C, 12 hours [98% $[Zn_5\mathbf{2}](BF_4)_{10}$]. (ii) 0.3 M solution of **3** (0.075 mmol, 1 equiv.), **4** (0.11 mmol, 1.5 equiv.), or **6** (0.089 mmol, 1.5 equiv.), Ph_3CBr (3.75 μmol, 5 mol %), CH_2Cl_2 (250 μl), RT, 8 hours (98% **5**; 82% **7**). (iii) $Na_4EDTA_{(aq)}$ CH_3CN/H_2O (1/1), rt, 3 hours (quantitative **2**). The use of a single knot enantiomer did not lead to enantiomeric enrichment of the Michael addition or Diels-Alder products (presumably the trityl cation is ion-paired with a BF_4^- anion rather than remaining associated with the knot).

vi). The Zn(II)-pentafoil knot binds a chloride or bromide anion within its central cavity approximately a tenth as strongly as its Fe(II) counterpart [$K_{Cl^-} \sim 2.9 \times 10^9$ M^{-1} (MeCN), $K_{Br^-} = 7.7 \pm 2.0 \times 10^8$ M^{-1} (MeCN)] (SM, section S9).

Substantial recent catalysis research has leveraged anion-binding molecules to influence reactions by ion pairing (*30*) or, in some cases, promoting carbon-halogen bond cleavage (*31*). Even with the relatively modest anion binding affinities of the host molecules generally employed to date, the approach has been shown to be effective across a range of reaction types (*31*). The empty-cavity metallated pentafoil knots are among the strongest noncovalent binding synthetic hosts of Cl^- and Br^- known, readily sequestering traces of Cl^- from the environment, including solvents and glassware. We wondered whether such a strong halide binder might be able to carry out reactions that have traditionally been the preserve of halophilic silver salts. We envisaged that the knot might be able to promote the formation of carbocations by stabilizing the Br^- counteranion formed by heterolytic carbon-bromine bond cleavage reactions.

We found that bromide ions bound within the cavities of either $[Fe_5\mathbf{2}\bullet Br](PF_6)_9$ or $[Zn_5\mathbf{2}\bullet Br](BF_4)_9$ react with methyl triflate to form bromomethane gas and the empty knots $[Fe_5\mathbf{2}](PF_6)_9OTf$ and $[Zn_5\mathbf{2}](BF_4)_9OTf$, respectively (SM, section S2.1). This reaction could be used to recycle the halide-binding cavity of the knot in situ—for example, using the Zn(II)–pentafoil knot as a catalyst for the hydrolysis of bromodiphenylmethane (Ph_2CHBr) (Fig. 4A and SM, section S2.2). MeOTf does not promote the hydrolysis reaction in the absence of the knot. Other nucleophiles (e.g., MeCN) also react efficiently with the catalytically generated benzhydryl (Ph_2CH^+) carbocation (SM, section S2.3).

In addition to acting as a catalyst in its own right, the metal-coordinated pentafoil knot could be used to generate other catalytic species, such as Lewis acidic trityl carbocations, through anion abstraction (Fig. 4B). The Michael addition and Diels-Alder reactions of acrolein (**3**) with 2-acetylcyclopentanone (**4**) and cyclohexadiene (**6**), respectively (Fig. 4B and tables S1 and S2), can each be promoted by Lewis acidic carbocations (*32*, *33*). We confirmed that neither of these reactions occurs in the absence of trityl bromide (tables S1 and S2, entry 1) and proceed only slowly in the presence of trityl bromide alone (tables S1 and S2, entry 2). The addition of Fe(II)$(bipy)_3$, the basic metal coordination unit of the knot, does not increase the reaction rate above the background level (tables S1 and S2, entries 3 and 4), nor does the addition of the tris(bipy) ligand strand **1**, even in the presence of $FeCl_2$ (any pentameric circular helicate formed would have a Cl^- anion already strongly bound to the halide binding site) (tables S1 and S2, entry 5). Neither the Fe(II)- nor Zn(II)–pentafoil knots {$[Fe_5\mathbf{2}](PF_6)_{10}$ and $[Zn_5\mathbf{2}](BF_4)_{10}$} lead to catalysis of the reactions in the absence of trityl bromide (tables S1 and S2, entries 11 and 14). However, in the presence of trityl bromide, both $[Fe_5\mathbf{2}](PF_6)_{10}$ (tables S1 and S2, entry 13) and $[Zn_5\mathbf{2}](BF_4)_{10}$ (tables S1 and S2,

Downloaded from http://science.sciencemag.org/ on June 28, 2016

entry 15) initiate catalysis of the reactions, effectively affording the endo-Diels-Alder (**7**) adduct in 62% [Fe(II)-knot] and 82% [Zn(II)-knot] and Michael adduct (**5**) in 83% [Fe(II)-knot] and 98% [Zn(II)-knot] yields, respectively (figs. S6 to S9).

Further evidence that the catalysis arises from in situ formation of the trityl cation by abstraction of a bromide anion into the knot cavity was provided by treating a solution of trityl bromide with $[Fe_5\mathbf{2}](PF_6)_{10}$. Ultraviolet-visible spectroscopy confirmed the presence of the trityl carbocation (fig. S14), showing its characteristic twin absorption features at λ = 425 and 405 nm, while ^{1}H NMR spectroscopy and mass spectrometry confirmed the contemporaneous formation of $[Fe_5\mathbf{2}\bullet Br](PF_6)_9$. In contrast, treating trityl bromide with the demetallated form of pentafoil knot **2** did not generate the carbocation (fig. S20), and no catalysis was observed upon the addition of ***3*** and **4** or **6** (tables S1 and S2, entry 12).

The binding of one type of molecular species (an effector) to induce structural change and alter binding or catalysis at a second site—allosteric regulation—is a central part of the enzyme feedback loops biology uses to maintain homeostasis (*34*). Allosteric control of Friedel-Crafts reactions has previously been demonstrated by a synthetic catalyst using coordination control of hydrogen bonding sites (*35*). However, treating the metal-free knot **2** with iron(II) salts led to broad ^{1}H NMR spectra and complex product mixtures rather than simple reformation of $[Fe_5\mathbf{2}]$, even under forcing conditions (figs. S2 and S3). The kinetics of bipy exchange at low-spin iron(II) centers is apparently too slow, given the number of intermediates and alternative unproductive pathways, for folding of the knot to the highly ordered five-fold symmetrical form to proceed within a useful time frame. In contrast, the fast and reversible coordination kinetics of zinc(II) ions allowed for allosteric initiation of the knot-promoted catalysis under mild conditions (Fig. 4B). Treating the metal-free knot **2** (inactive form) with $Zn(BF_4)_2$ in CD_2Cl_2/CD_3OD (3/1) at 40°C for up to 12 hours [depending on the amount of $Zn(BF_4)_2$ employed] smoothly generated the halide binding Zn(II)–pentafoil knot $[Zn_5\mathbf{2}](BF_4)_{10}$ (Fig. 4B, step i) (fig. S5). Addition of a 0.3-M solution of trityl bromide (5 mol %), and reagents ***3*** and **4** or **6**, formed products **5** or **7** in excellent yield (98 and 82%, respectively) (Fig. 4B, step ii) over 8 hours, together with a fine suspension of $[Zn_5\mathbf{2}\bullet Br](BF_4)_9$ (figs. S37 and S61). Filtration and washing with an aqueous solution of Na_4EDTA (Fig. 4B, step iii) quantitatively regenerated the demetallated knot, **2**.

Our results suggest that tying molecules in knots may prove to be a useful strategy for reducing the degrees of freedom of flexible macrocycles and chains, enabling them to adopt otherwise thermodynamically inaccessible conformations that can perform useful tasks. By analogy, it may be that one biological role of knotting is to prevent protein chains from adopting low energy, but inactive, folded states. The formation of a binding site by the organization of a long molecular strand by allosteric metal ion binding is also reminiscent of proteins. The use of a strongly halophilic, and chiral, metal-coordinated knot to promote the cleavage of carbon-halogen bonds may bring advantages of chemo- and stereoselectivity in chemical reactions traditionally promoted by silver salts.

REFERENCES AND NOTES

1. S. A. Wasserman, N. R. Cozzarelli, *Science* **232**, 951–960 (1986).
2. J. I. Sułkowska, E. J. Rawdon, K. C. Millett, J. N. Onuchic, A. Stasiak, *Proc. Natl. Acad. Sci. U.S.A.* **109**, E1715–E1723 (2012).
3. M. D. Frank-Kamenetskii, A. V. Lukashin, A. V. Vologodskii, *Nature* **258**, 398–402 (1975).
4. C. O. Dietrich-Buchecker, J.-P. Sauvage, *Angew. Chem. Int. Ed. Engl.* **28**, 189–192 (1989).
5. O. Safarowsky, M. Nieger, R. Fröhlich, F. Vögtle, *Angew. Chem. Int. Ed.* **39**, 1616–1618 (2000).
6. M. Feigel, R. Ladberg, S. Engels, R. Herbst-Irmer, R. Fröhlich, *Angew. Chem. Int. Ed.* **45**, 5698–5702 (2006).
7. J. Guo, P. C. Mayers, G. A. Breault, C. A. Hunter, *Nat. Chem.* **2**, 218–222 (2010).
8. P. E. Barran *et al.*, *Angew. Chem. Int. Ed.* **50**, 12280–12284 (2011).
9. N. Ponnuswamy, F. B. L. Cougnon, J. M. Clough, G. D. Pantoş, J. K. Sanders, *Science* **338**, 783–785 (2012).
10. T. Prakasam *et al.*, *Angew. Chem. Int. Ed.* **52**, 9956–9960 (2013).
11. J.-F. Ayme, J. E. Beves, C. J. Campbell, D. A. Leigh, *Chem. Soc. Rev.* **42**, 1700–1712 (2013).
12. N. Ponnuswamy, F. B. L. Cougnon, G. D. Pantoş, J. K. Sanders, *J. Am. Chem. Soc.* **136**, 8243–8251 (2014).
13. J.-F. Ayme *et al.*, *J. Am. Chem. Soc.* **136**, 13142–13145 (2014).
14. A. M. Saitta, P. D. Soper, E. Wasserman, M. L. Klein, *Nature* **399**, 46–48 (1999).
15. Y. Arai *et al.*, *Nature* **399**, 446–448 (1999).
16. W. R. Taylor, *Nature* **406**, 916–919 (2000).
17. J. R. Wagner, J. S. Brunzelle, K. T. Forest, R. D. Vierstra, *Nature* **438**, 325–331 (2005).
18. Y. Liu *et al.*, *Science* **351**, 365–369 (2016).
19. J.-F. Ayme *et al.*, *J. Am. Chem. Soc.* **137**, 9812–9815 (2015).
20. R. M. de Jong, B. W. Dijkstra, *Curr. Opin. Struct. Biol.* **13**, 722–730 (2003).
21. L. Tang *et al.*, *Biochemistry* **44**, 6609–6618 (2005).
22. J. W. Alexander, G. B. Briggs, *Ann. Math.* **28**, 562–586 (1926–1927).
23. B. Hasenknopf, J.-M. Lehn, B. O. Kneisel, G. Baum, D. Fenske, *Angew. Chem. Int. Ed. Engl.* **35**, 1838–1840 (1996).
24. J.-F. Ayme *et al.*, *Nat. Chem.* **4**, 15–20 (2011).
25. J.-F. Ayme *et al.*, *J. Am. Chem. Soc.* **134**, 9488–9497 (2012).
26. D. A. Leigh, R. G. Pritchard, A. J. Stephens, *Nat. Chem.* **6**, 978–982 (2014).
27. S. B. Garber, J. S. Kingsbury, B. L. Gray, A. H. Hoveyda, *J. Am. Chem. Soc.* **122**, 8168–8179 (2000).
28. P. G. de Gennes, *J. Chem. Phys.* **55**, 572–579 (1971).
29. B. Hasenknopf, J.-M. Lehn, N. Boumediene, E. Leize, A. Van Dorsselaer, *Angew. Chem. Int. Ed.* **37**, 3265–3268 (1998).
30. K. Brak, E. N. Jacobsen, *Angew. Chem. Int. Ed.* **52**, 534–561 (2013).
31. N. Busschaert, C. Caltagirone, W. Van Rossom, P. A. Gale, *Chem. Rev.* **115**, 8038–8155 (2015).
32. J. Bah, J. Franzén, *Chemistry* **20**, 1066–1072 (2014).
33. V. R. Naidu, S. Ni, J. Franzén, *Chem. Cat. Chem.* **7**, 1896–1905 (2015).
34. T. Traut, *Allosteric Regulatory Enzymes* (Springer, New York, 2008).
35. C. M. McGuirk, J. Mendez-Arroyo, A. M. Lifschitz, C. A. Mirkin, *J. Am. Chem. Soc.* **136**, 16594–16601 (2014).

ACKNOWLEDGMENTS

This research was funded by the European Research Council (advanced grant no. 339019) and the European Union's Seventh Framework Program (FP7-PEOPLE-2013-ITN-607602 'Hierarchical Self Assembly of Polymeric Soft Systems' SASSYPOL). The authors thank the Engineering and Physical Sciences Research Council National Mass Spectrometry Service Centre (Swansea, UK) for high-resolution mass spectrometry. CCDC-1443084 contains the supplementary crystallographic data for this paper. These data can be obtained free of charge via https://summary.ccdc.cam.ac.uk/structure-summary-form [or from the Cambridge Crystallographic Data Centre, 12 Union Road, Cambridge CB21EZ, UK; fax: (+44)1223-336-033; or deposit@ccdc.cam.ac.uk].

SUPPLEMENTARY MATERIALS

www.sciencemag.org/content/352/6293/1555/suppl/DC1
Materials and Methods
Figs. S1 to S66
Tables S1 to S3
References (*36*–*46*)

30 January 2016; accepted 17 May 2016
10.1126/science.aaf3673

DISTANT GALAXIES

Detection of an oxygen emission line from a high-redshift galaxy in the reionization epoch

Akio K. Inoue,[1]* Yoichi Tamura,[2] Hiroshi Matsuo,[3,4] Ken Mawatari,[1] Ikkoh Shimizu,[5] Takatoshi Shibuya,[6] Kazuaki Ota,[7,8] Naoki Yoshida,[9,10] Erik Zackrisson,[11] Nobunari Kashikawa,[3,4] Kotaro Kohno,[2] Hideki Umehata,[2,12] Bunyo Hatsukade,[3] Masanori Iye,[3] Yuichi Matsuda,[3,4] Takashi Okamoto,[13] Yuki Yamaguchi[2]

The physical properties and elemental abundances of the interstellar medium in galaxies during cosmic reionization are important for understanding the role of galaxies in this process. We report the Atacama Large Millimeter/submillimeter Array detection of an oxygen emission line at a wavelength of 88 micrometers from a galaxy at an epoch about 700 million years after the Big Bang. The oxygen abundance of this galaxy is estimated at about one-tenth that of the Sun. The nondetection of far-infrared continuum emission indicates a deficiency of interstellar dust in the galaxy. A carbon emission line at a wavelength of 158 micrometers is also not detected, implying an unusually small amount of neutral gas. These properties might allow ionizing photons to escape into the intergalactic medium.

The physical and chemical conditions of the interstellar medium (ISM) in galaxies can be revealed with forbidden atomic emission lines from the warm-phase ISM, such as ionized hydrogen (H II) regions and photodissociation regions (PDRs). A far-infrared (FIR) forbidden emission line, the [C II] 158-μm line predominantly coming from PDRs, has already been detected in many high-*z* objects (*1*, *2*). Recent observations with the Atacama Large

Downloaded from http://science.sciencemag.org/ on June 28, 2016

Millimeter/submillimeter Array (ALMA) have revealed the [C II] line emission from young star-forming galaxies emitting a strong hydrogen Lyα line, so-called Lyα emitters (LAEs), at redshift $z \sim 5$ to 6 (*3*, *4*). However, ALMA observations have also shown that LAEs at $z > 6$ have at least an order of magnitude lower luminosity of the [C II] line than that expected from their star formation rate (SFR) (*4*–*7*), suggesting unusual ISM conditions in these high-z LAEs (*8*).

Herschel observations of nearby dwarf galaxies, on the other hand, have revealed that a forbidden oxygen line, [O III] 88 μm, is much stronger than the [C II] line in these chemically unevolved galaxies (*9*–*11*). The Infrared Space Observatory and the Japanese infrared astronomical satellite AKARI have detected the [O III] line from the Large Magellanic Cloud and from many nearby galaxies (*12*, *13*). However, the [O III] line has rarely been discussed in a high-z context, because of the lack of instruments suitable to observe the redshifted line. Only a few detections from gravitationally lensed dusty starburst galaxies with active galactic nuclei at $z \sim 3$ to 4 have been reported (*14*, *15*) prior to ALMA. On the other hand, simulations predict that ALMA will be able to detect the [O III] line from star-forming galaxies with reasonable integration time even at $z > 8$ (*16*).

To examine the [O III] 88-μm line in high-z LAEs, we performed ALMA observations of an LAE at $z = 7.2$, SXDF-NB1006-2, discovered with the Subaru Telescope (*17*). We have also obtained ALMA data of the [C II] 158-μm line of this galaxy. [The observations and the data reduction are described in (*18*).] The [O III] line is detected with a significance of 5.3σ (Fig. 1A), and the obtained line flux is 6.2×10^{-21} W m^{-2}; the corresponding luminosity is 3.8×10^{35} W (Table 1). The [C II] line is not detected at the position of the [O III] emission line, and we take the 3σ upper limit for the [C II] line flux as $<5.3 \times 10^{-22}$ W m^{-2}. However, we note a marginal signal (3.5σ) that displays a spatial offset (≈ 0.4″ ≈ 2 kpc in the proper distance) from the [O III] emission (fig. S4). The continuum is not detected in either of the ALMA bands, resulting in a 3σ upper limit of the total IR luminosity of $<2.9 \times 10^{37}$ W when assuming a dust temperature of 40 K and an emissivity index of 1.5.

The spatial distribution of the ALMA [O III] emission overlaps with that of the Subaru Lyα emission (Fig. 1A), as expected because both emission lines are produced in the same ionized gas. On the other hand, the Lyα emission is well resolved (the image resolution is 0.4″) and spatially more extended than the [O III] line. This is because Lyα photons suffer from resonant scattering by neutral hydrogen atoms in the gas surrounding the galaxy. The systemic redshift of the galaxy is estimated at $z = 7.2120 \pm 0.0003$ from the [O III] emission line at an observed wavelength of 725.603 μm. The Lyα line is located at $\Delta v_{\mathrm{Ly}\alpha} = +1.1\ (\pm 0.3) \times 10^2$ km s^{-1} relative to the systemic redshift (Fig. 1C and fig. S6). This velocity offset, caused by scattering of neutral hydrogen, is relatively small by comparison to those observed in galaxies at $z \sim 2$ to 3 ($\Delta v_{\mathrm{Ly}\alpha} \sim 300$ km s^{-1}), given the ultraviolet (UV) absolute magnitude of this galaxy ($M_{\mathrm{UV}} = -21.53$ magAB) (*19*–*21*). The observed small $\Delta v_{\mathrm{Ly}\alpha}$ of SXDF-NB1006-2 may indicate an H I column density of $N_{\mathrm{H\,I}} < 10^{20}$ cm^{-2} (*21*, *22*). SXDF-NB1006-2 is in the reionization era where only the intergalactic medium (IGM) with a high hydrogen neutral fraction may cause an observation of $\Delta v_{\mathrm{Ly}\alpha} \approx +100$ km s^{-1} (*23*), implying an even smaller H I column density in the ISM of this galaxy.

We performed spectral energy distribution (SED) modeling to derive physical quantities such as the SFR of SXDF-NB1006-2 (Table 1). In addition to broadband photometric data from the United Kingdom Infra-Red Telescope (UKIRT) J, H, and K bands, Spitzer 3.6-μm and 4.5-μm bands, and Subaru narrowband photometry NB1006 (table S3), we have also used the [O III] line flux and the IR luminosity as constraints (Fig. 2) (*18*). The extremely blue rest-frame UV color of this galaxy [slope $\beta < -2.6$ (3σ) estimated from $J - H$, where the flux density $F_\lambda \propto \lambda^\beta$] gives an age of ~1 million years for the ongoing star formation episode. The nondetection of the dust IR emission suggests little dust and hence negligible attenuation. The observed strong [O III] line flux favors an oxygen abundance of 5% to 100% that of the Sun, but rejects 2% and 200% of the solar abundance at >95% confidence. The obtained oxygen abundance is similar to those estimated in galaxies at $z \sim 6$ to 7, for which UV C III] and C IV emission lines were detected (*24*, *25*). Because ~1 million years is insufficient to produce the inferred oxygen abundance, the galaxy must have had previous star formation episodes. Therefore, the derived stellar mass of ~300 million solar masses is regarded as a lower limit. We obtain a ~50% escape fraction of hydrogen-ionizing photons to the IGM in the best-fit model. Such a high escape fraction, although still uncertain, may imply a low H I column density of ~10^{17} cm^{-2} (*26*) or porous structure in the ISM of the galaxy.

The [O III]/far-UV luminosity ratio of SXDF-NB1006-2 is similar to those of nearby dwarf galaxies with an oxygen abundance of 10% to 60% that of the Sun (Fig. 3A), which suggests that the oxygen abundance estimated from the SED modeling is reasonable and chemical enrichment in this young galaxy has already proceeded. On the other hand, the dust IR continuum and the [C II] line of SXDF-NB1006-2 are very weak relative to those of the nearby dwarf galaxies (Fig. 3, B and C). The galaxies at $z \sim 3$ to 4, from which the [O III] line was detected previously, are IR luminous dusty ones (*14*, *15*). Their [O III]/IR and [O III]/[C II] luminosity ratios are similar to

[1]College of General Education, Osaka Sangyo University, 3-1-1 Nakagaito, Daito, Osaka 574-8530, Japan. [2]Institute of Astronomy, University of Tokyo, 2-21-1 Osawa, Mitaka, Tokyo 181-0015, Japan. [3]National Astronomical Observatory of Japan, 2-21-1 Osawa, Mitaka, Tokyo 181-8588, Japan. [4]Graduate University for Advanced Studies (SOKENDAI), 2-21-1 Osawa, Mitaka, Tokyo 181-8588, Japan. [5]Department of Earth and Space Science, Osaka University, 1-1 Machikaneyama, Toyonaka, Osaka 560-0043, Japan. [6]Institute for Cosmic Ray Research, University of Tokyo, 5-1-5 Kashiwanoha, Kashiwa, Chiba 277-8582, Japan. [7]Kavli Institute for Cosmology, University of Cambridge, Cambridge CB3 0HA, UK. [8]Cavendish Laboratory, University of Cambridge, Cambridge CB3 0HE, UK. [9]Department of Physics, University of Tokyo, 7-3-1 Hongo, Bunkyo, Tokyo 113-0033, Japan. [10]Kavli IPMU, University of Tokyo, 5-1-5 Kashiwanoha, Kashiwa, Chiba 277-8583, Japan. [11]Department of Physics and Astronomy, Uppsala University, SE-751 20 Uppsala, Sweden. [12]European Southern Observatory, D-85748 Garching, Germany. [13]Department of Cosmosciences, Graduate School of Science, Hokkaido University, N10 W8, Kitaku, Sapporo, Hokkaido 060-0810, Japan.
*Corresponding author. Email: akinoue@las.osaka-sandai.ac.jp

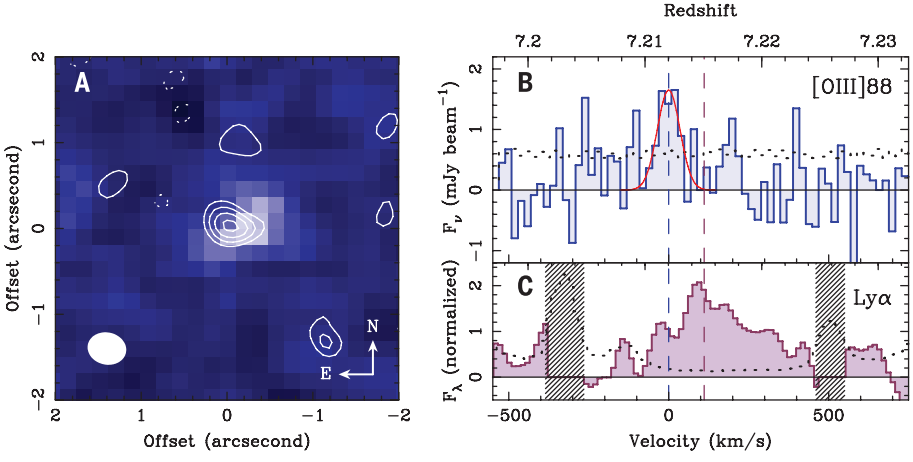


Fig. 1. [O III] 88-μm and Lyα emission images and spectra of SXDF-NB1006-2. (**A**) The ALMA [O III] 88-μm image (contours) overlaid on the Subaru narrow-band Lyα image (offsets from the position listed in Table 1). Contours are drawn at (−2, 2, 3, 4, 5) × σ, where σ = 0.0636 Jy beam^{-1} km s^{-1}. Negative contours are shown by the dotted line. The ellipse at lower left represents the synthesized beam size of ALMA. (**B**) The ALMA [O III] 88-μm spectrum with resolution of 20 km s^{-1} at the intensity peak position shown against the relative velocity with respect to the redshift $z = 7.2120$ (blue dashed line). The best-fit Gaussian profile for the [O III] line is overlaid. The RMS noise level is shown by the dotted line. (**C**) The Lyα spectrum (*17*) shown as a function of the relative velocity compared to the [O III] 88-μm line. The flux density is normalized by a unit of 10^{-18} erg s^{-1} cm^{-2} Å^{-1}. The sky level on an arbitrary scale is shown by the dotted line. The velocity intervals where Earth's atmospheric lines severely contaminate the spectrum are flagged (hatched boxes). The Lyα line shows a velocity shift $\Delta v \approx +110$ km s^{-1} relative to the [O III] line (red dashed line).

Downloaded from http://science.sciencemag.org/ on June 28, 2016

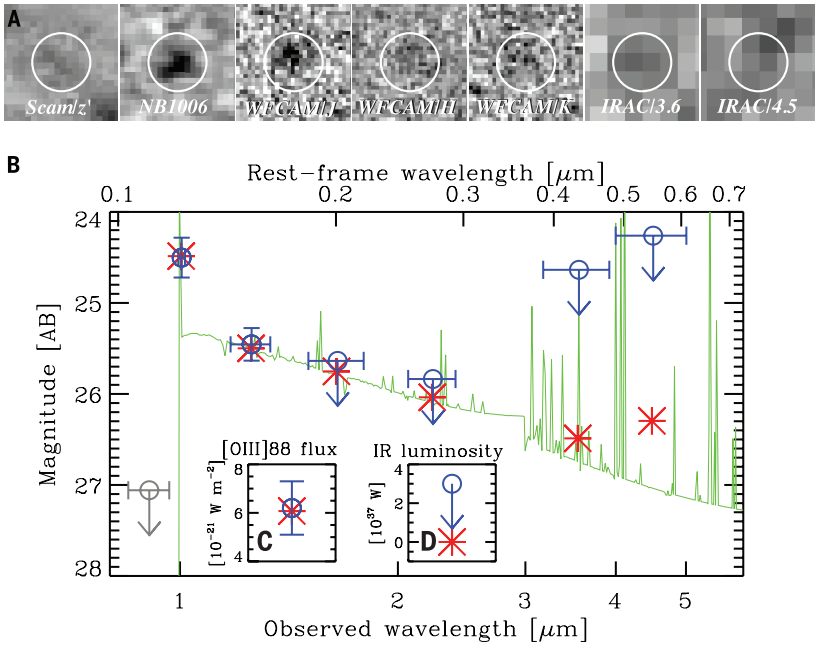


Fig. 2. Spectral energy distribution of SXDF-NB1006-2. (**A**) Thumbnail images (4″ × 4″; north is up, east is to the left) in the Subaru/Suprime-Cam z′, NB1006, UKIRT/WFCAM J, H, and K bands, and Spitzer/IRAC 3.6-μm and 4.5-μm bands, from left to right. (**B**) Near-infrared photometric data with the best-fit model. The bottom horizontal axis shows the wavelength in the observer's rest frame; the upper axis shows the wavelength in the source rest frame. The observations are marked by the circles. The horizontal error bars show the wavelength range of the band filters. The vertical error bars for detection bands represent ±1σ photometric uncertainties; the downward arrows for nondetections represent the 3σ upper limits. The z′ point in gray is not used for the model fit. The best-fit model spectrum is shown by the solid green line, and the corresponding magnitudes through the filters are indicated by asterisks. (**C**) The observed flux with the ±1σ uncertainty of the [O III] line and the best-fit model prediction (asterisk). (**D**) The 3σ upper limit on the total infrared luminosity with a dust temperature of 40 K and an emissivity index of 1.5. Also shown is the best-fit model prediction (asterisk; zero IR luminosity due to absence of dust in the best-fit model).

those of nearby spiral galaxies (*10*) and are at least one order of magnitude smaller than those of SXDF-NB1006-2. The high [O III]/IR ratio of SXDF-NB1006-2, despite a degree of chemical enrichment (or so-called metallicity) similar to that of the nearby dwarf galaxies, indicates a very small mass fraction of dust in elements heavier than helium (or dust-to-metal mass ratio) in SXDF-NB1006-2. The dust deficiency of this galaxy is in contrast to the discovery of a dusty galaxy at $z \approx 7.5$ (*27*), suggesting a diversity of the dust content in the reionization epoch. Because the [C II] line predominantly arises in gas where hydrogen is neutral, the nondetection of the [C II] line in SXDF-NB1006-2 suggests that this young galaxy has little H I gas.

We also compared the observed properties of SXDF-NB1006-2 with the galaxies at $z = 7.2$ in a cosmological hydrodynamic simulation of galaxy formation and evolution (*18*). This simulation yielded several galaxies with a UV luminosity similar to that of SXDF-NB1006-2 (fig. S10). Relative to these simulated galaxies, SXDF-NB1006-2 has the highest [O III] line luminosity, a similar oxygen abundance, and a lower dust IR luminosity by at least a factor of 2 to 3. This indicates a factor of >2 to 3 smaller dust-to-metal mass ratio within the ISM of SXDF-NB1006-2 relative to that in the simulated galaxies, where we assumed the dust-to-metal mass ratio of 50% as in the Milky Way ISM (*28*). Therefore, the dust-to-metal ratio of SXDF-NB1006-2 is implied to be <20%. The dust-to-metal ratio is determined by two processes: (i) dust growth by accretion of atoms and molecules onto the existing grains in cold dense clouds, and (ii) dust destruction by supernova (SN) shock waves consequent upon star formation (*28*). The dust-poor nature of SXDF-NB1006-2 may be explained by rapid dust destruction due to its high SN rate or by slow accretion growth due to a lack of cold dense clouds in the ISM.

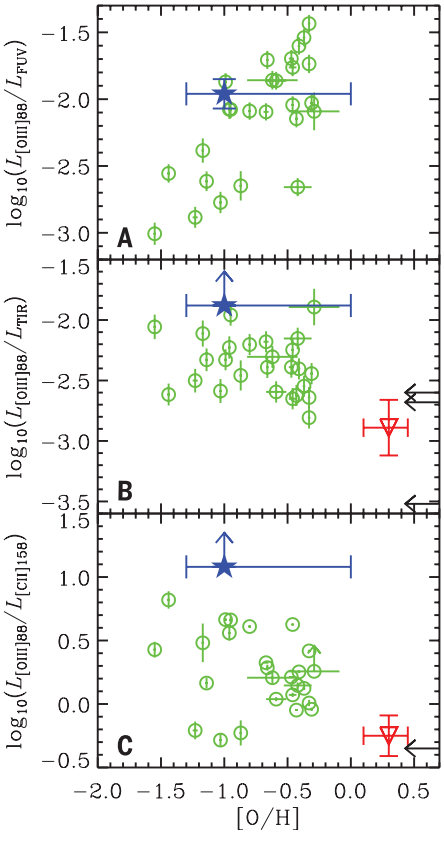


Fig. 3. Comparisons of SXDF-NB1006-2 and other galaxies detected in the [O III] line. The horizontal axis represents the oxygen abundance relative to the Sun on a logarithmic scale: [O/H] = $\log_{10}(n_O/n_H) - \log_{10}(n_O/n_H)_\odot$, where n_O and n_H are the number density of oxygen and hydrogen atoms, respectively, and the solar abundance is assumed to be $12 + \log_{10}(n_O/n_H)_\odot = 8.69$ (*30*). Circles with error bars represent data of nearby dwarf galaxies (*9*–*11*); inverted triangles with error bars are averages of nearby spiral galaxies (*13*). The arrows at the right-side axis show luminosity ratios of dusty galaxies at $z \sim 3$ to 4 whose oxygen abundances have not yet been measured (*10*, *14*, *15*). Data from SXDF-NB1006-2 are shown as five-pointed stars with error bars. (**A**) The [O III]/far-UV (FUV) luminosity ratio. The FUV luminosity is νL_ν at about 1500 Å in the source rest frame. (**B**) The [O III]/total infrared (IR) luminosity ratio. The IR wavelength range is 8 to 1000 μm in the source rest frame. Because the IR continuum of SXDF-NB1006-2 is not detected, we show a 3σ lower limit with a dust temperature of 40 K and an emissivity index of 1.5. (**C**) The [O III]/[C II] luminosity ratio. Because the [C II] 158-μm line of SXDF-NB1006-2 is not detected, we show a 3σ lower limit.

In the context of cosmic reionization studies, the most uncertain parameter is the product of the escape fraction of ionizing photons and the emission efficiency of these photons, $f_{esc}\xi_{ion}$ (*29*). From the SED modeling, we have obtained $\log_{10}[f_{esc}\xi_{ion}(\mathrm{Hz\ erg^{-1}})] = 25.44^{+0.46}_{-0.84}$ for SXDF-NB1006-2 (*18*). This ionizing photon emission efficiency is strong enough to reach (or even exceed) the cosmic ionizing photon emissivity at $z \sim 7$ estimated from various observational constraints on reionization (*29*) by an accumulation of galaxies that have already been detected ($M_{UV} < -17$), although this

Downloaded from http://science.sciencemag.org/ on June 28, 2016

Table 1. A summary of the observed and estimated properties of SXDF-NB1006-2.

Right ascension (J2000)	$2^h18^m56.536^s$ (±0.002^s)
Declination (J2000)	−5°19′58.87″ (±0.02″)
Redshift of [O III] 88-μm line	7.2120 ± 0.0003
Lyα velocity shift (km s^{-1})	+1.1 (±0.3) × 10^2
[O III] 88-μm luminosity (W)*	3.8 (±0.8) × 10^{35}
[C II] 158-μm luminosity (W)*	<3.2 × 10^{34} (3σ)
Total IR luminosity (W)*	<2.9 × 10^{37} (3σ)
Oxygen abundance [O/H]	$-1.0^{+1.0}_{-0.3}$
Star formation rate [$\log_{10}(M_\odot$ year^{-1})]†	$2.54^{+0.17}_{-0.71}$
Star formation age [$\log_{10}$(years)]	$6.00^{+1.00}$
Dust attenuation (E_{B-V} mag)	$0.00^{+0.04}$
Escape fraction of ionizing photons	$0.54^{+0.17}_{-0.54}$
Stellar mass ($\log_{10} M_\odot$)†	$8.54^{+0.79}_{-0.22}$

*Assuming a concordance cosmology with present-day Hubble parameter H_0 = 70 km s^{-1} Mpc^{-1}, density parameter of matter Ω_M = 0.3, and density parameter of the cosmological constant Ω_Λ = 0.7. †$M_\odot$ represents the solar mass (1.989 × 10^{30} kg).

does not rule out contributions of fainter, currently undetected galaxies to the ionizing emissivity. The ISM properties of SXDF-NB1006-2, with little dust and H I gas, may make this galaxy a prototypical example of a source of cosmic reionization.

REFERENCES AND NOTES

1. G. J. Stacey *et al.*, *Astrophys. J.* **724**, 957–974 (2010).
2. B. Gullberg *et al.*, *Mon. Not. R. Astron. Soc.* **449**, 2883–2900 (2015).
3. P. L. Capak *et al.*, *Nature* **522**, 455–458 (2015).
4. K. K. Knudsen *et al.*, http://arxiv.org/abs/1603.02277 (2016).
5. M. Ouchi *et al.*, *Astrophys. J.* **778**, 102 (2013).
6. K. Ota *et al.*, *Astrophys. J.* **792**, 34 (2014).
7. R. Maiolino *et al.*, *Mon. Not. R. Astron. Soc.* **452**, 54–68 (2015).
8. L. Vallini, S. Gallerani, A. Ferrara, A. Pallottini, B. Yue, *Astrophys. J.* **813**, 36 (2015).
9. S. C. Madden *et al.*, *Publ. Astron. Soc. Pac.* **125**, 600–635 (2013).
10. I. De Looze *et al.*, *Astron. Astrophys.* **568**, A62 (2014).
11. D. Cormier *et al.*, *Astron. Astrophys.* **578**, A53 (2015).
12. M. Kawada *et al.*, *Publ. Astron. Soc. Jpn.* **63**, 903–910 (2011).
13. J. R. Brauher, D. A. Dale, G. Helou, *Astrophys. J. Suppl. Ser.* **178**, 280–301 (2008).
14. C. Ferkinhoff *et al.*, *Astrophys. J.* **714**, L147–L151 (2010).
15. I. Valtchanov *et al.*, *Mon. Not. R. Astron. Soc.* **415**, 3473–3484 (2011).
16. A. K. Inoue *et al.*, *Astrophys. J.* **780**, L18 (2014).
17. T. Shibuya *et al.*, *Astrophys. J.* **752**, 114 (2012).
18. See supplementary materials on *Science* Online.
19. T. Hashimoto *et al.*, *Astrophys. J.* **765**, 70 (2013).
20. D. K. Erb *et al.*, *Astrophys. J.* **795**, 33 (2014).
21. T. Shibuya *et al.*, *Astrophys. J.* **788**, 74 (2014).
22. T. Hashimoto *et al.*, *Astrophys. J.* **812**, 157 (2015).
23. K. Kakiichi, M. Dijkstra, B. Ciardi, L. Graziani, http://arxiv.org/abs/1510.05647 (2015).
24. D. P. Stark *et al.*, *Mon. Not. R. Astron. Soc.* **450**, 1846–1855 (2015).
25. D. P. Stark *et al.*, *Mon. Not. R. Astron. Soc.* **454**, 1393–1403 (2015).
26. The photoionization cross section of a neutral hydrogen atom at the wavelength of 912 Å (Lyman limit) is σ = 6.3 × 10^{-18} cm^2. Then, the H I column density for a 50% escape is $N_{H\,I}$ = −ln 0.5/σ ≈ 1 × 10^{17} cm^{-2} in a uniform medium.
27. D. Watson *et al.*, *Nature* **519**, 327–330 (2015).
28. A. K. Inoue, *Earth Planets Space* **63**, 1027–1039 (2011).
29. R. J. Bouwens *et al.*, *Astrophys. J.* **811**, 140 (2015).
30. M. Asplund, N. Grevesse, A. J. Sauval, P. Scott, *Annu. Rev. Astron. Astrophys.* **47**, 481–522 (2009).

ACKNOWLEDGMENTS

This paper makes use of the following ALMA data: ADS/JAO.ALMA# 2013.1.01010.S and 2012.1.00374.S, which are available at https://almascience.nao.ac.jp/alma-data/archive. ALMA is a partnership of the European Southern Observatory (ESO) (representing its member states), NSF (USA), and NINS (Japan), together with NRC (Canada), NSC and ASIAA (Taiwan), and KASI (Republic of Korea), in cooperation with the Republic of Chile. The Joint ALMA Observatory is operated by ESO, the National Radio Astronomy Observatory/Associated Universities Inc., and the National Astronomical Observatory of Japan (NAOJ). Based in part on data collected at Subaru Telescope, which is operated by NAOJ; data are available at http://smoka.nao.ac.jp/ under project codes S08B-019, S08B-051, and S09B-055, and also at the W.M. Keck Observatory, which is operated as a scientific partnership among the California Institute of Technology, the University of California, and NASA; data are available at www2.keck.hawaii.edu/koa/public/koa.php under the project code S331D. When some of the data reported here were acquired, UKIRT was operated by the Joint Astronomy Centre on behalf of the Science and Technology Facilities Council of the UK; UKIDSS data are available at http://wsa.roe.ac.uk//dr10plus_release.html. Based in part on archival data obtained with the Spitzer Space Telescope, which is operated by the Jet Propulsion Laboratory, California Institute of Technology under a contract with NASA; data are available at www.cfa.harvard.edu/SEDS/data.html. Supported by JSPS KAKENHI grants 26287034 (A.K.I. and K.M.), 26247022 (I.S.), 25287050 (N.Y.), 24740112 (T.O.), 15H02073 (Y.T.), and 15K17616 (B.H.), and by a grant-in-aid for JSPS Fellows (H.U.), by a grant-in-aid for the Global COE Program "The Next Generation of Physics, Spun from Universality and Emergence" from MEXT of Japan (K.O.), the Kavli Institute Fellowship (at Kavli Institute for Cosmology, University of Cambridge) supported by the Kavli Foundation (K.O.), and the Swedish Research Council (project 2011-5349) and the Wenner-Gren Foundations (E.Z.).

SUPPLEMENTARY MATERIALS

www.sciencemag.org/content/352/6293/1559/suppl/DC1
Materials and Methods
Figs. S1 to S12
Tables S1 to S4
References (*31*–*75*)

14 December 2015; accepted 16 May 2016
10.1126/science.aaf0714

QUANTUM INFORMATION

Single-qubit gates based on targeted phase shifts in a 3D neutral atom array

Yang Wang, Aishwarya Kumar, Tsung-Yao Wu, David S. Weiss*

Although the quality of individual quantum bits (qubits) and quantum gates has been steadily improving, the number of qubits in a single system has increased quite slowly. Here, we demonstrate arbitrary single-qubit gates based on targeted phase shifts, an approach that can be applied to atom, ion, or other atom-like systems. These gates are highly insensitive to addressing beam imperfections and have little cross-talk, allowing for a dramatic scaling up of qubit number. We have performed gates in series on 48 individually targeted sites in a 40% full 5 by 5 by 5 three-dimensional array created by an optical lattice. Using randomized benchmarking, we demonstrate an average gate fidelity of 0.9962(16), with an average cross-talk fidelity of 0.9979(2) (numbers in parentheses indicate the one standard deviation uncertainty in the final digits).

The performance of isolated quantum gates has recently been improved for several types of qubits, including trapped ions (*1*–*3*), Josephson junctions (*4*), quantum dots (*5*), and neutral atoms (*6*). Single-qubit gate errors now approach or, in the case of ions, surpass the commonly accepted error threshold (error per gate < 10^{-4}) (*7*, *8*) for fault-tolerant quantum computation (*9*–*12*). It remains a challenge in all these systems to execute targeted gates on many qubits in close physical proximity to one another with fidelities comparable with those for isolated qubits (*13*, *14*). Neutral atom and ion experiments have to date demonstrated the most qubits in the same system, 50 and 18 respectively (*15*, *17*). The highest-fidelity gates in these systems are based on microwave transitions, but addressing schemes typically depend on either addressing light beams (*6*, *15*, *18*–*20*), which are difficult to make as stable as microwaves, or magnetic field gradients (*2*, *21*), which limit the number of addressed qubits. Here, we present a way to induce phase shifts on atoms at targeted sites in a 5 by 5 by 5 optical lattice that is highly insensitive to addressing laser beam fluctuations. We further show how to convert targeted phase shifts into arbitrary single-qubit gates.

Department of Physics, Pennsylvania State University, University Park, PA, USA.
*Corresponding author. Email: dsweiss@phys.psu.edu

Downloaded from http://science.sciencemag.org/ on June 28, 2016

In previous work, we performed single-site addressing in a three-dimensional (3D) lattice using crossed laser beams, to selectively induce ac Stark shifts in target atoms, and microwaves, to temporarily map quantum states from a field-insensitive storage basis to the Stark-shifted computational basis (*15*). Although we used most of the same physical elements in this work, the crucial difference is that the gates described here are based on phase shifts in the storage basis and do not require transitions out of it. Nonresonant microwaves are applied that give opposite-sign ac Zeeman shifts (analogous to ac Stark shifts, but for magnetic dipole transitions) for different atoms. A specific series of nonresonant pulses and global π-pulses on the qubit transition gives a zero net phase shift for nontarget atoms and a controllable net phase shift for target atoms. The resultant gate fidelity is much better than our previous gate because of this gate's extreme insensitivity to the addressing beam alignment and power, the insensitivity of the storage basis to magnetic fields and vector light shifts, and the independence on the phase of the nonresonant microwave pulses.

Detailed descriptions of our apparatus can be found in (*15*, *22*, *23*). We optically trapped and reliably imaged neutral ^{133}Cs atoms in a 5-μm spaced cubic optical lattice. The atoms were cooled to ~70% ground vibrational state occupancy and then microwave transferred into the qubit basis, the $6S_{1/2}$, $|3,0\rangle$, and $|4,0\rangle$ hyperfine sublevels, which we will call $|1\rangle$ and $|0\rangle$, respectively. Lattice light spontaneous emission is the largest source of decoherence, with a 7 s coherence time (T_2') that is much longer than the typical microwave pulse time of 80 μs, which could be shortened with more microwave intensity. We detected the qubit states by clearing atoms in the $|4,0\rangle$ states and imaging the $|3,0\rangle$ atoms that remain.

To target an atom, we crossed at a right angle two circularly polarized, 880.250-nm addressing beams (beam waist, ~2.7 μm; Rayleigh range, ~26 μm). The addressing beams can be directed to a new target in <5 μs by using micro-electro-mechanical-system (MEMS) mirrors (*24*). The addressing beams induce only a modest ac Stark shift on the $m_F = 0$ qubit states (~400 Hz), but they cause a vector light shift on the $m_F \neq 0$ levels. The vector light shifts are about twice as large for the target atom as for any other. This is illustrated in Fig. 1A, for which atoms are prepared in $|4,0\rangle$ and a microwave near the $|3,1\rangle$ transition is scanned. The resonances are visible for atoms at the intersection (orange, termed "cross" atoms), atoms in one addressing beam path (blue, termed "line" atoms), and the rest of the atoms (green, termed "spectator" atoms). The ac Stark shift for the line atoms, *f*, was chosen so that there is a region between the blue and orange peaks in which only a small fraction (2×10^{-4}) of atoms in any class (cross, line, or spectator) makes the transition. When a microwave pulse is applied in that frequency range, atoms experience different ac Zeeman shifts depending on their class.

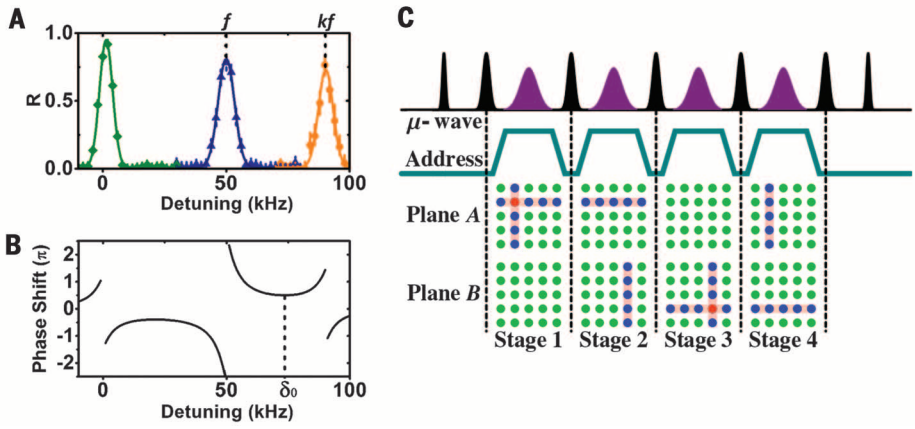


Fig. 1. Addressing spectrum, phase shift, and timing sequence. (**A**) Spectra of the $|4,0\rangle \rightarrow |3,1\rangle$ transition. We plot the ratio *R* of the number of detected $F = 3$ atoms to the initial number of atoms as a function of the phase-shifting microwave detuning from the non–ac-Stark–shifted resonance. There is a 570-mG bias field at 45° to the addressing beam axes. The green diamonds indicate spectators, the blue triangles indicate line atoms, and the orange circles indicate cross atoms. The solid lines are fits to Gaussians. The resonance frequencies of line atoms and cross atoms are marked by *f* and *kf*. (**B**) Exact calculation of the cumulative phase shift (ϕ_{Target}) on a target atom as a function of the microwave detuning from the unshifted resonance. The optimum operation point is marked by δ_0. Transitions out of the qubit basis are ignored. At δ_0, these occur less than 2×10^{-4} of the times. (**C**) Addressing pulse sequence. (Top row) Blackman-profiled (to minimize off-resonant transitions) (*35*) microwave pulse sequence. The black pulses (80 μs) are resonant on the $|0\rangle$ to $|1\rangle$ transition and affect all atoms; the narrower pulses are $\pi/2$ rotations, which first create and then measure superpositions, and the wider pulses are π rotations, which give spin echoes. The purple pulses (120 μs) are addressing pulses detuned from the $|4(3),0\rangle$ to $|3(4),1\rangle$ transitions by δ_0. (Second row from top) The addressing light intensity. The addressing light barely affects the trapping potential, so a linear ramp is optimal. It is effectively at full power for 252 μs. (Bottom two rows) Schematic of addressing beams in two planes. The atom color codes are as in (A).

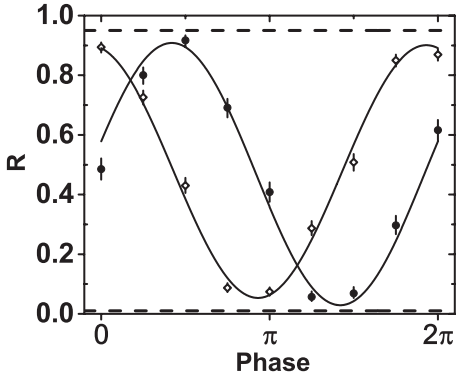


Fig. 2. Interference fringe of one $R_z(\pi/2)$ phase gate. The gate is applied to a succession of 48 randomly chosen sites (in pairs) in each implementation, and the data show averages over 10 implementations. The solid circles correspond to the target atoms, and the open diamonds correspond to nontarget atoms. Solid lines are fits to data. Dashed lines mark the maximum and minimum possible populations. After all these gates, the net fidelity $\mathcal{F}^2$ for target atoms is 0.94(3), and for the nontarget atoms it is 0.94(2). The average error per gate for both target and nontarget atoms is $13(7) \times 10^{-4}$.

The addressing pulse sequence for a pair of target atoms in two planes (Fig. 1C) consists of four stages (*15*). The qubit-resonant spin-echo pulses (Fig. 1C, black pulses on the microwave line) reverse the sign of the phase shifts, so that whatever phase shifts (ac Zeeman or ac Stark) a nontarget atom gets during the cross stages (Fig. 1C, stages 1 and 3) are exactly canceled by the shifts it gets during the dummy stages (Fig. 1C, stages 2 and 4), in which there is no cross atom. In contrast, the first target atom spends stage 1 as a cross, stage 3 as a spectator, and stages 2 and 4 as a line atom, and the second target atom spends stage 3 as a cross and stage 1 as a spectator. When the microwave frequency is chosen to be between the line and cross resonances, the change in the target atom's status from cross to line changes the sign of the ac Zeeman shift. Away from the resonances, the net phase shift for the target atoms is

$$\phi_{Target} \approx \frac{\Omega^2 T}{\delta - kf} - \frac{\Omega^2 T}{\delta - f} + \frac{\Omega^2 T}{\delta} - \frac{\Omega^2 T}{\delta - f} \quad (1)$$

where δ is the microwave detuning from the spectator resonance, *k* is the shift of cross atoms in units of *f* (*16*), Ω (typically 4 kHz) is the microwave Rabi frequency, and *T* is the pulse duration. Successive terms correspond to the integrated ac Zeeman shift on the first target atom during successive stages. The overall phase shift can be directly controlled by changing the power of the microwave field. The black curve in Fig. 1B shows the result of an exact

Downloaded from http://science.sciencemag.org/ on June 28, 2016

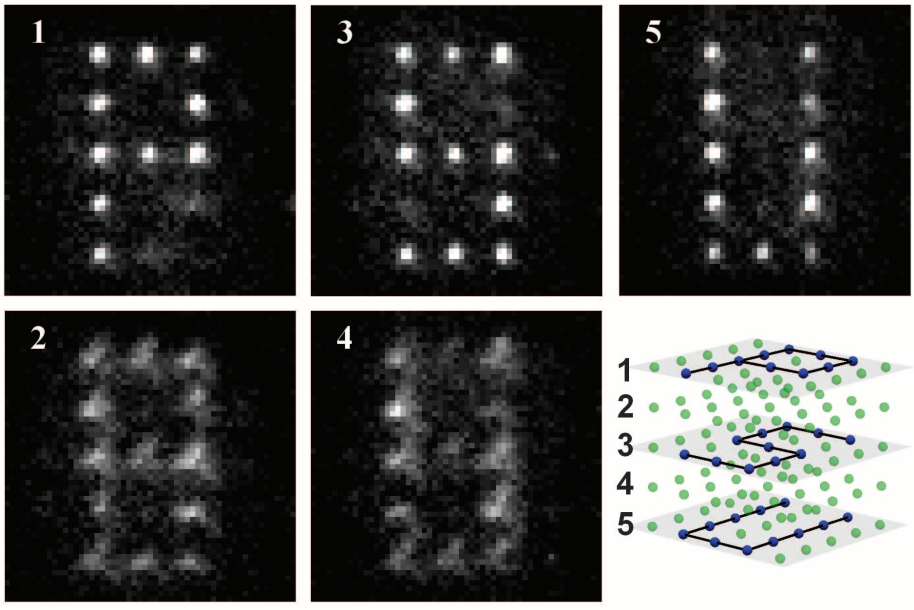


Fig. 3. $R_z(\pi)$ gates performed in a specific pattern. "1" to "5" are fluorescent images of five successive planes. Each image is the sum of 50 implementations. For clarity, the contrast is enhanced by using the same set of dark/bright thresholds on all pictures to account for the shot noise. There are no targeted sites in planes 2 and 4; the light collected there is from atoms in the adjacent planes. (Bottom right) Illustration marking the targeted sites in blue and the untargeted sites in green, with plane shading and blue lines to guide the eye.

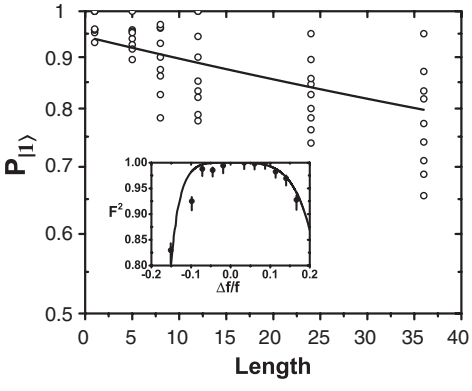


Fig. 4. Semi-log plot of fidelity from a randomized benchmarking sequence. We plot the probability of returning the two target atoms to $|1\rangle$ after a randomized benchmarking sequence versus the sequence length. At each length, we use three randomized CG sequences, each of which is combined with three sets of randomized PG sequences, for a total of nine points. Each data point is averaged over ~100 implementations. A least squares fit using the d_{if} = 0.1128(68) determined from the auxiliary RB measurement on nontarget atoms gives $\mathcal{E}_{2t} = (55 \pm 16) \times 10^{-4}$ (*16*). (**Inset**) Fidelity of an $R_z(\pi/2)$ gate as a function of the fractional change of the addressing ac Stark shift. The points are experimental data, and the curve is from the exact calculation.

calculation of the target atom's phase shift as a function of δ. The phase shift minimum at δ_0 = 74.9 kHz is the preferred operating point for the gate because in the vicinity of δ_0, the shift depends quadratically on the change in δ and thus also on the addressing beams, ac Stark shift, with the coefficient of 21 rad/$(\Delta f/f)^2$. For example, a 2% change in f gives an 8-mrad phase shift, which in turn leads to only a 1×10^{-4} gate error. Because the intensity changes quadratically with beam alignment, the gate is sensitive to beam-pointing only at fourth order.

The phase shift on target sites amounts to a rotation about the z axis [an $R_z(\theta)$ gate], but a universal single-qubit gate requires arbitrary rotations about any arbitrary axis. We can make an $R_y(\theta)$ gate by combining the $R_z(\theta)$ gate with global $R_x\left(\pm\frac{\pi}{2}\right)$ rotations

$$R_y(\theta) = R_x\left(-\frac{\pi}{2}\right)R_z(\theta)R_x\left(\frac{\pi}{2}\right) \qquad (2)$$

For nontarget atoms, which see the global microwave pulses but experience no $R_z(\theta)$, $R_x\left(-\frac{\pi}{2}\right)R_x\left(\frac{\pi}{2}\right)$ clearly has no net effect. It is straightforward to generalize this formula to obtain arbitrary rotations on a Bloch sphere for target atoms. The corresponding complete set of single-qubit gates on target atoms all leave the nontarget atoms unchanged.

We have demonstrated one $R_z(\pi/2)$ gate on a sequence of 48 randomly chosen sites (in 24 gate pairs) within a 5 by 5 by 5 array. Given the average initial site occupancy of ~40%, an average of 20 qubits experience the phase gate during each implementation, whereas 30 remain in their original quantum superposition. We probed the coherence of all the atoms by closing the spin echo sequence with a global π/2 pulse whose phase we scanned (Fig. 2). In Fig. 2, the open diamonds indicate nontarget atoms, and the solid circles indicate atoms at the 48 target sites. The corresponding curves are sinusoidal fits to the data. The dashed lines mark the maximum and minimum populations one expects given perfect gate fidelity, $\mathcal{F}^2$, defined as the square of the projection of the measured state onto the intended state, in the face of state preparation and measurement (SPAM) errors (*16*). From these curves, we determined that the error per gate pair, $\mathcal{E}_2$, is 25(13) × 10^{-4} for both target and nontarget atoms on average (numbers in parentheses indicate the 1 SD uncertainty in the final digits). At least for this particular gate, most of the error is clearly common to target and nontarget atoms. The good contrast of the target atom fringe illustrates the homogeneity of the phase shifts across the ensemble. The error per gate, $\mathcal{E}$, is thus 13(7) × 10^{-4} on average.

To graphically illustrate the flexibility of our gates, we have performed an $R_z(\pi)$ rotation on a 32-site pattern (Fig. 3). We rotated the superpositions of a sequence of pairs of target atoms from $\frac{1}{\sqrt{2}}(|0\rangle + |1\rangle)$ to $\frac{1}{\sqrt{2}}(|0\rangle - |1\rangle)$ and then used a π/2 detection pulse, phase-shifted by π, to return spectator atoms to $|0\rangle$ and target atoms to $|1\rangle$. Images from five planes summed over 50 implementations are shown in Fig. 3.

To confirm the robustness of this gate, we applied an $R_z(\pi/2)$ gate to 24 targets and measured the probability that atoms return to $|1\rangle$ after a π/2 pulse as a function of the fractional change in addressing beam intensity (Fig. 4, inset) (*16*). The data confirm the theoretical prediction (solid line) of extreme insensitivity to addressing beam intensity (Fig. 1B).

To fully characterize gate performance, we used the standard randomized benchmarking (RB) protocol (*25*), which has been used in nuclear magnetic resonance (*26*), quantum dots (*5*), ion systems (*27*), and neutral atoms systems (*6*, *28*, *29*). We implemented RB by choosing computation gates (CG) at random from $\left\{R_x\left(\pm\frac{\pi}{2}\right), R_y\left(\pm\frac{\pi}{2}\right)\right\}$ and Pauli gates (PG) at random from {$R_x(\pm\pi)$, $R_y(\pm\pi)$, $R_z(\pm\pi)$, I}, where I is the identity operation (*30*). After each randomized sequence, a detection gate is applied that in the absence of errors would return either the target qubits or the nontarget qubits to $|1\rangle$. For the targets, the average value of $\mathcal{F}^2$ decays exponentially with the length of the randomized sequence

$$\overline{\mathcal{F}^2} = \frac{1}{2} + \frac{1}{2}(1 - d_{if})(1 - 2\mathcal{E}_{2t})^l \qquad (3)$$

where $d_{if}/2$ is the SPAM error and l is the number of CG-PG operations applied to the pair of target atoms. A similar expression yields $\mathcal{E}_{2s}$ and $\mathcal{E}_{2l}$ for the spectator and line atoms, respectively—the unwanted changes wrought on the nontarget atoms when a random series of gates is executed on the

Downloaded from http://science.sciencemag.org/ on June 28, 2016

targets. In this way, we can characterize cross-talk and extract errors per gate from errors per gate pair. For target atoms, $\mathcal{E}_t = \mathcal{E}_{2t} - \mathcal{E}_s$; for spectator atoms, $\mathcal{E}_s = \mathcal{E}_{2s}/2$; and for line atoms, $\mathcal{E}_l = \mathcal{E}_{2l} - \mathcal{E}_s$.

First analyzing the nontarget data (fig. S2), we determined that $d_{if} = 0.11(1)$, $\mathcal{E}_s = 17(2) \times 10^{-4}$, and $\mathcal{E}_l = 46(9) \times 10^{-4}$. The cross-talk, defined as the average error per gate for nontarget atoms, is $\frac{107}{123}\mathcal{E}_s + \frac{16}{123}\mathcal{E}_l = 21(2) \times 10^{-4}$. Only global microwave pulse imperfections contribute to $\mathcal{E}_s$. Their contribution to $\mathcal{E}_l$ may differ because the microwave sequence is optimized for spectators. Spontaneous emission from the addressing beams adds to $\mathcal{E}_l$, with a calculable contribution of 8×10^{-4}. The RB data for the two target atoms are shown in Fig. 4. Using the d_{if} from the nontargets, the fit of Eq. 3 to the data yields $\mathcal{E}_t = 38(16) \times 10^{-4}$.

A summary of the errors for the target and nontarget atoms is shown in table S1. The errors can mostly be traced to microwave power stability (17×10^{-4} and 16×10^{-4}). We expect that reaching the state of the art (*2*, *27*), and perhaps tweaking our spin echo infrastructure (*31*) (fig. S1), can bring it below 10^{-4}. The next largest contribution is from the readily calculable spontaneous emission of addressing light (16×10^{-4} for target atoms). Its contribution is invariant with gate times because f must be changed inversely with gate time. Addressing with light between the D1 ($6S_{1/2} \rightarrow 6P_{1/2}$) and D2 ($6S_{1/2} \rightarrow 6P_{3/2}$) lines, as we do, locally minimizes spontaneous emission, but doubling the wavelength would further reduce spontaneous emission by a factor of 8 without dramatically compromising site-addressing. The required powerful addressing beams would exert a substantial force on line atoms, but deeper lattices and adiabatic addressing-beam turn-on would make the associated heating negligible. In our current experiment, we need to wait 70 μs after the addressing beams are turned on for our intensity lock to settle. Technical improvement there could halve the time the light is on, ultimately leaving the spontaneous emission contribution to the error just below 10^{-4} per gate. That limit is based on addressing with a differential light shift. It would disappear were the same basic scheme to be used on a three-level system, in which only one of the qubit states is strongly ac Stark–shifted by the addressing light. In that case, the phase-shifting microwaves (or light) would simply be off-resonant from the qubit transition, and the error caused by spontaneous emission would decrease proportional to the detuning. Because the dominant target errors have the same sources as the nontarget errors, improvements to the gate will correspondingly improve the cross-talk. Adapting this method to more common 1D and 2D geometries is straightforward. Only a single addressing beam is needed, and the dummy stages would be executed with half-intensity addressing beams. The same insensitivity to addressing beam power and alignment would follow.

Scalable addressing is an important step toward a scalable quantum computer. Future milestones that must be passed on the road to scalable neutral atom quantum computation include scalable addressing for two-qubit gates (*32*–*34*), reliable site filling (*19*), and the implementation of error correction (*7*).

REFERENCES AND NOTES

1. T. P. Harty *et al.*, *Phys. Rev. Lett.* **113**, 220501 (2014).
2. C. Piltz, T. Sriarunothai, A. F. Varón, C. Wunderlich, *Nat. Commun.* **5**, 4679 (2014).
3. A. C. Wilson *et al.*, *Nature* **512**, 57–60 (2014).
4. R. Barends *et al.*, *Nature* **508**, 500–503 (2014).
5. M. Veldhorst *et al.*, *Nat. Nanotechnol.* **9**, 981–985 (2014).
6. T. Xia *et al.*, *Phys. Rev. Lett.* **114**, 100503 (2015).
7. E. Knill, *Nature* **434**, 39–44 (2005).
8. A. M. Steane, *Phys. Rev. Lett.* **77**, 793–797 (1996).
9. J. Chiaverini *et al.*, *Nature* **432**, 602–605 (2004).
10. P. Schindler *et al.*, *Science* **332**, 1059–1061 (2011).
11. A. D. Córcoles *et al.*, *Nat. Commun.* **6**, 6979 (2015).
12. J. Benhelm, G. Kirchmair, C. F. Roos, R. Blatt, *Nat. Phys.* **4**, 463–466 (2008).
13. D. P. DiVincenzo, *Fortschr. Phys.* **48**, 771–783 (2000).
14. T. D. Ladd *et al.*, *Nature* **464**, 45–53 (2010).
15. Y. Wang, X. Zhang, T. A. Corcovilos, A. Kumar, D. S. Weiss, *Phys. Rev. Lett.* **115**, 043003 (2015).
16. Materials and methods are available as supplementary materials on *Science* Online.
17. C. Senko *et al.*, *Science* **345**, 430–433 (2014).
18. D. S. Weiss *et al.*, *Phys. Rev. A* **70**, 040302 (2004).
19. J. Vala *et al.*, *Phys. Rev. A* **71**, 032324 (2005).
20. C. Weitenberg *et al.*, *Nature* **471**, 319–324 (2011).
21. K. Lake *et al.*, *Phys. Rev. A* **91**, 012319 (2015).
22. K. D. Nelson, X. Li, D. S. Weiss, *Nat. Phys.* **3**, 556–560 (2007).
23. X. Li, T. A. Corcovilos, Y. Wang, D. S. Weiss, *Phys. Rev. Lett.* **108**, 103001 (2012).
24. C. Knoernschild *et al.*, *Appl. Phys. Lett.* **97**, 134101 (2010).
25. E. Knill *et al.*, *Phys. Rev. A* **77**, 012307 (2008).
26. C. A. Ryan, M. Laforest, R. Laflamme, *New J. Phys.* **11**, 013034 (2009).
27. K. R. Brown *et al.*, *Phys. Rev. A* **84**, 030303 (2011).
28. S. Olmschenk, R. Chicireanu, K. D. Nelson, J. V. Porto, *New J. Phys.* **12**, 113007 (2010).
29. J. H. Lee, E. Montano, I. H. Deutsch, P. S. Jessen, *Nat. Commun.* **4**, 2027 (2013).
30. S. Bravyi, A. Kitaev, *Phys. Rev. A* **71**, 022316 (2005).
31. A. M. Souza, G. A. Alvarez, D. Suter, *Philos. Trans. A Math Phys. Eng. Sci.* **370**, 4748 (2012).
32. K. M. Maller *et al.*, *Phys. Rev. A* **92**, 022336 (2015).
33. T. Keating *et al.*, *Phys. Rev. A* **91**, 012337 (2015).
34. T. Wilk *et al.*, *Phys. Rev. Lett.* **104**, 010502 (2010).
35. F. J. Harris, *Proc. IEEE* **66**, 51–83 (1978).

ACKNOWLEDGMENTS

This work was supported by the U.S. National Science Foundation grant PHY-1520976. The data presented in this report are available on request to D.S.W.

SUPPLEMENTARY MATERIALS

www.sciencemag.org/content/352/6293/1562/suppl/DC1
Materials and Methods
Figs. S1 to S3
Table S1
References (*36*–*39*)

14 January 2016; accepted 10 May 2016
10.1126/science.aaf2581

NANOMATERIALS

Polyelemental nanoparticle libraries

Peng-Cheng Chen,[1,2] Xiaolong Liu,[3] James L. Hedrick,[2,4] Zhuang Xie,[2,5] Shunzhi Wang,[2,5] Qing-Yuan Lin,[1,2] Mark C. Hersam,[1,3,5] Vinayak P. Dravid,[1,2] Chad A. Mirkin[1,2,4,5]*

Multimetallic nanoparticles are useful in many fields, yet there are no effective strategies for synthesizing libraries of such structures, in which architectures can be explored in a systematic and site-specific manner. The absence of these capabilities precludes the possibility of comprehensively exploring such systems. We present systematic studies of individual polyelemental particle systems, in which composition and size can be independently controlled and structure formation (alloy versus phase-separated state) can be understood. We made libraries consisting of every combination of five metallic elements (Au, Ag, Co, Cu, and Ni) through polymer nanoreactor–mediated synthesis. Important insight into the factors that lead to alloy formation and phase segregation at the nanoscale were obtained, and routes to libraries of nanostructures that cannot be made by conventional methods were developed.

Unary, binary, and even ternary nanostructures can be synthesized by incorporating up to three metals into a single nanoparticle (NP) in an alloyed or phase-segregated state with a variety of synthetic techniques (*1*–*9*). The controlled combination of multiple metals at the nanoscale offers an effective way to tune the chemical and physical properties of NPs, either (i) by facilitating hybrid chemical, electronic, and magnetic interactions between metal components (*2*, *3*, *10*, *11*); or (ii) by combining different properties associated with each pure component (*12*, *13*). These properties make multimetallic NPs promising materials for diverse applications, spanning catalysis (*2*, *3*, *10*, *14*–*16*), plasmonics (*11*, *17*), therapy (*12*), and biological imaging (*13*, *18*). Moreover, in the context of both catalysis and plasmonics, a multimetallic NP often has properties that exceed the capabilities of unary particles consisting of pure forms of each element (*2*, *3*, *14*–*17*).

To date, several tools have been developed for screening the composition space of macroscopic multicomponent materials. Notably, Mallouk *et al.* used ink-jet printing to prepare a combinatorial library of multimetallic catalysts that resulted in the discovery of a quaternary electrochemical catalyst (*19*). However, at the nanoscale, controlled synthesis and positioning of multimetallic nanofeatures become increasingly important for

[1]Department of Materials Science and Engineering, Northwestern University, Evanston, IL 60208, USA. [2]International Institute for Nanotechnology, Northwestern University, Evanston, IL 60208, USA. [3]Applied Physics Graduate Program, Northwestern University, Evanston, IL 60208, USA. [4]Department of Chemical and Biological Engineering, Northwestern University, Evanston, IL 60208, USA. [5]Department of Chemistry, Northwestern University, Evanston, IL 60208, USA.
***Corresponding author. Email: chadnano@northwestern.edu**

Downloaded from http://science.sciencemag.org/ on June 28, 2016

systematic study. In NP synthesis, important advances have been made in bulk solution–based (either one-pot or stepwise) (*5*–*7*), microfluidic (*8*), and microemulsion methods (*9*), but none of these offers the ability to systematically examine compositional diversity in a high-throughput manner or beyond three-element particles. In contrast, scanning-probe block copolymer lithography (SPBCL) (*20*–*23*), which can deliver attoliter-scale volumes of polymers with metal ion precursors to a desired location on a surface, can be used to generate nanoreactors, which upon thermal treatment can transform the precursors into individual site-isolated NPs. This method has proven useful for making bimetallic NPs (*22*, *23*) and even a single trimetallic alloy NP (*23*). Although this is an impressive demonstration of synthetic capabilities, such structures could also be made by other methods.

Because SPBCL can now be used with millions of tips over areas as large as square centimeters (*20*, *23*, *24*) to generate nanoscale features consisting of, in principle, a limitless number of polymer types, the technique could become a powerful approach to nanocombinatorics, in which new particle compositions, including those not accessible by conventional techniques, can be generated en masse and characterized and screened in a systematic and site-isolated fashion. To test this hypothesis, we investigated the combinatorial synthesis of particles consisting of five different elements, Au, Ag, Cu, Co, and Ni, via SPBCL. We showed that all combinations of the binary, ternary, quaternary, and quinary NPs could be independently synthesized by SPBCL and characterized by scanning transmission electron microscopy (STEM) and energy-dispersive x-ray spectroscopy (EDS).

We chose Au, Ag, Cu, Co, and Ni as example elements because they are often components of nanomaterials used in a wide variety of fields, spanning catalysis (*10*, *14*), plasmonics (*11*, *17*), magnetics (*25*), electronics (*26*), and biology (*12*, *13*). In addition, there are readily available salt precursors that can be easily incorporated into block copolymers such as poly(ethylene oxide)-*b*-poly(2-vinyl pyridine) (PEO-*b*-P2VP). To synthesize NPs composed of these elements, a polymer preloaded with the appropriate metal salt(s) was used as an ink and deposited onto a substrate as hemispherical domes via dip-pen nanolithography (DPN) (Fig. 1A) (*27*). After deposition, the polymer domes were thermally annealed in a two-step procedure. The first step was carried out in Ar at 120°C for 48 hours and induced aggregation of the metal salts within the polymer dome (*22*). The second step was carried out under flowing H_2 at 500°C for 12 hours, which results in decomposition of the polymer as well as reduction and coalescence of the aggregate metal ion precursors into a single-metal NP (*22*). Moreover, the long-term thermal treatment at relatively high temperature allows the constituent metals to adopt a stable configuration (alloy or phase-separated) based on the compatibility of the elements. This approach allows one to make and study all combinations of the unary, binary, ternary, quaternary, and quinary NPs in a systematic and controlled manner [Fig. 1, B to F, and figs. S1 to S4 (*28*)].

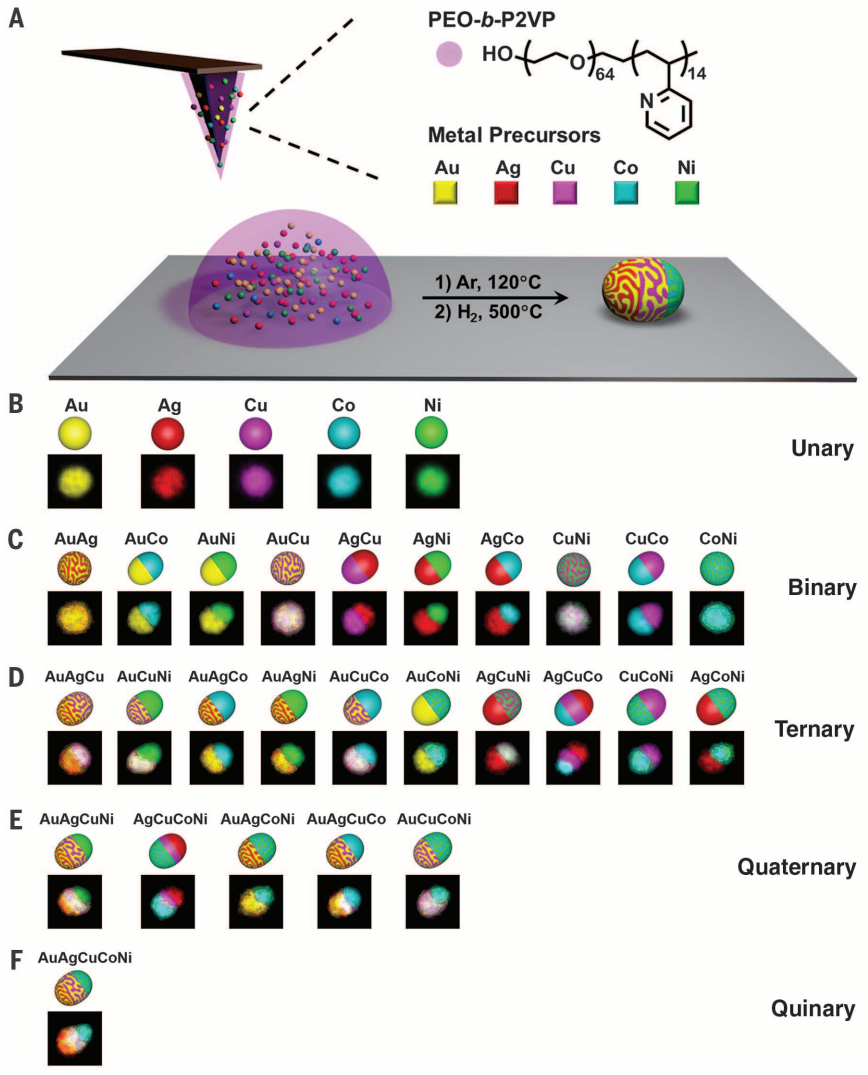


Fig. 1. The SPBCL-mediated synthesis of multimetallic NPs and a five-element library of unary and multimetallic NPs made via this technique. (**A**) Scheme depicting the process: A polymer loaded with metal ion precursor is deposited onto a substrate in the shape of a hemispherical dome via dip-pen nanolithography. After two-step thermal annealing, the metal precursors are aggregated and reduced, the polymer is decomposed, and individual NPs result from each dome feature. The interwoven patterns in the NP schemes are only meant to indicate the alloying of the elements and not the actual atomic structure. (**B**) Unary NPs (top row is a color-coded diagram of the anticipated result; bottom row is each particle, as characterized by EDS mapping). (**C**) Binary NPs consisting of every two-element combination of the five metals; the alloy versus phase-segregated state was consistent with the bulk phase diagrams for each two-element combination. (**D**) Ternary NPs consisting of every three-element combination of the five metals; the prediction of alloy versus phase-segregated state was based on the miscibility of the three components, extracted from the binary data. (**E**) Quaternary NPs consisting of every four-element combination of the five metals; the prediction of alloy versus phase-segregated state was based on the miscibility of the four components, extracted from the binary and ternary data. (**F**) A quinary NP consisting of a combination of Au, Ag, Cu, Co, and Ni; the prediction of alloy versus phase-segregated state was based on all of the previous data for the unary through quaternary systems.

To evaluate the capability of SPBCL to develop a combinatorial library of NPs, we first prepared the simplest structures, monometallic NPs, on TEM grids using ink solutions containing only one type of metal ion precursor. The resulting NPs were characterized by high-angle annular dark-field (HAADF) STEM and EDS. Fig. S1 (*28*) shows HAADF-STEM images of SPBCL-prepared Au, Ag, Cu, Co, and Ni NPs with diameters deliberately tailored to ~40 nm. The sizes of NPs were controlled by adjusting the volume and metal loading of the polymer nanoreactors, which

Downloaded from http://science.sciencemag.org/ on June 28, 2016

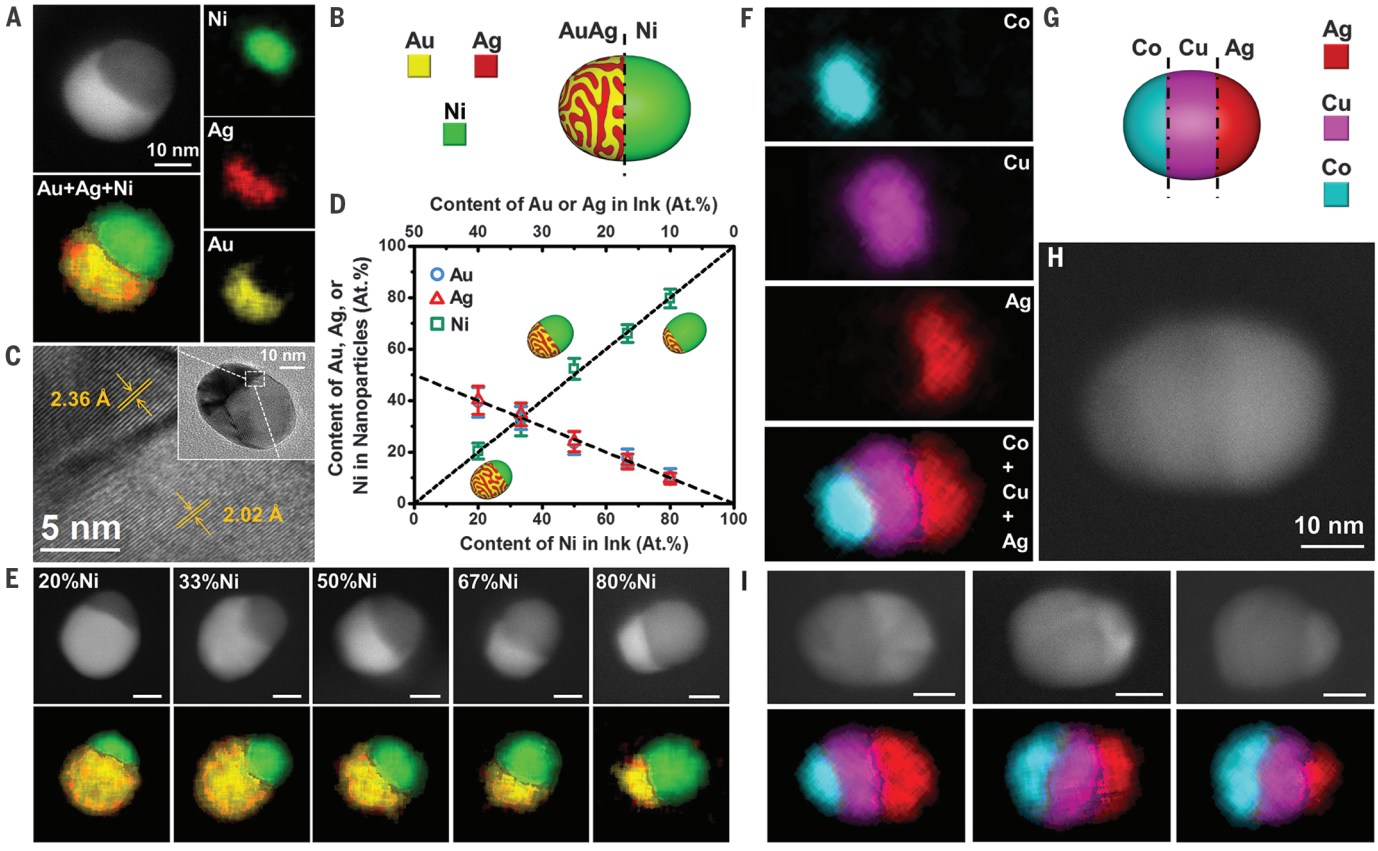


Fig. 2. AuAgNi and AgCuCo heterostructured NPs generated by SPBCL. (**A**) HAADF-STEM image and EDS elemental mapping, and (**B**) schematic illustration of a representative AuAgNi NP (24% Au, 24% Ag, 52% Ni). Au and Ag are miscible and both elements are immiscible with Ni, resulting in a heterodimer. (**C**) HR-TEM image of an AuAgNi NP. The observed lattice spacings near the interface are 2.36 and 2.02 Å (extracted from fast Fourier transform, fig. S5B), which closely match the AuAg alloy (111) and Ni (111) planes, respectively. (**D**) A comparison of the NP composition (20 to 60 nm) with the precursor ink composition. The dashed black line is the ideal 1:1 correlation case. (**E**) HAADF-STEM image and corresponding EDS mapping of AuAgNi NPs as a function of Ni content. Scale bars, 10 nm. (**F**) EDS elemental mapping, (**G**) schematic illustration, and (**H**) HAADF-STEM image of a representative AgCuCo NP (35% Ag, 38% Cu, 27% Co). The Ag, Cu, and Co are immiscible with each other, resulting in a heterotrimer. (**I**) Dark-field STEM images and EDS elemental mapping of AgCuCo NPs consisting of different compositions. From left to right, the content of Cu is approximately constant at 45% and the content of Ag is 39, 25, and 14%, respectively. Scale bars, 15 nm.

dictates the number of metal ions used for forming each NP (*20*–*22*). EDS analysis provides an effective way to reveal the chemical composition and elemental distribution of each NP product (Fig. 1B and fig. S1).

As part of the library, bimetallic NPs were accessed by equally loading two metal ion precursors into the polymer ink (Fig. 1C and fig. S2). Among the 10 binary combinations consisting of Au, Ag, Cu, Co, and Ni, four of them (AuAg, AuCu, CuNi, and CoNi) resulted in alloy NPs, as validated by the even contrast in HAADF-STEM images of NPs and the overlap of EDS element maps (Fig. 1C and fig. S2). In contrast, the other six combinations resulted in heterodimers, indicative of phase segregation in each binary mixture. The difference in contrast in the HAADF-STEM images of these heterostructured particles reflects the difference in atomic number between two metal domains, whereas EDS analysis confirms the separation of the majority of the elements that make up the NPs. Slight mixing between incompatible metals may still occur, but if so, it is below the detection limit of EDS. The orientation of phase boundaries in heterostructured NPs is random with respect to the substrate (i.e., the image plane). Here, particles with phase boundaries perpendicular to the substrate are used to clearly show the separation of metals. Although there is no reason to believe that nanostructures will necessarily follow the mixing behavior associated with bulk phase diagrams, the binary NPs we explored and prepared do (*23*, *29*). Because no one knows how three-, four-, and five-component particle systems will behave, it is important to build a library of nanostructures in successively more complex fashion, so that each layer of complexity can be used to understand the next series of entries (e.g., ternary structures).

The syntheses of ternary NPs via conventional methods are usually constrained by the difficulties in balancing the reduction kinetics of the different metal ion precursors (*1*, *30*), controlling the site-selective nucleation of each metal as opposed to forming multicomponent structures (*5*, *6*, *31*), and controlling phase separation at the nanoscale (*32*, *33*). However, trimetallic particles are easily accessible via SPBCL because this method preconfines precursor ions in a single nanoreactor and subsequently transforms them into a single particle, thus bypassing the issues involving precursor reduction potentials and element-specific nucleation. To evaluate the scope of this approach, we synthesized all of the ternary NPs consisting of every combination of Au, Ag, Cu, Co, and Ni. Although the study of binary particles shows the possibility of controlling particle structure based on metal compatibility, the combination of metal compatibility in ternary particles is more complicated, which includes four possible combination types. The first combination type (I) occurs when all three components are miscible with each other at any composition, which results in a single alloy particle (*23*). This combination type has been made before but was not observed in the library we generated. For the 10 ternary combinations of Au, Ag, Cu, Co, and Ni, the other combination types that occur are ones in which (II) two metals are miscible with each other but

Downloaded from http://science.sciencemag.org/ on June 28, 2016

the third is not with either, (III) all three metals are immiscible with each other, and (IV) two metals are immiscible and the other is miscible with the other two.

We first explored the combination of Au, Ag, and Ni (Fig. 2, A to E and figs. S5 to S9), which resulted in type II particles, in which the first two metals are miscible (Au and Ag) and the third one (Ni) is immiscible with the other two (*29*). We synthesized AuAgNi NPs on silicon substrates or on TEM grids using an ink solution with a metal loading ratio of 25% Au, 25% Ag, and 50% Ni. As shown by scanning electron microscopy (SEM) and HAADF-STEM images (figs. S5 and S6), arrays of AuAgNi NPs could be synthesized, and only one NP was observed in each position within the array. Increasing the magnification revealed that each AuAgNi NP was heterogeneously structured (Fig. 2, A and B, and fig. S6). Each AuAgNi NP was a dimeric heterostructure consisting of an AuAg alloy domain and a Ni domain. The contrast in the HAADF-STEM image arises from the difference in atomic number between the AuAg alloy and Ni. High-resolution TEM shows that the two domains in the AuAgNi NP are crystalline (Fig. 2C and fig. S5B). More than 10 million NPs were generated simultaneously over the centimeter scale by combining SPBCL with a large-area cantilever-free scanning probe technique such as polymer pen lithography (*24*) (fig. S8). Finally, in addition to AuAgNi, the other five ternary combinations that lead to type II particles are AuAgCo, AuCuCo, AuCoNi, AgCuNi, and AgCoNi (Fig. 1D and fig. S3).

One advantage of using SPBCL for generating NPs is the homogeneity of the patterned nanoreactor, which yields particles that have metallic constituent ratios reflecting those of the ink. This enables straightforward tuning of the particle composition (*23*). We used this ability to study the effect of altering metal ratios on the particle structure by examining five ink solutions (Fig. 2, D and E). The five solutions contained increasing Ni content from 20 to 80% while a 1:1 ratio of Au and Ag was maintained; the NPs were then investigated by EDS to determine elemental distribution and composition. As shown in Fig. 2E, the varying Ni content in the ink solution effectively changed the relative size of the Ni domains and AuAg alloy domains, respectively, while the dimeric heterostructure of AuAgNi NPs was maintained for all compositions studied. Experimentally, the majority of the AuAgNi NPs (yield, 80%; sample size, 50) matched the composition of the ink solutions, with a compositional variation of less than 10% (Fig. 2D and fig. S9). The remaining 20% of the NPs exhibited large composition fluctuations and even included bimetallic NPs (i.e., AuAg, AuNi, or AgNi), which is probably caused by the imperfect distribution of precursors in the ink solution. The formation of one NP per polymer reactor is crucial for this composition control. Indeed, attempts to synthesize NPs in a bulk polymer solution through a similar thermal annealing procedure resulted in heterogeneous mixtures of particles of varying size and composition (figs. S10 and S11), as is commonly observed in one-pot solution syntheses of multimetallic NPs, because different metal precursors exhibit different reduction kinetics and element-specific nucleation (*5*, *30*). In some polymer reactors (ones consisting of a features diameter >1 μm), failure of the atomic precursors to coalesce into a single NP was also observed, which prevented control over NP size and composition because of the formation of multiple particles (fig. S12).

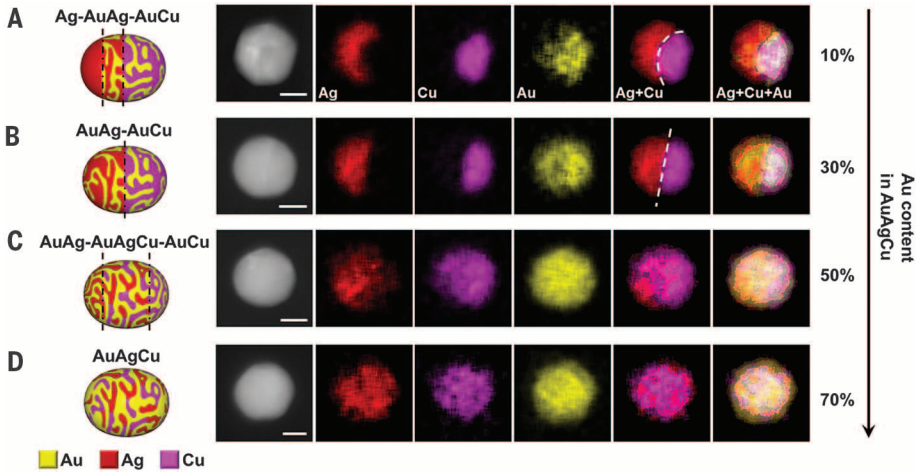


Fig. 3. AuAgCu heterostructured NPs. (**A** to **D**) Schematic illustration, HAADF-STEM images, and EDS elemental mapping of four representative AuAgCu NPs with different Au content. From (A) to (D), the Ag content and Cu content are equal in each NP and the Au content is 10, 30, 50, and 70%, respectively. The dashed white line in (A) and (B) indicates the position of the phase boundary. Scale bars, 20 nm.

In combination type III, the three constituent metals, such as Ag, Cu, and Co, are not miscible with each other, and trimeric heterostructures were expected. As a proof-of-concept experiment, we synthesized AgCuCo NPs using an ink solution with a metal loading of 33% for each metal. HAADF-STEM images along with EDS characterization confirm that Ag, Cu, and Co segregate into three segments in a AgCuCo NP (Fig. 2, F to H, and figs. S13 and S14), which is consistent with the compatibility of these metals (*29*). If the Cu content was kept constant while the relative loading ratio of Ag and Co in the ink solution was changed, the sizes of the Ag and Co domains, respectively, varied according to the ink formulation, but no apparent alloying of either two metals was observed for all compositions examined (Fig. 2I). In the case of all ink compositions studied, the three metal domains in the NPs shared a common structural feature: A central Cu domain is capped by an Ag or Co domain on each end. The phase boundaries between Ag-Cu and between Cu-Co are not always parallel, as evidenced by STEM and EDS (figs. S15 and S16). This structural motif for AgCuCo NPs suggests a higher interfacial energy between Ag and Co than the interfacial energy between Ag and Cu or between Cu and Co. Nevertheless, AgCuCo NPs with adjacent Ag-Co domains can be realized when the Cu content is <20%. Indeed, under these circumstances, the amount of Cu is not sufficient to completely segregate the Ag and Co domains (fig. S17).

For the final combination type, IV, two metals (Ag and Cu) are not miscible but the third one (Au) is miscible with the other two. Compared with the previous two types, the particle structure is more dependent on composition because of the increased complexity of interactions between the metals. To further show the advantage of SPBCL in studying composition-dependent phase separation in multimetallic NPs, we synthesized AuAgCu NPs using four ink formulations. The four solutions contained increasing Au content from 10 to 70% while the Ag and Cu contents were kept equal in each solution. The NPs obtained from these inks are shown in Fig. 3 and figs. S18 to S21. When the Au content in the NPs was only 10%, Ag and Cu phase-segregated into two domains (Fig. 3A and fig. S18). Experimentally, Au showed a higher affinity for Cu, as indicated by the enrichment of Au in the Cu domain. When the Au content was increased to 30%, Au diffused into the Ag domain, resulting in a Janus NP in which one part is an AuAg alloy and the other part is an AuCu alloy (Fig. 3B). Further increasing the Au content to 50% resulted in NPs without a distinct boundary between Ag and Cu (Fig. 3C). Instead, the Ag and Cu started to diffuse into each other's domains, indicating the formation of an intermediate region in the center that consists of an AuAgCu alloy. Finally, when the Au content was increased to 70%, Au was found throughout the entire NP structure and formed an alloy (Fig. 3D). In addition to AuAgCu, the other two ternary combinations that satisfy type IV are AuCuNi and CuCoNi. Similar to the AuAgCu system where Au shows preference for Cu over Ag, Cu had a higher affinity for Au than Ni in the AuCuNi system, and Ni had a higher affinity for Co than Cu in the CuCoNi system (Fig. 1D and fig. S3). Less noble metals such as Co, Ni, and Cu were readily reduced to a metallic state under an H_2 atmosphere under annealing conditions, as evidenced by XPS measurements (figs. S7, S14, and S21). Particles with these elements slowly oxidized upon exposure to air.

We further extended the library by synthesizing all quaternary combinations of Au, Ag, Cu, Co,

Downloaded from http://science.sciencemag.org/ on June 28, 2016

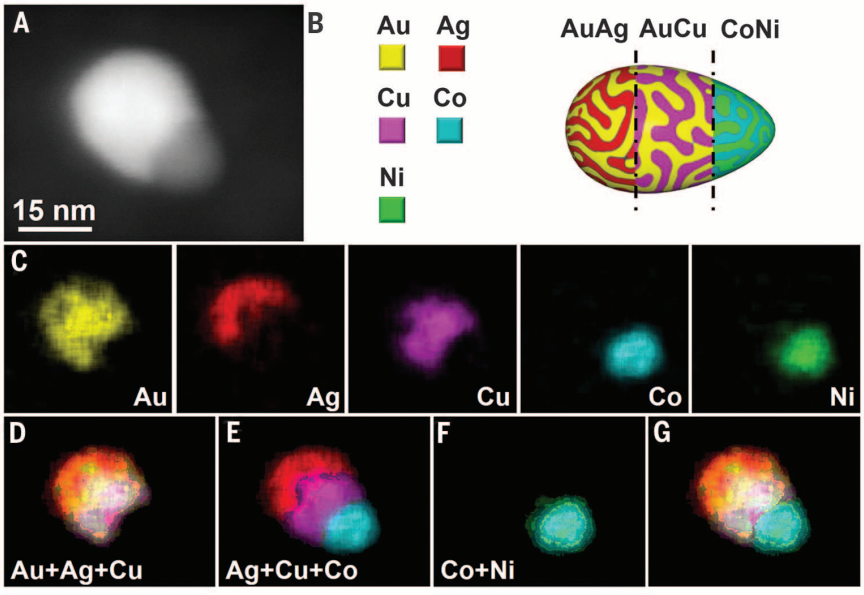


Fig. 4. Quinary heterostructured NPs. (**A**) HAADF-STEM image of a typical AuAgCuCoNi NP (19% Au, 24% Ag, 28% Cu, 14% Co, 15% Ni). (**B**) Schematic illustration of the structure of the AuAgCuCoNi NP in (A). The NP phase segregates into three domains: AuAg alloy, AuCu alloy, and CoNi alloy. (**C** to **G**) EDS elemental mapping of the AuAgCuCoNi NP in (A). (C) Distribution of each metal inside the NP. (D) Overlay of the element maps of Au, Ag, and Cu. (E) Overlay of the element maps of Ag, Cu, and Co. (F) Overlay of the element maps of Co and Ni. (G) Overlay of the element maps of all five metals.

and Ni. The structures of the quaternary NPs were highly dependent on particle composition. Here, we examined one specific ink composition for each combination of metals (Fig. 1E and fig. S4). The aforementioned studies on bimetallic and trimetallic systems are instructive for elucidating and assigning the structure of each quaternary NP. For example, the structure of the AuAgCoNi NP was assigned as an AuAgCo heterodimer primary particle and Ni as the fourth component. The location of the fourth component depends on its miscibility with the three components in the primary particle. Ni is miscible with Co but immiscible with Au and Ag. Thus, AuAgCoNi NPs still adopt a dimeric structure, with one part being an AuAg alloy and the other part a CoNi alloy. For the other quaternary particles synthesized, the structure can be similarly understood by the miscibility of components (fig. S4), which we previously described in the binary and ternary analysis. The incorporation of four components in one NP via SPBCL enables the creation of nanostructures with unprecedented compositional and structural complexity.

Creating combinatorial libraries with SPBCL even allowed for the synthesis of higher-order nanostructures, such as pentametallic NPs consisting of Au, Ag, Cu, Co and Ni, using an ink solution with an equal loading of the five ion precursors (Figs. 1F and 4 and fig. S4). Composition control was more difficult than with the lower-order NPs. Experimentally, we successfully formed quinary particles from half of the polymer reactors patterned by SPBCL (yield, 50%; sample size, 50; figs. S22 to S24). The remaining polymer reactors generated tetrametallic NPs. The AuAgCuCoNi NPs had three distinct structural domains (Fig. 4B and figs. S25 and S26). The overlay of EDS element maps revealed the distribution of metals and their spatial relationship. AgCuCo segregated into three domains, which formed the primary NP (Fig. 4E). Au was present in the Ag and Cu domains because it is compatible with Ag and Cu but immiscible with Co (Fig. 4D). Ni was only present in the Co domain because it phase-segregates from Au and has a higher affinity for Co than Cu (Fig. 4F). Therefore, AuAgCuCoNi NPs composed of three segments (i.e., an AuAg alloy, an AuCu alloy, and a CoNi alloy) were obtained via SPBCL (Fig. 4G). The structure of the AuAgCuCoNi NP was highly composition-dependent. Other substrates or annealing conditions may result in different particle structures, providing the potential for additional structure tuning. As such, this result validates SPBCL as a viable platform for synthesizing and studying previously undiscovered multimetallic NPs that are defined by fundamentally interesting and complex heterostructures.

The ability to synthesize and characterize such structures provides an experimental platform to study alloy formation and phase segregation at the nanoscale, which is important for understanding both structure and function. Given the enormous library of nanostructures that can be tailored based on particle composition and metal compatibility, this work advances the field of multimetallic NPs toward higher compositional diversity and structural complexity, which has the potential to affect a broad range of fields, such as catalysis (*10*, *14*, *19*), plasmonics (*11*, *17*), magnetics (*25*), electronics (*26*), biology (*13*, *18*), and medicine (*12*).

REFERENCES AND NOTES

1. M. R. Buck, R. E. Schaak, *Angew. Chem. Int. Ed.* **52**, 6154–6178 (2013).
2. C. Chen *et al.*, *Science* **343**, 1339–1343 (2014).
3. G. Chen *et al.*, *Science* **344**, 495–499 (2014).
4. L. Gan *et al.*, *Science* **346**, 1502–1506 (2014).
5. M. R. Buck, J. F. Bondi, R. E. Schaak, *Nat. Chem.* **4**, 37–44 (2011).
6. C. G. Read, T. R. Gordon, J. M. Hodges, R. E. Schaak, *J. Am. Chem. Soc.* **137**, 12514–12517 (2015).
7. W. Sang *et al.*, *Nano Lett.* **14**, 6666–6671 (2014).
8. Z. Nie, W. Li, M. Seo, S. Xu, E. Kumacheva, *J. Am. Chem. Soc.* **128**, 9408–9412 (2006).
9. A. K. Ganguli, A. Ganguly, S. Vaidya, *Chem. Soc. Rev.* **39**, 474–485 (2010).
10. C. George *et al.*, *Nano Lett.* **13**, 752–757 (2013).
11. A. Demortière *et al.*, *J. Am. Chem. Soc.* **136**, 2342–2350 (2014).
12. C. Xu, B. Wang, S. Sun, *J. Am. Chem. Soc.* **131**, 4216–4217 (2009).
13. I. Schick *et al.*, *J. Am. Chem. Soc.* **136**, 2473–2483 (2014).
14. J. C. Hill, A. T. Landers, J. A. Switzer, *Nat. Mater.* **14**, 1150–1155 (2015).
15. X. Huang *et al.*, *Science* **348**, 1230–1234 (2015).
16. L. Zhang *et al.*, *Science* **349**, 412–416 (2015).
17. M. B. Cortie, A. M. McDonagh, *Chem. Rev.* **111**, 3713–3735 (2011).
18. D. Rodriguez-Fernandez, J. Langer, M. Henriksen-Lacey, L. M. Liz-Marzan, *Chem. Mater.* **27**, 2540–2545 (2015).
19. E. Reddington *et al.*, *Science* **280**, 1735–1737 (1998).
20. J. Chai *et al.*, *Proc. Natl. Acad. Sci. U.S.A.* **107**, 20202–20206 (2010).
21. L. R. Giam *et al.*, *Nano Lett.* **12**, 1022–1025 (2012).
22. G. Liu *et al.*, *Proc. Natl. Acad. Sci. U.S.A.* **110**, 887–891 (2013).
23. P.-C. Chen *et al.*, *J. Am. Chem. Soc.* **137**, 9167–9173 (2015).
24. F. Huo *et al.*, *Science* **321**, 1658–1660 (2008).
25. H. Yu *et al.*, *Nano Lett.* **5**, 379–382 (2005).
26. T. Mokari, E. Rothenberg, I. Popov, R. Costi, U. Banin, *Science* **304**, 1787–1790 (2004).
27. R. D. Piner, J. Zhu, F. Xu, S. Hong, C. A. Mirkin, *Science* **283**, 661–663 (1999).
28. See the supplementary materials on *Science* Online.
29. P. Villars, H. Okamoto, K. Cenzual, Eds., ASM Alloy Phase Diagrams Database, http://www1.asminternational.org/AsmEnterprise/APD (ASM International, Materials Park, OH, 2006).
30. M. Sankar *et al.*, *Chem. Soc. Rev.* **41**, 8099–8139 (2012).
31. S. G. Kwon *et al.*, *Nat. Mater.* **14**, 215–223 (2015).
32. G. Guisbiers *et al.*, *Nano Lett.* **14**, 6718–6726 (2014).
33. F. Calvo, *Phys. Chem. Chem. Phys.* **17**, 27922–27939 (2015).

ACKNOWLEDGMENTS

This material is based on work supported by GlaxoSmithKline, the Air Force Office of Scientific Research (award FA9550-12-1-0141), and the Asian Office of Aerospace R&D (award FA2386-13-1-4124). The authors thank B. R. Meckes for helpful discussion. P.-C.C., S.W., and Q.-Y.L. gratefully acknowledge support from the Ryan Fellowship and the Northwestern University International Institute for Nanotechnology. X.L. and M.C.H. acknowledge support from the Materials Research Science and Engineering Center of Northwestern University (grant NSF DMR-1121262). V.P.D. acknowledges support by the Air Force Research Laboratory and the National Science Foundation under the Ceramics program. J.L.H. acknowledges support from the U.S. Department of Defense through the National Defense Science & Engineering Graduate Fellowship Program. This work made use of the EPIC facility of the NUANCE Center at Northwestern University, which has received support from the Soft and Hybrid Nanotechnology Experimental (SHyNE) Resource (NSF NNCI-1542205). A patent has been issued on this work: C. A. Mirkin, G. Liu, D. J. Eichelsdoerfer, K. A. Brown, "Method for synthesizing nanoparticles on surfaces" World Intellectual Property Organization Patent 2014039821-A1.

SUPPLEMENTARY MATERIALS

www.sciencemag.org/content/352/6293/1565/suppl/DC1
Materials and Methods
Figs. S1 to S26
Reference (*34*)

7 April 2016; accepted 20 May 2016
10.1126/science.aaf8402

Downloaded from http://science.sciencemag.org/ on June 28, 2016

NEURODEVELOPMENT

Reprogramming of avian neural crest axial identity and cell fate

Marcos Simoes-Costa[1,2] and Marianne E. Bronner[1]

Neural crest populations along the embryonic body axis of vertebrates differ in developmental potential and fate, so that only the cranial neural crest can contribute to the craniofacial skeleton in vivo. We explored the regulatory program that imbues the cranial crest with its specialized features. Using axial-level specific enhancers to isolate and perform genome-wide profiling of the cranial versus trunk neural crest in chick embryos, we identified and characterized regulatory relationships between a set of cranial-specific transcription factors. Introducing components of this circuit into neural crest cells of the trunk alters their identity and endows these cells with the ability to give rise to chondroblasts in vivo. Our results demonstrate that gene regulatory circuits that support the formation of particular neural crest derivatives may be used to reprogram specific neural crest–derived cell types.

Neural crest cells are characterized by their multipotency and migratory ability. During embryonic development, the neural crest differentiates into multiple cell types, including chondrocytes and osteocytes, melanocytes, and neurons and glia of the peripheral nervous system (*1*, *2*). Neural crest stem cells are retained postnatally in the skin and peripheral nerves, providing a potential target for replacement therapy in regenerative medicine (*3*, *4*). However, not all neural crest populations along the body axis are alike. Quail-chick grafting experiments demonstrated that the cranial and trunk neural crest differ in developmental potential: Whereas the cranial neural crest forms much of the craniofacial skeleton, the trunk crest fails to contribute to skeletal lineages, even when grafted in vivo to the head (*1*). Approaches for engineering and replacing specific cell types depend on a better understanding of the molecular mechanisms that underlie the establishment of specific cell types during embryonic development. We took advantage of differences in neural crest subpopulations (*1*, *5*–*7*) to identify the regulatory circuit that controls commitment of the cranial neural crest to a chondrocytic fate.

Expression of neural crest specifier genes such as *FoxD3* and *Sox10* is controlled by enhancers specific to particular axial levels, driving onset of their transcription in either the head or trunk neural crest but not both (*8*, *9*). The enhancers are activated by different inputs, suggesting that neural crest specification is driven by distinct genetic programs in different subpopulations (*2*, *9*). In order to identify the transcriptional program that endows the cranial neural crest with its ability to give rise to ectomesenchyme (the cartilage and bone of the face), we used the *FoxD3* enhancers *NC1* and *NC2* (*9*) (Fig. 1, A to C), active in the cranial and trunk neural crest, respectively, to isolate pure populations of neural crest cells for comparative transcriptional profiling. Embryos were electroporated with expression vectors driving green fluorescent protein (GFP) expression under the control of these enhancers, and early-migrating cranial and trunk neural crest cells were obtained by fluorescence-activated cell sorting (FACS) (*10*). RNA-seq analysis comparing these two populations identified 216 genes that were enriched in the cranial neural crest relative to the trunk (Fig. 1, D and E, and database S1), including 16 transcription factors (listed in Fig. 1F). We confirmed the expression of these regulators in the cranial neural crest by in situ hybridization; whereas six genes were expressed throughout the cranial neural crest (fig. S1, A to F), the remainder were detected in specific subsets of cells (fig. S1, G to L). Of these, we focused on the first group, which were expressed in all cranial neural crest cells, including Brain-Specific Homeobox Protein 3C (*Brn3c*), LIM Homeobox Protein 5 (*Lhx5*), Diencephalon/Mesencephalon Homeobox 1 (*Dmbx1*), Transcription Factor AP-2 Beta (*Tfap2b*), SRY Box 8 (*Sox8*), and the V-Ets Avian Erythroblastosis Virus E26 Oncogene Homolog 1 (*Ets1*).

Analysis of the spatiotemporal expression of these cranial-specific regulators demonstrated that *Brn3c*, *Lhx5*, and *Dmbx1* were first detected in the anterior regions of gastrula-stage embryos at Hamburger Hamilton stage 4 (HH4) and persisted through stages of neural crest specification (Fig. 2, A and E). These early cranial-specific genes were down-regulated after the neural crest delaminated from the neural tube. The onset of *Tfap2b*, *Sox8*, and *Ets1* expression was observed later at HH7 and HH8, in neural crest progenitors residing within the cranial neural folds (Fig. 2, B and E). These genes were maintained in the migratory neural crest cells during later stages of development (HH10 to 14; Fig. 2, B and E). Co-localization of neural plate border markers *Msh Homeobox 1* (*Msx1*) or *Paired Box* 7 (*Pax7*) with

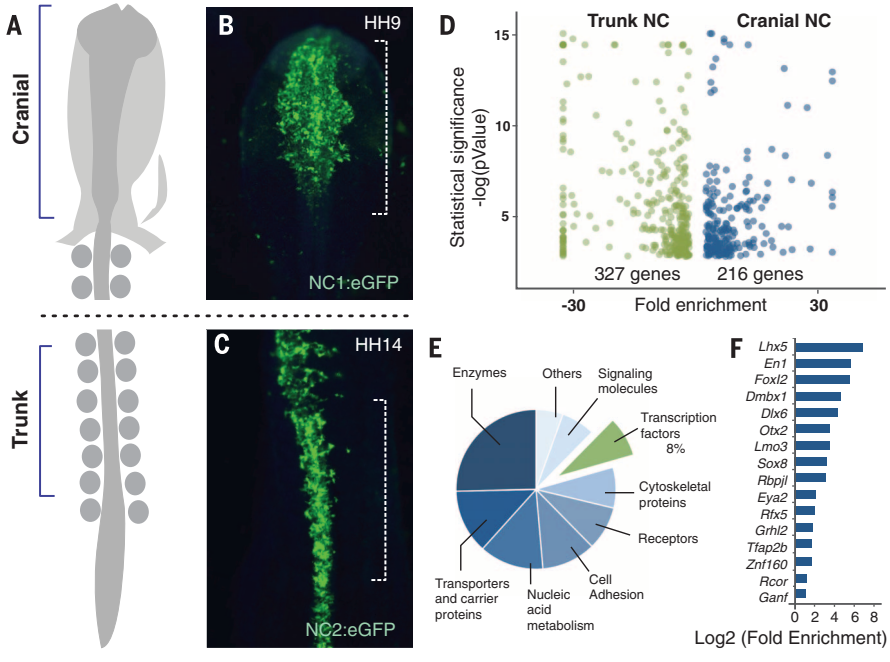


Fig. 1. Identification of cranial-specific regulators by comparative transcriptomics. (**A**) Diagram depicting dorsal view of chick embryo. (**B** and **C**) Embryos electroporated with *FoxD3* axial-specific enhancers *NC1* and *NC2*, active in cranial and trunk neural crest (NC), respectively. (**D**) Comparative transcriptome analysis of FACS-sorted cranial and trunk neural crest populations identified 216 cranially enriched genes. (**E**) Summary of gene ontology analysis for the cranial-enriched genes. (**F**) Enrichment levels of transcription factors expressed in the cranial neural crest.

[1]Division of Biology and Biological Engineering, California Institute of Technology, Pasadena, CA 91125, USA.
[2]Department of Molecular Biology and Genetics, Cornell University, Ithaca, NY 14853-2703, USA.
*Corresponding author. Email: mbronner@caltech.edu

Downloaded from http://science.sciencemag.org/ on June 28, 2016

Brn3c, *Lhx5*, and *Dmbx1* showed that the latter are expressed by an anterior subset of the neural crest progenitors (Fig. 2C). To verify that the cranial regulators mark the territory that contains cranial neural crest precursors, we analyzed the fate map of the neural plate border at the three-somite stage, using focal injections of a vital lipophilic dye (CM-DiI) to label cells along the anterior-posterior axis. The injected embryos were cultured until the 12-somite stage (HH11-), when the labeled cellular progeny were scored with respect to their fate as cranial or vagal/trunk neural crest cells. The results show that the domain of expression of the early regulators (*Brn3c*, *Lhx5*, and *Dmbx1*) demarcates the territory that contains the progenitors of the cranial neural crest in the early neurula (HH8-) (Fig. 2D).

We asked whether cranial-specific regulators are part of a transcriptional circuit that underlies cranial identity by knocking down each regulator individually and assaying for changes in expression levels of the other five genes. This was done via bilateral electroporations (*11*), with control transfections on the left side and function-blocking morpholinos or dominant negative constructs on the right side of the same embryo (Fig. 3, A to D). Transfected embryos were analyzed by in situ hybridization (Fig. 3, A to H) and quantitative polymerase chain reaction (qPCR) (Fig. 3I) for effects on putative targets; loss of the target gene in the experimental side of the embryo indicated the existence of a regulatory link between the two transcription factors. The diagram in Fig. 3J contains interactions confirmed by both qPCR and in situ hybridization. Morpholino knockdown efficiency was validated by in vivo translation-blocking assays (fig. S2).

By testing 25 putative regulatory links, we found that the early and late cranial-specific genes constitute different hierarchical levels of a gene regulatory network (Fig. 3J). *Brn3c*, which is placed at the top of the circuit, is necessary for

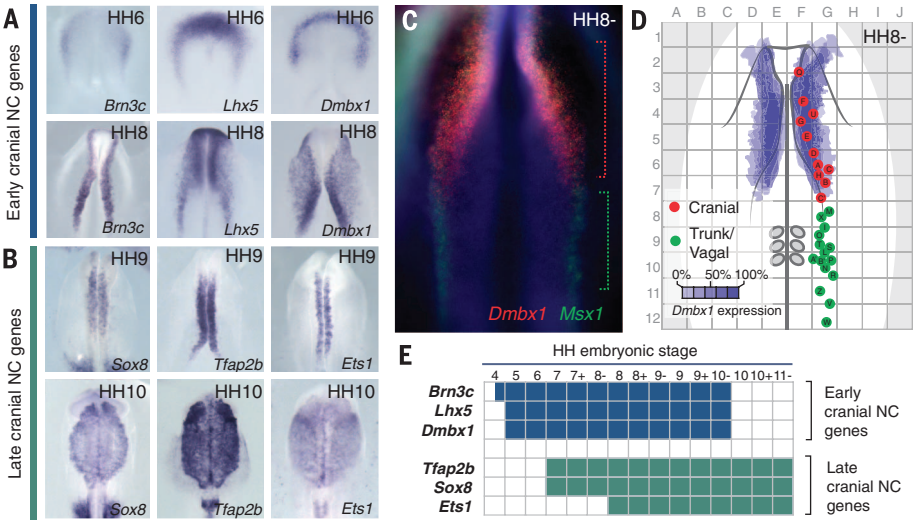


Fig. 2. Spatial and temporal expression of cranial neural crest transcription factors. (**A** and **B**) Dorsal views of embryos after in situ hybridization for cranial neural crest–specific transcription factors reveals expression at early (A) or later (B) stages. (**C**) Double in situ hybridization reveals that cranial regulator *Dmbx1* is expressed in the anterior neural plate border, whereas *Msx1* is expressed along the entire neural axis. (**D**) Fate map of neural crest progenitors (red and green dots) at stage HH8- confirms cranial specific expression of *Dmbx1* (purple). (**E**) Diagram summarizing the timing of the expression of early and late cranial regulators.

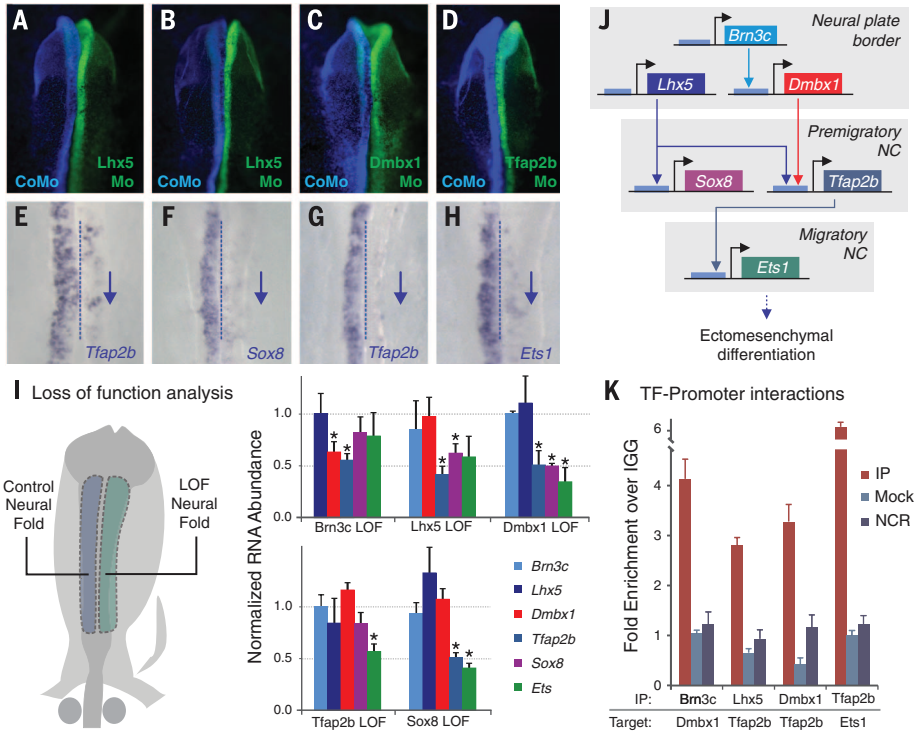


Fig. 3. Cranial-specific transcriptional circuit underlying neural crest axial identity. (**A** to **D**) Whole-mount dorsal views of embryos after morpholino (Mo) targeted to the indicated transcription factor was transfected to the right side (green) and control morpholino (CoMo) to the left side (blue) of each embryo. (**E** to **H**) Same embryos as above after in situ hybridization for the indicated downstream transcription factor; blue arrows indicate transcript down-regulation. (**I**) Comparing control to loss-of-function (LOF) neural folds by qPCR reveals differential regulation of downstream targets with significant changes indicated by an asterisk (Student's *t* test, $P < 0.05$). (**J**) Diagram summarizing cranial-specific gene regulatory circuit delineated by functional assays. (**K**) ChIP demonstrates direct association of cranial specific transcription factors with promoters of their downstream targets. No enrichment was observed for intergenic negative control regions (NCRs) or when the procedure was performed with mock-transfected embryos (see materials and methods for more information). IGG, immunoglobulin G. Error bars in (I) and (K) represent standard deviation.

Downloaded from http://science.sciencemag.org/ on June 28, 2016

the activation of *Dmbx1* in the anterior neural plate border (Fig. 3I and fig. S3). Subsequently, *Lhx5* and *Dmbx1* drive expression of *Tfap2b* and *Sox8* in the dorsal neural folds (Fig. 3, A to C, E to G, and I). Finally, *Tfap2b* activates expression of *Ets1* as the neural crest becomes specified (Fig. 3, D, H, and I). Chromatin immunoprecipitation (ChIP) experiments performed in microdissected neural crest cells showed the association of the cranial-specific transcription factors with promoters of predicted downstream target genes, suggesting that these regulatory links are direct (Fig. 3K and fig. S4).

Sox8, *Tfap2b*, and *Ets1* are all retained in the migrating cranial crest cells as they move ventrally to give rise to the facial mesenchyme during stages HH10 to 14. To investigate whether these genes play a role in the differentiation of neural crest cells into chondroblasts, we assayed the effects of disrupting the terminal module of the circuit on the expression of markers of chondrocytic differentiation. We found that *Ets1* was required for the expression of *ALX Homeobox 1* (*Alx1*, also known as *Cartilage Paired-Class Homeoprotein 1*) in the facial mesenchyme (fig. S5), indicating a link between cranial identity and chondrocytic differentiation. Thus, cranial-specific regulators are part of a transcriptional circuit that conveys regulatory information from the anterior neural plate border to the late migratory neural crest.

To test whether this cranial-specific regulatory circuit could be used to manipulate neural crest identity, we employed neural crest axial-specific enhancers as reporters of axial level identity. We electroporated expression constructs in the trunk neural tube of stage HH10 embryos, and found that transfection of the late cranial-specific factors (*Sox8*, *Tfap2b*, and *Ets1*) robustly activated the cranial enhancer *Sox10E2* (*9*, *11*) in the trunk neural crest [n = 15 out of 15 (15/15) embryos] (Fig. 4, A to E), consistent with a shift from trunk to cranial identity. Other axial-specific enhancers were similarly affected; trunk-specific enhancers *NC2* and *Sox10E1* were repressed after electroporation of the late factors (fig. S6). Early cranial-specific factors (*Brn3c*, *Lhx5*, and *Dmbx1*), or individual late factors, were unable to activate cranial enhancers in the trunk. To identify changes in the regulatory state of the reprogrammed trunk neural crest, we isolated transfected cells by FACS and analyzed their expression profile by qPCR, focusing on transcription factors involved in craniofacial differentiation. The results revealed elevated expression of chondrocytic genes *Runt-Related Transcription Factor 2 (Runx2)* and *Alx1*, in the trunk *Sox10E2*$^+$ cells as compared with native trunk crest (Fig. 4F). The reprogrammed trunk *Sox10E2*$^+$ cells also displayed a loss of genes enriched in the trunk neural crest, such as *Developing Brain Homeobox 1 (Dbx2)* and *Hairy And Enhancer Of Split 6 (Hes6)* (Fig. 4G). This confirmed that the reprogrammed cells adopt a cranial-like expression profile, and raised the possibility that these cells might display augmented chondrocytic potential.

Finally, we tested whether this cranial neural crest circuit could reprogram not only enhancer activity and expression of axial-specific neural crest genes, but also cell fate, so that reprogrammed trunk neural crest cells could differentiate into craniofacial cartilage. We cotransfected three constructs encoding late transcription factors *Sox8*, *Tfap2b*, and *Ets1* into the posterior epiblast of HH5 chicken embryos transgenic for GFP by electroporating DNA in the region posterior to the Hensen's node. The GFP$^+$ trunk neural folds then were microdissected at HH11 and immediately transplanted to the cranial regions of HH9 wild-type chick embryos (fig. S7). The grafted embryos were incubated until host embryonic day 7 (E7), by which time endogenous cartilage cells have differentiated. The fate of donor tissue was assayed using markers for neuronal, melanocytic, and chondrocytic differentiation. By E7, wild-type (host) and reprogrammed (donor) trunk neural crest migrated to the proximal part of the jaw. As observed with chick-quail chimeras (*5*–*7*), we found that wild-type or mock-transfected trunk neural crest cells grafted into the cephalic region gave rise to neurons and melanocytes but were unable to differentiate into chondroblasts (n = 0/5 embryos) (Fig. 4, H

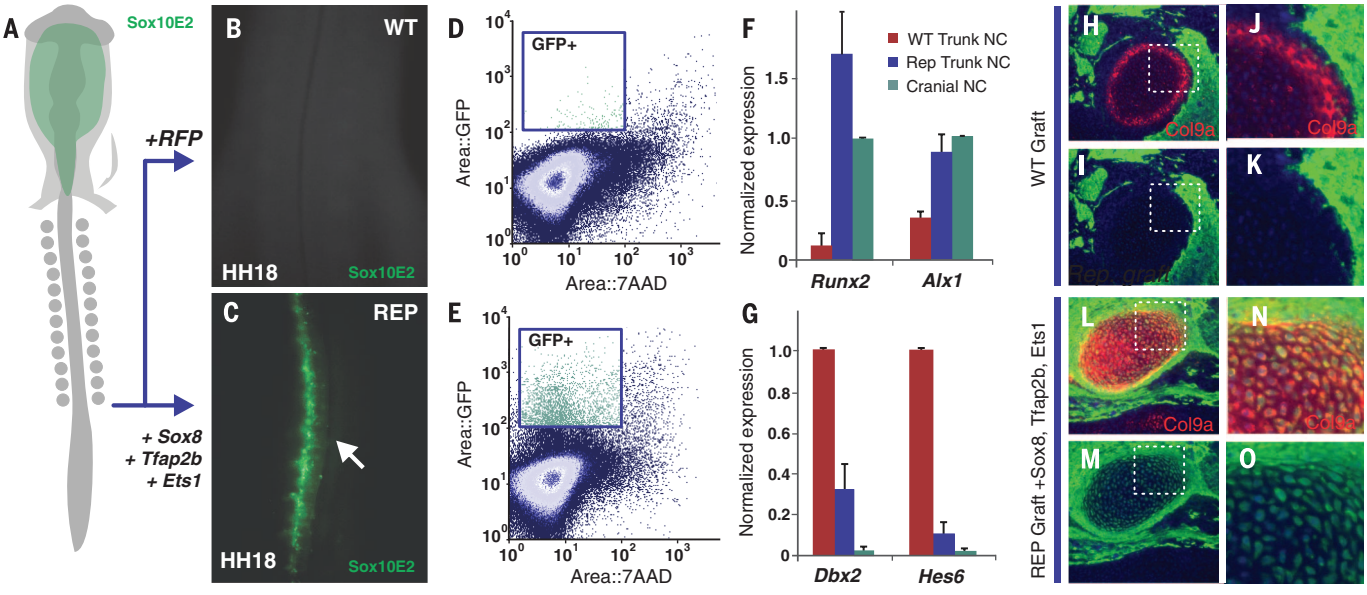


Fig. 4. Reprogramming of neural crest axial identity and fate. (**A**) Diagram of chick embryo electroporated with the *Sox10E2* enhancer, active only in migrating cranial neural crest. (**B**) Transfection of trunk neural crest cells with a control RFP expression vector shows no *Sox10E2* activity. (**C**) Reprogramming of trunk neural crest cells with cranial-specific regulators *Sox8*, *Tfap2b*, and *Ets1* results in robust activity of the cranial *Sox10E2* enhancer in the trunk region (n = 15/15 embryos). (**D** and **E**) Flow cytometry analysis of dissociated embryonic trunks shows a large number of *Sox10E2*$^+$ trunk neural crest cells after reprogramming. (**F** and **G**) Reprogrammed (Rep) trunk neural crest display increased expression of the chondrocytic genes *Runx2* and *Alx1*, whereas trunk genes *Dbx2* and *Hes6* are strongly down-regulated. Error bars represent standard deviation. (**H** and **I**) Histological sections of E7 embryonic heads show that wild-type (WT) trunk neural crest cells (GFP$^+$, green) fail to form cartilage (Col9a$^+$, red) after transplantation to the cranial region (n = 0/5 embryos). (**J** and **K**) Inset of (H) and (I), showing the absence of GFP$^+$ chondrocytes. (**L** and **M**) Reprogrammed trunk neural crest cells (expressing *Sox8*, *Tfap2b*, and *Ets1*) from GFP donor embryos transplanted to the head form ectopic cartilage nodules. (**N** and **O**) Inset of (L) and (M), showing chondrocytes derived from trunk neural crest cells (GFP$^+$ and Col9a$^+$).

Downloaded from http://science.sciencemag.org/ on June 28, 2016

to K). The same result was observed with trunk neural crest transfected with the early cranial-specific factors (n = 0/6 embryos). Reprogrammed trunk neural crest, however, acquired chondrogenic potential and formed ectopic cartilage nodules (n = 4/7 embryos) (Fig. 4, L to O) in the proximal jaw. Thus, introducing components of the cranial-specific transcriptional circuit is sufficient to reprogram trunk neural crest cells and to drive them to adopt an additional cartilaginous fate. These results definitively show that the cranial-specific regulatory circuit (Fig. 3J) we have defined confers chondrocytic potential to the trunk neural crest.

The development and differentiation of neural crest cells are controlled by a complex gene regulatory network, composed of transcription factors, signaling molecules, and epigenetic modifiers (*12*, *13*). We have expanded the known cranial neural crest gene regulatory network by identifying transcriptional interactions specific to the cranial crest and absent from other subpopulations. By linking anterior identity in the gastrula to the expression of drivers of chondrocytic differentiation, we have identified a cranial-specific circuit (Fig. 3J) that endows the neural crest with its potential to differentiate into the craniofacial skeleton of vertebrates. Our results highlight how transcriptional circuits can be rewired to alter progenitor cell identity and fate during embryonic development.

REFERENCES AND NOTES

1. N. Le Douarin, *The Neural Crest* (Cambridge Univ. Press, 1982).
2. M. Simões-Costa, M. E. Bronner, *Genome Res.* **23**, 1069–1080 (2013).
3. T. Uesaka, M. Nagashimada, H. Enomoto, *J. Neurosci.* **35**, 9879–9888 (2015).
4. V. Dyachuk *et al*., *Science* **345**, 82–87 (2014).
5. C. S. Le Lièvre, N. M. Le Douarin, *J. Embryol. Exp. Morphol.* **34**, 125–154 (1975).
6. C. S. Le Lievre, G. G. Schweizer, C. M. Ziller, N. M. Le Douarin, *Dev. Biol.* **77**, 362–378 (1980).
7. P. Y. Lwigale, G. W. Conrad, M. Bronner-Fraser, *Development* **131**, 1979–1991 (2004).
8. P. Betancur, M. Bronner-Fraser, T. Sauka-Spengler, *Proc. Natl. Acad. Sci. U.S.A.* **107**, 3570–3575 (2010).
9. M. S. Simões-Costa, S. J. McKeown, J. Tan-Cabugao, T. Sauka-Spengler, M. E. Bronner, *PLOS Genet.* **8**, e1003142 (2012).
10. M. Simões-Costa, J. Tan-Cabugao, I. Antoshechkin, T. Sauka-Spengler, M. E. Bronner, *Genome Res.* **24**, 281–290 (2014).
11. M. Simões-Costa, M. Stone, M. E. Bronner, *Dev. Cell* **34**, 544–554 (2015).
12. M. Simões-Costa, M. E. Bronner, *Development* **142**, 242–257 (2015).
13. S. A. Green, M. Simoes-Costa, M. E. Bronner, *Nature* **520**, 474–482 (2015).

ACKNOWLEDGMENTS

We thank J. Tan-Cabugao, M. Stone, B. Jun, and D. S. E. Koo for technical assistance. The Caltech Millard and Muriel Jacobs Genetics and Genomics Laboratory provided sequencing and bioinformatics support. We are indebted to D. Perez, K. Beadle, and R. Diamond for cell-sorting assistance at the Caltech Flow Cytometry Cell Sorting Facility. We also thank M. Barembaum for the Sox8 and Tfap2b expression constructs. This work was supported by NIH grants DE024157 and HD037105 to M.E.B. M.S.-C. was funded by a fellowship from the Pew Fellows Program in Biomedical Sciences and by NIH grant K99DE024232. The supplementary materials contain additional data.

SUPPLEMENTARY MATERIALS

www.sciencemag.org/content/352/6293/1570/suppl/DC1
Materials and Methods
Figs. S1 to S7
References (*14*–*26*)
Database S1

18 January 2016; accepted 23 May 2016
10.1126/science.aaf2729

ETHICS

The social dilemma of autonomous vehicles

Jean-François Bonnefon,[1] Azim Shariff,[2]* Iyad Rahwan[3]†

Autonomous vehicles (AVs) should reduce traffic accidents, but they will sometimes have to choose between two evils, such as running over pedestrians or sacrificing themselves and their passenger to save the pedestrians. Defining the algorithms that will help AVs make these moral decisions is a formidable challenge. We found that participants in six Amazon Mechanical Turk studies approved of utilitarian AVs (that is, AVs that sacrifice their passengers for the greater good) and would like others to buy them, but they would themselves prefer to ride in AVs that protect their passengers at all costs. The study participants disapprove of enforcing utilitarian regulations for AVs and would be less willing to buy such an AV. Accordingly, regulating for utilitarian algorithms may paradoxically increase casualties by postponing the adoption of a safer technology.

The year 2007 saw the completion of the first benchmark test for autonomous driving in realistic urban environments (*1*, *2*). Since then, autonomous vehicles (AVs) such as Google's self-driving car covered thousands of miles of real-road driving (*3*). AVs have the potential to benefit the world by increasing traffic efficiency (*4*), reducing pollution (*5*), and eliminating up to 90% of traffic accidents (*6*). Not all crashes will be avoided, though, and some crashes will require AVs to make difficult ethical decisions in cases that involve unavoidable harm (*7*). For example, the AV may avoid harming several pedestrians by swerving and sacrificing a passerby, or the AV may be faced with the choice of sacrificing its own passenger to save one or more pedestrians (Fig. 1).

Although these scenarios appear unlikely, even low-probability events are bound to occur with millions of AVs on the road. Moreover, even if these situations were never to arise, AV programming must still include decision rules about what to do in such hypothetical situations. Thus, these types of decisions need be made well before AVs become a global commodity. Distributing harm is a decision that is universally considered to fall within the moral domain (*8*, *9*). Accordingly, the algorithms that control AVs will need to embed moral principles guiding their decisions in situations of unavoidable harm (*10*). Manufacturers and regulators will need to accomplish three potentially incompatible objectives: being consistent, not causing public outrage, and not discouraging buyers.

However, pursuing these objectives may lead to moral inconsistencies. Consider, for example, the case displayed in Fig. 1A, and assume that the most common moral attitude is that the AV should swerve. This would fit a utilitarian moral doctrine (*11*), according to which the moral course of action is to minimize casualties. But consider then the case displayed in Fig. 1C. The utilitarian course of action, in that situation, would be for the AV to swerve and kill its passenger, but AVs programmed to follow this course of action might discourage buyers who believe their own safety should trump other considerations. Even though such situations may be exceedingly rare, their emotional saliency is likely to give them broad public exposure and a disproportionate weight in individual and public decisions about AVs. To align moral algorithms with human values, we must start a collective discussion about the ethics of AVs—that is, the moral algorithms that we are willing to accept as citizens and to be subjected to as car owners. Thus, we initiate the data-driven study of driverless car ethics, inspired by the methods of experimental ethics (*12*).

We conducted six online surveys (n = 1928 total participants) between June and November 2015. All studies were programmed on Qualtrics survey software and recruited participants (U.S. residents only) from the Amazon Mechanical Turk (MTurk) platform, for a compensation of 25 cents each. Studies described in the experimental ethics literature largely rely on MTurk respondents, with robust results, even though MTurk respondents are not necessarily representative of the U.S. population (*13*, *14*). A possible concern with MTurk studies is that some participants may already be familiar with testing materials, particularly when these materials are used by many research groups. However, this concern does not apply to our testing materials, which have never been used in a published MTurk study to date.

In all studies, participants provided basic demographic information. Regression analyses (see supplementary materials) showed that enthusiasm for self-driving cars was consistently greater for younger, male participants. Accordingly, all subsequent analyses included age and sex as covariates. The last item in every study was an easy question (e.g., how many pedestrians were on the

[1]Toulouse School of Economics, Institute for Advanced Study in Toulouse, Center for Research in Management, CNRS, University of Toulouse Capitole, Toulouse, France. [2]Department of Psychology, University of Oregon, Eugene, OR 97403, USA. [3]The Media Lab, Massachusetts Institute of Technology, Cambridge, MA 02139, USA.
*Present address: Department of Psychology and Social Behavior, 4201 Social and Behavioral Sciences Gateway, University of California, Irvine, Irvine, CA 92697, USA. †**Corresponding author. Email: irahwan@mit.edu**

Downloaded from http://science.sciencemag.org/ on June 28, 2016

road) relative to the traffic situation that participants had just considered. Participants who failed this attention check (typically 10% of the sample) were discarded from subsequent analyses.

Detailed statistical results for all studies are provided in the supplementary materials (tables S1 to S8). Overall, participants strongly agreed that it would be more moral for AVs to sacrifice their own passengers when this sacrifice would save a greater number of lives overall.

In study one (n = 182 participants), 76% of participants thought that it would be more moral for AVs to sacrifice one passenger rather than kill 10 pedestrians [with a 95% confidence interval (CI) of 69 to 82]. These same participants were later asked to rate which was the most moral way to program AVs, on a scale from 0 (protect the passenger at all costs) to 100 (minimize the number of casualties). They overwhelmingly expressed a moral preference for utilitarian AVs programmed to minimize the number of casualties (median = 85) (Fig. 2A). However, participants were less certain that AVs would be programmed in a utilitarian manner (67% thought so, with a median rating of 70). Thus, participants were not worried about AVs being too utilitarian, as often portrayed in science-fiction works. If anything, they imagined future AVs as being less utilitarian than they should be.

In study two (n = 451 participants), participants were presented with dilemmas that varied the number of pedestrians' lives that could be saved, from 1 to 100. Participants did not think that AVs should sacrifice their passenger when only one pedestrian could be saved (with an average approval rate of 23%), but their moral approval increased with the number of lives that could be saved (P < 0.001), up to approval rates consistent with the 76% observed in study one (Fig. 2B).

Participants' approval of passenger sacrifice was even robust to treatments in which they had to imagine themselves and another person, particularly a family member, in the AV (study three, n = 259 participants). Imagining that a family member was in the AV negatively affected the morality of the sacrifice, as compared with imagining oneself alone in the AV (P = 0.003). But even in that strongly aversive situation, the morality of the sacrifice was still rated above the midpoint of the scale, with a 95% CI of 54 to 66 (Fig. 3A).

Still, study three presents the first hint of a social dilemma. On a scale of 1 to 100, respondents were asked to indicate how likely they would be to buy an AV programmed to minimize casualties (which would, in these circumstances, sacrifice them and their co-rider family member), as well as how likely they would be to buy an AV programmed to prioritize protecting its passengers, even if it meant killing 10 or 20 pedestrians. Although the reported likelihood of buying an AV was low even for the self-protective option (median = 50), respondents indicated a significantly lower likelihood (P < 0.001) of buying the AV when they imagined the situation in which they and their family member would be sacrificed for the greater good (median = 19). In other words, even though participants still agreed that utilitarian AVs were the most moral, they preferred the self-protective model for themselves.

Study four (n = 267 participants) offers another demonstration of this phenomenon. Participants were given 100 points to allocate between different types of algorithms, to indicate (i) how moral the algorithms were, (ii) how comfortable participants were for other AVs to be programmed in a given manner, and (iii) how likely participants would be to buy an AV programmed in a given manner. For one of the algorithms, the AV would always swerve when it was about to run over people on the road. Figure 3B shows the points allocated to the AV equipped with this algorithm, in three situations: (i) when it swerved into a pedestrian to save 10 people, (ii) when it killed its own passenger to save 10 people, and (iii) when it swerved into a pedestrian to save just one other pedestrian. The algorithm that swerved into one to save 10 always received many points, and the algorithm that swerved into one to save one always received few points. The algorithm that would kill its passenger to save 10 presented a hybrid profile. Like the high-valued algorithm, it received high marks for morality (median budget share = 50) and was considered a good algorithm for other people to have (median budget share = 50). But in terms of purchase intention,

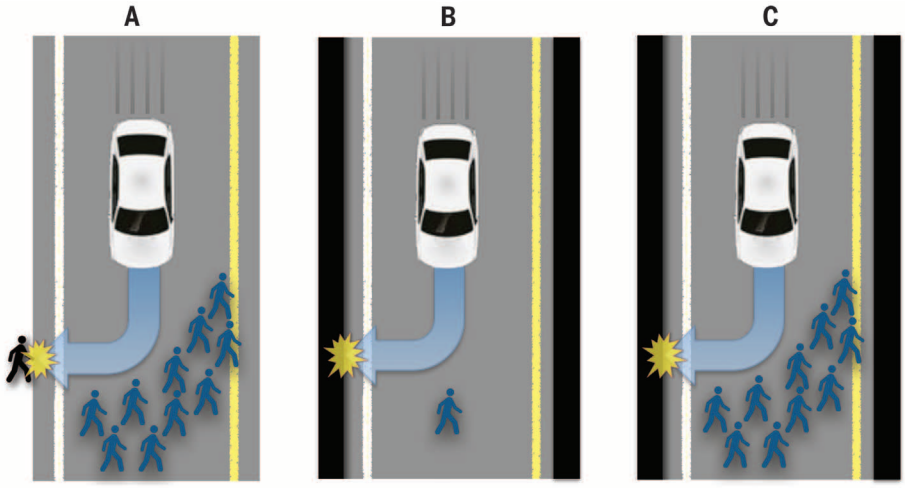
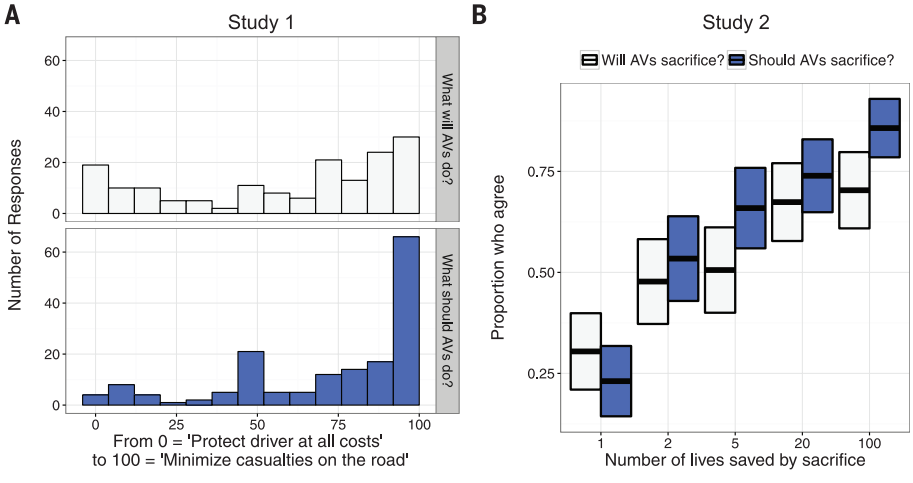


Fig. 1. Three traffic situations involving imminent unavoidable harm. The car must decide between (**A**) killing several pedestrians or one passerby, (**B**) killing one pedestrian or its own passenger, and (**C**) killing several pedestrians or its own passenger.

Fig. 2. Considering the greater good versus the life of the passenger. (**A** and **B**) In studies one and two, when asked which would be the most moral way to program AVs, participants expressed a preference for AVs programmed to kill their passengers for the greater good. This preference was strong, provided that at least five lives could be saved [(A) shows detailed results for 10 lives]. On average, participants were more confident that AVs should pursue the greater good than whether AVs would actually be programmed to do so. In (B), boxes show the 95% CI of the mean.



Downloaded from http://science.sciencemag.org/ on June 28, 2016

it received significantly fewer points than the high-valued algorithm ($P < 0.001$) and was, in fact, closer to the low-valued algorithms (median budget share = 33). Once more, it appears that people praise utilitarian, self-sacrificing AVs and welcome them on the road, without actually wanting to buy one for themselves.

This is the classic signature of a social dilemma, in which everyone has a temptation to free-ride instead of adopting the behavior that would lead to the best global outcome. One typical solution in this case is for regulators to enforce the behavior leading to the best global outcome. Indeed, there are many similar societal examples involving trade-off of harm by people and governments (*15*–*17*). For example, some citizens object to regulations that require children to be immunized before starting school. In this case, the parental decision-makers choose to minimize the perceived risk of harm to their child while increasing the risk to others. Likewise, recognition of the threats of environmental degradation have prompted government regulations aimed at curtailing harmful behaviors for the greater good. But would people approve of government regulations imposing utilitarian algorithms in AVs, and would they be more likely to buy AVs under such regulations?

In study five ($n = 376$ participants), we asked participants about their attitudes toward legally enforcing utilitarian sacrifices. Participants considered scenarios in which either a human driver or a control algorithm had an opportunity to self-sacrifice to save 1 or 10 pedestrians (Fig. 3C). As usual, the perceived morality of the sacrifice was high and about the same whether the sacrifice was performed by a human or by an algorithm (median = 70). When we inquired whether participants would agree to see such moral sacrifices legally enforced, their agreement was higher for algorithms than for human drivers ($P < 0.002$), but the average agreement still remained below the midpoint of the 0 to 100 scale in each scenario. Agreement was highest in the scenario in which algorithms saved 10 lives, with a 95% CI of 33 to 46.

Finally, in study six ($n = 393$ participants), we asked participants specifically about their likelihood of purchasing the AVs whose algorithms had been regulated by the government. Participants were presented with scenarios in which they were riding alone, with an unspecified family member, or with their child. As in the previous studies, the scenarios depicted a situation in which the algorithm that controlled the AV could sacrifice its passengers to minimize casualties on the road. Participants indicated whether it was the duty of the government to enforce regulations that would minimize the casualties in such circumstances, whether they would consider the purchase of an AV under such regulations, and whether they would consider purchasing an AV under no such regulations. As shown in Fig. 3D, people were reluctant to accept governmental regulation of utilitarian AVs. Even in the most favorable condition, when participants imagined only themselves being sacrificed to save 10 pedestrians, the 95% CI for whether people thought it was appropriate for the government to regulate this sacrifice was only 36 to 48. Finally, participants were much less likely to consider purchasing an AV with such regulation than without ($P < 0.001$). The median expressed likelihood of purchasing an unregulated AV was 59, compared with 21 for purchasing a regulated AV. This is a huge gap from a statistical perspective, but it must be understood as reflecting the state of public sentiment at the very beginning of a new public issue and is thus not guaranteed to persist.

Three groups may be able to decide how AVs handle ethical dilemmas: the consumers who buy the AVs; the manufacturers that program the AVs; and the government, which may regulate the kind of programming manufacturers can offer and consumers can select. Although manufacturers may engage in advertising and lobbying to influence consumer preferences and government regulations, a critical collective problem consists of deciding whether governments should regulate the moral algorithms that manufacturers offer to consumers.

Our findings suggest that regulation for AVs may be necessary but also counterproductive. Moral algorithms for AVs create a social dilemma (*18*, *19*). Although people tend to agree that everyone would be better off if AVs were utilitarian (in the sense of minimizing the number of casualties on the road), these same people have a personal incentive to ride in AVs that will protect them at all costs. Accordingly, if both self-protective and utilitarian AVs were allowed on the market, few people would be willing to ride in utilitarian AVs, even though they would prefer others to do so. Regulation may provide a solution to this problem, but regulators will be faced with two difficulties: First, most people seem to disapprove of a regulation that would enforce utilitarian AVs. Second—and a more serious problem—our results suggest that such regulation could substantially delay the adoption of AVs, which means that the

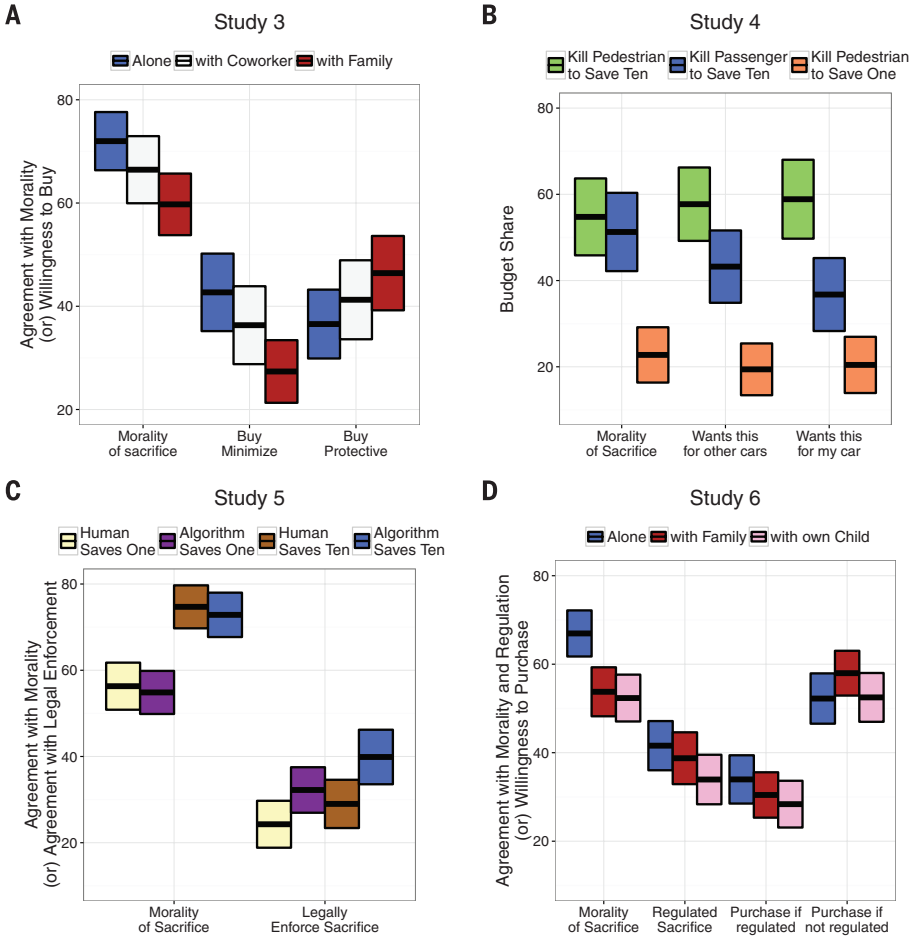


Fig. 3. Toward regulation and purchase (studies three to six). (**A** to **D**) Boxes show the 95% CI of the mean. In all studies, participants expressed a moral preference for AVs sacrificing their passengers to save a greater number of pedestrians. This moral preference was robust for situations in which participants imagined themselves in the AV in the company of a co-worker, a family member, or their own child. However, participants did not express a comparable preference for buying utilitarian AVs, especially when they thought of family members riding in the car [(A) and (B)]. Additionally, participants disapproved of regulations enforcing utilitarian algorithms for AVs and indicated that they would be less likely to purchase an AV under such regulations [(C) and (D)].

Downloaded from http://science.sciencemag.org/ on June 28, 2016

lives saved by making AVs utilitarian may be outnumbered by the deaths caused by delaying the adoption of AVs altogether. Thus, car-makers and regulators alike should be considering solutions to these obstacles.

Moral algorithms for AVs will need to tackle more intricate decisions than those considered in our surveys. For example, our scenarios did not feature any uncertainty about decision outcomes, but a collective discussion about moral algorithms will need to encompass the concepts of expected risk, expected value, and blame assignment. Is it acceptable for an AV to avoid a motorcycle by swerving into a wall, considering that the probability of survival is greater for the passenger of the AV than for the rider of the motorcycle? Should AVs account for the ages of passengers and pedestrians (*20*)? If a manufacturer offers different versions of its moral algorithm, and a buyer knowingly chose one of them, is the buyer to blame for the harmful consequences of the algorithm's decisions? Such liability considerations will need to accompany existing discussions of regulation (*21*), and we hope that psychological studies inspired by our own will be able to inform this discussion.

Figuring out how to build ethical autonomous machines is one of the thorniest challenges in artificial intelligence today (*22*). As we are about to endow millions of vehicles with autonomy, a serious consideration of algorithmic morality has never been more urgent. Our data-driven approach highlights how the field of experimental ethics can provide key insights into the moral, cultural, and legal standards that people expect from autonomous driving algorithms. For the time being, there seems to be no easy way to design algorithms that would reconcile moral values and personal self-interest—let alone account for different cultures with various moral attitudes regarding life-life trade-offs (*23*)—but public opinion and social pressure may very well shift as this conversation progresses.

REFERENCES AND NOTES

1. B. Montemerlo *et al.*, *J. Field Robot.* **25**, 569–597 (2008).
2. C. Urmson *et al.*, *J. Field Robot.* **25**, 425–466 (2008).
3. M. M. Waldrop, *Nature* **518**, 20–23 (2015).
4. B. van Arem, C. J. van Driel, R. Visser, *IEEE Trans. Intell. Transp. Syst.* **7**, 429–436 (2006).
5. K. Spieser *et al.*, in *Road Vehicle Automation*, G. Meyer, S. Beiker, Eds. (Lecture Notes in Mobility Series, Springer, 2014), pp. 229–245.
6. P. Gao, R. Hensley, A. Zielke, "A roadmap to the future for the auto industry," *McKinsey Quarterly* (October 2014); www.mckinsey.com/industries/automotive-and-assembly/our-insights/a-road-map-to-the-future-for-the-auto-industry.
7. N. J. Goodall, in *Road Vehicle Automation*, G. Meyer, S. Beiker, Eds. (Lecture Notes in Mobility Series, Springer, 2014), pp. 93–102.
8. K. Gray, A. Waytz, L. Young, *Psychol. Inq.* **23**, 206–215 (2012).
9. J. Haidt, *The Righteous Mind: Why Good People Are Divided by Politics and Religion* (Pantheon Books, 2012).
10. W. Wallach, C. Allen, *Moral Machines: Teaching Robots Right from Wrong* (Oxford University Press, 2008).
11. F. Rosen, *Classical Utilitarianism from Hume to Mill* (Routledge, 2005).
12. J. D. Greene, *Moral Tribes: Emotion, Reason, and the Gap Between Us and Them* (Atlantic Books, 2014).
13. S. Côté, P. K. Piff, R. Willer, *J. Pers. Soc. Psychol.* **104**, 490–503 (2013).
14. J. A. C. Everett, D. A. Pizarro, M. J. Crockett, *J. Exp. Psychol. Gen.* **145**, 772–787 (2016).
15. N. E. Kass, *Am. J. Public Health* **91**, 1776–1782 (2001).
16. C. R. Sunstein, A. Vermeule, *Stanford Law Rev.* **58**, 703–750 (2005).
17. T. Dietz, E. Ostrom, P. C. Stern, *Science* **302**, 1907–1912 (2003).
18. R. M. Dawes, *Annu. Rev. Psychol.* **31**, 169–193 (1980).
19. P. A. M. Van Lange, J. Joireman, C. D. Parks, E. Van Dijk, *Organ. Behav. Hum. Decis. Process.* **120**, 125–141 (2013).
20. E. A. Posner, C. R. Sunstein, *Univ. Chic. Law Rev.* **72**, 537–598 (2005).
21. D. C. Vladeck, *Wash. Law Rev.* **89**, 117–150 (2014).
22. B. Deng, *Nature* **523**, 24–26 (2015).
23. N. Gold, A. M. Colman, B. D. Pulford, *Judgm. Decis. Mak.* **9**, 65–76 (2014).

ACKNOWLEDGMENTS

J.-F.B. gratefully acknowledges support through the Agence Nationale de la Recherche–Laboratoires d'Excellence Institute for Advanced Study in Toulouse. This research was supported by internal funds from the University of Oregon to A.S. I.R. is grateful for financial support from R. Hoffman. Data files have been uploaded as supplementary materials.

SUPPLEMENTARY MATERIALS

www.sciencemag.org/content/352/6293/1573/suppl/DC1
Materials and Methods
Supplementary Text
Fig. S1
Tables S1 to S8
Data Files S1 to S6

15 January 2016; accepted 21 April 2016
10.1126/science.aaf2654

PROSTATE DEVELOPMENT

Identification of an NKX3.1-G9a-UTY transcriptional regulatory network that controls prostate differentiation

Aditya Dutta,[1]* Clémentine Le Magnen,[1]* Antonina Mitrofanova,[2]† Xuesong Ouyang,[3]‡ Andrea Califano,[4] Cory Abate-Shen[5]§

The *NKX3.1* homeobox gene plays essential roles in prostate differentiation and prostate cancer. We show that loss of function of *Nkx3.1* in mouse prostate results in down-regulation of genes that are essential for prostate differentiation, as well as up-regulation of genes that are not normally expressed in prostate. Conversely, gain of function of *Nkx3.1* in an otherwise fully differentiated nonprostatic mouse epithelium (seminal vesicle) is sufficient for respecification to prostate in renal grafts in vivo. In human prostate cells, these activities require the interaction of NKX3.1 with the G9a histone methyltransferase via the homeodomain and are mediated by activation of target genes such as *UTY (KDM6c)*, the male-specific paralog of *UTX (KDM6a)*. We propose that an NKX3.1-G9a-UTY transcriptional regulatory network is essential for prostate differentiation, and we speculate that disruption of such a network predisposes to prostate cancer.

Among the tissues of the male urogenital system, the prostate and seminal vesicle are secretory organs that develop in close proximity under the influence of androgens (fig. S1A) (*1*, *2*). However, the prostate develops from the urogenital sinus, an endodermal derivative, whereas the seminal vesicle develops from the Wolffian duct, a mesodermal derivative. Among genes that distinguish prostate and seminal vesicle, the *Nkx3.1* homeobox gene is among the earliest expressed in the presumptive prostatic epithelium during development, and its expression in adults is primarily restricted to prostatic luminal cells (*3*, *4*), which are secretory cells that are the major target of prostate neoplasia (*4*, *5*). Accordingly, in mouse models, loss of function of *Nkx3.1* results in impaired prostate differentiation and defects in luminal stem cells, as well as predisposes to prostate cancer (*3*, *4*).

Analyses of expression profiles from *Nkx3.1* wild-type ($Nkx3.1^{+/+}$) and *Nkx3.1* mutant ($Nkx3.1^{-/-}$) prostates revealed down-regulation of genes associated with prostate differentiation, such as *FoxA1* (*Forkhead Box A1*), *Pbsn* (*Probasin*), *HoxB13*, and *Tmprss2* (*Transmembrane Protease, Serine 2*), as well as luminal cells (*cytokeratins 8 and 18*), and up-regulation of basal cell markers (*cytokeratins 5 and p63*) (Fig. 1A, fig. S2A, and database S1) (*6*). Surprisingly, $Nkx3.1^{-/-}$ versus $Nkx3.1^{+/+}$ prostates display up-regulation of genes that are expressed, albeit not exclusively, in seminal vesicle, namely

[1]Departments of Medicine and Urology, Institute of Cancer Genetics, Herbert Irving Comprehensive Cancer Center, Columbia University Medical Center, New York, NY 10032, USA. [2]Department of Systems Biology, Columbia University Medical Center, New York, NY 10032, USA. [3]Department of Urology, Columbia University Medical Center, New York, NY 10032, USA. [4]Departments of Systems Biology, Biomedical Informatics, and Biochemistry and Molecular Biophysics, Center for Computational Biology and Bioinformatics, Institute of Cancer Genetics, Herbert Irving Comprehensive Cancer Center, Columbia University Medical Center, New York, NY 10032, USA. [5]Departments of Urology, Medicine, Systems Biology, and Pathology and Cell Biology, Institute of Cancer Genetics, Herbert Irving Comprehensive Cancer Center, Columbia University Medical Center, New York, NY 10032, USA.
*These authors contributed equally to this work. †Present address: Department of Health Informatics, Rutgers, The State University of New Jersey, 65 Bergen Street, Room 350B, Newark, NJ 07101, USA. ‡Present address: Crown Bioscience Inc., 6 West Beijing Road, Taicang, Jiangsu 215400, China. **§Corresponding author. Email: cabateshen@columbia.edu**

Downloaded from http://science.sciencemag.org/ on June 28, 2016

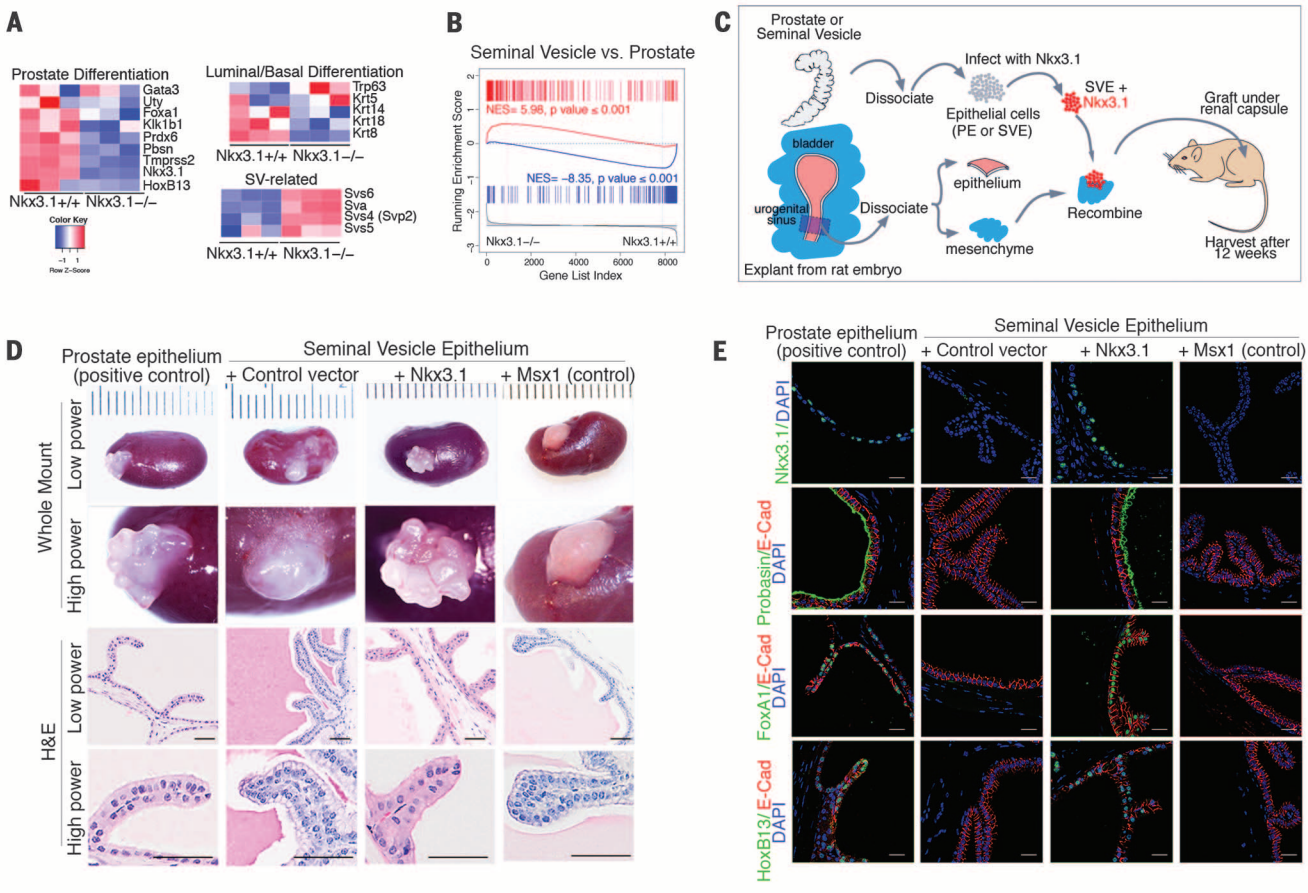


Fig. 1. Murine Nkx3.1 respecifies a nonprostatic epithelium to form prostate in vivo. (**A**) Heat map representations of differentially expressed genes from *Nkx3.1*$^{+/+}$ and *Nkx3.1*$^{-/-}$ prostate (*6*). (**B**) Gene set enrichment analysis, using as the query gene set differentially expressed genes from seminal vesicle versus prostate, compared with a reference gene signature of *Nkx3.1*$^{-/-}$ versus *Nkx3.1*$^{+/+}$ prostate. (**C**) Diagram of the tissue recombination assay. Dissociated epithelium from seminal vesicle (SVE) or prostate (PE) is infected with a lentivirus expressing Nkx3.1 (or control). Mesenchyme from rat embryonic urogenital sinus is combined with the epithelium and grown under the renal capsule of host mice. (**D** and **E**) Representative tissue recombinants. (D) (Top) Whole-mount images. (Bottom) Hematoxylin and eosin (H&E) images. (E) Confocal images of immunofluorescence using the indicated antibodies. Scale bars represent 50 μm in (D) and 20 μm in (E). A summary of tissue recombinant data is provided in table S4.

Svs6, *Sva*, *Svs4*, and *Svs5* (Fig. 1A and fig. S2A) (*7*). These differentially expressed genes were significantly enriched in a gene signature comparing seminal vesicle versus normal prostate, and this pattern was conserved in mouse and humans (Fig. 1B and figs. S1B and S2B). At the cellular level, we observed reduced expression of Probasin and a corresponding up-regulation of Svp2 in *Nkx3.1*$^{-/-}$ versus *Nkx3.1*$^{+/+}$ prostates (figs. S1, C to E, and S2C; and tables S1 to S3) (*8*).

Considering that loss of function of *Nkx3.1* leads to aberrant prostate epithelial differentiation, we asked whether its gain of function in a nonprostatic epithelium is sufficient to induce prostate differentiation. Toward this end, we performed tissue recombination assays, in which relevant epithelial and mesenchymal tissues are recombined in vitro, followed by growth under the kidney capsule of host mice in vivo (Fig. 1C) (*2*). It is well established that prostate formation requires both epithelial and mesenchymal tissues, as well as an appropriate source of androgens (fig. S3), and that nonendodermal epithelium, even those that are androgen-regulated, such as seminal vesicle, do not form prostate in this assay (*2*).

To explore whether *Nkx3.1* expression can induce prostate differentiation in tissue recombinants, we infected seminal vesicle epithelium with a lentivirus expressing *Nkx3.1* (or the control vector) (Fig. 1C). As expected, tissue recombinants made with prostate epithelium (PE) generate prostate-like grafts, which are distinguished by their prostate-like ductal structures, histological appearance resembling prostate epithelium, and expression of markers of prostate differentiation, including Nkx3.1, probasin, FoxA1, and HoxB13 (N = 19 recombinants) (Fig. 1, D and E; fig. S4A; and table S4). Also as expected, tissue recombinants made with seminal vesicle epithelium (SVE) lacking *Nkx3.1* generate seminal vesicle–like grafts, which are distinguished by their lack of discernible ductal morphology, histological appearance resembling seminal vesicle, and the absence of markers of prostate differentiation (N = 20 recombinants) (Fig. 1, D and E; fig. S4A; and table S4).

In contrast, tissue recombinants made with SVE expressing exogenous *Nkx3.1* more closely resemble prostate than seminal vesicle. In particular, the Nkx3.1-expressing SVE grafts are distinguished by their appearance of prostate-like ductal structures, histological appearance resembling prostate, and expression of markers of prostate differentiation, including probasin, FoxA1, and HoxB13 (N = 26 recombinants) (Fig. 1, D and E; fig. S4A; and table S4); this was not the case for tissue recombinants made with SVE expressing an unrelated homeobox gene, *Msx1* (N = 3 recombinants) (Fig. 1, D and E, and table S4). Moreover, expression profiling analyses showed that tissue recombinants made from SVE expressing *Nkx3.1* were significantly enriched with a signature of prostate versus seminal vesicle (fig. S4, B and C). Nkx3.1 is thus sufficient to respecify a fully differentiated nonprostate epithelium to form prostate in vivo.

To study the underlying mechanisms, we established a cell-based assay using an immortalized human prostate cell line, RWPE1, which

Downloaded from http://science.sciencemag.org/ on June 28, 2016

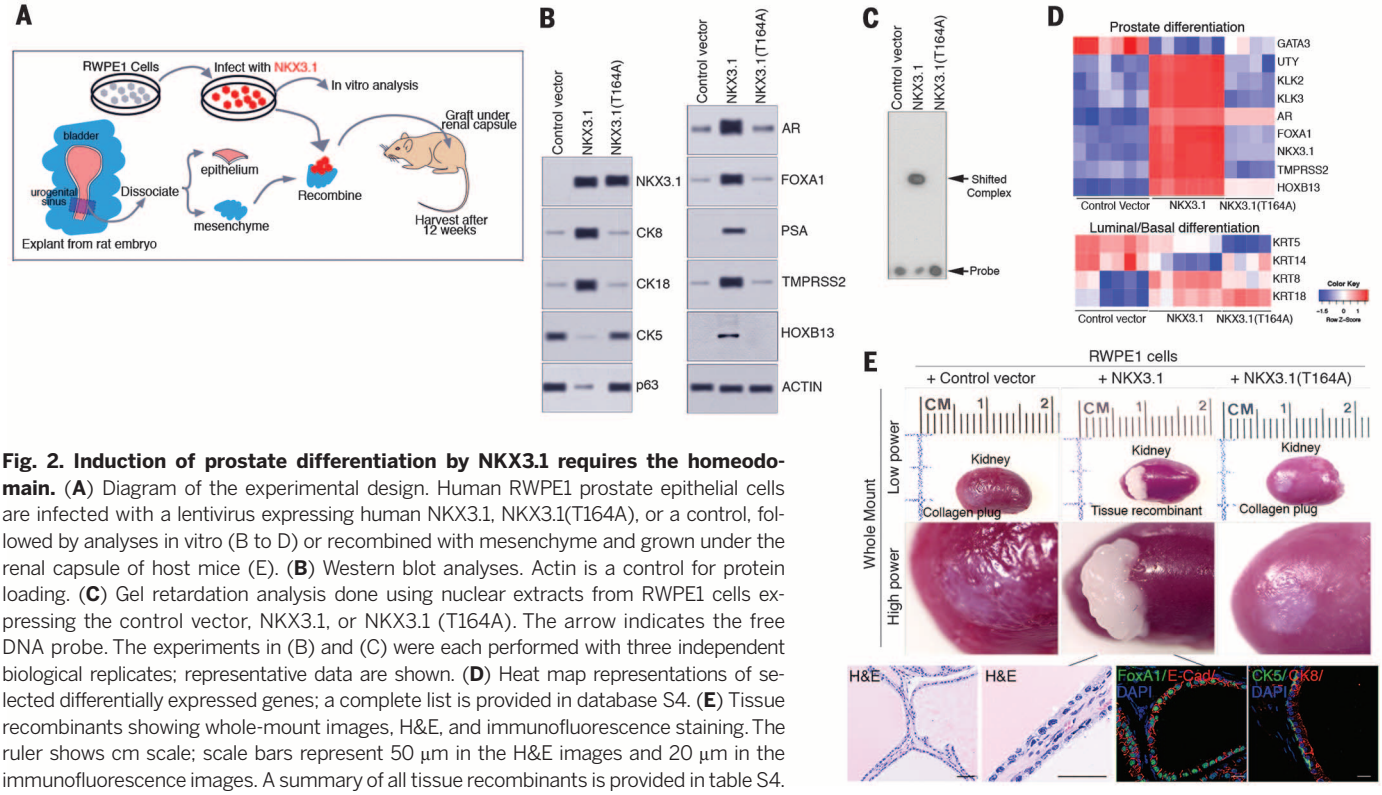


Fig. 2. Induction of prostate differentiation by NKX3.1 requires the homeodomain. (**A**) Diagram of the experimental design. Human RWPE1 prostate epithelial cells are infected with a lentivirus expressing human NKX3.1, NKX3.1(T164A), or a control, followed by analyses in vitro (B to D) or recombined with mesenchyme and grown under the renal capsule of host mice (E). (**B**) Western blot analyses. Actin is a control for protein loading. (**C**) Gel retardation analysis done using nuclear extracts from RWPE1 cells expressing the control vector, NKX3.1, or NKX3.1 (T164A). The arrow indicates the free DNA probe. The experiments in (B) and (C) were each performed with three independent biological replicates; representative data are shown. (**D**) Heat map representations of selected differentially expressed genes; a complete list is provided in database S4. (**E**) Tissue recombinants showing whole-mount images, H&E, and immunofluorescence staining. The ruler shows cm scale; scale bars represent 50 μm in the H&E images and 20 μm in the immunofluorescence images. A summary of all tissue recombinants is provided in table S4.

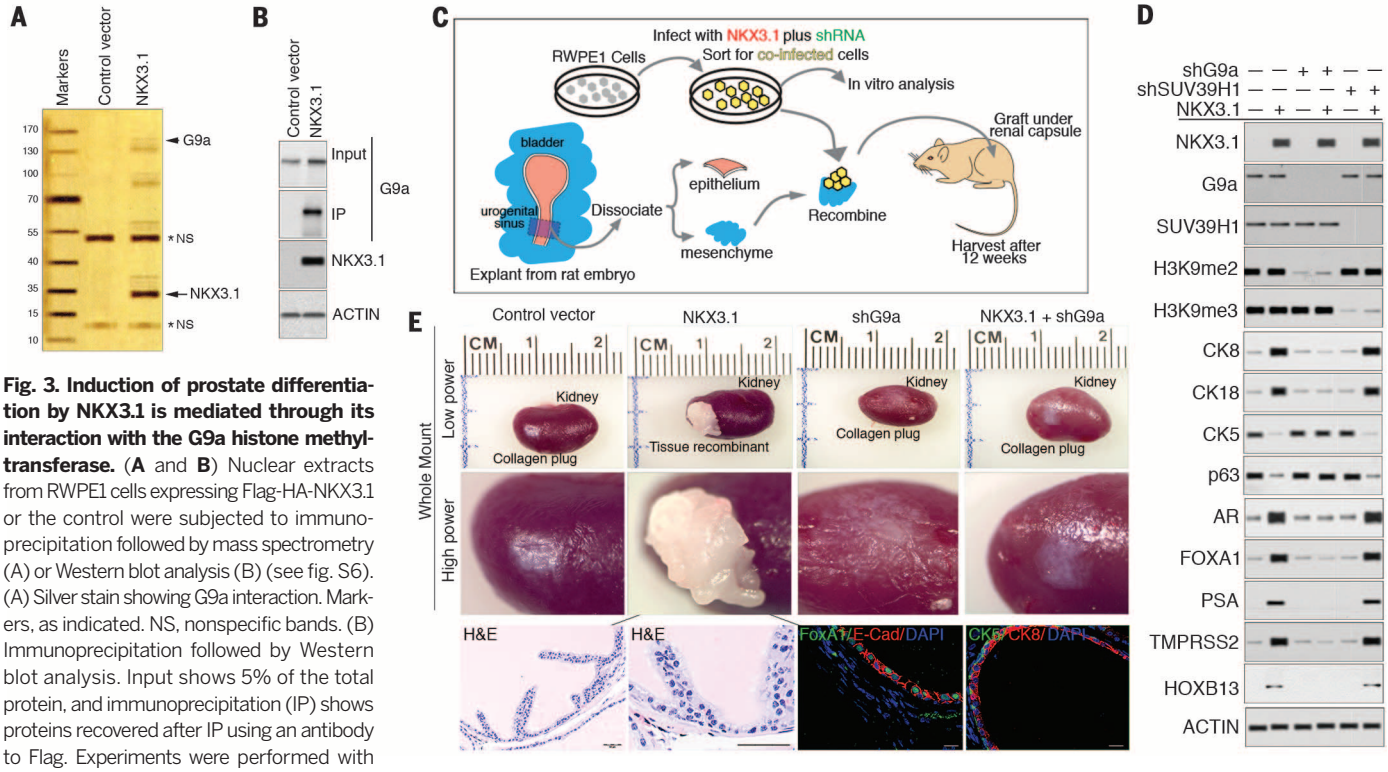


Fig. 3. Induction of prostate differentiation by NKX3.1 is mediated through its interaction with the G9a histone methyltransferase. (**A** and **B**) Nuclear extracts from RWPE1 cells expressing Flag-HA-NKX3.1 or the control were subjected to immunoprecipitation followed by mass spectrometry (A) or Western blot analysis (B) (see fig. S6). (A) Silver stain showing G9a interaction. Markers, as indicated. NS, nonspecific bands. (B) Immunoprecipitation followed by Western blot analysis. Input shows 5% of the total protein, and immunoprecipitation (IP) shows proteins recovered after IP using an antibody to Flag. Experiments were performed with three independent biological replicates; representative data are shown. (**C**) Diagram of experimental design for (D) and (E). Human RWPE1 prostate epithelial cells were infected with an NKX3.1-expressing lentivirus (expressing red fluorescent protein), followed by infection with an shRNA-expressing lentivirus (expressing green fluorescent protein). Coinfected cells were sorted by fluorescence-activated cell sorting, followed by analyses in vitro (D) or generation of tissue recombinants in vivo. (**D**) Western blot analysis. Experiments were performed with three independent biological replicates; representative data are shown. (**E**) Representative tissue recombinants showing whole-mount, H&E, and confocal images of immunofluorescence staining. Indicated is the kidney and the collagen plug (for the recombinants that did not grow) or the tissue recombinant. The ruler shows cm scale; scale bars represent 50 μm in the H&E images and 20 μm in the immunofluorescence images. A summary of tissue recombinants is provided in table S4.

Downloaded from http://science.sciencemag.org/ on June 28, 2016

expresses low levels of NKX3.1, low levels of luminal cytokeratins, high levels of basal cell markers, and low levels of markers of prostate differentiation, such as androgen receptor (AR), FOXA1, PSA, TMPRSS2, and HOXB13 (Fig. 2, A to D). Infection of RWPE1 cells with a lentivirus expressing *NKX3.1* resulted in high levels of NKX3.1 protein and robust DNA binding (Fig. 2, B and C). Expression profiling and Western blot analyses of the NKX3.1-expressing versus control RWPE1 cells revealed up-regulation of luminal cell markers (cytokeratins 8 and 18), down-regulation of basal cell markers (cytokeratin 5 and p63), and up-regulation of prostate differentiation markers (AR, FOXA1, PSA, TMPRSS2, and HOXB13) (Fig. 2, B and D). Furthermore, when combined with embryonic mesenchyme and grown under the renal capsule, NKX3.1-expressing RWPE1 cells generate prostate-like grafts that morphologically and histologically resemble prostate, including the presence of basal and luminal cell layers and expression of markers of prostate differentiation (N = 15 recombinants). In contrast, the control RWPE1 cells failed to grow in this assay (N = 12 recombinants) (Fig. 2E, fig. S5, and table S4). NKX3.1(T164A), which has a mutation in the homeodomain that impairs its DNA binding capacity (Fig. 2C) (*9*), did not induce prostate differentiation in vitro, nor did it promote prostate growth in tissue recombinants in vivo (N = 7 recombinants) (Fig. 2, B to E; fig. S5; and table S4). Therefore, the ability of NKX3.1 to induce prostate differentiation requires a functional DNA binding domain.

Many of the functions of homeoproteins are mediated by protein-protein interactions that often occur through the homeodomain (*10*). Among NKX3.1-interacting proteins identified by mass spectrometry (Fig. 3A and fig. S6) (*8*) was G9a [also called EHMT2 (euchromatic histone lysine N-methyltransferase 2)], a histone methyltransferase that forms a complex with a related histone methyltransferase, GLP [also called EHMT1 (euchromatic histone lysine N-methyltransferase 1)], to promote dimethylation of lysine 9 on histone 3 (H3K9me2) (*11*). G9a is essential for embryonic development (*12*) and interacts with other homeoproteins to mediate differentiation (*13*, *14*). In

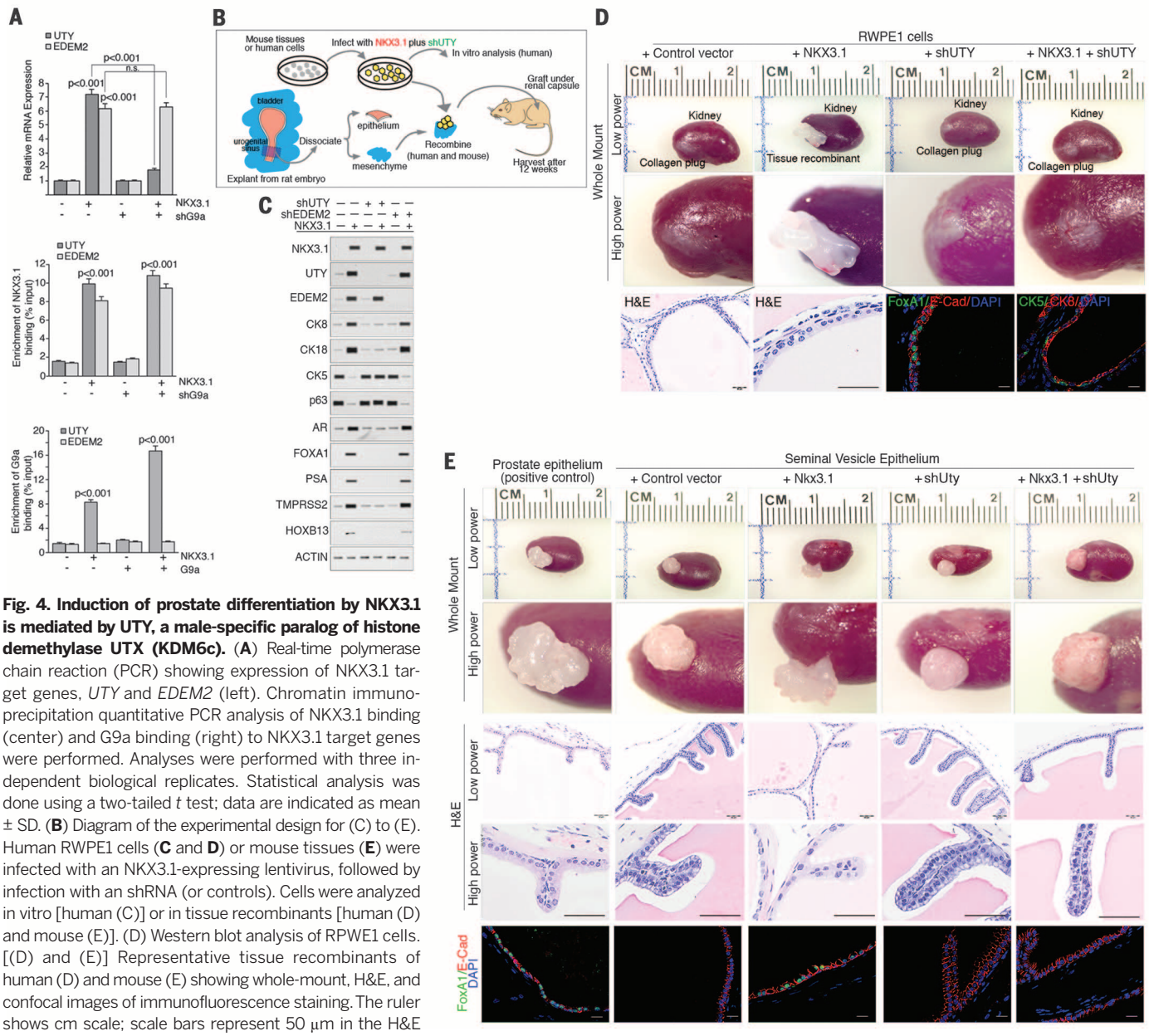


Fig. 4. Induction of prostate differentiation by NKX3.1 is mediated by UTY, a male-specific paralog of histone demethylase UTX (KDM6c). (**A**) Real-time polymerase chain reaction (PCR) showing expression of NKX3.1 target genes, *UTY* and *EDEM2* (left). Chromatin immunoprecipitation quantitative PCR analysis of NKX3.1 binding (center) and G9a binding (right) to NKX3.1 target genes were performed. Analyses were performed with three independent biological replicates. Statistical analysis was done using a two-tailed *t* test; data are indicated as mean ± SD. (**B**) Diagram of the experimental design for (C) to (E). Human RWPE1 cells (**C** and **D**) or mouse tissues (**E**) were infected with an NKX3.1-expressing lentivirus, followed by infection with an shRNA (or controls). Cells were analyzed in vitro [human (C)] or in tissue recombinants [human (D) and mouse (E)]. (D) Western blot analysis of RPWE1 cells. [(D) and (E)] Representative tissue recombinants of human (D) and mouse (E) showing whole-mount, H&E, and confocal images of immunofluorescence staining. The ruler shows cm scale; scale bars represent 50 μm in the H&E images and 20 μm in the immunofluorescence images. A summary of tissue recombinants is provided in table S4.

Downloaded from http://science.sciencemag.org/ on June 28, 2016

coimmunoprecipitation assays, NKX3.1 interacted with endogenous G9a, as well as GLP, which requires the homeodomain and is directly correlated with DNA binding by NKX3.1 (Fig. 3B and fig. S7, A to C). In contrast, NKX3.1 did not interact with other histone methyltransferases, including SUV39H1 (suppressor of variegation 3-9 homolog 1), which promotes trimethylation of lysine 9 on histone 3 (H3K9me3), and EZH2 (enhancer of zeste 2), which promotes trimethylation of lysine 27 on histone 3 (H3K27me3) (fig. S7, A and B).

To study the functional relevance of the interaction between NKX3.1 and G9a, we coinfected RWPE1 cells with an NKX3.1-expressing lentivirus together with a short hairpin RNA (shRNA) to deplete G9a (shG9a) or SUV39H1 (shSUV39H1) as a control (Fig. 3, C to E, and fig. S5). These shRNAs reduced expression of G9a or SUV39H1, as well as their respective histone marks, H3K9me2 and H2K9me3, while not affecting expression of NKX3.1 (Fig. 3D). However, depletion of G9a, but not SUV39H1, impaired the ability of NKX3.1 to induce prostate differentiation, as evidenced by Western blot analysis of cultured cells, as well as prostate growth in the tissue recombinant assay in vivo (N = 9 recombinants) (Fig. 3, D and E; fig. S5; and table S4). These findings demonstrate that the interaction of NKX3.1 with G9a is required for induction of prostate differentiation.

Considering that induction of differentiation by NKX3.1 requires its homeodomain and corresponding DNA binding activity (fig. S7), we reasoned that these functions are likely to be mediated by gene transcription. Among NKX3.1 target genes that have predicted functions for differentiation and are conserved between mice and humans (fig. S8) (*8*), we focused on *UTY*, using *EDEM2* as a control. In particular, G9a binds to the promoter of *UTY*, but not *EDEM2*, which is dependent on NKX3.1 binding and is required for NKX3.1-mediated up-regulation of *UTY* expression (Fig. 4A and fig. S9). Notably, UTY (KDM6c, ubiquitously transcribed tetratricopeptide repeat containing, Y-linked) is the male-specific paralog of UTX (KDM6a), a histone demethylase that is essential for viability and is frequently deregulated in cancer (*15*–*17*). Although its functions as a histone demethylase are uncertain (*16*), UTY is essential for male fertility as well as the development and differentiation of male-specific organs (*16*), and it has been linked to prostate cancer (*18*).

To study the consequences of UTY depletion on prostate differentiation, we coinfected NKX3.1-expressing or control RWPE1 cells with an shRNA to UTY (shUTY) or EDEM2 (shEDEM2) as a control (Fig. 4, B to D, and fig. S5). Expression of these shRNAs reduced expression of UTY or EDEM2, respectively, while not affecting expression of NKX3.1 (Fig. 4C). Moreover, depletion of UTY, but not EDEM2, impaired the ability of NKX3.1 to induce prostate differentiation in vitro as well as in tissue recombinants in vivo (N = 8 recombinants) (Fig. 4, C and D, and table S4).

We next investigated whether Uty is also required for prostate specification in vivo by performing analogous experiments using the mouse tissue recombinant model. Depletion of Uty (shUty) in *Nkx3.1*-expressing SVE abrogated the ability of Nkx3.1 to generate prostate, as was evident by the resulting tissue recombinants (SVE + Nkx3.1 + shUty), which more closely resemble seminal vesicle than prostate (N = 8 recombinants) (Fig. 4E). Moreover, expression profiling of tissue recombinants generated from the Uty-depleted *Nkx3.1*-SVE revealed their significant enrichment in a gene signature comparing seminal vesicle versus prostate (fig. S10).

Cumulatively, our findings support a model in which NKX3.1 regulates the expression of a gene program associated with prostate differentiation, while simultaneously inhibiting the inappropriate expression of nonprostatic genes (fig. S11A). In particular, *Nkx3.1* can respecify a fully differentiated mouse tissue to form prostate in vivo, and its expression in basal-like human prostate epithelial cells can promote their differentiation to luminal-like cells that form prostate in vivo. These functions of NKX3.1 are mediated by the coordinate actions of G9a and UTY (fig. S11, A and B). Notably, we find that G9a functions as a coregulator of NKX3.1, which is associated with activation, as well as repression, of NKX3.1 target genes. This further underscores the complexity of G9a function in transcriptional control. Indeed, although G9a is a histone methyltransferase for a "repressive" mark, it is active on euchromatin (*11*), and it has been shown that G9a can repress or activate transcription depending on the context (*19*, *20*). This includes the glucocorticoid receptor (*21*, *22*), which also interacts with NKX3.1, as assessed by mass spectrometry (fig. S6), and has been implicated in drug resistance in prostate cancer (*23*). Thus, we envision that our findings presage a role for G9a in both prostate differentiation and cancer.

Our findings also shed new light on UTY as an essential downstream mediator of NKX3.1 in prostate differentiation. Given the importance of UTY for male fertility, as well as for differentiation of male-specific organs (*16*, *24*), our current study provides an example of how, in addition to the well-known role of androgen signaling, the promotion of "maleness" may be essential for prostate differentiation.

Last, there are still relatively few examples in which a single gene can respecify an otherwise fully differentiated epithelium to a new fate, as we have observed for *NKX3.1*. Notably, our findings regarding *NKX3.1* in prostate are strikingly concordant with the functions of *NKX2.1* in lung differentiation and lung cancer (*25*–*28*). In particular, loss of function of *NKX2.1* leads to impaired lung differentiation, which is associated with the derepression of an aberrant gene expression program (*28*), while, conversely *NKX2.1* expression is associated with inhibition of lung metastases (*26*, *27*). Consistent with the action of *NKX3.1* in prostate, these actions of *NKX2.1* in lung are dependent upon its level of expression. Thus, these observations suggest that NK-class homeobox genes function as key regulators of tissue-specific differentiation, as well as key gatekeepers whose diminution of expression in specific tissue contexts may enhance susceptibility to cancer.

REFERENCES AND NOTES

1. C. Abate-Shen, M. M. Shen, *Genes Dev.* **14**, 2410–2434 (2000).
2. G. R. Cunha *et al.*, *Endocr. Rev.* **8**, 338–362 (1987).
3. R. Bhatia-Gaur *et al.*, *Genes Dev.* **13**, 966–977 (1999).
4. X. Wang *et al.*, *Nature* **461**, 495–500 (2009).
5. Z. A. Wang, R. Toivanen, S. K. Bergren, P. Chambon, M. M. Shen, *Cell Reports* **8**, 1339–1346 (2014).
6. X. Ouyang, T. L. DeWeese, W. G. Nelson, C. Abate-Shen, *Cancer Res.* **65**, 6773–6779 (2005).
7. M. C. Ostrowski, M. K. Kistler, W. S. Kistler, *J. Biol. Chem.* **254**, 383–390 (1979).
8. Materials and methods are available as supplementary materials on *Science* Online.
9. S. L. Zheng *et al.*, *Cancer Res.* **66**, 69–77 (2006).
10. T. R. Bürglin, M. Affolter, *Chromosoma* **2015**, 1–25 (2015).
11. Y. Shinkai, M. Tachibana, *Genes Dev.* **25**, 781–788 (2011).
12. M. Tachibana *et al.*, *Genes Dev.* **16**, 1779–1791 (2002).
13. J. Wang, C. Abate-Shen, *PLOS ONE* **7**, e37647 (2012).
14. B. Lehnertz *et al.*, *Genes Dev.* **28**, 317–327 (2014).
15. C. Wang *et al.*, *Proc. Natl. Acad. Sci. U.S.A.* **109**, 15324–15329 (2012).
16. K. B. Shpargel, T. Sengoku, S. Yokoyama, T. Magnuson, *PLOS Genet.* **8**, e1002964 (2012).
17. G. van Haaften *et al.*, *Nat. Genet.* **41**, 521–523 (2009).
18. Y. F. Lau, J. Zhang, *Mol. Carcinog.* **27**, 308–321 (2000).
19. C. P. Chaturvedi *et al.*, *Proc. Natl. Acad. Sci. U.S.A.* **106**, 18303–18308 (2009).
20. B. Lehnertz *et al.*, *J. Exp. Med.* **207**, 915–922 (2010).
21. D. Bittencourt *et al.*, *Proc. Natl. Acad. Sci. U.S.A.* **109**, 19673–19678 (2012).
22. D. Y. Lee, J. P. Northrop, M. H. Kuo, M. R. Stallcup, *J. Biol. Chem.* **281**, 8476–8485 (2006).
23. V. K. Arora *et al.*, *Cell* **155**, 1309–1322 (2013).
24. H. J. Cooke, P. T. Saunders, *Nat. Rev. Genet.* **3**, 790–801 (2002).
25. B. A. Weir *et al.*, *Nature* **450**, 893–898 (2007).
26. M. M. Winslow *et al.*, *Nature* **473**, 101–104 (2011).
27. C. M. Li *et al.*, *Genes Dev.* **29**, 1850–1862 (2015).
28. E. L. Snyder *et al.*, *Mol. Cell* **50**, 185–199 (2013).

ACKNOWLEDGMENTS

We are grateful to A. Aytes, F. Constantini, E. Gelmann, D. Reinberg, and M. Shen for comments on the manuscript. We thank C. Bieberich (University of Maryland) for Nkx3.1 antisera. We acknowledge support from the JP Sulzberger Columbia Genome Center and the Proteomics Shared Resource, which are shared resources of the Herbert Irving Comprehensive Cancer Center at Columbia University, supported in part by NIH/NCI grant P30 CA013696. This research is supported by funding to C.A.-S. from the National Cancer Institute (CA154293). A.D. was supported in part by the National Center for Advancing Translational Sciences, National Institutes of Health, grant UL1 TR000040. C.L.M. was supported by the Swiss National Science Foundation (PBBSP3_146959 and P300P3_151158). A.M. is a recipient of a Prostate Cancer Foundation Young Investigator Award. C.A.-S. is an American Cancer Society Research Professor supported in part by a generous gift from the F.M. Kirby Foundation.

SUPPLEMENTARY MATERIALS

www.sciencemag.org/content/352/6293/1576/suppl/DC1
Materials and Methods
Supplementary Text
Figs. S1 to S11
Tables S1 to S6
Databases S1 to S4
References (*29*–*44*)

29 November 2015; accepted 27 May 2016
10.1126/science.aad9512

Downloaded from http://science.sciencemag.org/ on June 28, 2016

MUCOSAL IMMUNOLOGY

Tissue adaptation of regulatory and intraepithelial CD4$^+$ T cells controls gut inflammation

Tomohisa Sujino,[1] Mariya London,[1] David P. Hoytema van Konijnenburg,[1,2] Tomiko Rendon,[1] Thorsten Buch,[3] Hernandez M. Silva,[4] Juan J. Lafaille,[4] Bernardo S. Reis,[1]* Daniel Mucida[1]*

Foxp3$^+$ regulatory T cells in peripheral tissues (pT$_{regs}$) are instrumental in limiting inflammatory responses to nonself antigens. Within the intestine, pT$_{regs}$ are located primarily in the lamina propria, whereas intraepithelial CD4$^+$ T cells (CD4$_{IELs}$), which also exhibit anti-inflammatory properties and depend on similar environmental cues, reside in the epithelium. Using intravital microscopy, we show distinct cell dynamics of intestinal T$_{regs}$ and CD4$_{IELs}$. Upon migration to the epithelium, T$_{regs}$ lose Foxp3 and convert to CD4$_{IELs}$ in a microbiota-dependent manner, an effect attributed to the loss of the transcription factor ThPOK. Finally, we demonstrate that pT$_{regs}$ and CD4$_{IELs}$ perform complementary roles in the regulation of intestinal inflammation. These results reveal intratissue specialization of anti-inflammatory T cells shaped by discrete niches of the intestine.

The gut mucosa is exposed daily to large amounts of both harmless and potentially pathogenic stimuli; hence, diverse immune regulatory mechanisms must operate to avoid inflammatory diseases (*1*). Peripheral Foxp3-expressing regulatory T cells (pT$_{regs}$) mediate suppression of a variety of immune cells and actively prevent inflammatory bowel diseases and food allergies (*2*–*7*). Similar to pT$_{regs}$, Foxp3$^-$CD8$\alpha\alpha^+$CD4$^+$ intraepithelial lymphocytes (CD4$_{IELs}$) depend on retinoic acid (RA) and transforming growth factor–β (TGF-β) signaling for their development and also have anti-inflammatory properties (*4*, *8*–*13*). However, whereas CD4$_{IELs}$ accumulate in the intestinal epithelium, few total T$_{regs}$ (including pT$_{regs}$ and thymically derived T$_{regs}$) can be found at this site (fig. S1, A and B). We asked whether and how the intestinal environment segregates pT$_{regs}$ and CD4$_{IELs}$, which transcriptional factors are involved in this regulation, and what the implications are for gut inflammation.

We used intravital multiphoton microscopy (IVM) to investigate whether T$_{regs}$ are actively excluded from the gut epithelium. For tracking in vivo T$_{reg}$ dynamics, we used tamoxifen-inducible *Foxp3*$^{CreER\text{-}eGFP}$:*Rosa26*$^{lsl\text{-}tdTomato}$ (i*Foxp3*^{Tomato}) mice (*14*), which allow T$_{reg}$ fate mapping and the ability to distinguish between cells that currently express and cells that once expressed Foxp3. We compared T$_{reg}$ movement patterns in these mice shortly (24 hours) after tamoxifen administration, which allows the visualization of bona fide T$_{regs}$ (Tomato$^+$), to thymically derived γδ IEL cell movement patterns (*15*). We found that more than 80% of TCRγδ^{GFP} cells preferentially remained in the epithelium, whereas 68 and 14% of Tomato$^+$ cells were considered lamina propria and IE residents, respectively, throughout the duration of image recordings (Fig. 1, A and B, and movies S1 and 2). Among the remaining (~18%) migrating Tomato$^+$ cells, cell tracking indicated that cells moved into the epithelial layer from the lamina propria more frequently than vice versa (Fig. 1, B and C, and movie S2). Because ex vivo analysis of the intestinal epithelium revealed a low frequency of Foxp3$^+$ T$_{regs}$ (fig. S1, A and B), these IVM results suggested either preferential cell death of T$_{regs}$ or T$_{reg}$ conversion into another T cell subtype.

Whereas all T$_{regs}$ express the CD4-lineage transcription factor T helper–inducing POZ/Krüppel-like factor (ThPOK), CD8$\alpha\alpha^+$CD4$^+$ and more than 50% of Foxp3$^-$CD8α^- CD4$^+$ cells in the small intestinal epithelium lack ThPOK expression (fig. S1C). We thus asked whether down-modulation of ThPOK influences CD4$^+$ T cell dynamics. We performed IVM using an ovalbumin (OVA)–specific T cell receptor (TCR) transgenic system (OT-II), in which oral OVA exposure leads to incremental ThPOK loss by intestinal CD4$^+$ T cells (*10*, *16*). To visualize T cells upon ThPOK loss, we crossed OT-II (*Rag1*$^{-/-}$) with *Thpok*^{GFP} knockin reporter and ubiquitous monomeric red fluorescent protein 1 (mRFP1) mice. Sorted naïve (RFP$^+$GFP$^+$) CD4$^+$ T cells from OT-II (RFP *Thpok*^{GFP}) mice were transferred to *Rag1*$^{-/-}$ mice kept on an OVA-containing diet for 1 week before IVM analysis. Computational tracking revealed that ~60% of the transferred cells that down-regulated ThPOK (RFP$^+$GFP$^-$), and only 20% of ThPOK^{high} cells (RFP$^+$GFP$^+$), remained in the epithelial layer (Fig. 1, D and E, and movie S3). Migrating ThPOK^{high} cells showed movement patterns similar to those of T$_{reg}$ cells, with preferential displacement from the lamina propria into the epithelial layer, suggesting that part of these cells convert into ThPOK^{low} cells, or die, in that compartment (Fig. 1F). These observations indicate that loss of ThPOK corresponds to an IEL-like behavior in CD4$^+$ T cells. Additionally, the discrepancy between the capacity of T$_{regs}$ to visit the intestinal epithelium and their low frequency in this layer suggests that this environment may favor T$_{reg}$ plasticity.

To directly examine T$_{reg}$ plasticity in the gut tissue, we performed T$_{reg}$ fate mapping using naïve adult *Foxp3*$^{Cre\text{-}YFP}$:*Rosa26*$^{lsl\text{-}DsRed}$ (*Foxp3*^{DsRed}) mice (*17*). Analysis of peripheral lymphoid tissues isolated from *Foxp3*^{DsRed} mice revealed an almost complete concurrence between Foxp3 reporter (YFP, yellow fluorescent protein) and DsRed expression, confirming previously described stability of the T$_{reg}$ lineage (*14*, *18*). However, more than 40% of DsRed$^+$ CD4$^+$ T cells in the small intestinal epithelium did not express Foxp3 (YFP$^-$), indicating that many T$_{regs}$ lost Foxp3 expression (fig. S2A). Because previous studies have demonstrated that most "ex-Foxp3" cells in the steady state were derived from uncommitted precursors that transiently up-regulated Foxp3 (*18*), we also performed fate mapping after pulse labeling i*Foxp3*^{Tomato} mice with tamoxifen (*14*), a strategy more likely to target bona fide T$_{regs}$ (*19*). Nevertheless, although stable Foxp3 expression was again observed in several peripheral tissues examined, more than 50% of Tomato$^+$ CD4$^+$ T cells that accumulated in the small intestinal epithelium and almost 10% that accumulated in the large intestinal epithelium isolated from i*Foxp3*^{Tomato} mice no longer expressed Foxp3 5 weeks after tamoxifen administration (fig. S2, B and C). The contribution of Tomato$^+$ cells to the CD8$\alpha\alpha^+$ and CD8$\alpha\beta^+$ CD4$_{IEL}$ pools was roughly 10 and 25%, respectively (fig. S2D). Consistent with a ThPOK-dependent process, ex-T$_{regs}$ that underwent IEL differentiation showed low amounts of ThPOK (fig. S2E). These results indicate that a substantial proportion of intestinal T$_{regs}$ physiologically convert to CD4$_{IELs}$.

Commensal bacteria play a major role in the induction of large intestine lamina propria pT$_{regs}$ (*3*, *5*–*7*, *20*). In contrast, we observed an increased frequency of pT$_{regs}$ (Neuropilin-1$^-$ Foxp3$^+$) in the small intestinal epithelium isolated from germ-free (GF) mice when compared to specific-pathogen–free (SPF) controls (Fig. 2A). The total number of T$_{regs}$ in the epithelial compartment was comparable between GF and SPF mice, even though GF mice showed an almost 10-fold reduction in the number of intraepithelial CD4$^+$ T cells (Fig. 2A). Consistent with a reciprocal ThPOK or Foxp3 expression and CD4$_{IEL}$ differentiation, we found an increased frequency of ThPOK^{high} CD4$^+$ T cells and significantly reduced numbers of CD4$_{IELs}$ in GF mice (Fig. 2B). We therefore reasoned that the instability of T$_{regs}$ in the gut epithelium was influenced by the microbiota. To address this possibility, we treated i*Foxp3*^{Tomato} mice with broad-spectrum antibiotics for 5 weeks, immediately after tamoxifen exposure. We observed that microbiota depletion prevented Foxp3 loss within the Tomato$^+$ CD4$^+$ T cell population, resulting in an accumulation of T$_{regs}$ in the epithelial compartment

[1]Laboratory of Mucosal Immunology, The Rockefeller University, New York, NY 10065, USA. [2]Laboratory of Translational Immunology, University Medical Center Utrecht, the Netherlands. [3]Institute of Experimental Immunology, University of Zurich, Zurich, Switzerland. [4]Skirball Institute, New York University School of Medicine, New York, NY 10016, USA.
*Corresponding author. Email: breis@rockefeller.edu (B.S.R.); mucida@rockefeller.edu (D.M.)

Downloaded from http://science.sciencemag.org/ on June 28, 2016

(Fig. 2, C and D). The direct contribution of microbial metabolites versus microbial or dietary antigens to the differentiation of $CD4_{IELs}$ or pT_{regs} occupying the small intestinal epithelium (*21*) remains to be fully determined. Nevertheless, provision of a TCR ligand can overcome the strict microbiota requirement for $CD4_{IEL}$ differentiation, as demonstrated by the relatively normal $CD4_{IEL}$ differentiation in antibiotic-treated OT-II *Thpok*^{GFP} *Rag1*$^{-/-}$ mice exposed to oral OVA (fig. S2F). Along with the above data, these observations substantiate a microbial-induced plasticity of T_{reg} cells in the epithelium, corroborating intratissue specialization and conversion of gut $CD4^+$ T cells.

Next, we analyzed whether the reciprocal properties of pT_{regs} and $CD4_{IELs}$ were influenced by lineage-defining transcription factors. We first determined the role of ThPOK by crossing *Thpok*$^{fl/fl}$ (*22*) with *Cd4*^{CreER} mice (*23*) for *Thpok* depletion upon tamoxifen treatment (*16*) (fig. S3A). In vivo administration of tamoxifen to i*Cd4*(Δ*Thpok*) mice (*16*) 1 week before analysis resulted in a 32 to 48% reduction in the frequency of $Foxp3^+$ T_{regs} in lymphoid and intestinal tissues, respectively, whereas an increase in $CD4_{IELs}$ was observed only in intestinal tissues (Fig. 3, A and B). To examine the T_{reg} cell–intrinsic nature of these findings, we crossed *Thpok*$^{fl/fl}$ with *Foxp3*$^{CreER\text{-}eGFP}$ (fig. S3B) (*16*). Ex vivo analysis of T cells from i*Foxp3*(Δ*Thpok*) mice 1 week after tamoxifen treatment did not show a significant decrease in amounts of Foxp3 in the tissues examined, suggesting that ThPOK was not required for short-term stability of the lineage. However, analysis of T cells from i*Foxp3*(Δ*Thpok*) mice 5 weeks after tamoxifen pulse labeling revealed a significant reduction in the frequency and amounts of Foxp3 in $CD4^+$ T cells located in most compartments analyzed, with the exception of the large intestine (Fig. 3, C and D). Reciprocally, we found an accumulation of $CD4_{IELs}$ in the small intestine (Fig. 3, C and D). These data further support a ThPOK role in the regulation of the T_{reg} de novo conversion and stability.

To target the $CD4_{IEL}$ lineage defining transcription factors, we generated mice with conditional deletion of *Runx3* or *Tbx21* (encoding T-bet), which mediate down-regulation of ThPOK in developing $CD4_{IELs}$ (*9*, *10*). We analyzed the epithelial compartment of *Cd4*(Δ*Runx3*) mice and found a reduction in the frequency and number of $CD4_{IELs}$ and, conversely, enrichment in T_{regs} (Fig. 3E). Next, we analyzed mice in which *Tbx21* was excised early [driven by *Ox40*^{Cre} (*24*)] or late [driven by $E8_I^{Cre}$ (*25*)] during the $CD4_{IEL}$ differentiation (*16*). *Ox40*(Δ*Tbx21*) mice also showed reduced numbers of $CD4_{IELs}$ and roughly a twofold increase in T_{regs} in the epithelium, whereas $E8_I$(Δ*Tbx21*) mice showed reduced numbers of $CD4_{IELs}$ but normal numbers of T_{regs} in the epithelium when compared to Cre^- control mice (Fig. 3E). Collectively, the above data provide a possible mechanism for the reduced number of T_{regs} in the gut epithelium, where collaboration between Runx and T-bet results in down-modulation of ThPOK, and Foxp3, in $CD4^+$ T cells (*9*, *10*).

Oral exposure to TCR ligands results in both pT_{reg} and $CD4_{IEL}$ differentiation in a TGF-β–dependent manner (*4*, *8*, *10*, *11*, *13*, *26*). We asked whether the intratissue adaptation of pT_{regs} and $CD4_{IELs}$ influences the outcome of T cell responses to dietary antigens by using a transcription factor–based targeting of these lineages in OVA-specific TCR transgenic mice on a *Rag1*$^{-/-}$ background (*16*). Conditionally targeting *Runx3* in the OT-II model [OT-II(Δ*Runx3*)] prevented ThPOK loss and $CD4_{IEL}$ differentiation and also affected pT_{reg} differentiation in the large intestine, although no differences in cytokine production were found when compared to control OT-II mice (fig. S4, A to D). Whereas OVA-challenged control OT-II mice showed few or no signs of intestinal inflammation, OT-II(Δ*Runx3*) mice readily developed diarrhea and severe pathology, as confirmed by fecal lipocalin-2 concentrations (Fig. 4, A to C). We concluded that prevention of ThPOK loss and $CD4_{IEL}$ differentiation resulted in a local inflammatory response toward dietary antigens, although the reduction in pT_{reg} numbers could also contribute to the exaggerated inflammatory phenotype observed in the large intestine of OT-II(Δ*Runx3*) mice. In contrast, conditionally targeting *Thpok* by administering tamoxifen to OVA-fed iOT-II(Δ*Thpok*) mice (*16*) severely impaired pT_{reg} development in all tissues examined with a concomitant increase in $CD4_{IELs}$ in the intestine, although no inflammatory phenotype was observed (fig. S4, E to G). We then tested whether the OT-II(Δ*Runx3*) disease phenotype could be rescued, or prevented, by wild-type or *Thpok*-deficient

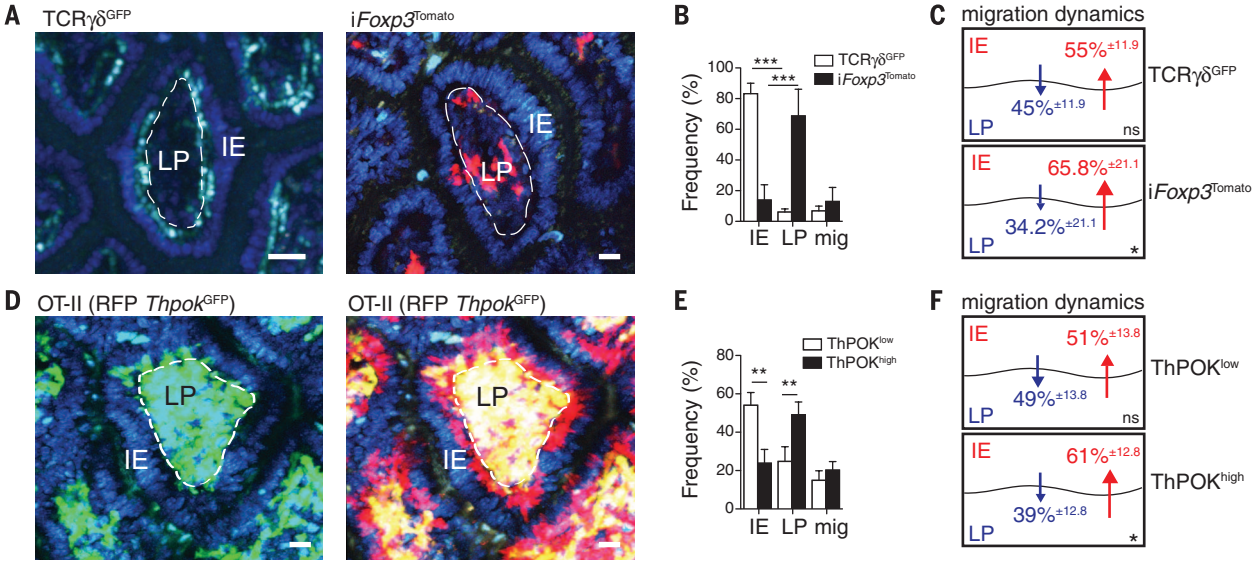


Fig. 1. ThPOK levels correlate with reciprocal T_{reg} and $CD4_{IEL}$ localization and migration dynamics in the intestine. (**A** to **F**) IVM analysis of ileal villi. Mice were injected with Hoechst before imaging to visualize all nuclei (blue). Scale bars, 10 μm. (A) Time-stacked image of TCRγδ^{GFP} (left, green channel) mice and i*Foxp3*^{Tomato} (right, red channel) mice, 24 hours after tamoxifen administration. Images are representative of 20 to 22 villi from at least three independent experiments. (B and C) Frequency of intraepithelial (IE), lamina propria (LP), or migratory TCRγδ^{GFP} and iFoxp3^{Tomato} cells. (C) Percentages within migrating cells. (D to F) Sorted naïve $CD4^+$ T cells from OT-II (RFP *Thpok*^{GFP}) mice were transferred to *Rag1*$^{-/-}$ mice, and recipient mice were fed an OVA-containing diet for 7 days before IVM analysis. (D) Time-stacked image of GFP^+ (left, green channel and blue channel overlay) and GFP^+ (yellow) and GFP^- (red) cells (right, green, red and blue channel overlay). Time-stacked images are representative of at least 50 villi from four independent experiments. (E) Quantification of tracked GFP^+ and GFP^- cell dynamics from four different movies (total six paired villi) in two independent experiments. (F) Percentages within migrating cells. Cells were tracked with *Imaris* software (Bitplane UK). Data are expressed as mean ± SD from three to six independent movies. ns: not significant, $*P < 0.05$, $**P < 0.01$, $***P < 0.001$ (Student's *t* test).

Downloaded from http://science.sciencemag.org/ on June 28, 2016

OT-II cells (*16*). We found that transferred wild-type CD45.1 OT-II cells, which could differentiate to both pT_{reg} and $CD4_{IELs}$, as well as $CD4^+$ T cells from tamoxifen-treated iOT-II(Δ*Thpok*) mice, which could only differentiate to $CD4_{IELs}$, rescued the diarrhea and inflammatory phenotype observed in OT-II(Δ*Runx3*) mice (Fig. 4, B and C, and fig. S4, H and I). These data indicate that a balance in ThPOK levels regulates inflammatory, $CD4^+$ T cell–mediated responses to dietary antigens. Additionally, these results suggest that $CD4_{IELs}$ exert a cell-extrinsic control of local intestinal inflammation.

To investigate whether pT_{regs} and $CD4_{IELs}$ play complementary anti-inflammatory roles in the intestine, we compared T cell responses to dietary OVA using BALB/c background monoclonal OVA-specific TCR strains, carrying either wild-type Foxp3 or a *scurfy* mutation ($Foxp3^{sf}$) (*16*), which results in a Foxp3 loss of function (*27*). In contrast to OT-II mice (C57BL/6 background), TBmc $Foxp3^{wt}$ mice fed an OVA diet showed a high rate of pT_{reg} induction in all tissues examined, but less ThPOK loss and fewer $CD4_{IELs}$ in the epithelium (fig. S4, A to C and J to N). Conversely, TBmc $Foxp3^{sf}$ showed a high degree of ThPOK loss and increased $CD4_{IEL}$ development in the small intestine, with a frequency that mirrored the relative amounts of pT_{regs} in TBmc $Foxp3^{wt}$ mice (fig. S4, J to N). However, no inflammatory phenotype or diarrhea was observed, even in the absence of functional Foxp3 in this monoclonal model (Fig. 4, D to F). To examine whether exaggerated $CD4_{IEL}$ differentiation could compensate for the absence of pT_{regs} in TBmc $Foxp3^{sf}$ mice, we depleted $CD4_{IELs}$ using antibodies against CD8α (anti-CD8α) during OVA feeding (fig. S4, M and N). We found that TBmc $Foxp3^{sf}$ mice treated with anti-CD8α, but not TBmc $Foxp3^{wt}$ treated with anti-CD8α or TBmc

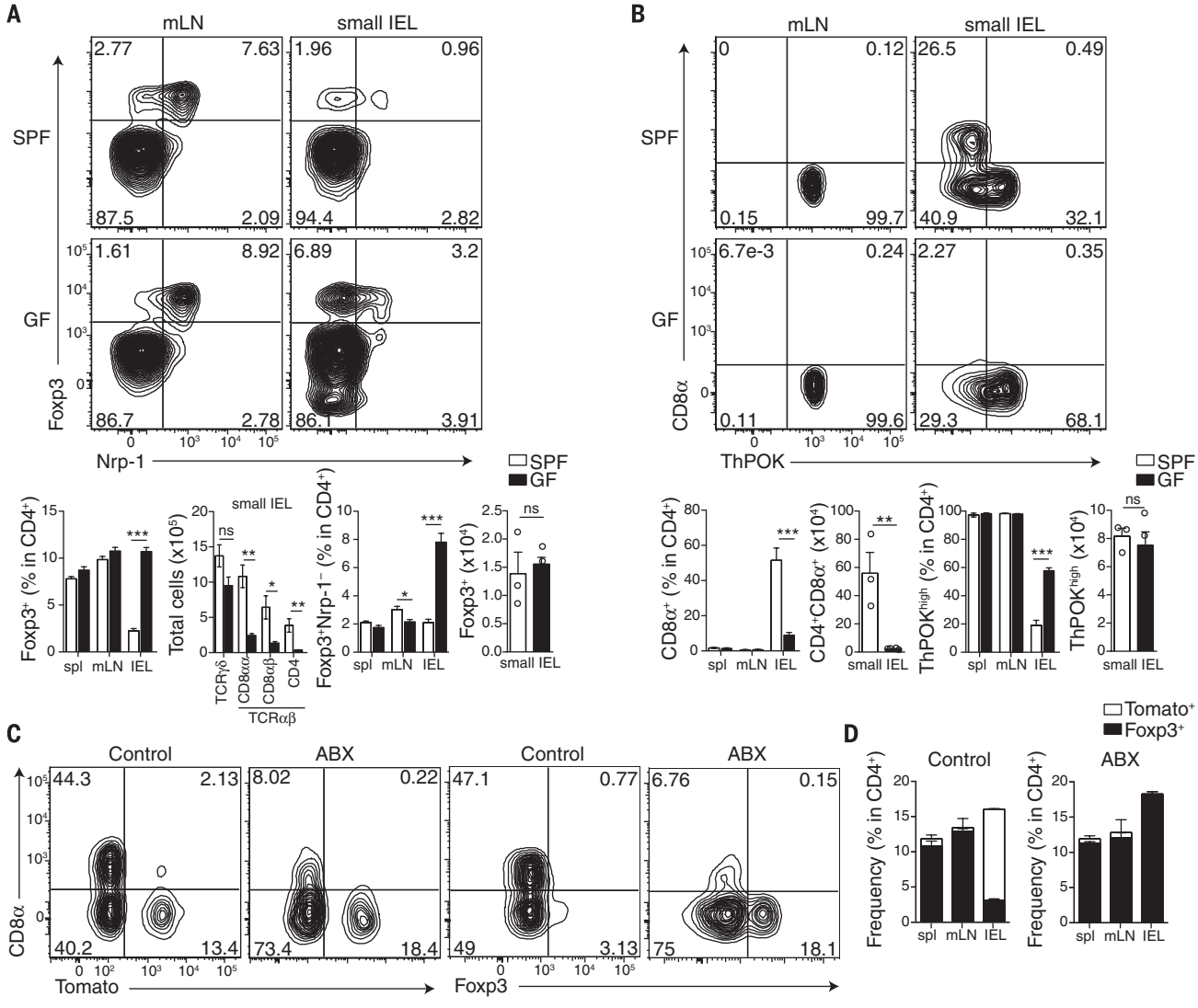


Fig. 2. Microbiota-dependent plasticity of T_{regs} in the intestinal epithelium. (**A** and **B**) Flow cytometry analysis of lymphocytes from spleen (spl), mesenteric lymph nodes (mLN), and small intestine epithelium (IEL) of wild-type C57BL/6 mice maintained under specific pathogen-free (SPF) or germ-free (GF) conditions. (A) Surface neuropilin-1 (Nrp-1) and intracellular Foxp3 expression by $TCRβ^+CD4^+CD8β^-$ cells. Bar graphs represent frequency and total number of $Foxp3^+$ (left) or $Foxp3^+Nrp\text{-}1^-$ (pT_{regs}) (right) among $TCRβ^+CD4^+CD8β^-$ cells. Total cell number for T cell populations isolated from the sIELs is also shown. (B) Surface CD8α and intracellular ThPOK expression by $TCRβ^+CD4^+CD8β^-$ cells. Bar graphs represent frequency and total number of $CD8α^+$ (left) or $ThPOK^{high}$ (right) among $TCRβ^+CD4^+CD8β^-$ cells. Data are expressed as mean ± SD of individual mice (n = 6), representative of three independent experiments. (**C** and **D**) Flow cytometry analysis of lymphocytes from spl, mLN, and small intestine IEL of *Foxp3*$^{CreER\text{-}eGFP}$:*Rosa26*$^{lsl\text{-}tdTomato}$ (i*Foxp3*^{Tomato}) mice treated with tamoxifen and maintained with broad-spectrum antibiotics for 5 weeks (ABX) or sucralose (Control). (C) Surface CD8α and Tomato expression or intracellular Foxp3 among $TCRβ^+CD4^+$ cells. (D) Frequency of $Foxp3^+$ (black) and $Tomato^+$ (white) among $TCRβ^+CD4^+$ cells in each tissue. Data are expressed as mean ± SD of individual mice (n = 3), representative of three independent experiments. *P < 0.05, **P < 0.01, ***P < 0.001 (Student's t test).

Downloaded from http://science.sciencemag.org/ on June 28, 2016

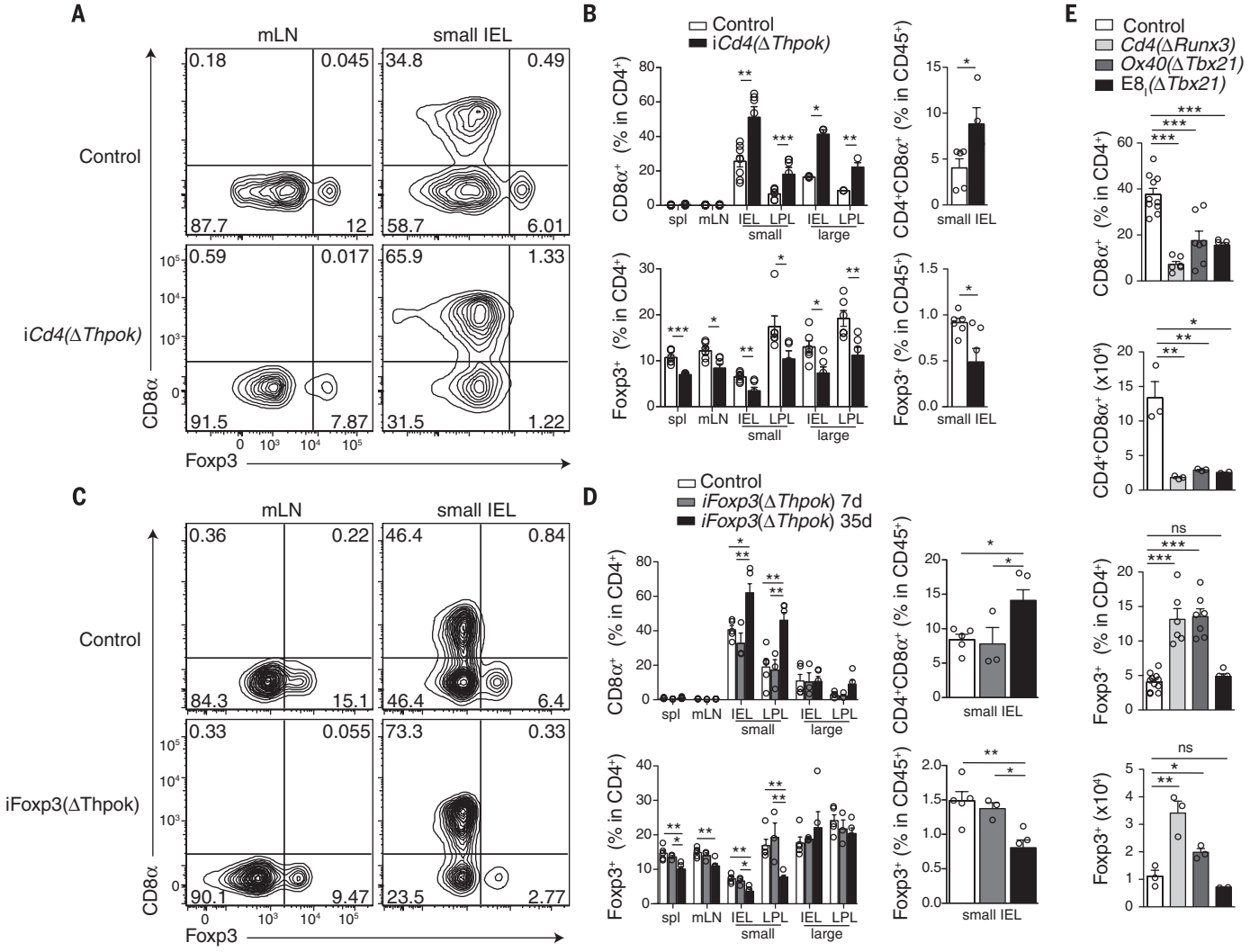


Fig. 3. ThPOK expression by intestinal epithelial CD4$^+$ T cells plays a key role in the reciprocal development of T_{regs} and $CD4_{IELs}$. (**A** to **D**) Flow cytometry analysis of lymphocytes from spleen (spl), mesenteric lymph nodes (mLN), small and large intestine epithelium (IEL), and lamina propria (LPL) of inducible conditional *Thpok*-deficient mice. (A and B) *Cd4*^{CreER}:*Thpok*$^{fl/fl}$ [i*Cd4*(Δ*Thpok*)] and (Cre$^-$) *Thpok*$^{f/f}$ littermate control mice 7 days after tamoxifen administration. (A) Representative contour plot for surface CD8α and intracellular Foxp3 among TCRβ$^+$CD4$^+$CD8β$^-$ cells. (B) Frequency of CD8α$^+$ (upper) and Foxp3$^+$ (lower) among TCRβ$^+$CD4$^+$CD8β$^-$ or among total CD45$^+$ cells in the indicated tissues. Data are expressed as mean ± SD of individual mice (n = 3 to 6), representative of six independent experiments. (C and D) *Foxp3*^{CreER}:*Thpok*$^{fl/fl}$ [i*Foxp3*(Δ*Thpok*)] and (Cre$^+$)*Thpok*$^{+/+}$ littermate control mice 7 days [shown in (D)] or 35 days after tamoxifen administration. (C) Representative contour plot for surface CD8α and intracellular Foxp3 among TCRβ$^+$CD4$^+$CD8β$^-$ cells. (D) Frequency of CD8α$^+$ (upper) and Foxp3$^+$ (lower) among TCRβ$^+$CD4$^+$CD8β$^-$ or among total CD45$^+$ cells in the indicated tissues. Data are expressed as mean ± SD of individual mice (n = 3 to 8), representative of three independent experiments. (**E**) Frequency and total number of CD8α$^+$ and Foxp3$^+$ among TCRβ$^+$CD4$^+$CD8β$^-$ cells from sIEL of *Ox40*(Δ*Tbx21*), *Cd4*(Δ*Runx3*), E8$_I$(Δ*Tbx21*), and wild-type (WT) mice. Data are expressed as mean ± SD of individual mice (n = 3 to 9), representative of three independent experiments. *P < 0.05, **P < 0.01, ***P < 0.001 [Student's t test (B), one-way analysis of variance (ANOVA) with Tukey post-test (D, E)].

Foxp3^{sf} treated with control antibodies, showed severe intestinal inflammation and diarrhea (Fig. 4, D to F, and fig. S4O). These results support a model in which $CD4_{IELs}$ and pT_{regs} cooperate in the regulation of local intestinal inflammation.

The single-layered intestinal epithelium constitutes a uniquely challenging location for immune regulatory processes, given its proximity to highly stimulatory luminal contents and limited spatial organization. It is currently thought that T_{regs} use several redundant and complementary mechanisms to suppress inflammatory responses, and their capacity to sense specific environmental cues plays a major role in their function (*28*–*30*). The physiological instability that we observe in the T_{reg} lineage within the intestinal epithelium may represent an important modulation of regulatory activity that is coordinated by this particular environment (*3*, *20*, *28*, *31*, *32*). Although our targeting strategies do not discriminate between the function of "ex-T_{regs}" and "directly converted" $CD4_{IELs}$, natural or forced ThPOK down-modulation was previously associated with an impaired helper function in CD4$^+$ T cells, including reduced production of proinflammatory cytokines and reduced expression of costimulatory molecules (*8*, *10*, *33*). The data presented here support a cell-extrinsic suppressive role for $CD4_{IELs}$, although the likely epithelium-specific mechanism used by these cells to actively regulate or prevent tissue inflammation remains unclear. However, a role for $CD4_{IELs}$ in triggering inflammation via their cytotoxic activity, in specific contexts, is conceivable (*8*, *34*). Nevertheless, the observation that particular environmental cues, such as the microbiota, induce plasticity of seemingly stable lymphocyte

Downloaded from http://science.sciencemag.org/ on June 28, 2016

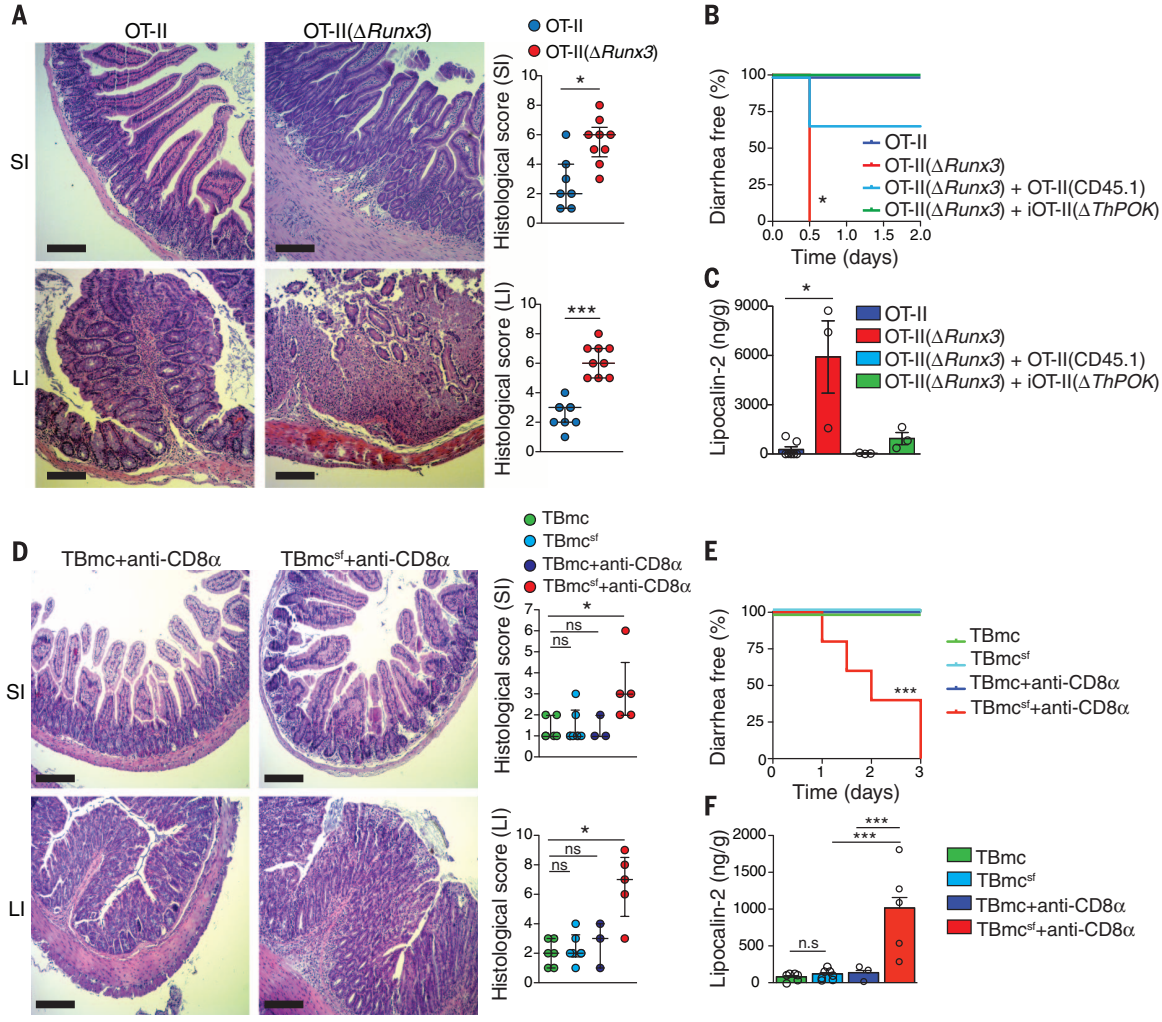


Fig. 4. Complementary roles for pT_{regs} and $CD4_{IELs}$ in regulating local inflammatory response toward dietary antigens. OVA-specific TCR transgenic mice (*Rag1*$^{-/-}$ background) were fed an OVA-containing diet for 7 days. (**A** to **C**) *Thpok*^{GFP} OT-II(Δ*Runx3*) and control *Thpok*^{GFP} OT-II mice were analyzed. (A) Hematoxylin and eosin staining of the small intestine jejunum (SI) (upper panels) and the large intestine colon (LI) (lower panels). Original magnification, 40×. Graphs represent histological scores of the SI (upper) and the LI (lower) (each symbol represents one mouse). (B and C) Sorted naïve OVA-specific TCR transgenic cells (TCRVα2^{+}CD4^{+}CD62L^{+}CD44^{low}) from wild-type CD45.1 OT-II or tamoxifen-treated iOT-II(Δ*Thpok*) were transferred to host OT-II(Δ*Runx3*) before treatment, as in (A). (B) Frequency of diarrhea-free mice after oral OVA challenge. (C) Quantification of fecal Lipocalin-2. (**D** to **F**) TBmc Foxp3^{sf} (*scurfy*) and TBmc control were treated as in (A) and injected with isotype control or anti-CD8α depleting antibody. (D) Hematoxylin and eosin staining of the SI (upper) and the LI (lower). Original magnification, 40×. Graphs represent histological scores of the SI (upper) and the LI (lower) (each symbol represents one mouse). (E) Frequency of diarrhea-free mice after oral OVA challenge. (F) Quantification of fecal Lipocalin-2. Data are expressed as mean +SD or median ± interquartile range (A and D), representative of at least two independent experiments (n = 3 to 8 per group). Scale bar, 200 μm. *P < 0.05, **P < 0.01, ***P < 0.001 [Student's t test or Mann-Whitney test (A), one-way ANOVA with Tukey post-test (C and F), log-rank test (B and E), and Kruskal-Wallis with Dunns post-test (D)].

lineages may contribute to the understanding of how specialized tissue-adaptation pathways function to balance efficient immune protective responses with tissue tolerance.

REFERENCES AND NOTES

1. M. Shale, C. Schiering, F. Powrie, *Immunol. Rev.* **252**, 164–182 (2013).
2. A. M. Bilate, J. J. Lafaille, *Annu. Rev. Immunol.* **30**, 733–758 (2012).
3. Y. Furusawa *et al.*, *Nature* **504**, 446–450 (2013).
4. D. Mucida *et al.*, *J. Clin. Invest.* **115**, 1923–1933 (2005).
5. P. M. Smith *et al.*, *Science* **341**, 569–573 (2013).
6. N. Arpaia *et al.*, *Nature* **504**, 451–455 (2013).
7. K. Atarashi *et al.*, *Nature* **500**, 232–236 (2013).
8. D. Mucida *et al.*, *Nat. Immunol.* **14**, 281–289 (2013).
9. B. S. Reis, D. P. Hoytema van Konijnenburg, S. I. Grivennikov, D. Mucida, *Immunity* **41**, 244–256 (2014).
10. B. S. Reis, A. Rogoz, F. A. Costa-Pinto, I. Taniuchi, D. Mucida, *Nat. Immunol.* **14**, 271–280 (2013).
11. J. L. Coombes *et al.*, *J. Exp. Med.* **204**, 1757–1764 (2007).
12. J. A. Hall, J. R. Grainger, S. P. Spencer, Y. Belkaid, *Immunity* **35**, 13–22 (2011).
13. C. M. Sun *et al.*, *J. Exp. Med.* **204**, 1775–1785 (2007).
14. Y. P. Rubtsov *et al.*, *Science* **329**, 1667–1671 (2010).
15. K. L. Edelblum *et al.*, *Proc. Natl. Acad. Sci. U.S.A.* **109**, 7097–7102 (2012).
16. Materials and methods are available as supplementary materials on *Science* Online.
17. Y. P. Rubtsov *et al.*, *Immunity* **28**, 546–558 (2008).
18. T. Miyao *et al.*, *Immunity* **36**, 262–275 (2012).
19. T. Tanoue, K. Atarashi, K. Honda, *Nat. Rev. Immunol.* **16**, 295–309 (2016).
20. K. Atarashi *et al.*, *Science* **331**, 337–341 (2011).
21. K. S. Kim *et al.*, *Science* **351**, 858–863 (2016).
22. T. Egawa, D. R. Littman, *Nat. Immunol.* **9**, 1131–1139 (2008).
23. A. Śledzińska *et al.*, *PLOS Biol.* **11**, e1001674 (2013).
24. M. Klinger *et al.*, *J. Immunol.* **182**, 4581–4589 (2009).
25. Y. Maekawa *et al.*, *Nat. Immunol.* **9**, 1140–1147 (2008).
26. M. O. Li, Y. Y. Wan, R. A. Flavell, *Immunity* **26**, 579–591 (2007).
27. M. A. Curotto de Lafaille *et al.*, *Immunity* **29**, 114–126 (2008).
28. S. Z. Josefowicz, L. F. Lu, A. Y. Rudensky, *Annu. Rev. Immunol.* **30**, 531–564 (2012).
29. C. Ohnmacht *et al.*, *Science* **349**, 989–993 (2015).
30. E. Sefik *et al.*, *Science* **349**, 993–997 (2015).
31. L. V. Hooper, A. J. Macpherson, *Nat. Rev. Immunol.* **10**, 159–169 (2010).

Downloaded from http://science.sciencemag.org/ on June 28, 2016

32. J. Bollrath, F. M. Powrie, *Semin. Immunol.* **25**, 352–357 (2013).
33. M. S. Vacchio *et al.*, *Nat. Immunol.* **15**, 947–956 (2014).
34. B. Jabri, V. Abadie, *Nat. Rev. Immunol.* **15**, 771–783 (2015).

ACKNOWLEDGMENTS

We are indebted to K. Velinzon and N. Thomas for sorting cells and to members of the Nussenzweig lab and The Rockefeller University employees for continuous assistance. We thank S. Hemmers (Memorial Sloan Kettering Cancer Center) for generating *Cd4*^{CreER} mice. We especially thank A. Rogoz for outstanding technical support. We thank members of our laboratory, particularly V. Pedicord, and D. Esterhazy, for discussions and critical reading and editing of the manuscript. The data reported in this manuscript are tabulated in the main paper and in the supplementary materials. This work was supported by Leona M. and Harry B. Helmsley Charitable Trust (T.S., D.P.H.v.K., B.S.R., D.M.), Japan Foundation for Applied Enzymology and Uehara Memorial Foundation (T.S.), Alexandre Suerman Stipend, Royal Netherlands Academy of Sciences, and the Prince Bernhard Cultural Foundation (D.P.H.v.K.), Deutsche Forschungsgemeinschaft 1410/1 grant and Swiss National Science Foundation 0310030-11620 grant (T.B.), National Multiple Sclerosis Society (J.J.L.), the Crohn's & Colitis Foundation of America (B.S.R., D.M.), the Irma T. Hirschl Award (D.M.), and National Institutes of Health grant NIH R01 DK093674 (D.M.). The Rockefeller University Bio-Imaging Resource Center is supported by the Empire State Stem Cell Fund through New York State Department of Health C023046. D.M. conceived of and D.M. and B.S.R. supervised this study; T.S., J.J.L., B.S.R., and D.M. designed experiments; T.S., M.L., D.P.H.v.K., T.R., H.M.S., and B.S.R. performed and analyzed experiments; T.B. provided the *Cd4*^{CreER} strain (*23*); T.S., M.L., D.P.H.v.K. and B.S.R. prepared figures and helped with manuscript preparation; and D.M. wrote the paper.

SUPPLEMENTARY MATERIALS

www.sciencemag.org/content/352/6293/1581/suppl/DC1
Materials and Methods
Figs. S1 to S4
Movies S1 to S3
Reference (*35*)

3 February 2016; accepted 10 May 2016
Published online 2 June 2016
10.1126/science.aaf3892

NEUROGENOMICS

Neuronal subtypes and diversity revealed by single-nucleus RNA sequencing of the human brain

Blue B. Lake,[1]* Rizi Ai,[2]* Gwendolyn E. Kaeser,[3,4]* Neeraj S. Salathia,[5]* Yun C. Yung,[3] Rui Liu,[1] Andre Wildberg,[2] Derek Gao,[1] Ho-Lim Fung,[1] Song Chen,[1] Raakhee Vijayaraghavan,[5] Julian Wong,[3] Allison Chen,[3] Xiaoyan Sheng,[3] Fiona Kaper,[5] Richard Shen,[5] Mostafa Ronaghi,[5] Jian-Bing Fan,[5]† Wei Wang,[2]† Jerold Chun,[3]† Kun Zhang[1]†

The human brain has enormously complex cellular diversity and connectivities fundamental to our neural functions, yet difficulties in interrogating individual neurons has impeded understanding of the underlying transcriptional landscape. We developed a scalable approach to sequence and quantify RNA molecules in isolated neuronal nuclei from a postmortem brain, generating 3227 sets of single-neuron data from six distinct regions of the cerebral cortex. Using an iterative clustering and classification approach, we identified 16 neuronal subtypes that were further annotated on the basis of known markers and cortical cytoarchitecture. These data demonstrate a robust and scalable method for identifying and categorizing single nuclear transcriptomes, revealing shared genes sufficient to distinguish previously unknown and orthologous neuronal subtypes as well as regional identity and transcriptomic heterogeneity within the human brain.

Although substantial progress has been achieved in mice (*1*–*3*), comprehensive classification of adult human brain neurons on the basis of their single-cell transcriptomes has yet to be realized. Examination of individual neuronal gene expression profiles for functional patterns could provide unbiased insights into subtypes from defined neuroanatomical regions, which are missed by gross anatomical studies that report limited transcriptomic differences across the neocortex (*4*–*7*). Previous analyses of single adult human neurons have been dependent on methods compatible with freshly isolated neurosurgical tissues (*8*), which can be difficult to obtain, with limited regional sampling and depth. In contrast, postmortem tissues provide a vastly more accessible source of both normal and diseased brain, in which challenges to interrogating single neuronal genomes can be overcome by using single nuclei (*9*, *10*) combined with RNA sequencing. Here, we report the development of a scalable pipeline from postmortem brain through nuclear transcriptome analyses that identifies both known and previously unknown neuronal subtypes across the cerebral cortex in humans.

With the goal of defining transcriptomic profiles of single neurons, neuronal nuclear antigen (NeuN) was used (*9*) to isolate neuronal nuclei (fig. S1) from the postmortem brain of a normal, 51-year-old female (Fig. 1A). We focused on six classically defined Brodmann Areas (BAs) with well-documented anatomical and electrophysiological properties that were derived from a single cortical hemisphere because interhemispheric and interindividual transcriptome differences were reported to be minimal (*4*–*7*). Isolation of nuclei was used to reduce transcriptomic contamination from other cells or degradation encountered with whole-neuron dissociation or laser caption microdissection (fig. S2). Furthermore, sequencing of RNA from single nuclei on a limited scale has found gene expression values comparable with that of the whole cell (*11*, *12*). Therefore, we developed and implemented a highly scalable, single-nucleus RNA sequencing (SNS) pipeline (*13*) (Fig. 1A and figs. S1 and S3 to S8) that has broad applicability for postmortem brains derived from multiple brain banks or repositories (fig. S4F).

Using this pipeline, we processed 86 Fluidigm C1 chips and sequenced 4488 single nuclei to an average depth of 8.34 million reads (table S1 and fig. S5). Genomic mapping rates revealed a high proportion of reads that corresponded to intronic sequences (Fig. 1A and fig. S5A). The low percentage of intergenic reads argues against possible genomic contamination. Instead, the intronic reads likely captured an abundance of nascent RNA transcripts present in the nuclei. Intronic reads can be used to predict de novo expression (*14*), as well as whole-cell gene transcription levels (*15*). Additionally, our single-nuclei expression data inclusive of intronic reads accurately predicted cellular identity (fig. S7), providing initial validation for our SNS pipeline.

After quality filtering, including removal of doublets misclassified as single nuclei (Fig. 1A and fig. S6) (*13*), we achieved 3227 data sets across the six cortical regions (Fig. 1A and table S2). To identify neuronal subtypes, we developed a clustering and classification strategy that was capable of resolving 17 clusters (fig. S8A) (*13*) on the basis of differential expression of neuronally annotated marker genes (tables S3 and S4 and fig. S8B). These clusters showed distinct subgroup aggregation (Fig. 1B and fig. S9A) and specific gene expression profiles associated with neuronal ontologies (Fig. 1C, fig. S9B, and tables S5 and S6). With the exception of a single cluster (NoN, $n = 44$ data sets) deriving from one C1 chip having reduced mapping rates, 16 of these clusters were generated independent of detectable batch effects (table S2 and fig. S10). Differential expression of inhibitory markers associated with GABAergic interneurons (table S3) distinguished potential inhibitory (In) from excitatory (Ex) neuronal subtypes (Fig. 1B), which is consistent with mutually exclusive positivity of associated marker genes using a fraction of positive (FOP) thresholding method (Fig. 2A) (*2*). As such, our data set first differentiated two major classifications within the cerebral cortex: 972 inhibitory

[1]Department of Bioengineering, University of California, San Diego, La Jolla, CA, USA. [2]Department of Chemistry and Biochemistry, University of California, San Diego, La Jolla, CA, USA. [3]Department of Molecular and Cellular Neuroscience, Dorris Neuroscience Center, The Scripps Research Institute, La Jolla, CA, USA. [4]Biomedical Sciences Graduate Program, University of California, San Diego, La Jolla, CA, USA. [5]Illumina, San Diego, CA, USA.
*These authors contributed equally to this work. †Corresponding author. Email: kzhang@bioeng.ucsd.edu (K.Z.); jchun@scripps.edu (J.C.); wei-wang@ucsd.edu (W.W.); jianbing_fan@yahoo.com (J.-B.F.)

Downloaded from http://science.sciencemag.org/ on June 28, 2016

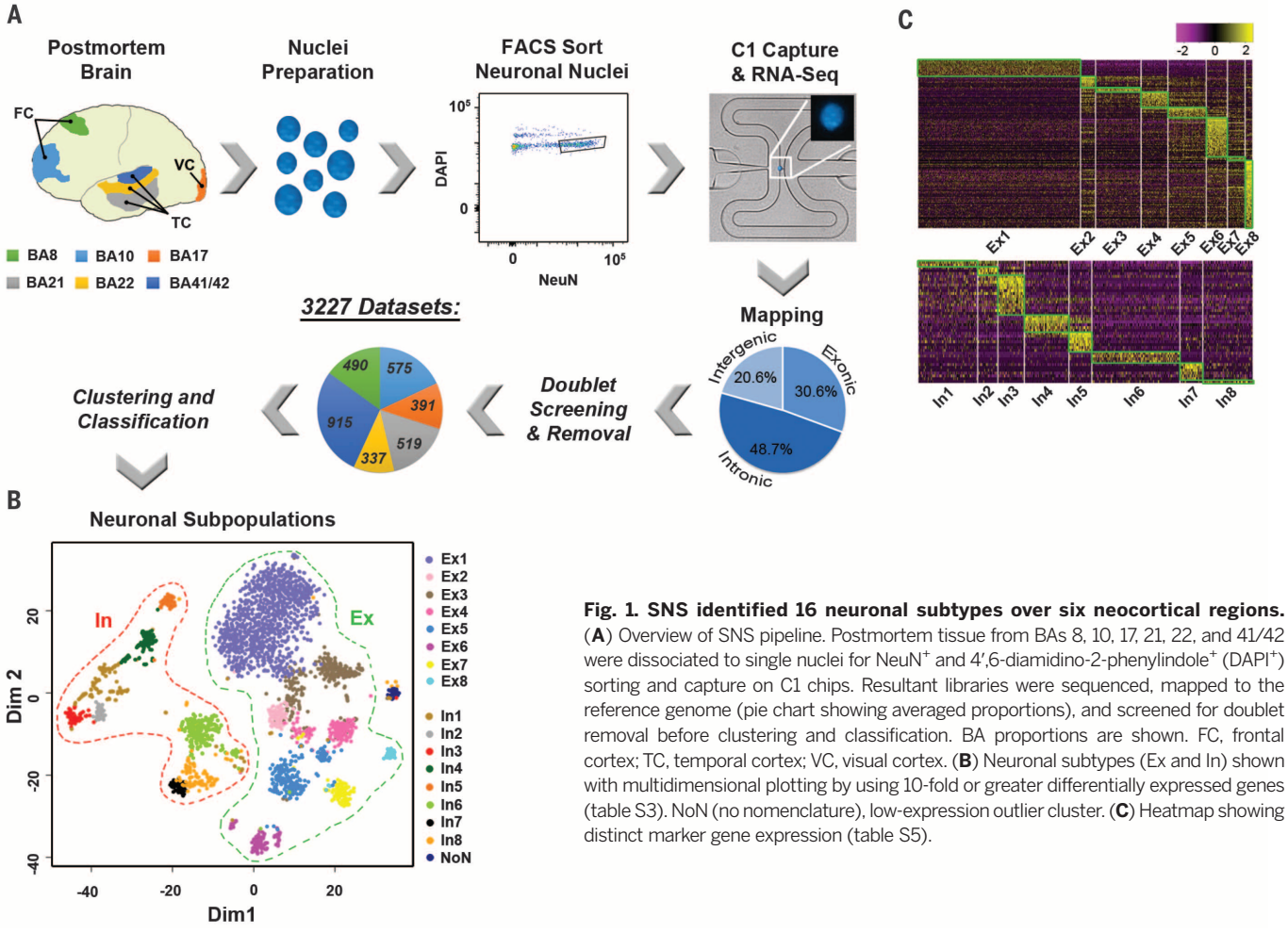


Fig. 1. SNS identified 16 neuronal subtypes over six neocortical regions. (**A**) Overview of SNS pipeline. Postmortem tissue from BAs 8, 10, 17, 21, 22, and 41/42 were dissociated to single nuclei for NeuN$^+$ and 4′,6-diamidino-2-phenylindole$^+$ (DAPI$^+$) sorting and capture on C1 chips. Resultant libraries were sequenced, mapped to the reference genome (pie chart showing averaged proportions), and screened for doublet removal before clustering and classification. BA proportions are shown. FC, frontal cortex; TC, temporal cortex; VC, visual cortex. (**B**) Neuronal subtypes (Ex and In) shown with multidimensional plotting by using 10-fold or greater differentially expressed genes (table S3). NoN (no nomenclature), low-expression outlier cluster. (**C**) Heatmap showing distinct marker gene expression (table S5).

neurons that generally encompass interneurons and 2253 excitatory neurons that generally encompass pyramidal or projection neurons (*16*). Furthermore, each subgroup within these classifications showed distinct contributions from each brain region (Fig. 2A and table S7), likely reflecting varied proportions of these neuronal subtypes across BAs, with most variability present in the visual cortex (BA17), which is known to have distinct cytoarchitecture and gene expression profiles (*7*, *17*).

In order to further annotate inhibitory neuron subtypes, we examined expression of known marker genes associated with cortical layers, developmental origin, and interneuron classification (Fig. 2B) (*13*). On the basis of in situ human brain expression data (fig. S11) (*17*), our inhibitory neuron subtypes were found to distribute spatially from the pial surface (most superficial boundary) to white matter (deepest boundary) of the neocortex and could be grouped by the developmental origin of interneurons from subcortical regions of the medial, lateral, or caudal ganglionic eminences (MGE, LGE, or CGE) (Fig. 2B) (*18*, *19*). Furthermore, distinct profiles of interneuron classification markers revealed subtypes that parallel those identified from the mouse somatosensory cortex (Fig. 2, B and C, and fig. S12A) (*3*). Cortical regional heterogeneity within subtypes was also observed, as evident by a layer 3 population (In4) that showed a specific absence of *RELN*/*SST* expression in BA17 (Fig. 2C and fig. S11, B and D). As such, our data distinguished inhibitory neuron subtypes having heterogeneous distributions within the neocortex.

Most excitatory cortical projection or pyramidal neurons can be categorized by their layer position established during neocortical development (*17*) combined with their axonal projections (Fig. 3A) (*16*). Our excitatory neuron subgroups, which were also in high concordance with subtypes identified in mice (fig. S12B) (*3*), expressed known markers associated with a superficial-to-deep cortical distribution (Fig. 3, B to D, and fig. S13) (*13*), with more than one subtype occupying most layers. Our data set was able to resolve cortical region specificity, as seen for the *BHLHE22*-positive (Fig. 3C and fig. S13, A and D) layer 4 subtypes Ex2 and Ex3 (Fig. 4A), where Ex2 derived predominantly from rostral regions, BA8 and BA10, and Ex3 from caudal regions, BA17 and BA41/42 (Figs. 2A and 4B). Consistently, these subgroups showed distinct gene expression (Fig. 4C and table S8) associated with neuronal electrophysiology and connectivity (table S9). Furthermore, we were able to resolve intrasubtype heterogeneity, in terms of BA-specific expression patterns, which was observed in all subtypes (Fig. 4B), such as within the Ex3 subtype between BA17 and BA41/42 regions (Fig. 4, B and D, and table S10). As such, regional neurophysiological differences in cortical regions may be attributed to not only variations in the proportions of interneuron and projection neuron subtypes, but also to cell-intrinsic transcriptomic differences among single neurons within a subtype. Consistent with this possibility, we found that genes having known variability between the visual and temporal cortices from in situ hybridization (ISH) studies (*17*) also had transcriptomic differences that could be attributed to subtypes defined by our data set (fig. S14A and table S11) (*13*). Therefore, our data highlight subtle yet region-defining gene expression signatures among specific neuronal subtypes that could not be detected from bulk analyses (fig. S14B).

To further understand the extent of heterogeneity that may exist within subtypes, we identified genes varying globally (table S12 and fig. S15A) or expressed differentially within each BA (table S13 and fig. S15B) for each subgroup. Although a subset of In and Ex subgroup-variable genes was associated with differential expression between brain regions, a large proportion were distinct (fig. S15C).

Downloaded from http://science.sciencemag.org/ on June 28, 2016

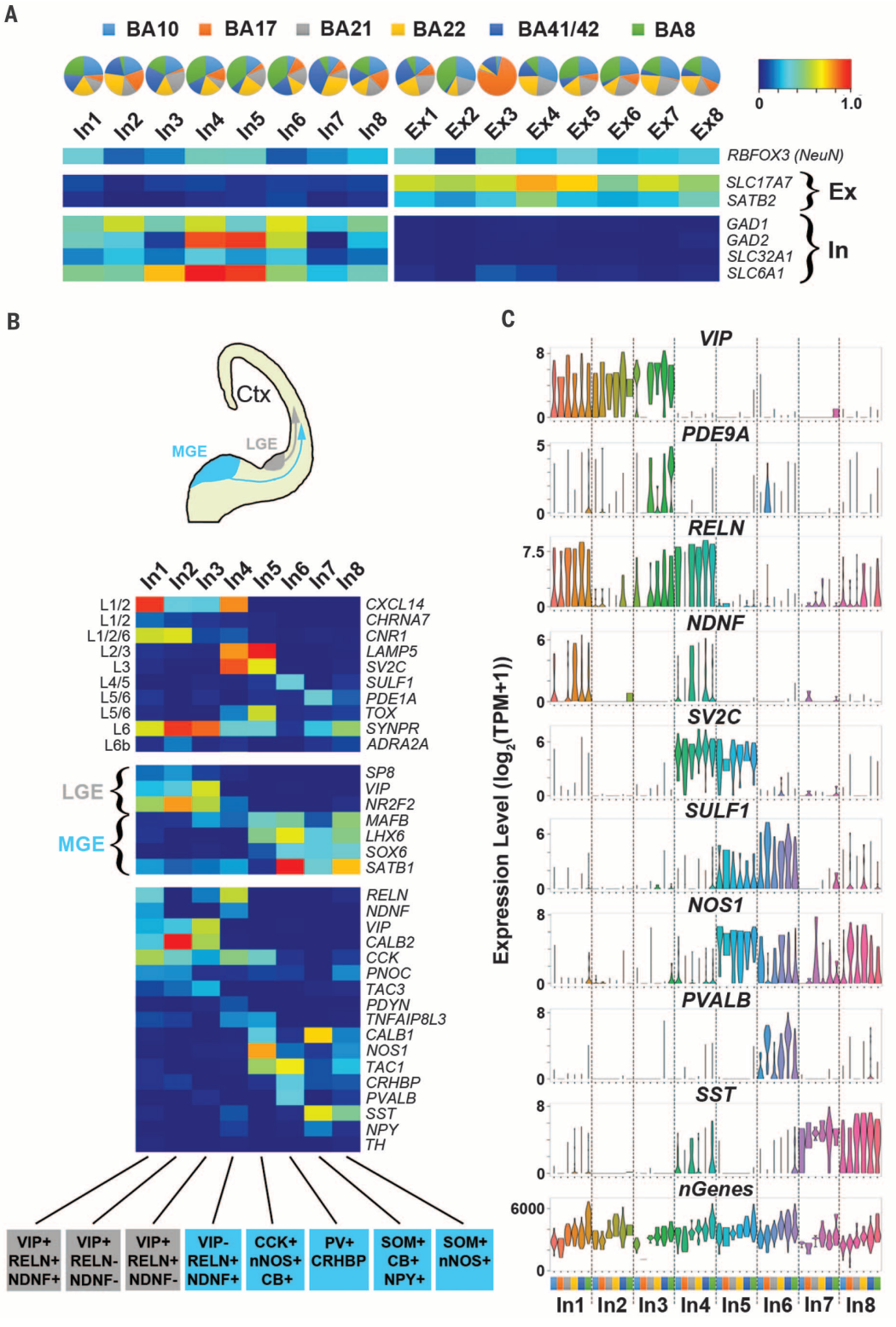


Fig. 2. SNS reveals distinct interneuron subtypes. (**A**) Pie charts display relative proportions of subtypes among BAs and FOP heatmaps for In and Ex marker genes. (**B**) Diagram of subpallial origins of interneurons from either the LGE or MGE with FOP heatmaps [scale as in (A)] for marker genes associated with cortical layer (L) (top), subpallial origin (middle), and interneuron classification (bottom). Potential interneuron subtypes are indicated below. SOM, *somatostatin* or *SST*; NPY, *neuropeptide Y*; CB, *calbindin-D-28k* or *CALB1*; VIP, *vasoactive intestinal peptide*; RELN, *reelin*; nNOS, *neuronal nitric oxide synthase* or *NOS1*; PV, *parvalbumin* or *PVALB*; CCK, *cholecystokinin;* NDNF, *neuron-derived neurotrophic factor*; CRHBP, *corticotropin releasing hormone binding protein*. (**C**) Violin plots showing select marker gene expression values by BA [colors as in (A)] for each inhibitory neuron subtype. *nGenes*, total number of genes identified.

Downloaded from http://science.sciencemag.org/ on June 28, 2016

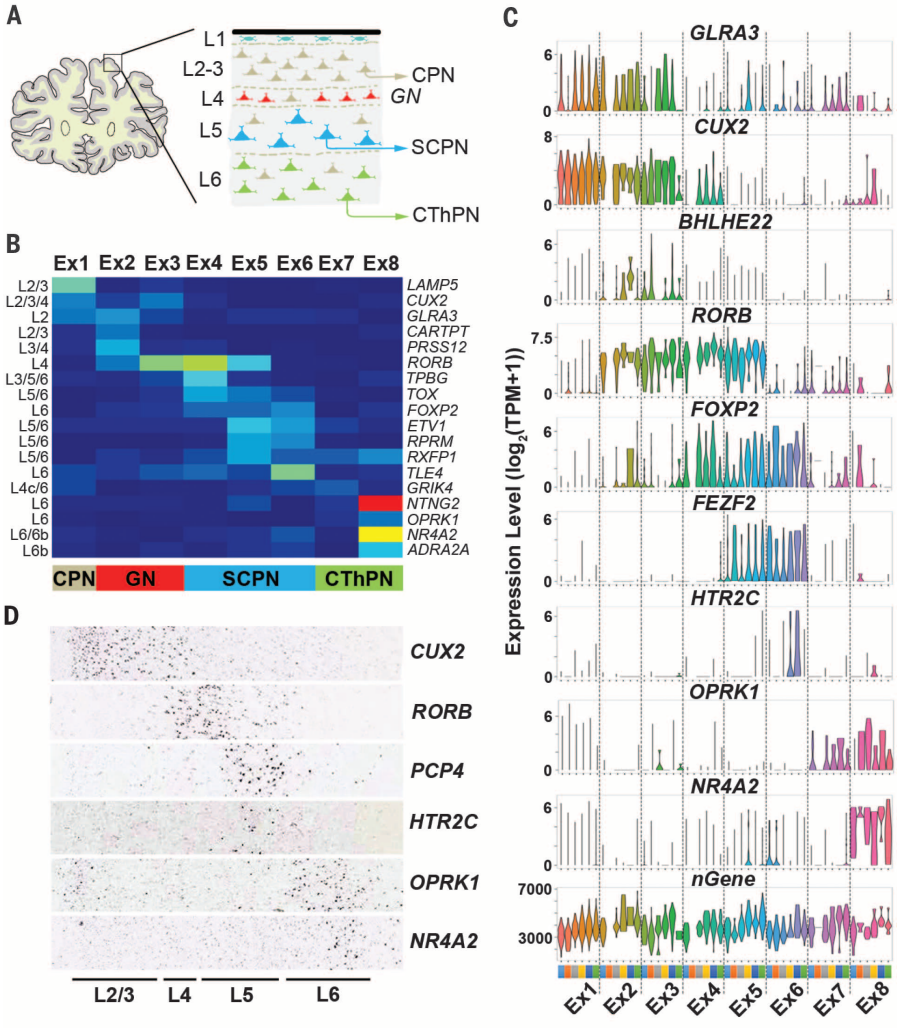


Fig. 3. Excitatory neuronal subtypes show distinct spatial organization. (**A**) Schematic of the prefrontal cortex showing projection neuron layers (L) and expected axonal projection destinations (layer 4 granule neurons typically receive outside inputs for distribution of signals locally). (**B**) FOP heatmap (scale as in Fig. 2A) for layer-specific marker genes showing expected cortical layer identity (L2-L6b) and excitatory neuron subclassification. CPN, cortical projection neuron; GN, granule neuron; SCPN, subcortical projection neuron; CThPN, corticothalamic projection neuron. (**C**) Violin plots showing selected marker gene expression values by Ex subtype and BA represented by colors (Fig. 2A). *nGenes*, total number of genes identified. (**D**) RNA ISH showing layer-specific expression of selected markers in the temporal cortex (Allen Human Brain Atlas, table S11).

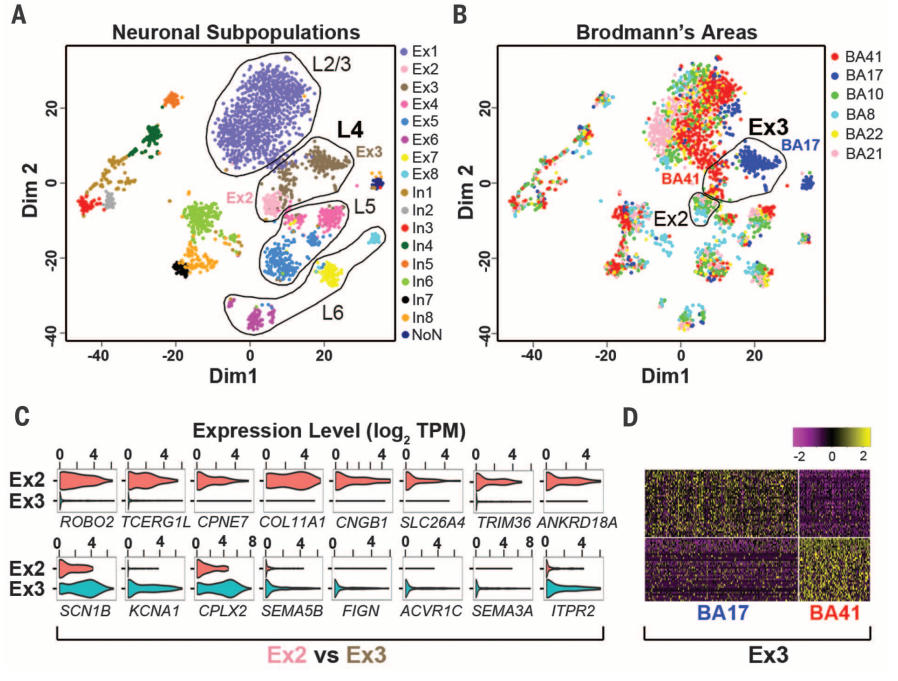


Fig. 4. Neuronal subtypes reveal heterogeneity among BAs. (**A**) Multidimensional plot showing projection neuron subtypes distributed according to their predicted cortical layer (L) identity. Layer 4 Ex2 and Ex3 subtypes are indicated. (**B**) Clusters shown in (A) colored by BA and with BA41/42 and BA17 subpopulations of Ex3 indicated. (**C**) Violin plots showing differentially expressed genes between Ex2 and Ex3 subtypes (table S8). (**D**) Heatmap showing genes differentially expressed between BA17 and BA41/42 within the Ex3 subtype (table S10).

Downloaded from http://science.sciencemag.org/ on June 28, 2016

Therefore, the potential exists for not only intraregional cortical transcriptomic differences, but also further intrasubtype heterogeneity. This might reflect a technical need for increased sampling depth for further subtype resolution, yet may also indicate the potential for even more diversity within subtypes associated with a broader range of individualized neuronal activities. Consistent with these observations, proportions of subgroup-variable genes were associated with neuronal subtype classification, postsynaptic function, and known regional expression variability (fig. S15C). These data support further local and regional functional heterogeneity existing among defined subtypes.

Our results demonstrate that postmortem SNS can identify expected and previously unidentified neuronal subtypes that provide insight into brain function through distinct profiles of activity-defining genes (fig. S16 and table S14). Furthermore, given that only a very small subset of layer-specific markers used in our analyses (*CARTPT*, *CHRNA7*, *PDYN*, and *RELN*) was found to have ISH differences between individual donors (*17*), our subtypes can be expected to be globally representative. Indeed, our subtypes remain highly conserved in mice (*3*), with differences highlighting evolutionary changes in potential orthologs (fig. S12). Our data sets reveal shared gene expression signatures that can distinguish subtypes and regional identity, supporting a transcriptional basis for well-known differences in cortical cytoarchitecture. Additional heterogeneity found within single neuronal transcriptomes may further reflect activities of complex neuronal networks that vary with function and time, as well as underlying genomic mosaicism that exists in human cortical neurons (*10*, *20*–*23*). Our study thus lays the groundwork for high-throughput global human brain transcriptome mapping using nuclei derived from readily available postmortem tissues for analyses of normal individuals, as assessed here, as well as myriad diseases of brain and mind.

REFERENCES AND NOTES

1. E. Z. Macosko *et al.*, *Cell* **161**, 1202–1214 (2015).
2. D. Usoskin *et al.*, *Nat. Neurosci.* **18**, 145–153 (2015).
3. A. Zeisel *et al.*, *Science* **347**, 1138–1142 (2015).
4. M. J. Hawrylycz *et al.*, *Nature* **489**, 391–399 (2012).
5. H. J. Kang *et al.*, *Nature* **478**, 483–489 (2011).
6. M. B. Johnson *et al.*, *Neuron* **62**, 494–509 (2009).
7. M. Hawrylycz *et al.*, *Nat. Neurosci.* **18**, 1832–1844 (2015).
8. S. Darmanis *et al.*, *Proc. Natl. Acad. Sci. U.S.A.* **112**, 7285–7290 (2015).
9. D. M. Bushman *et al.*, *eLife* **4**, e05116 (2015).
10. J. Gole *et al.*, *Nat. Biotechnol.* **31**, 1126–1132 (2013).
11. R. V. Grindberg *et al.*, *Proc. Natl. Acad. Sci. U.S.A.* **110**, 19802–19807 (2013).
12. S. R. Krishnaswami *et al.*, *Nat. Protoc.* **11**, 499–524 (2016).
13. Materials and methods are available as supplementary materials on *Science* Online.
14. A. Graf *et al.*, *Proc. Natl. Acad. Sci. U.S.A.* **111**, 4139–4144 (2014).
15. D. Gaidatzis, L. Burger, M. Florescu, M. B. Stadler, *Nat. Biotechnol.* **33**, 722–729 (2015).
16. L. C. Greig, M. B. Woodworth, M. J. Galazo, H. Padmanabhan, J. D. Macklis, *Nat. Rev. Neurosci.* **14**, 755–769 (2013).
17. H. Zeng *et al.*, *Cell* **149**, 483–496 (2012).
18. D. V. Hansen *et al.*, *Nat. Neurosci.* **16**, 1576–1587 (2013).
19. T. Ma *et al.*, *Nat. Neurosci.* **16**, 1588–1597 (2013).
20. M. A. Lodato *et al.*, *Science* **350**, 94–98 (2015).
21. M. J. McConnell *et al.*, *Science* **342**, 632–637 (2013).
22. S. K. Rehen *et al.*, *J. Neurosci.* **25**, 2176–2180 (2005).
23. J. W. Westra *et al.*, *J. Comp. Neurol.* **518**, 3981–4000 (2010).

ACKNOWLEDGMENTS

Flow cytometry was performed both at the University of California, San Diego (UCSD) Human Embryonic Stem Cell Core and The Scripps Research Institute Flow Cytometry Core. Initial C1 runs were performed at the UCSD Stem Cell Genomics Core. The data tables accompanying this work are provided as Excel files in the supplementary materials. Clustering-and-Classification code used to identify neuronal subtypes and instructions (Readme.txt) for its operation in R are provided as supplementary files. We thank Fluidigm (M. Ray, R. C. Jones, and P. Steinberg) for instrument support and technical advice in adaptation of the C1 protocol for nuclei. Sequencing data has been deposited with dbGaP (accession phs000833.v3.p1), curated by the NIH Single Cell Analysis Program–Transcriptome (SCAP-T) Project (www.scap-t.org), and annotated in the supplementary materials (table S2). We thank G. Kennedy for help with RNAscope. Funding support was from the NIH Common Fund Single Cell Analysis Program (1U01MH098977). G.E.K. was additionally supported by a Neuroplasticity of Aging Training Grant (5T32AG000216-24).

SUPPLEMENTARY MATERIALS

www.sciencemag.org/content/352/6293/1586/suppl/DC1
Materials and Methods
Supplementary Text
Figs. S1 to S16
Tables S1 to S16
Supplementary Files
References (*24*–*38*)

18 December 2015; accepted 19 May 2016
10.1126/science.aaf1204

BIOCHEMISTRY

Synthetic evolutionary origin of a proofreading reverse transcriptase

Jared W. Ellefson,* Jimmy Gollihar, Raghav Shroff, Haridha Shivram, Vishwanath R. Iyer, Andrew D. Ellington*

Most reverse transcriptase (RT) enzymes belong to a single protein family of ancient evolutionary origin. These polymerases are inherently error prone, owing to their lack of a proofreading (3′- 5′ exonuclease) domain. To determine if the lack of proofreading is a historical coincidence or a functional limitation of reverse transcription, we attempted to evolve a high-fidelity, thermostable DNA polymerase to use RNA templates efficiently. The evolutionarily distinct reverse transcription xenopolymerase (RTX) actively proofreads on DNA and RNA templates, which greatly improves RT fidelity. In addition, RTX enables applications such as single-enzyme reverse transcription–polymerase chain reaction and direct RNA sequencing without complementary DNA isolation. The creation of RTX confirms that proofreading is compatible with reverse transcription.

The molecular basis for life rests on the information flow between DNA, RNA, and proteins (*1*). Early notions of a unidirectional central dogma were amended after the discovery of the reverse transcriptase (RT) enzyme (*2*, *3*). The RT family has a single ancient evolutionary origin based on amino acid homology and the presence of RT across multiple domains of life (*4*). RTs are involved in processes such as telomere addition, mitochondrial plasmid replication, transposition, and the proliferation of retroviral genomes (*5*). It is also hypothesized to be the catalyst in the transition of the RNA to DNA world by providing an avenue to copy RNA into more stable DNA genomes (*6*).

The progenitor of RT is postulated to be an RNA-dependent RNA polymerase. Because RNA polymerases generally lack an error-checking 3′-5′ exonuclease domain (*4*, *7*), proofreading activity is also not present across the RT family, resulting in low-fidelity reverse transcription and characteristic quasispecies behavior in organisms that rely upon it for replication (*8*). In contrast to RTs, other DNA polymerase families have evolved exquisite proofreading mechanisms to increase DNA synthesis fidelity during genome replication (*9*).

To determine whether the evolutionary divide between RTs and DNA polymerases is a matter of history or function, we have attempted to directly evolve a reverse transcription xenopolymerase (RTX; Fig. 1A) from an error-correcting DNA polymerase using a modified directed evolution strategy (*10*), reverse transcription–compartmentalized self-replication (RT-CSR) (Fig. 1B). RT-CSR enables the simultaneous screening of up to 10^9 polymerase variants for RT activity.

We chose the Archaeal family-B DNA polymerases (*polB*) for directed evolution of the RTX as they are monomeric, hyperthermostable, highly processive, and contain proofreading domains. Attempts to rationally design these enzymes to use RNA templates have met with limited success (*11*, *12*), and initial experiments confirmed that two common *polB* enzymes from *Pyrococcus furiosus* and *Thermococcus kodakarensis* (KOD) (*13*, *14*) failed to polymerize across five template RNA bases (fig. S1). Modeling to identify mutations enabling RT activity was deemed impractical, given the extensive contacts these polymerases make with the template (>50 direct interactions). We initiated evolution using low-stringency RT-CSR (10 RNA residues) with a random library

Center for Systems and Synthetic Biology, Institute for Cellular and Molecular Biology, Department of Molecular Biosciences, University of Texas, 2500 Speedway, Austin, TX 78712, USA.
*Corresponding author. Email: jaredwellefson@gmail.com (J.W.E.); ellingtonlab@gmail.com (A.D.E.)

Downloaded from http://science.sciencemag.org/ on June 28, 2016

(one or two amino acid mutations per gene) of KOD polymerase variants. As polymerases were enriched, we gradually increased RT-CSR stringency with the stepwise addition of RNA bases into primers (table S1). By cycle 18, primers were entirely composed of RNA—requiring reverse transcription of 176 residues to occur every thermal cycle to maintain exponential amplification in the emulsion polymerase chain reaction (PCR).

Profiling of polymerases revealed one variant, B11, which contained 37 mutations. RT-CSR enriched for RT activity, and B11 was capable of reverse transcription of at least 500 base pairs; however, sequencing and testing confirmed inactivation of the proofreading domain (fig. S2). Kinetic analyses established that B11 uses both DNA and RNA templates with similar efficiencies by greatly lowering the Michaelis constant (K_m) on RNA:DNA heteroduplexes. We attempted to restore proofreading by transplantation of the wild-type 3′-5′ exonuclease, which reactivated

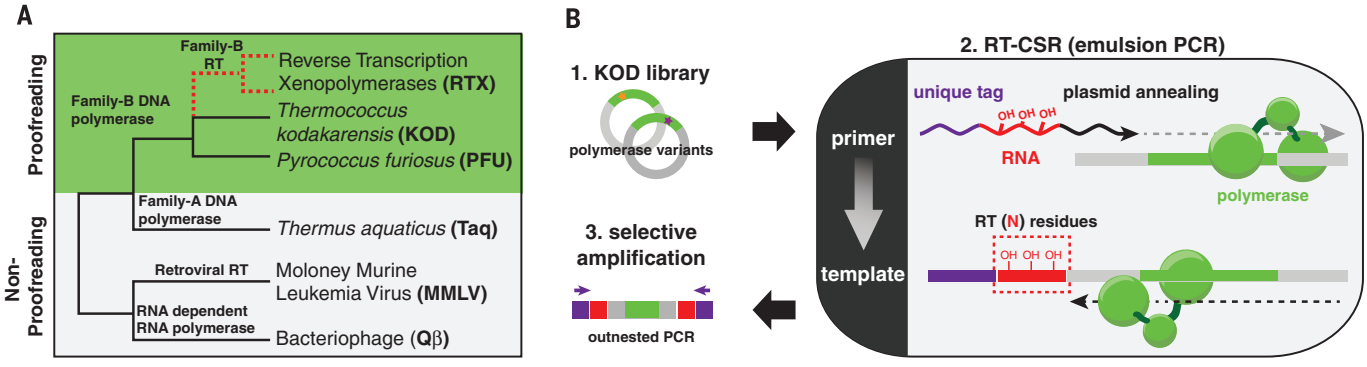


Fig. 1. Evolution of a synthetic family of reverse transcriptases by RT-CSR. (**A**) Polymerase phylogeny depicts reverse transcription xenopolymerases (RTX) as a second, evolutionarily distinct, origin of RT function. (**B**) Framework for the directed evolution of hyperthermostable RT using reverse transcription compartmentalized self-replication (RT-CSR). Libraries of polymerase variants are created, expressed in *Escherichia coli*, and in vitro compartmentalized. During emulsion PCR, primers flanking the polymerase enable self-replication but are designed with a variable number of RNA bases separating the plasmid annealing portion from the unique recovery tag.

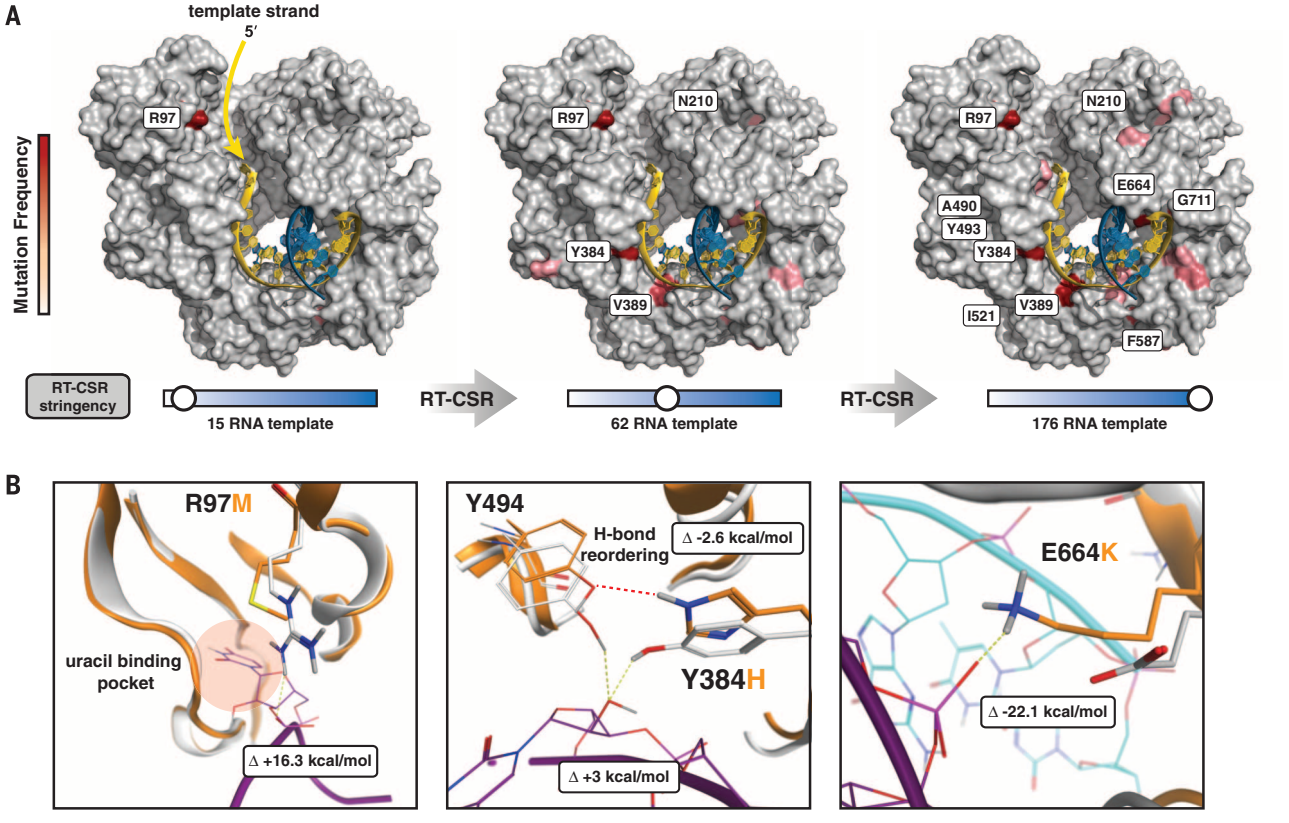


Fig. 2. Molecular checkpoints involved in template recognition. (**A**) Structural heat map of mutated residues over the RT-CSR process. Conserved mutations are colored incrementally darker shades of red to indicate frequency in the polymerase pool. Amino acid residues that were mutated in more than 50% of the population are labeled. [Figure was adapted from KOD structure PDB 4K8Z.] (**B**) Computer modeling of KOD (gray) and RTX mutations (orange) at checkpoints responsible for DNA and RNA template recognition at R97, Y384, and E664. Free-energy changes between wild-type KOD and RTX mutations are inlet displayed. Single-letter abbreviations for the amino acid residues are as follows: A, Ala; E, Glu; F, Phe; G, Gly; H, His; I, Ile; K, Lys; M, Met; N, Asn; R, Arg; V, Val; and Y, Tyr.

Downloaded from http://science.sciencemag.org/ on June 28, 2016

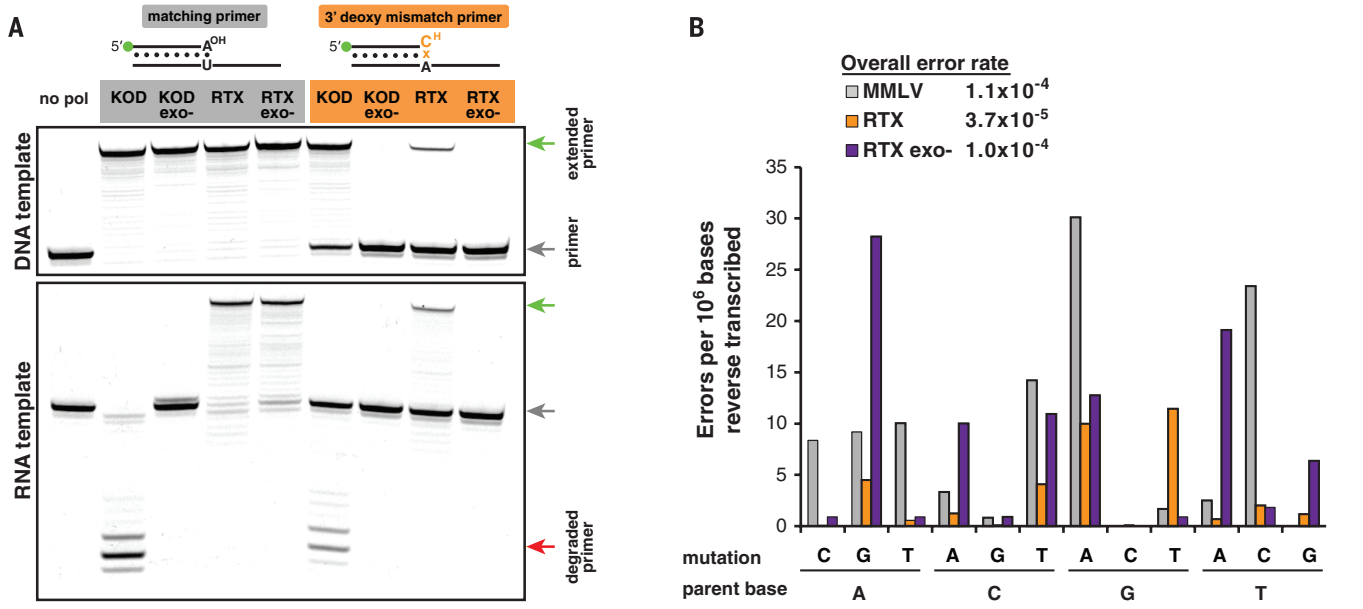


Fig. 3. RTX polymerase proofreads during reverse transcription. (**A**) Primer extension reactions of KOD and RTX polymerases and their proofreading-deficient counterparts (exo-), on both DNA and RNA templates. Extension reactions were performed with matched 3′ primer:templates (gray) or a 3′ deoxy mismatch (orange), which must be excised before extension can proceed. The primer is denoted by a gray arrow, extended product is in green, and exonuclease-degraded primer is in red. (**B**) Deep sequencing of reverse transcription reaction on *HSPCB* gene. The overall error rate was determined by dividing the sum of base substitutions and insertions or deletions by the total number of bases sequenced. The error profile of MMLV, RTX, and RTX exo- is shown as frequency of errors per million bases sequenced.

proofreading capabilities, albeit to barely detectable levels. Encouraged that minimizing extraneous mutations could restore proofreading activity, we sought to design polymerases with a minimal set of mutations.

To understand how our process reshaped KOD polymerase to use RNA templates, we deep-sequenced RT-CSR cycles to recapitulate the evolutionary path to RT activity (Fig. 2A and table S2). Mutations were identified throughout the polymerase and accumulated along the template-binding interface so as to progressively increase the length of RNA that could be accommodated. The mutated positions are hypothesized to be molecular checkpoints used to enforce strict DNA template utilization: as the template enters, near the active site, and at the nascent duplex. Given the likely importance of these regions, we used computer modeling to determine the molecular basis for RNA utilization (figs. S3 and S4).

The first selected mutation localized near the template entry site of the polymerase at position R97 (Fig. 2B). Proximal to this site, native *polB* scans for uracils (typically caused by cytosine deamination) by flipping template bases into a specialized pocket to halt polymerization until the mutation can be corrected by repair machinery (*15*, *16*). Evolved polymerases contained a variety of amino acid mutations at R97, all of which destabilize a salt bridge to the phosphate backbone that presumably regulates base flipping into the pocket.

As template residues near the active site, they encounter mutation Y384H, which prevents Y384 and Y494 from hydrogen bonding to the 2' hydroxyl of template RNA by reorganizing a hydrogen bonding network. After polymerization, in the thumb domain, the most prevalent mutations (E664K, G711V, and E735K) promote tighter homo- and heteroduplex binding in both A- and B-form conformations. The E664K mutation alone has been shown to increase binding to RNA:DNA heteroduplexes (*17*). To further validate that we had established an optimized set of mutations, we fully randomized several positions and repeated the RT-CSR. In support of our modeling, many amino acids solutions were viable at position R97, but other positions (Y384 and E664) had strong preferences for particular amino acids (fig. S5).

Modeled designs of several polymerases with favorable RT mutations were synthesized and tested empirically (fig. S6). The best-performing RTX contained fewer than half the mutations found in B11, without sacrificing catalytic efficiency or K_m on RNA (fig. S7). Mutations in RTX did not affect desirable properties of parental KOD polymerase. Thermostability was maintained, with optimal RT occurring at ~70°C, and consequently RTX was capable of single-enzyme RT-PCR (in which RTX performs both first-strand RT synthesis and PCR amplification). Across several RNA samples and gene loci, RTX demonstrated high processivity on RNA templates, performing RT-PCR on RNAs more than 5 kb in length (fig. S8).

Initial testing of RTX using dideoxy mismatch primers in PCR demonstrated robust proofreading activity on DNA template (fig. S9), but it was unclear whether the proofreading mechanism was compatible during reverse transcription because RNA:DNA heteroduplexes can adopt A-form helical structures (*18*). Primer extension reactions with a canonical matched base pair or a 3′ deoxy mismatched pair (preventing extension until terminator excision) were tested. Both wild-type KOD and RTX were capable of extending mismatched primers on DNA templates, unlike exonuclease-deficient mutants. When tested on an RNA template, KOD's exonuclease was stimulated—actively degrading the priming oligonucleotide. In contrast, RTX could extend the mismatched primer with activity indistinguishable from that of DNA templated proofreading (Fig. 3A).

Given that RTX is capable of proofreading during reverse transcription, we hypothesized that it may have increased RT fidelity compared to natural polymerases. Barcoded primers used during RT of several human mRNAs allowed multiple reads of a single cDNA during deep sequencing—reducing background sequencing errors by several orders of magnitude (fig. S10) (*19*). Sequencing analyses revealed that the control retroviral RT [Moloney murine leukemia virus (MMLV)] had an error rate of 1.1×10^{-4} to 4.8×10^{-4}, whereas RTX had an error rate of 3.5×10^{-5} to 3.7×10^{-5} (3- to 10-fold lower) (Fig. 3B). The mutational spectra of RTX favored G-to-A transitions and G-to-T transversions, which accounted for nearly half the observed mutations. Inactivating the RTX's proofreading capabilities increased error frequency nearly threefold, supporting evidence that active proofreading was occurring during RT. Inactivating the proofreading of RTX shifted the mutational bias (Fig. 3B and table S3). Given that the barcoding error detection limit is identical to the observed error of RTX (table S3) (*19*), we anticipate the true error rate for RTX to be even lower than reported.

RTX has the potential to streamline workflows (combining RT and PCR steps) and increase the precision of transcriptomics, reducing biases and

Downloaded from http://science.sciencemag.org/ on June 28, 2016

errors introduced in the reverse transcription step of RNA-sequencing protocols (*20*). To demonstrate its utility, we introduced RTX into a commonly used platform for RNA sequencing. Analysis revealed nearly identical coverage and expression profiles (fig. S11), suggesting that RTX is compatible with established workflows. In addition, we developed a more streamlined protocol to directly sequence RNA. Using a traditional Sanger sequencing approach (*21*), we directly sequenced a $GATC_5$ RNA repeat (fig. S12). Direct RNA sequencing should be adaptable to single-molecule sequencing platforms, enabling high-throughput and high-fidelity sequencing of complex RNA samples by eliminating the biases created in cDNA synthesis and subsequent amplification.

The expanded template specificity of the RTX lineage may presage the ability to use entirely new chemistries in genetics. Primer extension reactions were performed on a ribose sugar analog [2' O-methyl (Me) DNA] that indicated that RTX reverse transcription could extend alternative templates but with much lower efficiency, indicating a preference for RNA substrates (fig. S13). However, RTX was still far more efficient at using 2'-OMe DNA than the parental wild-type, allowing the possibility of further optimization and, owing to 2'-OMe stability, potential therapeutic applications.

The RTX RNA reverse transcriptase function is fundamentally distinct from that of the retroelement lineage. Using RT-CSR, we have altered the substrate specificity of a high-fidelity DNA polymerase, highlighting the plasticity of highly conserved molecular machinery. Ostensibly, the mutations identified unlocked molecular checkpoints in the discrimination of DNA and RNA, but did not disrupt the proofreading capabilities of the polymerase. This was unexpected, especially given that RNA:DNA hybrid duplexes often form A-helical structures unlike DNA:DNA duplexes, and may provide insights into the transition from polymerization to editing modes of the polymerase.

Only a handful of mutations were required to impart RT activity, suggesting that the evolutionary hurdle for forming high-fidelity reverse transcription is relatively low. Nevertheless, all known retroelements use proofreading-deficient RTs, suggesting that high error rates are either a historical coincidence or an evolutionary strategy to promote diversity. Another possible explanation is that high fidelity was never required simply because RNA genomes are small as a result of their inherent instability (*22*). Given the plasticity of these polymerases for modified templates and the adaptability of the RT-CSR framework (as primers are simply programmed to contain modified bases), RTX evolution should be compatible with many base and sugar analogs (*23*–*26*). Combination with previously evolved XNA polymerases could enable synthesis of genomes entirely composed of artificial nucleic acids (*27*).

REFERENCES AND NOTES

1. F. Crick, *Nature* **227**, 561–563 (1970).
2. H. M. Temin, S. Mizutani, *Nature* **226**, 1211–1213 (1970).
3. D. Baltimore, *Nature* **226**, 1209–1211 (1970).
4. Y. Xiong, T. H. Eickbush, *EMBO J.* **9**, 3353–3362 (1990).
5. J. D. Boeke, J. P. Stoye, in *Retroviruses*, J. M. Coffin, S. H. Hughes, H. E. Varmus, Eds. (Cold Spring Harbor Laboratory Press, Cold Spring Harbor, NY, 1997).
6. J. E. Darnell, W. F. Doolittle, *Proc. Natl. Acad. Sci. U.S.A.* **83**, 1271–1275 (1986).
7. T. M. Nakamura *et al.*, *Science* **277**, 955–959 (1997).
8. A. Meyerhans *et al.*, *Cell* **58**, 901–910 (1989).
9. T. A. Kunkel, K. Bebenek, *Annu. Rev. Biochem.* **69**, 497–529 (2000).
10. F. J. Ghadessy, J. L. Ong, P. Holliger, *Proc. Natl. Acad. Sci. U.S.A.* **98**, 4552–4557 (2001).
11. M. J. Moser *et al.*, *PLOS ONE* **7**, e38371 (2012).
12. S. K. Jozwiakowski, B. A. Connolly, *ChemBioChem* **12**, 35–37 (2011).
13. K. S. Lundberg *et al.*, *Gene* **108**, 1–6 (1991).
14. M. Takagi *et al.*, *Appl. Environ. Microbiol.* **63**, 4504–4510 (1997).
15. M. A. Greagg *et al.*, *Proc. Natl. Acad. Sci. U.S.A.* **96**, 9045–9050 (1999).
16. M. J. Fogg, L. H. Pearl, B. A. Connolly, *Nat. Struct. Biol.* **9**, 922–927 (2002).
17. C. Cozens, V. B. Pinheiro, A. Vaisman, R. Woodgate, P. Holliger, *Proc. Natl. Acad. Sci. U.S.A.* **109**, 8067–8072 (2012).
18. A. H.-J. Wang *et al.*, *Nature* **299**, 601–604 (1982).
19. M. W. Schmitt *et al.*, *Proc. Natl. Acad. Sci. U.S.A.* **109**, 14508–14513 (2012).
20. F. Ozsolak, P. M. Milos, *Nat. Rev. Genet.* **12**, 87–98 (2011).
21. F. Sanger, S. Nicklen, A. R. Coulson, *Proc. Natl. Acad. Sci. U.S.A.* **74**, 5463–5467 (1977).
22. J. W. Huff, K. S. Sastry, M. P. Gordon, W. E. C. Wacker, *Biochemistry* **3**, 501–506 (1964).
23. D. A. Malyshev *et al.*, *Proc. Natl. Acad. Sci. U.S.A.* **109**, 12005–12010 (2012).
24. Z. Yang, F. Chen, J. B. Alvarado, S. A. Benner, *J. Am. Chem. Soc.* **133**, 15105–15112 (2011).
25. R. Yamashige *et al.*, *Nucleic Acids Res.* **40**, 2793–2806 (2012).
26. K. Schöning *et al.*, *Science* **290**, 1347–1351 (2000).
27. V. B. Pinheiro *et al.*, *Science* **336**, 341–344 (2012).

ACKNOWLEDGMENTS

We thank the University of Texas Genomic Sequencing and Analysis Facility for DNA sequencing support. This work was supported by Defense Advanced Research Projects Agency (HR0011-12-2-0001), National Security Science and Engineering Faculty Fellowship (FA9550-10-1-0169), NASA (NNX15AF46G), and the Welch foundation (F-1654). J.W.E. conceived of the project. J.W.E., J.G., R.S. performed research with contributions from H.S and V.R.I. J.W.E, J.G., R.S., and A.D.E. wrote the manuscript. The authors declare competing financial interests. A.D.E. was a paid consultant for Enzymatics. A provisional patent has been filed on the sequence composition of the reverse transcriptase.

SUPPLEMENTARY MATERIALS

www.sciencemag.org/content/352/6293/1590/suppl/DC1
Materials and Methods
Figs. S1 to S13
Tables S1 to S3
Sequences

24 February 2016; accepted 31 May 2016
10.1126/science.aaf5409

Downloaded from http://science.sciencemag.org/ on June 28, 2016

NEW ENGLAND BioLabs® Inc.

PASSION IN SCIENCE AWARDS™

What is your PASSION?

New England Biolabs® is pleased to announce our 2016 Passion In Science Awards™, recognizing those within the scientific community working to make a difference in the world through their scientific mentorship, humanitarian efforts, environmental stewardship, or arts and creativity.

Through July 31st, 2016, we invite you to nominate yourself or a colleague for one of these awards. Award winners will be our guests at a celebration at the NEB® campus in Ipswich MA, USA and will also receive a donation to help further their cause. Remember, no act is too big or too small.

Help us celebrate those individuals who demonstrate true passion in science.

Tell us your story.

Visit NEBPassionInScience.com

Content is covered by one or more patents, trademarks and/or copyrights owned or controlled by New England Biolabs, Inc. For more information, please contact NEB's Global Business Development team at gbd@neb.com. Terms and conditions apply.

Science and art come together in the artwork displayed outside the NEB laboratory facility in Ipswich, MA, USA. Building artwork created by Nicole Gordon. Sculpture by Dale Rogers.



CALL FOR ENTRIES

Apply for the 2017 Award now!

http://www.sciencemag.org/prizes/boyalife
Questions/Inquiries:BoyalifeSciencePrize@aaas.org

Stem cells and regenerative medicine is the new frontier in life sciences. Boyalife, *Science*, and *Science Translational Medicine* jointly establish a global annual prize to recognize and reward scientists in the fields of stem cells and regenerative medicine with a focus on developing cell-based treatments for cancer, degenerative disorders, immunotherapy and stem cells transplantation.

2016 WINNER

Li Qian, Ph.D.
(UNC-Chapel Hill)

Exploring the reprogramming approaches for cardiac regeneration and disease modeling

★ The winners will receive: A Grand Prize of $25,000 and a Runner-Up Prize of $5,000 will be awarded.

★The Grand Prize Winning Essay and an abstract of the Runner-Up Essay will be published in *Science*.

The 2016 winners are Dr. Li Qian and Dr.Yossi Buganim, You can read their winning essays in the June 17 issue of *Science*.

BOYALIFE Science & Science Translational Medicine Award | in Stem Cells and Regenerative Medicine

BOYALIFE For Better Health

Science AAAS

Science Translational Medicine AAAS

life science EXPERT and e-commerce leader

The life science leaders of
EMD Millipore + Sigma-Aldrich
have joined together and, with our agile e-commerce and global distribution, we can help to simplify your world.
So you can focus with confidence on tackling life science's biggest challenges.



MilliporeSigma now offers:

- **An extended global network** across more than 66 countries
- **A world-class e-commerce platform** to simplify transactions
- **A vast portfolio** that has grown to over 300,000 products

Our combined strengths will deliver the **knowledge, know-how, and best-in-class resources.**

Learn more at **milliporesigma.com**

The life science business of Merck KGaA, Darmstadt, Germany operates as MilliporeSigma in the U.S. and Canada.

EMD Millipore, MilliporeSigma and the vibrant M are trademarks of Merck KGaA, Darmstadt, Germany and its affiliates.
Sigma-Aldrich is a trademark of Sigma-Aldrich Co. LLC and its affiliates.
Copyright © 2016 EMD Millipore Corporation. All Rights Reserved.

MilliporeSigma

life science EXPERT and e-commerce leader

The life science leaders of
Merck Millipore + Sigma-Aldrich
have joined together and, with our
agile e-commerce and global distribution,
we can help to simplify your world.
So you can focus with confidence on
tackling life science's biggest challenges.



The life science business of Merck now offers:

- **An extended global network** across more than 66 countries
- **A world-class e-commerce platform** to simplify transactions
- **A vast portfolio** that has grown to over 300,000 products

Our combined strengths will deliver the **knowledge, know-how, and best-in-class resources.**

Learn more at **merckgroup.com/life-science**

The life science business of Merck operates as MilliporeSigma in the U.S. and Canada.

Merck, Merck Millipore and the vibrant M are trademarks of Merck KGaA and its affiliates.
Sigma-Aldrich is a trademark of Sigma-Aldrich Co. LLC and its affiliates.
Copyright © 2016 Merck KGaA. All Rights Reserved.

MERCK

2016 WORLD LIFE SCIENCE CONFERENCE

www.wlsc2016.com

Nov. 1st-3rd, 2016, Beijing, China

Organized by the China Association of Science and Technology

Conference Chairs



Qide Han
Honorary President of China Associations for Science and Technology (CAST)



David Baltimore
1975 Nobel Laureate in Physiology or Medicine, California Institute of Technology

Confirmed Invited Plenary Speakers



David Baltimore
1975 Nobel Laureate in Physiology or Medicine, California Institute of Technology



Roger N. Beachy
2001 Wolf Prize Laureate in Agriculture, Washington University in St. Louis



Robert Eric Betzig
2014 Nobel Laureate in Chemistry, HHMI Janelia Research Campus



Zhu Chen
Shanghai Jiao Tong University



Zhangliang Chen
China Association for Science and Technology



Johann Deisenhofer
1988 Nobel Laureate for Chemistry, University of Texas Southwestern Medical Center



Robert T. Fraley
2013 World Food Prize Laureate, Monsanto Company



Jules A Hoffmann
2011 Nobel Laureate in Physiology or Medicine, University of Strasbourg



Robert Huber
1988 Nobel Laureate in Chemistry, Technical University Munich



Brian Kobilka
2012 Nobel Laureate in Chemistry, Stanford University



Marc Van Montagu
2013 World Food Prize Laureate, Ghent University



Erwin Neher
1991 Nobel Laureate in Physiology or Medicine, Max Planck Institute for Biophysical Chemistry



Venkatraman Ramakrishnan
2009 Nobel Laureate in Chemistry, University of Cambridge



Bengt Samuelsson
1982 Nobel Laureate in Physiology or Medicine, Stockholm University



Karl Barry Sharpless
2001 Nobel Laureate in Chemistry, 2011 Wolf Prize Laureate in Chemistry, Massachusetts Institute of Technology



Youyou Tu
2015 Nobel Laureate in Physiology or Medicine, China Academy of Chinese Medical Sciences



Kurt Wüthrich
2002 Nobel Laureate in Chemistry, The Scripps Research Institute and ETH Zurich



Ada E. Yonath
2009 Nobel Laureate in Chemistry, Weizmann Institute of Science



Longping Yuan
2001 Wolf Prize Laureate in Agriculture, 2004 World Food Prize Laureate, Hunan Agricultural University

Organizing Committee Chairs



Zihe Rao
Tsinghua University



Xiaofan Wang
Duke University

Scientific and Program Committee Chairs



Xuetao Cao
Chinese Academy of Medical Sciences



Marcia McNutt
Editor-in-chief of Science

Hosted by the China Union of Life Science Societies:

CHINA ZOOLOGICAL SOCIETY · BOTANICAL SOCIETY OF CHINA · THE ENTOMOLOGICAL SOCIETY OF CHINA · CHINESE SOCIETY FOR MICROBIOLOGY
THE CHINESE SOCIETY OF BIOCHEMISTRY AND MOLECULAR BIOLOGY · CHINESE SOCIETY FOR CELL BIOLOGY · CHINESE SOCIETY FOR PLANT BIOLOGY
BIOPHYSICAL SOCIETY OF CHINA · GENETICS SOCIETY OF CHINA · CHINESE ASSOCIATION FOR LABORATORY ANIMAL SCIENCES · THE CHINESE NEUROSCIENCE SOCIETY
CHINESE SOCIETY OF BIOTECHNOLOGY · CHINESE ASSOCIATION FOR PHYSIOLOGICAL SCIENCES · CHINESE SOCIETY FOR ANATOMICAL SCIENCES
CHINESE SOCIETY OF BIOMEDICAL ENGINEERING · CHINESE NUTRITION SOCIETY · CHINESE SOCIETY FOR IMMUNOLOGY · CHINESE SOCIETY FOR COGNITIVE SCIENCE

Be Among the First to Publish in *Science Robotics*



Image: jim/AdobeStock

NOW ACCEPTING MANUSCRIPTS

ScienceRobotics.org

Science Robotics is a unique journal created to help advance the research and development of robotics for all environments. *Science Robotics* will provide a much-needed central forum to share the latest technological discoveries and to discuss the field's critical issues.

Join in the excitement for the Fall 2016 debut!

Science Robotics

AAAS

Scavenger Screening Kit

The new Metal Scavenger Screening Kit contains a selection of Biotage industrial metal scavengers in an easy-to-use format, with detailed instructions that enable researchers to screen active pharmaceutical ingredient product mixtures and identify an optimum scavenger for their downstream metal-removal process. The kit includes five 1-g prepacked tubes of ISOLUTE Si-TMT, ISOLUTE SCX-2, ISOLUTE Si-Trisamine, ISOLUTE Si-Thiol, and Biotage MP-TMT metal scavengers. Biotage metal scavengers are industry proven, supported by a comprehensive regulatory qualification-support package, and produced in an ISO9001:2008-compliant manufacturing facility. Each scavenger is batch controlled and has served the pharmaceutical, drug discovery, and fine chemical industries for many years.

Biotage
For info: 800-446-4752
www.biotage.com

Chiral Columns

The 3-µm particle size is the latest addition to Phenomenex's new chiral selector, Lux Amylose-1, amylose tris (3,5-dimethylphenylcarbamate). These high-efficiency Lux polysaccharide columns are ideal for ultra-high-performance liquid chromatography (UHPLC), HPLC, and supercritical fluid chromatography (SFC) chiral screening and analysis. Now with two sizes—the new 3-µm and existing 5-µm particles—method scalability from analytical work to preparative purification is seamless. The affordable Lux Amylose-1 provides valuable enantioselectivity and is a guaranteed alternative to other phases with the same chiral selector. The 3-µm particle media is available in analytical columns, while the 5-µm particle media is available in both analytical columns and Phenomenex-patented Axia preparative column hardware, both of which are stable in normal phase, reversed phase, polar organic, and SFC conditions. The Phenomenex Lux amylose and cellulose chiral column line of six chiral selectors comprise an affordable and complementary kit for chiral separations, featuring high efficiency, excellent loading capacity, and pressure stability up to 300 bar in a wide range of conditions.

Phenomenex
For info: 310-212-0555
www.phenomenex.com



Sample Tracking Rack/Reader

Designed to improve sample tracking and protection, a new barcoded latch rack and wireless barcode reader enhance Thermo Fisher Scientific's broad portfolio of automated and semiautomated laboratory instruments and related consumables for secure sample collection and storage. Barcoded tubes and racks—with both 2D and linear barcodes—can now be read with the VisionMate wireless reader. Unlike currently available wireless barcode readers, the unit is designed to lay flat, allowing users to set it directly on the benchtop and scan tubes or racks without holding it. For samples that should not be exposed to ambient conditions, the reader can easily be used as a handheld instrument, reading samples while they remain safely in storage. The VisionMate wireless reader can read tubes in a cold environment, capturing and sending data via Bluetooth to a paired computer.

Thermo Fisher Scientific
For info: 800-955-6288
www.thermofisher.com

Small-Scale Crossflow Device

The single-use ultrafilter Sartocon Slice 50 is a new crossflow filter device designed for use in biotechnological applications, especially for membrane screening and small-volume process development. Sartocon Slice 50 is offered as an encapsulated and ready-to-use crossflow module with a filter area of 50 cm^2 and a wide variety of molecular weight cutoffs. The current good manufacturing process (cGMP)-validated, self-contained unit eliminates the need for a compression holder and is available in a choice of two polymers: The Hydrosart membrane is a stable polymer suitable for a broad pH range and can be depyrogenated using NaOH at elevated temperatures. It is extremely hydrophilic, making it non-protein-binding and virtually nonfouling, and delivers an exceptional high flux. The polyethersulfone membrane, which is well established in the biotechnological and pharmaceutical industries, is a stable polymer that is ideal for a broad pH and temperature range.

Sartorius Stedim Biotech
For info: 800-368-7178
www.sartorius.com

One-Step Conjugation Kits

New red, black, and blue 400-nm LATEX conjugation kits are one-step kits for the covalent conjugation of antibodies and proteins to specially treated latex beads. The new conjugation kits are easy to use and allow quick, effective conjugation of antibodies, proteins, and peptides to latex beads, potentially simplifying and improving assay development while reducing development timelines. Additionally, the range of available colors enables multiplexing and therefore maximum flexibility in assay design. The kits are suitable for development of diagnostics, in lateral flow assays, and across a range of other applications, and are fully compatible with human serum. Conjugation to latex particles using conventional methodology is complex, time consuming, and typically requires extensive optimization and relatively large quantities of antibodies, with aggregation often a major problem associated with covalent conjugations, and extensive pH optimization required for passive conjugation techniques.

Innova Biosciences
For info: +44-(0)-1223-496170
www.innovabiosciences.com

Electronically submit your new product description or product literature information! Go to www.sciencemag.org/about/new-products-section for more information.

Newly offered instrumentation, apparatus, and laboratory materials of interest to researchers in all disciplines in academic, industrial, and governmental organizations are featured in this space. Emphasis is given to purpose, chief characteristics, and availability of products and materials. Endorsement by *Science* or AAAS of any products or materials mentioned is not implied. Additional information may be obtained from the manufacturer or supplier.

Don't miss the debut of *Science Immunology*.

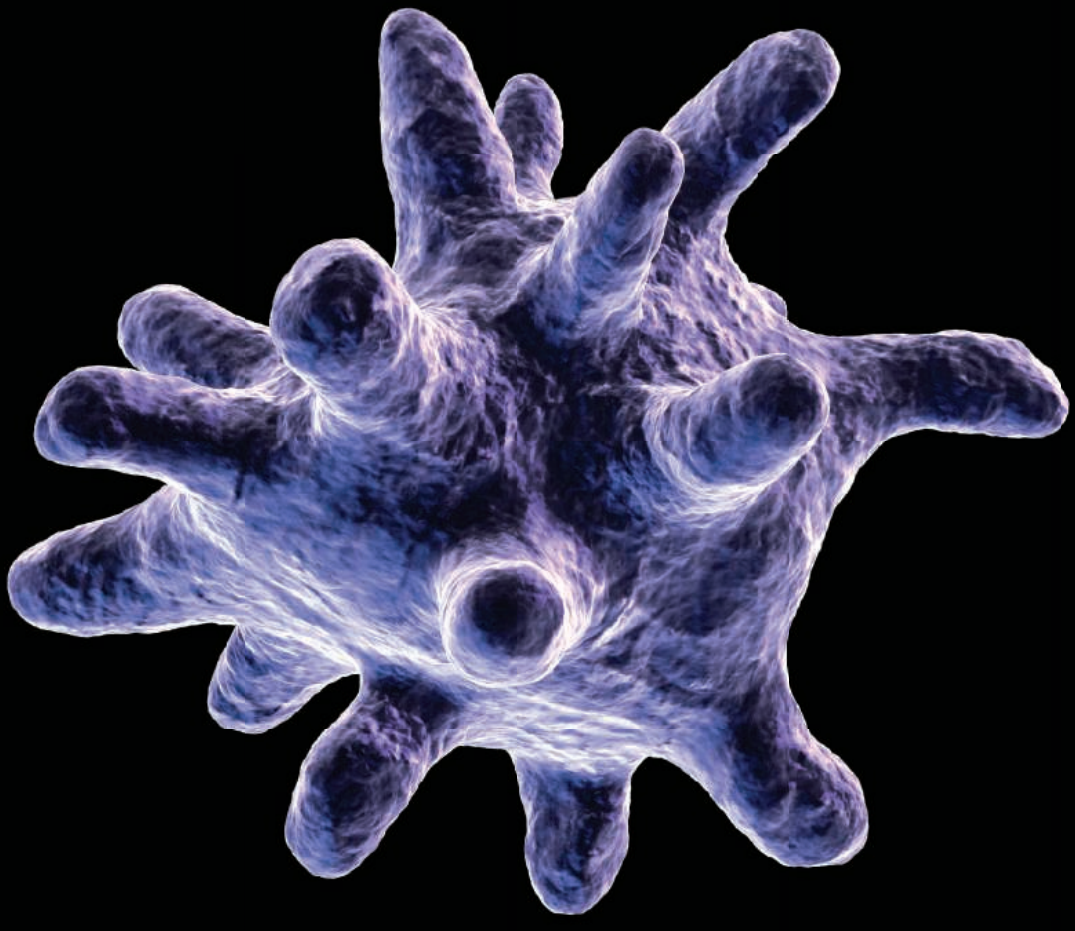


Image: Eraxion / iStockPhoto

NOW ACCEPTING PAPERS

Science is expanding its reach into immunology—now offering the newest online-only, weekly journal in the *Science* family of publications. *Science Immunology* will provide original, peer-reviewed research articles that report critical advances in all areas of immunological research, including studies that provide insight into the human immune response in health and disease.

Be a part of the *Science Immunology* debut issue publishing Summer 2016!

Submit your manuscript today at **ScienceImmunology.org.**

Science Immunology

AAAS

CELL SIGNALING TECHNOLOGY

Deciphering Cancer

Antibodies to evaluate key signaling networks in growth and differentiation.





Download pathways at www.cellsignal.com/cancerpathways

For Research Use Only. Not For Use In Diagnostic Procedures.
© 2016 Cell Signaling Technology, Inc. Cell Signaling Technology and CST are trademarks of Cell Signaling Technology, Inc.
16PADDBIO0072ENG

Cell Signaling TECHNOLOGY®



There's only one Science

Science Careers Advertising

For full advertising details, go to ScienceCareers.org and click For Employers, or call one of our representatives.

Tracy Holmes
Worldwide Associate Director
Science Careers
Phone: +44 (0) 1223 326525

THE AMERICAS

E-mail: advertise@sciencecareers.org
Fax: +1 (202) 289 6742

Tina Burks
Phone: +1 (202) 326 6577

Nancy Toema
Phone: +1 (202) 326 6578

Online Job Posting Questions
Phone: +1 (202) 312 6375

EUROPE / INDIA / AUSTRALIA / NEW ZEALAND / REST OF WORLD

E-mail: ads@science-int.co.uk
Fax: +44 (0) 1223 326532

Sarah Lelarge
Phone: +44 (0) 1223 326527

Kelly Grace
Phone: +44 (0) 1223 326528

Online Job Posting Questions
Phone: +44 (0) 1223 326528

JAPAN

Katsuyoshi Fukamizu (Tokyo)
E-mail: kfukamizu@aaas.org
Phone: +81 3 3219 5777

Hiroyuki Mashiki (Kyoto)
E-mail: hmashiki@aaas.org
Phone: +81 75 823 1109

CHINA / KOREA / SINGAPORE / TAIWAN / THAILAND

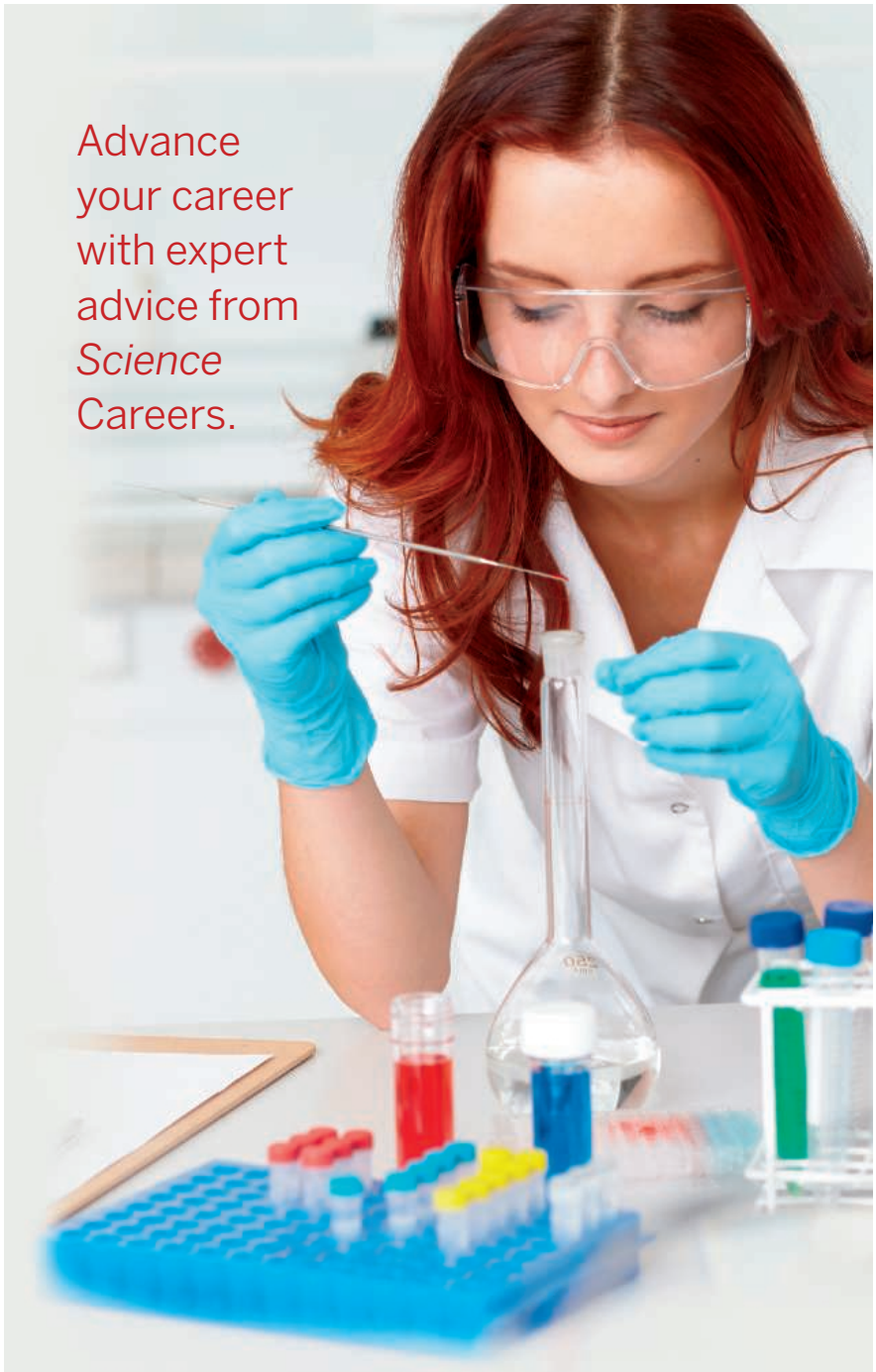
Ruolei Wu
E-mail: rwu@aaas.org
Phone: +86 186 0082 9345

Danny Zhao
E-mail: dzhao@aaas.org
Phone: +86 131 4114 0012

All ads submitted for publication must comply with applicable U.S. and non-U.S. laws. *Science* reserves the right to refuse any advertisement at its sole discretion for any reason, including without limitation for offensive language or inappropriate content, and all advertising is subject to publisher approval. *Science* encourages our readers to alert us to any ads that they feel may be discriminatory or offensive.

ScienceCareers
FROM THE JOURNAL SCIENCE AAAS

ScienceCareers.org



Download Free Career Advice Booklets!
ScienceCareers.org/booklets

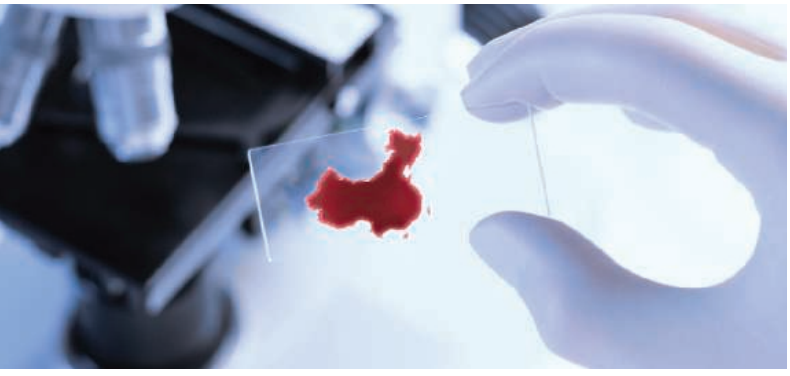
Featured Topics:

- Networking
- Industry or Academia
- Job Searching
- Non-Bench Careers
- And More



ScienceCareers
FROM THE JOURNAL SCIENCE AAAS

ScienceCareers online @sciencecareers.org





Building a translational medicine powerhouse in China

Those involved in translational medicine research in China admit that it has its challenges; but they know that their hard work is rewarded with the opportunity to make a real difference to patients. And with funding still on the rise despite a flagging economy, demand for skilled researchers is likely to continue to grow. That's because the field has been receiving special attention from China's central and regional governments in recent years. As a result, translational medicine—defined as a partnership between basic and clinical research to develop new pharmaceuticals, devices, and other medical products—presents many opportunities for researchers to build careers in biomedicine.
By Shawna Williams

Rui Shi, the associate chief physician of orthopedic oncology at West China Hospital in Chengdu, first heard the term "translational medicine" in 2008, when he took a temporary post in the hospital's technology transfer office. Both the hospital and a provincial agency had put aside funds for translational research, and part of Shi's new job was to help with presentations to hospital faculty about how to apply for the new grants—and how to conduct a successful project. In translational medicine, "the research question has to arise from clinical needs, and the needs of the clinic have to be solved by the lab," Shi explains. "The clinic and the lab have to be combined, and the outcome has to be a new medication, a new device, or a new therapy—a new solution for a clinical problem."

A major challenge, Shi says, is that clinical and basic researchers tend to have their own entrenched ways of approaching their work. To bridge the gap between bench and bedside, institutions like his must find ways to encourage the two camps to communicate with one another.

A culture shift

Luming Li, who heads the National Engineering Laboratory for Neuromodulation in Beijing, agrees. "Translational medicine research is multidisciplinary research," he says. "It needs the right environment."

Only relatively recently has China's central government made fostering that environment a priority, but the shift is beginning to have an impact. Members of his laboratory, for example, collaborate closely with surgeons, engineers, and basic researchers, Li says. In 2014, China's National Development and Reform Commission announced plans for five new translational medicine research centers, where basic scientists and clinicians will work side by side.

The first of these, the National Centre for Translational Medicine, is slated to complete construction in 2017 in Shanghai. With one building on the main campus of Shanghai Jiao Tong University and another at the affiliated Ruijin Hospital, the center "will promote the merger of basic and clinical techniques and methods in translational innovations," says **Guang Ning,** Ruijin's deputy director.

With 50 principal investigators and 300 beds for clinical trials, the center will focus on cancer as well as metabolic and cardiovascular diseases, he says. And to ensure that products make it to the market quickly, "there is enough space for pharmaceutical companies, and [we will] invite them to open their offices or laboratories in our building," he adds.

To foster an interdisciplinary environment, one trait Ning looks for in potential recruits is "broad knowledge and skills in multiple disciplines." That advice is echoed by **Yuquan Wei,** director of the National Key Laboratory of Biotherapy at Sichuan University in Chengdu. "Students in clinical medicine who are interested in translational medicine should gain experience in basic research and have a strong background … [in] diverse disciplines such as genomics, proteomics, structural biology, genetic engineering, developmental biology, immunology, the mechanism of human diseases, chemistry, and materials, among others," he says, adding that similarly, "students in basic research who are interested in translational medicine should gain some knowledge of clinical medicine." cont.>

PHOTOS: (FROM LEFT) © 18PERCENTGREY/PER BENGTSSON/SHUTTERSTOCK.COM; XIXINXING/SHUTTERSTOCK.COM

Upcoming Features

Focus on Manchester—July 15 ■ *Postdoc Careers—August 26* ■ *Faculty Careers—September 16*



南昌大学
www.ncu.edu.cn

南昌航空大学
www.ncu.edu.cn

江西师范大学
www.jxnu.edu.cn

江西财经大学
www.jxufe.edu.cn

Looking for more positions?

Please send your CV to acabridge@163.com
or call the direct line: 86-10-62603551

www.edu.cn/jxzp

Shi concurs that translational medicine researchers need to build a strong knowledge base to succeed. "You need to discover the clinical needs … you have to know how the lab works, and how basic research can provide the solution. At the same time you need to understand the basic concept of how to do technology transfer… [and] how research results could be finally transferred into the market," he says.

Another critical skill, says Li, is communication. "I ask my students to visit hospitals and talk to patients so we can find how to help them," he says.

So far, Chinese institutions have been more successful at attracting basic science researchers with the right experience than physician-scientists, says **Xiao-Fan Wang,** a professor of pharmacology and cancer biology at Duke University School of Medicine in Durham, North Carolina, who serves on the international advisory boards of two of the new translational medicine centers. But he notes the difference in salaries for physicians in the United States versus China: According to a 2014 survey by the news website Phoenix Innovation, the salaries of experienced Chinese physicians range from $5,520 to $18,480 per year, while the news website Medscape found in 2015 that primary care physicians in the United States bring in an average of $195,000 per year, and specialists annually earn $284,000. As a consequence, Chinese labs generally "don't have people who really have the expertise to set up clinical trials to withstand the scrutiny of international experts when they publish their results," says Wang. To cope, Chinese universities are beginning to develop their own equivalent of M.D./Ph.D. programs, he says, and are recruiting practicing clinicians domestically to join research teams.

Many newer initiatives also set up their facilities so that basic researchers share space with medical doctors. At the Shanghai Institutes for Biological Sciences (SIBS) of the Chinese Academy of Sciences, for example, "We ask the [basic science] researchers … to work in our hospital one day per week and talk to doctors to try to find solutions to clinical problems," says **Ying Mao,** vice president at Huashan Hospital and a principal investigator and adjunct professor at SIBS.



"The clinic and the lab have to be combined, and the outcome has to be a new medication, a new device, or a new therapy."
—Rui Shi

Translational medicine with Chinese characteristics

In collaborating with colleagues from different fields to push innovations to the bedside, many in the translational medicine field see a unique opportunity to improve health care in China. The five new translational medicine research centers "really want to recruit people to target some of the diseases more prevalent in China," says Wang. For example, he says, the incidence of stroke and certain cancers of the digestive system is much higher in China than in the United States. Finding ways to prevent and treat such illnesses is a priority for many translational research institutions.

Keeping product costs down is another way in which researchers seek to meet local needs, says Li. "We want to help people not only in the cities, but also in the [relatively poor] countryside," he says. "Those patients can be very sensitive to price."

Shi recounts how his colleague Hao Liu, also a spinal surgeon, noted that imported artificial vertebral discs cost thousands of dollars each, so he set out to develop his own version. The resulting prototype, made by a Chinese company, is not only less expensive, but is as durable as commercially available artificial discs and more suited to the average anatomy parameters of Chinese patients, Shi says. It is currently in clinical trials.

Other projects seek to harness aspects of traditional Chinese medicine. Li, for example, collaborated with a doctor who is an expert in using acupuncture for pain control to develop an implantable device to mimic acupuncture's effects. The device is currently being tested in animals to pave the way for human trials.

Another feature of translational medicine research in China is the relative ease of recruiting large cohorts of patients for clinical trials, researchers say. "You have this enormous population from which to collect samples," Wang says. "It is relatively easy to get a patient population big enough for statistical analysis."

And Wang says that a favorable funding environment is a critical element in the blossoming of translational medicine research. "The funding is much better now in China than in the United States, so a lot of young people make the tough decision to come back to China after training overseas, because it's easier for them to build up their lab," he says, and he expects that trend to continue.

Luyang Yu, a professor of cell biology at Zhejiang University who worked as a postdoctoral associate and associate research scientist at Yale from 2006 to 2012, is one of those returnees. In addition to his academic research, Yu is working to launch a startup company with three other scientists in Hangzhou—two of whom are friends he met at Yale. The company, CedarMed, is developing a test to predict atherosclerosis earlier than previously possible, which could enable doctors to better prevent negative outcomes such as heart attacks and strokes. "We feel that Zhejiang is a very good environment" for biomedicine, Yu says, citing startup funding the company has already received from the central, provincial, and city governments. He has also been cultivating contacts in the private sector and is confident that the startup will have no trouble attracting investment once more data has been generated. cont.>

PHOTO: COURTESY OF RUI SHI

中国科学院遗传与发育生物学研究所
INSTITUTE OF GENETICS AND DEVELOPMENTAL BIOLOGY
CHINESE ACADEMY OF SCIENCES

Faculty Positions

The Institute of Genetics and Developmental Biology (IGDB), Chinese Academy of Sciences is a leading life science institution in China, and aims to address fundamental questions in modern agriculture and human health, making internationally recognized contributions in these fields.

IGDB invites applicants for ten faculty positions. The appointment of all positions will be at Full Professor Level. We are particularly interested in candidates in the areas of genetics, crop design, genome engineering, stem cell, organ development and regenerative medicine, computational biology and systems biology. In addition, positions are also open for biotech IP management and product development.

Successful candidates will be expected to also apply to the CAS Pioneer Hundred Talents Program or the National Thousand Talents Program. Applications will be welcomed until all positions are filled.

More information about IGDB can be found at http://www.genetics.ac.cn or http://english.genetics.cas.cn. Interested candidates should submit a cover letter, curriculum vitae, representative publications, a statement of research experience and interests as well as the names and contact information of three referees to the Institute director Professor Weicai Yang by e-mail (wcyang@genetics.ac.cn), copied to Ms. Jing Wang (jwang@genetics.ac.cn).








Don't hit the pavement for your job search.

- Search thousands of job postings
- Create job alerts based on your criteria
- Get career advice from our Career Forum experts
- Download career advice articles and webinars
- Complete an individual development plan at "myIDP"

Target your job search using relevant resources on **ScienceCareers.org**.

ScienceCareers
FROM THE JOURNAL SCIENCE AAAS

The 2017-2018 Fulbright U.S. Scholar Competition is open

Opportunities in over 125 countries for faculty, administrators, postdocs, professionals, artists, independent scholars and many others.

For more information on recent program innovations, including flexible, multi-country opportunities, please visit:
www.iie.org/cies

Fulbright
SCHOLAR PROGRAM

FEATURED PARTICIPANTS

Huashan Hospital (Chinese only)
www.huashan.org.cn

Nanjing Drum Tower Hospital (Nanjing Gulou Hospital)
www.njglyy.com/en/index.htm

National Engineering Laboratory for Neuromodulation
www.neuromodulation.cn

National Key Laboratory of Biotherapy
sklb.scu.edu.cn summary/?type=detail&id=3

Ruijin Hospital
www.rjh.com.cn/chpage/c1352

Shanghai Institutes for Biological Sciences
english.sibs.cas.cn/

Sun Yat-Sen University
www.sysu.edu.cn/2012/en/index.htm

West China Hospital
eng.cd120.com

Zhejiang University
www.zju.edu.cn/english


Lingyun Sun

Looking to the future

At the meeting of the National People's Congress in Beijing in March 2016, Premier Keqiang Li outlined the central government's economic plans for the next five years, including a 9.1% boost in science funding in 2016, and priorities that include brain research, applications of genetic knowledge, and big data. The new plan "will strongly support translational medicine innovation in China," says Ning. He adds that the government is reforming the regulatory system to make translational medicine research "more compliant."

Andy Peng Xiang, a professor at Sun Yat-Sen University in Guangzhou, credits what he sees as accelerated progress in translational medicine research over the past decade not only to government funding but also to changes at universities and with researchers themselves. As he explains it, "A lot of universities in mainland China have formulated special policies to help their faculties accelerate the translation of basic research findings into practice or products," such as establishing centers that put "researchers, doctors, and patients under one roof," and encouraging collaboration with industry. And more researchers have become interested in the field as a way of directly benefiting patients, he adds.

China is not building its translational medicine capability from scratch, however; some internationally recognized researchers there have been doing strong work in the field for decades. Among them is **Lingyun Sun,** a professor of medicine at Nanjing Drum Tower Hospital. Sun has been exploring the possibility of transplanting stem cells since the late 1990s, and for the past 15 years has studied the question of whether so-called allogeneic mesenchymal stem cells (MSCs) can effectively treat autoimmune diseases such as lupus. With approximately 700 patients treated in clinical trials, MSCs are showing great promise, he says. The project has thus far attracted about US$10 million in funding from pharmaceutical companies and from national and local governments.

The five translational medicine centers planned by the National Development and Reform Commission are part of a movement toward strengthening the connection between bench and bedside, says Wang. The National Centre for Translational Medicine in Shanghai will be joined in a few years by two Beijing institutes, one for geriatrics and another for rare and refractory diseases: the Translational Science Center for Molecular Medicine at the Fourth Military Medical University in Xi'an, which will focus on precision medicine and cancer; and the National Translational Medicine Center for Biotherapy, part of the National Key Laboratory of Biotherapy in Chengdu. The latter will boast some 500 faculty members when it opens in 2018 or 2019, working in nearly 180,000 square meters on the main and medical campuses of Sichuan University, says Wei. Wei adds that the new center's emphases will include gene therapies, vaccines and other immunotherapies, monoclonal antibodies and engineered T-cells, stem cells and regenerative medicines, and synthetic and natural small-molecule drugs, and that it will "establish a whole key technology chain from genomics to the research and development of innovative drugs, pilot-scale production, preclinical safety evaluations, clinical trials, and clinical treatment, all in a single institute."

Moreover, the Translational Science Center for Molecular Medicine, funded with an initial investment of more than US$125 million, will aim to answer research questions such as how biological signals are regulated and what molecular mechanisms lie behind inflammation-linked diseases and cancer, says its director, **Zhinan Chen.** He expects the new center, which will boast state-of-the-art instruments, to rank among the top international translational medicine research centers.

Even under the best of circumstances, researchers say, translational medicine is challenging. Asked for his advice for younger researchers, Sun says, "It is essential that they should overcome many difficulties and challenges, even failure, before realizing successful translational medicine in the clinic." His team, for example, spent seven years running animal studies to clarify issues such as whether MSC transplantation is safe, the optimal type of stem cell for transplantation, and correct dosage and timing; and evaluating long-term effectiveness before clinical trials could begin, he says.

But for those who persevere, the rewards are great, says Xiang. "Although translational medicine is time-consuming and challenging research, most of the time I do enjoy the process," he adds.

Shawna Williams is a freelance writer based in Baltimore, Maryland.

DOI: 10.1126/science.opms.r1600164

TOP RESEARCH DEMANDS BRILLIANT MINDS – WE'RE ALWAYS LOOKING FOR THE BEST

THE ONSAGER FELLOWSHIPS

11 tenure-track positions available at NTNU

The Norwegian University of Science and Technology (NTNU) is Norway's primary institution for educating scientists and engineers for the future. The university also has strong programmes across a range of academic fields, including the social sciences, teacher education, the arts and humanities, medicine and health sciences, architecture and fine art. NTNU's cross-disciplinary research delivers creative innovations that have far-reaching social and economic impact and help to create a better world. Two of NTNU's researchers were named Nobel Laureates in 2014.

The Onsager Fellowship programme at NTNU is designed to attract the most talented scholars with an established reputation for high-quality research and a commitment to learning and teaching at the university level.

APPLY FOR A TENURE-TRACK POSITION AS AN ASSOCIATE PROFESSOR IN:

- Complex analysis
- Integrated Power and Energy Systems
- Fluid mechanics
- Risk-based marine systems design for Arctic operations
- Operations research in maritime transportation
- Public and/or urban economics
- Political communication
- Psychopathology and development
- Modern Political and Economic History, 1870–2000
- Biostatistics
- Experimental environmental toxicology

More info at: www.ntnu.edu/onsager-fellowship

Application deadline: 2 September 2016



KNOWLEDGE FOR A BETTER WORLD

NTNU
Norwegian University of Science and Technology

ScienceCareers online @sciencecareers.org

ScienceCareers online @sciencecareers.org

myIDP: A career plan customized for you, by you.



For your career in science, there's only one Science

my IDP ScienceCareers

Recommended by leading professional societies and the NIH

Features in myIDP include:

- Exercises to help you examine your skills, interests, and values.
- A list of 20 scientific career paths with a prediction of which ones best fit your skills and interests.
- A tool for setting strategic goals for the coming year, with optional reminders to keep you on track.
- Articles and resources to guide you through the process.
- Options to save materials online and print them for further review and discussion.
- Ability to select which portion of your IDP you wish to share with advisors, mentors, or others.
- A certificate of completion for users that finish myIDP.

Visit the website and start planning today!
myIDP.sciencecareers.org

ScienceCareers In partnership with:

advancing the life sciences 1912-2012 FASEB Federation of American Societies for Experimental Biology

UCSF University of California San Francisco

Medical College of Wisconsin

Burroughs Wellcome Fund

FRED HUTCH
CURES START HERE™

Senior Faculty Leadership Position in Immunology at Fred Hutchinson Cancer Research Center

The Vaccine and Infectious Disease Division (VIDD) of the Fred Hutchinson Cancer Research Center seeks exceptional applicants for a full-time senior faculty leadership position in immunology at the Full Member rank (comparable to Professor). The primary responsibility of this position will be to develop and lead a comprehensive, cross-disciplinary integrated research center (IRC) involving multiple investigators that will focus on pathogen-induced cancers. The candidate will be expected to conduct laboratory-based translational immunology research as part of this IRC and within VIDD, and an emphasis on mechanisms of memory/effector cell induction and immune dysfunction in the context of cancer or cancer-associated infections is highly desirable.

Candidates for this position must have a well established, robust, funded program that is nationally and internationally recognized for excellence in immunology, immunotherapeutic design, or viral oncogenesis.

Applicants must have an MD (or foreign equivalent) or PhD (or foreign equivalent). Selection criteria include excellence in scholarship, creativity in research, and demonstrated leadership in the profession.

VIDD scientists integrate clinical care, computational methods, and basic science research in immunology, virology, and vaccine design to reduce the global burden of infectious disease.

The Fred Hutchinson offers a vibrant intellectual environment within a beautiful, lakeside campus in Seattle's South Lake Union biotech hub. VIDD occupies a new building that is connected by walking trails to Seattle Cancer Care Alliance and the other four Divisions of the Fred Hutch and by trolley to major research partners such as the University of Washington School of Medicine, Seattle Children's Research Institute, Center for Infectious Disease Research (formerly Seattle Biomedical Research Institute), and the Infectious Disease Research Institute.

Interested candidates should submit a CV, a concise research plan statement, and the names and contact information for three (3) references to: **fredhutch.org/job/6653**. Specific inquiries can be directed to **Julie McElrath** at **206-667-1858**. Applications should be received by **August 15, 2016** to assure consideration and will be evaluated as received.

The Fred Hutchinson Cancer Research Center is an Affirmative Action, Equal Opportunity Employer. All qualified applicants will receive consideration for employment without regard to, among other things, race, religion, color, national origin, sex, age, status as protected veterans, or status as qualified individuals with disabilities. We strongly encourage applications from women, minorities, individuals with disabilities and covered veterans.

UCDAVIS

Department Chair and Professor of Plant Sciences

The University of California, Davis College of Agricultural and Environmental Sciences is pleased to announce an open recruitment for a tenured professor and chair of the Department of Plant Sciences (http://www.plantsciences.ucdavis.edu). The department portfolio covers a broad array of research and extension activities in the areas of ecology, genetics, and physiology of agricultural and natural systems in California, the U.S. and abroad. The department has a large effort in cooperative extension programming and mission-oriented research activities consistent with the CA Agricultural Experiment Station.

Criteria for appointment: a Ph.D. in plant sciences or a related discipline, a record of excellence in scholarly research in plant sciences that aligns with the interdisciplinary foci of the department, and demonstrated ability to establish a competitively-funded research program. The candidate is expected to have a record of strong teaching/mentoring of undergraduates and graduates, and evidence of strong outreach and stakeholder engagement experiences. Administrative experiences and skills are expected commensurate with the capacity to chair a large and diverse unit of faculty, students and staff.

Applicants should submit materials via the following website: **http://apptrkr.com/829458**

Additional inquiries should be directed to Search Committee co-chairs Ed Lewis eelewis@ucdavis.edu or Jeffrey Ross-Ibarra rossibarra@ucdavis.edu.

The position will remain open until filled but to ensure consideration, applications should be received by August 31, 2016.

The University of California, Davis, and the College of Agricultural and Environmental Sciences are interested in candidates who are committed to the highest standards of scholarship and professional activities, and to the development of a campus climate that supports equality and respect for differences based on gender, cultural ethnicity, level of disability, and sexual orientation. UC Davis is an affirmative action/equal employment opportunity employer and is dedicated to recruiting a diverse faculty community. We welcome all qualified applicants to apply, including women, minorities, veterans, and individuals with disabilities. **EOE**

Pharmacology & Therapeutics Faculty Position

Roswell Park Cancer Institute

Roswell Park Cancer Institute (RPCI), an NCI-Designated Comprehensive Cancer Center in Buffalo, NY, invites applications for individuals at the Assistant Professor level in the Department of Pharmacology and Therapeutics. The mission of the department is to identify and develop novel anti-cancer therapeutics. The department currently consists of more than a dozen faculty studying genetic mechanisms of tumor initiation and progression, biochemical mechanisms of cell death, drug response and steroid hormone receptor actions, cancer stem cells, noncoding RNAs, and epigenetic mechanisms in cancer. Outstanding candidates with strong training and publication track records are encouraged to apply. Candidates can work in the areas that complement the departmental current research and in areas of metastasis, drug resistance and drug development, pharmacogenomics, and chemical biology. Applicants will be selected based on a track record of research excellence, ability to develop a robust basic or translational cancer research program, and the potential for sustained peer-reviewed funding. The successful candidate will be expected to participate in an NCI T32-supported Ph.D. training program, administrative responsibilities of the department and institute, disease site working groups, and the RPCI Comprehensive Cancer Center core grant (CCSG) programmatic activities. Applications will close by July 31.

RPCI, the nation's first cancer center founded in 1898, has made fundamental contributions to reducing the cancer burden and has successfully maintained a leadership role in setting national standards for cancer care, research, and education. Laboratory space will be located in a modern 300,000 square foot Life Sciences Complex, which includes a new Center for Personalized Medicine with capabilities for state-of-the-art genomic analysis in a CLIA certified laboratory and the NY State Center for Excellence in Bioinformatics. In this multidisciplinary research environment, the successful candidate will have access to numerous additional core facilities, the opportunity to interact with scientists and clinicians from many programs and departments, and the ability to conduct patient-oriented translational research in collaboration with clinicians. The successful candidate will receive a competitive start-up package and salary commensurate with their experience.

Candidates should e-mail their CV, a brief research statement (3-5 pages), and the names of 3 references to: David Goodrich, Ph.D., Chair, Search Committee, c/o Ms. Susan Bechtel, Department of Pharmacology and Therapeutics, Roswell Park Cancer Institute: **Susan.Bechtel@Roswellpark.org**

Roswell Park Cancer Institute is an Affirmative Action/Equal Opportunity Employer.

ROSWELL PARK
CANCER INSTITUTE

ScienceCareers online @sciencecareers.org

10 ways that *Science* Careers can help advance your career

1. Register for a free online account on **ScienceCareers.org**.
2. Search thousands of job postings and find your perfect job.
3. Sign up to receive e-mail alerts about job postings that match your criteria.
4. Upload your resume into our database and connect with employers.
5. Watch one of our many webinars on different career topics such as job searching, networking, and more.
6. Download our career booklets, including Career Basics, Careers Beyond the Bench, and Developing Your Skills.
7. Complete an interactive, personalized career plan at "my IDP."
8. Visit our Career Forum and get advice from career experts and your peers.
9. Research graduate program information and find a program right for you.
10. Read relevant career advice articles from our library of thousands.



Visit **ScienceCareers.org** today — all resources are free

ScienceCareers

FROM THE JOURNAL SCIENCE AAAS

SCIENCECAREERS.ORG

WILL YOUR RESEARCH LEAD TO BETTER LIVES FOR PATIENTS?



Gopinath Sutendra and Evangelos D. Michelakis, "Pulmonary Arterial Hypertension: Challenges in Translational. Research and a Vision for Change", *Sci. Transl. Med.* 5, 208sr5 (2013) Credit: *Science* Source

Science Translational Medicine | AAAS
INTEGRATING SCIENCE, ENGINEERING, AND MEDICINE

Find out more about the scope of the journal and submit your research today. **ScienceTranslationalMedicine.org**

Institut Pasteur

Parasites & Insectes vecteurs

NEW JUNIOR FACULTY RECRUITMENT IN PARASITOLOGY AND INSECT VECTOR BIOLOGY

The Department of Parasites and Insect Vectors (**https://research.pasteur.fr/en/department/parasites-and-insect-vectors**) is selecting outstanding Junior Group Leaders* to postulate for a faculty position at the Institut Pasteur – Paris. All aspects of parasitology and insect vector biology including both laboratory and field based research will be considered and candidates with ambitious and original research projects are strongly encouraged to apply.

A highly attractive package matching the experience of the successful candidate will be provided, including salaries for the successful candidate and scientific staff (technician, post-doctoral fellows), a substantial contribution to laboratory equipment and to annual running costs, as well as support for relocation expenses. In addition, Institut Pasteur provides access to state-of-the-art technology platforms and to laboratories and research infrastructure in disease-endemic regions through the Pasteur International Network.

Potential candidates should communicate directly with the department by sending a letter of intent, brief research statement and CV by **31 August 2016**, addressed to **parasitology@pasteur.fr.** Full applications will be requested from selected candidates in fall 2016, short-listed candidates will be invited for interviews in early 2017 and decisions will be announced by mid 2017.

** Institut Pasteur is an equal opportunity employer. Junior group leaders should be less than 8 years after PhD at the time of submission. Women are eligible up to 11 years after their PhD if they have one child and up to 14 years after their PhD if they have two or more children.*

SCIENCE & DIPLOMACY

A quarterly publication from the AAAS Center for Science Diplomacy

SCIENCE & DIPLOMACY

provides an open access forum for rigorous thought, analysis, and insight to serve stakeholders who develop, implement, or teach all aspects of science and diplomacy. Learn more about the latest ideas in science diplomacy and receive regular updates by following @SciDip on Twitter, liking the quarterly's page on Facebook (www.facebook.com/sciencediplomacy), and registering for free at **www.sciencediplomacy.org/user/register**.



WWW.SCIENCEDIPLOMACY.ORG

AAAS
ADVANCING SCIENCE, SERVING SOCIETY

Science Careers online @sciencecareers.org

By **Sarah Fankhauser**

A winding path to satisfaction

When I speak with my students about their future careers, it is clear that many feel there is only one path to success and that any deviations will be catastrophic. My own academic path might seem to support this belief. On the surface, it appears quite linear: undergrad, grad student, postdoc, faculty member. But if you look deeper, you will see the series of roadblocks and revised plans that led me to where I am today. Using my own experience as an example, I try to convince students not to fear bends in the road. In fact, these deviations often help us develop, both as scientists and as people, and lead us to our true passions.

When I started my undergraduate studies, I had wanted to be a medical doctor for as long as I could remember. I dutifully took my premed prerequisites and fluffed my resume with medical-related activities that were interesting but didn't inspire me. During my second year of college, everything changed. I took a microbiology course and became fascinated with bacteria—and with the way that researchers studied them. I more or less begged the professor to let me join his lab, and I soon became hooked on research life.

As I got close to graduating, I started thinking about how I could make research part of my long-term career. I was terrified by the thought that my many years of methodical planning for a medical degree would be for naught, and I had no idea if I was properly prepared to pursue a Ph.D. But my passion for research trumped my insecurities, so I applied to several schools. I received one stinging rejection—but also a few acceptances. After deliberating for a while, and convincing my parents that changing my career path was not the end of the world, I enrolled in a Ph.D. program.

My road was set again. I would get my degree in 4 years (maybe 5), do a postdoc, and become a professor at a research-intensive university. Everything was falling back into place—or so I thought.

My first 3 years of grad school were rough, to say the least. I enjoyed the science, but I didn't feel I was on the path to becoming a thoughtful, independent researcher. I wondered whether going to grad school had been a mistake, and I found myself again struggling with the possibility of leaving a path in which I had invested significant time and energy. After much soul-searching, I decided to stay in grad school but move to a different lab. I found a fantastic mentor who gave me the freedom to make mistakes, self-correct, and grow as a scientist. And I did get my Ph.D.—in about 6 years, not the 4 or 5 I had initially expected.



"Instead of pursuing the ... track I had initially planned on, I shifted my outlook."

My struggles made me realize the importance of good advisers and teachers, and I found that I wanted to play the role of enthusiastic mentor myself. So, when I finished my degree, instead of pursuing the high-powered research track I had initially planned on, I shifted my outlook once again and applied for college teaching positions. But a dearth of responses stimulated me to pursue a different kind of teaching opportunity: a postdoc position with a microbiologist who is also a dedicated educator. Fortunately, she was willing to take a chance on me and my less-than-stellar publication record and to support my desire to teach, so I readjusted my trajectory once more. I meticulously crafted a 5-year plan that included a research project, a strategy to improve my publication record, and some teaching at the graduate level. I even bought a house nearby.

Then, less than a year into my postdoc, a job announcement caught my eye. It was for a tenure-track position focused on teaching, where I could also pursue research with undergraduates. I wasn't sure I was ready, but I knew I couldn't pass it up. Exactly 1 year after starting my postdoc, I got the job, and I absolutely love it.

Is my story complete? Nowhere near. And as it continues to unfold, I know that I will need to be flexible and remain open to the interesting, unexpected possibilities that arise. ■

Sarah Fankhauser is an assistant professor of biology at Oxford College of Emory University in Georgia. Send your story to SciCareerEditor@aaas.org.

ILLUSTRATION: ROBERT NEUBECKER

Downloaded from http://science.sciencemag.org/ on June 28, 2016

Published by AAAS